Single crystal and polycrystalline niobium and OFE copper for SRF cavities applications : mechanical characterization at low to high strain rates and microstructural investigations

Jean-François Croteau

DOCTORAT BRETAGNE SCIENCES LOIRE POUR L'INGENIEUR

ENSTA Bretagne

THESE DE DOCTORAT DE

L'ECOLE NATIONALE SUPERIEURE
DE TECHNIQUES AVANCEES BRETAGNE

ECOLE DOCTORALE N° 602
Sciences pour l'Ingénieur
Spécialité : *Mécanique des solides, des matériaux, des structures et des surfaces*

Par
Jean-François CROTEAU

Single Crystal and Polycrystalline Niobium and OFE Copper for SRF Cavities Applications: Mechanical Characterization at Low to High Strain Rates and Microstructural Investigations

Thèse présentée et soutenue en visioconférence, le 28 mai 2021
Unité de recherche : Institut de Recherche Dupuy de Lôme – UMR CNRS 6027

Composition du Jury :

Président :	Guillaume Kermouche	Professeur des Universités, École des Mines de Saint-Étienne
Rapporteurs :	Salima Bouvier	Professeur des Universités, Université de Technologie de Compiègne
	Alexis Rusinek	Professeur des Universités, Université de Lorraine
Examinatrice :	Claire Antoine	Directrice de Recherche, CEA/DRF/IRFU
Dir. de thèse :	Nicolas Jacques	Maître de Conférences HDR, ENSTA Bretagne
Co-encadrante de thèse :	Elisa Cantergiani	Ingénieure-docteure, I-Cube Research / Bmax

Invité(s)
Gilles Mazars Ingénieur, I-Cube Research / Bmax

SINGLE CRYSTAL AND POLYCRYSTALLINE NIOBIUM AND OFE COPPER FOR SRF CAVITIES APPLICATIONS: MECHANICAL CHARACTERIZATION AT LOW TO HIGH STRAIN RATES AND MICROSTRUCTURAL INVESTIGATIONS

by

Jean-François Croteau

A thesis submitted to the École Nationale Supérieure de Techniques Avancées Bretagne in partial fulfillment of the degree of

Doctor of Philosophy

in Engineering Science
Specialization: Solid, Material, Structure, and Surface Mechanics

École Nationale Supérieure de Techniques Avancées Bretagne
Brest, France

July 2021

Supervised by

Dr. Elisa Cantergiani: I-Cube Research, Toulouse, France
Associate Professor Nicolas Jacques: École Nationale Supérieure de Techniques Avancées Bretagne, Brest, France
Gilles Mazars: I-Cube Research, Toulouse, France

Abstract

Manufacturing of superconducting radiofrequency (SRF) cavities with high performances is paramount to increase the collision energy in new particle accelerators that will push the limits of fundamental research in particle physics. The use of high-speed sheet forming techniques, such as electro-hydraulic forming, can be beneficial for cavity performances, but requires a detailed understanding of the mechanical properties of the materials being deformed and the consequence on their microstructures. The main objective of this thesis is then to characterize materials to improve different forming techniques and ultimately increase the performances of SRF cavities.

The dissertation is separated in two parts, based on the material studied. Part I focuses on high-purity niobium single crystals and Part II studies polycrystalline niobium and oxygen-free electronic (OFE) copper sheets. In Part I, the effect of strain rate, from 10^{-4} to 10^{3} s^{-1}, on the mechanical properties and on the microstructure of niobium single crystals is studied. In Part II, the forming limit diagrams of polycrystalline OFE copper and high-purity niobium were measured. The effect of strain rate on electron beam welded sheets of the same materials is also presented.

Chapter 1 introduces the motivation behind this study of the mechanical properties and the microstructure of OFE copper and high-purity niobium for sheet forming of SRF cavities for CERN's Future Circular Collider and more. An overview of the role of SRF cavities in a particle accelerator and different SRF cavity manufacturing routes, e.g. different sheet forming processes, seamless SRF cavities, and tube manufacturing, are also presented in this chapter.

The fundamental theories required to perform this study, a survey of relevant literature for single crystalline niobium, forming limit diagrams, and electron beam welds, and the scientific contributions of this study are presented for Parts I and II in Chapters 2 and 6, respectively. Chapters 3 and 7 present the materials characterized in the study and the experimental methodology used for all tests and analyses performed in each part. In Chapter 3, the method used to select niobium single crystal tensile orientations from a large-grain disk is presented. Finally, all experimental equipment used to measure the mechanical properties (e.g. mechanical and servo-hydraulic universal testing machines and split Hopkinson bars) and investigate the microstructure (e.g. scanning and transmission electron microscopes) of the different specimens are presented.

Chapter 4 presents the mechanical properties of niobium single crystals with different crystallographic orientations deformed in tension and compression at strain rates of about 10^{-4} to 10^{3} s^{-1}. A reduction of anisotropic mechanical properties was measured in tension for increasing strain rates. The effect of crystal orientation and strain rates on the resulting microstructures, i.e. crystal orientations and dislocation substructures, are reported in Chapter 5. Tensile specimens deformed at quasi-static strain rates and with an initial crystal orientation with similar Schmid factors for two {112}<111> slip systems with Burgers vectors in different directions showed shear bands in IPF orientation maps, compared to rotated single crystals for other orientations. A reduction in hardness from nanoindentation measurements on specimens previously deformed at high strain rates instead of quasi-static strain rates was measured and likely caused by differences in dislocation substructures. At high strain rates, homogeneously distributed dislocations with a higher dislocation dipole density were observed. At low strain rates, dislocation cells with a high density of long dislocations were observed.

Chapter 8 presents the forming limit diagrams of annealed OFE copper and polycrystalline high-purity niobium, obtained at a quasi-static strain rate of 10^{-3} s^{-1}. A higher formability (higher major strain) was measured for niobium for all linear strain paths between uniaxial tension and equi-biaxial tension.

Chapter 9 presents the mechanical properties of electron beam welded annealed OFE copper and polycrystalline niobium deformed in tension and in compression at strain rates of 10^{-3} to 10^{3} s^{-1}. The effect of strain rate on the mechanical properties and the ductility was negligible for OFE copper, while an increase in yield and ultimate tensile stress was measured for increasing strain rates for niobium and a reduction in nominal strain to failure was measured between strain rates of 2.0×10^{-1} s^{-1} and about 400 s^{-1}.

Résumé

La fabrication de cavités supraconductrices à radiofréquence (SRF) à haute performance est essentielle pour augmenter l'énergie de collision dans de nouveaux accélérateurs de particules qui poussent les limites de la recherche fondamentale en physique des particules. L'utilisation de procédés de fabrication à haute vitesse, telle que l'électro-hydro formage, peut être bénéfique pour la performance des cavités, mais requiert une compréhension détaillée des propriétés mécaniques des matériaux déformés et de l'impact sur leurs microstructures. L'objectif principal de cette thèse est la caractérisation de matériaux pour améliorer différentes techniques de formage pour ultimement augmenter les performances de cavités SRF.

Le manuscrit est séparé en deux parties, basées sur les matériaux étudiés. La partie I se concentre sur les monocristaux de niobium à haute pureté et la partie II étudie les tôles polycristallines de niobium et de cuivre OFE. Dans la partie I, l'effet du taux de déformation, de 10^{-4} à 10^{3} s^{-1}, sur les propriétés mécaniques et la microstructure de monocristaux de niobium est étudié. Dans la partie II, les courbes limites de formage de tôles polycristallines de cuivre OFE et de niobium à haute pureté sont mesurées. L'effet du taux de déformation sur des tôles des mêmes matériaux polycristallins soudées par faisceau d'électrons est aussi présenté dans cette partie.

Le chapitre 1 introduit la motivation de cette étude des propriétés mécaniques et de la microstructure du cuivre OFE et du niobium à haute pureté pour le formage de cavités SRF pour le Future Circular Collider du CERN et d'autres accélérateurs. Une introduction du rôle des cavités SRF dans un accélérateur de particules et différentes méthodes pour fabriquer une cavité SRF, e.g. différents procédés de formage, des cavités sans-soudures dites *seamless* et la fabrication de tubes, sont aussi présentées dans ce chapitre.

Les théories requises pour réaliser cette étude, une revue de la littérature pour les monocristaux de niobium, les courbes limites de formage et les soudures par faisceau d'électrons, et les contributions scientifiques de cette étude sont présentées en parties I et II dans les chapitres 2 et 6, respectivement. Les chapitres 3 et 7 présentent les matériaux caractérisés dans cette étude et les méthodes expérimentales pour les essais et analyses faits dans chaque partie. La méthode utilisée pour sélectionner l'orientation cristalline des monocristaux de niobium déformés en traction est décrite dans le chapitre 3. Finalement, l'équipement utilisé pour mesurer les propriétés mécaniques (e.g. machines d'essai universelles électromécaniques et hydrauliques et des barres de Hopkinson) et observer la

microstructure (e.g. microscope électronique à balayage et à transmission) des différentes éprouvettes est présenté.

Le chapitre 4 présente les propriétés mécaniques de monocristaux de niobium avec différentes orientations cristallographiques déformés en traction et en compression à des taux de déformation d'environ 10^{-4} à 10^{3} s^{-1}. Une réduction d'anisotropie des propriétés mécaniques a été mesurée en traction lors d'augmentation du taux de déformation au régime dynamique. L'effet de l'orientation des cristaux et du taux de déformation sur les microstructures qui en résultent, i.e. l'orientation des cristaux et les sous-structures de dislocations, sont présentés dans le chapitre 5. Une réduction de la dureté, mesurée par nanoindentation, pour les éprouvettes déformées au préalable à de hauts taux de déformation plutôt qu'au régime quasi-statique a été mesurée et probablement causée par différentes sous-structures de dislocations. À hauts taux de déformation, une distribution homogène de dislocations avec une plus haute densité de dipôles a été observée. À bas taux de déformation, des cellules de dislocations avec une haute densité de longues dislocations ont été observées.

Le chapitre 8 présente les courbes limites de formage du cuivre OFE recuit et de tôles polycristallines de niobium à haute-pureté obtenues à un taux de déformation quasi-statique de 10^{-3} s^{-1}. Une formabilité plus élevée (déformation majeure plus élevée) a été mesurée pour le niobium pour tous chemins de déformation linéaires entre la traction uniaxiale et la traction équi-biaxiale.

Le chapitre 9 présente les propriétés mécaniques d'éprouvettes de cuivre OFE recuites et de tôles de niobium polycristallines soudées par faisceau d'électron et déformées en traction et en compression à des taux de déformation de 10^{-3} à 10^{3} s^{-1}. L'effet du taux de déformation sur les propriétés mécaniques et la ductilité était négligeable pour le cuivre OFE. Pour le niobium, une augmentation de la contrainte à l'écoulement et de la résistance à la traction ont été mesurées pour des augmentations du taux de déformation et une réduction de la déformation nominale à la rupture a été mesurée entre des taux de déformation de $2.0x10^{-1}$ s^{-1} et d'environ 400 s^{-1}.

Acknowledgement

The research presented in this thesis could not have been performed without the financial support of the European Commission. This Marie Sklodowska-Curie Action (MSCA) Innovative Training Network (ITN) received funding from the European Union's H2020 Framework Programme under grant agreement no. 764879. I am also equally grateful to the management of I-Cube Research for its financial support, for hosting me in Toulouse for the entire duration of my PhD, and for being understanding of the different challenges I faced.

I am grateful to Dr. Elisa Cantergiani, Professor Nicolas Jacques, and Gilles Mazars for their supervision. This work would not have been possible without your support, help, and the long conversations we had. I sincerely thank you.

Merci aux membres de mon jury de thèse, soit Dr. Claire Antoine, Dr. Salima Bouvier, Dr. Guillaume Kermouche et Dr. Alexis Rusinek, pour vos commentaires qui n'ont qu'amélioré la qualité de ce mémoire.

Thank you to everyone at CERN who directly or indirectly supported this project. A special thanks to Said Atieh for his constant support and his openness to new research ideas. This study would not have been possible without your help. For the EASITrain project, I am thankful to Johannes Gutleber, Émilie, Coralie, and Ani for managing this long and complex project. Thank you to Anité, Elisa, Adrienn, and your entire group for the countless hours spent in front of the SEM, for giving me access to your facilities, and your hospitality during my stays.

I must thank my colleagues and good friends of the Simulation Team and the other departments of I-Cube Research. Thanks to Jon, Maxime, and everybody else for the great time I spent in Toulouse, both in and out of the office. I hope that our friendship will last forever.

Un merci particulier à Marilyne pour m'avoir récupéré à l'aéroport ou chez moi à toute heure de la journée. Ta bonne humeur était toujours appréciée.

I would also like to thank the collaborators from the many labs where I have worked. My time at MSU would not have been the same without the warmth of Dr. Thomas Bieler and his wife. Thank you to Eureka for accepting to work long hours with me and everything else during my month in East Lansing, especially the last-minute drive to the airport after I had a flight change. Thank you again to Dr. Bieler and Dr. Philip Eisenlohr for your attention to

details, patience, and for sharing your knowledge with me and to all your research groups, including Zhuowen, Satya, Aritra, Di, and many more, for your kindness.

Thank you to Chaintanya Kale for the great help and hospitality during my time at ASU and to Dr. Kiran Solanki for accepting to collaborate and for your multiple inputs.

Thank you to Derek Siu of Imperial College for the great tests campaigns we had and for our non-technical discussions. Dr. Daniel Balint, Dr. Paul Hooper, and Dr. Michael Cox are also acknowledged for their support and for accepting to collaborate on this study.

Merci à Guillaume, Marion, Sébastien et tous les membres du LEM3 pour m'avoir très bien accueilli à Metz. Guillaume, ce fut un réel plaisir de travailler à tes côtés et je te remercie de ta constante bonne humeur, ta patience et ta motivation, malgré les longues heures que nous avons travaillées.

Merci à Célia, Aboulghit et tous les membres de l'IRDL avec qui j'ai pu travailler. Je n'étais pas souvent présent au labo, mais toutes mes visites furent très agréables et enrichissantes grâce à vous.

Thank you to Marco for performing all the tensile and compression tests at the JRC on your own due to COVID-19 restrictions. I am really looking forward for this pandemic to end to visit your lab and thank you in person.

Thanks to Leonardo and Anna of BAM for their hard work despite all the waves of restrictions that the pandemic brought to us and, more importantly, for your kind hospitality both in and outside of the lab.

I must thank all my collaborators one last time. I could not have asked for more passionate, knowledgeable, patient, and kind individuals.

I want to thank all my colleagues of the EASITrain project: Aisha, Alice, Andrea, Dmitry, Dorothea, Jakub, Johannes, Linn, Mattia Donato, Mattia Ortino, Maxime, Paola, Sofiya, Stewart, and Vanessa. It was a pleasure to learn with you and from you during our weeks spent together. I will always remember our great moments spent at CERN, in Vienna, Amsterdam, Brussels, Padova, Saclay, Paris (for the morning guys!), and Grenoble. I wish you all the best in your future endeavors and hope that we will stay in touch. A special thanks to Jakub for driving to Arizona for a weekend and for hosting me in your apartment, to Stewart for our thousands of conversations and support during the project, and to Dorothea for your kindness during my stays at CERN and beyond.

Merci à ma mère, Chantal, mon père, Alain, et mes sœurs, Anne-Marie et Émilie, pour votre support durant ces trois dernières années passées à l'étranger et toutes les années précédentes.

Finally, I must thank my wife Audrey for her patience, understanding, support, and a lot more. I would not be where I am today without you.

Contribution of the Author

Due the sheer amount of results obtained and analyzed in the three years of the project and the disruptions created by the SARS-CoV-2 pandemic that placed most of Europe under lockdown in March 2020 and had consequences through the rest of the year, not all experiments were performed by the author. A chapter-by-chapter breakdown of the author and collaborators' contributions for experimental testing, setup design, data collection, and data analysis are presented below. Note that most of the raw material (oxygen-free electronic copper sheets, large-grain niobium disks and polycrystalline niobium sheets) was supplied by the European Organization for Nuclear Research (CERN) and that annealing heat treatments of copper sheets were performed at CERN.

Part I – Niobium Single Crystals

Chapter 4: Mechanical Properties of Niobium Single Crystals

Dr. Di Kang of Michigan State University (MSU) measured the crystal orientation of 10 large grains in two niobium disks at MSU using a Laue X-ray diffraction method. The author and Eureka Pai Kulyadi (MSU) analyzed the orientation data to determine the test matrix and performed quasi-static tensile and compression tests at MSU. The author and Dr. Chaitanya Kale of Arizona State University (ASU) performed compression and tensile split Hopkinson bar tests at ASU. Dr. Chaitanya Kale analyzed the raw split Hopkinson bar data. The author analyzed all quasi-static data obtained at MSU and the stress–strain curves obtained from split Hopkinson bar tests at ASU.

The author and Derek Siu of Imperial College London (ICL) performed the intermediate strain rate tensile tests at ICL. The author analyzed the raw data obtained at ICL, including digital image correlation, stress–strain curves, and in-situ thermal measurements.

Chapter 5: Microstructural Investigations of Deformed Niobium Single Crystals

The author prepared the niobium specimens for electron backscatter diffraction (EBSD) and nanoindentation analyses. Ana Teresa Perez Fontenla and Dr. Elisa García-Tabarés Valdivieso (CERN) performed the EBSD scans and the fracture surface imaging. The author analyzed the data from the EBSD scans (orientation, LAM, misorientation). Dr. Adrienn Baris (CERN) prepared a scanning transmission electron microscopy (STEM) lamella with a focused ion beam (FIB) and acquired the dark and bright field images. Dr. Leonardo Agudo Jácome of the Federal Institute for Materials Research and Testing (BAM) in Berlin prepared and analyzed the transmission electron microscopy (TEM) specimens. Dr. Anna Manzoni (BAM) also helped for the TEM analysis. Dr. Célia Caër of the École Nationale Supérieure

de Techniques Avancées (ENSTA) Bretagne performed the nanoindentation tests. The author was present during all or most of the EBSD, FIB and STEM, TEM, and nanoindentation analyses performed in different laboratories to select the regions of interest.

Part II – Polycrystalline Niobium and OFE Copper

Chapter 8: Forming Limits of OFE Copper and Polycrystalline High-Purity Niobium

The author and Dr. Guillaume Robin of the Université de Lorraine performed the Marciniak formability tests on annealed OFE copper at the Laboratoire d'Étude des Microstructures et de Mécanique des Matériaux (LEM3). Dr. Guillaume Robin performed the Marciniak formability tests, tensile tests, and plane strain tests on polycrystalline niobium. The author analyzed the raw data with digital image correlation and determined the forming limit diagram of both materials.

Chapter 9: Mechanical Properties of Electron Beam Welded OFE Copper and Niobium

The author and Dr. Elisa Cantergiani (I-Cube Research) prepared the research proposal to access the European Commission Joint Research Centre's (JRC) testing facility. Manuel Redondas Monteserin (CERN) performed the electron beam welds on the OFE copper and polycrystalline niobium specimens. Dr. Marco Peroni (JRC) developed the tensile split Hopkinson fixtures, performed the tensile and compression tests at the JRC, and extracted stress–strain curves from the raw data using MATLAB post-processing codes he developed. The niobium weld was polished, etched, and imaged at the Max-Planck-Institut für Eisenforschung (MPIE). The author analyzed the images acquired for digital image correlation, the corrected stress–strain curves, the microstructure of a copper weld, and performed microhardness measurements on niobium and copper welds.

Book of Appendices

Appendix E: Mechanical Characterization of OFE Copper

The author performed compression split Hopkinson bar tests on annealed OFE copper and quasi-static tensile tests on hard and annealed OFE copper at the Institut de Recherche Dupuy de Lôme (IRDL) of the ENSTA Bretagne under the supervision of faculty members. Dr. Nicolas Jacques and Dr. Aboulghit El Malki (IRDL/ENSTA Bretagne) performed compression tests at quasi-static strain rates on annealed and hard OFE copper and compression split Hopkinson bar tests on hard OFE copper at ENSTA Bretagne.

Derek Siu (ICL) designed the lost motion and grip device for tensile tests in a servo-hydraulic machine. The author and Derek Siu performed the tensile tests on annealed and hard OFE copper at ICL. Derek Siu designed the data acquisition system of the high speed

and thermal cameras. The author analyzed the raw data obtained at ICL, including digital image correlation, stress–strain curves, and in-situ thermal measurements.

All additional analyses were performed by the author.

Scientific Contributions

To the best knowledge of the author, the following contributions have been made to the current scientific knowledge.

The mechanical properties of niobium single crystals, presented in Chapter 3, were unknown in tension for strain rates higher than 10^{-1} s^{-1}. Consequently, all analyses of the resulting microstructure and dislocation substructures are also firsts. The use of high-speed sheet forming for the fabrication of superconducting radiofrequency cavities from large-grain niobium disks will benefit from this knowledge. As a future work and a new scientific contribution, the influence of the dislocation substructure in specimens deformed at a high strain rate of about 10^{3} s^{-1} on the superconducting properties of niobium should be studied on the specimens that were used by the author. These specimens were analyzed with transmission electron microscopy and homogeneously distributed short dislocation segments and loops were observed, compared with cell walls in specimens deformed at quasi-static strain rates.

The quasi-static forming limit curve of high-purity polycrystalline niobium is the first public record since 1986 [1] and is believed to be more complete and accurate than the previous FLC. These experimental data are expected to help manufacturers of SRF cavities by better predicting the formability of high-purity niobium sheets.

The mechanical properties in tension and compression of electron beam welded OFE copper and polycrystalline niobium sheets were unknown at strain rates greater to approximately 10^{-3} s^{-1} and have now been measured at up to 10^{3} s^{-1}. These results should provide valuable information to the SRF community for the fabrication of seamless cavities and other complex components where welded sheets and tubes are used as starting material.

Table of Contents

List of Figures

List of Tables

Nomenclature

To avoid confusion with readers from different countries, please note the following convention. Based on the ISO 80000-1:2009 standard [2], a *thin space* is used as Thousands separator instead of a comma, the commonly symbol in English. For example, one thousand will be written as 1 000.

Below are lists of symbols and constants used in this thesis with corresponding SI units and descriptions, and acronyms.

List of Symbols

Symbol	Unit	Description
a_0	[m]	Lattice constant
b	[m]	Burgers vector amplitude
$\underline{b}$	[m]	Burgers vector
$\underline{b}_1$	[m]	Burgers vector of the slip system with the highest Schmid factor
$\underline{b}_2$	[m]	Burgers vector of the slip system with the second highest Schmid factor
$\hat{b}$	[m]	Burgers unit vector
c_b	$\left[\frac{\mathrm{m}}{\mathrm{s}}\right]$	Speed of sound in a split Hopkinson bar
f_{gage}	$[\mathrm{V}^{-1}]$	Strain gage factor
$\underline{\underline{g}}$	$[-]$	Orientation matrix
h_{ijk}	[m]	Kink height of the $\{ijk\}$ slip plane
$k_{effective}$	$\left[\frac{\mathrm{N}}{\mathrm{m}}\right]$	Effective stiffness coefficient of a specimen and machine
$k_{machine}$	$\left[\frac{\mathrm{N}}{\mathrm{m}}\right]$	Stiffness coefficient of a machine
$k_{specimen}$	$\left[\frac{\mathrm{N}}{\mathrm{m}}\right]$	Stiffness coefficient of a specimen
m	$[-]$	Strain rate sensitivity exponent
m_m	$[-]$	Mean strain rate hardening exponent
n	$[-]$	Strain hardening exponent
n_m	$[-]$	Mean strain hardening rate
$\underline{n}$	[m]	Slip plane normal vector

$\underline{n_1}$	$[-]$	Slip plane normal vector of the slip system with the highest Schmid factor
$\underline{n_2}$	$[-]$	Slip plane normal vector of the slip system with the second highest Schmid factor
$\hat{n}$	[m]	Slip plane normal unit vector
r_m	$[-]$	Mean plastic strain anisotropy
r_m^{ε}	$[-]$	Mean plastic strain anisotropy at a true strain of ε
r_θ^{ε}	$[-]$	Plastic strain anisotropy in the θ rolling direction and a true strain of ε
$\underline{r}$	[m]	Rotation normal vector
t_{pulse}	[s]	Pulse duration in split Hopkinson bar
v_d	$\left[\frac{\mathrm{m}}{\mathrm{s}}\right]$	Mean dislocation velocity
v_i	$\left[\frac{\mathrm{m}}{\mathrm{s}}\right]$	Velocity of split Hopkinson input bar
v_o	$\left[\frac{\mathrm{m}}{\mathrm{s}}\right]$	Velocity of split Hopkinson output bar
v^*	$[b^3]$	Activation volume, normalized in cubic Burgers vector
w	[m]	Width of kink loop
w_0	[m]	Initial width of a tensile specimen
w_f	[m]	Final width of the gage section of a tensile specimen
A	$[\mathrm{m}^2]$	Cross-sectional area of a specimen
A_b	$[\mathrm{m}^2]$	Cross-sectional area of split Hopkinson bar
A_s	$[\mathrm{m}^2]$	Cross-sectional area of split Hopkinson bar specimen
B	[Pa. s]	Dislocation viscosity coefficient
E	[Pa]	Elastic modulus
E_{acc}	$\left[\frac{\mathrm{MV}}{\mathrm{m}}\right]$	Accelerating gradient
E_b	[Pa]	Elastic modulus of split Hopkinson bar
F	[N]	Applied load
F_1	[N]	Front load of split Hopkinson input bar
F_2	[N]	Back load of split Hopkinson output bar
$\underline{F}$	[N]	Applied load vector
G	[J]	Gibbs free energy
L	[m]	Dislocation segment length

L_0	[m]	Initial gage length of a tensile specimen
L_b	[m]	Length of split Hopkinson striker bar
L_f	[m]	Final gage length of a tensile specimen
L_s	[m]	Initial length of split Hopkinson bar specimen
L_{tot}	[m]	Initial total length of a tensile specimen
Q_0	$[-]$	Quality factor
$\underline{\underline{R}}$	$[-]$	Rotation matrix
SF	$[-]$	Schmid factor
SF_1	$[-]$	Schmid factor of the slip system with the highest Schmid factor
SF_2	$[-]$	Schmid factor of the slip system with the second highest Schmid factor
T	[K]	Temperature
T_0	[K]	Reference temperature
T_c	[K]	Critical superconducting temperature
T_D	[K]	Debye temperature
T_m	[K]	Melting temperature
U_k	$[J]$	Kink nucleation energy
U_n	$[J]$	Kink pair nucleation energy
V_{bar}	[V]	Voltage of strain gage on a split Hopkinson bar
(x, y, z)	[m]	Specimen or crystal coordinate system
(X, Y, Z)	[m]	Sheet or disk coordinate system
α	[m]	Distance between Peierls valleys
α	$[-]$	Projection angle on the $[101]$–$[111]$ boundary of an IPF
$\dot{\gamma}$	$[s^{-1}]$	Shear strain rate
ε_1	$[-]$	Major strain
ε_2	$[-]$	Minor strain
ε_{bar}	$[-]$	Strain measured from a strain gage in a split Hopkinson bar
ε_f	$[-]$	Nominal strain to failure
ε_i	$[-]$	Incident wave in split Hopkinson test
ε_r	$[-]$	Reflected wave in split Hopkinson test
ε_t	$[-]$	Transmitted wave in split Hopkinson test
$\dot{\varepsilon}$	$[s^{-1}]$	Strain rate

$\dot{\varepsilon}_0$	$[\mathrm{s}^{-1}]$	Reference strain rate
$\dot{\varepsilon}_{eng}$	$[\mathrm{s}^{-1}]$	Engineering strain rate
θ	$[-]$	Projection angle on the $[001]$–$[111]$ boundary of an IPF
λ	$[-]$	Angle between the loading and slip directions
ν	$[\mathrm{s}^{-1}]$	Debye frequency
ϕ	$[-]$	Angle between the loading direction and slip plane normal
ϕ_1	$[-]$	First Bunger Euler angle
$\phi_{1_{rotation}}$	$[-]$	Counter-clockwise specimen Bunge Euler angle rotation
$\phi_{1_{measured}}$	$[-]$	Measured first Bunge Euler angle
$\phi_{1_{desired}}$	$[-]$	Desired first Bunge Euler angle for a specimen
ϕ_2	$[-]$	Third Bunger Euler angle
ρ	$[\mathrm{m}^{-2}]$	Mobile dislocation density
ρ_b	$\left[\frac{\mathrm{kg}}{\mathrm{m}^3}\right]$	Mass density of split Hopkinson bar
σ_{eng}	[Pa]	Engineering stress
σ_y	[Pa]	Yield stress
σ_A	[Pa]	Athermal stress component
σ_P	[Pa]	Peierls stress at 0 K
σ_T	[Pa]	True stress
σ_{UTS}	[Pa]	Ultimate tensile strength
σ^*	[Pa]	Thermally activated stress component
$\underline{\underline{\sigma}}_{crystal}$	[Pa]	2nd order stress tensor of a crystal
$\underline{\underline{\sigma}}_{disk}$	[Pa]	2nd order stress tensor of a disk or sheet
τ	[Pa]	Shear stress
τ_0	[Pa]	Reference shear stress
τ_{CRSS}	[Pa]	Critical resolved shear stress
τ_{RSS}	[Pa]	Resolved shear stress
χ	$[-]$	Angle between the $[\bar{1}01]$–$[111]$ plane and the MRSS plane
Δr^{ε}	$[-]$	Planar anisotropy at a true strain of ε
Δt	[s]	Change in time
$\Delta y_{crosshead}$	[m]	Vertical displacement of a machine's crosshead
$\Delta y_{specimen}$	[m]	Vertical displacement of a specimen

Δy_{DIC}	[m]	Specimen elongation at failure from DIC
ΔL	[m]	Change in gage length
Φ	$[-]$	Second Bunger Euler angle
$\emptyset_b$	[m]	Split Hopkinson bar diameter

List of Constants

Symbol	Unit	Value	Description
k_B	$\left[\frac{\mathrm{m^2 kg}}{\mathrm{s^2 K}}\right]$	1.38065×10^{-23}	Boltzmann constant
h	[J. s]	6.626×10^{-34}	Planck constant

List of Acronyms

Acronym	Description
ASTM	American Society for Testing and Materials
ASU	Arizona State University
BAM	Bundesanstalt für Materialforschung und -prüfung
BCC	Body-centered cubic
BCP	Buffered chemical polishing
BF	Bright field
CBED	Convergent-beam electron diffraction
CCD	Charged-couple device
CMOS	Complementary metal–oxide–semiconductor
CEA	Commissariat à l'énergie atomique et aux énergies alternatives
CERN	European Organization for Nuclear Research
CTEM	Conventional transmission electron microscope/microscopy
CSV	Comma separated value
D	Dynamic
DESY	Deutsches Elektronen-Synchrotron
DF	Dark field
DIC	Digital image correlation
EASITrain	European Advanced Superconductivity Innovation and Training
EB	Electron beam
EBSD	Electron backscattered diffraction

ECAE	Equal channel angular extrusion
ECCI	Electron channeling contrast imaging
EDM	Electrical-discharge machine
EDS	Energy dispersive X-ray spectroscopy
EHF	Electro-hydraulic forming
ENSTA	École Nationale Supérieure de Techniques Avancées
EP	Electropolishing
FCC	Future Circular Collider
FCC	Face-centered cubic
FE	Finite element
FIB	Focused ion beam
FLC	Forming limit curve
FLD	Forming limit diagram
GND	Geometrically necessary dislocation
HAZ	Heat affected zone
HCP	Hexagonal close-packed
HopLab	Hopkinson bar laboratory
HPP	High-pulsed power
HV	Hardness Vickers
ICL	Imperial College London
IHEP	Institute of High Energy Physics
ILC	International Linear Collider
INFN	Istituto Nazionale di Fisica Nucleare
IPF	Inverse pole figure
IRDL	Institut de Recherche Dupuy de Lome
ISO	International Organization for Standardization
ITN	Innovation Training Network
JLab	Jefferson Laboratory
JRC	Joint Research Centre
KEK	Japan’s High Energy Accelerator Research Organization
LAGB	Low angle grain boundary
LAM	Local average misorientation

LED	Light emitting diode
LEM3	Laboratoire d'Étude des Microstructures et de Mécanique des Matériaux
LHC	Large Hadron Collider
LNL	Legnaro National Laboratory
MSCA	Marie Skłodowska-Curie action
MRSS	Maximum resolved shear stress
MSU	Michigan State University
NADDRG	North American Deep Drawing Research Group
OFE	Oxygen-free electronic
OFHC	Oxygen-free high conductivity
PE	Polyethylene
PKU	Peking University
PTFE	Polytetrafluoroethylene (Teflon^{TM})
PVC	Polyvinyl chloride
QS	Quasi-static
RRR	Residual resistivity ratio
SAD	Selected-area diffraction
SEM	Scanning electron microscope/microscopy
SHPB	Split Hopkinson pressure bar
SHTB	Split Hopkinson tensile bar
SRF	Superconducting radiofrequency
STEM	Scanning transmission electron microscope/microscopy
T/AT	Twinning/Anti-twinning
T/C	Tension/Compression
TEM	Transmission electron microscope/microscopy
TU	Technische Universität
UTS	Ultimate tensile strength
XRD	X-ray diffraction
YS	Yield strength

Foreword

The results obtained in this study have partially been published in Open Access journal articles or presented at conferences. Below is a list of journal articles that have been published or are currently under review and conferences where the author presented relevant results or contributed to the results. Since all articles emerging from this study are Open Access with a Creative Commons license, in compliance with the rules of European Commission's H2020 projects, the content of these articles can be and has been reproduced in this thesis.

Journal articles – Published

1. **J.-F. Croteau**, E. Pai Kulyadi, C. Kale, D. Siu, D. Kang, A. T. Perez Fontenla, E. García-Tabarés Valdivieso, T.R. Bieler, P. Eisenlohr, K.N. Solanki, D. Balint, P.A. Hooper, S. Atieh, N. Jacques, E. Cantergiani, "Effect of strain rate on tensile mechanical properties of high-purity niobium single crystals for SRF applications," *Materials Science and Engineering: A*, p. 140258, Sep. 2020, doi: 10.1016/j.msea.2020.140258.
2. **J.-F. Croteau**, M. Peroni, S. Atieh, N. Jacques, E. Cantergiani, "Effect of strain rate on the tensile mechanical properties of electron beam welded OFE copper and high-purity niobium for SRF applications", *Journal of Dynamic Behavior of Materials*, accepted Jan. 2021, doi: 10-1007/s40870-021-00293-9

Journal articles – Under review

3. **J.-F. Croteau**, G. Robin, E. Cantergiani, S. Atieh, N. Jacques, G. Mazars, M. Martiny, "Characterization of the formability of high-purity polycrystalline niobium sheets for SRF applications", *Journal of Engineering Materials and Technology*, submitted Feb. 2021

Conference talks (*: presenter)

1. **J.-F. Croteau***, E. Pai Kulyadi, L. Agudo Jácome, C. Kale, E. García-Tabarés Valdivieso, A. T. Perez Fontenla, D. Siu, D. Kang, P. Eisenlohr, T. R. Bieler, K. N. Solanki, A. M. Manzoni, S. Atieh, D. Balint, P. Hooper, N. Jacques, E. Cantergiani, "Electro-Hydraulic Forming of SRF Cavities: Effect of Strain Rate on Niobium Single Crystals", *Oral presentation: FCC Week 2021*, Online, June 2021
2. **J.-F. Croteau***, E. Pai Kulyadi, C. Kale, D. Siu, D. Kang, A.T. Perez Fontenla, E. García-Tabarés Valdivieso, T.R. Bieler, P. Eisenlohr, K.N. Solanki, D. Balint,

P.A. Hooper, S. Atieh, N. Jacques, G. Mazars, E. Cantergiani, "Effect of Strain Rate on the Anisotropic Tensile Mechanical Properties of High Purity Niobium Single Crystals", *Oral presentation: TMS 2020,* San Diego, CA, USA, Feb. 2020

3. E. Pai Kulyadi*, **J.-F. Croteau**, P. Eisenlohr, C. Kale, K.N. Solanki, T.R. Bieler, D. Kang, E. Cantergiani, "Mechanical Properties of Single Crystal Niobium from Uniaxial Deformation Experiments and Crystal Plasticity Modeling", *Oral presentation: MS&T 2019*, Seattle, WA, USA, Oct. 2019
4. **J.-F. Croteau***, E. Cantergiani, D. Siu, N. Jacques, A. El Malki, G. Mazars, P. Hooper, G. Avrillaud, D. Balint, "Mechanical Characterization of OFE-Cu at Low and High Strain Rates for SRF Cavity Fabrication by Electro-Hydraulic Forming", *Oral presentation: Congrès Français de mécanique (CFM) 2019*, Brest, France, Aug. 2019
5. E. Cantergiani, G. Avrillaud, C. Abajo Clemente, S. Atieh, **J.-F., Croteau***, "Surface Quality and Improvements on the SRF Cavity Manufacturing by Electrohydraulic Forming", *Oral presentation: 8th International workshop on thin films and new ideas for pushing the limits of RF superconductivity*, Legnaro, Italy, Oct. 2018
6. **J.-F. Croteau***. "Designing future particle colliders: Accelerating particles and innovation - Superconducting Radio Frequency Cavity Fabrication by Electrohydraulic Forming", *Oral presentation and panelist: European Science Open Forum (ESOF) 2018*, Toulouse, France, Jul. 2018
7. **J.-F. Croteau***, "High Velocity Forming of Superconducting Structures with Bulk Nb and Cu Substrate", *Oral presentation: FCC Week 2018*, Amsterdam, Netherlands, Apr. 2018

Poster sessions (*: presenter)

1. **J.-F. Croteau***, E. Pai Kulyadi, L. Agudo Jácome, C. Kale, E. García-Tabarés Valdivieso, A. T. Perez Fontenla, D. Siu, D. Kang, P. Eisenlohr, T. R. Bieler, K. Solanki, A. M. Manzoni, S. Atieh, D. Balint, P. Hooper, N. Jacques, E. Cantergiani, "Effect of Strain Rate on the Mechanical Properties and the Dislocation Substructure of Niobium Single Crystals", *Poster: SRF 2021*, East Lansing, USA, June 2021
2. **J.-F. Croteau***, E. Pai Kulyadi, C. Kale, T.R. Bieler, P. Eisenlohr, K.N. Solanki, D. Kang, E. Cantergiani, N. Jacques, S. Atieh, "Mechanical Characterization of Large Grain Niobium Sheets for High-Velocity Forming of SRF Cavities", *Poster: FCC Week 2019*, Brussels, Belgium, Jul. 2019
3. **J.-F. Croteau***, E. Cantergiani, C. Abajo Clemente, N. Jacques, A. El Malki Alaoui, G. Avrillaud, S. Atieh, "Mechanical Characterization of OFE-Cu for SRF Cavity

Fabrication by Electrohydraulic Forming", *Poster: International Conference on the Strength of Materials (ICSMA) 18*, Columbus, OH, USA, Jul. 2018

Marie Curie project meetings (*: presenter)

1. **J.-F. Croteau***, "EASITrain Mid-Term Review", *Oral presentation: EASITrain Marie Curie fellow mid-term review meeting*, Brussels, Belgium, Dec. 2018

A picture is worth a thousand words – Fred R. Barnard

Chapter 1 Introduction

The fabrication of particle accelerators with higher collision energy is paramount for the fundamental understanding of particle physics and the origin of the universe, the development of more powerful synchrotrons and accelerator-driven subcritical reactors, and more. The reliable manufacturing of superconducting radiofrequency (SRF) cavities with higher accelerating gradients is a first step in that direction. The main objective of the thesis is to characterize materials to improve different forming techniques and ultimately increase the performances of SRF cavities. Compared with previous studies, a particular interest is given to the effect of strain rate, from quasi-static (10^{-4} s^{-1}) to dynamic (10^{3} s^{-1}), on the mechanical properties and resulting microstructures. The two materials of interest are oxygen-free electronics (OFE) copper and high-purity niobium. More precisely, for niobium, the mechanical properties are studied for single crystals and electron beam welded polycrystalline sheets and the formability is studied for polycrystalline sheets.

The motivation to study the dynamic properties of those materials arises from recent promising results from high-speed forming of SRF cavities with electro-hydraulic forming (EHF) compared with traditional sheet forming using deep-drawing or spinning [3], [4]. During EHF, the blank deforms at low strain rates when EHF is preceded by a hydrostatic hydroforming step and at high strain rates of up to 10^{4} s^{-1} in confined regions of the blank or upon impact with the die [3]. The range of strain rates during the forming process and the high deformation required to form a cavity motivate the following characterization study.

The different length scales studied, from the activation of slip systems in niobium single crystals to the determination of a forming limit diagram, an engineering tool used to predict sheet formability, are all intended to support the SRF community for future particle accelerator projects such as the European Organization for Nuclear Research's (CERN) Future Circular Collider (FCC). Figure 1.1 shows a simplified schematic of the SRF cavity fabrication starting with a sheet or a tube. The main contributions of this study are grouped in three categories: (1) the mechanical properties at low and high strain rates, (2) the forming limit at low strain rate, and (3) the mechanical properties of electron beam (EB) welds at low and high strain rates. The mechanical properties of niobium single crystals and OFE copper are presented in different chapters due to the high amount of characterization work performed for the former material. The thesis is also separated in two parts to clearly distinguish between results for single niobium crystals and polycrystalline OFE copper and niobium sheets.

The following sections introduce the European project in which this PhD was performed, particle accelerators and SRF cavities, sheet forming processes to manufacture SRF cavities, tube fabrication for seamless cavity manufacturing, and a breakdown of the structure of this dissertation.

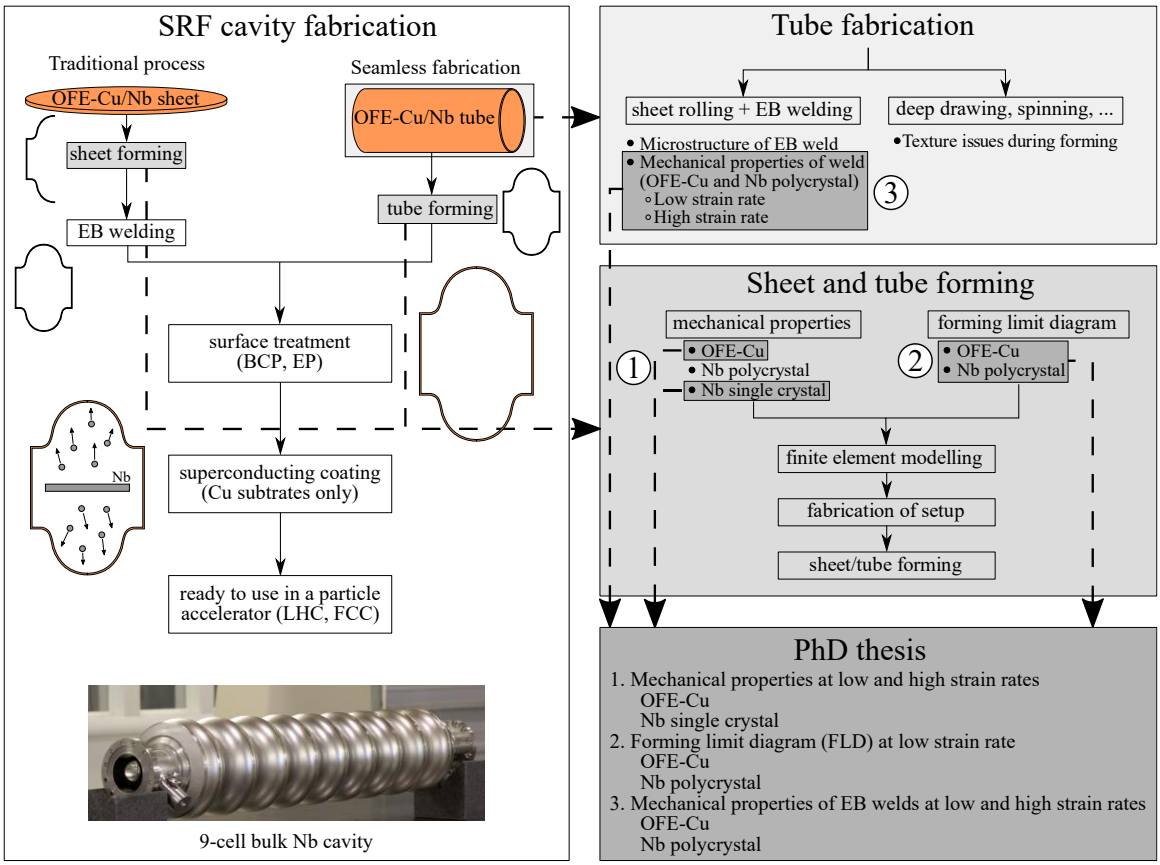

Figure 1.1: Simplified schematic of the fabrication of SRF cavities and the contribution of the different characterization works conducted during the doctoral study.

1.1. Future Circular Collider and EASITrain Program

This PhD study was performed at a private company based in Toulouse, France, called I-Cube Research and was sponsored by a Marie Skłodowska-Curie action (MSCA) Innovation Training Network (ITN) program called European Advanced Superconductivity Innovation and Training (EASITrain). The EASITrain program (grant agreement no. 764879) is composed of 15 early stage researchers, the majority of whom are PhD students, working in universities (Technische Universität (TU) Dresden, TU Wien, Universität Siegen, Universität Stuttgart, Vienna University of Economics and Business), research institutes (Commissariat à l'énergie atomique et aux énergies alternatives (CEA), CERN, Consiglio Nazionale delle Ricerche (CNR) SPIN, Istituto Nazionale di Fisica Nucleare (INFN) Legnaro National Laboratory (LNL)) or private companies (ASG Superconductors, Bruker, I-Cube Research) across Europe, see Figure 1.2 for the locations where the beneficiaries are based.

The main objectives of the EASITrain program are to study and improve the performances of different superconducting particle accelerator components, e.g. SRF cavities, cryogenics, and superconducting cables, for CERN's Future Circular Collider. Technological improvements are required in the next decades to reach the FCC's target collision energies. The FCC is a proposed 100 km-long circular particle accelerator that will operate first as a lepton (electron–positron) collider and later as a hadron (proton–proton) collider [5], [6]. The increase in collision energy from 13 TeV in the current Large Hadron Collider (LHC) that provided the first detection of the Higgs boson in 2012 [7] to 100 TeV makes it a compelling device for new fundamental particle physics research.

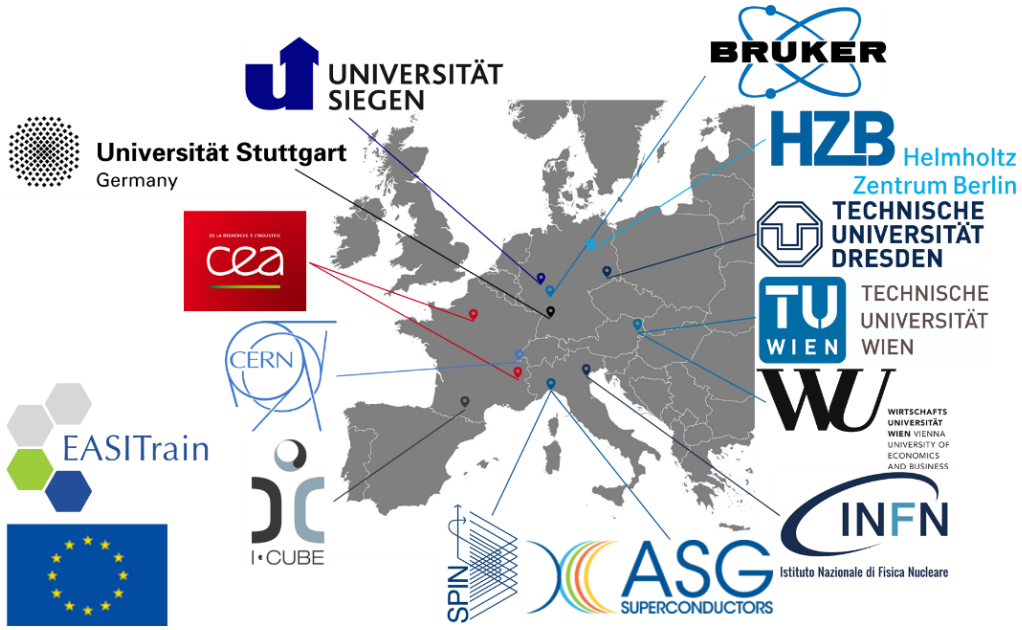

Figure 1.2: Location of the beneficiaries (universities, national laboratories, and companies) of the EASITrain program.

I-Cube Research's role in the EASITrain program was to investigate high-velocity forming of SRF cavities made of niobium or copper. This investigation is accomplished with the study of mechanical properties and formability of cavity substrate materials.

In addition to collaborating with members of the EASITrain program, testing and characterization was conducted at different universities and research institutes to benefit from the expertise of different research groups. For the characterization of niobium single crystals, a large collaboration with CERN, Michigan State University (MSU), Arizona State University (ASU), Imperial College London (ICL), the Bundesanstalt für Materialforschung und -prüfung (BAM) in Berlin, and the Institut de Recherche Dupuy de Lome (IRDL) of the École Nationale Supérieure de Techniques Avancées (ENSTA) Bretagne was initiated. The formability tests were performed at the Laboratoire d'Étude des Microstructures et de Mécanique des Matériaux (LEM3) of the Université de Lorraine and the tests on EB welded

specimens were conducted at the European Commission Joint Research Centre (JRC) in Ispra. Finally, multiple additional tests and analyses were performed at IRDL/ENSTA Bretagne.

1.2. Particle Accelerator and SRF Cavities

Particle accelerators are used in a variety of applications, the main industries being medical (hadron therapy and the production of radioactive isotopes), semi-conductors (ion implantation), and fundamental physic research [8]–[10]. The nature (electron, proton, ions) and energy (keV to TeV) of the charged particles vary for the different applications. Superconducting accelerators, like CERN's Large Hadron Collider, can operate at high proton beam energies of up to 6.5 TeV due to the near absence of electrical resistivity in the magnets, cavities, and cables delivering electrical power.

The role of superconducting radiofrequency cavities in particle accelerators is to accelerate the beam of hadrons (protons) or leptons (electrons and positrons). An overview of the SRF field is available in the following textbooks [11], [12]. The cavities are designed to operate at a specific frequency that represents its fundamental mode, which is geometrically dependent. For example, a 400 MHz cavity used in the LHC has inner diameters of 300.0 and 688.0 mm at the iris and the equator, respectively, (see Figure 1.4 for SRF cavity nomenclature) compared with 20.0 mm and 45.5 mm for a much smaller 6 GHz cavity used at the Legnaro National Laboratories of the Italian National Institute for Nuclear Physics (INFN LNL). High shape accuracy during forming, assembling, and tuning is paramount for the cavity to operate at the desired frequency. The design frequency is chosen based on the targeted beam energy, equivalent to the velocity of the particle bunch. The acceleration of charged particles is explained by the inversion of polarity at a cavity's iris, due to an alternating current at the resonance frequency of the cavity, that is attracting and repelling each particle bunch at accelerating gradients of up to 45 MV/m [13]. Figure 1.3 shows a schematic of the acceleration of protons in an 8-cell 400 MHz resonator used in the LHC. Finally, the type of particles being accelerated influences the required accelerating energy. For example, in the FCC-ee, a 100 km-long circular lepton collider, the energy losses from synchrotron radiation, compared with the FCC-hh (hadron collider), are overcome by the addition of more SRF cavities [5], [6].

1.2.1. SRF Cavities and Material

SRF cavities are structural and functional parts. First, they act as pressure vessels due to the high vacuum required for the charged particles to travel without impacting undesired atoms or molecules. The cavities are also subject to stresses from thermal gradients and are contracted during cooldown of the accelerator from ambient temperature to as low as

1.9 K. Figure 1.4a shows a schematic of a single-cell SRF cavity. Second, they must operate in a superconducting state and avoid quenches, sudden losses of superconductivity caused by localized heating. Therefore, the material used to fabricate SRF cavities must have sufficient structural rigidity, have a high thermal conductivity to maximize heat transfer between the heat generated by the high magnetic field on the inner (RF) surface and the liquid helium on the outer surface, and be superconductive at the operating temperature, electric current, and magnetic field. For those reasons, current state of the art SRF cavities are made of bulk niobium or high conductivity copper coated on the inner surface with niobium. Figure 1.4b shows a 9-cell 1.3 GHz bulk niobium resonator.

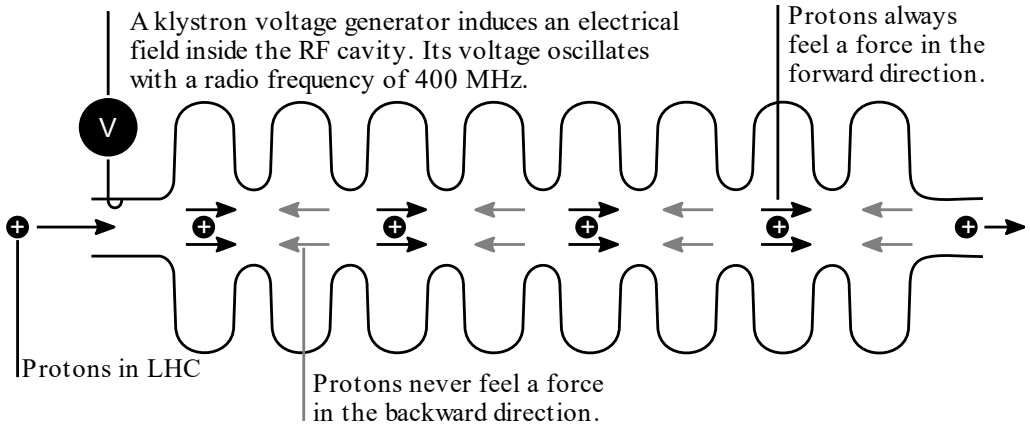

Figure 1.3: Schematic of protons accelerated in a 5 MV/m field by a 400 MHz 8-cell resonator in the LHC. Redrawn from [14].

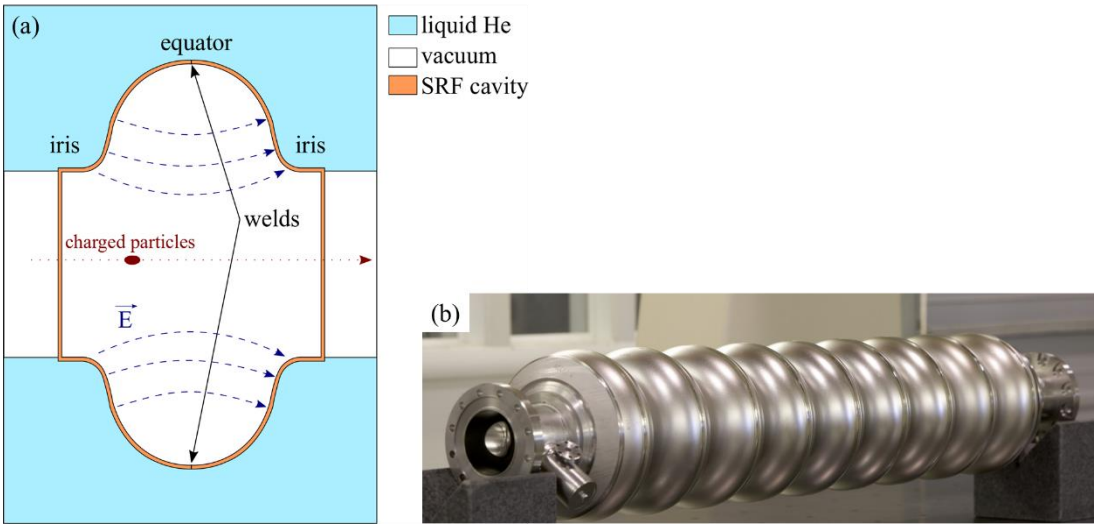

Figure 1.4: (a) Schematic of the cross-section of an SRF cavity with important elements and (b) a 9-cell 1.3 GHz bulk niobium resonator [19].

Niobium is used because it is the element with the highest superconducting critical temperature (T_c) at 9.2 K, in the absence of a magnetic field and current, and has a high formability. The development of coatings with superconducting materials with higher critical temperature, such as Nb_3Sn or MgB_2, is still being studied [15]. Nb_3Sn is a potential

candidate (T_c of ~18 K), but is challenging to produce since the A15 superconducting phase must be obtained and this superconducting phase has a low thermal conductivity and is brittle, often resulting in cracks during thermal contraction of the cavity or during heat treatment [16]–[18].

Since the purpose of this thesis is to characterize the substrate materials, the nature of the superconducting coating will not be further discussed. Focus will be on bulk niobium with fine (tens of micrometers) and large (few centimeters) grains and fine-grain oxygen-free electronic copper. The following distinction is made between the niobium with fine and large grains: a niobium *sheet* has been rolled and has fine grains, while a niobium *disk* was simply cut from an ingot and has large grains.

1.2.2. Large Grain SRF Cavities

The interest in large-grain niobium disks to manufacture SRF cavities arose more than 10 years ago due to the lower cost to obtain a disk ready for forming [20]. Large-grain disks are produced by slicing one or multiple, providing mass production capabilities, disks simultaneously from a long cylindrical ingot purified by electron beam melting. Figure 1.5a shows five large-grain disks from Tokyo Denkai [21]. Fine-grain sheets, however, require forging, grinding, rolling, polishing, cutting, and more steps after cutting a slice from the high-purity ingot [21]–[23]. This results in expensive sheets (~800 €/kg [24]) and becomes a significant cost for future large circular and linear accelerator projects with up to 153 000 and 2 400 cells with frequencies of 1.3 GHz and 800 MHz for the International Linear Collider (ILC) and the Future Circular Collider, respectively [5], [25]. The number of processing steps for large-grain disks is reduced from 16 to 7 [21]. However, the anisotropic mechanical properties in each grain and at the grain boundaries complexify the forming process. More details about the mechanical properties of niobium single crystals are provided in section 2.3.

Large-grain niobium half-cells have been fabricated by deep drawing at Jefferson Laboratory (JLab) [20], [26], Deutsches Elektronen-Synchrotron (DESY) [27], Peking University (PKU) [28], [29], and the Institute of High Energy Physics (IHEP) [30], [31]. As expected, forming of large grain disks with anisotropic mechanical properties resulted in non-uniform deformation and forming defects such as earing at the equator and the iris, but high accelerating gradients were still measured in the SRF cavities [20], [26], [30]. Kneisel et al. [32] published a detailed review paper presenting the material properties, cavity fabrication, and performances measured in different institutes. Figure 1.5b and c show the earing defect in a deep drawn half-cell and an assembled 3.5-cell 1.3 GHz cavity, respectively.

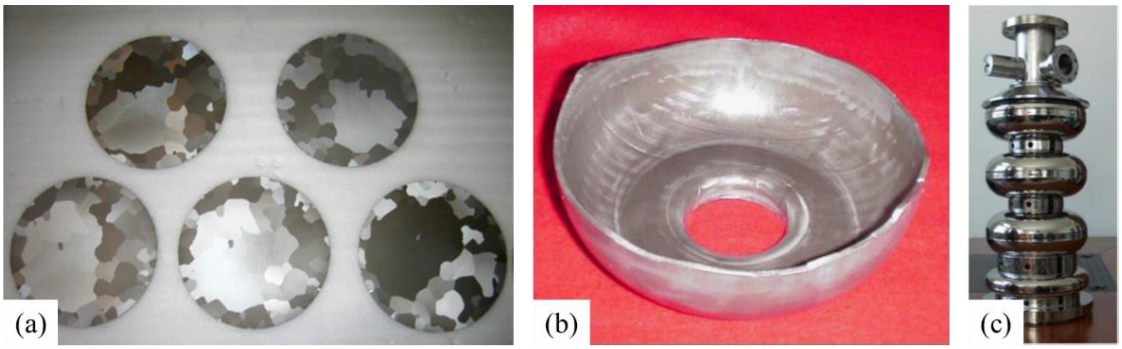

Figure 1.5: Large-grain niobium (a) disks produced at Tokyo Denkai, (b) half-cell deep drawn at JLab with earing defects and (c) 3.5-cell 1.3 GHz cavity manufactured at PKU [21], [29], [32].

1.2.3. SRF Cavity Fabrication

The majority of the elliptical SRF cavities currently used are built by forming two half-cells and weld them together at the equator. Figure 1.6 shows a simplified sequence to manufacture a 400 MHz copper–coated SRF cavity for the LHC. More detailed sequences from different laboratories are available in the literature [23], [33]. First, the half-cells are fabricated by plasticly deforming the copper or niobium blanks using different forming processes such as deep drawing, spinning, hydroforming, or electro-hydraulic forming. Second, the formed half-cells are controlled to ensure that the high shape tolerances are respected. Third, the excess material is removed from the half-cells. Fourth, two half-cells are electron beam welded at the equator. Fifth, a chemical polishing or electropolishing step is used to remove up too few hundreds of micrometers from the inner surface of the cavity. Removal of the damaged layer, developed during forming and machining, is essential to ensure proper film growth for copper substrates and to remove any defect that would hinder the performances of a cavity [34]. Finally, if the substrate of the cavity is made of OFE copper, a superconducting thin film of few micrometers is deposited on the inner surface of the SRF cavity. A thick film approach has also been proposed by Palmieri et al. [35] in an attempt to obtain performances similar to bulk niobium cavities [36]. One or multiple tuning steps are also added in the sequence to ensure that the fundamental frequency of the formed cavity is equal to the designed one. Hydrogen interstitial atoms trapped in the cavity during the manufacturing process are removed with a high temperature heat treatment. The addition of nitrogen atoms in the cavity, a process called *nitrogen doping*, showed increased performances by affecting hydride nucleation [13], [37]. Another fabrication route is to form cavities with no weld, hereafter *seamless cavities*, starting with circular blanks or tubes [38].

For this thesis only sheet forming and electron beam welding steps are of interest. The different sheet forming techniques are presented in the following section and electron beam welding is described in section 1.4.

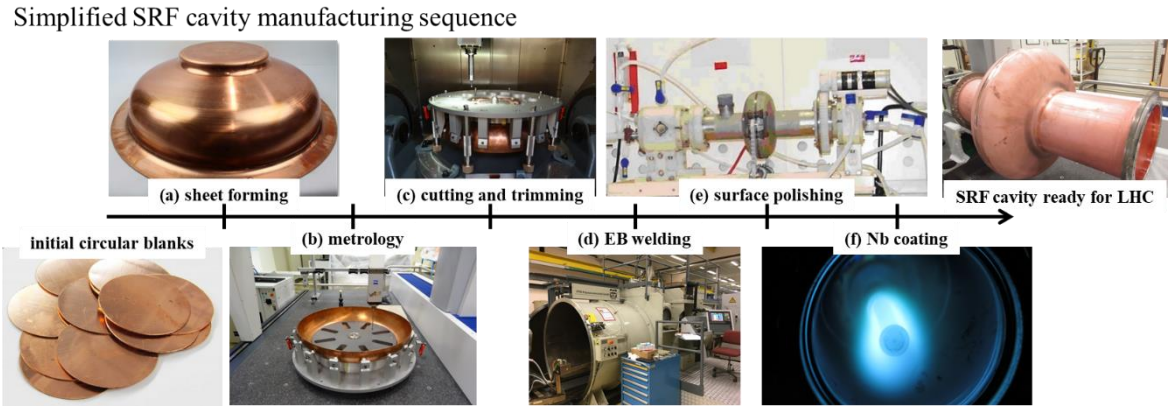

Figure 1.6: Simplified SRF cavity manufacturing sequence for a 400 MHz Cu/Nb cavity for the LHC [39]–[41].

1.3. Sheet Forming Processes

Predicting the material response to low and high strain rate loading in order to improve the sheet forming step in the manufacturing process of SRF cavities, presented in Figure 1.6, is an objective of this thesis. The sheet forming technique used to manufacture half-cells changes between different research institutes and companies. Traditional low strain rate techniques like deep drawing, hydroforming, and spinning are used at JLab, DESY, and INFN LNL, respectively. Electro-hydraulic forming is used at I-Cube Research/Bmax to produce half-cells at a high strain rate of up to 10^4 s^{-1} [3]. An understanding of the fundamental principles and differences between the different techniques are essential to understand the different characterization experiments performed during this thesis.

1.3.1. General Principles of Sheet Forming

Sheet–metal forming is used across a wide variety of industries including consumer electronics, automotive, food packaging, and more [42]. See Figure 1.7 for an example from the automotive industry, where structural beams are often made of high-strength steel and body panels of aluminum. In all cases, a flat and thin sheet, from few hundreds of microns for fuel-cells up to 4 mm in thickness for SRF cavities, of metal is deformed in a final and often complex geometry. Depending on the application, the final parts can have structural, esthetic, or functional roles. Recall that SRF cavities are both structural and functional parts.

To accurately design the setup, e.g. punch and die geometries, and forming sequences, the mechanical properties of the materials must be known. For example, the elastic modulus E, yield stress σ_y, and hardening behavior are experimentally determined using tensile tests of specimens extracted from the sheet metal. Specimens are cut in different orientations (for instance, tensile axis aligned at 0°, 45°, and 90° with respect to the sheet rolling direction) to measure anisotropic properties caused by the texture developed during the rolling process. For the specific case of high-speed sheet forming the strain rate sensitivity m is an important

parameter. Identifying these parameters is required for accurate modeling of the plastic domain during deformation and springback after removal of the applied load in finite element (FE) models. A detailed overview of mechanical properties at different strain rates and the parameters mentioned in this paragraph are presented in section 2.1.

Figure 1.7: Car chassis showing assembled structural sheet–metal parts [43].

1.3.2. Standard Low Strain Rate Forming Techniques

Deep drawing is a process commonly used to form copper and niobium sheets into half-cells and a variety of other applications such as forming of car components, see the schematic in Figure 1.8a. During this process, a metallic punch forces a flat blank into a die machined with a geometry close to the final part's geometry. The sheet is hold into place by the applied pressure of a press on a blankholder. The applied load, blankholder design, and the addition of draw beads allows the control of material draw-in during forming. Controlling the draw-in prevents excessive thinning for deep forming operations, tear and wrinkling of the sheet. Effective lubrication, forming large radii and adequate design of the blank are additional important parameters to control to avoid forming defects [42].

Spinning is also used to form half-cells, see Figure 1.8b for a schematic of the process. It is used at the INFN LNL to form seamless cavities starting with circular sheets or tubes, see section 1.3.4. for details on seamless cavity forming. During this process, a load is applied with a rolling tool on a sheet or tube. The blank is affixed to a rotating mandrel that has the shape of the internal surface of a half-cell. Parts formed with spinning are axisymmetric. This process is similar to clay pottery, where fingers are used as the rolling tool, but with a defined final shape on the mandrel.

In hydroforming, a tube or sheet is formed on a one-sided die cavity by increasing the pressure in a fluid or elastomer to expand the part, see Figure 1.9 for a schematic of the process. To avoid significant wall thinning, the process is done in sequences, starting with an open die. Figure 1.12 shows the multi-step process used to form seamless cavities with

hydroforming. The term *bulging* is used to define free-forming blanks with hydroforming and the biaxial strain in the sheet makes it a suitable process to determine the forming limit diagram of a material [44]. An advantage of this technique and electro-hydraulic forming for SRF cavities is the reduced risk of contamination on the RF surface from the inclusion of metallic particles caused by the contact with the punch in deep drawing or the mandrel in spinning, since the inner surface is only in contact with water [3].

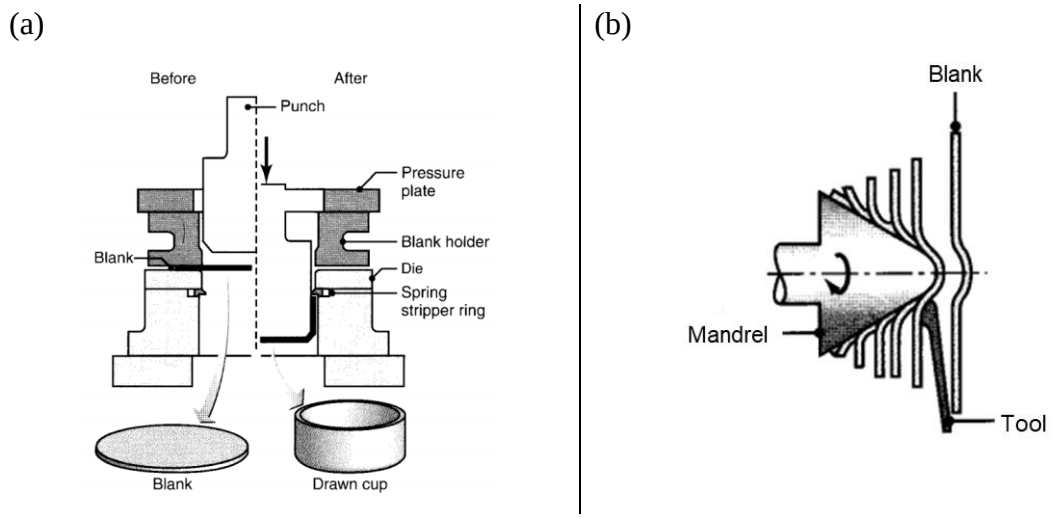

Figure 1.8: (a) schematic of the deep-drawing process to form a circular cup and (b) Schematic of the spinning process starting with a sheet [42].

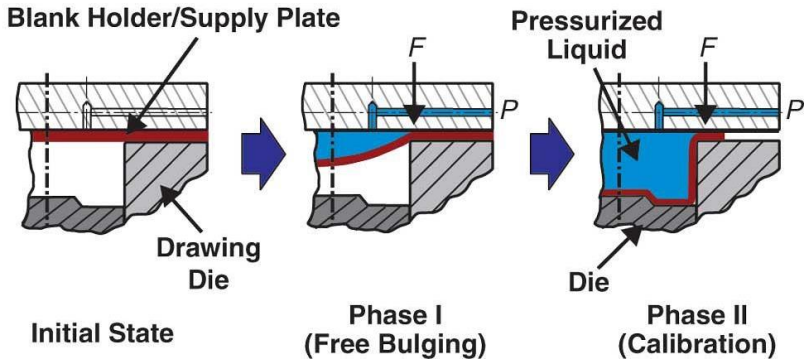

Figure 1.9: Schematic of sheet hydroforming process with the bulging and calibration phases [45].

1.3.3. Electro-hydraulic Forming

Electro-hydraulic forming is a high strain rate sheet metal forming technology that uses a high voltage electric discharge in a fluid, often water, to deform a blank into a final desired shape. This high-pulsed power (HPP) technique discharges the electrical energy stored in capacitor banks in a small wire that explodes under the electrical power or between an anode and a cathode. The low resistance of the exploding wire yields high current discharge, while the high resistance of water as it heats up and ionize to form a conductive gas phase results in higher losses. In both cases, a plasma is formed and expands in the fluid, resulting in pressure waves that impact the blank and accelerate it to speeds of up to hundreds of meters per second. Depending on the discharge chamber and geometry of the parts, reflected waves

can locally increase the pressure above the pressure of the incident wave. Therefore, multi-physics FE models are used to predict how the pressure evolves in the chamber as the part is formed. The process is repeated with additional discharges until the blank is formed to the shape of the die below it. See Figure 1.10 for a schematic of an EHF chamber with an exploded wire. The water tank is often closed with a hydraulic or mechanical press to maximize the pressure in the discharge chamber and prevent water leakages or jets. The region between the blank and the die is placed under vacuum to improve the forming efficiency at each discharge and avoid defects due to the presence of compressed air.

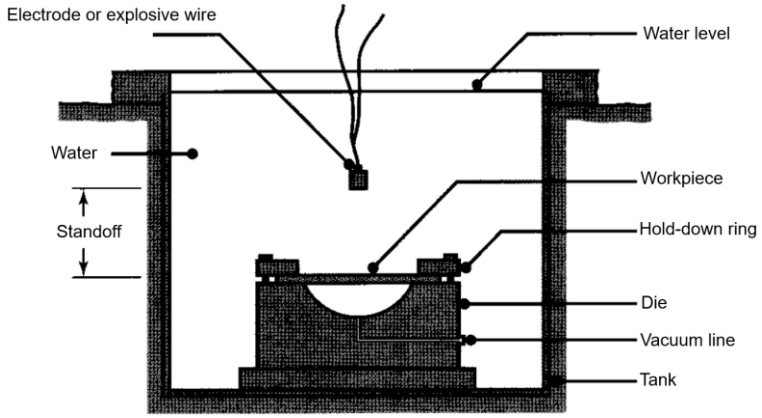

Figure 1.10: Schematic of an electro-hydraulic forming chamber with an exploded wire [42].

The technique has been used to manufacture small and large parts for the luxury, aerospace, automotive, consumer electronics, and other industries [46]. Golovashchenko [47] published a detailed report of the application of EHF in automotive panels for forming, trimming, and calibration operations and the numerical modeling of the process.

The advantages of EHF to form niobium half-cells were reported by Cantergiani et al [3]. Some of the advantages below can also be generalized to EHF of other metals. First, the surface in contact with water is less deformed after forming, proved by the presence of twins on the outer surface of niobium sheets, but not on the inner surface and the lower local average misorientation angle [3]. Second, the high strain rate deformation leads to a higher formability for multiple materials by delaying the onset of necking [48]–[50]. The inertial ironing, defined as the rapid deceleration of the blank upon impact with the tool, is also expected to increase formability [49], [51]. This tool–sheet interaction during high-speed forming results in non-linear strain paths and multi-axial stress states that can lead to strong compressive hydro-static stresses reducing damages and delaying sheet fracture [51], [52]. Third, intermediate heat treatments, used to reduce residual stresses in the deformed sheet, are generally not required with EHF. Fourth, as mentioned in the description of the hydroforming process, the inner surface is not in contact with a metallic part that generates a thick damaged layer with possible inclusions. Finally, the roughness of the blank is

preserved during forming [4]. Low roughness and low contamination content are paramount in copper–coated cavities to maximize the heat conduction between the niobium thin film and the copper substrate [53]–[55]. Similar results were expected for copper half-cells formed with EHF and an increase in Nb/Cu cavity performance for a 400 MHz copper cavity manufactured with EHF was indeed measured at CERN [56]. As shown in the quality factor as function of accelerating voltage (Q_0–E_{acc}) plot of Figure 1.11, the performance measured for the EHF Nb/Cu 400 MHz cavity were the highest ever measured.

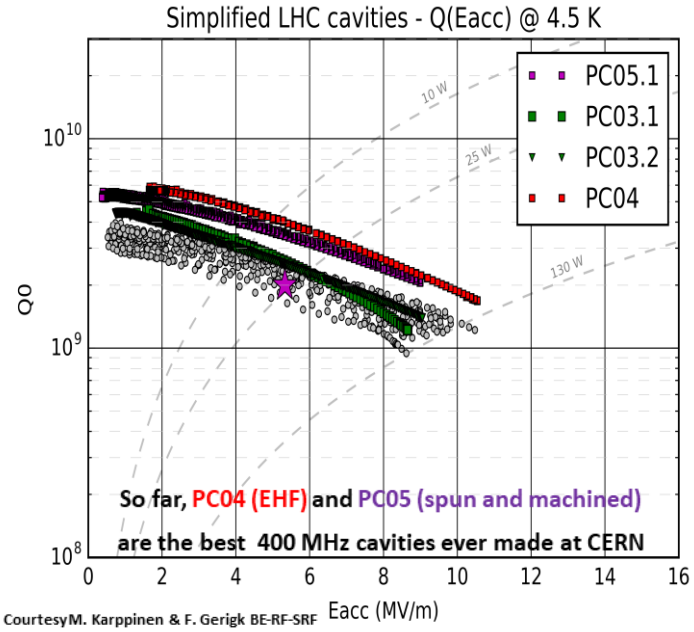

Figure 1.11: 400 MHz SRF cavity performances measured at CERN and comparing substrates manufactured with EHF (PC04) and spinning and machining (PC05.1) [56].

1.3.4. Seamless Cavities

Seamless cavities have been formed since the end of the 1980s with the objectives to increase RF performances and reduce production cost and time. Both of those objectives are reached by removing the complex and expensive electron beam welding of half-cells, which can generate potential defects (e.g. contamination, welding projections, voids or holes) that are prone to act as quenching sites during operation [11], [57], [58].

Hydroformed seamless cavities were first proposed by Kirchgessner of Cornell University in 1987 [59]. CERN later formed cavities at resonance frequencies of 352 MHz, 1.5 GHz, and 2.1 GHz with hydroforming [60], [61]. In 1994, Palmieri of INFN LNL formed the first 1.5 GHz cavities using spinning, which eliminated the need for intermediate annealing steps, and allowed him to use flat circular blanks instead of tubes [62]. The following year, Japan's High Energy Accelerator Research Organization (KEK) presented results on 1.3 GHz cavities formed with a combination of hydroforming and explosive forming [63]. CEA and

DESY each hydroformed 1.3 GHz cavities [64], [65], while Michigan State University worked on hydroforming of 3.9 GHz prototypes [66]. In the recent years, work was published on 1.3 GHz cavities formed with a combination of necking at the iris and hydroforming at the equator by both KEK and DESY [67], [68]. This forming sequence is ideal to avoid material thinning at the equator and is presented in Figure 1.12. The resulting 1.3 GHz 3-cell copper and niobium seamless cavities are presented in Figure 1.13.

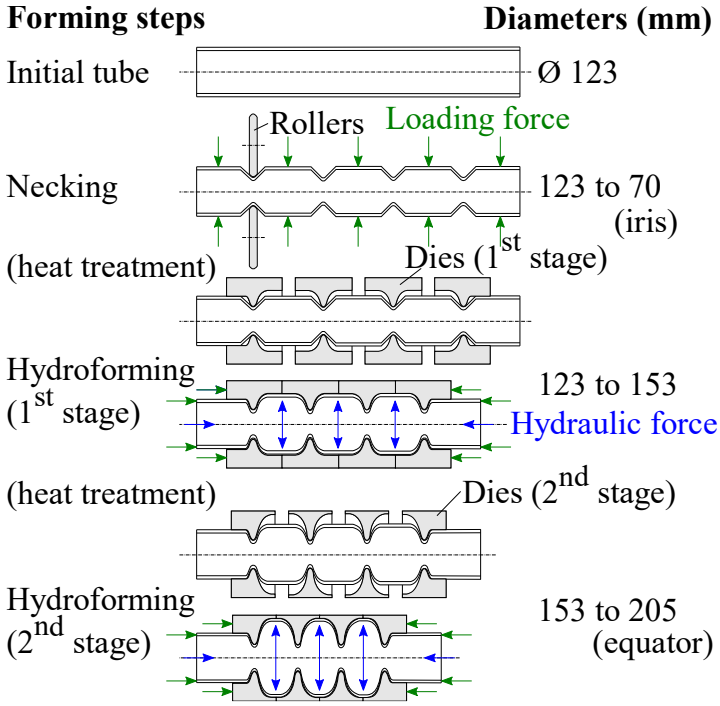

Figure 1.12: Necking and hydroforming steps to manufacture seamless cavities starting with a tube at KEK and similarly at DESY. Redrawn from [67].

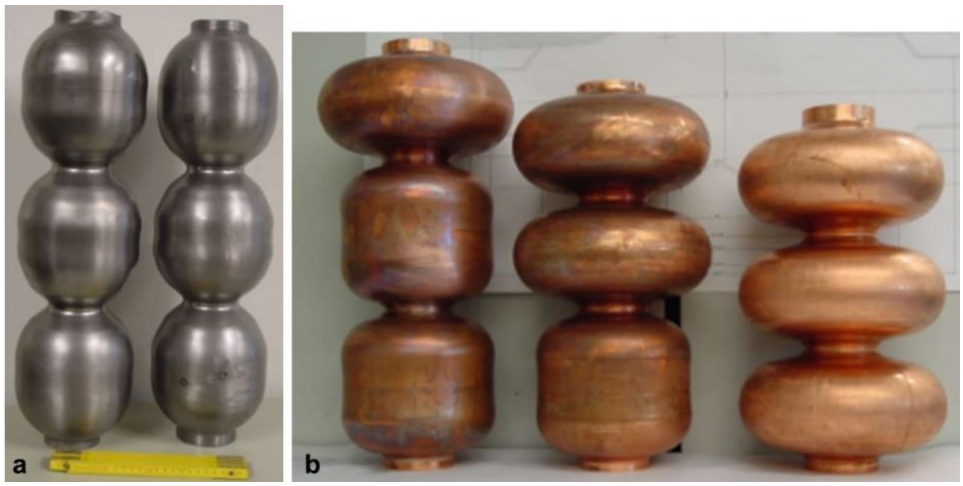

Figure 1.13: (a) niobium tubes deformed after the necking step and (b) copper tubes at different stages of the 1.3 GHz 3-cell fabrication at DESY [68].

The latest development in 1.3 GHz seamless cavities was motivated by the design of the International Linear Collider, which might become the accelerator with the largest number of cavities and operate at a collision energy of up to 500 GeV [69].

Miniature 6 GHz seamless cavities formed by spinning, as shown in Figure 1.14, are still used at the INFN LNL for research purposes, such as the EASITrain project. The small cavities are economically ideal to test different deposition parameters and to develop novel surface preparation techniques [70].

Figure 1.14: Seamless 6 GHz cavities fabricated at INFN LNL with spinning and different materials [71].

1.4. Tube Fabrication

All the work around seamless cavities led to R&D projects on the fabrication of copper and niobium tubes. The manufacturing of niobium tubes with an inner diameter of about 150 mm, for hydroforming, and suitable for the SRF industry is complex due to the following requirements: (1) high purity (RRR ~300), (2) high ductility (elongation > 25% before localized necking), (3) low anisotropy (absence of significant texture), (4) high wall thickness tolerances (± 0.1 to 0.2 mm), and (5) high surface quality [68].

Tubes for SRF applications were manufactured by bending and welding a sheet or with one or a combination of the following seamless techniques: (1) forward extrusion, (2) backward extrusion, (3) spinning, (4) deep drawing, (5) flow forming, and (6) tube equal channel angular extrusion (ECAE). In forward (direct) extrusion, the billet is forced through a fixed die, while in backward (indirect) extrusion, the die moves toward the billet [42]. The same nomenclature is often used for forward and backward flow forming. A billet is used as starting material for tube ECAE and forward and backward extrusion. Except for tube ECAE, the grain size of the billet is not significantly changed during tube manufacturing. Therefore, niobium billets with large grains, which are produced by successive EB melting steps, are not ideal for forward and backward extrusion as this results in tubes with large grains and anisotropic properties.

This is not a problem for bent and welded sheets, deep drawing, and spinning, because a thin flat sheet is used as a starting material and the production of fine-grain niobium sheets with equiaxed grains suitable for SRF applications has been well controlled for decades now. In flow forming, a hollow cylindrical blank that fits on a mandrel is required as starting

material. The microstructure of the blank is dependent on its manufacturing process, e.g. deep drawing or back extrusion. During this process, the tube wall thickness can be reduced by 90% and the tube length increased by a tenfold [62]. The large through-thickness plastic deformation leads to tubes with increased strength, but possibly with a texture, resulting in anisotropic mechanical and physical properties. Table 1.1 presents a summary of the starting material, and main advantages and disadvantages of the different tube forming techniques used to manufacture SRF cavities.

Table 1.1: Overview of different tube fabrication techniques for the SRF industry, grouped by starting material.

Technique	**Starting material**	**Advantages**	**Disadvantages**
Backward / Forward extrusion	Billet	Few production steps [68]	Not sufficient work hardening (especially problematic for billets with large grains) [68], [72] High tonnage for large tubes [38]
Tube ECAE		Important grain size reduction	Still in R&D phase [73]
Deep drawing	Sheet	Low anisotropy [68]	Requires multiple sets of expansive dies High wall thickness variation [68]
Spinning		Low anisotropy [68]	High wall thickness variation [68]
Bending + welding		Low anisotropy Simple to implement Control of length and thickness	Potential defects at the weld Lower formability in HAZ [68]
Flow turning	Hollow cylindrical blank	High wall thickness tolerance ±0.1 mm Large increase in length Heavy work hardening	Higher anisotropy (elongated grains)

Combinations of the different tube forming techniques presented above have been used by private companies, national laboratories and universities to manufacture tubes for the SRF industry. Spinning and deep drawing combined with flow forming was used by Palmieri at the INFN LNL to manufacture niobium and copper tubes [38]. Extrusion and flow forming was used by Antoine at CEA Saclay to manufacture niobium and copper tubes [22]. At their first attempt, the high-purity niobium jammed the tool, which required a redesign. Similarly, larger radii were machined in the dies used at the INFN LNL for deep drawing and more redrawing steps were required for niobium [38].

WC Heraeus manufactured seamless niobium tubes by back extrusion only [72]. Upon hydroforming, the high-purity tubes (RRR ~300) burst due to a reduced formability from heterogeneous grain sizes, see Figure 1.15a [72]. DESY concluded that tubes formed by a combination of deep drawing or spinning with flow forming, which allows the manufacturer to use a sheet with fine grains instead of a billet with large grains, was ideal for the fabrication of seamless cavities by hydroforming [68]. The ductility was sufficient to form cavities, but anisotropic mechanical properties were measured in the tube.

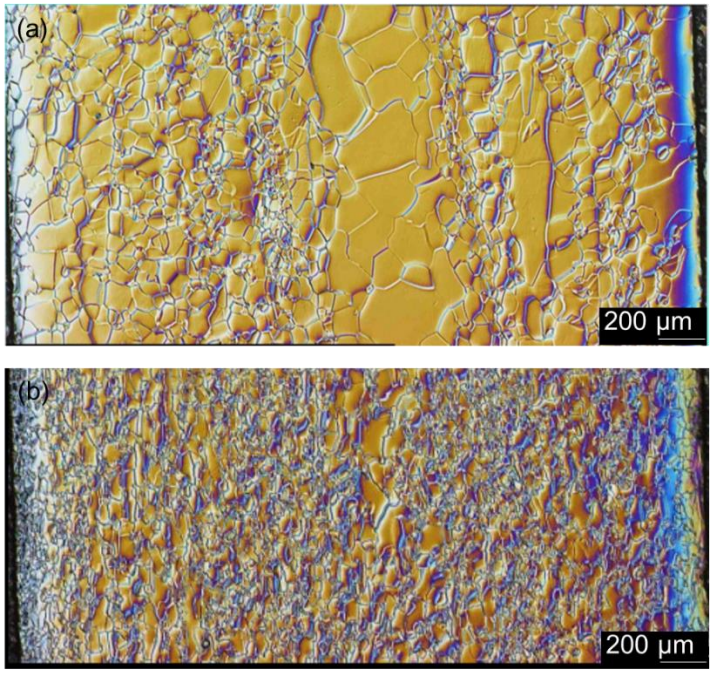

Figure 1.15: Optical microscopy image of etched niobium tube cross-sections formed by backward extrusion at Heraeus and showing (a) different and (b) similar grain sizes from the surface to the center, for tubes with RRR of 300 and 100, respectively [74].

Black Laboratories LLC and JLab used backward extrusion, forward extrusion, and flow forming, starting from a billet with 11 µm grains [75], [76]. The fine-grained billet was produced using equal channel angular extrusion. Four passes in a 90° die and an annealing heat treatment were required to reduce the billet grain size from 110 to 15 µm [77]. Texas A&M University also used billets with a fine microstructure produced by ECAE, but removed the material in the center of the cylindrical billet by drilling, forward extrusion and symmetric shear processing, a process where the tube was expanded and contracted back to its initial shape by undergoing important plastic shear deformation [78], [79]. The reduced grain size obtained by ECAE resulted in tubes and seamless cavities with a low roughness. However, a reduction in ductility was also measured [68]. A compromise between grain size and texture in the microstructure is then required.

Non-seamless tubes produced by bending and welding a sheet were manufactured at CEA Saclay (without success) [22], INFN LNL [38], and DESY [68]. A low ductility (failure at < 20% strain) was measured at DESY during a bulge test and was explained by the large grains in the heat affected (HAZ) zone, see Figure 1.16. The risk of a reduced ductility due to potential contamination, e.g. lubricant or gas particles, in the HAZ during welding is also increased [38]. Therefore, seamless tube manufacturing approaches are currently preferred [38]. However, the complexity associated with the manufacturing of tubes that respect strict requirements for SRF cavities and forming of more complex geometries where welds are required, like in crab cavities [80], motivate the characterization of EB welds deformed at high strain rates.

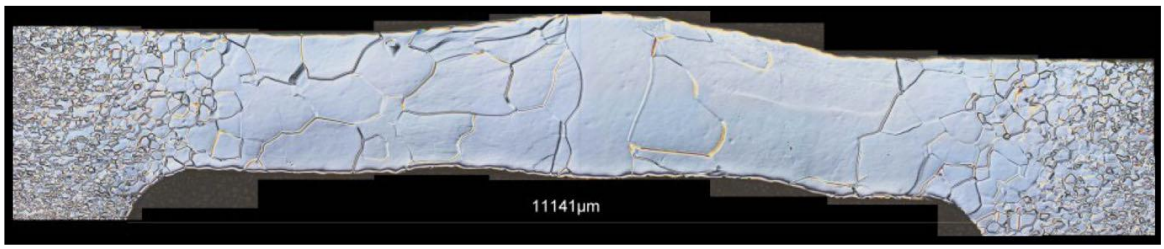

Figure 1.16: Optical microscopy image of an etched niobium tube cross-section in the HAZ of a weld at DESY [68].

1.5. Thesis Overview

Recall that the main objective of the thesis is to characterize materials to improve different forming techniques and ultimately increase the performances of SRF cavities. The materials characterized are niobium single crystals, polycrystalline niobium and OFE copper sheets. The thesis is then separated in two parts, based on the material studied. Part I presents the study on the mechanical properties and the microstructure of niobium single crystals with different crystal orientations deformed in tension and compression at strain rates between 10^{-4} s^{-1} and 1 000 s^{-1}. Part II presents studies on polycrystalline niobium and OFE copper in terms of sheet formability at low strain rate and the effect of strain rate on electron beam welded sheets. Figure 1.17 presents a flowchart of the structure of this dissertation.

Each part has a *Background* chapter (Chapters 2 and 6) that provides a survey of the relevant literature and theories required to perform each study and to contribute to the scientific knowledge and a *Materials and Methods* chapter (Chapters 3 and 7) that describes the materials characterized, the experimental procedures for the different tests performed, and the analysis techniques used. Fundamental theories and methods that are important for both parts are only presented in Part I.

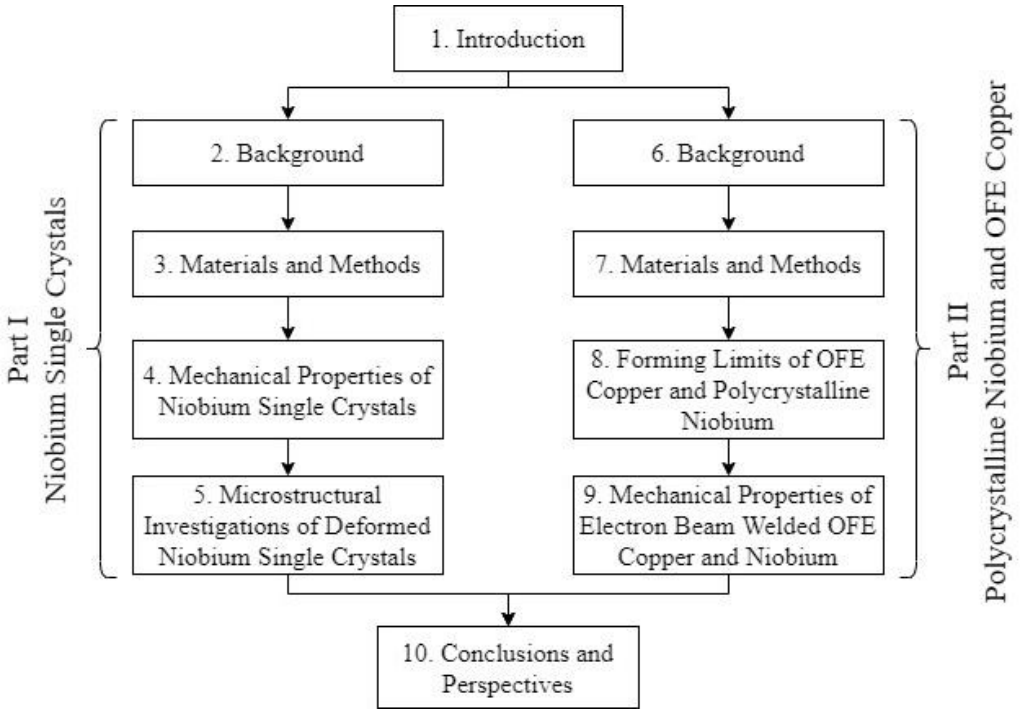

Figure 1.17: Flowchart of the structure of the dissertation with associated chapter numbers.

The results in Part I are separated in two chapters. First, Chapter 4, *Mechanical Properties of Niobium Single Crystals*, presents the tensile and compressive mechanical properties of niobium single crystals with different crystallographic orientations deformed at strain rates between 10^{-4} s^{-1} and 1 000 s^{-1}. Second Chapter 5, *Microstructural Investigations of Deformed Niobium Single Crystals*, focuses on the microstructure and dislocation substructures in the deformed specimens, observed with scanning and transmission electron microscopy, respectively. The effects of the different microstructures are also quantified with nanoindentation measurements and presented.

The results in Part II are also separated in two chapters. First, Chapter 8, *Forming Limits of OFE Copper and Polycrystalline Niobium*, focuses on the determination of the quasi-static forming limit diagrams of annealed OFE copper and polycrystalline niobium sheets. Second, Chapter 9, *Mechanical Properties of Electron Beam Welded OFE Copper and Niobium*, presents the mechanical properties of electron beam welded OFE copper and niobium sheets deformed at strain rates between 10^{-3} s^{-1} and 10^{3} s^{-1} for the future development of seamless SRF cavities using tubes formed with rolled and welded sheet.

Chapter 10, *Conclusion and Perspectives*, highlights the main conclusions of the different chapters, proposes future work that could not be performed in the time constraint of the project, and highlights the potential applications of the results.

PART I

NIOBIUM SINGLE CRYSTALS

Chapter 2 Background

2.1. Mechanical Properties of Metals

The mechanical properties of materials, and more specifically of metals, can be found by performing tensile or compression tests. A stress–strain curve is obtained from those uniaxial tests, as shown in Figure 2.1, and important quantities such as the elastic modulus E, the yield stress σ_y, the ultimate tensile stress (UTS) σ_{UTS}, and the nominal strain to fracture ε_f are found. Stretching of metallic bonds between atoms occurs during elastic (temporary) deformation. The elastic regime is characterized in the stress–strain plot by the initial linear segment described by Hooke's law:

$$\sigma_T = E\varepsilon_T \tag{2.1}$$

In most metals deformed at room temperature and low strain rate, plastic (permanent) deformation is characterized by the motion of dislocations, i.e. linear crystal defects (see section 2.3.1.), and hardening (or softening) of the material during plastic deformation is numerically described with often non-linear constitutive equations. Robust and representative constitutive models are required for finite element modeling of sheet–metal forming processes.

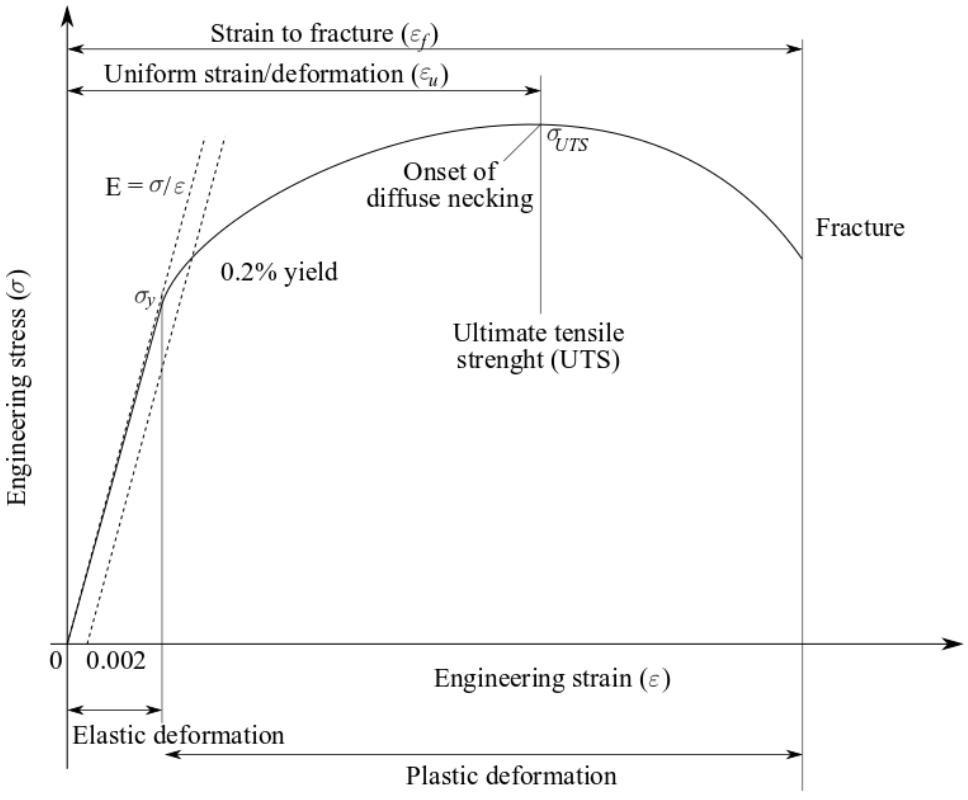

Figure 2.1: Schematic of a typical tensile stress–strain curve with important quantities. Redrawn from [91].

For polycrystalline materials, many advanced phenomenological and physical constitutive equations have been developed and are applicable in different conditions such as varying temperature, strain rate, lattice structure, and more. Salvado et al. [81] reviewed strain rate dependent constitutive equations for FCC metals. The Johnson–Cook equation [82], an empirical equation, is commonly used in finite element models of dynamic processes. This equation is versatile to characterize the flow stress of many face-centered cubic (FCC) metals, such as OFE copper, at different strain rates and temperatures due to the multiplicative effect of each term. However, for strain rate sensitive body-centered cubic (BCC) materials, such as niobium, an additive strain rate hardening term is required to be representative of the response of the material. Therefore, constitutive equations such as the Zerilli–Armstrong equation [83], dependent on physical constants as well as empirical values, are often more appropriate. Other constitutive equations, such as the Steinberg–Cochran–Guinan–Lund (SCGL) [84], [85], Mechanical Threshold Stress (MTS) [86], [87], Preston–Tonks–Wallace (PTW) [88], and the Rusinek and Klepaczko (RK) [89], [90], are also often used to predict the stress in specimens deformed at high strain rates. For single crystalline materials, like niobium single crystals, those constitutive equations are often not representative and crystal plasticity models are used.

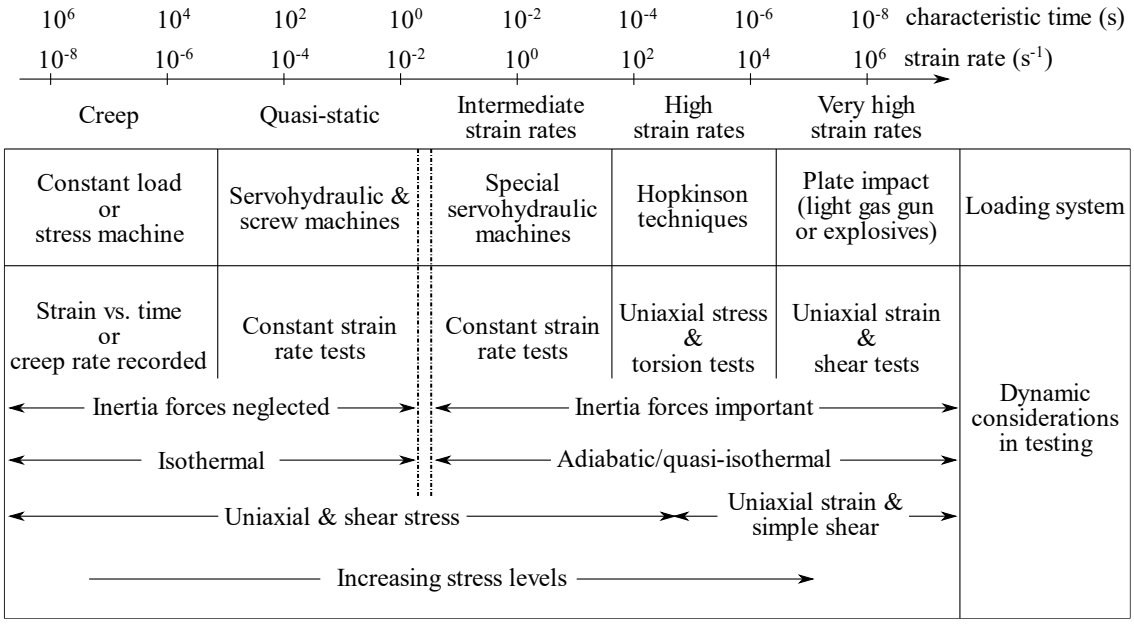

Figure 2.2: Different considerations for changing regimes of strain rate and load duration. Redrawn from [93].

Several machines are required to perform tensile and compression tests at different strain rates and many aspects, such as adiabatic heating, are important at high strain rates. Figure 2.2 shows the different strain rate regimes with associated considerations, loading systems, and characteristic times. For a maximum strain rate in the order of 10^3 s^{-1}, the maximum strain rate used in this study, inertia forces and adiabatic heating cannot be neglected. The

effect of inertia and adiabatic heating are generally only negligible at quasi-static strain rates of up to ~10^{-1} s^{-1}. Screw and hydraulic machines and split Hopkinson bars must be used to perform tests at quasi-static, intermediate, and high strain rates. Tests with a screw-driven machine are commonly used and do not require special explanations or considerations. Tests at an intermediate strain rate with a hydraulic machine need special devices at high speeds, such as a lost-motion rod [92], to ensure that the piston is at a constant speed as a specimen is being deformed. Finally, the split Hopkinson bar tests are different than the ones with screw and hydraulic machines since the specimen is deformed by an elastic strain wave that is usually generated by the impact of two bars with a high yield strength. More details on split Hopkinson tests are presented in the next subsection.

2.2. Split Hopkinson Bars

The split Hopkinson (Kolsky) pressure bar technique has been extensively used to measure the mechanical properties at strain rates of about 10^2 s^{-1} to 10^4 s^{-1} in tension, compression, and torsion for ductile and brittle materials. A brief overview of the method and important equations are presented below. More details about the technique are available in the review papers of Gray [94] and Gama et al. [95] and the book of Chen and Song [96].

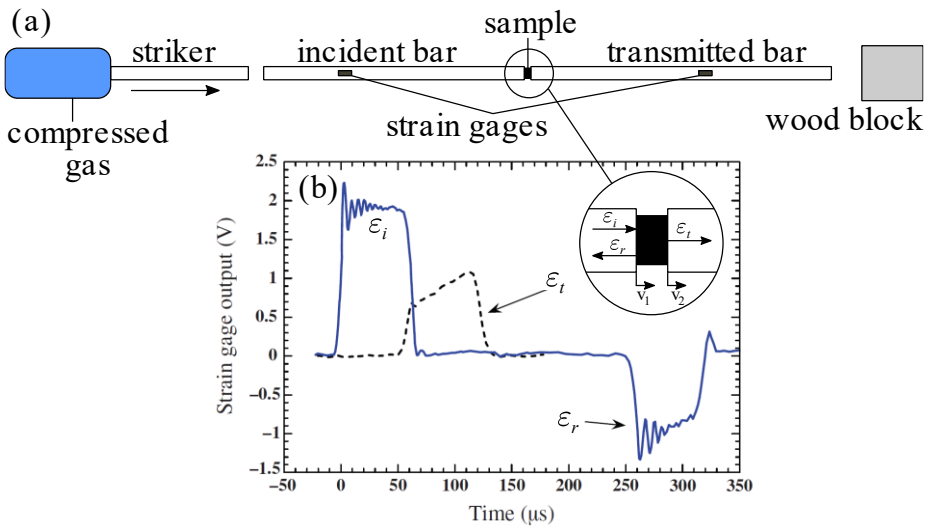

Figure 2.3: (a) Main components of a compression split Hopkinson bar setup and (b) typical strain gage data from [94] with (inset) a schematic of the different strain waves and bar velocities at the bar–specimen interface. The incident (ε_i) and transmitted (ε_t) waves are compressive waves and the reflected wave (ε_r) represents tensile loading.

Figure 2.3a shows the main components of a compression split Hopkinson bar setup. During that test, a striker bar made of a high strength material, e.g. maraging steel, is propelled, often by compressed gas, at a high velocity toward an incident bar. The yield stress of all bars in the setup must be high to ensure that the strain wave generated upon impact of the striker with the incident bar is elastic. The incident compression strain wave travels in the incident bar up to the surface in contact with the specimen, where a portion is reflected as a

tensile wave and travels back in the incident bar and the rest of the compression wave is transmitted through the specimen and travel in the transmitted bar. This results in a difference in velocity of the incident and transmitted bars at the bar–specimen interface and a deformation of the specimen. Typical strain signals measured with strain gages attached to the incident and transmitted bars are shown in Figure 2.3a.

Figure 2.4 shows a schematic of a dynamically loaded compression split Hopkinson bar system with the corresponding simplified $x-t$ diagram. Pictures of four different split Hopkinson bar systems with tensile and compression loading used in this study are presented in the *Materials and Methods* chapters in Parts I and II of this thesis. The simplified x–t diagram shows that a compression wave is generated upon impact of the striker with the incident bar. Tensile waves are generated upon reflection of the compression wave at the free end of the striker and at the end of the incident bar in contact with the specimen. The duration of the pulse t_{pulse} is dependent on the material and the length of the striker L_b as follow:

$$t_{pulse} = \frac{2L_b}{c_b} \tag{2.2}$$

where c_b is the speed of sound in the striker, which is given by:

$$c_b = \sqrt{\frac{E_b}{\rho_b}} \tag{2.3}$$

where E_b is the elastic modulus of the striker and ρ_b is the density of the striker. The striker, incident, and transmission bars are often made of high-strength materials since the maximum stress that can be produced to deform the specimen is limited by the yield stress of the bars.

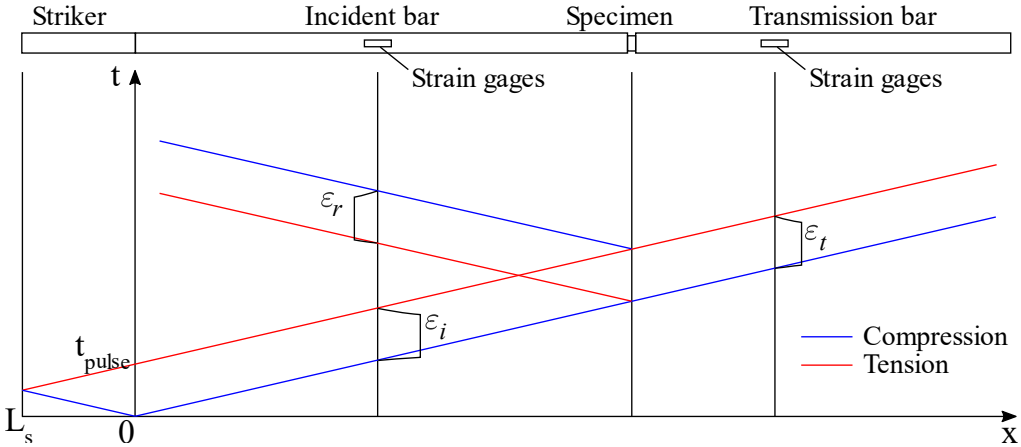

Figure 2.4: Schematic of a compression split Hopkinson bar system with the corresponding simplified x–t diagram. Redrawn from [96].

Three strain waves of interest are measured with strain gages on the incident (input) and transmission (output) bars. For a compression (tensile) test, the incident compression (tension) wave ε_i is generated at the impact of the striker and travels towards the specimen. The difference in impedance of the specimen results in partial transmission of the wave. The reflected tensile (compressive) component of the wave ε_r travels back in the incident bar and the transmitted compressive (tensile) component of the wave ε_t travels in the transmission bar. The sum of the incident and reflected waves is equal to the transmitted wave:

$$\varepsilon_t = \varepsilon_i + \varepsilon_r \tag{2.4}$$

The determination of the specimen's force–displacement behavior in split Hopkinson bar tests is based on the principle of one-dimensional elastic wave propagation within pressure loading bars. At equilibrium, the forces on each side of the sample are equal ($F_1 = F_2$) and given by

$$F_1(t) = A_b E_b\big(\varepsilon_i(t) + \varepsilon_r(t)\big) \tag{2.5}$$

$$F_2(t) = A_b E_b \varepsilon_t(t) \tag{2.6}$$

where A_b is the cross-sectional area of the input and output bars and E_b is the elastic modulus of the bars. Note that the subscript b was also used for calculations associated with the striker bar since the same material is often used for the three bars. The loads F_1 and F_2 are often referred as the *front* and *back loads*, respectively.

The engineering stress in the sample, $\sigma_{eng}(t)$, can be calculated using the back load. This is referred as a *one-wave analysis*. This approach is often used since the transmitted strain wave has low oscillations due to damping of the high-frequency oscillations as the specimen is deformed and is given by

$$\sigma_{eng}(t) = \frac{F_2(t)}{A_s} \tag{2.7}$$

where A_s is the initial cross-sectional area of the specimen. The stress can also be calculated using the average of the front and back loads. This is referred as a *three-wave analysis*. At equilibrium, the loads should be equal, but oscillations are often measured in the front load. The engineering stress with the three-wave analysis is calculated as follow

$$\sigma_{eng}(t) = \frac{F_1(t) + F_2(t)}{2A_s} = \frac{A_b E_b}{2A_s}(\varepsilon_i + \varepsilon_r + \varepsilon_t) \tag{2.8}$$

Equilibrium in the stress state is verified by comparing the one- and three-wave analyses. Figure 2.5 shows a stress–strain plot with a stress state at equilibrium and a nearly constant strain rate.

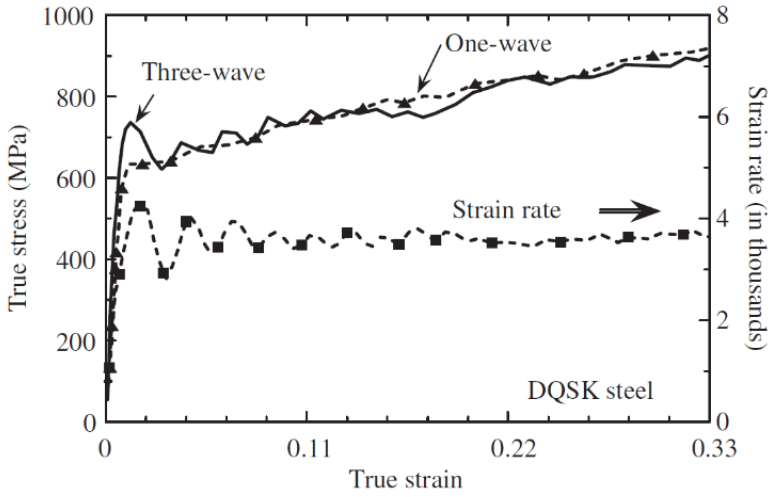

Figure 2.5: Comparison of the three and one-wave methods to confirm that equilibrium is reached and stabilization of the strain rate curve [94].

The nominal strain rate in the specimen is calculated with the reflected strain wave as follow

$$\dot{\varepsilon}\,(t) = \frac{v_i(t) - v_o(t)}{L_s} = \frac{2c_b\varepsilon_r(t)}{L_s} \tag{2.9}$$

where L_s is the initial length of the specimen, $v_i(t)$ and $v_o(t)$ are the face velocities of the input and output bars, respectively. Note that the equation on the right-hand side of the second equal sign is valid for bars of equal dimensions and properties. In the following, for tests with a varying strain rate during the deformation of the specimen, the average of the strain rate from loading (increase) to unloading (decrease) in the nearly square strain rate signal is given. The engineering strain in the sample is obtained by time integration of the strain rate signal.

2.2.1. Strain Rate Sensitivity and Deformation Mechanisms

The strain rate sensitivity of a metal is highly dependent on its lattice structures. FCC metals tend to show a multiplicative increase in flow stress at higher strain rates, i.e. a nearly constant yield stress and an increase in strain hardening rate for increasing strain rates [97]. BCC metals are more strain rate sensitive and often have an additive strain rate sensitivity, i.e. an increase in yield stress and similar strain hardening rates for increasing strain rates [97]. The (logarithmic) strain rate sensitivity m of a material is equal to the slope of the log–log plot of flow stress, preferably at a low strain to minimize the influence of the developed substructure, as function of the stain rate. This parameter is calculated as follow, at a given strain:

$$m = \frac{d \ln \sigma_y}{d \ln \dot{\varepsilon}}\bigg|_{\varepsilon} \tag{2.10}$$

A high strain rate sensitivity indicates a high increase in flow stress for increasing strain rates. A higher post-necking strain is positively correlated with a high strain rate sensitivity, as shown in Fig. 4c of [98], since the material locally hardens in the neck due to a higher strain rate [99]. Thus, a high strain rate sensitivity tends to delay failure of the specimen.

A change in strain rate sensitivity slope, usually a sharp increase in flow stress at a critical strain rate, may indicate a change in dominant deformation mechanism. A calculation of the activation volume v^* at a given flow stress, as shown in section 4.1.4., can estimate the thermally activated mechanisms [100]. The activation volume is defined as the partial derivative of the activation free energy with respect to stress at a constant temperature [101]–[104]. The different thermally activated deformation mechanisms are defined based on the short-range barriers affecting dislocation motion. Figure 2.6 shows schematics of five different thermally activated mechanisms ((a) overcoming Peierls–Nabarro stress, (b) intersection of forest dislocations, (c) non-conservative motion of jogs, (d) cross-slip, and (e) climb) with corresponding values of activation volume in units of cubic Burgers vector b^3.

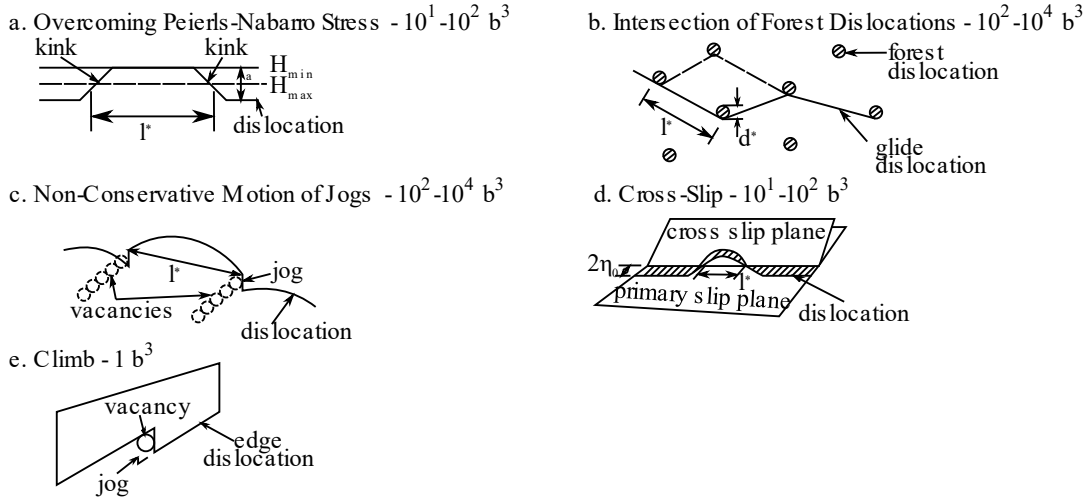

Figure 2.6: Schematic of different thermally activated mechanisms related to plastic deformation with corresponding activation volumes. Redrawn from [100].

2.3. Niobium Single Crystals

The study of the mechanical properties of single crystals requires an understanding of dislocations and their role in strain hardening. The following subsections provide a brief overview of the important theories required for the study presented in chapters 4 and 5, and a literature review of previous work performed on niobium single crystals.

2.3.1. Dislocations: Linear Defects in Crystalline Materials

Most of pure metallic elements have face-centered cubic, body-centered cubic, or hexagonal close-packed (HCP) lattice structures, as shown in Figure 2.7. Real materials all have imperfections with different length scales. Point, line, surface, and volume defects are such imperfections that affect the properties of the material. Dislocations are linear defects that reduce the required shear stress for atoms to move (*slip*) from one stable position in the lattice to the next one. Such slip motion of atoms defines a permanent (*plastic*) deformation and occurs along the *Burgers vector*. Figure 2.8 shows schematics of *edge* and *screw dislocations* and the directions of their respective dislocation line and Burgers vector. In BCC metals, such as niobium, plasticity, i.e. the study of plastic deformation, is mostly governed by the nucleation and motion of screw dislocations. Dislocations glide on preferred slip systems, composed of a *slip plane* and a *slip direction*. Figure 2.9a shows an example of a {110}<111> slip system. More specifically, it shows the (110) slip plane and the $[\bar{1}11]$ slip direction in a BCC lattice and the arrangement of atoms on that plane and along that direction. Miller–Bravais indices are used to define both planes and directions. The indices of a slip plane define a vector normal to the plane while the indices of a slip direction define a vector aligned with the slip direction. A more thorough understanding and description of dislocations is available in the *Introduction to Dislocations* textbook of Hull and Bacon [105].

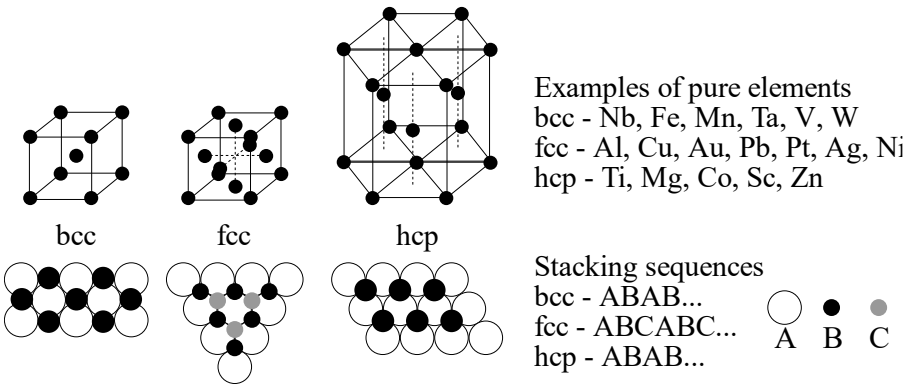

Figure 2.7: Lattice structures of most pure metals with (top) unit cells and (bottom) atomic stacking sequences for the plane with the highest atomic density.

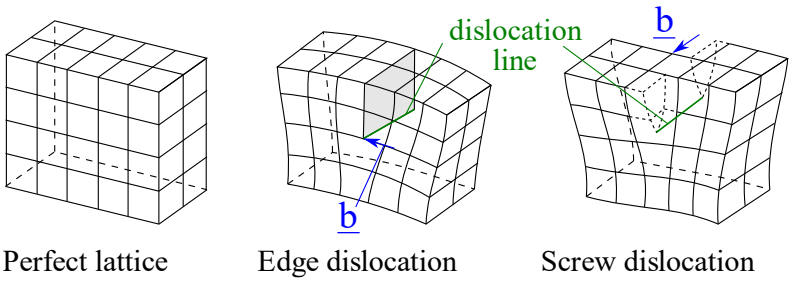

Figure 2.8: Schematics of distorted lattices with edge or screw dislocations with their dislocation lines and Burgers vectors.

2.3.2. Calculation of the Schmid Factor and Slip Systems in BCC Metals

Deformation in single crystalline specimens occurs by the motion of dislocations on specific slip planes and in defined slip directions. This is also true for polycrystalline specimens, but not considered at the scale of the specimen due to an averaging effect from the multiple grains with different crystal orientations. The applied load is resolved on the slip system as a shear stress, namely the *resolved shear stress* τ_{RSS}. According to the Schmid law, plastic deformation occurs on the slip system where the resolved shear stress is larger than the *critical resolved shear stress* τ_{CRSS}, which is strain rate and temperature dependent. However, it has been reported that BCC metals, which have a non-closed-packed lattice structure, do not follow Schmid's law due to the non-planar components of a screw dislocation [106], see section 2.3.7. for more details. Knowing the high likelihood that the niobium single crystals deformed in this study did not follow Schmid's law, the Schmid factor was still identified and used as the most relevant metric to predict the slip systems that will most likely activate for a given crystal orientation.

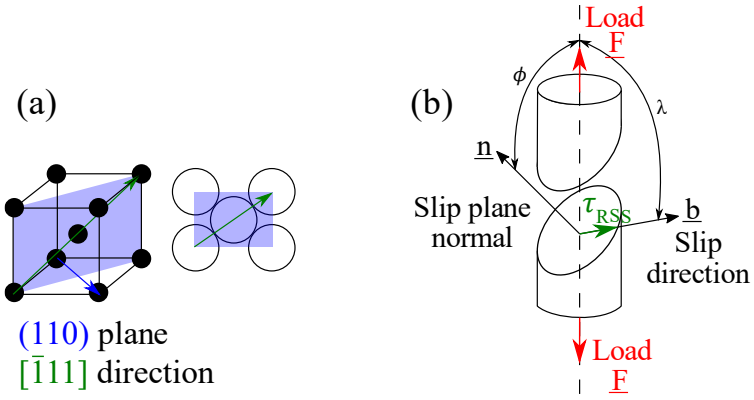

Figure 2.9: (a) Schematic of a slip plane (110) and a slip direction [$\bar{1}$11] in a BCC lattice and (b) schematic of a slip system with variables to calculate the Schmid factor for uniaxial stress. Redrawn from [107].

For a uniaxial stress state, the resolved shear stress is given by:

$$\tau_{RSS} = \frac{F}{A}\cos\phi\cos\lambda \tag{2.11}$$

where F is the applied load in uniaxial tension or compression, A is the cross-sectional area of the specimen, ϕ is the angle between the direction of the load and the normal of the slip plane, and λ is the angle between the direction of the load and the slip direction. Figure 2.9b shows a schematic of the resolved shear stress on a slip system with a slip plane normal vector $\underline{n}$ and a slip direction along the Burgers vector $\underline{b}$. From this figure and from equation 2.11, the Schmid factor SF, a variable dependent on the geometry of the crystal and the loading direction, is defined as:

$$SF = \cos\phi\cos\lambda \tag{2.12}$$

Based on the Schmid law and by substitution of equation 2.12 in equation 2.11, slip should occur on the slip system with the highest Schmid factor (if the critical resolved shear stress is similar for all slip systems). If the Schmid factor is equal on multiple slip systems, dislocations would then likely simultaneously glide on multiple slip planes.

Using the Miller-Bravais indices of a slip plane $\underline{n}$ and slip direction $\underline{b}$ and knowing the components of the load vector $\underline{F}$, the cosine angles in equation 2.12 are calculated as follow:

$$\cos\phi = \frac{\underline{n}\cdot\underline{F}}{\|\underline{n}\|\|\underline{F}\|} \text{ and } \cos\lambda = \frac{\underline{b}\cdot\underline{F}}{\|\underline{b}\|\|\underline{F}\|}$$

This notation is especially important when calculating the Schmid factor on all slip systems that could activate during the deformation of niobium single crystals.

2.3.3. Activated Slip Systems

In BCC metals, slip can occur on 48 different slip systems. The Burgers vector (slip direction) in all slip systems is always in the direction of highest packing factor, i.e. <111> and <101> in BCC and FCC metals, respectively. The three families of slip systems in BCC metals are the {110}<111>, {112}<111>, and {123}<111> families. For the specific case of niobium, slip was only experimentally observed on the {110}<111> and {112}<111> slip systems [108]–[110]. Similarly, numerical models near 273 K and at low temperatures predicted slip on the {112}<111> and {110}<111> slip systems, respectively [111], [112]. Therefore, only the 24 slip systems of those families are considered and listed in Table 2.1.

Table 2.1: Potentially activated slip systems in niobium for the {110}<111> and {112}<111> slip systems.

{110} family			{112} family		
$(0\bar{1}1)\ [\bar{1}11]$	$(101)\ [\bar{1}11]$	$(110)\ [\bar{1}11]$	$(211)\ [\bar{1}11]$	$(\bar{1}21)\ [\bar{1}11]$	$(1\bar{1}2)\ [\bar{1}11]$
$(011)\ [\bar{1}\bar{1}1]$	$(101)\ [\bar{1}\bar{1}1]$	$(110)\ [\bar{1}\bar{1}1]$	$(2\bar{1}1)\ [\bar{1}\bar{1}1]$	$(\bar{1}21)\ [\bar{1}\bar{1}1]$	$(112)\ [\bar{1}\bar{1}1]$
$(0\bar{1}1)[111]$	$(\bar{1}01)[111]$	$(1\bar{1}0)[111]$	$(\bar{2}11)[111]$	$(1\bar{2}1)[111]$	$(\bar{1}\bar{1}2)\ [111]$
$(011)[1\bar{1}1]$	$(\bar{1}01)\ [1\bar{1}1]$	$(110)\ [1\bar{1}1]$	$(\bar{2}\bar{1}1)\ [1\bar{1}1]$	$(121)\ [1\bar{1}1]$	$(\bar{1}12)\ [1\bar{1}1]$

The crystallography textbook *The mechanics of crystals and textured polycrystals* of William F. Hosford [113] is recommended to gain a better understanding of crystal orientation, rotation, and slip systems. However, most of the analyses and schematics are related to an FCC lattice structure. Therefore, the paragraphs below expand the work presented by Hosford to BCC metals and provides analyses on the activated slip systems with useful figures.

The Schmid factor of the primary slip system in a standard [001]–[101]–[111] inverse pole figure (IPF) triangle is schematically shown in Figure 2.10 by identifying the ϕ and λ angles in the stereographic projection of a unit sphere on the plane normal to [001]. Analyzing the {110}<111> family of slip systems is trivial due to similarities with the {111}<110> family in FCC metals. The Schmid factor of the primary {110}<111> slip system is maximum and equal to 0.5 for angles of 45° and loading along an axis close to the center of the IPF. This is schematically shown in Figure 2.10a by drawing a line between the projection of the normal to the (011) plane and the $[1\bar{1}1]$ slip direction. On the [001]–[111] boundary of the standard triangle, the Schmid factor is equal for the primary and conjugate planes. Similarly, the Schmid factor is equal on the primary and critical slip systems on the [001]–[101] boundary. The effect of equal Schmid factors will be further discussed in the *Single Crystal Orientation and Rotation* section below.

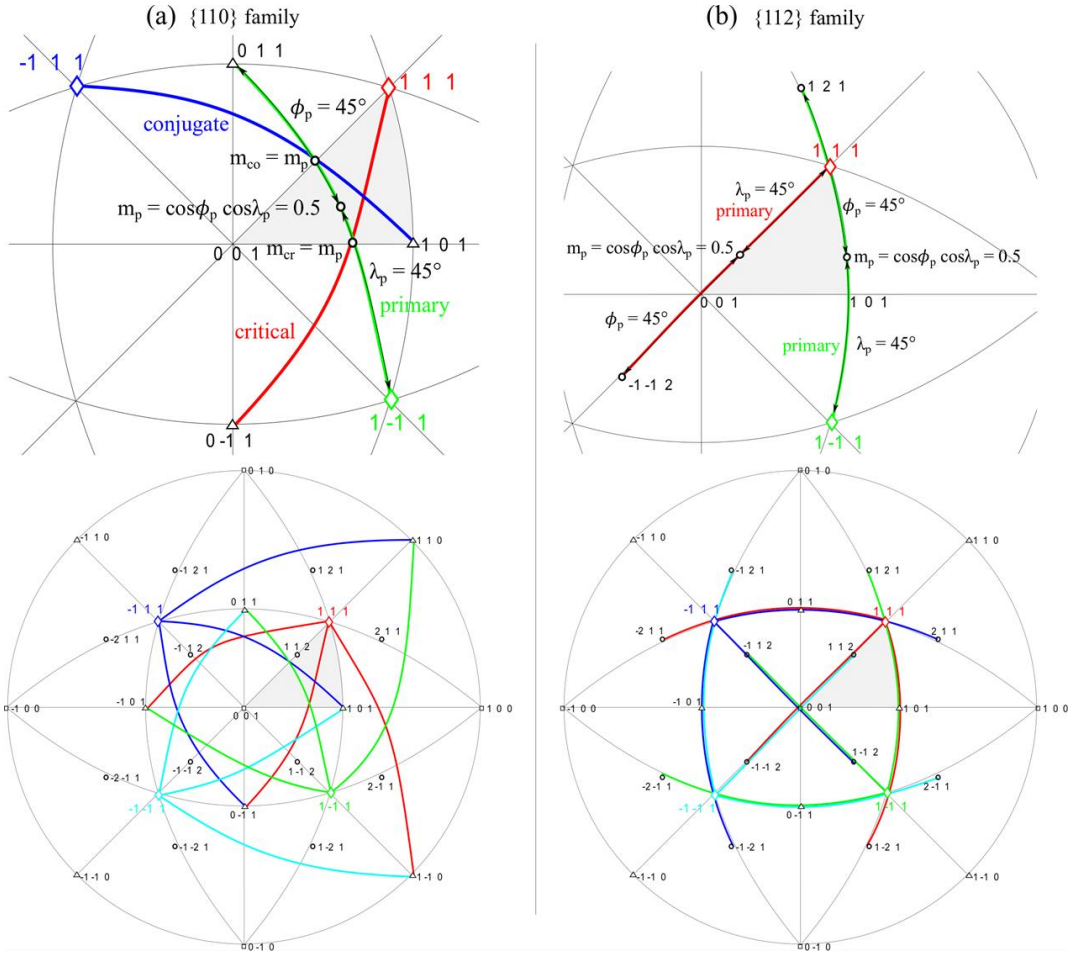

Figure 2.10: Schematic of the different slip systems on the stereographic projection for (a) the {110} and (b) the {112} slip families. Lines with the same color are for slip systems with the same slip direction (cross-slip systems) and (in grey) the standard triangle IPF used in orientation analyses. Variable m denotes the Schmid factor (SF) in this figure.

For the {112}<111> family of slip systems, the analysis from the schematic on the stereographic projection is more complicated. The lines drawn between the slip plane normal

and the slip direction lie on the boundaries of the standard triangle. The maximum Schmid factor for the {112} slip plane lies on the [001]–[111] and [101]–[111] boundaries of the standard triangle. Compared with the $(011)[1\bar{1}1]$ primary slip system for the {110} family, the $(\bar{1}\bar{1}2)[111]$ and $(121)[1\bar{1}1]$ slip systems could be defined as "primary slip systems of the {112} family". However, the $(121)[1\bar{1}1]$ slip system shares the same slip direction as the $(011)[1\bar{1}1]$ primary slip system and is then considered a *cross-slip* system. The cross-slip systems are visually identified in Figure 2.10 as the lines drawn from the same slip direction have the same color. Note that six slip planes share the same Burgers vector. Slip systems with the same slip plane, but different slip directions are called *coplanar* systems. The nature of the different active slip planes affects the interaction of the moving dislocations and, therefore, strain hardening.

From the definition of the Schmid factor in equation 2.12 and the 24 slip systems identified in Table 2.1, the Schmid factor can be calculated for all crystal orientations and displayed in an inverse pole figure. Figure 2.11 shows contour plots of the Schmid factor for the slip systems with the highest value. As shown in Figure 2.10, contour plots of the {110} and {112} slip systems have maximum Schmid factors close to the center and on the boundaries of the IPF, respectively. The combination of both slip systems explains *pencil-glide* in BCC metals [113]. However, the equi-Schmid factor lines would not be continuous as the Schmid factor drops between the regions of highest Schmid factors for {110} and {112}. The addition of the {123}<111> slip system, which could theoretically be activated in BCC metals, reduces this discontinuity and also agrees with pencil-glide (not shown).

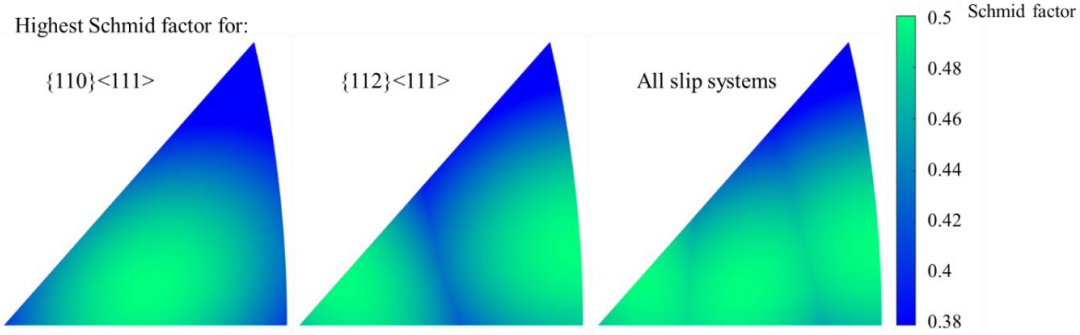

Figure 2.11: Schmid factor contour plots for different slip systems and all orientations in an IPF.

Since the primary slip system and its interaction with the secondary slip system affect slip and hardening, the identification of the two slip systems with the highest Schmid factor for different crystal orientations is calculated and presented in Figure 2.12a. This representation of the IPF was proposed as a tool to select crystal tensile orientations with different hardening behaviors. A similar approach for slip directions of the two slip systems with the highest Schmid factor is also calculated to identify regions where the slip directions are the

same or different (Figure 2.12b). Both plots in Figure 2.12 must be considered together when analyzing different hardening behaviors, because different slip systems sharing the same Burgers vector will not interact like slip systems with intersecting Burgers vectors.

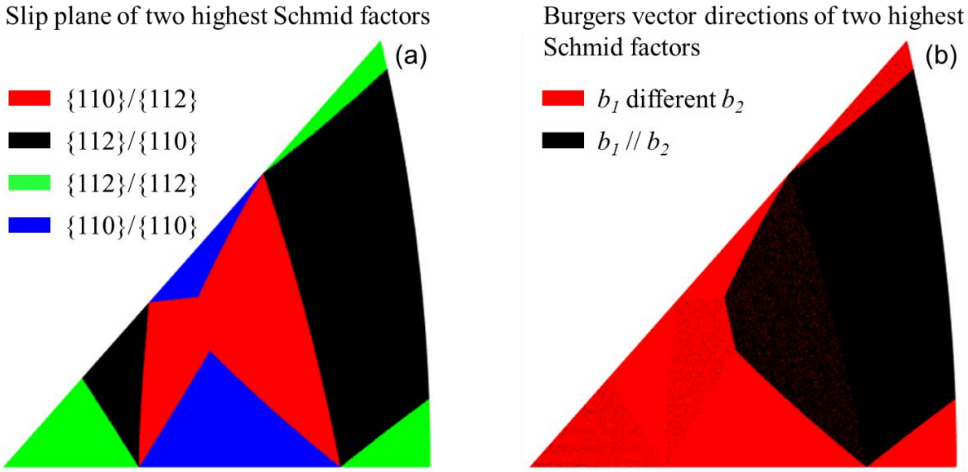

Figure 2.12: Inverse pole figures of the two slip systems with the highest Schmid factors for (a) the ratios of slip plane families and (b) the directions of the Burgers vectors. Small black and red dots in (b) are artefact of the resolution (number of points used in the calculation) and not physical.

2.3.4. Motion of Screw Dislocations: Kink Pair Nucleation and Motion

As previously mentioned, an accurate prediction of the activated slip systems in BCC metals for a given temperature and strain rate remains complicated [114]. Slip of screw dislocations is dominant during the deformation of BCC metals. Due to the non-planar core structure of screw dislocations, discussed in section 2.3.7., the lattice friction is more important than for edge dislocations. This difference in core structure explains the lower mobility of screw compared to edge dislocations. The nucleation of kink pairs to overcome a Peierls potential and move a dislocation, as shown in Figure 2.13, is likely responsible for the high lattice friction. This thermally activated mechanism is highly dependent on temperature and strain rate as thermal fluctuations provide some energy to reduce the stress required for the nucleation of a kink pair and the motion of a dislocation. The kink height is directly related to its enthalpy and is slip system specific. The kink heights for the {110} and {112} slip planes are respectively:

$$h_{110} = a_0\left(\frac{2}{3}\right)^{1/2} \approx 0.82a_0 \qquad h_{112} = a_0(2)^{1/2} \approx 1.4a_0$$

where h_{ijk} is the kink height for the $\{ijk\}$ slip plane, a_0 is the lattice constant.

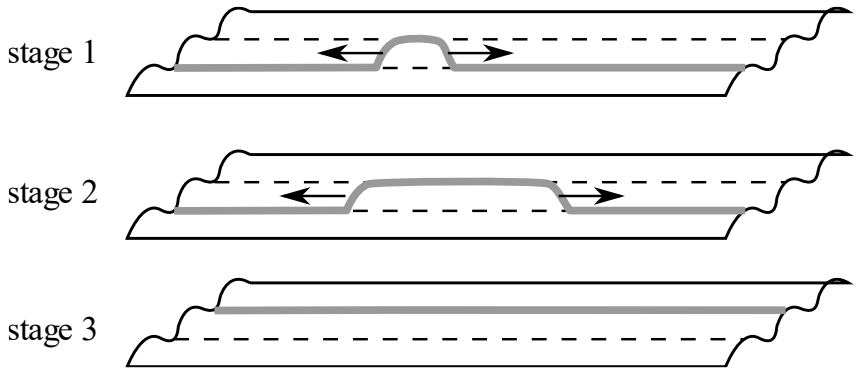

Figure 2.13: Motion of a dislocation over Peierls barrier by (stage 1) the nucleation and (stage 2) movement of a pair of kinks due to thermal fluctuation and an applied load. Redrawn from [115].

By analogy between the kink height and enthalpy, the energy required for the nucleation of kink pairs is lowest for the {110} planes and highest for the {112} planes. Thus, the activation of {110} planes should be dominant. However, temperature and strain rate affect the enthalpy, so elasticity theory models and atomistic simulations have been performed to determine the active slip systems for different BCC metals in different conditions [114].

For niobium single crystals, Seeger [112] developed a kink pair model to calculate the resolved shear stress on the {110}<111> slip system with the highest Schmid factor as a function of temperature to predict the activated slip planes in different temperature or stress regimes. The model predicted that the primary slip plane activated for all shear stress ranges studied (from 0 to 160 MPa) would be {112}. A kink pair model developed by Butt [116] was adapted by Ali [111] for niobium single crystals. This model predicted that slip will occur on the primary {110} plane for temperatures between 10 and 195 K and on the {112} plane for temperatures between 195 and 295 K. Finally, models of infinitely long screws at 0 K predicted that the effective slip plane would be the {112} alone [117], [118] or both {110} and {112} planes [119], [120].

The different predictions of all models show again the non-trivial prediction of the activated slip planes during the deformation of a niobium specimen. In addition, high strain rate tests have not been studied with these models. However, an analogy with low temperature can be made due to the lower time for thermal activation and the consequent higher flow stresses observed, but additional effects such as adiabatic heating and viscous drag could also affect the slip behavior at high strain rates. Since the highest strain rates obtained in this study in compression and tension are in the order of 10^3 s^{-1}, these two factors are not expected to be predominant, but should be kept in mind for future work at higher strain rates.

2.3.5. Dislocation Velocity

The velocity of dislocations depends on the applied shear stress, the purity of the crystal, the temperature, and the type of dislocation [105]. It can be measured by etching the surface of

a specimen to reveal dislocation pits and measuring the displacement of the pits following an imposed deformation. Repeating this experiment for different levels of stress yields the following empirical velocity relation at a constant temperature, valid for low speeds between 10^{-9} m/s and 10^{-3} m/s:

$$v_d \propto \left(\frac{\tau}{\tau_0}\right)^{1/m}$$

where v_d is the mean dislocation velocity, τ is the resolved shear stress, τ_0 is a reference shear stress (often at 1 m/s), and m is a positive material constant [105]. As previously mentioned, the nature of the dislocation affects its velocity. At low velocities, edge dislocations move about 50 times faster than screw dislocations [105]. The lower mobility of screw dislocation partially explains the higher mechanical properties of BCC metals at low dislocation velocities. At higher velocities, the above relation is no longer valid.

Figure 2.14 schematically shows the different dislocation velocity regimes as function of stress [121]. At stresses lower than a threshold stress $\hat{\tau}$ to overcome a short-range obstacle, the thermal activation and drag regimes operate. At higher stresses, the mean dislocation velocity rapidly increases and a linear regime of pure phonon, or viscous, drag is observed. As the velocity nears the speed of sound c in the material, relativistic effects are not negligible and explain the higher rate of increasing stress.

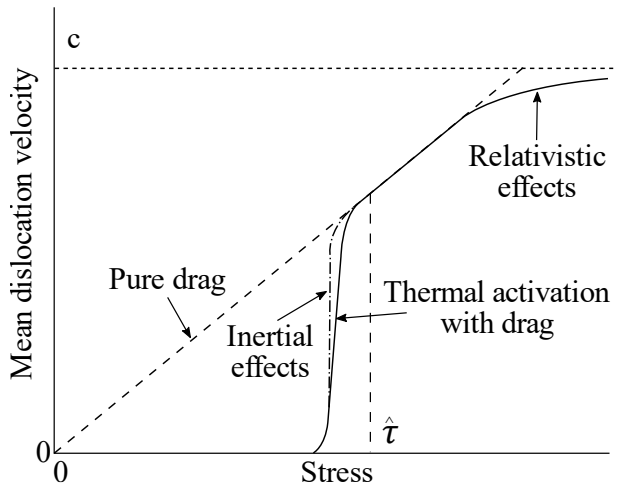

Figure 2.14: Mean dislocation velocity as function of stress showing the main regimes (1) thermal activation with drag, (2) pure drag, and (3) relativistic effects. Redrawn from [121].

The shear strain rate on a slip plane is defined by Orowan's equation as:

$$\dot{\gamma} = \rho b v_d \tag{2.13}$$

where $\dot{\gamma}$ is the shear strain rate, ρ is the mobile dislocation density (total length of the dislocations per unit volume), and b is the Burgers vector. As previously discussed, real

crystals have a non-zero initial dislocation density. A typical dislocation density for an annealed specimen is in the order of 10^9 to 10^{11} m^{-2} [122]. During a uniaxial test, the increase in dislocation density and in mean dislocation velocity are competing factors accommodating for the imposed strain rate. As shown in Figure 2.14, three dislocation velocity regimes exist. At strain rates below ~10^3 s^{-1}, the velocity of dislocation is generally defined by thermal activation mechanisms and a small contribution from phonon drag. At higher strain rate, the pure drag regime is dominant. As previously mentioned, the transition in deformation mechanism is experimentally observed as a change in slope on a stress as function of strain rate plot.

The contribution of viscous drag is then often considered in numerical models of specimens deformed at high strain rate. However, Lim et al. [123], [124] only considered thermally activated mechanisms for Taylor bar tests, with a maximum strain rate of about $5x10^5$ s^{-1}, performed on tantalum single crystals with four different orientations and observations and modeling supported slip on {112}. The contribution of the drag component of the flow stress for tantalum single crystals was only significant in the Livermore Multiscale Strength (LMS) model at strain rate greater than 10^7 s^{-1}, which provides a baseline critical strain rate for niobium [125]. The influence of viscous drag was considered at lower strain rates by Hoge and Mukherjee [126] to model the flow stress of tantalum polycrystalline specimens as a function of strain rate for a strain rate of up to ~10^3 s^{-1}. The effect of viscous drag is likely not significant in the current study due to the maximum strain rate of ~10^3 s^{-1}. However, the models used by Hoge and Mukherjee [126] are still described below since they are used in Chapter 4 in an attempt to explain an experimentally measured increase in flow stress by a change in deformation mechanism.

2.3.6. Strain Rate Analytical Modeling for Kink Pair Nucleation and Motion, and Viscous Drag

The strain rate at a given flow stress can be estimated for low strains when the dominant mechanisms by which screw dislocations move is known. The velocity of a dislocation is extrapolated to the strain rate of the specimen and the latter is calculated using the following simplification of Orowan's equation with the normal strain rate instead of the shear strain rate:

$$\dot{\epsilon} = \rho b v_d \tag{2.14}$$

The Burgers vectors of a screw dislocation in niobium is known to be along the <111> slip direction and its magnitude is calculated with the following equation:

$$b = \frac{1}{2}\|< 111 >\| = \frac{1}{2}\sqrt{a_0^2 + a_0^2 + a_0^2} = \frac{1}{2}\sqrt{3}a_0 \quad (2.15)$$

where a_0 is approximately equal to 3.3068 Å ($1\ Å = 10^{-10}$ m) for niobium [127], and $\|< 111 >\|$ is the distance in the lattice in the <111> direction.

As previously discussed, the dislocation velocity v_d depends on the dominant deformation mechanisms, which are dependent of temperature and strain rate. In this study, specimens were deformed at strain rates of up to about 1 000 s^{-1} in tension and 4 000 s^{-1} in compression. Also, an activation volume v^* of about 10 to 10^2 b^3 at all strain rates would suggest that the nucleation of kink pairs to overcome Peierls potential, shown in Figure 2.6a and Figure 2.13, is the dominant deformation mechanism [112], [114], [115], [128], [129]. The activation volume is then calculated from experimental tests in Chapter 4 to identify a potential change in deformation mechanism. A contribution of viscous drag would also affect the dislocation velocity and is therefore considered. The different components of the strain rate equation (eq. 2.14) for thermal activation and dislocation drag are presented in the following sections.

2.3.6.1. Thermal Activation and Kink Pair Nucleation

For the thermal activation mechanism, the flow stress is low compared with the Peierls stress since thermal fluctuations provide an important amount of energy to the dislocations to overcome barriers. The strain rate equation of plastic flow controlled by thermal fluctuations at ambient temperature follows an Arrhenius equation:

$$\dot{\epsilon} = \dot{\epsilon}_0 \exp\left(-\frac{G(\sigma)}{k_B T}\right) \quad (2.16)$$

where $\dot{\epsilon}_0$ is a reference strain rate that is mainly dependent on the dislocation density and vibrational frequency (Debye frequency), G is the Gibbs free energy, k_B is Boltzmann constant, and T is the absolute temperature [130].

Hoge and Mukherjee [126] expended equation 2.16 for thermal activation of screw dislocations in their study of tantalum to the following equation:

$$\dot{\epsilon} = \frac{\rho b^2 L a \nu}{2w^2} \exp\left(-\frac{U_n}{k_B T}\right) \quad (2.17)$$

where L is the dislocation segment length, a is the distance between Peierls valleys, ν is the Debye frequency (SI unit: s^{-1}), w is the width of a kink loop, and U_n is the energy to nucleate a pair of kinks.

The distance between Peierls valleys a, often defined as the shortest lattice translation, of niobium used by Seeger and Holzwarth [112] of 4.78×10^{-10} m is used in this study. Note that other studies often use the approximation $a \approx b$, which would be approximately 1.7 times smaller than the value used in [112], but this is not exactly valid in screw or mixed dislocations [115].

The Debye frequency of niobium is calculated using the following relation with the Debye temperature T_D:

$$\nu = \frac{k_B}{h} T_D \tag{2.18}$$

where h is the Planck constant, a relation between a phonon's energy and frequency, ($\sim 6.626 \times 10^{-34}$ J. s). For a Debye temperature of 260 K at room temperature (298 K) [131], the Debye frequency of niobium is $\sim 5.42 \times 10^{12}$ s^{-1}.

The width of a kink loop w for niobium is equal to 21.5 b or ~6.157×10^{-9} m [129] and the dislocation segment length L was not found in the literature. The parameter of tantalum, a similar BCC metal, is then used and is equal to $L = 10^4 b$. The energy to nucleate a pair of kinks U_n can be expressed as a function of the flow stress. First, the flow stress in decomposed in a strain rate and temperature dependent effective stress, also referred as the thermally activated stress, $\sigma^*(\dot{\epsilon}, T)$ and a strain dependent athermal component $\sigma_A(\epsilon)$:

$$\sigma_T = \sigma^*(\dot{\epsilon}, T) + \sigma_A(\epsilon) \tag{2.19}$$

The effective (thermally activated) component is related to the stress required to overcome the lattice friction. The athermal component is related to long range barriers, such as grain boundaries, second phases, and dispersion. At high temperature, above a critical value dependent on the strain rate, the flow stress is equal to the athermal component, meaning that no additional effective load is required for dislocation motion since the thermal energy contribution is sufficient to overcome short range obstacles. Figure 2.15 shows the relation between stress and temperature for materials where the Peierls mechanism is dominant, e.g. BCC metals.

From Hoge and Mukherjee [126], the athermal stress component at room temperature is calculated with the following equation:

$$\sigma_{A,293} = \sigma_{A,T} \frac{G_{293}}{G_T} \tag{2.20}$$

where G_{293} is the shear modulus at 293 K, and $\sigma_{A,T}$ and G_T are the athermal stress and the shear modulus at a temperature T.

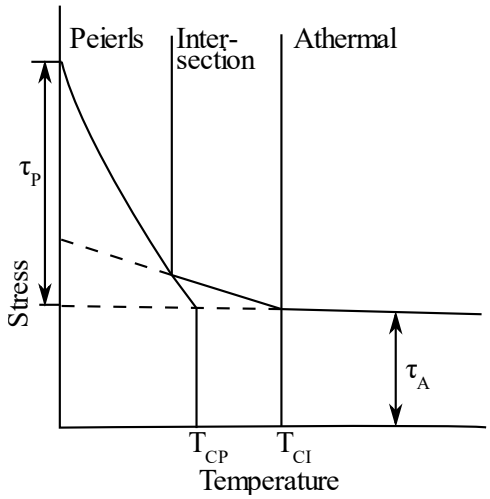

Figure 2.15: Relation between shear flow stress and temperature for material undergoing Peierls mechanism. Redrawn from Dorn and Rajnak [132].

Guyot and Dorn [133] showed that for sinusoidal hills, a reasonable approximation for this model that does not consider non-Schmid behaviors, the relation between the kink (U_k) and pairs of kink nucleation (U_n) energies and the effective and Peierls stress (σ_P) at 0 K is given by:

$$\frac{U_n}{2U_k} = \left(1 - \frac{\sigma^*}{\sigma_P}\right)^2 \tag{2.21}$$

Combining equations 2.17 and 2.21, the following equation relating the strain rate and effective stress for dislocation glide described by the nucleation of pair of kinks by thermal activation is obtained:

$$\dot{\epsilon} = \frac{\rho b^2 La\nu}{2w^2} \exp\left(\frac{2U_k}{k_B T}\left(1 - \frac{\sigma^*}{\sigma_P}\right)^2\right) \tag{2.22}$$

Different values of kink pair nucleation energy are available in the literature. Seeger and Holzwarth [112] used 0.68 eV for their model, Takeuchi et al. used 0.62 eV [134], and density-functional theory (DFT) calculations from Dezerald et al. [129] yielded kink pair nucleation energy of energy of 1.28 eV. The experimental values of 0.62 and 0.68 eV are used as starting points in the model.

2.3.6.2. Dislocation Drag

The dislocation drag mechanism is dominant at strain rates high enough for dislocations to overcome barriers without assistance from thermal fluctuations, i.e. when the applied load is greater than the Peierls and the pinning forces [115]. This leads to a sharp increase in stress

and a dislocation velocity dependent load, as per the *viscous* drag appellation. More details about this mechanism are available in review articles like the one of Shilo and Zolotoyabko [115].

The force exerted by a dislocation in the assumption that viscous drag is the only mechanism is given by:

$$\sigma^* b = B v_d \tag{2.23}$$

where σ^* is the effective shear stress and B is the viscosity coefficient (SI unit: Pa. s).

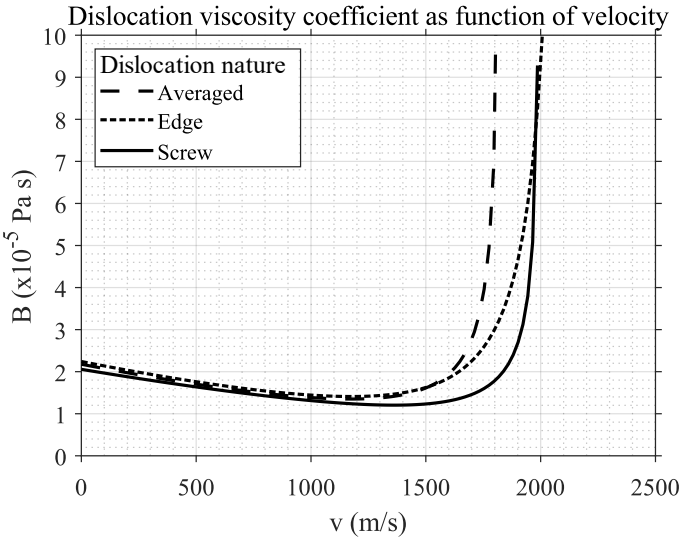

Figure 2.16: Dislocation viscosity coefficient of niobium for edge and screw dislocations as function of dislocation velocity [137].

B was experimentally measured by Al'Shitz and Indenbom [135] for niobium and equal to 0.17 mPoise (1.7×10^{-5} Pa.s). This value will be used as a starting point in Chapter 4, but might be changed due to the large error, in the order of hundreds of percent [115], in the determination of the viscosity coefficient. As a comparison, Steinberg and Lund [84] used a viscosity coefficient of 10^{-4} Pa.s for tantalum. Hoge and Mukherjee [126], whose work was used by Steinberg and Lund, used a coefficient equal to 100 Pa.s. The large difference between the two papers citing the same original work and the comparison with the niobium value reported by [135] lead us to believe that the 10^{-4} Pa.s value is the correct one. Note that the original work reporting this value was published in a conference proceeding that could not be found [136]. The 1.7×10^{-5} Pa.s value reported by Al'Shitz and Indenbom [135] is also in agreement with recent theoretical work of Blaschke [137]. However, it is important to note that the dislocation viscosity coefficient found by Blaschke is dependent on the velocity and the nature of the dislocation, i.e. screw or edge dislocations, as shown in Figure 2.16. A sharp increase in B is expected at a critical dislocation speed. For a screw dislocation in niobium, the critical speed v_c^s is equal to 1 997 m/s [137].

The combination of the thermal activation and viscous drag models, equations 2.22 and 2.23, gives the following equation that was used by Hoge and Mukherjee [126] for tantalum and will be used for niobium in Chapter 4:

$$\dot{\epsilon} = \frac{\rho b^2}{\frac{2w^2}{Lav}\exp\left(\frac{2U_k}{k_B T}\left(1-\frac{\sigma^*}{\sigma_P}\right)^2\right)+\frac{B}{\sigma^*}} \tag{2.24}$$

The objectives of analytical modeling of strain rate as a function of the applied stress for niobium single crystals are twofold. First, to investigate if an increase in flow stress at high strain rate is caused by viscous drag. This would indicate a change in deformation mechanisms at a strain rate between 10^{-4} to 10^{3} s^{-1} for specimens deformed in tension and in compression. Second, to identify parameters that could be used by other researchers in future crystal plasticity models.

2.3.7. Non-Schmid Behaviors

According to Schmid law, plastic flow, or the motion of a dislocation, occurs when the resolved shear stress (equation 2.13) is larger than the critical resolved shear stress τ_{CRSS}. Deviations from this law have been reported for BCC metals was first discussed by Taylor [138] in his study of β-brass where the resistance to slip in opposite directions for a given plane was found to be different. This observation was made on measurements of different yield stress for single crystals with the same crystal orientation deformed in tension and in compression. This tension/compression (T/C) asymmetry is due to non-glide shear stress components in the core structure of screw dislocations and can result in the activation of different slip systems for crystals deformed in tension and compression. More precisely, the non-planar core structure of a <111> screw dislocation is explained by spreading of the dislocation on three symmetric {110} or {112} slip planes that share the same <111> direction. This is shown schematically in Figure 2.17 from Po et al. [139] with stress components accounting for non-Schmid effects in their crystal plasticity model and mathematically defined as follow:

$$\tau_{crss}(\alpha) = \tau^{\alpha} + \sum_{i=1}^{N_{ns}} a_i \tau_i^{\alpha} \tag{2.25}$$

where α represents the slip system in the glide direction, N_{ns} is the number of slip systems with non-glide components considered in the model, a_i is the non-Schmid coefficient for the i^{th} non-Schmid component, often temperature or strain rate dependent, and τ^{α} and τ_i^{α} are the shear stress resolved on their respective slip systems.

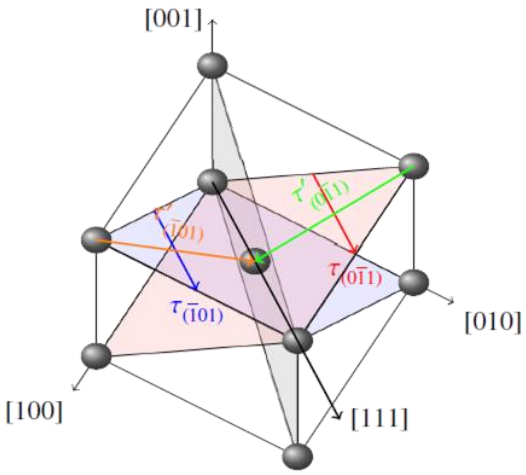

Figure 2.17: Schematic of the stress components used by Po et al. [139] to model non-Schmid effects for slip in the [111] direction. The $\tau_{(\bar{1}01)}$ shear stress component has the highest Schmid factor and the $\tau_{(0\bar{1}1)}$, $\tau'_{(\bar{1}01)}$, and $\tau'_{(0\bar{1}1)}$ shear stress components are responsible for the non-Schmid effects. From Po et al. [139].

A lower resistance to dislocation glide, i.e. a lower τ_{CRSS}, in the twinning slip direction, compared to the anti-twining direction, was also reported for BCC metals [106], [117], [140]. This phenomenon is defined as the twinning/anti-twinning (T/AT) asymmetry. The theoretical yield stress considering T/AT asymmetry is given by:

$$\sigma_y = \frac{\sigma_o}{\cos\chi + a_1 \cos(\chi + 30°)} \tag{2.26}$$

where σ_y is the yield stress for the considered orientation, σ_o is a reference stress, often the Peierls stress, a_1 is a material constant, and χ is the previously defined angle, in degrees. Without the second term of the denominator, the yield stress in equation 2.26 would be symmetric and follow Schmid's law.

The development of a crystal plasticity model with non-Schmid effects that would account for the T/C and T/AT asymmetries is beyond the scope of this study. The reader is then invited to read the PhD thesis of Aboozar Mapar [141], [142], where two hardening laws were used to model the anisotropic mechanical properties of niobium single crystals deformed at low strain rates. A main conclusion of this work was that the hardening laws were capturing the general hardening behavior, but not accurately predicting the different hardening stages.

For niobium single crystals, Duesbery et al. [108] identified the slip systems activated during tensile and compression tests and grouped them by families of slip plane to investigate T/C asymmetry. Figure 2.18 shows the experimental results obtained in that study and the translation of the boundaries separating regions where the {110} and {112} slip planes should theoretically be activated. Based on the experimental results of Duesbery et al. [108],

the theoretical boundaries in tension shifted closer to the [101]–[111] boundary and the theoretical boundary in the right-half of the IPF in compression shifted closer to the [001] direction, effectively reducing the amount of orientations prone to activate the primary {110}<111> slip system.

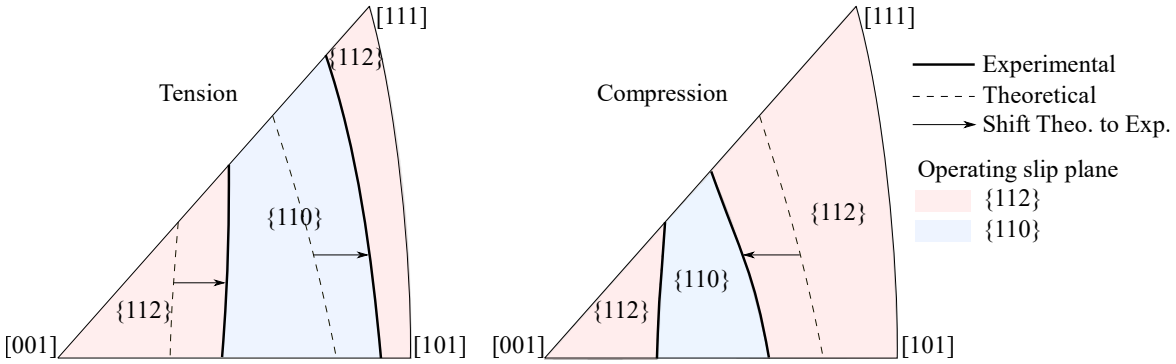

Figure 2.18: Superposition of the theoretical operative slip system boundaries with experimental results from Duesbery et al. [108] showing a shift in the transition of operative slip system for single crystals loaded in tension and compression at room temperature.

Experimental results report that non-Schmid effects are more important at low temperatures since the contribution of non-Schmid stress components to the yield stress is more significant, e.g. Spitzig and Keh [143] for iron single crystals. For thermally activated deformation mechanisms, an analogy between low temperature and high strain rate due to the low contributions to reducing the effective stress, could be observed in this study. The importance of non-Schmid effects at different strain rates is then investigated for niobium single crystals.

More details about non-Schmid behaviors are available in Christian's review on plastic deformation of BCC metals [106] and Duesbery and Vitek's article on plastic anisotropy in BCC transition metals [117].

2.3.8. Single Crystal Orientation and Rotation

While an accurate determination of the activated slip system is not trivial in BCC metals, as discussed in the previous sections, crystal rotation during a tensile or compression test is predictable. Figure 2.19 schematically shows the deformation of single crystals at the scale of the specimen for an ideal case with a free end that translates away from the original loading axis and the more realistic case where the crystal is forced to rotate since both ends are fixed. During a tensile test, the ends of the specimens are held by the fixture of the testing machine and results in a rotation of the specimen toward the tensile axis. This results in a rotation of the lattice in the tensile direction toward the Burgers vector of the active slip system or the effective Burgers vectors if multiple slip systems are activated. As previously discussed, the $(011)[1\bar{1}1]$ slip system is the primary system. Therefore, the crystal rotates

towards the $[1\bar{1}1]$ direction. However, if the tensile axis of the crystal is oriented in region B of Figure 2.19a, the Schmid factor is higher for the $(\bar{1}\bar{1}2)[111]$ slip system, which leads to a rotation toward the [111] direction (see black arrows in region B of Figure 2.19a). As the crystal rotates and the tensile axis orientation crosses to region A, slip occurs on the $(011)[1\bar{1}1]$ system and the crystal rotates toward the $[1\bar{1}1]$ direction. For a tensile orientation along the [001]–[101] boundary, the Schmid factor is equal on the primary and critical ($(0\bar{1}1)[111]$) slip systems. The activation of both slip systems and the rotations toward the $[1\bar{1}1]$ and [111] directions result in an effective rotation toward the [101] direction. The [101] direction is then considered the *stable end orientation* for BCC single crystals deformed in tension.

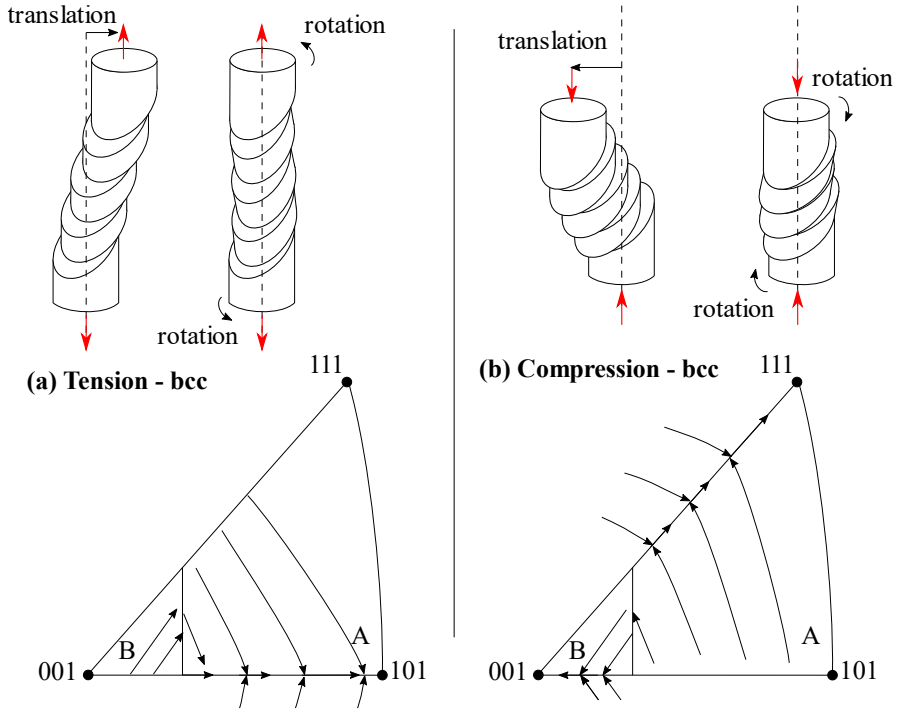

Figure 2.19: (a) Tensile and (b) compression rotation paths for BCC metals with their respective end stable orientations, [121] and [110] respectively, for the [100]-[110]-[111] standard triangle. Redrawn from [113].

In compression, the motion of the top and bottom faces of the cylindrical specimen is restricted due to friction forces. The single crystal tends to rotate away from the loading axis and away from the Burgers vector. The opposite rotation paths than the ones described in tension are then expected in regions A and B, as shown in Figure 2.19b. The [001] and [111] directions are the stable end orientations for BCC single crystals deformed in compression with initial crystal orientations in regions B and A, respectively.

A significant rotation of a single crystalline specimen leads to the activation of one or multiple different slip systems. This geometric hardening, or softening, is expected to occur during the tests performed in this study since the tensile specimens will be deformed up to

rupture and high-purity niobium has a high ductility. Experimentally, the crystal orientation can be measured during testing using X-ray diffraction (XRD) or before and after testing using XRD or electron backscattered diffraction (EBSD). Also, when possible, the test can be interrupted to acquire orientation related data at different levels of strain.

Orientation related data are often given by EBSD or XRD measurements as three Bunge Euler angles ϕ_1, Φ, and ϕ_2. Figure 2.20 shows the effect of each angle to convert the sheet coordinate system (X, Y, Z) to the crystal coordinate system (x, y, z). The first angle, ϕ_1 is a counterclockwise (ccw) rotation about the Z axis of the sheet coordinate system. The second angle, Φ is the ccw rotation about the x' axis. The third angle, ϕ_2, is the ccw rotation about the z'' axis. The Bunge Euler angles are intrinsic, meaning that the order of the successive rotations matters.

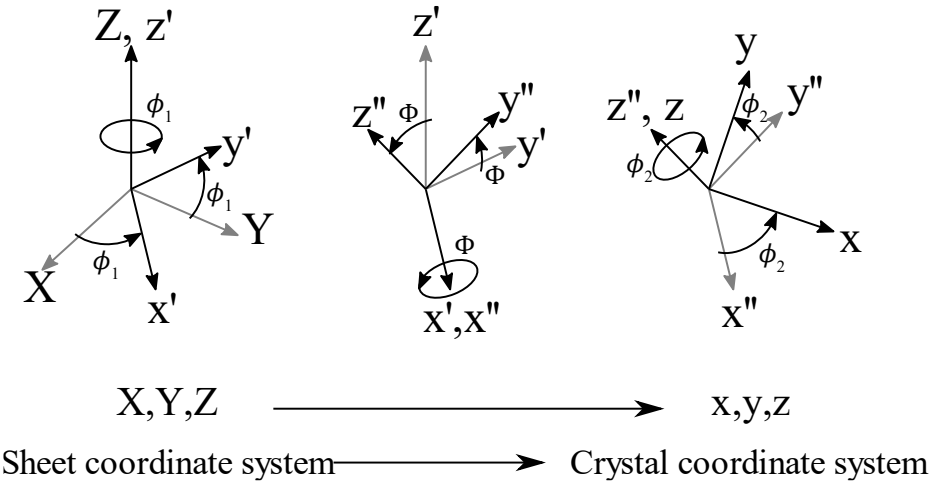

Figure 2.20: Schematic of the rotation from the sheet coordinate system to the crystal coordinate system with the ϕ_1, Φ, and ϕ_2 Bunge Euler angles. At each step, the axes in grey are along the original direction (before rotation) and black arrows are the rotated axes.

To calculate the crystal coordinate system or, more importantly in this study, to calculate the Schmid factor for different crystal orientations, the Euler angles are used to find a unique orientation matrix $\underline{\underline{g}}$ defining the crystal coordinate system. Different combinations of Euler angles can result in the same transformation of coordinate systems and will all yield the same orientation matrix. For example, the Schmid factor was calculated for all slip systems in Table 2.1 for millions of different loading directions covering an entire inverse pole figure to generate Figure 2.11 and Figure 2.12.

The orientation matrix is obtained from rotation matrices. A rotation matrix is used to rotate a vector into a different coordinate system by performing a ccw rotation of a given angle around a defined axis. The rotation matrices of the three Bunge Euler angles are defined below.

First, a rotation matrix of ϕ_1 radians around the Z-axis is defined as:

$$\underline{\underline{R_Z}}(\phi_1) = \begin{bmatrix} \cos\phi_1 & -\sin\phi_1 & 0 \\ \sin\phi_1 & \cos\phi_1 & 0 \\ 0 & 0 & 1 \end{bmatrix} \tag{2.27}$$

Similarly, a rotation matrix of Φ radians around the x'-axis is defined as:

$$\underline{\underline{R_{x'}}}(\Phi) = \begin{bmatrix} 1 & 0 & 0 \\ 0 & \cos\Phi & -\sin\Phi \\ 0 & \sin\Phi & \cos\Phi \end{bmatrix} \tag{2.28}$$

Finally, a rotation matrix of ϕ_1 radians around the z''-axis is defined as:

$$\underline{\underline{R_{z''}}}(\phi_2) = \begin{bmatrix} \cos\phi_2 & -\sin\phi_2 & 0 \\ \sin\phi_2 & \cos\phi_2 & 0 \\ 0 & 0 & 1 \end{bmatrix} \tag{2.29}$$

By multiplication of the rotation matrices in the order given in Figure 2.20 with a vector in the sheet coordinate system, the resulting vector will be in the crystal coordinate system.

First, the (x', y', z') coordinate system is obtained by rotation of the sheet coordinate system (X, Y, Z) by the rotation matrix $\underline{\underline{R_Z}}(\phi_1)$:

$$\begin{bmatrix} x' \\ y' \\ z' \end{bmatrix} = \underline{\underline{R_Z}}(\phi_1) \begin{bmatrix} X \\ Y \\ Z \end{bmatrix}$$

Second, the (x'', y'', z'') coordinate system is obtained by rotation of the (x', y', z') vector by the rotation matrix $\underline{\underline{R_{x'}}}(\Phi)$:

$$\begin{bmatrix} x'' \\ y'' \\ z'' \end{bmatrix} = \underline{\underline{R_{x'}}}(\Phi) \begin{bmatrix} x' \\ y' \\ z' \end{bmatrix}$$

Finally, the (x, y, z) crystal coordinate system is obtained by rotation of the (x'', y'', z'') vector by the rotation matrix $\underline{\underline{R_{z''}}}(\phi_2)$:

$$\begin{bmatrix} x \\ y \\ z \end{bmatrix} = \underline{\underline{R_{z''}}}(\phi_2) \begin{bmatrix} x'' \\ y'' \\ z'' \end{bmatrix}$$

The orientation matrix is defined as the transpose of the rotation matrix. For the three Euler angles, the corresponding orientation matrices are defined as:

$$\underline{\underline{g}}_{\phi_1} = \underline{\underline{R_z}}(\phi_1)^T \qquad \underline{\underline{g}}_{\Phi} = \underline{\underline{R_{x'}}}(\Phi)^T \qquad \underline{\underline{g}}_{\phi_2} = \underline{\underline{R_{z''}}}(\phi_2)^T$$

Finally, the orientation matrix of the crystal coordinate system is defined as a combination of the orientation matrix of each Euler angle as:

$$\underline{\underline{g}} = \underline{\underline{g}}_{\phi_2}\underline{\underline{g}}_{\Phi}\underline{\underline{g}}_{\phi_1} \tag{2.30}$$

The second order stress tensor for a tensile test along the sheet (disk) Y-axis is defined as:

$$\underline{\underline{\sigma}}_{disk} = \begin{bmatrix} 0 & 0 & 0 \\ 0 & 1 & 0 \\ 0 & 0 & 0 \end{bmatrix} \tag{2.31}$$

To transform stress tensor in the crystal coordinate system, the orientation matrix is used as follow:

$$\underline{\underline{\sigma}}_{crystal} = \underline{\underline{g}}\,\underline{\underline{\sigma}}_{disk}\,\underline{\underline{g}}^{T} \tag{2.32}$$

Finally, the Schmid factor of a given slip system with normal unit vector to a plane direction $\hat{n}$ and unit slip direction $\hat{b}$ is given by:

$$SF = \left(\underline{\underline{\sigma}}_{sheet}\,\hat{b}^{\mathrm{T}}\right) \cdot \hat{n} \tag{2.33}$$

A numerical example of the calculation of the Schmid factor using measured crystal orientations is provided in section 3.1.1.1. to help future students or professionals to implement these equations in a software.

2.3.9. Single Crystal Stress–Strain Curves

The mechanical properties of single crystals are often presented on plots of the resolved shear stress as function of the resolved shear strain. The normal stress σ is resolved on the slip system with the highest Schmid factor for single glide. However, the activation of multiple slip systems, the rotation of a crystal leading to the activation of different slip systems (geometrical hardening), and non-Schmid behaviors in BCC metals all complexify the calculation of the resolved shear stress. Therefore, multiple studies on the mechanical properties of niobium single crystals up to failure in tension report the mechanical properties with the engineering stress and strain. The mechanical properties obtained in this study are reported with engineering stress–strain curves. The resolved shear stress–resolved shear strain curve is however still discussed in this section since it is used to explain the three hardening stages often measured during tensile or compression tests.

Figure 2.21a shows the theoretical resolved shear stress–resolved shear strain curve with the three hardening stages. Stage I, called *easy glide*, has a low linear hardening rate and can be absent or extend up to large strains. During this stage, slip occurs on only one slip system.

The low interaction of dislocations gliding on parallel planes and in parallel directions with the elastic field of neighboring dislocations explains the low strain hardening rate. The transition to stage II indicates the activation of a second slip system and, therefore, depends on the rotation of the single crystal. The extent of stage I is then highly dependent on the initial orientation of the crystal along the loading direction. Stage II has the highest hardening rate due to dislocation entanglement and is characterized by an approximately linear stress–strain curve. Finally, parabolic hardening is observed in stage III, which is associated with dynamic recovery [144], and explained by a saturation of the dislocation density and flow stress due to the annihilation of dislocations.

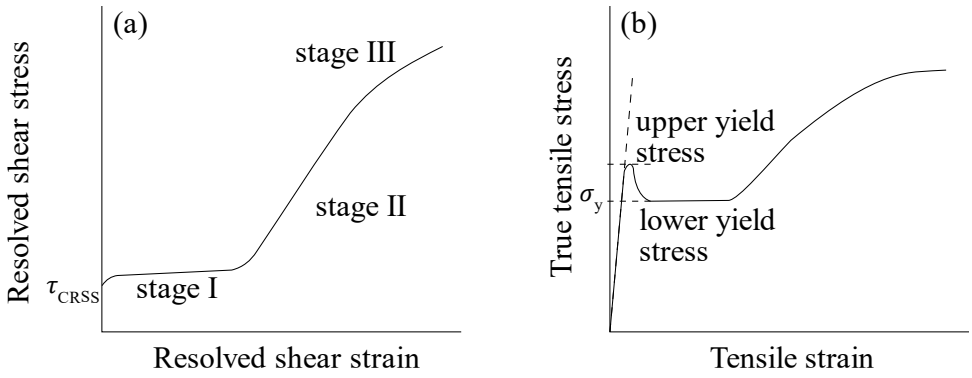

Figure 2.21: Stress-strain curve of BCC metals with (a) the shear components for single crystals and (b) Lüders band. Redrawn from [105].

Figure 2.21b shows a true stress–strain curve with a yield drop and Lüders band that indicate a plastic strain heterogeneity. Dislocations are multiplying at the band front that is rapidly moving in the specimen, often visible with digital image correlation, until the strain is uniform and strain hardening begins. This phenomenon is common in steels due to the interaction of dislocations with carbon interstitial atoms.

2.3.10. Mechanical Properties of Niobium Single Crystals

The mechanical properties of niobium single crystals at low strain rates have been investigated since the 1950s, when the element was still called Columbium [110]. Extensive research on the mechanical properties for different orientations, purity levels, heat treatments, temperatures, and strain rates of high-purity single crystals mostly took place in the 1960s. More interest arose in the 2000s for the fabrication of large grain SRF cavities. The tensile mechanical properties of niobium single crystals cut from large-grain disks used for the fabrication of SRF cavities have been measured at several universities and research laboratories, but never at strain rates larger than 10^{-1} s^{-1}. The effects of crystal orientation [140], [145]–[149], heat treatment [108], [146], [149]–[152], interstitial hydrogen content [150]–[152], testing temperature [146], [153], [154] and strain rate [145], [146], [151], [152], [155] on mechanical properties of niobium single crystals have been published in literature.

Figure 2.22 shows a summary of the number of publications, including peer-reviewed journal articles, conference papers, and relevant presentations, on the mechanical properties of niobium single crystals, based on the literature review of the author.

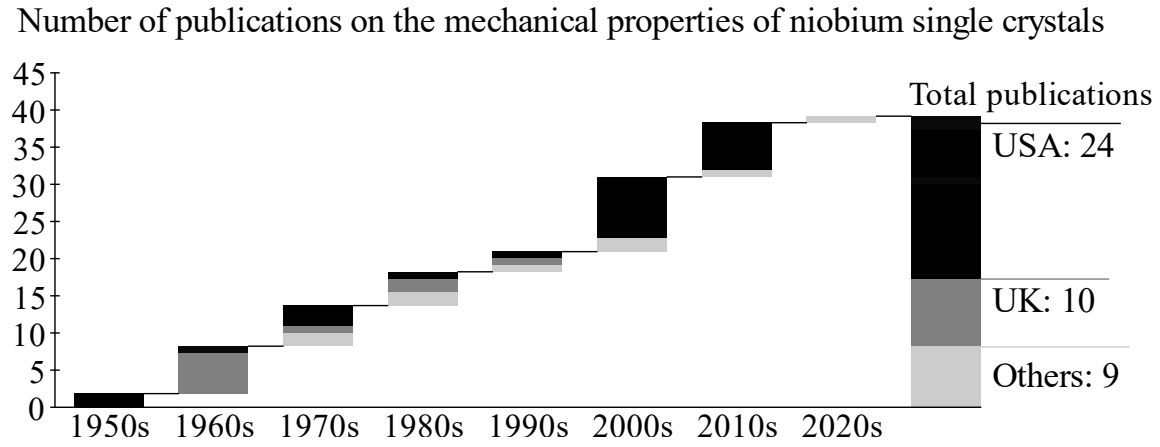

Figure 2.22: Number of publications (journal articles and conference papers) and available relevant presentations on the mechanical properties of niobium single crystals per decade and region of the first author, based on the literature review of the author [20], [27], [32], [108]–[110], [117], [130], [134], [140], [145]–[176].

Mitchell et al. [145] performed tensile tests at a nominal strain rate of 4.5×10^{-5} s^{-1} in seven different orientations. No trends were observed for most of the hardening parameters, i.e. the hardening rate of the three stages of single crystal deformation and the shear stress at their beginning and end. The extent of hardening stages I and II were lower for orientations closer to the [001]–[101] symmetry boundary. Specimens on the boundary showed no stage I (easy glide), higher yield stress [146], and the lowest strain at failure [145]. The [101] orientation is the terminal stable tensile orientation of BCC metals [113].

Duesbery et al. [146] observed slip traces on only {110} and {112} planes in niobium single crystals with differences in the critical resolved shear stress (τ_{CRSS}) for the two families. Ermakov et al. [147] observed anisotropic tensile properties in the plastic regime with different hardening behaviors and strain at fracture for three different orientations. According to Gnäupel-Herold et al. [151], the differences in yield stress, hardening stages, and the presence or absence of a yield drop cannot be solely attributed to anisotropy but are also probably affected by sample inhomogeneities and purity.

Baars et al. [148] calculated the Schmid factor of the 24 {110} and {112} potential slip system families for large grains within a sliced sheet of a niobium ingot to select the tensile orientations of specimens such that the resolved shear stress on selected slip systems is maximized. Tests were interrupted before failure and lattice orientation gradients were measured to quantify the rotation of the single crystals. A larger misorientation spread within the crystal after deformation was measured for three orientations close to the

[001]–[111] and [001]–[101] boundaries of the IPF, and these showed the highest strain hardening. This could be explained by dislocation tangles in cases where the active systems have Burgers vectors in different directions [148]. Finally, it was concluded that the highest resolved shear stress might not lead to the activation of that slip system but that a more complicated criterion involving non-Schmid behavior governs slip [148].

The effects of heat treatment on the tensile mechanical properties were reported by Duesbery et al. [108], [146], Myneni [150], Gnäupel-Herold et al. [151], Ricker et al. [152], and Kang et al. [149]. A reduction of yield stress caused by annihilation of dislocations after high temperature exposure was generally reported. However, an increase in yield stress reported by Gnäupel-Herold et al. was explained by the outgassing of interstitial hydrogen atoms absorbed during electrical-discharge wire cutting of specimens [151]. Hydrogen atoms are known to enhance screw dislocation mobility at room temperature and increase dislocation velocity, which could account for softening prior to removing hydrogen [177], [178]. Since most heat treatments of niobium are performed in vacuum at temperatures greater or equal to 800°C, it is expected that the reduction of dislocation density and the partial outgassing of hydrogen are competing factors with opposing influence on mechanical properties. While absorption of hydrogen in interstitial sites during the heat treatment could take place during the furnace cooldown [150], most of the atoms are expected to be removed from the furnace during the high temperature vacuum heat treatment. Kang et al. [149] reported that the primary slip system for as-extracted specimens (by electrical-discharge machining (EDM) followed by a brief buffered chemical polishing (BCP) etch) was for a {112} plane, in contrast to predominant slip on {110} planes for vacuum heat-treated specimens. This was established by ranking the ratio of Schmid factor of the primary and secondary slip systems, identifying the rotation axes, and by slip trace analyses. The observed change in the preferred slip system could be due to an alteration of the core structure of screw dislocations by removal of interstitial hydrogen atoms during vacuum heat treatment [149]. Finally, Duesbery et al. [108], [146], Myneni [150], and Ricker et al. [152] observed an increase in strain at failure for annealed specimens.

The effect of hydrogen interstitials was studied independently of the heat treatment by Myneni [150] following buffered chemical polishing of specimens and by Gnäupel-Herold et al. [151] and Ricker et al. [152] following electrical discharge machining of specimens immersed in water. A reduction of yield stress was reported in all studies with increasing hydrogen content. Ricker et al. [152] noted that residual stresses on the surfaces from EDM could affect the mechanical properties and potentially result in greater stresses at that surface compared to the bulk of the specimen. The presence of hydrogen interstitial atoms also leads

to a reduction of ductility. At a high hydrogen concentration, much higher than the level found in SRF cavities, hydrogen embrittlement can occur and it results in a reduction of ultimate tensile strength and a change in fracture mode that is detrimental for all sheet forming processes [179], [180]. The lack and difficulty of quantification of the hydrogen (and other impurity) content in published results complicates any attempt for quantitative comparison between different studies.

The effect of testing temperature on yield stress in niobium single crystals was published by Duesbery and Foxall [146], Nagakawa and Meshii [153] and Byun et al. [154] for temperature ranges of 77 to 523 K, 4.2 to 77 K, and 77 to 295 K, respectively. A reduction of yield stress with increasing temperature was reported in all studies. Nagakawa and Meshii compared tensile properties at low temperature of two distinct crystal orientations, one near the center of the IPF and the other on the boundary of the IPF, between the [110] and [111] orientations. Different stress–strain curves were obtained for the different orientations. A load drop was observed for a specimen located on the [110]–[111] boundary of the IPF and was caused by the formation of a macroscopic shear band. This specimen also mostly deformed by primary slip until severe necking. Duesbery and Foxall [146] and Byun et al. [154] observed a reduction in ductility with decreasing temperatures for specimens with different tensile orientations.

The effect of strain rate on the tensile properties were reported by Mitchell et al. [145], Duesbery and Foxall [146], Gnäupel-Herold et al. [151], and Ricker et al. [152] for quasi-static strain rate ranges between 4.5×10^{-6} s^{-1} and 1×10^{-1} s^{-1}. Mitchell et al. and Duesbery and Foxall observed significant increases in yield stress for increasing strain rates, a common result for BCC metals. Ricker et al. however obtained the opposite trend at nominal strain rates of 4×10^{-5} and 3×10^{-6} s^{-1} [152]. Ricker et al. explained the strain rate effect by the influence of oxygen and hydrogen based upon the work of Ravi and Gibala [161], [181]. At very low strain rates and room temperature, the diffusion rate of hydrogen is significant enough to produce strain rate effects due to an increased interaction time between the dislocations and the mobile interstitial atoms. At higher strain rates, the dislocations break free and travel unimpeded in the grain. This could also explain the reduction in failure strain for the case with the smallest strain rate. However, Mitchell et al. [145] performed tests at similar rates but observed an increase in yield stress with increasing strain rate. Since the impurity content in both studies are not reported no conclusion can be made on the effect of strain rate on the yield stress at such low rates.

Mitchell et al. [145] and Duesbery and Foxall [146] compared the different hardening stages of specimens with a similar crystal tensile orientation. The transition from stage I to II was

not well defined at the higher strain rates and a lower hardening rate was measured during stage II for increasing strain rates. Strain rate sensitivities observed in the two studies are different. Mitchell et al. [145] reported a logarithmic dependence of the yield stress with strain rate with two slopes, where the higher rate slope occurred from $5x10^{-3}$ s^{-1} to $1x10^{-1}$ s^{-1}. The bi-logarithmic trend was not observed by Duesbery and Foxall whose results had a significantly lower yield stress for all rates.

In compression, Edington [155] performed tests at strain rates of 10^{-4} to 10^{3} s^{-1} with a universal testing machine and split Hopkinson bars. Niobium single crystals with the same orientation (near the center of an IPF) were machined in cylindrical specimens with two geometries. Stage I hardening was not observed at all strain rates despite the specimens being preferably oriented for single slip. The evolution of the lower yield stress as function of the strain rate showed two linear regimes on a semi–log plot. A lower strain rate sensitivity was measured at strain rates below 10 s^{-1}. The lower purity of the single crystals used in this study, compared with the study of Mitchell et al. [145][145], could explain the differences in strain rate sensitivity and hardening.

Finally, Gnäupel-Herold et al. [151] performed tests at a constant speed on specimens with different gage lengths. No effect of the strain rate was reported in this study, but all tests were performed at rates in the same order of magnitude. This result is consistent with the logarithmic dependency of the strength on the strain rate observed by Mitchell et al [145]. These observations will be compared with the present study later in the manuscript.

The author and collaborators [176] published tensile mechanical property results on niobium single crystals deformed at orders of magnitude of strain rates of 10^{-4} to 10^{3} s^{-1}. Those tensile results and compression results, first presented in this thesis, are the part of the first study on the mechanical properties of niobium single crystals deformed at strain rates greater than about 10^{-1} s^{-1}. Note that the high strain rate mechanical properties of polycrystalline high-purity niobium specimens have been reported by Peroni and Scapin [182]. An important increase in yield stress and a transition from hardening to softening were measured for increasing strain rates [182].

2.3.11. Observation of Dislocations in Niobium Single Crystals

Foxall et al. [109] performed an in-depth study of dislocation content as function of strain, crystal orientation, and loading direction (tension vs compression) in niobium single crystals using transmission electron microscopy (TEM). Tensile and compression specimens were all deformed at a constant temperature of 295 K and a strain rate of $1.3x10^{-4}$ s^{-1}. First, during stage I, clusters of edge dipoles and short elongated loops were observed in all sections

parallel to the primary (011) plane [109]. A screw mechanism was suggested for the formation of those dipoles or a representation of the interactions between screw dislocations and short loops were observed. During stage II, bundles of dislocations joined to form cell walls with decreasing size for increasing stress [109]. About 50% of the dislocations observed in the middle of stage II were from the secondary slip systems. Finally, dislocation substructures similar to the ones described for stage II were observed during stage III.

Edington [155] studied the effect of strain rate on the dislocation substructure in niobium single crystals with an initial orientation close to the center of an IPF deformed in compression at strain rates of $1.2x10^{-4}$ s^{-1} and $1.5x10^{3}$ s^{-1}. The purity of the specimens in that study was lower purity than current state of the art niobium ingots with a RRR greater than 300. TEM analyses were performed on specimens deformed at shear strains of about 0.037, 0.054, 0.126, 0.199, and 0.297 for specimens deformed at a low strain rate of $1.2x10^{-4}$ s^{-1} and at shear strains of 0.028, 0.06, 0.12, and 0.3 for specimens deformed at a high strain rate of $1.5x10^{3}$ s^{-1}. A linear increase in dislocation density was measured for increasing shear strains at the same rate for the specimens deformed at low and high strain rates. This result suggests that the dislocation density is independent of the strain rate [155]. Edge and screw dislocations with different Burgers vectors, indicating the activation of multiple slip systems, were observed at low and high strain rates. However, differences in dislocation substructure were observed at the different strain rates. At a low strain rate, dislocation cells formed at a strain of about 0.297. At a high strain rate, no dislocation cells formed and a higher density in homogeneously distributed dislocation dipoles (about twice as high as the specimens deformed at a low strain rate) was observed. Finally, since the dislocation density was independent of strain rate, the higher strain hardening rate at low strain rate (measured from shear stress–shear strain curves) was explained by Edington [155] by cell walls acting as more effective hardeners than the homogenously distributed dislocation dipoles.

Ikeno and Furubayashi [162] performed in-situ TEM measurements of pierced niobium single crystal foils deformed in tension at room temperature. The nucleation and motion of, mostly screw, dislocations were observed. Note that the stress-state was complex and not uniaxial due to the hole in the foil. Ikeno [165] also performed in-situ TEM measurements of niobium foils prepared in a similar way but deformed at temperatures of 40 to 300 K. It was concluded that edge dipoles from jogs are at the origin of the formation of cells [165].

Sung et al. [183] studied the microstructure of tensile specimens deformed up to a strain of 0.05 at low strain rate with TEM. Cell structures with dense dislocation walls were observed and are shown in Figure 2.23. A high dislocation density was also observed in low angle grain boundaries (LAGB), with a misorientation angle between 1° and 5° [183].

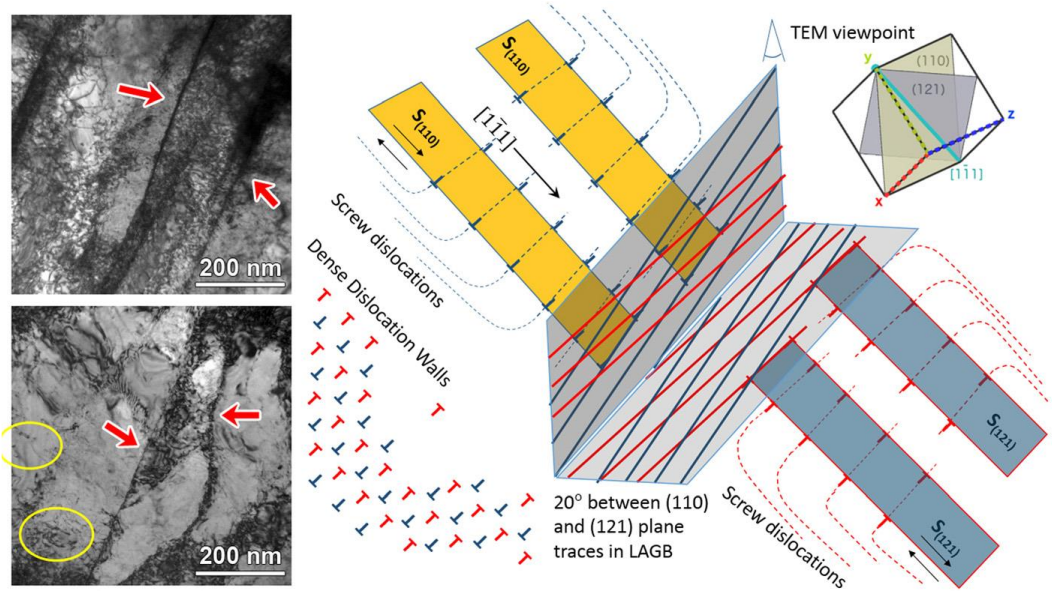

Figure 2.23: Bright field transmission electron microscope images of cross-sectional microstructure (normal to the tensile direction) of tensile specimen strained a 0.05, and a schematic of the possible dislocation arrangement on sub-boundaries parallel and perpendicular to the tensile axis. (Reprint with permission from the journal [183]).

Dislocations were also observed in niobium single crystal specimens by Wang et al. [184] using electron channeling contrast imaging (ECCI). Tensile specimens with different levels of work hardening and heat treatments were analyzed. A reduction of dislocation density from 9 to 2 μm^{-2} was measured for undeformed specimens following an annealing heat treatment at 800°C for 2h [184]. Slip was observed on {110} and {112} slip systems for specimens deformed up to a strain of 0.4, but some of the dislocations on the {112} slip systems were pre-existing [184]. Srinivasan et al. [185] studied the dislocation substructure of cold rolled niobium single crystals with different orientations. The deformed specimens showed regions with a high dislocation density and thick cell walls.

Finally, Dobromyslov et al. [186] observed dislocations in a niobium single crystal that was loaded by spherically converging shock waves. The strain rate in that study was not reported but was likely much higher than 10^3 s^{-1}, the highest order of magnitude presented in this thesis. The very high pressure converted the single crystal in a polycrystalline structure. Also, the temperature increase in the specimen was sufficient to partially melt the niobium single crystal, as droplets were found at the surface of the broken spherical specimen. TEM observations showed that the plastic deformation occurred through slip and the formation of a vortex structure [186]. Twinning played a small role in the plastic deformation since only few twins were found at the microscopic scale.

In the present study, the TEM measurements performed on specimens deformed in tension at 10^{-3} s^{-1} and about 1 000 s^{-1} will be compared with Edington's study [155] on niobium

single crystal specimens deformed in compression at similar strain rates. The observation of dislocations in niobium single crystals deformed in tension at a strain rate greater than the quasi-static regime of about 10^{-5} s^{-1} to 10^{-3} s^{-1} is a first and will provide information about potential change in deformation mechanisms at high strain rate.

2.3.12. Effect of Dislocations on Superconducting Properties

As previously mentioned, SRF cavities are not only structural components acting as pressure vessels, but also functional components since they must operate in a superconducting state. Therefore, an understanding of the effect of dislocations and other crystalline defects on the superconducting properties of niobium is essential. Only a short overview of this topic is presented here, since this study focused on the mechanical properties and on the microstructure of niobium single crystals, and not on the superconducting properties.

Antoine [34] reviewed the effect of different crystalline structures, e.g. voids, grain boundaries, and dislocations, on the superconducting properties of niobium used in radiofrequency applications. Three-dimensional defects, like voids, with a dimension larger than the penetration depth have the strongest flux pinning energy, followed by two-dimensional structures, e.g. grain boundaries. Individual dislocations are linear defects and, therefore, have a smaller pinning energy. However, the dislocation density in deformed niobium sheets is high, about 10^{14} m^{-2} for specimens deformed at a strain of 0.10 [187], which results in a high effective pinning energy for dislocations. Also, as shown in Figure 2.23, dislocations can accumulate on preferred slip planes and form cell walls or low angle grain boundaries which act like 2D structures [34]. The influence of a LAGB on the superconducting properties was measured by Sung et al. [183] using magneto optical imaging and flux penetration was observed at this microstructural defect. The development of the LAGB in that study was likely caused by the interaction of dislocations on competing slip planes in the specimen deformed at a low strain rate [183].

In conclusion, an investigation of the dislocation substructure at low and high strain rates for specimens deformed in tension is essential, since a change in dislocation substructure could lead to different superconducting properties.

2.3.13. Nanoindentation Characterization of Niobium Single Crystals

To the best knowledge of the author, nanoindentation measurements have not previously been performed on deformed niobium single crystals. Wang and Ngan [188] performed nanoindentation measurements on annealed niobium specimens with grain size of 500 ± 200 μm. However, the main objective of their study was to measure the hardness and pop-ins for indents at the vicinity of grain boundaries, which is different than this study. For

SRF applications, extensive work has been performed at Old Dominion University by Dr. Elmustafa on niobium nitride deposited layers [189]–[192]. Therefore, this study presents the first nanoindentation measurements performed on niobium single crystals and, more precisely, on specimens deformed in tension and compression at strain rates ranging from 10^{-3} to 10^{3} s^{-1}.

The main objectives were to measure the influence of the different dislocation substructures in specimens with different initial crystal orientations and deformed at different strain rates on the hardness. Undeformed reference specimens with different crystallographic orientations were also indented to measure anisotropic elastic properties and compare hardness values due to the nucleation and motion of dislocations on different slip systems.

2.4. Conclusions and Research Objectives

Plastic deformation in niobium single crystals will be governed by the motion of screw dislocations, which will lead to non-Schmid effects, such as a tension/compression asymmetry. By analogy with low temperature tests, more important non-Schmid effects could be measured at high strain rate. For the range of strain rate studied, the screw dislocations are expected to move between Peierls potentials by the nucleation and motion of kink pairs, a thermally activated deformation mechanism. An increase in yield stress is expected for increasing strain rate due to smaller thermal contributions to the activation energy required to overcome short-range obstacles. A change in dominant deformation mechanism could occur at the highest strain rate. Therefore, the activation volume will be calculated and analytical modeling of the strain rate as function of the flow stress is used with a model considering the nucleation and motion of kink pairs and viscous drag to study if the latter mechanism explains a potential increase in flow stress at the highest strain rate.

The mechanical properties of high-purity niobium single crystals have been extensively studied in the literature. However, the effect of crystal orientation on the anisotropic mechanical properties have not been studied at strain rates greater than the quasi-static regime (10^{-5} to 10^{-3} s^{-1}). The effect of strain rate on one crystal orientation has also not been studied at strain rates greater than 10^{-1} s^{-1}. This study will fill the gaps in the literature by performing tensile tests at strain rates of up to 10^{3} s^{-1} and by studying different crystal orientations deformed in tension and compression at strain rates of up to 10^{3} s^{-1}. The tensile tests at strain rates greater than 10^{-1} s^{-1} will answer questions about (1) the strain-rate sensitivity at strain rates of up to 10^{3} s^{-1} and (2) if a change in dominant deformation mechanism is measured expected. The tensile and compression tests at different strain rate and for different crystal orientations will answer questions about (1) potential changes in anisotropic mechanical properties for an increasing strain rate, (2) the effect of crystal

orientation on the strain-rate sensitivity, and (3) the contribution of non-Schmid effects, measured at high strain rate.

Observations of dislocation substructures with a TEM in specimens deformed at low strain rates showed slip on preferred orientations and the formation of cell walls. The only study on single crystals deformed in compression at a strain rate of about 10^3 s^{-1} measured the same dislocation density as specimens deformed at 10^{-4} s^{-1}, but observed a higher concentration in dislocation dipoles [155]. The dislocation substructure of specimens deformed in tension greater than the quasi-static regime has not been reported in the literature. Also, dislocations and cell walls are known to act as flux pinning centers, which are detrimental for the superconductive properties of SRF cavities. The effect of strain rate on the dislocation substructure of niobium single crystals deformed in tension at strain rates of 10^{-3} s^{-1} to about 10^3 s^{-1} is studied with TEM in this thesis. This investigation of the microstructure will answer questions about (1) a potential change in the dominant deformation mechanism and (2) the effects on superconducting properties. Combined with the TEM observations, analyses from EBSD measurements will help explain the measured mechanical properties.

Chapter 3 Materials and Methods

Experiments and microstructure analyses were performed at different institutes on niobium single crystals. In order to ensure repeatability between measurements and analyses performed in different laboratories, it is paramount to develop and respect detailed experimental procedures. This chapter describes the method for crystal orientation selection and the different sample geometries. The experimental procedures that were used for the different mechanical tests (uniaxial tensile and compression tests at strain rates between 10^{-4} s^{-1} and 10^{3} s^{-1}), microstructure analyses (sample preparation for EBSD, nanoindentation, and TEM), and data analysis are presented.

3.1. Materials

3.1.1. Niobium Single Crystals

Niobium single crystal specimens were extracted from a 322 mm diameter and 3.8 mm thick disk supplied by CERN, see Figure 3.1a. Two identical disks were available, but only one was used for the characterization of the mechanical properties. The ten largest grains in the disk have principal diagonals between approximately 45 mm x 60 mm and 120 mm x 170 mm. This allowed for the extraction of small tensile specimens with different crystal orientations. The high purity niobium disk with a residual resistivity ratio (RRR) greater than 300 is normally used for the fabrication of superconducting radiofrequency cavity half-cells. The low impurity content is essential for the final application, since the formed components are functional and structural parts: the niobium SRF cavity must operate in a superconductive state at the applied electromagnetic field and it acts as a pressure vessel.

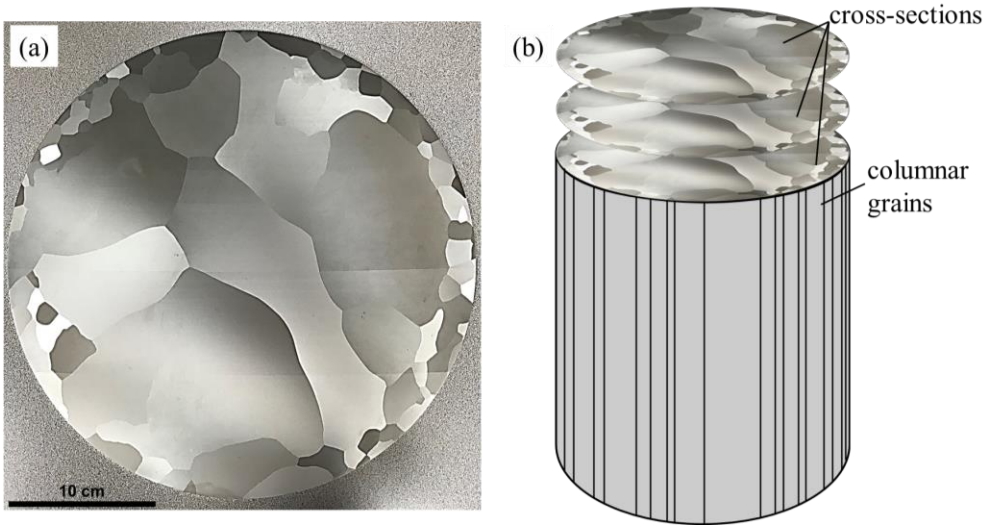

Figure 3.1: (a) High-purity large grain niobium disk used for single crystal specimens' extraction. (b) Schematic of the disk location in a section of a cylindrical niobium ingot with columnar grains.

The disk is a slice of a long electron beam melted cylindrical ingot, see Figure 3.1b for a schematic of the disk extraction from an ingot. The large grains in the disk are sections of the ingot's columnar grains. Thus, multiple disks with the same grain dimensions and crystallographic orientations can be produced. Buffered chemical polishing (BCP) was used on the disks after cutting, which revealed the grain boundaries and resulted in smooth surfaces. The reader is invited to refer to the review paper on SRF cavities published by Singer [23] for additional details on ingot and disk fabrication.

3.1.1.1. Grain Orientation Measurement

The crystal orientation of the ten largest grains in the disk was measured at Michigan State University using a non-destructive Laue X-ray diffraction method developed by Kang et al. [174]. Measurements were performed at multiple locations in the largest grains of the disk used for mechanical testing. No orientation gradients were measured within grains. See Figure 3.2a for the measurement locations, Figure 3.2b for a normal orientation map with unit cells, and Table 3.1 for the measured Bunge Euler angles (the frame of reference is shown in Figure 3.2b). Additional measurements were performed on the adjacent disk extracted from the same ingot. The same grain orientations were measured in the second disk. An average difference in Bunge Euler angles of 0.3 ± 0.1°, 0.2 ± 0.2° and 0.9 ± 0.4° for ϕ_1, Φ, and ϕ_2, respectively, was measured between the two disks for three locations in grains 4, 8, and 10. The approximate resolution limit for the method is ~0.1°.

Table 3.1: Measured Bunge Euler angles for multiple locations in disks 1 and 2 (identified in Figure 3.2a).

	Disk 1 (used for mechanical testing)			Disk 2		
	ϕ_1 (°)	Φ (°)	ϕ_2 (°)	ϕ_1 (°)	Φ (°)	ϕ_2 (°)
1	30.1	148.7	158.1			
2-a	352.1	146.0	185.9			
2-b	353.3	146.9	184.6			
2-c	353.1	145.6	186.3			
3	24.3	147.7	186.8			
4-a	86.3	130.7	124.8	85.9	130.2	123.6
4-b	85.8	130.6	124.8			
4-c	86.0	130.9	124.9			
5-a	53.7	129.0	164.0			
5-b	53.5	129.2	163.9			
5-c	53.0	129.1	163.4			
5-d	53.1	129.8	163.4			
6	240.9	152.1	154.6			

7	150.8	152.6	134.2			
8-a	44.8	132.9	168.3	44.6	133.0	168.7
8-b	44.1	132.6	168.0			
9	97.7	167.5	143.4			
10-a	350.3	147.6	185.2			
10-b	350.4	147.6	185.1	350.2	147.7	184.0

3.1.1.2. Tensile Specimen Orientation Selection

From the measured crystal orientations, it is possible to cut tensile specimens with orientations where, upon deformation, specific slip systems will likely activate or multiple systems will be competing and simultaneously activate. This orientation selection is made with the assumption that Schmid's law is valid and that the critical resolved shear stress is equal on all slip systems. Therefore, slip will initiate on the slip system with the highest Schmid factor. However, it is well known that the core structure of a screw dislocation leads to non-Schmid effects and that BCC metals mostly deform, at room temperature, by the motion of screw dislocations (see section 2.3. for more details). Therefore, the assumption of the Schmid law is not perfectly accurate for niobium single crystals, but it is believed to be the best approximation for the purpose of orientation selection. The Schmid factor calculation, for the purpose of tensile specimen orientation selection, is presented below with different approaches. The first method is inspired on the work performed by Dr. Baars during his PhD thesis [140], also on niobium single crystals.

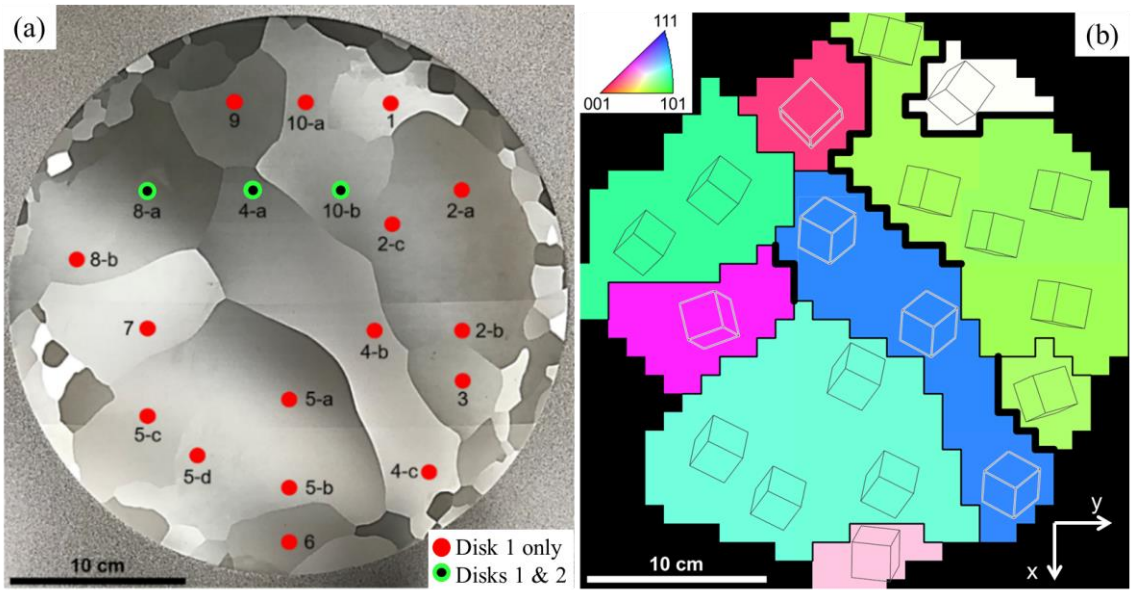

Figure 3.2: (a) locations where orientation measurements were performed in the ten largest grains of the used disk (disk 1) and a second disk (disk 2) and (b) grain normal direction orientation map with unit cells showing crystal orientations.

Recall from section 2.3. that slip in niobium single crystals was only experimentally observed on the {110}<111> and {112}<111> slip systems [108]–[110]. Therefore, only the 24 slip systems of those families, listed in Table 2.1, are considered. Knowing the slip systems that can be activated, the Schmid factor SF can be calculated for each of them for specific loading direction in each grain.

The Schmid factors for all known active slip systems are calculated for varying Bunge Euler angle ϕ_1 between 0 and 180 degrees for each grain. The rotation by ϕ_1 is equivalent rotating the tensile loading direction of a specimen in a grain. The blue and green lines in Figure 3.3 show the change in Schmid factor for each slip system for a rotating tensile specimen in grain 2. Orientations with a high Schmid factor for a specific slip system indicate a high likelihood for slip to occur on that slip system for a tensile specimen pulled in that tensile direction. Similarly, orientations where the highest Schmid factors are equal for more than one slip systems indicate that slip will likely compete on those systems. To align the tensile direction of a specimen with the desired ϕ_1 angles, the rotation angle $\phi_{1_{rotation}}$, is calculated and equal to the difference between the measured and desired angles:

$$\phi_{1_{rotation}} = \phi_{1_{measured}} - \phi_{1_{desired}} \tag{3.1}$$

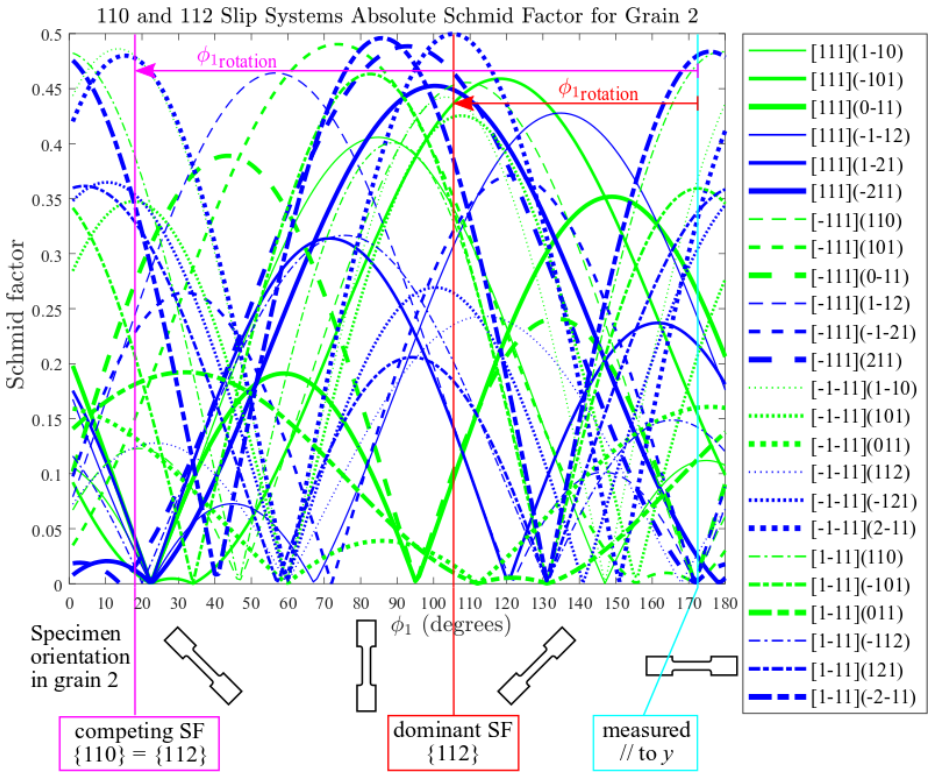

Figure 3.3: Schmid factors for all possible tensile orientations and 24 slip systems of a tensile test in grain two. The specimen orientation for the measured orientation (parallel to *y* in Figure 3.2b) and examples of orientations with competing or dominant Schmid factors are shown.

The specimen is rotated counterclockwise, from an initially horizontal position, by $\phi_{1_{rotation}}$ on the disk. This operation was repeated for the 33 different tensile specimen orientations. This approach is ideal to identify specific slip systems, but it does not give information about the crystal orientation along the tensile axis. A second and complimentary method was then used to ensure that specimens with different crystal orientations covering most of a tensile axis inverse pole figure were cut in the large grain sheet. Since the tensile specimens can only be rotated around the direction normal to the sheet, an inverse pole figure with the possible crystal orientations for the rotation of the specimen from 0 to 180° was generated for each grain. Figure 3.4 shows such IPF for grains 2 and 5. This figure clearly shows that not all crystal orientations are accessible for a given grain and helps in the decision making of crystal orientations. In combination with the IPFs of the two slip systems with the highest Schmid factor and the relation between their Burgers vectors in Figure 2.12, this method becomes an efficient visual tool for orientation selection. Appendix B shows the IPFs, like in Figure 3.4, with the possible crystal tensile orientations for all grains.

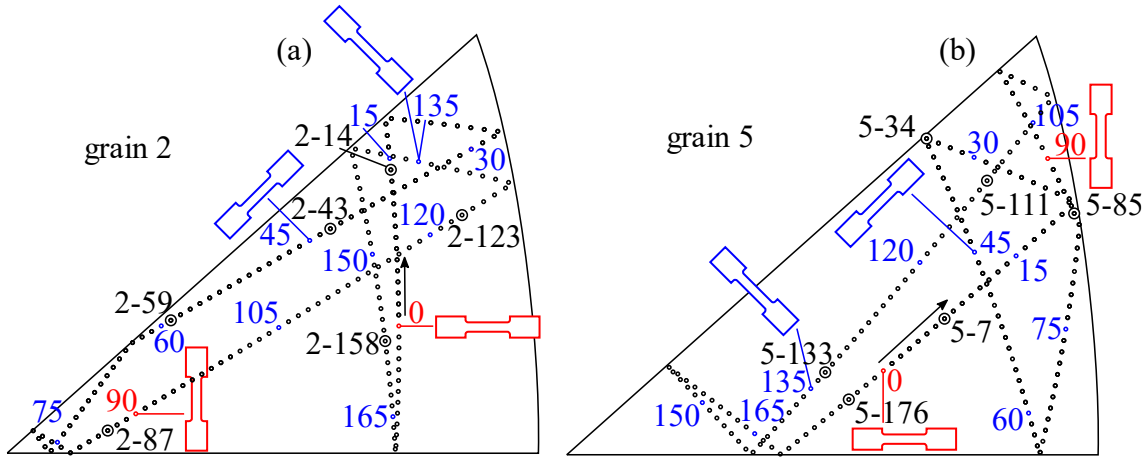

Figure 3.4: Possible crystal orientations in the tensile direction for grains 2 and 5. Colored numbers are the counterclockwise rotation angles in degree of a horizontal specimen to obtain the crystal orientation at the location of the tensile axis IPF.

Figure 3.5a shows the final disk layout with tensile specimens colored based on the tensile axis IPF, presented in Figure 3.5b. The long tensile specimens were used for tests at up to ~100 s^{-1} and the short tensile specimens were used with split Hopkinson bars (more details about the sample geometries in section 3.2.). The layout was converted to the dxf format for specimen cutting with wire electrical-discharge machining (EDM). The specimen nomenclature in Figure 3.5b and through the thesis is: grain number-rotation angle. For example, specimen 1-95 is from grain 1 and the specimen was rotated counter-clockwise about a vector normal to the face of the disk by 95°, from an originally horizontal position, i.e. along the y-axis in Figure 3.2b. Details about each specimen orientation, Schmid factors,

and Burgers vectors, for the two slip systems with the highest Schmid factors, are presented in Table 4.1.

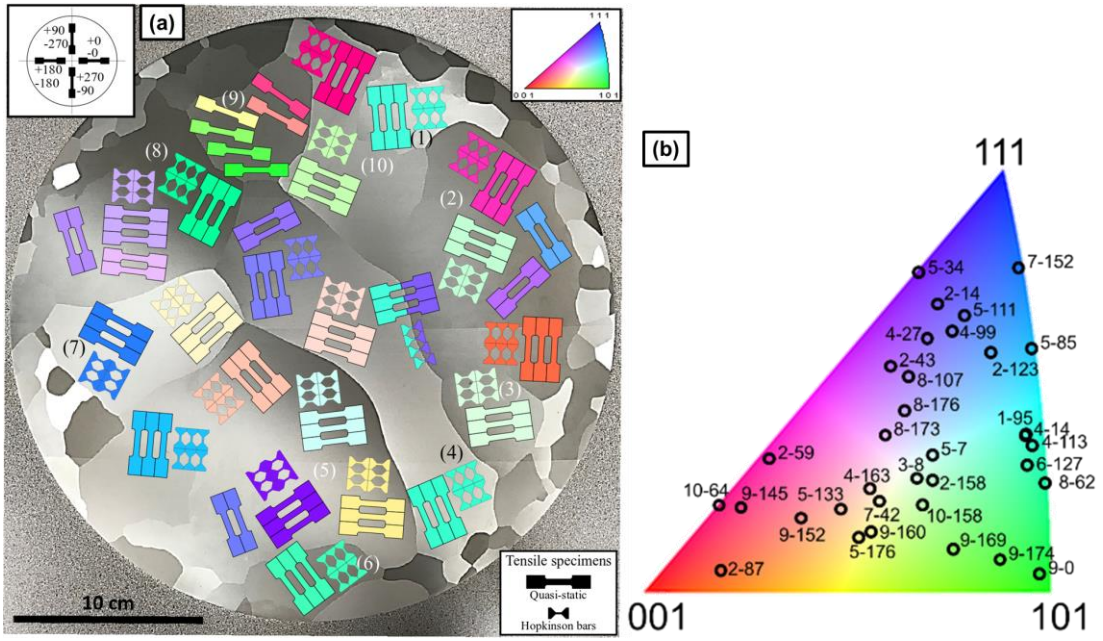

Figure 3.5: (a) Tensile specimen layout in the nine measured grains and (b) tensile axis IPF of the different specimens. The specimen's color in (a) represent the tensile axis IPF colors in (b).

The following grey shaded section provides a numerical example of the Schmid factor calculation for different specimen tensile directions and a measured crystal orientation. This methodology was implemented in MATLAB to perform the same calculations for all grains and Appendix B presents the flowcharts of the different MATLAB codes written for that purpose.

Example of Schmid factor calculation for different slip planes

The calculation of the Schmid factors for all possible tensile orientations by rotating the tensile axis from 0 to 180° around the normal direction of the disk is explained below with a numerical example. This approach was used to select tensile orientations of interest in niobium and can be adapted for different lattice structures.

The calculation of the Schmid factors for different regions of the IPF is a purely geometrical relationship between the direction of applied stress and the slip system, i.e. the slip and slip-plane normal directions.

1. Measure grain orientations

First, the orientation of the crystal in each grain of the physical sheet are measured. The approach used for this study was developed by Kang specifically for large–grain niobium disks [174]. However, a small specimen could also be extracted and measured with EBSD

to obtain the grain orientation. Three Euler angles ϕ_1, Φ, and ϕ_2 are obtained from this experimental step. The Bunge Euler convention is used throughout this thesis. The angles describe the crystal orientation compared with the sheet orientation see Figure 3.6. The three standard sheet directions (X,Y,Z) are used. Since we are working with single crystals, X and Y are based on the reference system used during grain orientation measurement due to absence of rolling. These directions must be clearly identified to avoid confusion during following calculations.

Grain 1 is used for this numerical example: ϕ_1 = 30.0°, Φ = 148.7°, and ϕ_2 = 158.1°.

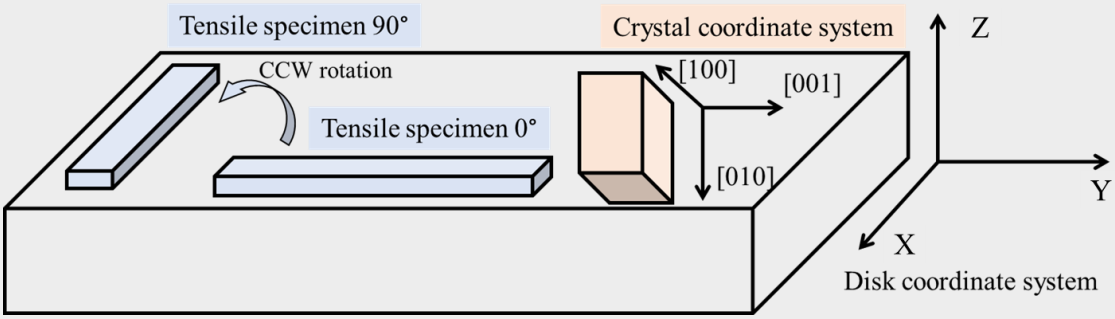

Figure 3.6: Disk and the crystal coordinate systems and tensile specimens' orientations for different rotation angles.

2. Identify the slip systems that could activate for the lattice structure of the material

Since niobium is a BCC metal, slip occurs on the direction with the highest packing density, i.e. <111>, and on three possible slip planes families: {110}, {112}, and {123}. As previously mentioned, slip was experimentally observed and numerically predicted on the {110} and {112} slip planes. A total of 24 slip systems exist for the {110}<111> and {112}<111> families and are presented in Table 2.1.

The example below for the $(\bar{1}01)[111]$ slip system must be repeated for the other slip systems. The slip direction and slip-plane normal direction are:

$$\underline{b} = [1,1,1] \text{ and } \underline{n} = [-1,0,1]$$

These vectors are normalized as follow:

$$\hat{b} = \left[\frac{1}{\sqrt{3}}, \frac{1}{\sqrt{3}}, \frac{1}{\sqrt{3}}\right] \text{ and } \hat{n} = \left[-\frac{1}{\sqrt{2}}, 0, \frac{1}{\sqrt{2}}\right]$$

3. Define the stress tensor

The stress tensor representative of the loading that the specimen is subjected to is established. The directions used to define the stress tensor are with respect to the X and Y axes defined during the measuring case and the 0° initial position of the specimen. In this

study, the X and Y directions were defined as pointing downward and to the right, respectively, during the orientation measuring phase (see Figure 3.2b as a complement to Figure 3.6). The specimens for the uniaxial tensile tests had an initial horizontal position, which indicates that the tensile axis is oriented along Y. The 2nd order stress tensor was then defined as follow:

$$\underline{\underline{\sigma}}_{disk} = \begin{bmatrix} 0 & 0 & 0 \\ 0 & 1 & 0 \\ 0 & 0 & 0 \end{bmatrix}$$

4. Rotation of the stress tensor in the crystal reference system

To calculate the Schmid factor, the stress tensor orientation must be rotated to be in the reference frame of the crystal and not of the disk. This is accomplished by first calculating the orientation matrix $\underline{\underline{g}}$:

$$\underline{\underline{g}} = \underline{\underline{g}}_{\phi_2}\underline{\underline{g}}_{\Phi}\underline{\underline{g}}_{\phi_1}$$

where the individual orientation matrices are defined as:

$$\underline{\underline{g}}_{\phi_2} = \begin{bmatrix} \cos\phi_2 & \sin\phi_2 & 0 \\ -\sin\phi_2 & \cos\phi_2 & 0 \\ 0 & 0 & 1 \end{bmatrix}, \underline{\underline{g}}_{\Phi} = \begin{bmatrix} 1 & 0 & 0 \\ 0 & \cos\Phi & \sin\Phi \\ 0 & -\sin\Phi & \cos\Phi \end{bmatrix} \text{ and}$$

$$\underline{\underline{g}}_{\phi_1} = \begin{bmatrix} \cos\phi_1 & \sin\phi_1 & 0 \\ -\sin\phi_1 & \cos\phi_1 & 0 \\ 0 & 0 & 1 \end{bmatrix}$$

For the specific case of grain 1 and $\phi_1 = 0°$:

$$\underline{\underline{g}} = \begin{bmatrix} \cos 158.1 & \sin 158.1 & 0 \\ -\sin 158.1 & \cos 158.1 & 0 \\ 0 & 0 & 1 \end{bmatrix}\begin{bmatrix} 1 & 0 & 0 \\ 0 & \cos 148.7 & \sin 148.7 \\ 0 & -\sin 148.7 & \cos 148.7 \end{bmatrix}\begin{bmatrix} \cos 0 & \sin 0 & 0 \\ -\sin 0 & \cos 0 & 0 \\ 0 & 0 & 1 \end{bmatrix}$$

$$\underline{\underline{g}} \approx \begin{bmatrix} -0.928 & 0.373 & 0 \\ -0.373 & -0.928 & 0 \\ 0 & 0 & 1 \end{bmatrix}\begin{bmatrix} 1 & 0 & 0 \\ 0 & -0.854 & 0.520 \\ 0 & -0.520 & -0.854 \end{bmatrix}\begin{bmatrix} 1 & 0 & 0 \\ 0 & 1 & 0 \\ 0 & 0 & 1 \end{bmatrix}$$

$$\approx \begin{bmatrix} -0.928 & -0.319 & 0.194 \\ -0.373 & 0.793 & -0.483 \\ 0 & -0.520 & -0.854 \end{bmatrix}$$

Second, the stress tensor is modified as follow:

$$\underline{\underline{\sigma}}_{crystal} = \underline{\underline{g}}\,\underline{\underline{\sigma}}_{disk}\,\underline{\underline{g}}^{T}$$

$$\underline{\underline{\sigma}}_{crystal} \approx \begin{bmatrix} -0.928 & -0.319 & 0.194 \\ -0.373 & 0.793 & -0.483 \\ 0 & -0.520 & -0.854 \end{bmatrix} \begin{bmatrix} 0 & 0 & 0 \\ 0 & 1 & 0 \\ 0 & 0 & 0 \end{bmatrix} \begin{bmatrix} -0.928 & -0.373 & 0 \\ -0.319 & 0.793 & -0.520 \\ 0.194 & -0.483 & -0.854 \end{bmatrix}$$

$$\underline{\underline{\sigma}}_{crystal} \approx \begin{bmatrix} 0.102 & -0.252 & 0.166 \\ -0.252 & 0.628 & -0.412 \\ 0.166 & -0.412 & 0.270 \end{bmatrix}$$

To rotate the stress tensor in all possible tensile orientations in the grain, the measured angle ϕ_1 is not used and angles from 0 to 180° are used instead. Recall that angle ϕ_1 defines a rotation about the normal direction of the grain. Angles Φ and ϕ_2 are the measured angles of the specific grain.

5. Schmid factor calculation

Finally, the Schmid factor is calculated. For this specific example, the Schmid factor is calculated as follow. First, the load along the slip direction is calculated:

$$\underline{F} = \underline{\underline{\sigma}}_{crystal} \hat{b}^T$$

$$\underline{F} = \begin{bmatrix} 0.102 & -0.252 & 0.166 \\ -0.252 & 0.628 & -0.412 \\ 0.166 & -0.412 & 0.270 \end{bmatrix} \begin{bmatrix} 1/\sqrt{3} \\ 1/\sqrt{3} \\ 1/\sqrt{3} \end{bmatrix} \approx \begin{bmatrix} 0.009 \\ -0.021 \\ 0.014 \end{bmatrix}$$

Second, the load is projected on the slip plane and gives the Schmid factor:

$$SF = \underline{F} \cdot \hat{n}$$

$$SF = \begin{bmatrix} 0.009 \\ -0.021 \\ 0.014 \end{bmatrix} \begin{bmatrix} -1/\sqrt{2} & 0 & 1/\sqrt{2} \end{bmatrix} \approx 0.0033$$

This procedure is repeated for the all the slip systems in Table 2.1 and for all ϕ_1 angles.

3.1.1.3. Specimen Cutting

All niobium single crystal specimens were cut with a water immersed wire EDM machine to avoid work hardening the side surfaces of the specimens, reduce material consumption, and cut at accurate angles to test the selected crystal orientations. Disk alignment, to respect the layout presented in Figure 3.5a, was done using a horizontal saw mark left on the disk during sectioning of the ingot, visible in Figure 3.1a. Tensile specimens were all cut through their thickness to double the number of available specimens.

Markings with permanent markers were applied on the disk to identify the original locations of the cut specimens. Texts were written in black and red in different languages and in perpendicular directions. Random lines were also traced with a ballpoint pen. For future

references, it is recommended to use fine point markers or ballpoint pens since the small specimens might only have a fraction of a letter on their entire surface after cutting, which can make the “puzzle” difficult to assemble. Figure 3.7 shows the disk after cutting of all tensile and compression specimens. A total of 372 tensile and 161 compression specimens were cut.

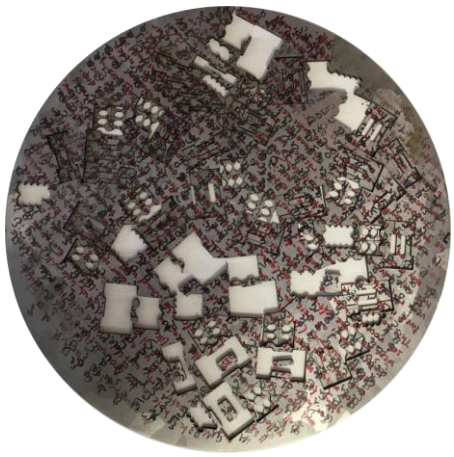

Figure 3.7: Large grain niobium disk after cutting with markings to identify specimens’ original location.

3.1.1.4. EBSD Sample Preparation

Deformed tensile and compression specimens were analyzed with electron backscatter diffraction (EBSD). The following procedure was used to prepare the surface of specimens for adequate indexing of the Kikuchi patterns of niobium.

First, specimens were cut lengthwise using a diamond wire saw (Well Diamond Wire Saw Series 3000) to analyze the microstructure in the gage section. Second, the cut specimens were cold mounted in a methyl-methacrylate based resin (Lam Plan resin 609). Third, grinding of the excess resin and flattening of the specimen was performed with silicon carbide (SiC) grinding papers P800. Additional grinding and polishing of the specimen were done with SiC grinding papers P1200, P2400, and P4000. Polishing clothes with 3 µm and 1 µm diamond suspension solutions for soft materials were used. The final polishing step used vibratory polishing (Buehler Vibromet 2) with a colloidal silica solution for 4 to 12 hours. The colloidal silica solution had the following content: 200 mL of distilled water (H_2O), 200 mL of colloidal silica (0.05 µm), and 20 mL of hydrogen peroxide (H_2O_2) with a concentration of 30%.

Before analysis in the scanning electron microscope, the specimens were extracted from the resin by dissolving the resin in acetone for approximately 48 hours. The specimens were mounted in a holder with screws applying pressure on the grip section, see Figure 3.8a. The specimen holder was securely installed in a 70° tilted stage for alignment of the reflecting electron beam with the EBSD detector. The resulting microstructure showed a low

geometrically necessary dislocation (GND) density in undeformed regions and high confidence index through the whole specimen, which confirmed that the sample preparation methodology was adequate.

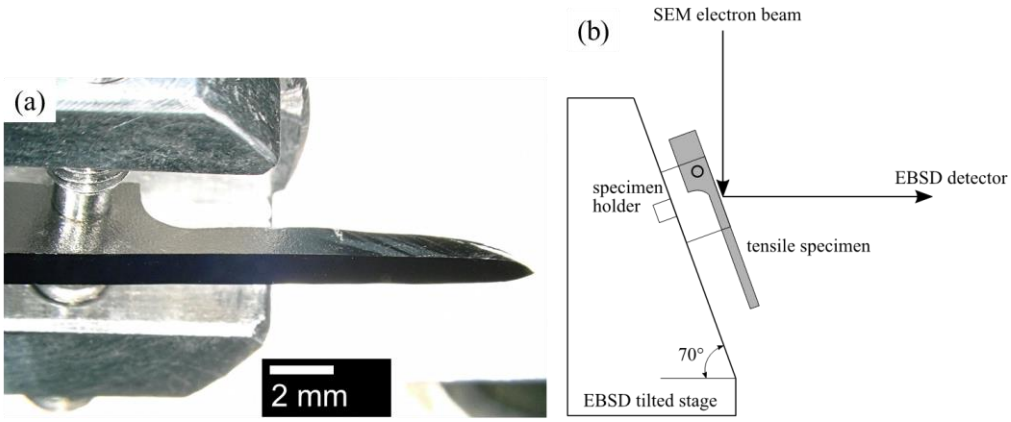

Figure 3.8: (a) Mounted tensile specimen in holder and (b) specimen holder location on a tilted stage for EBSD scans.

3.1.1.5. Nanoindentation Sample Preparation

Tensile and compression specimens deformed at low and high strain rates were analyzed with nanoindentation. The surface that was analyzed for the EBSD measurements was also used for the nanoindentation and was not repolished between the two studies. Since the cross-section of the specimen was polished and the resin was dissolved for EBSD measurements, cold mounting with a methyl-methacrylate resin was used to provide a flat surface on the opposite side of the polished surface. Figure 3.9 shows three specimens in the chamber of the nanoindenter and a schematic of the cold mounted specimen. The niobium single crystal specimen was held with a plastic support with the polished surface facing upward. After cold mounting, the bottom surface was not polished since it was sufficiently flat. However, a thin glass lamella, used in light microscope for observation of biological samples, was glued at the bottom of the specimen with a cyanoacrylate adhesive. This insured a more uniform contact with the stage of the nanoindenter and removed the high amount of noise found in load–indentation depth curves of specimens with no glass lamella.

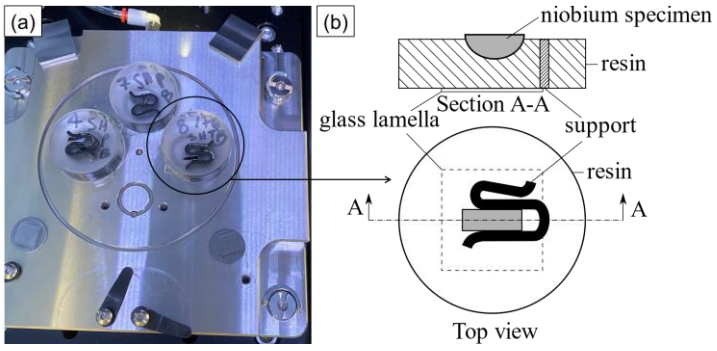

Figure 3.9: (a) Three niobium single crystal specimens in the chamber of the nanoindenter and (b) a schematic of the cold mounted specimen.

3.1.1.6. TEM Sample Preparation

Tensile specimens deformed at low and high strain rates were analyzed with a transmission electron microscope (JEOL JEM-2200FS). All samples were prepared by Dr. Leonardo Agudo Jácome and Dr. Anna Manzoni of BAM. To avoid ion implantation, mechanical polishing and electropolishing were used instead of focused ion beam (FIB). Figure 3.10 shows a schematic of the steps followed to prepare electron-transparent niobium single crystal specimens. This method was developed to analyze the cross-section of specimens. First, a diamond wire saw was used to cut slices with a thickness of about 0.5 mm. Second, two slices were affixed to a steel block with parallel top and bottom surfaces using a wax with a melting point of 120°C. Third, the specimens were manually polished using rotating silicon carbide papers (P320, P600, and P1200) and water. The thickness of the slices was measured during the polishing process to remove about 200 μm. At that point, the wax was melted, the slices were flipped upside down, and reattached to the steel block. The mechanical polishing was then repeated to remove again about 200 μm. The wax was then melted and the ~100 μm thick slices were removed. The thickness of each slice was measured with an optical microscope to adjust the electropolishing time. A circular punch was used to cut 3 mm holes in the slice. Each 3 mm long specimens, hereafter *disks*, were placed in a numbered TEM grid storage box. The order and identification number of each disk was tracked to ensure that specimens in the deformed gage length were analyzed and to know the proximity with the fracture surface.

Finally, a disk was electropolished (Struers Tenupol-3) with a solution of 895 mL of methanol, 525 mL of ethylene glycol, and 90 mL of perchloric acid. The solution was cooled at a temperature of −16.5°C and a flow rate machine parameter of ~3.1 was used with a current and voltage of 0.1 A and 30 V, respectively. The electropolishing was performed in two steps. First, a small circular platinum aperture (Ø 500 μm) was used for 3 to 5 minutes to create a thinner region at the center of the specimen. Second, a larger circular platinum aperture (Ø 1250 μm) was used until a hole was detected by the photosensitive detector of the machine. The specimen was then taken out of the polishing machine and rinsed in methanol and ethanol to remove all traces of the electrolytic solution. A one-step procedure was originally used, but the holes were consistently on the edge of the aperture which resulted in excessive thinning or polishing artefacts. Figure 3.11 shows pictures of the equipment used and the step numbers correspond to the numbers in the schematic presented in Figure 3.10.

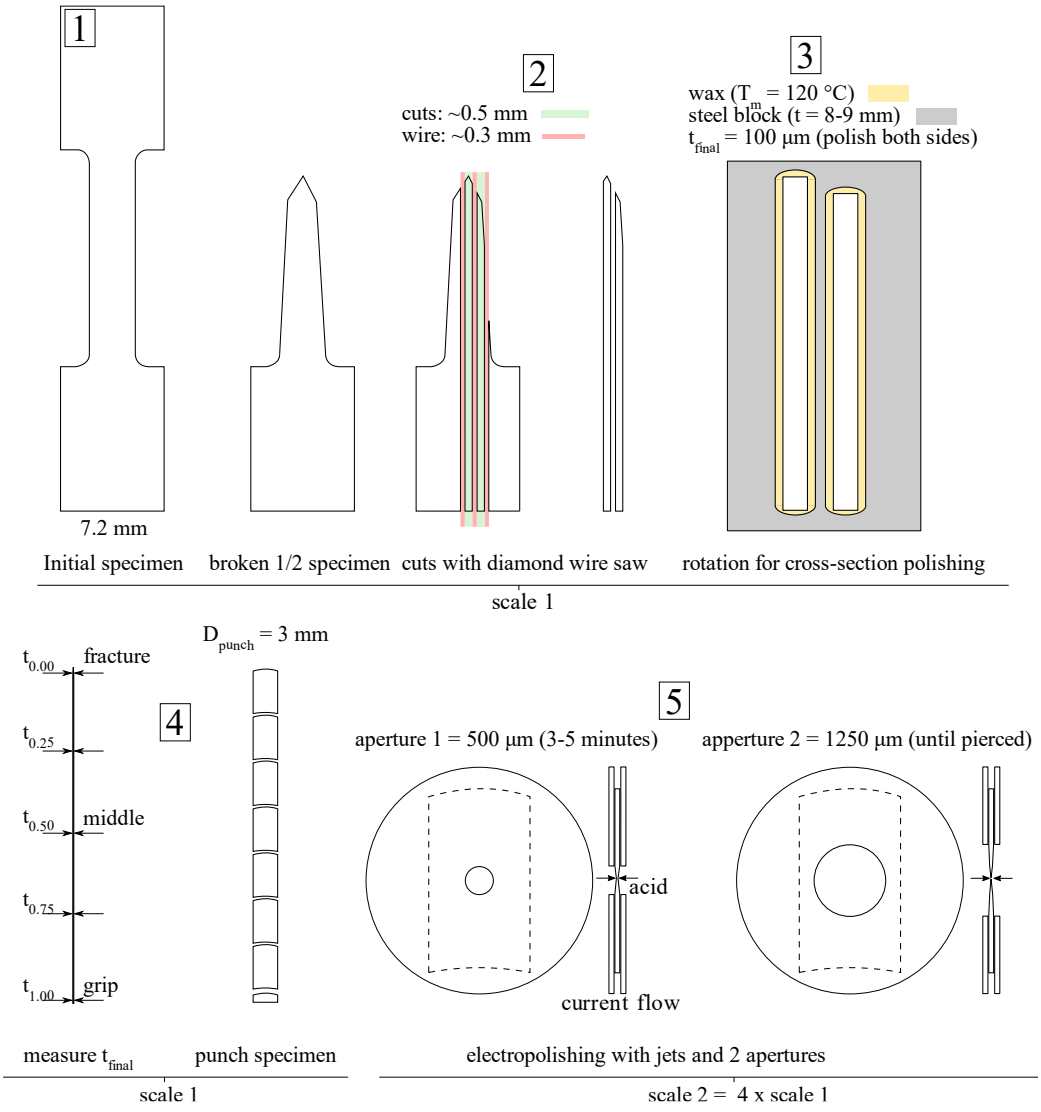

Figure 3.10: Sample preparation for TEM analysis at BAM for cross-section analysis using mechanical polishing and electropolishing. The scales used are for a low strain rate tensile specimen. Numbers correspond to the pictures in Figure 3.11.

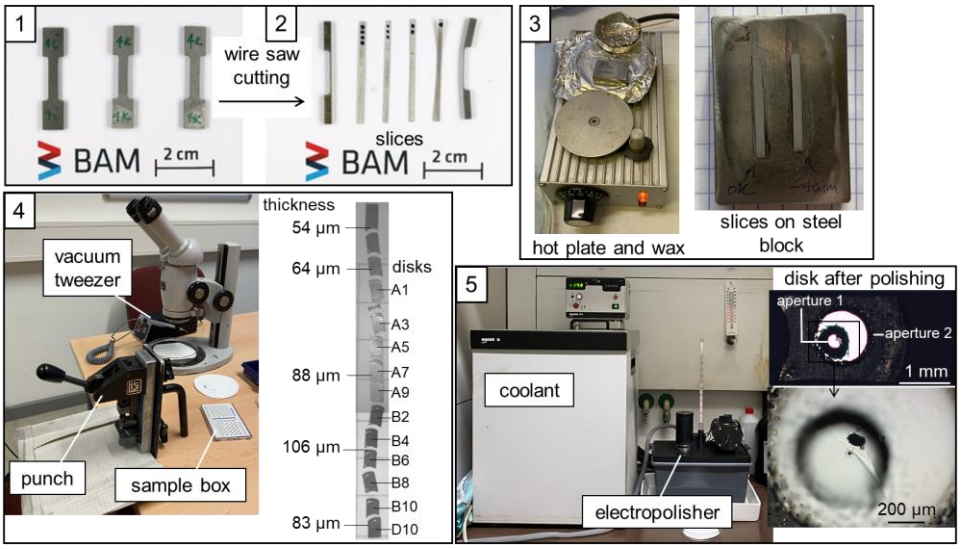

Figure 3.11: Pictures of the specimen and the equipment used at different steps of the TEM sample preparation of the cross-section of tensile specimens with mechanical polishing and electropolishing.

3.2. Specimen Geometries and Surface Preparation for Digital Image Correlation

3.2.1. Tensile and Compression Tests

Two different tensile sample geometries with rectangular cross-sections were used: (a) a miniature coupon for niobium single crystals using a split Hopkinson bar system and (b) short dog bones with or without holes in the fixture for low and intermediate strain rate tests on niobium single crystals. Figure 3.12 shows the different specimens with labels for their main dimensions. The applied strain rates and the length of the main dimensions are listed in Table 3.2.

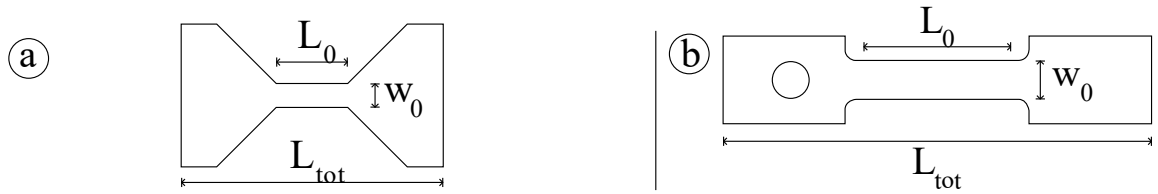

Figure 3.12: Tensile specimen geometry and main dimensions for all tests performed on niobium single crystals. Specimen (b) was used in two different configurations, with or without the hole shown on the left side.

The geometry of the miniature tensile specimen (Figure 3.12a) was developed and used at ASU in studies of nanocrystalline materials with gage lengths of 3 mm, 4.75 mm, and 5 mm, gage widths of 1 mm and 2 mm, and specimen thicknesses of 1 mm and 2 mm [193]–[195]. The geometry in Figure 3.12b was based on recommendations in the ASTM E8 standard [196] for a reduced version of the proposed subsize specimen. Compression tests were performed on cylindrical specimens and had an equal thickness and diameter of 3.8 mm.

Table 3.2: Characteristics of the different tensile specimens used in Part I of this study.

	Strain rate (s^{-1})	**L_0 (mm)**	**L_{tot} (mm)**	**t_0 (mm)**	**w_0 (mm)**
a	1 000	3	11	~1.8	1
b	10^{-4} to 100	13	35	~1.8	3.2

3.3. Methods for Material Characterization

Tensile and compression tests were performed at strain rates of 10^{-4} to 10^{3} s^{-1} in different institutes. Screw-driven (mechanical) and hydraulic systems were used for tests at strain rates lower or equal to about 100 s^{-1}. Tests at higher strain rates were performed with split Hopkinson bar systems. Table 7.2 provides a summary of the different institutes where the tests were performed and the range of strain rate and materials studied. The following acronyms are used in the table for the name of the institutes: Arizona State University (ASU), Imperial College London (ICL), and Michigan State University (MSU). Detailed procedures

for the different test rigs and the relevant equations for the data analysis are provided in the following subsections.

Table 3.3: Summary of the different tensile and compression tests performed during this study, grouped per testing system and institutes. (All acronyms are defined in the text.)

System	Institute	Strain rate (s^{-1})	Tension/Compression
Mechanical	MSU	10^{-4}–10^{-1}	T, C
Hydraulic	ICL	1–100	T
Split Hopkinson	ASU	10^{3}	T, C

3.3.1. Low Strain Rate Testing Methodologies (10^{-4} to 1 s^{-1})

3.3.1.1. Michigan State University – Niobium Single Crystals

A screw-driven table-top Instron 4302 was used at Michigan State University (MSU) to perform tensile and compression tests on niobium single crystals, as shown in Figure 3.13 with the camera used for DIC analyses. All tensile tests were performed at constant crosshead speeds of 0.1 mm/min, 1 mm/min, 10 mm/min, 50 mm/min, and 100 mm/min, equivalent to nominal strain rates of $1.28x10^{-4}$ s^{-1}, $1.28x10^{-3}$ s^{-1}, $1.28x10^{-2}$ s^{-1}, $6.41x10^{-2}$ s^{-1}, and $1.28x10^{-1}$ s^{-1}. The compression tests were performed at constant crosshead speeds of 0.1 mm/min, 1 mm/min, and 10 mm/min, equivalent to nominal strain rates of $4.39x10^{-4}$ s^{-1}, $4.39x10^{-3}$ s^{-1}, and $4.39x10^{-2}$ s^{-1}. In compression, no lubricant was used between the niobium specimen and the steel anvils.

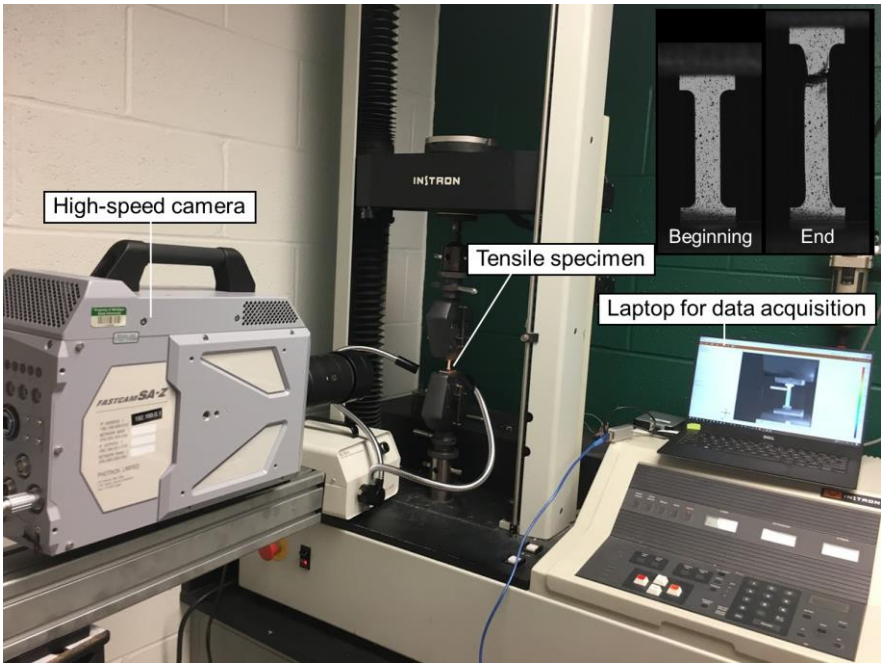

Figure 3.13: Screw-driven machine used for tensile and compression tests at MSU configured for digital image correlation. (Inset) Pictures of the specimens acquired by the high-speed camera at the beginning and the end of the test.

Figure 3.14 shows a typical load–displacement curve obtained at MSU for tensile tests. Five important features of the curve are numbered and described. First, a plateau of constant load is observed at the beginning of each test. Since all curves presented the same feature, this is likely an artefact of the tensile machine, such as the stretching of different gaps in the grips and the machine, and not a response of the specimens. The same plateau was observed in experimental curves obtained by Dr. Baars who used the same instrument during his thesis [140]. Points 2 and 3 show the upper and lower yield points, respectively. This phenomenon was not observed for all tests. Finally, points 4 and 5 show the onset of diffused and localized necking, respectively.

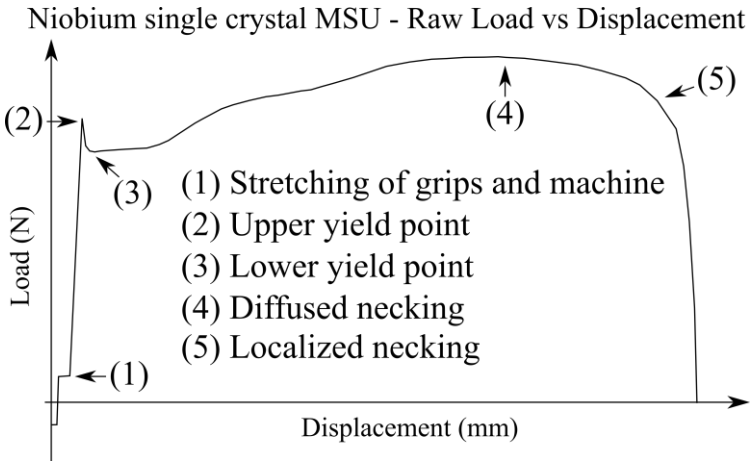

Figure 3.14: Typical load vs displacement curve obtained at the Michigan State University.

All tensile curves were corrected to remove the constant load plateau. A modulus correction was performed to remove the influence of the machine and grip stiffness in the measured crosshead displacement since no extensometer was used. Displacements larger than the length of the initial gage length of 13 mm were measured at fracture, which limits the type of extensometer that can be used. Digital image correlation of three tensile tests on specimens with different crystal orientations was used to accurately measure the elastic modulus of each specimen. A detailed study of elastic anisotropic properties was not conducted and an average machine stiffness value was instead used. Figure 3.15 shows a schematic of the stiffness of the machine, the specimen, and the effective (total) stiffness.

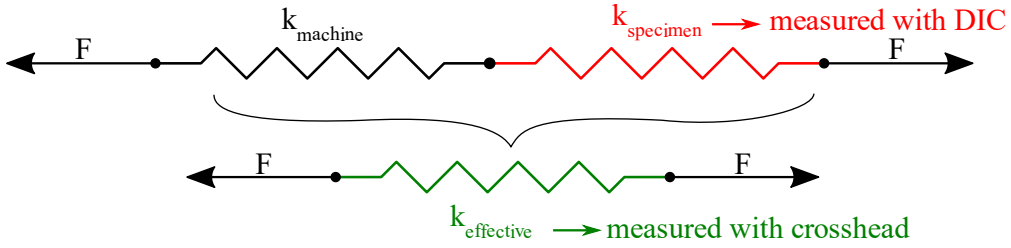

Figure 3.15: Schematic of the machine and specimen stiffness for the modulus correction.

Since the machine–specimen stiffness is considered as two springs in series, the following equation of the effective stiffness is used:

$$k_{\text{effective}} = \left(k_{machine}^{-1} + k_{specimen}^{-1}\right)^{-1} \tag{3.2}$$

Rearranging the terms yield the following equation to calculate the stiffness of the machine:

$$k_{machine} = \frac{k_{\text{effective}}\, k_{specimen}}{k_{specimen} - k_{\text{effective}}} \tag{3.3}$$

Three tests were performed with DIC at a constant crosshead speed of 10 mm/min for specimens 2-59, 7-152, and 10-158. A Photron FASTCAM SA-Z high speed camera was used at 60 frames per second and all specimens were painted in the gage section following the methodology presented in section 7.2.3. The GOM Correlate software was used for the 2D DIC analysis. The machines stiffness was calculated for the different orientations. An average stiffness of 2 060.3 N/mm and a standard deviation of 1 193.6 N/mm were calculated. The large standard deviation is not ideal, but no additional tensile tests with DIC were performed. The correction also looked reasonable for all the crystal orientations tested, i.e. no over corrected elastic modulus, that would have resulted in a negative strain, was obtained. The following equation was used to correct the stiffness for all tests:

$$\Delta y_{specimen} = \Delta y_{crosshead} - \frac{F}{k_{machine}} \tag{3.4}$$

where $\Delta y_{specimen}$ and $\Delta y_{crosshead}$ are the vertical displacements of the specimen after correction and measured with the crosshead of the machine, respectively.

Finally, since no pre-loading was used to remove potential gaps between the specimen and the grip and differences in manual grip tightening between the specimens is expected, a final correction was performed. A vertical translation of the load–displacement curve was performed for specimens where the load after rupture was different than zero. All final load should be equal to zero, since the load cell was tarred before inserting a new specimen. However, this curve correction is useful to ensure uniformity between the results since human errors, such as zeroing the load cell after tightening the specimen, are likely to have happened due to the high quantity of tests that were performed.

3.3.2. Intermediate Strain Rate Testing Methodologies (1 to 100 s^{-1})

3.3.2.1. Imperial College London – Annealed and Hard OFE Copper and Niobium Single Crystals

Tensile tests at intermediate nominal strain rates in the order of 1 s^{-1}, 10 s^{-1}, and 100 s^{-1} were performed using a servo-hydraulic (Instron VHS) tensile machine at Imperial College London. Annealed and hard OFE copper and niobium single crystal specimens with the geometry presented in Figure 3.12b with a circular hole in the grip were tested. The hole could not transfer the entire load without deforming the specimen in the region of the grip. Therefore, an aluminum holder clamping the specimen was used to partially transfer the machine's load to the specimen through friction forces.

A lost-motion rod [92] was used to ensure that the tests were performed at constant hydraulic piston speeds of approximately 0.013 m/s, 0.13 m/s, and 1.3 m/s, equivalent to nominal strain rates of 1 s^{-1}, 10 s^{-1}, and 100 s^{-1}. A schematic of the working principle of the lost motion rod during a tensile test is presented in Figure 3.16. The test is divided in three important steps: (1) acceleration of the piston to the desired testing speed without deforming the specimen, (2) the lost motion rod engages with the cylinder to start deforming the specimen, and (3) specimen deformation until rupture. No ringing issues due to the impact of the lost motion rod with the piston were measured at piston speeds of up to 1.3 m/s.

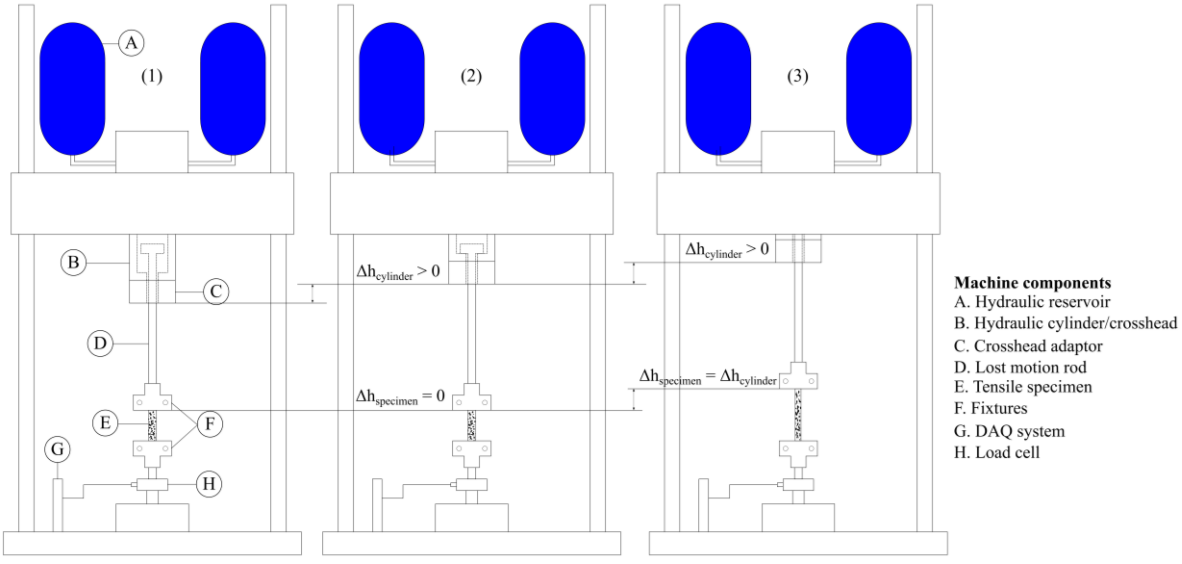

Figure 3.16: Servo-hydraulic tensile test sequence. (1) Motion of the piston, (2) engagement with the lost motion rod, and (3) deformation of the specimen until rupture.

The load was measured with a load cell located at the bottom of the assembly and the displacement was measured using digital image correlation. A high-speed camera (Phantom Miro M310) was used at up to 65 000 frames per second, resulting in images with square pixels of approximately 150 μm side lengths. Individual slip bands could not be observed at

this resolution and only the overall specimen deformation was measured. An uncooled thermal camera (FLIR A655sc) was used at 200 frames per second to measure the temperature evolution of specimens in time and space during the tests. The sample preparation method described in section 7.2.3. was used for DIC and for the thermal camera since the matte paint provided a high and uniform emissivity.

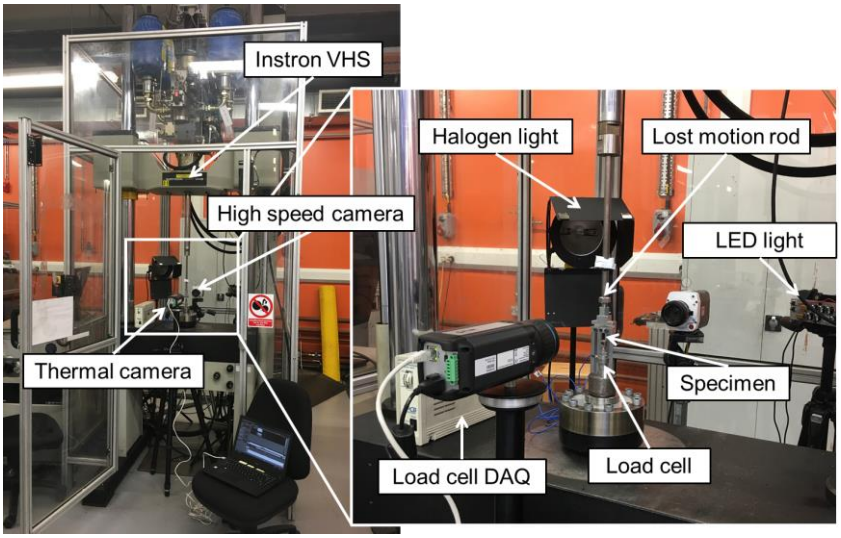

Figure 3.17: Servo-hydraulic tensile machine setup with high-speed and thermal camera.

The high-speed camera pictures were imported in the GOM Correlate software for 2D DIC analysis. The specimen displacement between two points at the boundaries of the gage section was exported from the software. This approach, shown in Figure 3.18, was used since the strain in the single crystal is not uniform across the gage section. An average engineering strain was calculated in MATLAB by dividing the increase in measured length with the initial length of about 13 mm. The stiffness of the machine and the grip is not affecting the result since the strain is measured directly on the specimen.

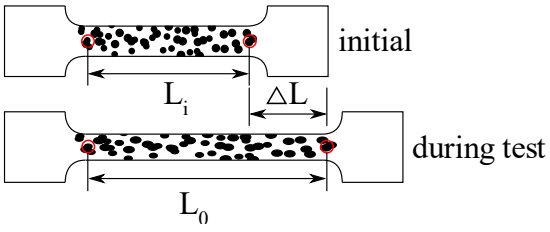

Figure 3.18: Schematic of engineering strain measurement method using DIC.

Different acquisition rates were used for the high-speed camera and the load cell. The data acquisition systems of the camera and the load cells were not synchronized, which complicated the calculation of stress–strain curves. The signals were manually adjusted by removing the zero load and absence of deformation during the displacement of the lost motion rod to have both signals starting at approximately the same time. This visual correction of the different data sets proved to be crucial, due to the high sensitivity of an

incorrect data alignment. Repeatable stress–strain curves were measured for specimens with the same crystal orientation, which confirmed the adequacy of the technique. Due to large deformations of the speckle pattern and a lower resolution at high strain rates, a loss of image correlation sometimes occurred at large strains. A linear fit of the increasing rate of specimen extension was used to account for the missing data points.

3.3.2.2. Imperial College London – Thermal Camera Calibration

The infrared thermal camera was calibrated in a static manner by measuring the cool down of a tungsten–tantalum (WTa) block and an OFE copper sheet, see Figure 3.19. Half of the WTa block was painted with a stochastic pattern, like for DIC, and a uniform white matte coat was applied on half of the copper sheet. Thermocouples were tapped on the painted and bare metal regions on the front and back faces of the metallic pieces.

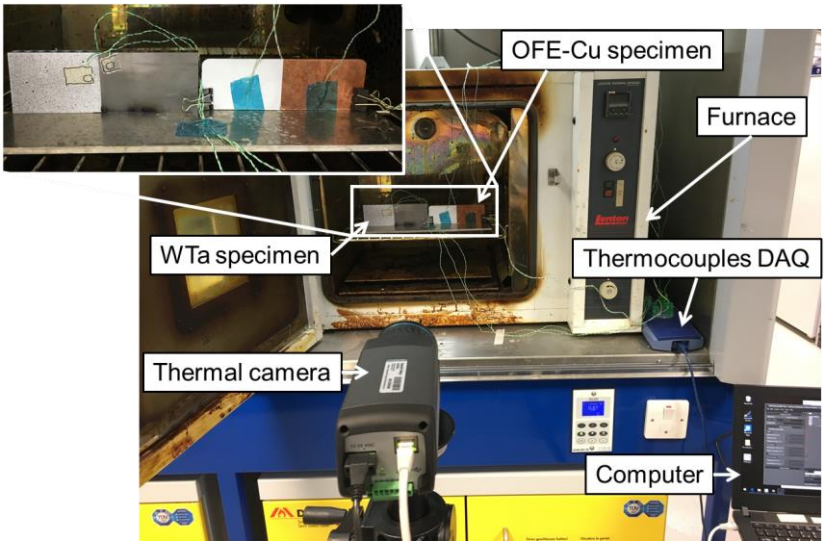

Figure 3.19: Thermal camera calibration setup on a tungsten–tantalum alloy block and an OFE copper sheet.

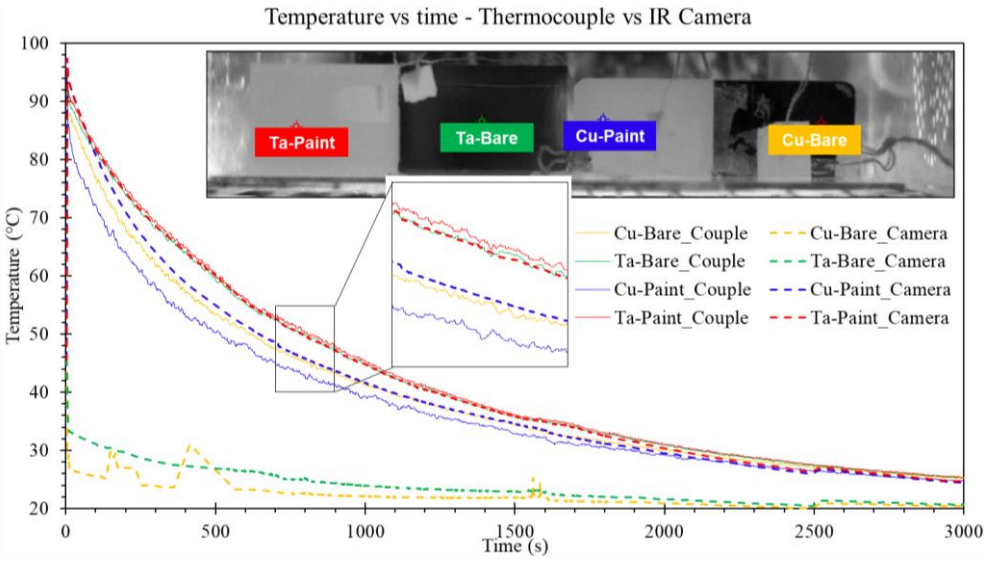

Figure 3.20: Thermal camera calibration measurements on bare metal and painted surface with thermocouples and camera.

The instrumented WTa block and the OFE copper sheet were placed in a furnace and heated to approximately 100°C. The furnace was opened and the thermal camera measured the cooldown of both pieces on the painted and bare metal regions. The temperature measured with the infrared camera was compared with the one measured with the thermocouples, see Figure 3.19. It was concluded that the thermal camera was well calibrated for the painted surfaces and that the speckled and uniformly white surfaces both provided a uniform emissivity. Note that the lower temperature of the thermocouple taped to the painted copper (blue line in Figure 3.19) was due to a poor contact between the thermocouple and the sheet due to a peeling-off tape. Access to spot welding to weld a thermocouple on a tensile specimen would have been ideal to ensure that the calibration is also accurate for higher heating rates by repeating the calibration with in-situ measurements during a tensile test.

3.3.3. High Strain Rate Testing Methodologies (> 1 000 s^{-1})

3.3.3.1. Arizona State University – Niobium Single Crystals

Tensile and compression tests at high strain rates of about 1 000 s^{-1} in tension and 4 000 s^{-1} in compression were performed at Arizona State University (ASU) with different split Hopkinson bar systems. The tensile specimen geometry used in the split Hopkinson bars is presented in Figure 3.12a and cylindrical specimens with equal diameter and thickness of 3.8 mm were used in compression.

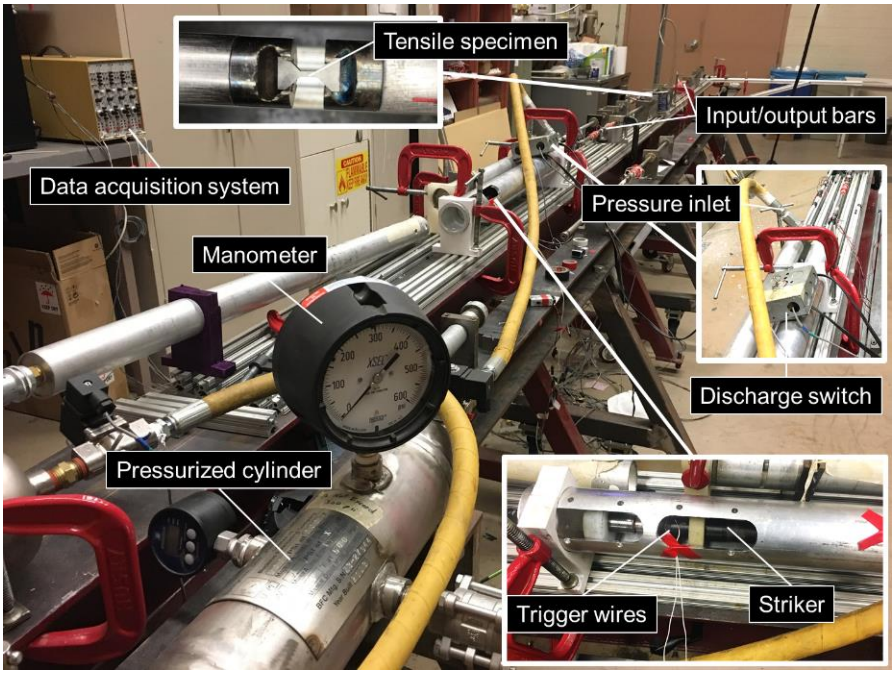

Figure 3.21: Split Hopkinson setup used at ASU for tensile tests with its main components.

Figure 3.21 shows the tensile split Hopkinson setup used at ASU and its main components. The striker, input and output bars of the tensile split Hopkinson system were made of maraging steel (E_b = 200 GPa) [197]–[200]. The input and output bars were 0.5″ (~12.7 mm)

in diameter. Thin copper rings were used as pulse shapers to obtain nearly constant strain rate deformation in the single crystals [96]. Strains were acquired at a frequency of 2 MHz. The strain data acquisition system was triggered by a contact of two wires pushed together by the striker before impacting the input bar. This approach proved to be very efficient and reliable. The compression bars were also 0.5″ in diameter but made of aluminum (E_b = 71.7 GPa). The pressurized cylinder was filled to 90 psi (~6.2 bar) with nitrogen for tensile and compression tests.

A few specimens were also painted for DIC measurements and pictures were acquired with a high-speed camera (Photron FASTCAM SA-Z) at 100 000 frames per second. Figure 3.22 shows the tensile split Hopkinson setup with the high-speed camera and lighting fixtures. The camera was lent and operated by Larry Vladic of Elite Motion LLC.

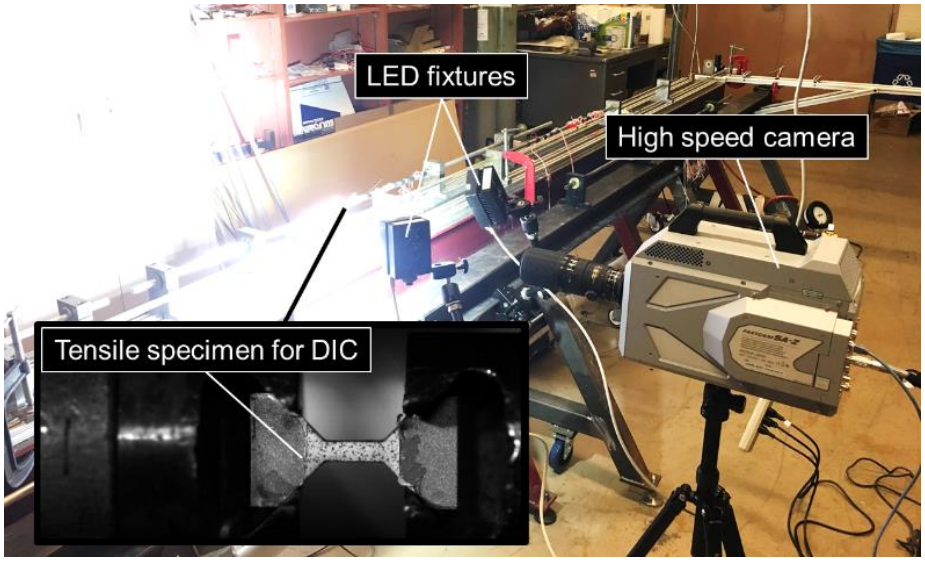

Figure 3.22: High-speed camera setup used at ASU for DIC at high strain rates tensile tests with split Hopkinson bars. (Inset) Picture of the tensile specimen acquired by the high-speed camera.

The raw voltage signal from the input and output bars were converted to engineering stress and strain using the equations presented in section 2.2. for the tensile and compression tests. Additional details about the methodology used at ASU are presented below. The voltage measured by the strain gages V_{bar} on the tension (compression) bars was converted to bar strain ε_{bar} with a strain gage factor f_{gage} of 6.285x10^{-4} V^{-1} (6.254x10^{-4} V^{-1}):

$$\varepsilon_{bar} = V_{bar}\, f_{gage}$$

To confirm that an equilibrium stress state was obtained during the test, the engineering stresses calculated with the one- and three-wave approximations were compared. The start and end of the incident, reflected, and transmitted strain waves were manually identified to synchronize the signals. Figure 3.23 shows an example of stress-state equilibrium validation

for a split Hopkinson bar tensile test performed at ASU. For this specimen, equilibrium is achieved for a nominal strain of about 0.02.

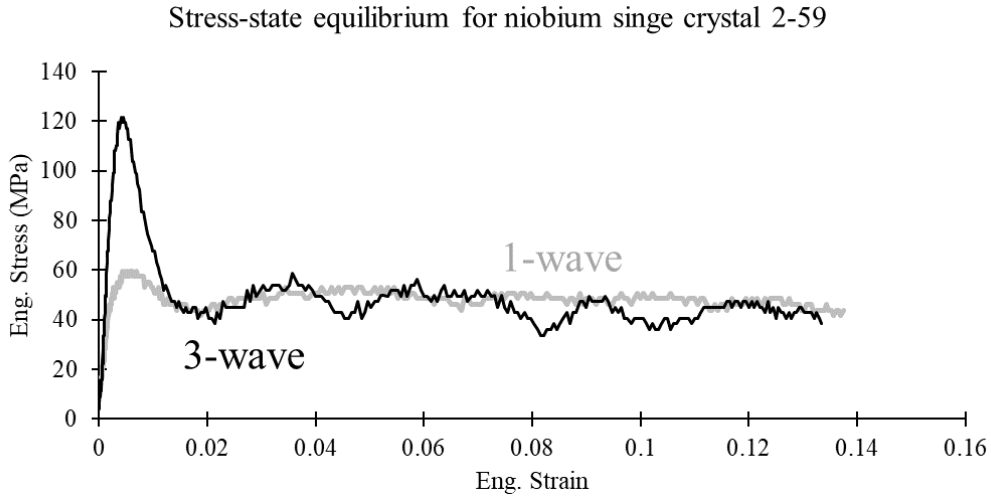

Figure 3.23: Stress-state equilibrium for a niobium single crystal deformed at high strain rate in tension.

The strain of the specimen was calculated from the strain rate of the specimen and the sampling rate of the data acquisition. The engineering strain rate $\dot{\varepsilon}_{eng}$ was calculated at each data point, acquired at intervals of 0.5 μs. This time interval Δt was multiplied by the strain rate of the specimen during each interval and summed to obtain the total strain at any instance j as follow:

$$\varepsilon_{eng_j} = \sum_{i=1}^{j} \dot{\varepsilon}_{eng_i} \Delta t$$

Finally, the average strain rate of the test was calculated by averaging the strain rate of the plateau of the near-square strain rate signal.

3.3.4. Nanoindentation Analysis

Figure 3.24 shows the nanoindenter (Bruker Hysitron TI980) used at ENSTA Bretagne to analyze niobium single crystal specimens. All indentations were performed at room temperature and elastic modulus and hardness values were calculated for each indent by the software of the machine. Generally, 16 indents (4x4) were taken to measure the average properties of a region. A maximum load of 500 μN, corresponding to an indent width of about 1.5 μm with a Berkovich tip, was always used. To avoid thermal drift issues, the specimens were left in the chamber for 1–2 hours before starting the measurements. Analyses of the evolution of the hardness and elastic modulus along the *x*- or *y*-directions of the stage or approximately along the tensile direction of a specimen were performed using MATLAB.

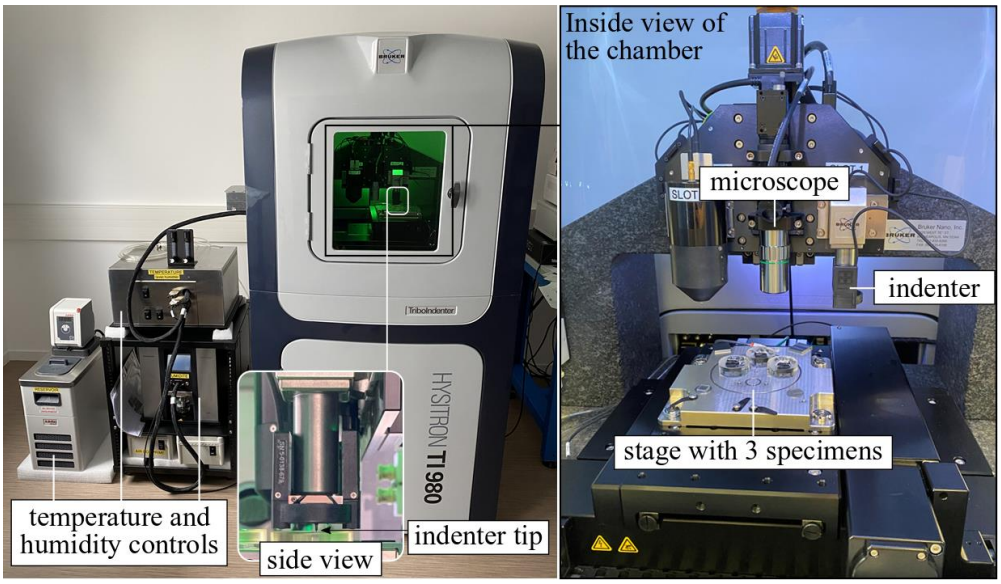

Figure 3.24: Nanoindentation system used at ENSTA Bretagne for the analysis of niobium single crystals. (Inset) Side view picture of the indenter during testing.

3.3.5. Microstructure Characterization

3.3.5.1. Scanning Electron Microscopy Analyses

Figure 3.25 shows the scanning electron microscopes used at CERN. The SEM in Figure 3.25a (ZEISS FEG-SEM Sigma and Oxford Instruments' Nordlys detector) was used for electron backscatter diffraction measurements. EBSD scans with varying step sizes, from about 0.5 to 2 μm, were acquired. All EBSD analyses were performed using the free MATLAB toolbox MTEX [201]. The SEM in Figure 3.25b (ZEISS Crossbeam 540) was equipped with a gallium ion focused ion beam. The FIB was used to machine a thin lamella for scanning transmission electron microscopy (STEM) analysis in the same microscope. This SEM was also used for fracture surface analyses and elemental analysis using an energy dispersive X-ray spectroscopy (EDS) detector.

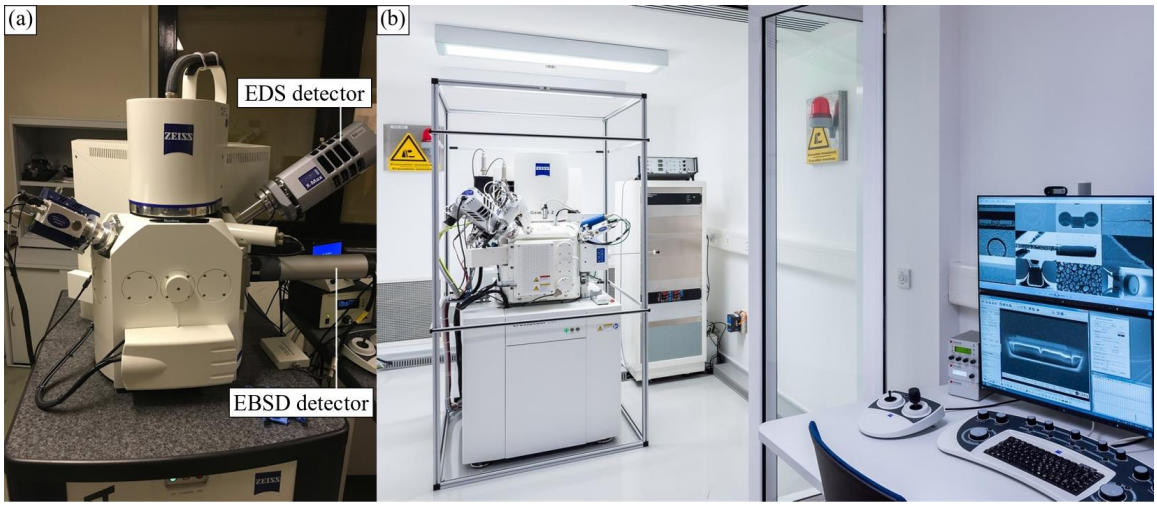

Figure 3.25: (a) SEM used for EBSD measurements and (b) SEM with a gallium FIB used for STEM lamella preparation and fracture surface analysis at CERN [202].

3.3.5.2. Transmission Electron Microscopy Analysis

Figure 3.26 shows the main components of the field emission TEM (JEOL JEM-2200FS) used at BAM for the analysis of niobium single crystal specimens. A specimen holder with an additional tilt direction was used and the specimen, prepared following the methodology shown in Figure 3.11, was held between beryllium washers. Different tilt angles were used for each specimen to optimize the imaging condition for the observation of dislocations.

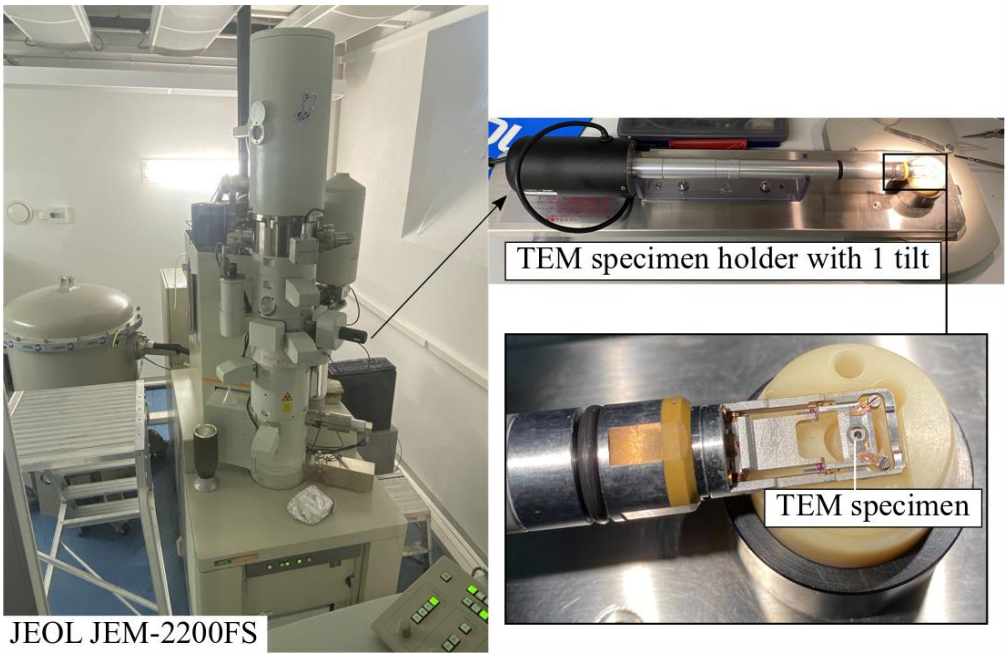

Figure 3.26: Main components of the TEM used at BAM for the analysis of niobium single crystals and closer views of the specimen holder.

Chapter 4 Mechanical Properties of Niobium Single Crystals

The tensile and compressive mechanical properties of high-purity niobium single crystals deformed at strain rates varying from approximately 10^{-4} to 10^{3} s^{-1} for different crystallographic orientations are presented in this chapter. The results are organized in the following subsections: (1) the effect of crystal orientation and strain rate on uniaxial tensile tests; (2) macroscopic spatial heterogeneity using in-situ digital image correlation on tensile specimens deformed at quasi-static and dynamic strain rates and (3) a comparison with in-situ temperature measurements at intermediate strain rate; (4) the effect of crystal orientation and strain rate on uniaxial compression tests; (5) tension/compression asymmetry for similar crystal orientations and strain rates; and (6) modeling of the flow stress as a function of strain rate, based on the nucleation and motion of kink pairs. Figure 4.1 shows the crystal orientation in the loading direction of the tensile and compression specimens, as previously discussed in section 3.1.1.2. and shown in Figure 3.5 for tensile specimens. Note that some tensile specimens were not tested.

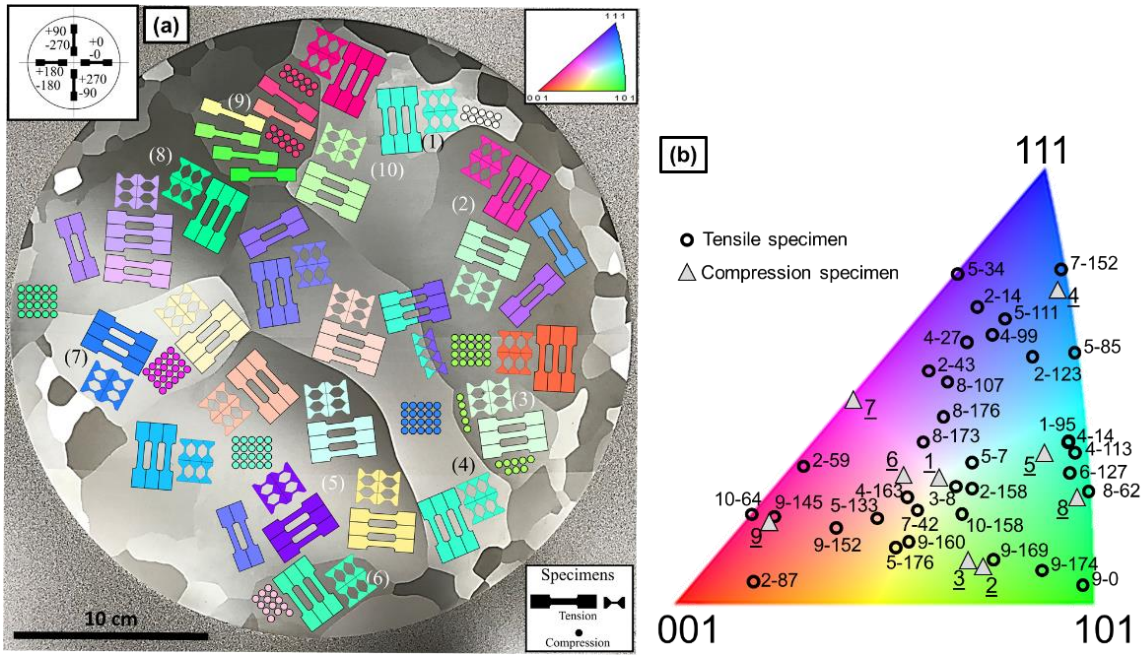

Figure 4.1: (a) Specimen layout in the large-grain niobium disk and (b) loading axis inverse pole figure for tensile and compression specimens. The color of the specimens in (a) represent the loading (tensile or compression) axis IPF colors in (b).

The slip plane normal and slip direction of the two slip systems with the highest Schmid factor were calculated for each tensile and compression specimen and are presented in Table 4.1. According to Schmid's law, dislocations will initially glide on the slip system with the

highest resolved shear stress, equivalent to the highest Schmid factor. Recall from Chapter 6 that Schmid's law is often not followed in BCC metals due to the out of plane stress components in the core of a screw dislocation. However, using Schmid's law remains, to the best of the author's knowledge, the most appropriate approach to predict which slip systems will likely activate, if dislocation glide will simultaneously take place on multiple systems, and allows for an orientation-based comparison of mechanical properties.

Table 4.1: Slip systems with the highest Schmid factors for all tensile (T) and compression (C) specimens, comparison of the slip directions of the two slip systems (S=same, D=different), ratios of Schmid factors and the strain rate of the tests performed on the specimens (QS=quasi-static, D=dynamic, N/A=no test performed). n_i, b_i, and SF_i denote, respectively, the slip normal, slip direction, and Schmid factor of slip system i.

Specimen #	$\underline{n}_1$	$\underline{b}_1$	SF_1	$\underline{n}_2$	$\underline{b}_2$	SF_2	Slip dir	SF_2/SF_1	Tests
1-95 (T)	$(\bar{1}\bar{1}2)$	[111]	0.497	$(\bar{1}01)$	[111]	0.438	S	0.881	QS, D
2-14 (T)	$(\bar{2}\bar{1}1)$	$[1\bar{1}1]$	0.412	(110)	$[1\bar{1}1]$	0.393	S	0.954	N/A
2-43 (T)	$(\bar{1}01)$	[111]	0.437	$(\bar{1}\bar{1}2)$	[111]	0.428	S	0.979	N/A
2-59 (T)	$(2\bar{1}1)$	$[\bar{1}\bar{1}1]$	0.471	$(\bar{1}01)$	[111]	0.459	D	0.975	QS, D
2-87 (T)	$(\bar{2}\bar{1}1)$	$[1\bar{1}1]$	0.496	(211)	$[\bar{1}11]$	0.483	D	0.974	QS, D
2-123 (T)	$(1\bar{1}2)$	$[\bar{1}11]$	0.459	(101)	$[\bar{1}11]$	0.418	S	0.911	N/A
2-158 (T)	$(1\bar{1}0)$	$[\bar{1}\bar{1}1]$	0.484	$(2\bar{1}1)$	$[\bar{1}\bar{1}1]$	0.479	S	0.990	QS, D
3-8 (T)	$(1\bar{1}0)$	$[\bar{1}\bar{1}1]$	0.487	$(2\bar{1}1)$	$[\bar{1}\bar{1}1]$	0.473	S	0.971	QS, D
4-14 (T)	(112)	$[\bar{1}\bar{1}1]$	0.495	(101)	$[\bar{1}\bar{1}1]$	0.439	S	0.887	N/A
4-27 (T)	(112)	$[\bar{1}\bar{1}1]$	0.430	(101)	$[\bar{1}\bar{1}1]$	0.418	S	0.972	N/A
4-99 (T)	$(2\bar{1}1)$	$[\bar{1}\bar{1}1]$	0.436	(101)	$[\bar{1}\bar{1}1]$	0.413	S	0.947	QS, D
4-113 (T)	$(2\bar{1}1)$	$[\bar{1}\bar{1}1]$	0.497	$(1\bar{1}0)$	$[\bar{1}\bar{1}1]$	0.438	S	0.881	QS, D
4-163 (T)	$(0\bar{1}1)$	[111]	0.495	$(\bar{1}\bar{1}2)$	[111]	0.450	S	0.909	D
5-7 (T)	$(1\bar{1}0)$	[111]	0.479	$(1\bar{2}1)$	[111]	0.477	S	0.996	QS, D
5-34 (T)	$(1\bar{2}1)$	[111]	0.377	$(2\bar{1}1)$	$[\bar{1}\bar{1}1]$	0.373	D	0.989	QS, D
5-85 (T)	$(\bar{2}\bar{1}1)$	$[1\bar{1}1]$	0.464	(110)	$[1\bar{1}1]$	0.403	S	0.869	QS, D
5-111 (T)	$(\bar{1}\bar{1}2)$	[111]	0.429	$(\bar{1}01)$	[111]	0.399	S	0.930	N/A
5-133 (T)	$(\bar{1}01)$	[111]	0.497	(101)	$[\bar{1}\bar{1}1]$	0.454	D	0.913	QS
5-176 (T)	$(1\bar{1}0)$	[111]	0.500	(110)	$[1\bar{1}1]$	0.468	D	0.936	D
6-127 (T)	$(\bar{1}\bar{1}2)$	[111]	0.499	$(0\bar{1}1)$	[111]	0.443	S	0.888	QS, D
7-42 (T)	$(0\bar{1}1)$	[111]	0.496	$(\bar{1}\bar{1}2)$	[111]	0.454	S	0.915	QS, D
7-152 (T)	$(1\bar{1}2)$	$[\bar{1}11]$	0.408	$(0\bar{1}1)$	$[\bar{1}11]$	0.354	S	0.868	QS, D
8-62 (T)	$(\bar{2}\bar{1}1)$	$[1\bar{1}1]$	0.500	$(\bar{1}01)$	$[1\bar{1}1]$	0.434	S	0.868	QS, D

8-107 (T)	$(\bar{1}01)$	[111]	0.445	$(\bar{1}\bar{1}2)$	[111]	0.443	S	0.996	QS
8-173 (T)	$(1\bar{1}0)$	[111]	0.477	$(1\bar{2}1)$	[111]	0.452	S	0.948	N/A
8-176 (T)	$(1\bar{1}0)$	[111]	0.465	$(1\bar{2}1)$	[111]	0.455	S	0.978	QS, D
9-0 (T)	$(\bar{1}\bar{1}2)$	[111]	0.480	(112)	$[\bar{1}\bar{1}1]$	0.461	D	0.960	N/A
9-145 (T)	$(\bar{1}21)$	$[\bar{1}\bar{1}1]$	0.494	$(0\bar{1}1)$	[111]	0.464	D	0.939	N/A
9-152 (T)	$(0\bar{1}1)$	[111]	0.492	$(\bar{1}21)$	$[\bar{1}\bar{1}1]$	0.470	D	0.955	N/A
9-160 (T)	$(0\bar{1}1)$	[111]	0.499	(011)	$[\bar{1}\bar{1}1]$	0.463	D	0.928	N/A
9-169 (T)	$(0\bar{1}1)$	[111]	0.477	$(\bar{1}\bar{1}2)$	[111]	0.476	S	0.998	N/A
9-174 (T)	$(\bar{1}\bar{1}2)$	[111]	0.482	$(0\bar{1}1)$	[111]	0.452	S	0.938	N/A
10-64 (T)	$(2\bar{1}1)$	$[\bar{1}\bar{1}1]$	0.498	$(\bar{1}01)$	[111]	0.450	D	0.904	QS, D
10-158 (T)	$(1\bar{1}0)$	$[\bar{1}\bar{1}1]$	0.490	$(2\bar{1}1)$	$[\bar{1}\bar{1}1]$	0.474	S	0.967	QS, D
1 (C)	$(\bar{1}01)$	[111]	0.489	$(\bar{2}11)$	[111]	0.464	S	0.949	QS, D
2 (C)	(101)	$[\bar{1}11]$	0.481	(211)	$[\bar{1}11]$	0.468	S	0.973	QS, D
3 (C)	(101)	$[\bar{1}11]$	0.487	(211)	$[\bar{1}11]$	0.465	S	0.955	QS, D
4 (C)	$(\bar{1}21)$	$[\bar{1}\bar{1}1]$	0.425	(011)	$[\bar{1}\bar{1}1]$	0.373	S	0.877	QS, D
5 (C)	$(\bar{2}11)$	[111]	0.495	$(1\bar{1}0)$	[111]	0.454	S	0.917	QS, D
6 (C)	$(\bar{1}01)$	[111]	0.490	$(\bar{2}11)$	[111]	0.445	S	0.908	QS, D
7 (C)	(011)	$[\bar{1}\bar{1}1]$	0.443	$(\bar{1}01)$	[111]	0.437	D	0.986	QS, D
8 (C)	$(\bar{2}11)$	[111]	0.499	$(1\bar{1}0)$	[111]	0.442	S	0.886	QS, D
9 (C)	$(1\bar{1}2)$	$[\bar{1}11]$	0.497	$(\bar{1}01)$	[111]	0.461	D	0.927	QS, D

4.1. Tensile Mechanical Properties

Tensile tests were performed at constant crosshead speeds of 1 mm/min and 10 mm/min, equivalent to nominal strain rates of 1.28×10^{-3} s^{-1} and 1.28×10^{-2} s^{-1}, at MSU for 17 different tensile orientations. Additional quasi-static tests were conducted at speeds of 0.1, 50, and 100 mm/min for an orientation close to the center of the IPF. Tests at intermediate strain rates, of approximately 1, 10, and 100 s^{-1}, were performed at Imperial College for few orientations. Finally, tensile split Hopkinson bars were used at ASU to conduct tests at strain rates of ~1 000 s^{-1}. More details about the different testing procedures are available in Chapter 7. Note that the majority of the tensile test results, e.g. mechanical properties and microstructure analysis, have been published by the author [176]. The article is open access, which allows for the reproduction of the original work. The sections below are then reproduced from the article and more details and analyses are provided when available.

4.1.1. Effect of Orientation

Figure 4.2a and b show engineering stress–strain curves for 17 and 18 different samples deformed in tension at nominal strain rates of $1.28x10^{-3}$ s^{-1} and $1.28x10^{-2}$ s^{-1}, respectively. Tensile axis IPF colors are used on a gray background to identify trends related to initial orientation. A minimum of two tests were performed for each orientation, but only one curve is presented for orientations that were highly repeatable. Large differences in hardening behavior are observed between the different orientations, for both quasi-static strain rates. Since plasticity in niobium single crystals is related to the thermal activation of dislocations gliding on slip planes, the anisotropy results from the activation and interaction of different slip systems.

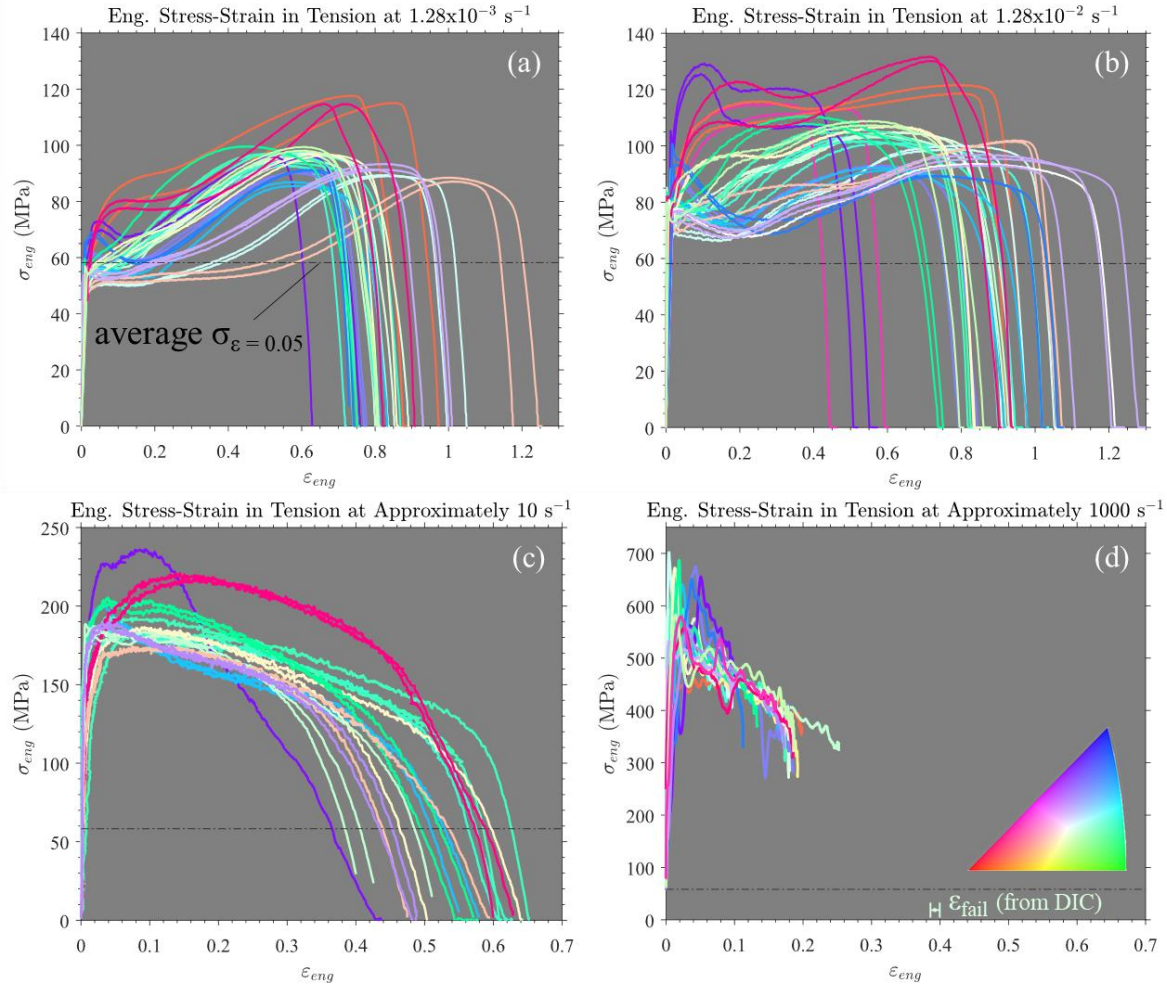

Figure 4.2: Engineering stress–strain curves of tensile specimens with different crystallographic orientations at nominal strain rates of (a) $1.28x10^{-3}$ s^{-1}, (b) $1.28x10^{-2}$ s^{-1}, approximately (c) 10 s^{-1}, and (d) 1 000 s^{-1}, colored by initial crystallographic tensile axis (see IPF inset). Split Hopkinson results are not up to fracture, since only the first strain wave was used for analysis. However, the strain to failure of specimen 3-8, measured with DIC, is plotted for reference. The black dash-dotted line represents the mean flow stress at 0.05 strain at a strain rate of $1.28x10^{-3}$ s^{-1} to enable comparison between the different stress scales [176].

A comparison of Figure 4.2a and b shows an increase in yield stress with increasing strain rate. An initial strain softening is observed for most samples deformed at $1.28x10^{-2}$ s^{-1}, but

is only visible for a few samples at the lower strain rate. Figure 4.2c shows engineering stress–strain curves for 9 different tensile orientations deformed at an intermediate nominal strain rate of approximately 10 s^{-1}. All curves show an initial hardening, followed by softening at some strain level. Different softening behaviors are observed for the different orientations, especially for orientations near [001] and [111]. Temperature increases of approximately 40°C and 85°C were measured using an infrared camera at the onset of necking and in the neck before rupture, respectively. These values are low compared to the melting point of niobium (~2 477°C). Moreover, as softening is observed at very low strain for some orientations, it cannot be attributed only to adiabatic heating effects. The apparent softening could be a consequence of presenting the results with the engineering stress, since a constant true stress would show as a reduction in engineering stress due to the reducing cross-sectional area that is not considered in the calculation of the latter. Different dislocation substructures at low at high strain rate, could also explain the apparent softening if the dislocation substructure generated during a high strain rate test offers less resistance to dislocation motion.

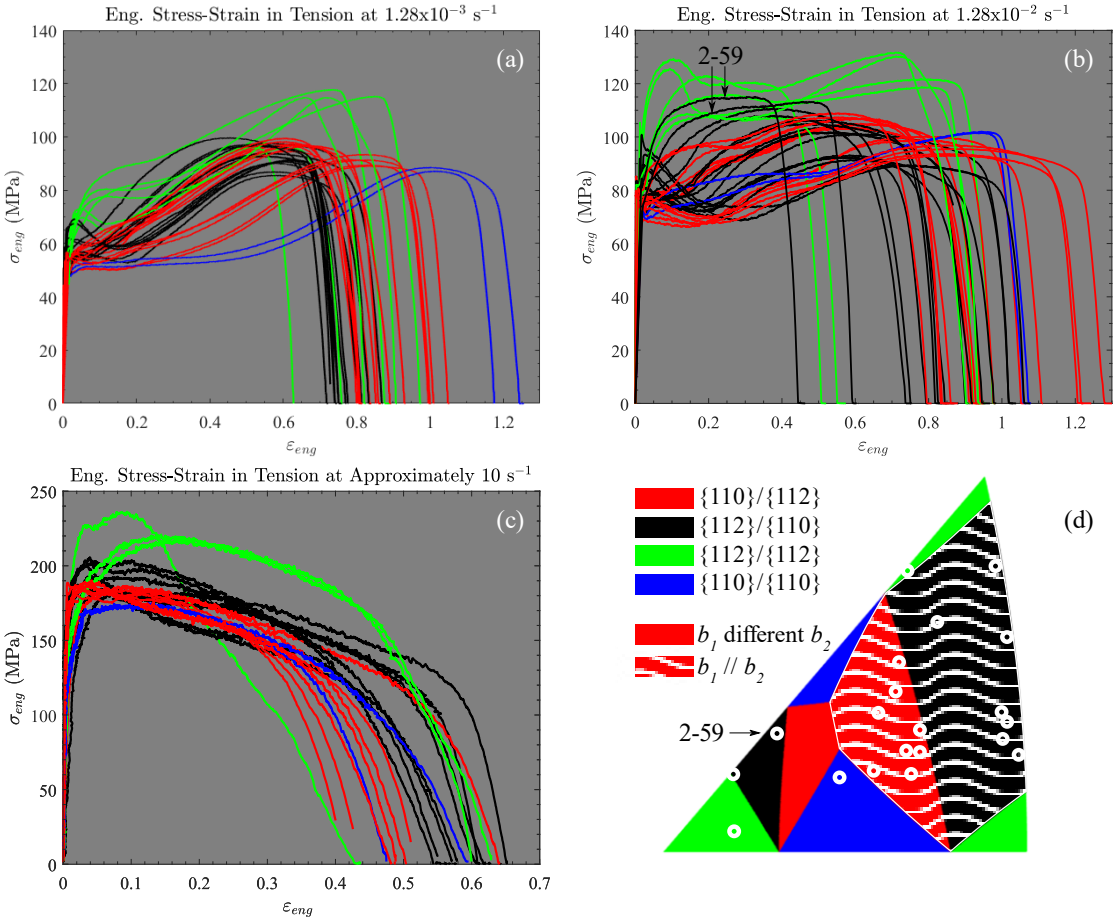

Figure 4.3: Engineering stress–strain curves of tensile specimens with different crystallographic orientations at nominal strain rates of (a) 1.28x10^{-3} s^{-1}, (b) 1.28x10^{-2} s^{-1}, and approximately (c) 10 s^{-1}, colored based on the slip plane of the two dominant slip systems for the initial crystallographic tensile axis (d). Orientations in the region of the IPF (d) with wavy white lines have parallel Burgers vectors on the two dominant slip systems.

Figure 4.3 shows the same stress–strain curves as in Figure 4.2a–c, but colored based on the slip plane of the two slip systems with the highest Schmid factor. For example, the slip plane fraction notation {110}/{112} in Figure 4.3d indicates that the first and second highest Schmid factors are for {110}<111> and {112}<111> slip systems, respectively. In addition, the relation between the orientation of the Burgers vectors for the different slip systems (same or different) are presented based on the wavy pattern (see Table 4.1 for more information about the two dominant slip systems of each specimen and section 2.3.2. for more details about the IPF in Figure 4.3d).

Crystals oriented in the {112}/{112} regions of the IPF (green) show the highest flow stress at strain rates between $1.28x10^{-3}$ s^{-1} and ~10 s^{-1}. Bieler et al. [156] also measured the highest flow stress for tensile specimens with a similar initial tensile orientation. Dislocations in those specimens are likely intersecting due to their different Burgers vectors and the impeded motion results in important strain hardening. However, the different Burgers vectors condition is not sufficient alone. The lowest flow stress measured at a strain rate of $1.28x10^{-3}$ s^{-1} was for the tensile specimen in the blue region (5-133) which also has Burgers vectors in different directions. The stress–strain curves in Figure 4.3 and the IPF in Figure 4.3d suggest that the dominant slip system must be of the {112}<111> family for the condition to be valid. The only specimen with an orientation in the black region and with Burgers vectors in different directions (2-59) also shows a higher flow stress than the average specimen deformed at a strain rate $1.28x10^{-2}$ s^{-1}, which confirms this hypothesis.

The effect of orientation on the mechanical properties at an engineering strain of 0.05 is presented in Figure 4.4 for all crystal orientations tested and at strain rates of $1.28x10^{-3}$ to ~1 000 s^{-1}. The distribution in flow stress appears to change between the different strain rates, but it is consistently high for specimen 5-34 (identified in Figure 4.4a) at all strain rates and low around the center of the IPF at all strain rates lower or equal to ~10 s^{-1}. The effect of strain rate on mechanical properties and strain rate sensitivity are further discussed in section 4.1.3. Specimens with an initial tensile orientation on the right dashed-boundary of the IPF (with equal Schmid factors for {110}<111> and {112}<111> slip systems) do not show higher flow stresses, which was originally expected due to the interaction of dislocations on different slip planes. As discussed in the previous paragraph and based on Figure 4.3d, this is likely due to Burgers vectors sharing the same direction for the slip systems with different slip planes.

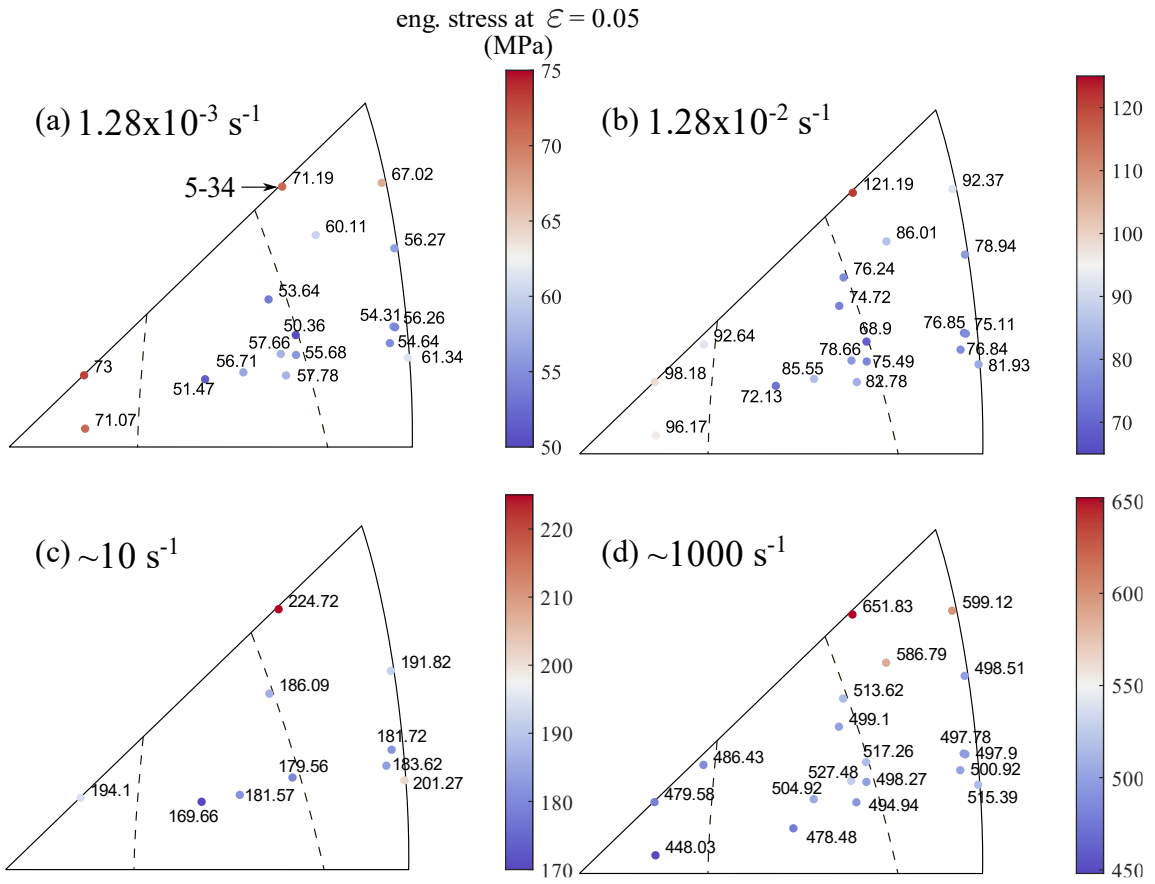

Figure 4.4: Engineering stress at a strain of 0.05 plotted in tensile axis IPFs of the initial crystal orientations at strain rates of (a) 1.28x10^{-3} s^{-1}, (b) 1.28x10^{-2} s^{-1}, (c) ~10 s^{-1}, and (d) ~1 000 s^{-1}.

4.1.1.1. Hardening Stages

Stress–strain curves of single crystals are often described with three hardening stages. Stage I, also called *easy glide*, has a low strain hardening rate and one primary slip system is active. Stage II starts with the increasing activation of secondary slip systems and the interaction of primary and secondary dislocations causes a higher and nearly constant hardening rate. Finally, stage III features a decreasing hardening rate and a saturating flow stress due to the dynamic annihilation of dislocations by cross-slip. Figure 4.5 shows the same engineering stress–strain curves shown in Figure 4.2, but for only four initial crystal orientations to ease the identification of different hardening stages and other differences in flow stress.

The tensile specimens deformed at the lowest strain rate of 1.28x10^{-3} s^{-1} and with the lowest yield stress all show the three hardening stages, as shown in Figure 4.2a and Figure 4.5a. At a strain rate of 1.28x10^{-2} s^{-1} (Figure 4.2b and Figure 4.5b), most tensile orientations exhibit a qualitatively very similar three-stage hardening behavior as observed at 1.28x10^{-3} s^{-1}. Consistent with this observation, Gnäupel–Herold et al. [151] observed three stages in their tensile tests at strain rates of 10^{-4} s^{-1} or smaller with different hardening rates and strain intervals between the stages for different orientations. As demonstrated for a particular tensile orientation in Figure 4.7, the presence of a clear stage I and II hardening gradually

disappears at strain rates between 10^{-1} and 10 s^{-1} (see also Figure 4.2c and Figure 4.5c). This implies that multiple slip systems are activated after yield. Such behavior is not unexpected because of the high strain-rate sensitivity of niobium. It is likely that the initially most stressed slip system gradually reaches the limit of its capacity (given by mobile density and maximum dislocation velocity) to accommodate ever higher imposed deformation rates. Therefore, part of the imposed (total) deformation rate results in increasing elastic deformation until further slip systems become sufficiently active at higher stress. The immediate (in terms of plastic strain) interaction of dislocations on intersecting slip planes then results in the absence of stage I hardening. The activation of multiple slip planes directly after yield was not directly observed because it would have required slip trace analysis, such as done in-situ by Kang et al. [20] for low strain rates up to $2.2x10^{-4}$ s^{-1}. The disappearance of stage I for increasing strain rate up to about 10^{-1} s^{-1} was also observed by Mitchell et al. [145].

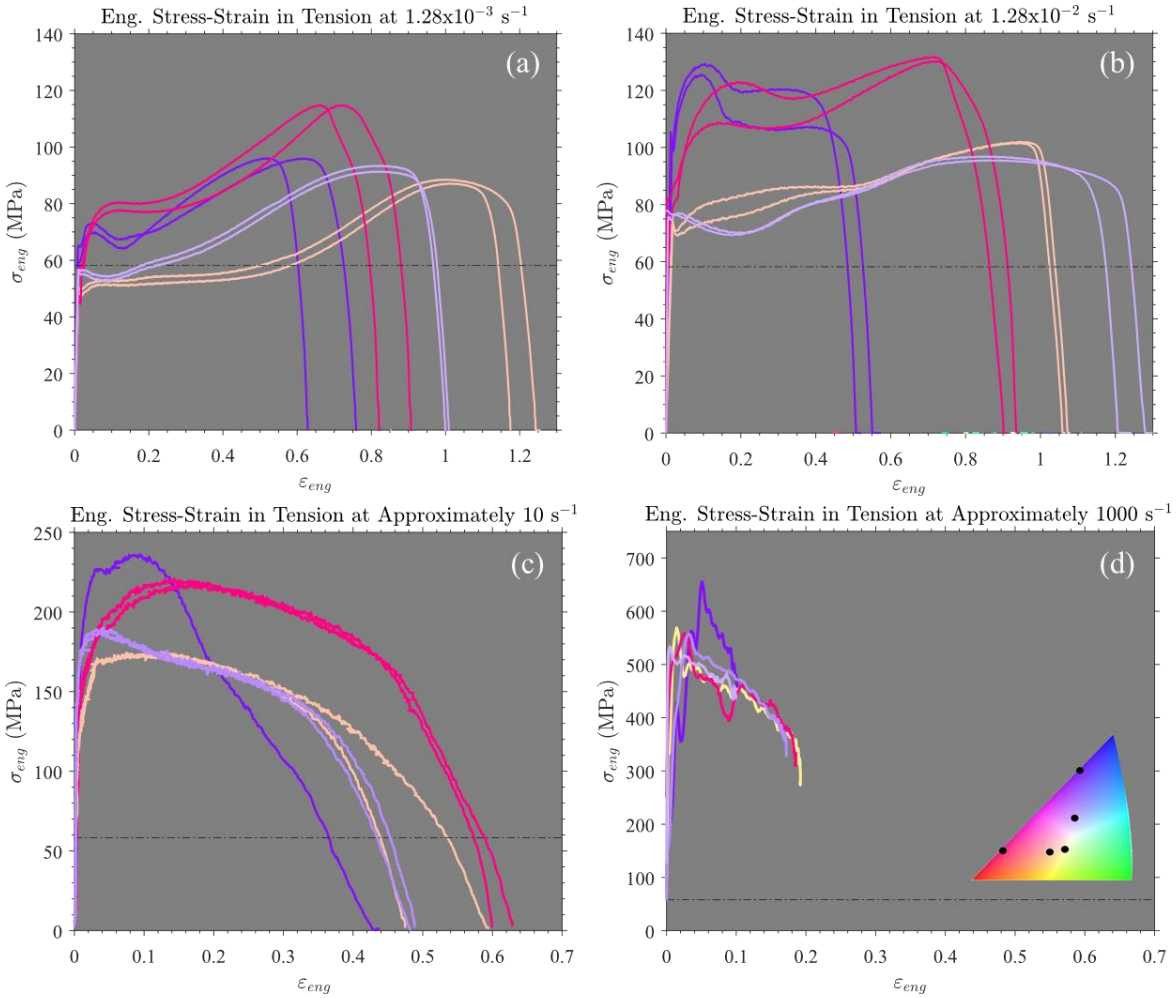

Figure 4.5: Engineering stress–strain curves of tensile specimens with different crystallographic orientations at nominal strain rates of (a) $1.28x10^{-3}$ s^{-1}, (b) $1.28x10^{-2}$ s^{-1}, approximately (c) 10 s^{-1}, and (d) 1 000 s^{-1}, colored by initial crystallographic tensile axis (see IPF inset). Split Hopkinson results are not up to fracture, since only the first strain wave was used for analysis. The black dash-dotted line represents the mean flow stress at 0.05 strain at a strain rate of $1.28x10^{-3}$ s^{-1} to enable comparison between the different stress scales.

The absence of stage II for strain rates greater or equal to ~10 s^{-1}, shown in Figure 4.2c and d, is probably due to a combination of different parameters: (1) the annihilation of dislocations by cross-slip, which is linked to the motion of dislocations on multiple slip systems (e.g. cross slip from {110} to {112} planes, and *vice versa*), (2) diffuse necking happened sooner, as indicated by the maximum flow stress at a lower strain in the stress-strain curves for higher strain rates and, and (3) thermal softening. These conclusions are based on the changes in the hardening and softening behavior exhibited in the stress-strain curves and especially the reduction of anisotropy at the highest strain rate. Mitchell and Spitzig [203] studied the mechanical properties of tantalum single crystals deformed at different strain rates and observed a similar behavior. They suggested that the hardening effects were "masked by unstable plastic flow and rapid necking" due to the initially high flow stress at high strain rate or low temperature.

4.1.1.2. Orientation-Dependent Strain to Failure

Figure 4.6 shows the average engineering strain to failure, defined as the value at the intersect of an engineering stress–strain curve with the strain-axis in Figure 4.2, at constant cross-head speeds of 1 mm/min and 10 mm/min, equivalent to nominal strain rates of $1.28x10^{-3}$ s^{-1} and $1.28x10^{-2}$ s^{-1}. The values are plotted on a tensile axis IPF with inner boundaries (dashed lines) at regions where the Schmid factor is equal on the {110} and {112} slip planes. The lowest strain to failure were 0.520 and 0.691 lower than the most ductile specimens at strain rates of $1.28x10^{-3}$ s^{-1} and $1.28x10^{-2}$ s^{-1}, respectively. Those values were measured for orientations close to the [001]–[101] boundary of the IPF and in regions with similar Schmid factors on different slip planes. The most ductile specimens had initial tensile orientations close to the center of the IPF and the right inner boundary of similar Schmid factors. At that boundary, the slip systems with different slip planes share the same Burgers vectors.

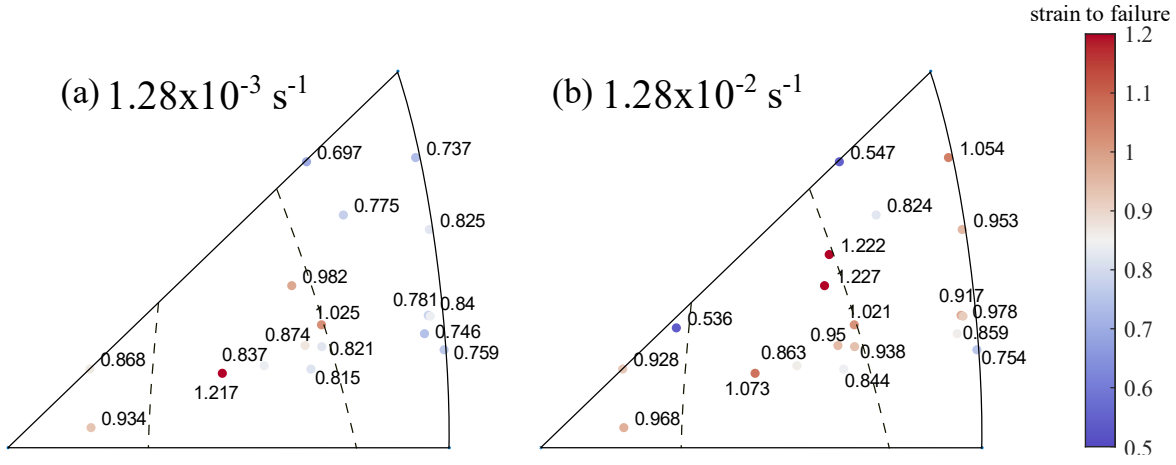

Figure 4.6: Strain to failure at nominal strain rates of (a) $1.28x10^{-3}$ s^{-1} and (b) $1.28x10^{-2}$ s^{-1} as function of the initial crystal orientation along the tensile axis.

4.1.2. Split Hopkinson Tensile Bars

Figure 4.2d shows the tensile properties of niobium single crystals deformed in 19 different crystallographic orientations with split Hopkinson bars at strain rates close to 10^3 s^{-1}. The high strain rate tests show a significant increase in the 500–650 MPa yield stress compared to the 50–70 MPa for the tests performed at the lowest strain rate ($1.28x10^{-3}$ s^{-1}). Moreover, the anisotropy is significantly reduced as the flow curves are much more similar for many orientations. This could also be explained by the combined effects of activation of multiple slip systems to accommodate for the imposed plastic strain at high rate, adiabatic heating effects, and strain heterogeneity from the split Hopkinson bar tests (see section 4.2.2.). The flow stress in all orientations reduces directly after yielding and through all the plastic domain. However, this apparent softening behavior does not necessarily imply a plastic flow localization. The high strain-rate sensitivity of the material may contribute to stabilize the plastic flow and delay the onset of localized necking [98], [204]. The high-speed camera observation did not reveal any occurrence of localized necking during the loading induced by the first incoming wave, but significant strain heterogeneities due to sample length and the nature of the split Hopkinson bar tests, as shown in Figure 4.12 [205], [206].

The maximum engineering strains measured during the SHTB tests are around 0.2. This value is however not the strain at fracture, but the strain of the specimen after deformation from the first incoming strain wave. The use of a high-speed camera showed that specimens usually failed after the third strain wave. Since the second and third waves are the consequences of the reflection of the initial wave at the end of the bars, the signal becomes difficult to analyze and consequently mechanical properties are only presented for the first wave.

Due to the dynamic nature of the tests, adiabatic heating from dissipation of mechanical energy into heat is expected. If significant enough, the concentration of heat in the neck leads to a strength reduction. In-situ measurements of the temperature were performed on single crystals deformed at 1 s^{-1}, 10 s^{-1}, and 100 s^{-1}. An average maximum temperature of 85°C was measured in the necks before failure for three specimens deformed at 10 s^{-1}. The temperature is expected to be higher for the tests performed at 1 000 s^{-1}. However, the experimental results of Mitchell et al. [145] showed that the temperature dependence of flow stress of niobium single crystals is low for temperatures above 298 K. Moreover, the apparent softening observed in the SHTB tests cannot be attributed only to adiabatic heating effects as it takes place directly after yield. A decrease in the peak force strain and a decrease in hardening at high strain rates is often observed for BCC polycrystalline metals, as reported by Peroni and Scapin [182] for niobium and Hoge and Mukherjee [126] for tantalum. This

phenomenon has been analyzed by Ghosh [98] and Zerilli and Armstrong [207]. The strain rate sensitivity of BCC materials is almost independent on the dislocation density and the plastic strain for polycrystalline materials [208]. In other words, an increase in strain rate causes an overstress with a magnitude independent on the plastic strain level. For this reason, the Considère criterion is met at a smaller strain when the strain rate is increased.

The observation made in section 4.1.1.1. on the activation of multiple slip systems after yield for higher strain rates is extrapolated to the dynamic tests. Since anisotropy is enhanced by the activation of limited slip systems, the activation of multiple slip systems for all crystallographic orientations leads to similar flow behavior for different orientations.

4.1.3. Effect of Strain Rate

The effect of strain rate on crystals with tensile directions near the center of the tensile axis IPF (crystals 2-158 and 3-8), for nine different strain rates is compared. Because the two orientations are very similar, results for both crystals are presented on the same plot to determine the strain rate sensitivity. Figure 4.7 combines the stress–strain curves for both orientations across all strain rates.

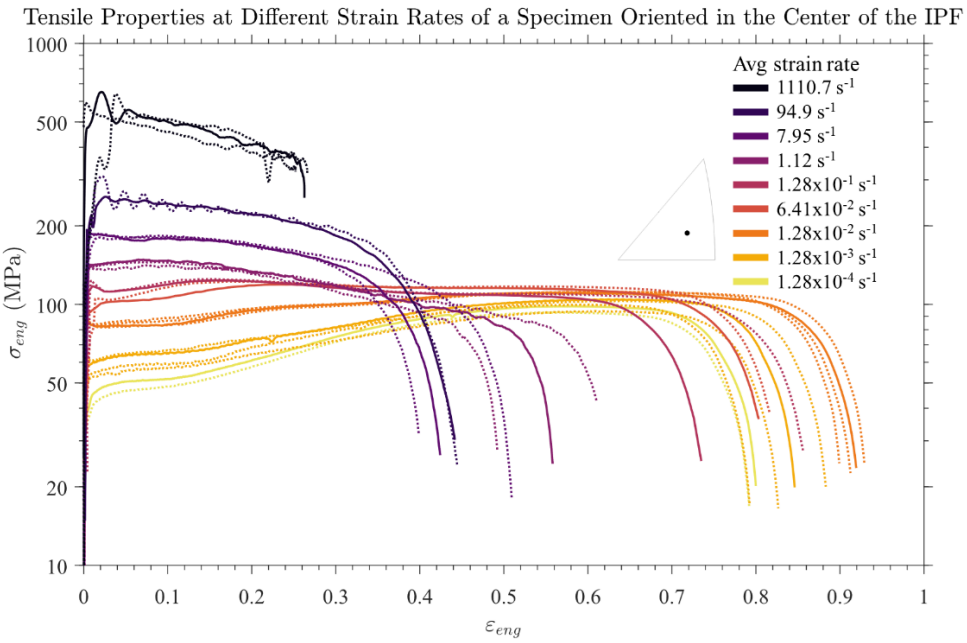

Figure 4.7: Tensile engineering stress–strain curves with a logarithmic stress scale for strain rates from 1.28×10^{-4} to approximately 1 000 s^{-1} on specimens 2-158 and 3-8 with a crystallographic orientation near the center of the IPF. (Dotted lines are repeat measurements for the same strain rate [176].)

Figure 4.7 reveals a systematic increase in flow stress with increasing strain rate. The elongation to failure is maximal at about 6.41×10^{-2} s^{-1}, and drops quickly with increasing strain rate as the work hardening rate becomes level or negative. A larger dispersion in fracture strain occurred for tests performed at 1 s^{-1} and 10 s^{-1}. This transition also corresponds

with a notable yield drop at about 120 MPa (~10^{-1} s^{-1}). The lack of yield drops at lower strain rates is probably caused by longer times for thermal activation of dislocation motion and hence a higher probability for dislocation detachment from pinning sites. Pinning is more dominant when there is less opportunity for thermally assisted detachment, so that the upper yield point (and its disappearance at higher rates) represents a locally saturated interstitial atom concentration in the dislocation core [200], [209]. Barely noticeable yield drops, less than 1 MPa in magnitude, were also observed by Gnäupel-Herold et al. [151] for different orientations, but for tensile tests performed at strain rates of 10^{-4} s^{-1} or lower.

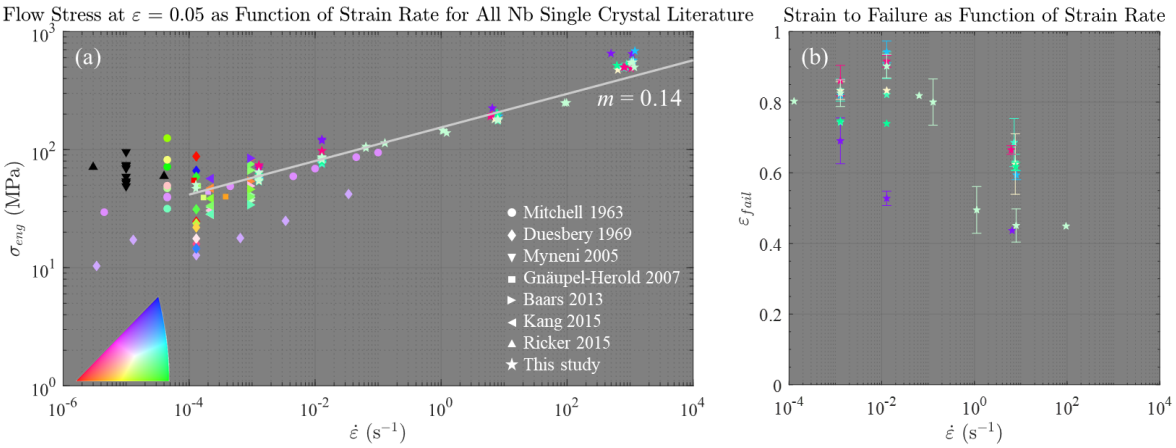

Figure 4.8: (a) flow stress at ε = 0.05 from the literature and this study with symbols colored by the tensile axis (black if not known) and (b) strain to failure across eight orders of magnitude of strain rate for an orientation near the center of the tensile axis IPF (specimens 2-158 and 3-8) and for three orders of magnitude of strain rate for 7 additional orientations. A white line of constant strain rate sensitivity slope of 0.14 is plotted in (a). (Error bars are not plotted when the standard deviation is smaller than the marker size or only one test was performed [176].)[1]

To compare properties of specimens with similar dislocation substructures at the different strain rates, strain rate change tests are often conducted to calculate the strain rate sensitivity. In this study, the strain rate sensitivity was calculated for engineering strains of 0.05 since no rate change tests were performed and stress equilibrium in split Hopkinson bars is often not reached at strains lower than 0.05 [94]. The flow stress in tension for the same crystal orientation as function of strain rate across eight orders of magnitude is presented in Figure 4.8a in light green together with seven additional crystal orientations colored according to their respective tensile axis IPF colors and tested over three orders of magnitude in strain rate. The strain rate sensitivity of the specimen near the center of the tensile axis IPF deformed at room temperature, $m = (\partial \ln \sigma_T / \partial \ln \dot{\varepsilon})_{\varepsilon=0.05} = 0.14$, is consistent over all but

[1] The flow stress in Duesbery's study [146] was calculated assuming that the specimen geometry was the same as in the study of Mitchell [145] (tests performed at same laboratory and the difference in calculated axial stresses is similar to the difference in reported shear stresses). The flow stress in Myneni's study [171] required to extract data from two sources to obtain the load [171] and calculate the likely specimen cross-sectional area by extracting the stress of one specimen [150].

the highest strain-rate data, as shown with the line of equal slope in Figure 4.8a. The resistance from the inertial forces opposing the deformation were estimated to be about 12 MPa [49]. This contribution is too small to explain the deviation at the highest rate. Figure 4.8a also provides a comparison with the literature. Despite different single crystal processing techniques and purity levels, the flow stresses at strain rates of the same order of magnitude are similar.

Figure 4.8b shows a reduction of the strain to failure with decreasing strain rates below 10^{-2} s^{-1} for different orientations. A similar result was obtained by Mitchell et al. [145] at a similar strain rate and by Ricker et al. [152] for tests at 10^{-5} s^{-1} and 10^{-6} s^{-1} and was explained by the increased interaction time between dislocations and mobile hydrogen interstitial atoms at the lowest strain rate, i.e. dynamic strain aging. The opposite trend is observed for the specimens deformed at intermediate strain rates, where the strain to failure is lower compared with the quasi-static specimens, for all orientations.

4.1.4. Activation Volume

Crossing of short range dislocation barriers, such as the Peierls–Nabarro stress, point defects (e.g. vacancies and self-interstitials) and other dislocations intersecting the slip plane, are temperature and strain rate dependent [100]. The resistance to dislocation motion is then dependent on a thermal term and the identification of the dominant thermally activated mechanism is possible by calculating the activation volume [100]. The activation volume is defined as the derivative of the activation enthalpy with respect to the thermal component of the stress and is calculated as

$$v^* = \frac{\sqrt{3}k_B T}{\sigma_T}\left(\frac{\partial \ln \dot{\varepsilon}}{\partial \ln \sigma_T}\right)_T \tag{4.1}$$

where k_B is the Boltzmann constant, T is the absolute temperature and $\partial \ln \dot{\varepsilon} / \partial \ln \sigma_T$ is the inverse of the strain rate sensitivity. Mitchell et al. calculated activation volumes for high-purity niobium single crystals using the strain rate sensitivity at yield, and activation volumes of 75 b^3 and 30 b^3 were obtained at strain rates of 4.5×10^{-6} s^{-1} and 1×10^{-1} s^{-1}, respectively [145], [210]. Using the same method, the activation volumes are calculated for specimens 2-158 and 3-8 for all strain rates using constant ($m = 0.14$) and rate-specific strain rate sensitivities at $\varepsilon = 0.05$ from Figure 4.8. Figure 4.9 shows excellent agreement between Mitchell et al. [145] and the present study, where v^* decreases from 60.6 b^3 to 2.6 b^3 with increasing flow stress. The decrease in activation volume in inverse proportion to the flow stress is consistent with a constant strain rate sensitivity and not uncommon for the range of

strain rates studied. An increase in strain rate sensitivity at the highest strain rate, as shown in Figure 4.8, results in a higher rate of reduction of activation volume.

According to Conrad [100], the decreasing activation volume from quasi-static to dynamic rates corresponds to the thermal activation of two mechanisms observed in BCC metals. First, overcoming of the Peierls–Nabarro stress, which is probably responsible for the increase in flow stress at the higher strain rates [211], [212]. See Figure 2.13 for a schematic of the kink pair nucleation mechanism to overcome Peierls–Nabarro stress. Second, cross-slip, i.e. a change in slip plane during dislocation glide (see Figure 2.6d), as observed by Duesbery et al. [108] in shear bands on the surface of deformed single crystals. The increasing activation volume with decreasing flow stress represents the volume over which thermal activation must operate to dissociate a dislocation from an interstitial pinned atmosphere.

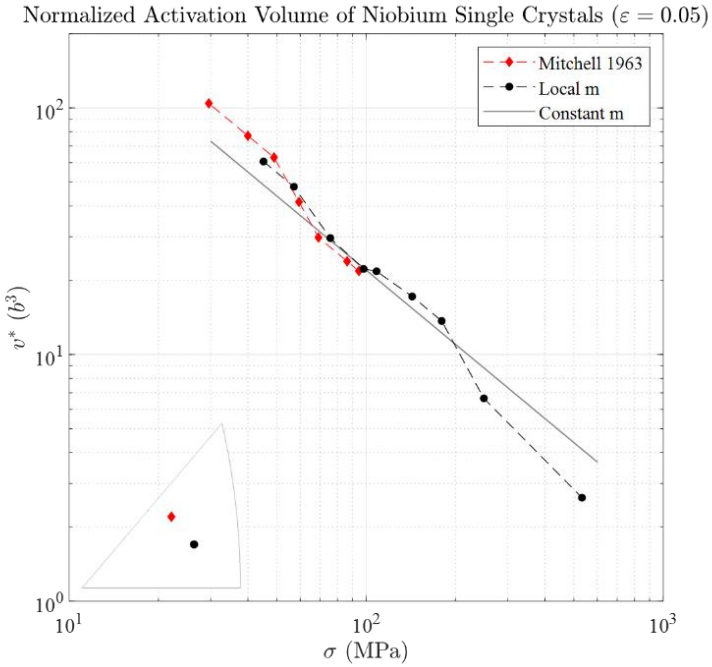

Figure 4.9: Activation volume as a function of the flow stress at ε = 0.05 [176].

4.2. Digital Image Correlation and Spatial Strain Heterogeneity in Tensile Specimens

4.2.1. Quasi-Static Strain Rate Spatial Strain Heterogeneity

Digital image correlation (DIC) was used to measure the distribution of total strain for three different specimens. Figure 4.10 shows the strain distribution at six different engineering strains in specimen 7-152, with a tensile orientation near the [111] direction, deformed at a nominal strain rate of 1.28×10^{-2} s^{-1}. Strain maps are numbered with their corresponding strains to show the strain distribution in the softening and hardening regimes at the

macroscopic scale. Plots of the total tensile strain distribution in the gage section of each strain map are presented for quantitative comparison in the top right of Figure 4.10. Pictures 3 and 4 show a region of high strain at the bottom of the specimen, indicating the onset of localized necking with thinning through the specimen thickness. However, the specimen did not fail in this region because it started to harden and did not deform further at a global strain of 0.25. Pictures 5 and 6 show more uniformly distributed total strain in the gage length, which corresponds to the hardening section of the curve.

The activation of different slip systems due to a rotation of the crystal could explain the transition from softening to hardening, since crystal rotation was measured with EBSD orientation maps. A change in the interaction of dislocations with each other or with interstitial atoms is also potentially responsible for the change in hardening rates. An expanding band, similar to a Lüders band in steel, was not observed with DIC, but the successive increase in strain in adjacent regions represents a strain propagation band in the specimen.

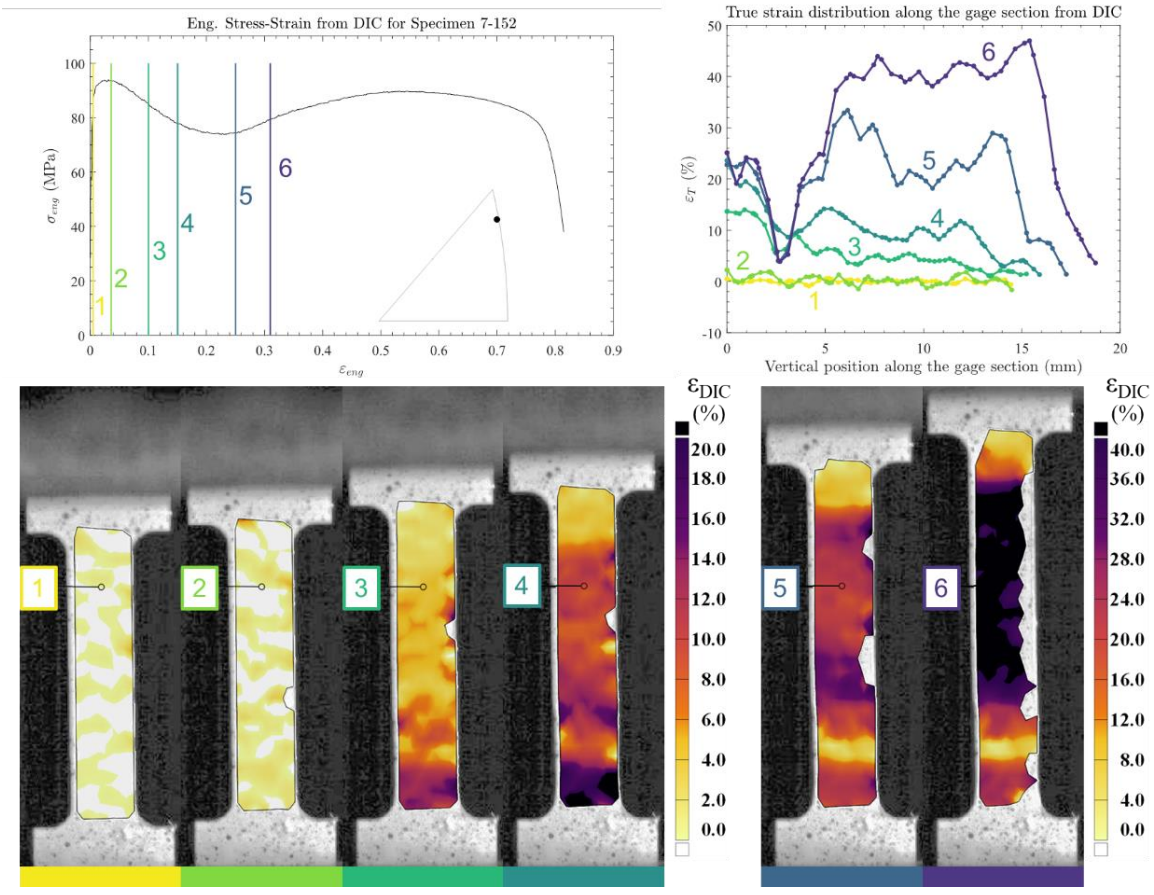

Figure 4.10: Strain localization in specimen 7-152 with a [111] tensile orientation deformed at 1.28×10^{-2} s^{-1}. (The strain reduction in the neck in 5 and 6 is not physical, but an artefact of the 2D DIC method [176].)

Figure 4.11 shows a similar analysis for specimen 2-59, with a tensile orientation on the lower half of the [001]–[111] boundary of the IPF and deformed at a nominal strain rate of

$1.28x10^{-2}$ s^{-1}. The stress–strain curve of this specimen has no softening component and a much lower elongation at failure than the specimen with a tensile orientation near [111]. From Table 4.1, the $(2\bar{1}1)[\bar{1}\bar{1}1]$ and $(\bar{1}01)[111]$ slip systems have similar Schmid factors of 0.471 and 0.459, respectively. The high hardening behavior and the absence of stage I hardening is then likely caused by the interaction of dislocations on the different slip systems. Finally, picture 3 of Figure 4.11 shows that strain localizes in the top of the specimen, where a neck forms and where the specimen ultimately fails.

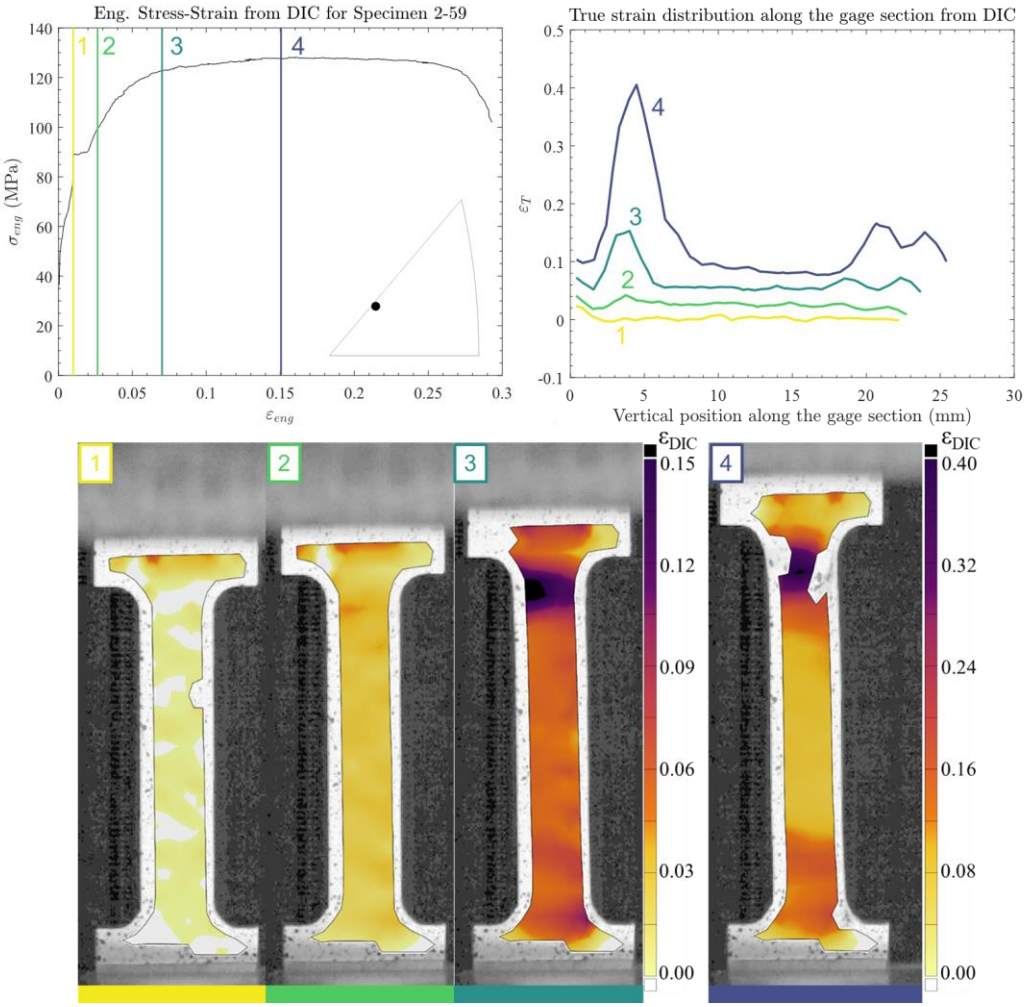

Figure 4.11: Strain localization of specimen 2-59 with a tensile orientation on the [001]–[111] boundary of the IPF deformed at $1.28x10^{-2}$ s^{-1}.

A third specimen (10-158) with a tensile orientation in the center of the IPF was deformed at a nominal strain rate of $1.28x10^{-2}$ s^{-1} and analyzed with DIC. This specimen showed a more uniform strain distribution, a strain to failure of ~0.72, and failed in the middle of the gage section. The different strain heterogeneities measured with DIC for three different crystal orientations are directly correlated to the anisotropic hardening behaviors observed in Figure 4.2. Finally, as mentioned in section 3.3.1.1., the elastic strain measured with DIC in the gage section of the three specimens deformed at a nominal strain rate of $1.28x10^{-2}$ s^{-1}

was used for stiffness correction of all stress-strain curves obtained at MSU for nominal strain rates of $1.28x10^{-4}$ to $1.28x10^{-1}$ s^{-1}.

4.2.2. High Strain Rate Spatial Strain Heterogeneity

Figure 4.12 shows strain localization in four specimens deformed at high strain rates with split Hopkinson tensile bars with different crystallographic orientations. Strain heterogeneities appears rapidly in the specimen. It is also interesting to observe that the region where the strain reaches its maximum is generally not located at the center of the specimen. This phenomenon is probably related to wave propagation effects [205], [213]. Moreover, the rather short length of the specimens used in the slip Hopkinson bar tests probably also contributes to the strain field heterogeneity [205], [206]. However, the heterogeneity of the strain distribution does not grow very much during the deformation of the specimen and localized necking is not reached during the first wave loading as the specimens failed after the third wave loading.

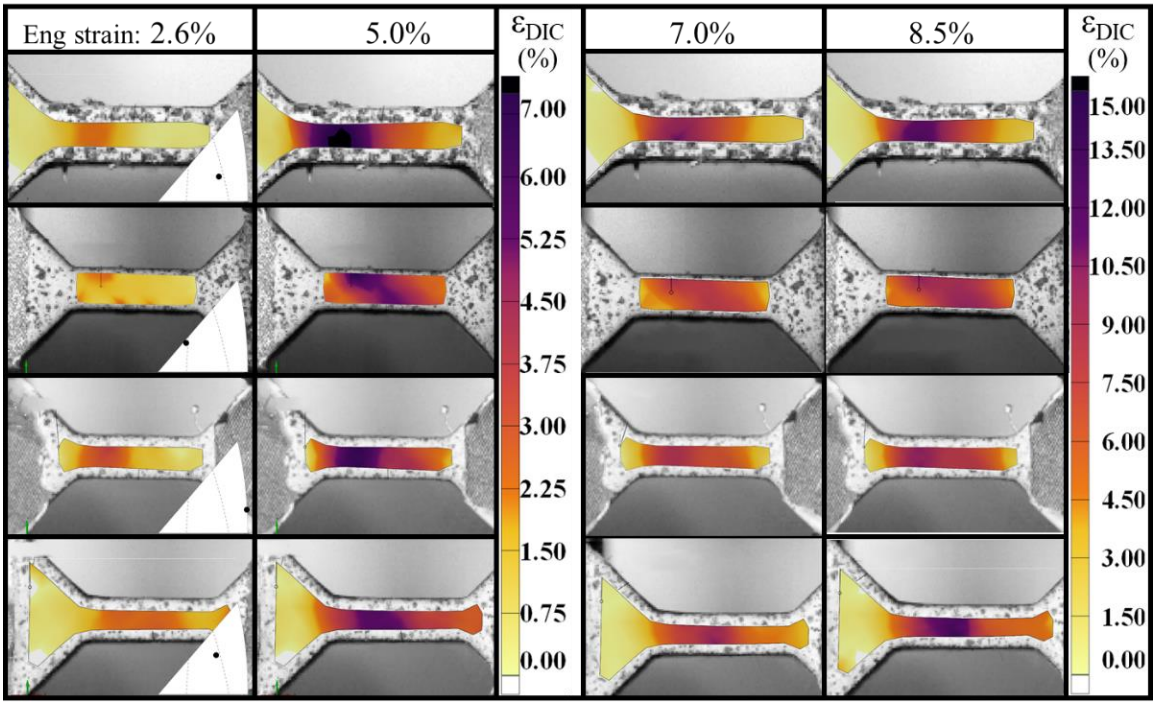

Figure 4.12: DIC strain maps of four specimens deformed at high strain rates (~1 000 s^{-1}) showing strain localization at low engineering strains. The initial tensile direction for each specimen is shown as dots on the inverse pole figure in the lowest strain image of each sample [176].

4.2.3. Strain to Failure in Split Hopkinson Bar Tests after Three Strain Waves

Figure 4.13a shows a plot of the engineering strain as function of time for the three waves required to break specimen 3-8, with a tensile orientation in the center of the IPF. From this figure, the strain rate can be approximated as the slope of a linear regression of each wave. The strain rate of the first, second, and third waves are approximately equal to 893 s^{-1}, 734 s^{-1}, and 597 s^{-1}. A 33.2% reduction in strain rate between the first wave, during

which the stress–strain curves in Figure 4.2 were calculated, and the strain to failure was measured and caused by losses in the split Hopkinson bars. The engineering strain at failure of the specimen was calculated using two DIC measurements and is equal to 0.39–0.40.

Figure 4.13b shows the strain distribution in the specimen during the first wave. The strain distribution indicates that the strain reaches is maximum at the center of the specimen, as discussed for other orientations in Figure 4.12. The large increase in engineering strain of about 0.20 between the end of the first wave and failure indicates that the apparent necking in Figure 4.13b is diffused and that the high strain rate sensitivity of niobium single crystal, about 0.14 for a similar orientation, stabilizes the post-necking deformation.

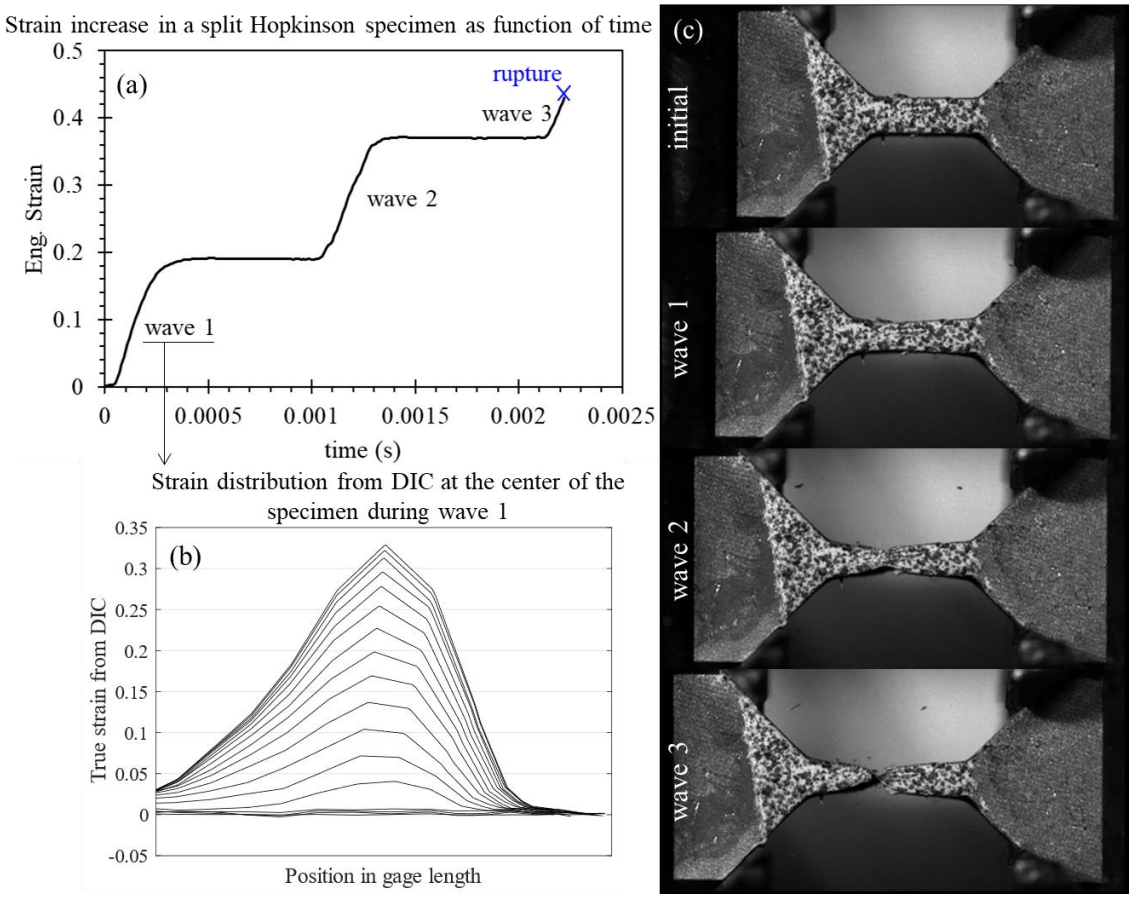

Figure 4.13: Evolution of (a) the engineering strain as a function of time for specimen 3-8 deformed high strain rate for three strain waves to calculate the strain to failure, (b) the strain distribution at the center of the specimen during the first wave, and (c) in-situ pictures from the high-speed camera at the beginning of the test and at the end of each wave.

Finally, the in-situ pictures of the specimen (Figure 4.13c) show that rupture occurs close to the center of the gage section. Flakes of paint, visible at the end of waves 2 and 3, caused issues for all other specimens deformed with split Hopkinson bars. The strain to failure could only be calculated for this specimen since the paint did not flake in the gage section. A loss of image correlation at large strains for the other specimens made the analysis impossible and this motivated the need to use a different paint or other strain measurement techniques

for future tests with ductile specimens deformed at high strain rates. Few specimens were tested without the white paint layer, but too much reflection from the lighting system made the image correlation impossible. Note that this approach was successfully used during the analysis of larger electron beam welded specimens, presented in Chapter 9.

4.3. Intermediate Strain Rate In-Situ Temperature Measurements

Thermal and high-speed cameras were used at Imperial College to investigate potential heterogeneities in the gage section, such as multiple necks or other elements that could not have been observed with digital image correlation. Figure 4.14 shows the temperature distribution along a line in the center of the gage length of specimens 5-34, 8-62, and 10-64 deformed at a strain rate of ~10 s^{-1}. The temperature was extracted from the beginning of the test up to the fracture of the specimen. However, since data was acquired at a low frequency of 200 Hz, the last frame is not always equal to the time of failure for different specimens. Therefore, the final and highest temperature in Figure 4.14 is constantly lower than the maximum temperature at failure and comparisons of absolute values can lead to wrong conclusions. The short analysis presented below is then based on the temperature distribution at the different frames.

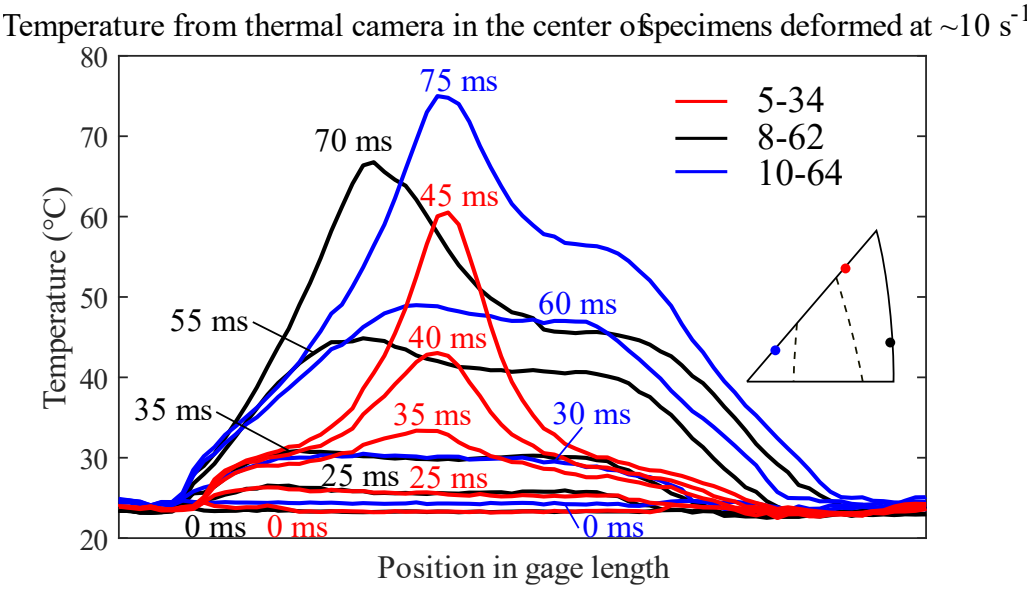

Figure 4.14: Temperature distribution along the center of the gage length of specimens 5-34, 8-62, and 10-64 deformed at ~10 s^{-1}, from the beginning of the test to fracture.

The specimen selection was based on the different hardening behaviors observed in Figure 4.2c. Specimen 5-34 has the highest flow stress, but the lowest strain to failure. Specimen 10-64 has the second largest flow stress and a strain to failure similar to most other crystal orientations, resulting in the largest plastic strain energy. Finally, the hardening behavior of specimen 8-62 is similar to all other crystal orientations.

All orientations show only one peak, indicating that only one neck was formed. The low ductility of specimen 5-34 correlates with a more acute neck, as shown by the narrower temperature peak and high temperature reached after 45 ms in Figure 4.14. Necking, and ultimately failure, did not occur in the center of the gage section for specimens 8-62 and 10-64. This behavior was not uncommon, as previously shown with DIC for specimen 2-59 deformed at a low nominal strain rate of 1.28×10^{-2} s^{-1}. Due to a lack of correlation at in some regions of the gage section at large strains, the strain history of the specimens is not compared with the thermal data. For this reason, the thermal data was used to identify the number of necks at intermediate strain rates and to evaluate the temperature rises during the tests, but not used for quantitative analyses. The modest measured temperature increases suggest that adiabatic heating effects are unlikely to play a significant role in the present experiments.

4.4. Compression Results

Compression tests were performed along the thickness of the large grain sheet presented in Figure 4.1a. Specimens from grains 1 to 9, with initial crystal orientations given in Figure 4.1b, were deformed at a constant crosshead velocity equivalent to a nominal quasi-static strain rate of 4.4×10^{-3} s^{-1}. Additional quasi-static tests at nominal strain rates of 4.4×10^{-4} s^{-1} and 4.4×10^{-2} s^{-1} were performed on specimens from grains 4, 5, 6, 7, and 9. Finally, high strain rate (~4 000 s^{-1}) split Hopkinson bar tests were performed on specimens with all crystal orientations. More details about the experimental procedures are provided in section 7.3.

Similar to the tensile tests, the effect of crystal orientation and strain rate is studied. The tensile and compression results are also compared for similar orientations and strain rates in the next subsection to quantify tension/compression (T/C) asymmetry.

4.4.1. Effect of Orientation

Figure 4.15 shows the mechanical properties of niobium single crystals deformed in compression at nominal strain rates of (a) 4.4×10^{-4} s^{-1}, (b) 4.4×10^{-3} s^{-1}, (c) 4.4×10^{-2} s^{-1}, and ~4 000 s^{-1} for nine different crystal orientations. The colors of the different true stress–true strain curves represent the crystal initial orientation in the loading direction. The majority of the stress–strain curves show at least two hardening stages at quasi-static strain rates and a gradient of hardening properties for orientations with stage I and II at a strain rate of 4.4×10^{-3} s^{-1} (Figure 4.15b). To quantitatively compare the different crystal orientations with the hardening behaviors and flow stresses, the projection angles θ and α on the [001]–[111] and [101]–[111] boundaries of the inverse pole figure were calculated for crystals in region A of Figure 4.16c. Angles θ and α are schematically shown for a unit sphere and an IPF in Figure 4.16a and b. This choice of projection angles is based on the

expected crystal rotation for BCC metals deformed in compression. Single crystals with an initial orientation along the loading direction in region A or B in Figure 4.16c will rotate toward the [111] or [001] end stable orientations, respectively [113] (more details in section 2.3.8.).

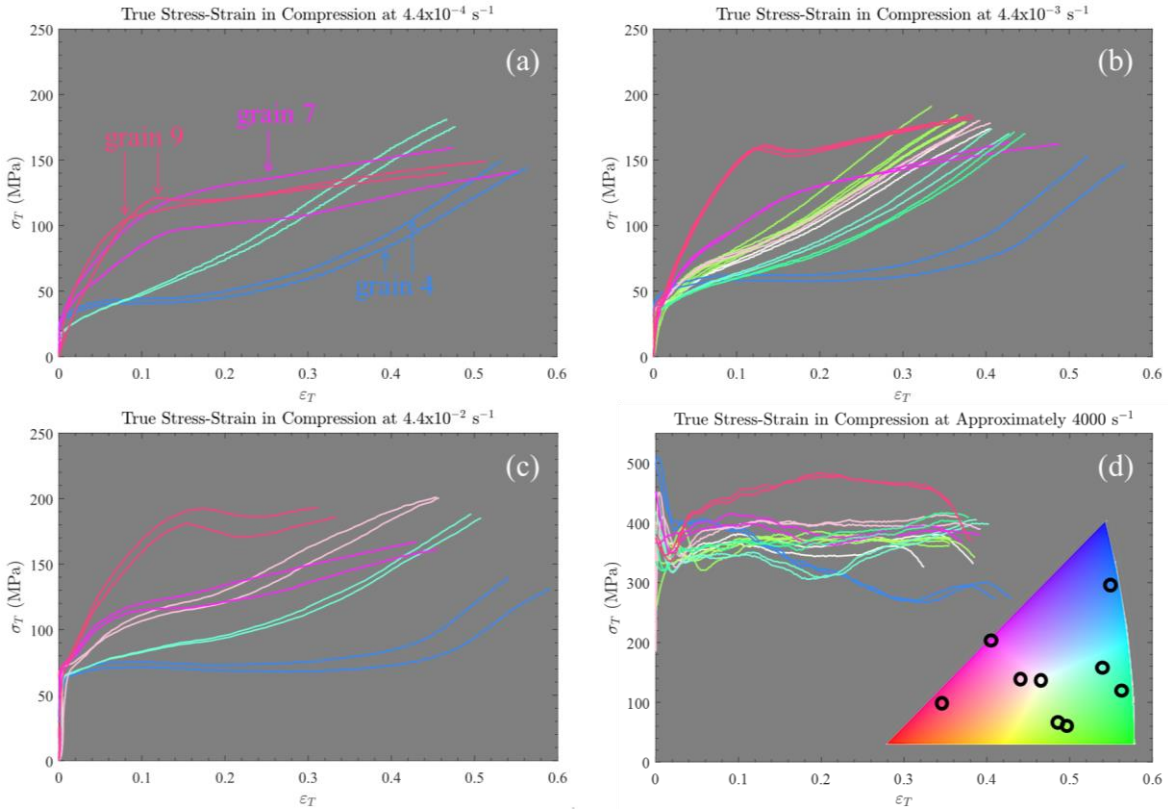

Figure 4.15: True stress–strain compression curves for specimens deformed at nominal strain rates of (a) 4.4x10^{-4} s^{-1}, (b) 4.4x10^{-3} s^{-1}, (c) 4.4x10^{-2} s^{-1}, and (d) ~4 000 s^{-1}. Colors represent the initial compression axis orientation.

The single crystal specimens deformed in this study all have an initial crystal orientation in zone A, except for grain 9 that is in zone B (orientation shown in Figure 4.15d). Specimens from grain 9 show the highest flow stress at all strain rates and softening, followed by an additional hardening stage, at a true strain of approximately 0.15. The latter was not observed for specimens from region A. Finally, parabolic, compared with three-stage, hardening is observed for specimens cut in grains 9 and 7. The initial orientation of grain 7 specimens is on the [001]–[111] boundary IPF, which indicates that the Schmid factor is equal on the primary and conjugate slip systems. The activation of both slip systems and the interaction of dislocations explain the absence of stage I hardening.

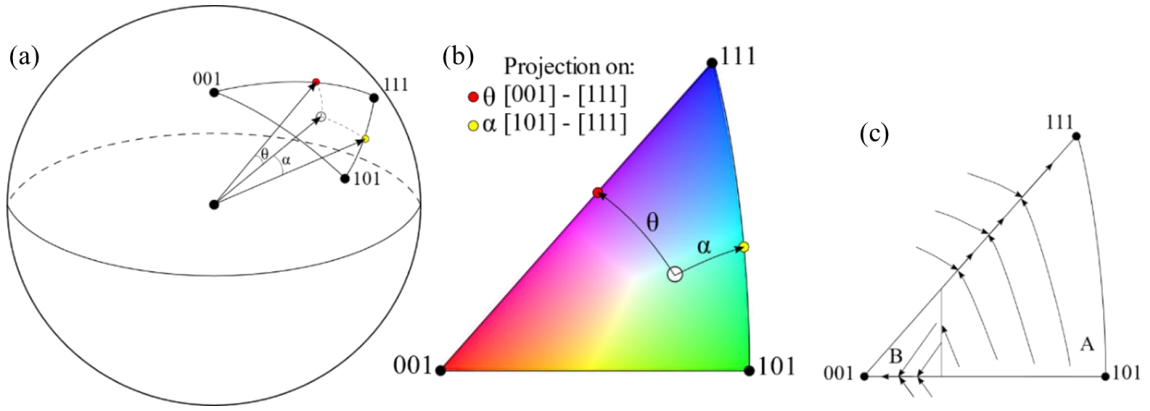

Figure 4.16: Projection of crystal compression direction on the [001]-[111] and [101]-[111] boundaries of the IPF in (a) 3D and (b) 2D on an inverse pole figure and (c) stable end orientations for BCC crystals deformed in compression, reproduced from Hosford [113].

Figure 4.17a shows the calculated projection angles θ and α, and their sum for the initial crystal orientations of grains 1 to 8. The crystal rotation toward the [001]–[111] boundary by θ represents the theoretical extent of single-slip and stage I hardening. The activation of the conjugate slip system, corresponding with the onset of stage II hardening, is only expected upon rotation of the crystal up to the [001]–[111] boundary. The parabolic hardening and absence of stage I hardening of specimen 7, as previously discussed, is quantitatively confirmed by the small θ projection angle.

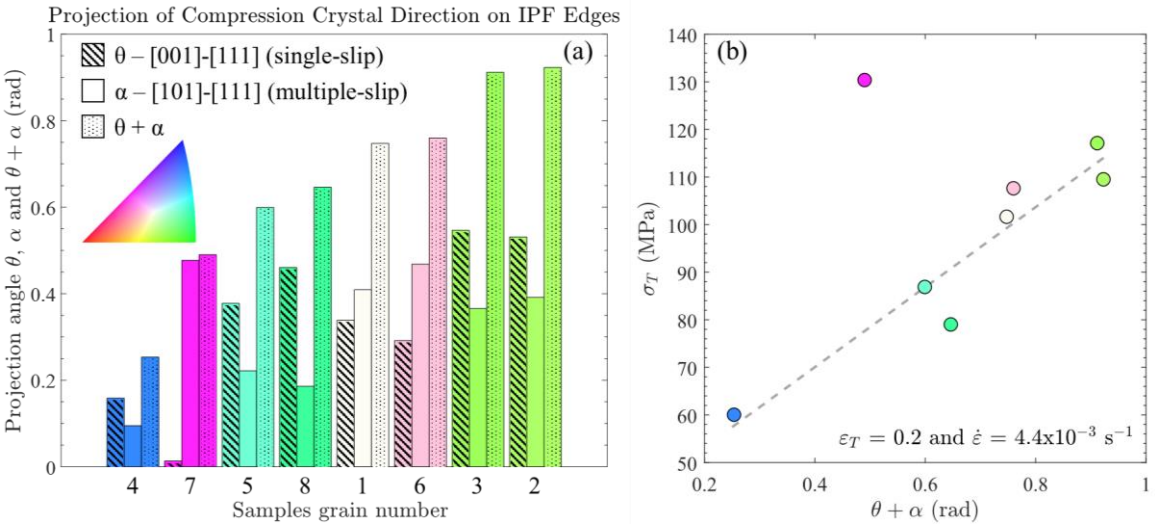

Figure 4.17: (a) Projection angles θ, α, and θ+α on the boundaries of the IPF for specimens with an initial crystal orientation in region A of the IPF (the projections are sorted by increasing θ+α). (b) True stress at a true strain of 0.2 for tests at a nominal strain rate of $4.4\text{x}10^{-3}$ s^{-1} as function of θ+α. Colors represent the initial compression axis orientation.

For specimens with stage I and II hardening, the reduction in the extent of stage I, and corresponding increase in flow stress, is positively correlated with the increasing sum of the projection angles (θ + α). The sum of the projection angles is analogous to the total rotation required to reach the [111] stable end orientation. This result indicates that the θ projection angle is not dictating the extent of single slip. The activation of a second slip system is then

expected to occur before the specimen orientation in the compression axis has reached the [001]–[111] boundary. In-situ measurements of the change in crystal orientation and the activated slip systems during the compression tests would be required to confirm this hypothesis. Finally, the correlation between the flow stress and the total projection angles in Figure 4.17b, for a nominal strain rate of $4.4x10^{-3}$ s^{-1} at a true strain of 0.2, is likely caused by the activation of multiple slip systems during crystal rotation, leading to impeded dislocation motion and strain hardening.

The effect of the initial crystal orientation on the three hardening stages was reported by Mitchell et al. [145] for niobium single crystals deformed in tension at room temperature and at a strain rate of $4.5x10^{-5}$ s^{-1}. The extent of easy glide (stage I) for specimens with an initial orientation closer to the [001]–[101] boundary, the double-glide boundary analogous to the [001]–[111] boundary in compression, was the smallest. This result is again in agreement with the hardening behavior of grain 7 specimens deformed in compression, but not with the specimens from other grains, such as grain 4. Mitchell et al. [145] also observed that the onset of double glide (stage II) was premature compared with the sample rotation reaching that IPF boundary, which would support the hypothesis of the previous paragraph. However, those trends were not observed for tensile tests performed during this study (Figure 4.2) and could be caused for by the lowest strain rate used in the literature.

4.4.2. Effect of Strain Rate

A large increase in yield stress from approximately 30 to 400 MPa was measured in Figure 4.15 for strain rates of $4.4x10^{-4}$ s^{-1} and 4 000 s^{-1}, respectively. Similar strength anisotropies were observed at quasi-static and high strain rate, e.g. the specimens with the highest and lowest flow stresses are from grains 9 and 4, respectively. This differs from the tensile specimens deformed at ~1 000 s^{-1} where the strength anisotropy was reduced. The reduction of anisotropy is then not only caused by the increase in strain rate and the activation of multiple slip systems, but appears to be dependent on the nature of the test and potentially necking. However, on a logarithmic stress scale, as presented in Figure 4.18, the flow stress at a true strain of 0.05 is less scattered at a high strain rate.

The three-stage hardening behavior is not observed at high strain rate and the stress–strain curve of the specimen with an orientation close to [111] is softening through the whole plastic domain (Figure 4.15d). Specimens from this orientation were heavily deformed, with a large relative displacement of the top and bottom surfaces and large shear strain. Figure 5.21 shows a schematic of the final geometry of specimens from grain 4 compared with other specimens (with a visible barreling effect). The activation of one slip system and the extent of easy glide at a strain rate of $4.4x10^{-2}$ s^{-1} in Figure 4.15c are probably responsible for the

final geometry of grain 4 specimens. Softening at ~4 000 s^{-1} is then likely a consequence of the activation of only the primary slip system.

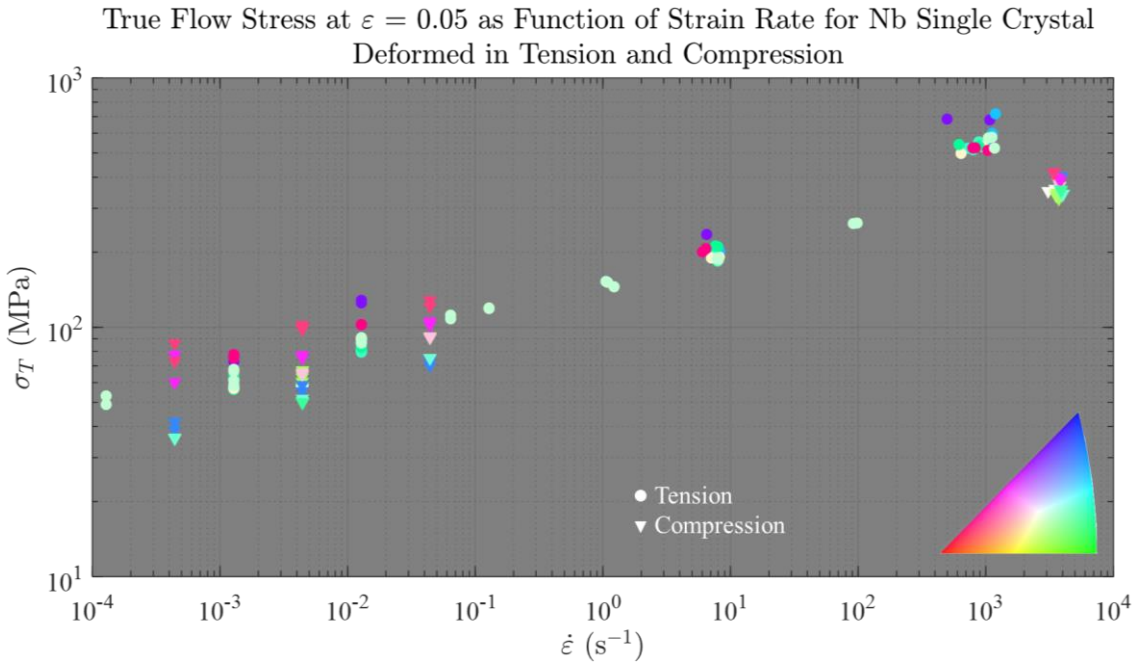

Figure 4.18: True flow stress as function of strain rate at a strain of 0.05 for compression and tensile specimens for strain rates between 1.28x10^{-4} s^{-1} and 4 000 s^{-1}. Colors represent the initial crystal orientation in the loading direction.

4.5. Tension/Compression and Twinning/Anti-Twinning Asymmetries

To assess the effect of non-Schmid behaviors on tension/compression (T/C) asymmetry at low to high strain rates, the flow stress measured in tension and compression are compared. Figure 4.18 shows the true flow stress as function of strain rate at a true strain of 0.05 for compression specimens deformed at strain rates between 4.4x10^{-4} s^{-1} and ~4 000 s^{-1} and for tensile specimens deformed at strain rates of 1.28x10^{-4} to ~1 000 s^{-1} for all crystal orientations tested in this study. The compression results follow a linear distribution in the log–log plot, indicating that the same deformation mechanism operates for the entire range of strain rates studied. This is not the case in tension, where the increase in flow stress in at ~1 000 s^{-1} suggests a change in dominant deformation mechanism, such as the occurrence of viscous drag effects. However, as further discussed in section 4.6., this is unlikely the case based on modeling of kink pair nucleation and motion and the high viscous drag coefficient required to model the higher flow stress.

The higher T/C asymmetry at the highest strain rate is then likely caused by more important non-Schmid effects due to a reduction of thermal energy to assist in the nucleation and motion of kink pairs, as measured by Chang et al. [166] at low temperature. The consistently higher flow stress in tension for a variety of orientations with positive and negative values of χ, the angle defining the twinning and anti-twinning (T/AT) slip directions, schematically

shown in Figure 4.19, also differs from ideal T/AT asymmetry in BCC metals [214] and experimental data at low temperature [215] for cyclic tests. This suggests that the contribution of non-Schmid effects for T/C asymmetry, e.g. the activation of different slip systems in each loading direction, is sufficiently high for the T/AT asymmetry phenomenon to differ from the literature that states that the critical resolved shear stress is smaller in the twinning direction [106], [117], [140].

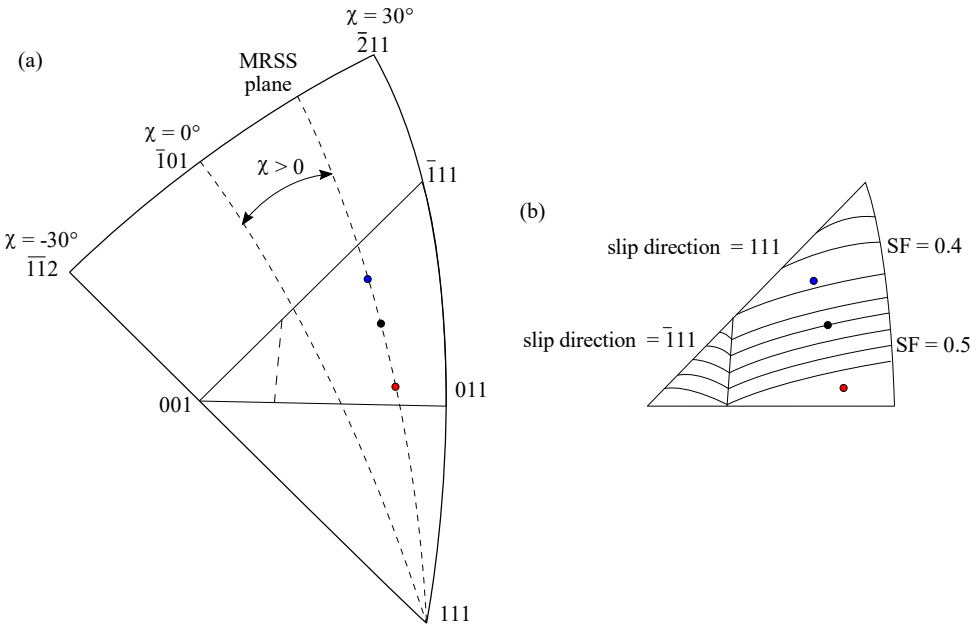

Figure 4.19: (a) Definition of the χ angle for different orientations in an IPF and (b) the corresponding iso-Schmid factor IPF plot assuming pencil-glide [113].

Figure 4.20 shows the flow stress as function of strain rate for orientations close to [001] ($\chi < 0$) and [111] ($\chi > 0$), where slip is expected to occur on different {112} planes, and close to the center of the IPF ($\chi \approx 0$), where slip is expected to occur on a {110} plane. The theoretical and experimental boundaries between orientations where slip occurs on the {110} or {112} slip planes are shown in the IPF in the inset of the figure (also shown in Figure 2.18). The experimental boundaries for tensile and compression tests are based on results of Duesbery et al. [108].

To assess T/C asymmetry for tests performed at strain rates lower than 1 000 s^{-1}, log–log linear regression trend lines of the flow stress at a strain of 0.05 as function of the strain rate are traced in Figure 4.20. For this comparison, the dynamic results obtained in tension are not used in the log–log linear regression due to the upturn in flow stress that does not follow the linear trend observed at low and intermediate strain rates. For orientations close to the [001] direction ($\chi < 0$), the flow stress is higher in compression at quasi-static and intermediate strain rates. The opposite asymmetry was measured for specimens close to the [111] direction ($\chi > 0$). The same T/C asymmetry trends were observed by Duesbery et al.

[108] for high-purity niobium specimens deformed at ~10^{-4} s^{-1}. Finally, specimen with a crystal orientation at the center of IPF ($\chi \approx 0$) have similar flow stresses in tension and compression.

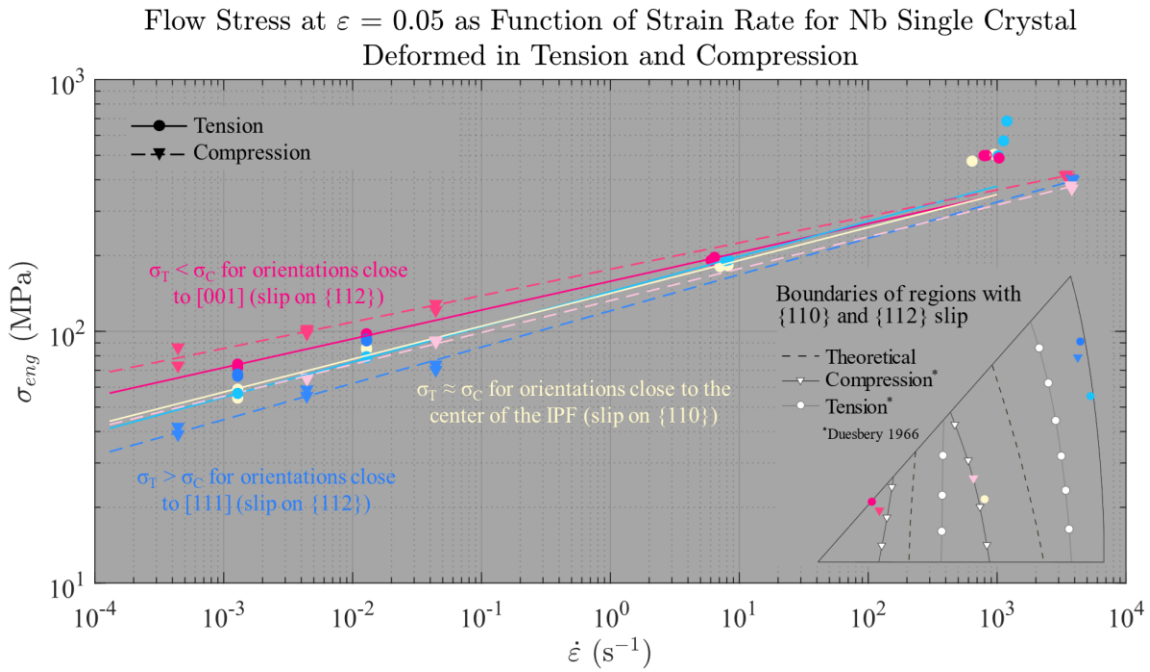

Figure 4.20: Flow stress as function of strain rate for orientations close to [001], [111], and the center of the IPF and (inset) IPF with the theoretical and experimental boundaries of the regions where slip occurs on the {110} or {112} slip planes. The experimental boundaries are from the literature [108].

T/AT asymmetry was assessed by measuring the flow stress at strains of 0.05, 0.1, and 0.2 for specimens with different crystal orientations, i.e. different χ angles, deformed at the same strain rate. The distribution of flow stress as function of χ for specimens deformed in tension and compression at strain rates of 10^{-4} to 10^{3} s^{-1} did not follow equation 2.26. More precisely, in compression, the difference in flow stress as function of χ is more pronounced at low strain rate and the flow stress is higher for orientations with $\chi < 0$, which is the opposite of the result expected from equation 2.26. In tension, plots of the flow stress as function of χ at strain rates of 1.28x10^{-3} s^{-1} and 1.28x10^{-2} s^{-1} and for all orientations tested during this study showed no angle-based trends. From previous analyses presented in section 4.1.1. and Figure 4.3, the flow stress appears to be dependent on the slip systems with the highest Schmid factor and the slip planes and Burgers vectors of the two dominant slip systems. As shown in Figure 4.19b, orientations with the same angle χ can have different Schmid factors. Therefore, the dependence of the flow stress as function of χ, i.e. the T/AT asymmetry, is not further investigated.

Figure 4.21 shows a comparison of the average strain rate sensitivity, $m = \partial \ln \sigma_T / \partial \ln \dot{\varepsilon}$, in tension and compression for orientations with experimental results at more than two strain

rates. The strain rate sensitivity m in tension, considering the high strain rate results, is consistently higher than in compression and varies between 0.141 and 0.169. To continue the comparison from the previous paragraphs, the strain rate sensitivity in tension without the high strain rate results is compared in Figure 4.21 and discussed below.

The strain rate sensitivity in tension for tests performed at strain rate below 1 000 s^{-1} reduces by ~0.29 to 0.113–0.140 and is now comparable to the strain rate sensitivity of 0.105–0.144 for compression tests performed at all strain rates. Specimens with initial crystal orientations along the loading axis close to the [001] direction and on the [001]–[111] boundary of the IPF have some of the highest flow stress at all strain rates in tension (specimen 10-64) and compression (grains 7 and 9), but the lowest strain rate sensitivity. The highest strain rate sensitivity was measured for specimens close to the [111] direction and on the [101]–[111] boundary of the IPF. The compression specimen with this orientation (grain 4) had the lowest flow stress at all strain rates. These results suggest that the strain rate sensitivity is orientation dependent and similar for specimens loaded in tension and compression.

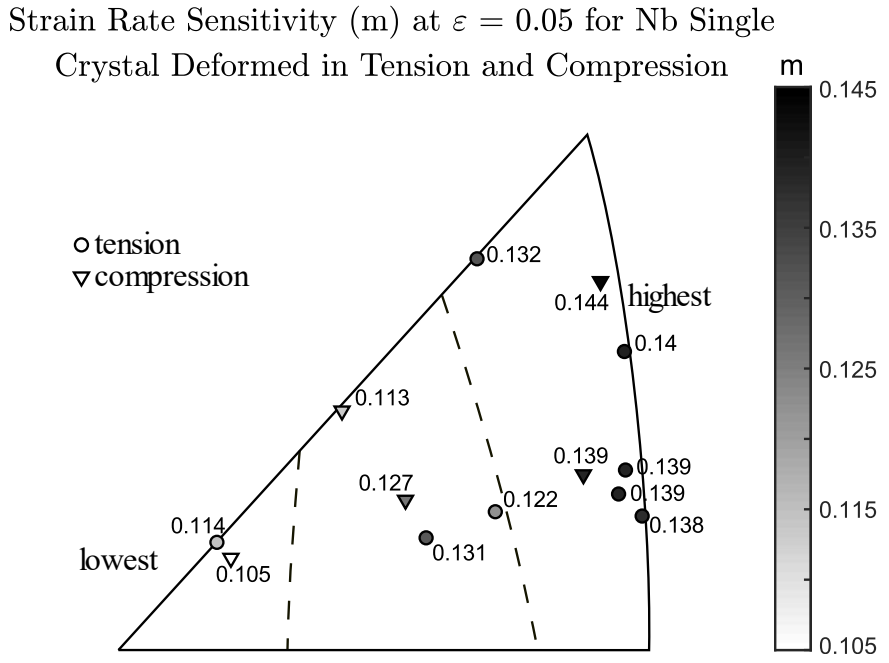

Figure 4.21: Strain rate sensitivity at a strain of 0.05 in compression and tension as function of the initial orientations along the loading axis. High strain rate tensile tests were not considered in the calculation of the strain rate sensitivity.

4.6. Modeling of the Flow Stress at Different Strain Rates

In this section, modeling of the flow stress measured in tension and compression as function of strain rate, based on the nucleation and motion of kink pairs and on viscous drag, is presented. The objectives of this study are (1) to identify parameters that accurately model the general strain rate dependency in tension and compression for single crystals by force fitting the experimental data, and (2) to assess if viscous drag accurately models the apparent

increase in flow stress at 10^3 s^{-1} for the tensile specimens. The models used for the numerical fitting of experimental data are presented in section 2.3.6. This section is separated in three sub-sections.

First, the experimental results and parameters of the models measured and estimated by Hoge and Mukherjee [126] and Steinberg and Lund [84], respectively, for polycrystalline tantalum deformed in tension and compression at strain rate of up to 10^4 s^{-1} are used to assess the implementation of the models in MATLAB.

Second, the experimental flow stress as a function of strain rate from polycrystalline niobium specimens deformed at strain rates of up to 10^3 s^{-1} are used to assess the validity of the material parameters of niobium found in the literature. The study of Peroni and Scapin [182] on specimens deformed in tension at strain rates of up to 10^3 s^{-1} and the experimental results of electron beam welded polycrystalline niobium sheets deformed at similar strain rates, presented in Part II of this thesis, were used.

Third, the experimental results measured for niobium single crystals deformed in tension and compression at strain rates between 10^{-4} s^{-1} and 10^3 s^{-1} are used with the analytical models. The experimental data of individual single crystal specimens are not considered separately and a detailed modelling of the measured anisotropic properties is not performed. Finally, the parameters identified for niobium single crystals are compared with the parameters obtained for polycrystalline niobium specimens.

4.6.1. Model Validation with Tantalum

The model implementation in MATLAB was validated by comparing the experimental results obtained by Hoge and Mukherjee [126] for polycrystalline tantalum, which were manually extracted using WebPlotDigitizer [216]. The parameters used for this material were extracted from the work of Steinberg and Lund [84], who also fitted the data of Hoge and Mukherjee and modified their model to include specimens deformed at higher strain rates. The Peierls stress was lowered from 880 to 800 MPa for a more accurate fit and all other parameters were not modified and are presented in Figure 4.22 with the experimental data [126] and the predicted curves. Despite the slight change in Peierls stress, this short analysis confirms that the thermal activation and thermal activation and drag models presented in equations 2.22 and 2.24, respectively, were properly implemented in MATLAB and can be used for niobium.

4.6.2. Validation of Material Parameters for Niobium with Polycrystalline Experimental Results

The objective of the second part of the analytical modeling of Orowan's equation is to validate if the material parameters for niobium identified in the literature and discussed in section 2.3.6. are accurate. Since the models of Hoge and Mukherjee were [126] used for a polycrystalline material, experimental results for polycrystalline niobium specimens deformed at strain rates of 10^{-3} to 10^{3} s^{-1} are used for this validation. First, estimations of the initial dislocation density and the athermal stress for an annealed niobium single crystal is presented. These single crystal parameters are used in the polycrystalline niobium models and summarized in subsection 4.6.2.3.

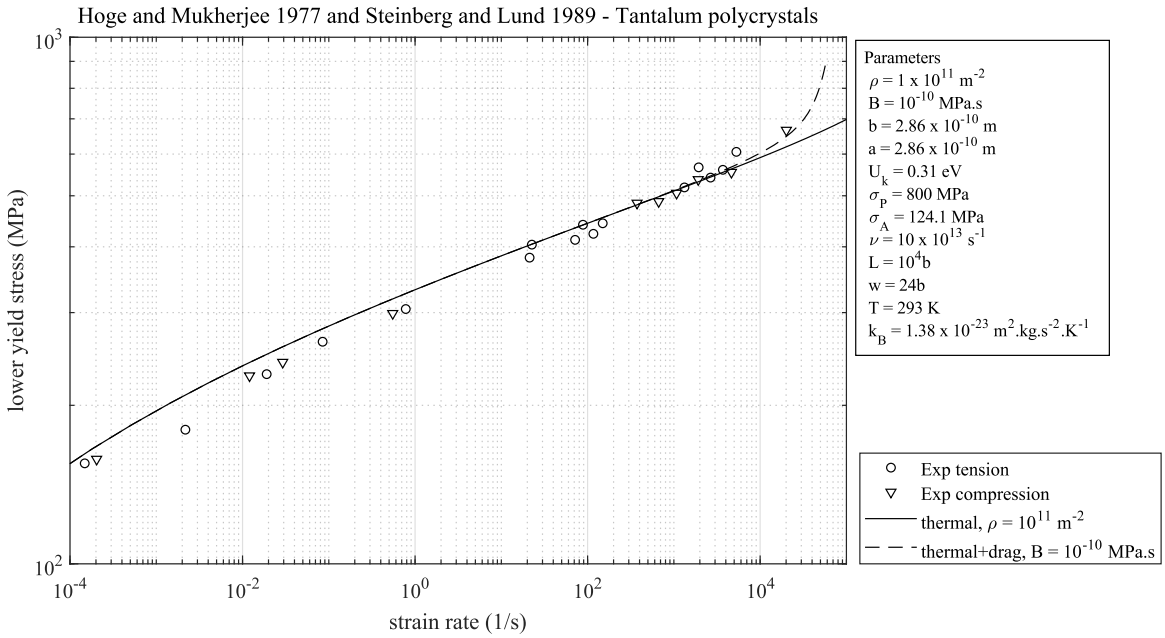

Figure 4.22: Validation of the model given by Hoge and Mukherjee [126] with parameters identified by Steinberg and Lund [84], but with a lower Peierls stress of 800 MPa.

4.6.2.1. Initial Dislocation Density

The mobile dislocation density in the annealed high-purity niobium single crystals was not measured in this study. Different types of analyses could have been performed, such as X-ray diffraction (XRD) [217], electron channel contrast imaging (ECCI) or transmission electron microscopy, to predict the dislocation density of the undeformed crystals. However, it was reported [187] that "well annealed" and 10% strained niobium single crystals have dislocations densities in the order of 10^{10} and 10^{14} m^{-2}, respectively. These values are reasonable and comparable to the mobile dislocation density used in the modeling of high-purity polycrystalline tantalum specimens (~10^{11} m^{-2} [84]) and were used as a starting point in the models to fit the experimental data.

4.6.2.2. Athermal Stress and Shear Modulus

From experimental tests, the flow stress σ_T is known. Since no high temperature tests were performed in this study or in the study of Peroni and Scapin [182], the athermal stress component σ_A was approximated from the literature by extracting the flow (resolved shear) stress at elevated temperatures from Mitchell et al. [145]. The purity of the niobium used in that study is assumed to be similar to this study due to the similar results obtained at different strain rates (see Figure 4.8a). The temperature dependent shear stress–shear strain curves were extracted and converted to engineering stress–strain curves, as shown in Figure 4.23. The identical stress–strain curves obtained at 473 and 513 K indicate that the majority of the measured stress at those temperature is equal to the athermal component. The engineering stress at a strain of 0.05 was then extracted for the specimens tested at 473 K and 513 K and are approximately equal to 25.03 MPa and 24.85 MPa.

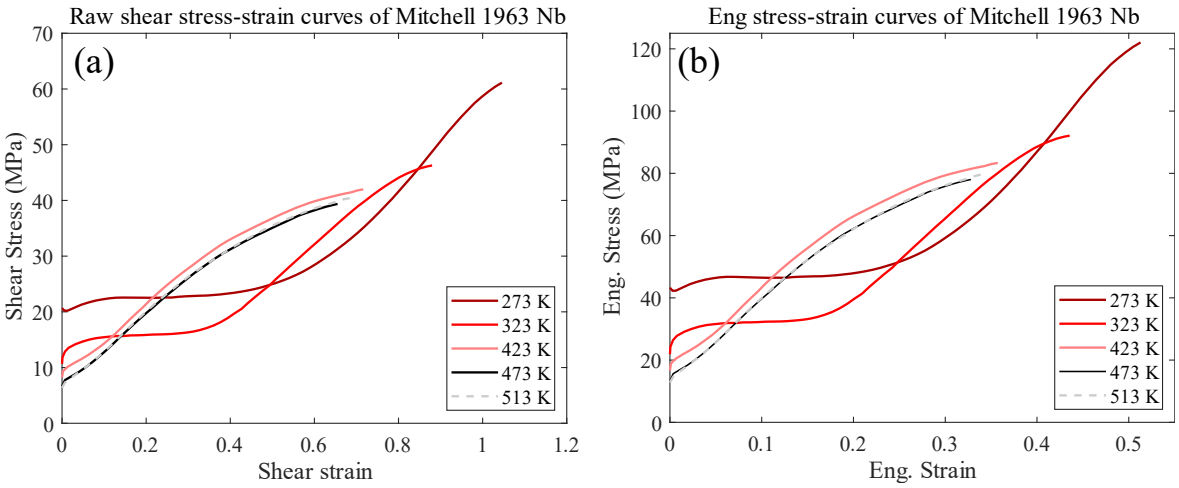

Figure 4.23: (a) Raw shear stress-shear strain curves and (b) calculated engineering stress-strain curves at different testing temperature and at a strain rate of 4.5×10^{-5} s^{-1} from [145].

The shear modulus was then extracted from different studies in the literature [218]–[223] to approximate its value at 293 K, 473 K, and 513 K. Figure 4.24 shows all the data available from the literature and the large distribution found between these studies. The shear modulus measured by Armstrong and Dickinson [222] is used since values are available at all temperatures of interest and the data is in agreement with the work of Hubbell and Brotzen [219] for temperatures of 105–373 K and with Wasilewski [221] at 293 K. The G_{293}/G_T ratio is equal to 0.989 and 0.983 at temperatures T of 473 and 513 K, respectively, for an average room temperature athermal stress of 24.77 ± 0.35 MPa.

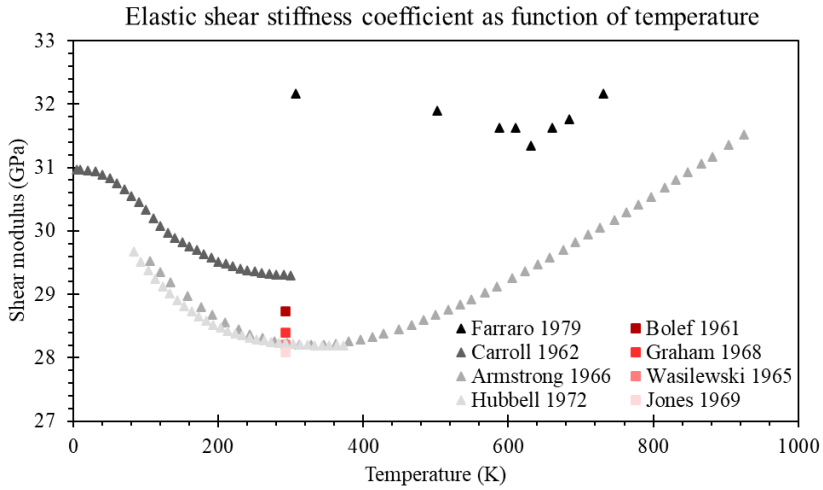

Figure 4.24: Shear modulus as function of temperature from different studies [218]–[223].

4.6.2.3. Summary of Parameters and Model Validation

Finally, the material parameters are summarized in Table 4.2. The values used in the analytical models for niobium were based on literature discussed in Chapter 2 and on estimates made in the two previous subsections. The parameters used for polycrystalline tantalum are presented for comparison.

Table 4.2: Materials parameteris for niobium and tantalum used in the numerical models.

Variable	Description	Unit	Nb	Ta [84], [126]
B	Viscosity coefficient	MPa. s	1.7×10^{-11} [135]	10^{-10}
U_k	Kink nucleation energy	eV	0.34 [112]	0.31
b	Burgers vector	m	2.8585×10^{-10}	2.86×10^{-10}
a_0	Lattice constant	m	3.3068×10^{-10} [127]	–
ρ	Mobile dislocation density	m^{-2}	10^{10}–10^{14}	10^{11}
T	Absolute test temperature	K	293	300
ν	Debye frequency	s^{-1}	5.42×10^{12}	10^{13}
w	Kink pair width	m	21.5 b [129]	24 b
a	Distance between Peierls valleys	m	4.78×10^{-10} [112]	b
L	Length of dislocation segment	m	-	$10^4 b$
σ_P	Peierls (shear) stress at 0 K	MPa	450–890 [129], [134]	999.8 and 880
σ_A	Athermal (shear) stress component	MPa	24.77 [145]	124.1

The accuracy of the parameters presented in Table 4.2 was verified by fitting the engineering flow stress at a strain of 0.05 of Peroni and Scapin [182] and of electron beam welded specimens from this study (see Chapter 9) as function of strain rate for high-purity polycrystalline niobium sheets. The specimens were deformed in tension at strain rates of

10^{-3} to 1 600 s^{-1}, a range of strain rates similar to the one of the single crystal specimens. The optimized material parameters for the polycrystalline specimens were used as a first step in the modeling of the behavior of single crystals deformed in tension and compression.

All parameters but the Peierls stress σ_P, the mobile dislocation density ρ, and the athermal stress σ_A were fixed. The large dispersion of Peierls stress values in the literature, the unknown initial dislocation density, and the approximated athermal stress motivated the decision to vary those parameters. The optimization material parameters were limited at physically reasonable lower and upper bounds (350 MPa $\leq \sigma_P \leq$ 1 500 MPa, 10^{10} $m^{-2} \leq \rho \leq 10^{14}$ m^{-2}, and 5 MPa $\leq \sigma_A \leq$ 50 MPa) and the initial parameters were as follow σ_P = 890 MPa, $\rho = 10^{12}$ m^{-2}, and σ_A = 24.9 MPa.

Figure 4.25 shows the thermal activation and thermal activation and drag models for optimized material parameters σ_P = 723.96 MPa, $\rho = 10^{12}$ m^{-2}, and σ_A = 43.30 MPa and the polycrystalline niobium experimental data. The flow stress calculated with the two models is the same at all strain rates, meaning that the viscous drag term has no influence at strain rates of 10^{-5} to 10^{4} s^{-1}. This is likely a consequence of a niobium viscosity coefficient B about one order of magnitude lower than for tantalum. This also indicates that the dislocation velocity is far from the critical velocity of 1 997 m/s around which the viscosity coefficient rapidly increases [137]. The agreement between the models and the experimental data at strain rates of up to 1 600 s^{-1} confirms that the parameters found in the literature or estimated in this study are reasonable for niobium and are used in the next subsection for niobium single crystals.

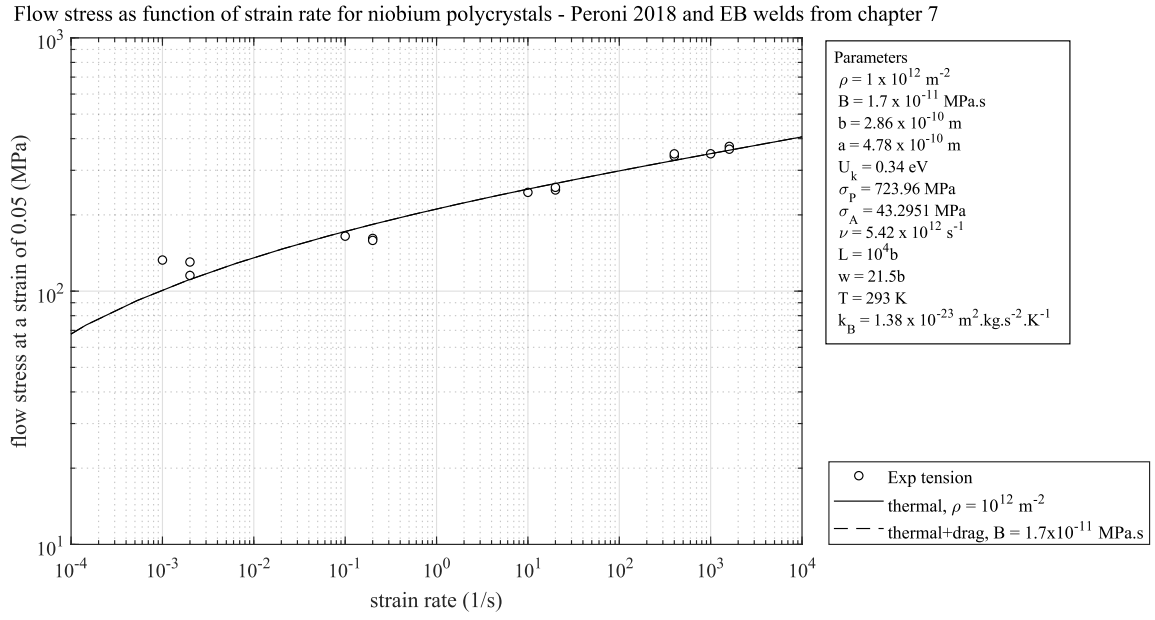

Figure 4.25: Validation of the model with experimental tensile data from Peroni and Scapin [182] and from EB welds characterized at the JRC (Chapter 9) for polycrystal niobium.

4.6.3. Application to Niobium Single Crystals

Finally, after validation of the models' implementation with polycrystalline tantalum and of the material parameters identified for niobium, the models are used with the experimental tensile and compression results obtained for niobium single crystals and presented in sections 4.1. and 4.4. As discussed at the beginning of section 4.6., accurate modeling of the anisotropic mechanical properties measured for tensile and compression tests is outside of the scope of this study. The main difficulties associated with an accurate modelling of anisotropic mechanical properties are (1) proper calculation of the resolved shear stress based on the active slip systems, (2) consideration of out-of-plane slip components, (3) orientation dependent critical resolved shear stress, (4) initial dislocation density, and (5) impurity content impeding dislocation motion. For practicality reasons, the material is then considered as a continuum and modeling of the experimental data is performed by force fitting equations 2.22 and 2.24. As previously stated, the objective is to capture the general strain rate dependency of the single crystals in tension and in compression and compare the obtained parameters with those of the polycrystalline specimens.

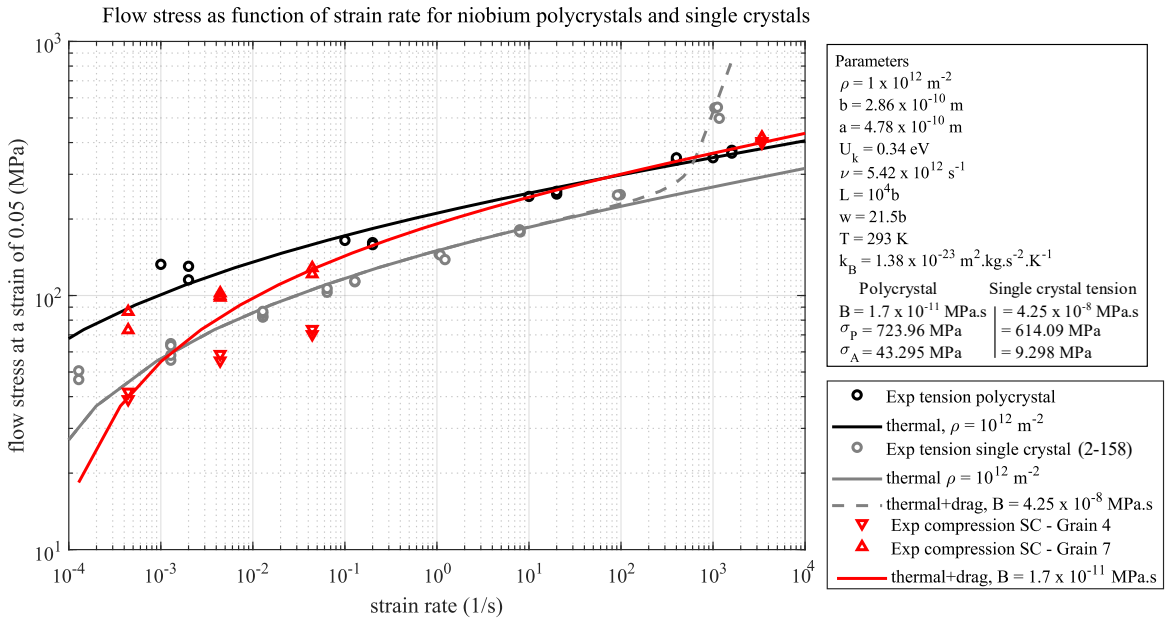

Figure 4.26: Modeling of the flow stress as function of strain rate for polycrystalline and single crystalline niobium single crystals deformed in tension and compression.

First, only the tensile specimens are considered. Figure 4.26 shows the experimental tensile data and predicted curves for the polycrystalline specimens, as shown in Figure 4.25, and a niobium single crystal specimen (2-158) with a crystal orientation in the center of the tensile axis IPF. The flow stress in tension of the polycrystalline specimens is higher at all strain rates below ~400 s^{-1} and this is probably due to pile-up of dislocations at grain boundaries (Hall-Petch effect). The lower flow stress of the single crystal specimens is modeled by

changes in the Peierls and athermal stresses, from 723.96 to 614.09 MPa and from 43.30 to 9.30 MPa, respectively. Note that the lower Peierls stress remains in the 450–890 MPa range found in the literature [129], [134]. Compared with the athermal stress estimated from the data of Mitchell et al. [145], the value found for single crystal specimens is about 62.5% lower.

Second, the compression specimens are considered. Figure 4.26 also shows the experimental data in compression for grains 4 and 7, with the lowest and highest hardening at low strain rates, respectively, and the average fit for both crystal orientations. Since there is no upturn in flow stress in compression at ~4 000 s^{-1}, the viscosity coefficient found in the literature is used. Like for the polycrystalline specimens, the influence of viscous drag is not visible, which indicates that dislocation motion is mainly caused due to thermal activation mechanisms. Peierls and athermal stresses of 870.54 MPa and 12.71 MPa were respectively found. The large difference in flow stress at strain rates lower or equal to 4.4×10^{-2} s^{-1}, discussed in section 4.4., suggests that different parameters would be more suited for the different crystal orientations.

The sudden increase in flow stress in tension at ~10^3 s^{-1} for the single crystal, which could be explained by a change in dominant deformation mechanism from thermal activation to viscous drag, does not follow the thermal activation and drag model using the viscosity coefficient B of 1.7×10^{-5} Pa.s. To force the numerical fitting of those results, the viscosity coefficient was increased to 4.25×10^{-2} Pa.s. Note that a lower estimate of the dislocation density would lead to a lower and more reasonable B to fit the experimental data, e.g. a ρ of 10^{10} m^{-2} would require an increase of B from 1.7×10^{-5} Pa.s to about 3.4×10^{-4} Pa.s. For both higher viscosity coefficient, the high contribution of viscous drag suggests that screw dislocations are traveling at close to the critical velocity. However, if dislocations are travelling at the critical velocity in the single crystals deformed in tension ($\dot{\varepsilon} \approx 1\,000$ s^{-1}), the velocity of the dislocations travelling in compression specimens ($\dot{\varepsilon} \approx 4\,000$ s^{-1}) should not be at such a lower speed that viscous drag is not the dominant deformation mechanism. Therefore, the stress upturn observed with niobium single crystals loaded in tension could be caused by more important tension/compression asymmetry at high strain rate. Since analytical modeling suggests that the dominant deformation mechanism remains a thermally activated mechanism at high strain rate, the analogy between low temperature, where more important non-Schmid behaviors have been reported, and high strain rate could explain this higher T/C asymmetry at 10^3 s^{-1}.

Note that an experimental artefact also cannot be excluded. However, the specimen geometries used in tension were previously used for other materials [193]–[195] and finite

element modeling of the high strain rate tensile test was performed to measure the stress-state in the gage length and the inertial forces. Isotropic material properties were used in the numerical model to study the effect of the specimen geometry. The stress-state extracted in the gage length was uniaxial and inertial forces were small, which confirms the validity of the specimen geometry used in split Hopkinson bar tensile tests.

4.7. Conclusions on the Mechanical Properties of Niobium Single Crystals

In conclusion, a lower anisotropy was measured in niobium single crystals deformed in tension at about 1 000 s^{-1} and is likely a consequence of dislocation glide on multiple slip systems. A reduction of nominal strain to failure was measured at strain rates greater than $1.28x10^{-2}$ s^{-1}.

Digital image correlation was used on tensile specimens deformed at strain rates of $1.28x10^{-3}$ s^{-1} and ~1 000 s^{-1}. Different spatial heterogeneities were measured in the specimens deformed at a low strain rate and the effect of orientation hardening due to the rotation of the single crystals during the tests was observed. At high strain rate, a more homogeneous strain distribution was observed for all orientations.

In-situ temperature measurements of specimens deformed at an intermediate strain rate of about 10 s^{-1} showed that only one hot spot, analogous to one neck, was observed and a low maximum temperature of less than 80°C was measured.

In compression, the reduction of anisotropy was not as pronounced at high strain rate. A positive linear relation between the flow stress at a true strain of 0.2 and the total projection angle from the initial crystal orientation to the [111] stable end orientation was measured.

Tension/compression asymmetry was also measured at low strain rates, with a higher flow stress in tension close to the [111] orientation and in compression close to the [001] orientation. At high strain rate in the order of 10^3 s^{-1}, the flow stress was higher in tension for all crystal orientations. This is likely caused by more important non-Schmid effects at high strain rate.

An orientation dependent strain rate sensitivity was also measured. The lowest logarithmic strain rate sensitivity exponent of 0.105 was measured for an initial crystal orientation close to the [001] direction and the highest exponent of 0.144 was close to the [111] direction and near the [101]–[111] boundary of an inverse pole figure.

The relationship between the measured flow stress at a low strain of 0.05 as function of the applied strain rate was modeled without taking anisotropic properties in account (a single set of parameters is used for all orientations loaded in tension or in compression). The model

suggests that the dominant deformation mechanism in tension and compression is thermally activated and not dependent of viscous drag effects.

Chapter 5 Microstructural Investigations of Deformed Niobium Single Crystals

In this chapter, the deformed niobium single crystals discussed in the previous chapter are analyzed with different optical and electron microscopy techniques, and with nanoindentation measurements. First, the fracture surface of tensile specimens deformed at quasi-static and high strain rates are analyzed with a scanning electron microscope. The same specimens are used to investigate the chemical composition of impurity particles found at the surfaces cut with wire EDM. Second, the crystal orientation in the cross-section of tensile and compression specimens deformed at quasi-static and dynamic strain rates is measured with electron backscatter diffraction. Inverse pole figure orientation maps and kernel average misorientation maps are used to assess to rotation of the single crystalline specimens and strain distributions, respectively. Third, electron-transparent tensile specimens were prepared and analyzed with a transmission electron microscope to observe the influence of strain rate and initial crystal orientation on the dislocation substructures. Finally, nanoindentation measurements were performed to quantify the hardness and elastic modulus of specimens with different crystal orientations and previously deformed at different strain rates, and therefore with different dislocation substructures, and in regions with different densities of geometrically necessary dislocations.

5.1. Fracture Surface Analysis

Tensile specimens deformed at low and high strain rates were analyzed to measure the effect of strain rate and crystal orientation on the fracture surface. Secondary electron pictures of the top surface (along the tensile axis) and the front of the specimens were taken at MSU and CERN. Figure 5.1 shows the setup used at MSU to acquire low and high resolutions images of the top surface of multiple high strain rate specimens.

Figure 5.2 compares top views of fracture surfaces of tensile specimens with three different initial tensile orientations and deformed at strain rates of 1.28×10^{-2} s^{-1} and ~1 000 s^{-1}. The macroscopic specimen rotation is often similar at quasi-static and dynamic strain rates, as in specimens 2-158 and 7-152. However, the longer gage section and nominal strain to failure in quasi-static specimens leads to a larger rotation, as shown for specimen 5-85 in Figure 5.2e.

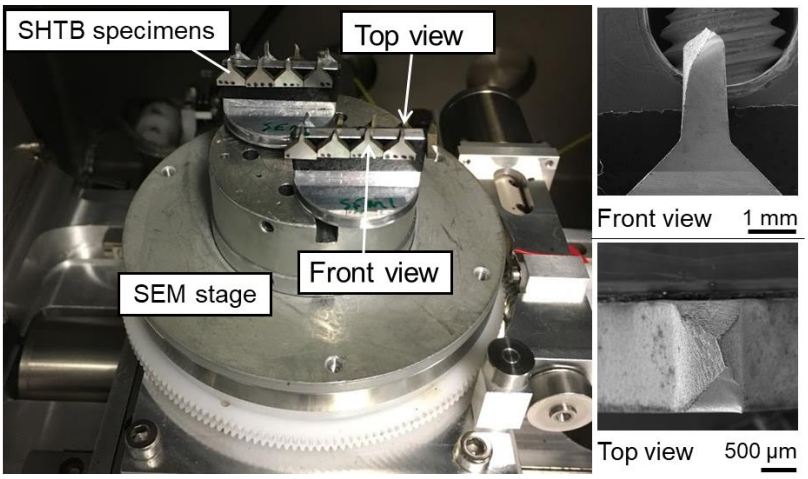

Figure 5.1: SEM layout for analysis of the fracture surface of SHTB specimens.

Figure 5.3 shows secondary electron front and top views of fracture surfaces of all tensile specimens deformed at about 1 000 s^{-1}. For these specimens, the strain rate at rupture is expected to be lower than 1 000 s^{-1} since fracture occurred after being deformed by the third strain wave passing through the bars, which had dissipated energy after each wave.

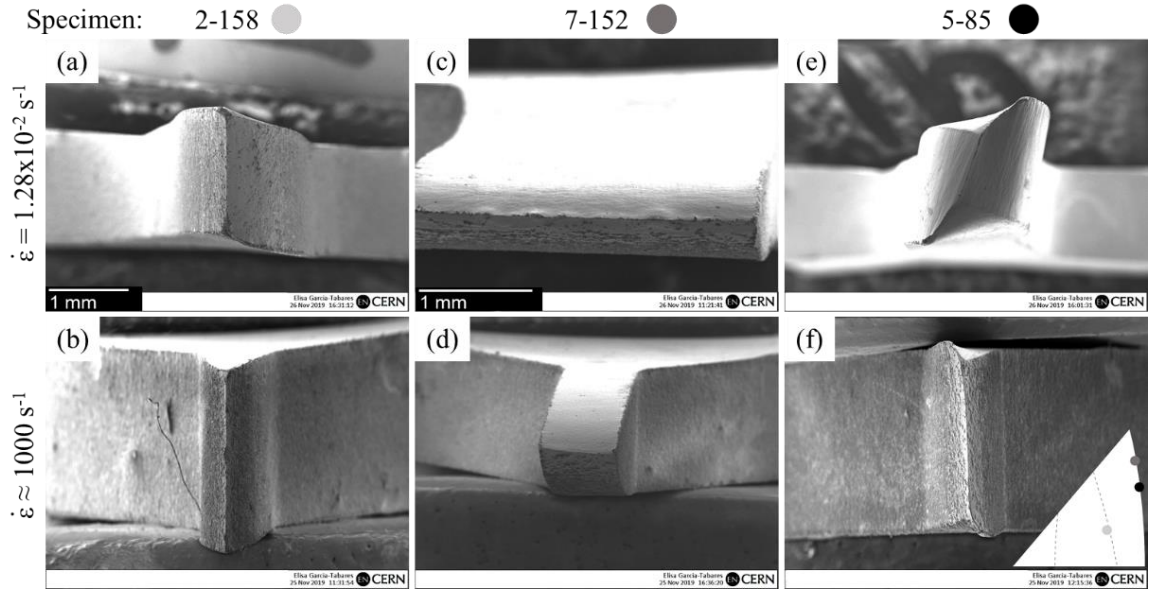

Figure 5.2: Secondary electron top views of rupture surfaces of specimens 2-158 (a, b), 7-152 (c, d), and 5-85 (e, f) deformed at quasi-static and high strain rates. The initial tensile direction for each specimen is shown as dots on the inverse pole figure in (f). (a, b, d, e, and f share the same scale bar [176].)

To ease the identification of trends based on the initial crystal orientation in the tensile direction, the unit cell of specimens from six different orientations are drawn for the front and top views and their exact tensile orientations are indicated in the IPF of Figure 5.4. Considerable variations in fracture surface morphology for specimens deformed at high strain rate are visible. However, no orientation-based trends in fracture surface edge rotation and length are observed. Specimens with initial tensile orientations in the center or on the

[101]–[111] boundary of the tensile axis IPF showed both short and rotated (specimens 7-42 and 6-127), and long and straight (specimens 2-158 and 7-152) fracture surface edges.

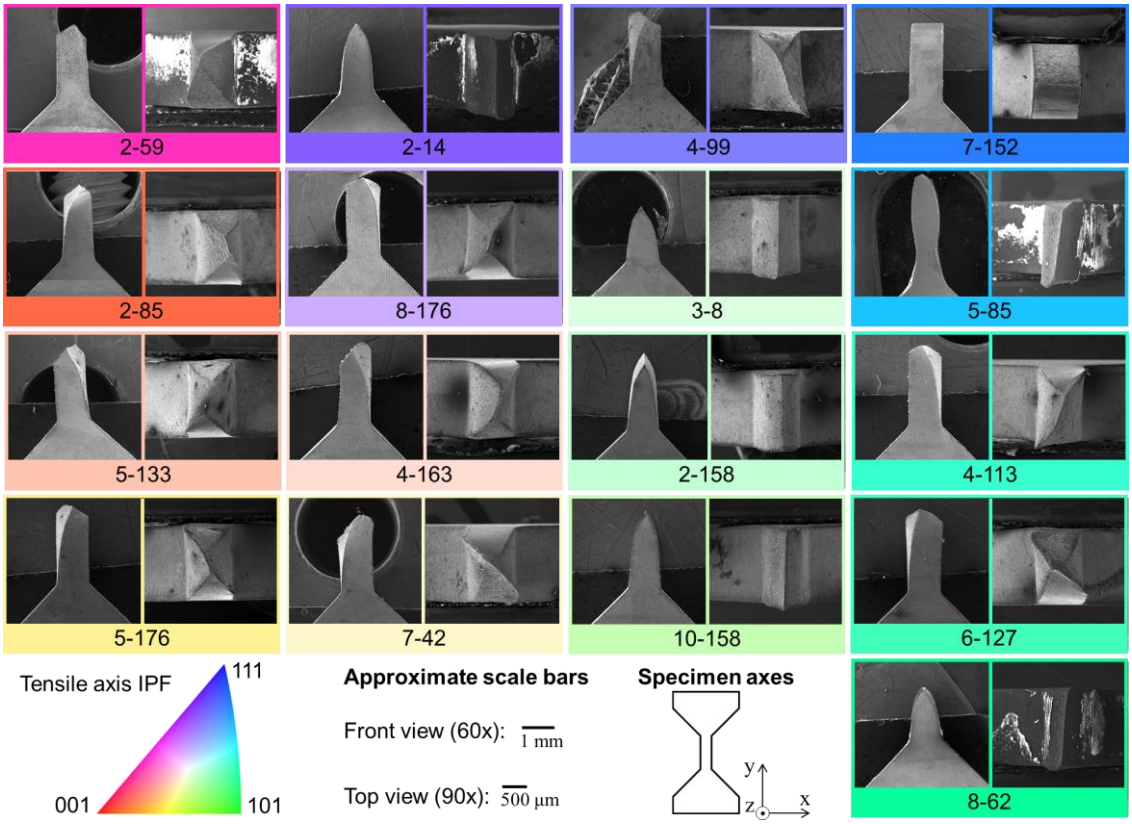

Figure 5.3: Front and top views, along the *z*- and *y*-axes, respectively, of 17 different SHTB specimens arranged by approximate location in the tensile axis (*y*-axis) IPF. The color of the borders is the initial orientation in the tensile axis IPF.

The number of active slip systems at rupture should influence the rupture surface morphology, i.e. the crystal rotation and neck geometry, as schematically shown in Figure 5.5. The case of slip on only one slip system (Figure 5.5a) was not expected for the tensile tests performed at low and high strain rate, because the ends of the specimens are fixed in the tensile machine and the split Hopkinson bars. As previously discussed, this forces the single crystal to rotate as it elongates, which changes the Schmid factor of all slip systems. A change in the slip system with the highest resolved shear stress results in the activation of a different or of multiple slip systems. Fracture surfaces with two- and four-fold symmetries were observed in the literature for copper single crystals deformed at different temperatures by Simoto et al. [224] and presented in Figure 5.6.

The long and straight fracture surface of specimens 2-14, 2-158, 3-8, 7-152, 8-62, and 10-158 in Figure 5.3 and Figure 5.4 suggest that the deformation took place on two slip systems. However, no orientation-based trends were identified to explain this fracture surface morphology. Studies were conducted using the length and rotation angle of all fracture surfaces and the specimen x, y, and z axes, as defined in Figure 5.3, and the rotation

normal vector $\underline{r}$, equal to the cross-product of the active plane normal $\underline{n}$ and slip direction (Burgers vector) $\underline{b}$ ($\underline{r} = \underline{n} \times \underline{b}$). There appears to be a relationship between long and straight fracture surfaces and the initial crystal orientation along the specimen x-axis (specimen transverse direction). Figure 5.7 shows that all long fracture surfaces, with a length of more than 950 µm, are located close to the [001]–[101] boundary of the x-axis IPF, except for specimen 2-14. The causation of this orientation-based trend is currently unknown.

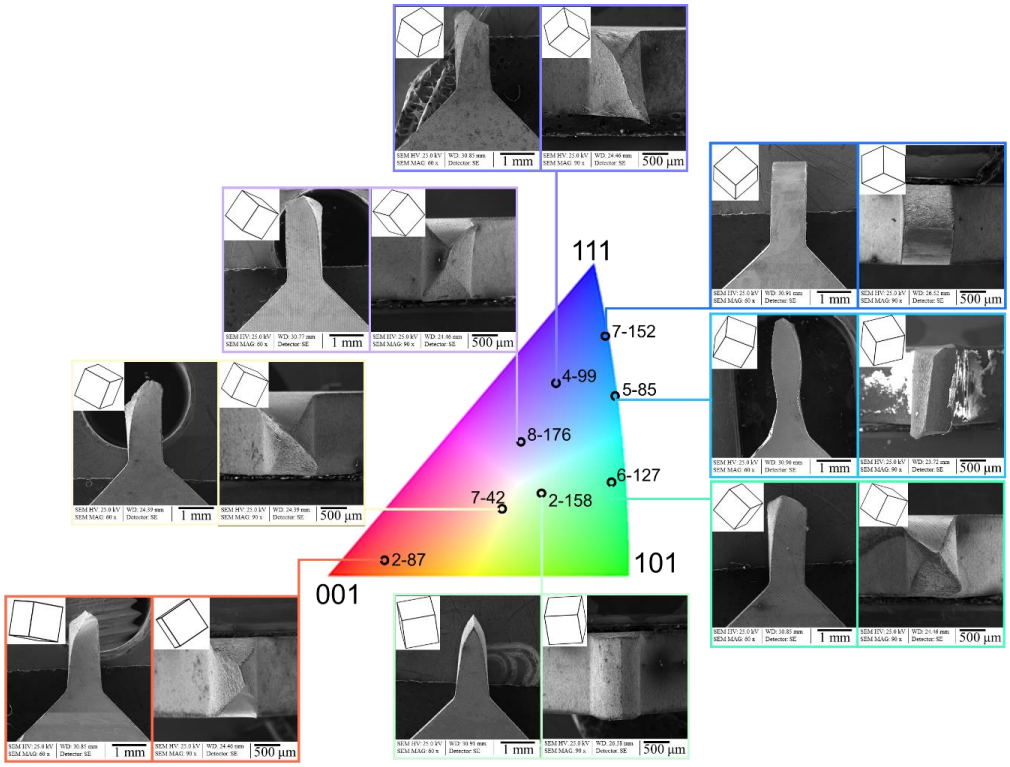

Figure 5.4: Fracture surface of niobium single crystals deformed at high strain rate in tension for six different orientations with unit cells of undeformed initial orientations normal to each view [176].

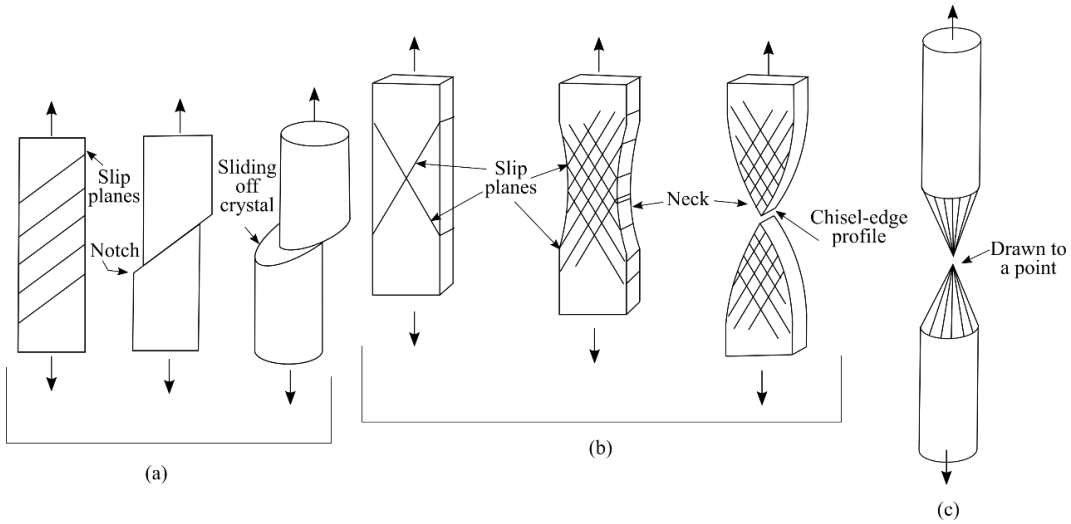

Figure 5.5: Different types of ductile rupture in single crystals for slip on (a) one, (b) two or (c) multiple slip systems. Redrawn from [225].

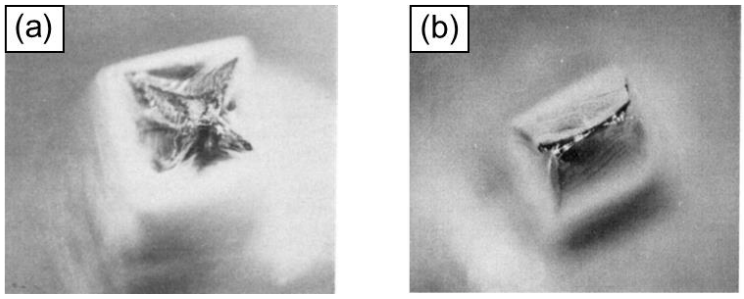

Figure 5.6: (a) Appearance of fracture in a [001] copper crystal pulled at 78 K showing the symmetry from equal slip on four {111} planes. (b) Appearance of fracture in a [001] copper crystal pulled at 273 K showing the two-fold symmetry from slip on only two {111} planes. Images are at 13x magnification [224].

A ductile rupture with a chisel-edge profile was observed in all specimens, as shown in the high-magnification fracture surface images in Figure 5.8. This is common for single crystals of high purity deformed at low strain rates [203], [226] and also the case for the niobium single crystals deformed at high strain rate. Despite the rotation and activation of multiple slip systems, especially for the high strain rate specimens, no specimen shows a single crystal drawn to a point, as schematically presented in Figure 5.5c. This could be a consequence of the lower strain rate at fracture since the specimens fail at the third strain wave.

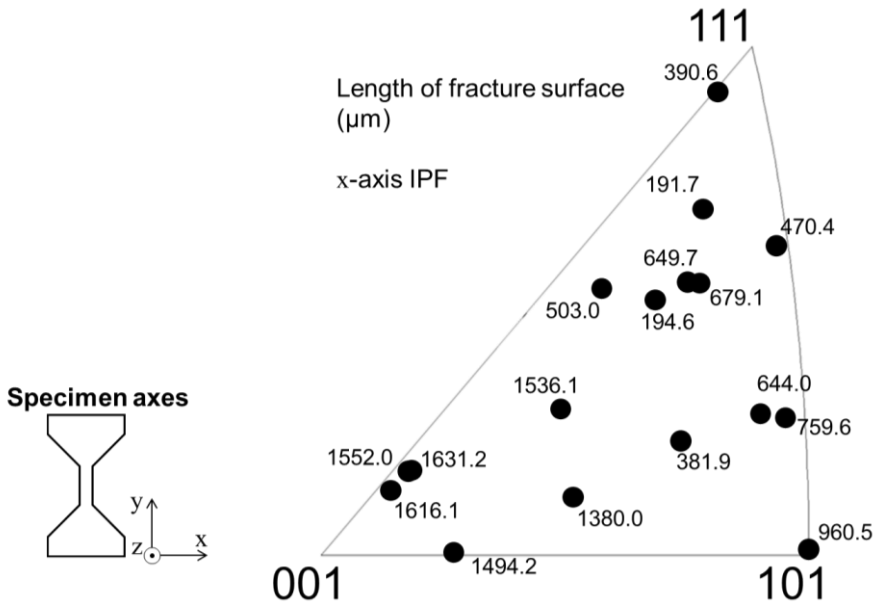

Figure 5.7: Length of the fracture surfaces of high-strain rate specimens on a specimen x-axis IPF.

In Figure 5.8a and c, i.e. specimens 4-99 and 5-85 deformed at high strain rate, more impurities (darker particles) are visible on the side of the specimens and close to the fracture surface than for specimen 4-99 deformed at a low strain rate (Figure 5.8b). Note that no impurities are visible in specimen 5-85 deformed at low strain rate (Figure 5.8d) since it was chemically polished before testing and about 44 μm was removed on all sides of the specimen.

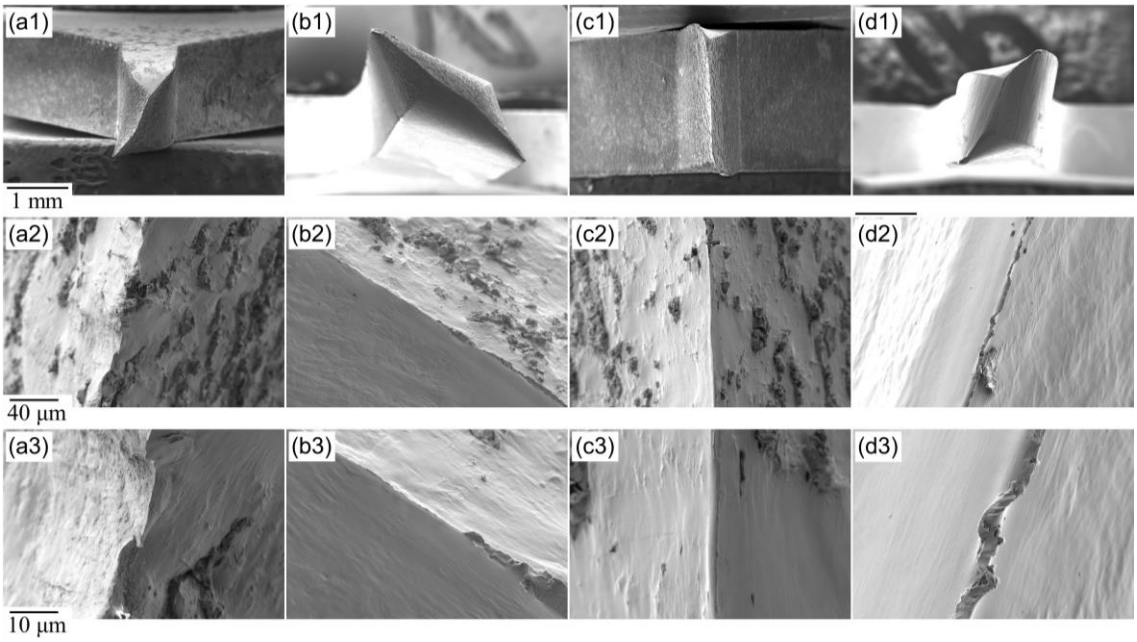

Figure 5.8: Secondary electron images of the fracture surface of specimen 4-99 deformed at (a#) $1.28x10^{-2}$ s^{-1} and (b#) ~1 000 s^{-1} and specimen 5-85 deformed at (c#) $1.28x10^{-2}$ s^{-1} and (d#) ~1 000 s^{-1}. The scale bar for images acquired at magnifications of 25x (x1), 500x (x2), and 2 000x (x3) are indicated in sample a#. The number sign (#) and the letter "x" represent numbers 1–3 and letters a–d, respectively.

5.1.1. Chemical Composition of Impurity Particles near the Fracture Surfaces

Large particles (5–50 μm) were observed on the sides of all non-chemically polished specimens during fracture surface analysis with an SEM. Electron diffraction X-ray spectroscopy was used to identify the elements in the particles and investigate the source of the contamination.

A high concentration of copper and zinc was found in the particles. Those two elements are the main components of the brass (CuZn37) electron discharge machining wire used at Michigan State University (AC Brass 900, Georg Fisher Machining Solutions). In addition, the particles were only visible on the cut surfaces. Therefore, the Nb-Cu-Zn particles are deposits of the material being vaporized and condensing during EDM and can be removed with buffered chemical polishing (BCP), as it was done for grain 5 specimens to obtain a mirror finish for post-mortem slip trace analysis. Carbon traces were also found on the large particles and are probably due to contamination during the cutting, testing or shipping steps. Figure 5.9 to Figure 5.11 show the EDS maps of three specimens deformed at ~1 000 s^{-1}. Source currents of 5 kV and 20 kV were used to identify the presence of niobium, copper, and zinc due to the values of their major transmission lines (Nb: Kα = 16.581 keV and Lα = 2.166 keV, Cu: Kα = 8.040 keV and Lα = 0.930 keV, and Zn: Kα = 8.630 keV and Lα = 1.012 keV).

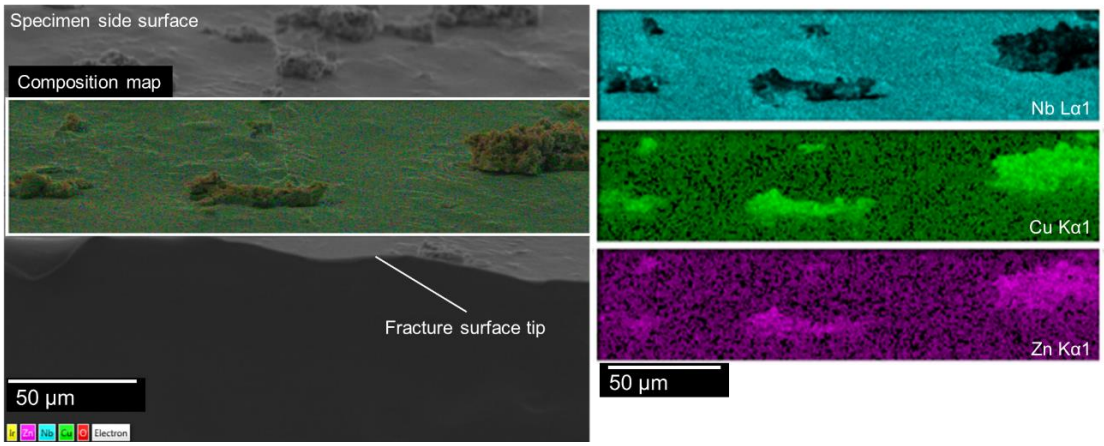

Figure 5.9: EDS composition map at 20 kV of particles on the side of specimen 7-152 deformed at a high strain rate of ~1 000 s^{-1}.

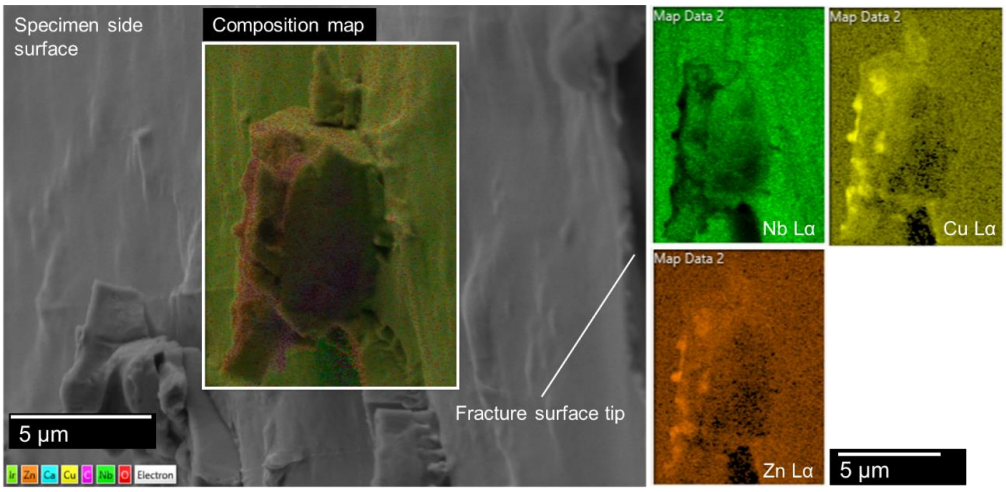

Figure 5.10: EDS composition map at 5 kV of particles on the side of specimen 5-85 deformed at a high strain rate of ~1 000 s^{-1}.

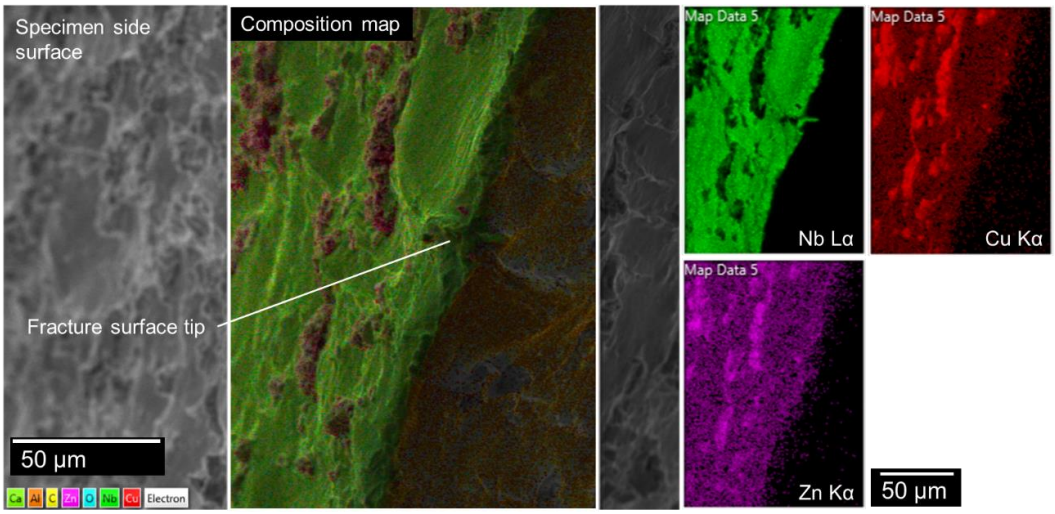

Figure 5.11: EDS composition map at 20 kV of particles on the side of specimen 4-99 deformed at a high strain rate of ~1 000 s^{-1}.

The presence of foreign metallic particles on the sides of specimens could affect the observed fracture surface and ductility. The presence of a Nb-Cu-Zn particle in the chisel-edge, as

seen in Figure 5.12 for sample 4-99 deformed at high strain rate, is a site prone to the presence of voids that can reduce the specimen's ductility. However, only few similar occurrences were observed and since the particles are only on the surfaces machined with EDM, the influence on the bulk properties is likely not significative.

The pickup of hydrogen during the EDM step could affect the mechanical properties by diffusion in the bulk [151]. The use of chemical etchants to remove the particles can also increase the hydrogen content in the specimen. The author believes that the effect of EDM on the specimen contamination depends on the system and parameters used. Polycrystalline niobium specimens cut with deionized water jet cooled EDM produces specimens with a blue-oxidized surface, while specimens cut in deionize water-immersed systems, like at MSU, do not change the specimen's color from heating and oxidation. A systematic study on the effect of the two different EDM systems on the increase in interstitial hydrogen atom content should be conducted to better understand the ideal system to avoid degrading the mechanical and superconducting properties of niobium specimens.

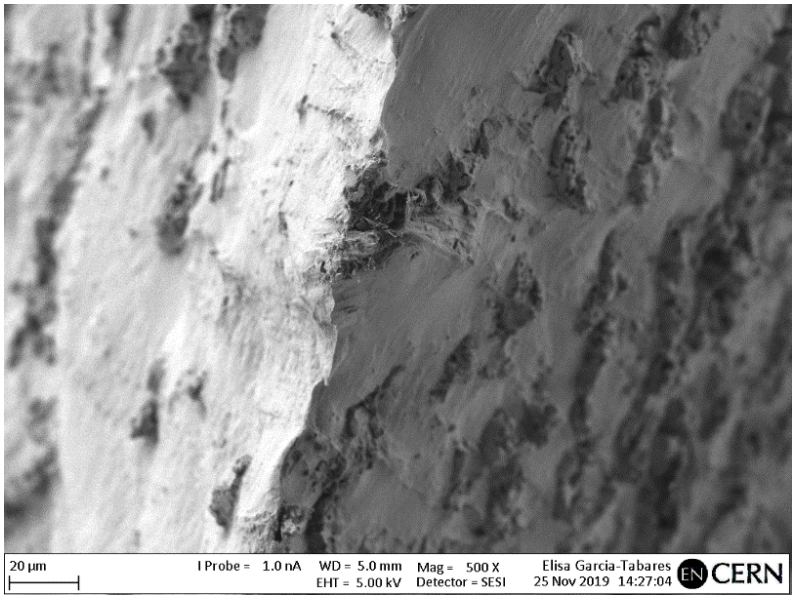

Figure 5.12: Fracture surface of specimen 4-99 SHTB showing a foreign particle in the chisel-edge.

5.2. Microstructural Analyses – Crystal Orientation and Rotations

EBSD measurements were performed on polished cross-sections of low and high strain rate tensile specimens to measure the change in crystal tensile orientation between the undeformed grip section and the fracture surface, schematically shown in Figure 5.13. Similarly, for compression specimens, EBSD measurements of a large section of the specimen, approximately from the bottom to the top surface of the cross-section, were performed. All specimens were polished following the methodology described in section 3.1.1.4.

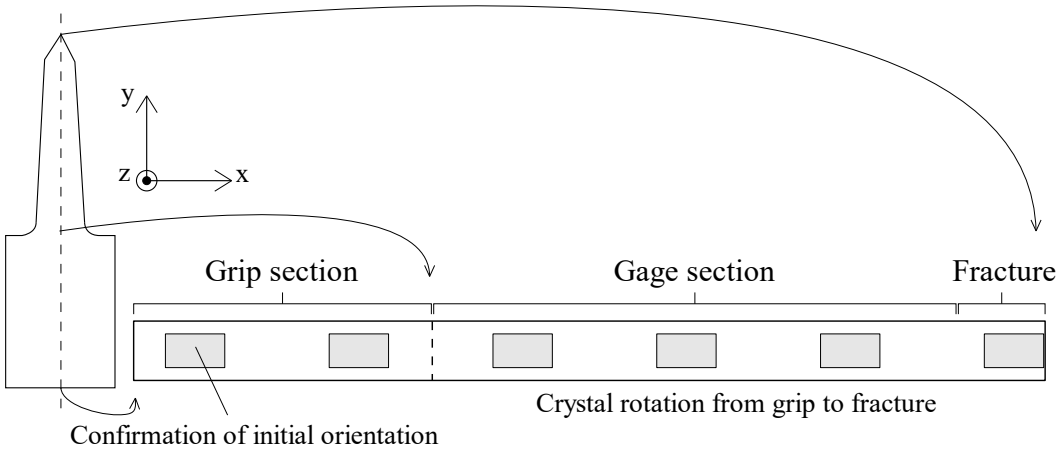

Figure 5.13: Location of different EBSD scans in the cross-section of broken tensile specimens to measure the crystal rotation from the grip to the fracture surface.

5.2.1. Microstructure of Tensile Specimens

Based on slip theories [113], all tensile BCC single crystal specimens should rotate toward the terminal stable [101] orientation. While no macroscopic rotation is observed in the fracture surfaces of specimens 2-158 and 7-152 deformed at high strain rate in Figure 5.4, microscopic orientation rotations toward [101] were measured with EBSD.

While stress anisotropy is reduced at dynamic rates the crystal rotation appears to be a macroscopic kinematic strain-driven process. The specimen dimensions, which affect the post necking behavior and consequently the strain-to-failure, could be the main factor influencing the extent of the rotation occurring in single crystals with the same orientation. The direction of the rotation should be the same for crystals with similar initial orientations as it is dictated by the active slip systems. EBSD measurements confirmed similar rotations for the quasi-static and dynamic specimens with the same initial tensile orientation, see Figure 5.14b and Figure 5.15b.

Figure 5.14a shows the crystallographic orientation, in the tensile direction, and local average misorientation (LAM) maps for five different sections of specimen 8-176, with an initial orientation near the center of the IPF (white areas on the orientation maps are regions with poor pattern indexation and artifacts of polishing). The rotation occurs around the previous defined rotation normal vector r, equal to the cross product of the slip plane normal and slip direction of the active slip system, which is approximately the out-of-plane direction in Figure 5.14a. This was observed for all specimens with no shear bands. A rotation toward the terminal stable [101] direction was measured for this orientation and three others shown in Figure 5.14b. An increase in GND density between the fixture and the fracture surface is evident in the local average misorientation map. Interestingly, the orientation in the grip differs from the original orientation for few specimens and is likely caused by alignment

errors during specimen cutting and measurements, and also because measurements were taken in a region of the grip where biaxial strain probably took place, as schematically shown in light red on a half-tensile specimen in Figure 5.14b and Figure 5.15b.

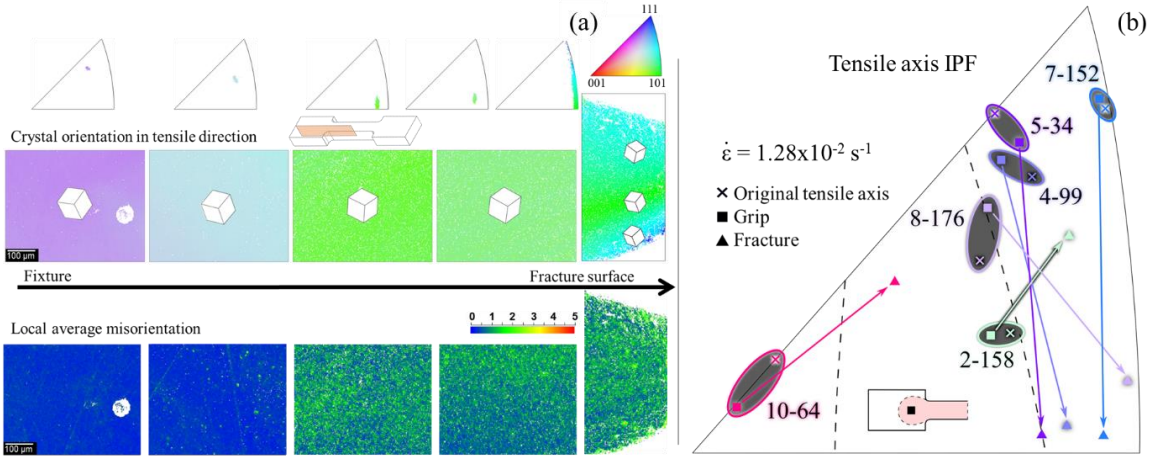

Figure 5.14: (a) EBSD orientation map in the tensile direction and misorientation of specimen 8-176 with an initial crystallographic orientation near the center of the IPF deformed in tension at 1.28×10^{-2} s^{-1}. (b) Orientations in the grip (square), near the fracture surface (triangle) and theoretical (crosses) for six specimens deformed at low strain rates. A half-specimen schematically shows the location of the grip measurement and possibly deformed region within the grip in light red [176].

Figure 5.15a shows EBSD scans for a specimen with the same tensile orientation as in Figure 5.14a, but deformed at high strain rate. In contrast to the quasi-static specimen that has a gradually increasing GND density from the fixture to the fracture, the dynamic specimen has a high GND density at the fracture surface and a low misorientation elsewhere. This is probably caused by the formation of a neck at a lower strain and a more intense straining in the neck region in the dynamic test. The deformation, and consequently the highest GND density, is then concentrated in the vicinity of the fracture surface. Similar observations in local misorientation distribution between low and high strain rate specimens were made for specimens 2-158 (Figure 5.16) and 7-152.

The insets in Figure 5.15a show higher resolution maps (step size of 0.5 μm compared to 2 μm). Note that the bands of higher misorientation angle (~1–2°) converging at the fracture surface edge in the low-resolution scan are an artefact of the large step size and represent the overall specimen rotation. Figure 5.15b compares the crystal rotation from the grip to the fracture surface for three specimens deformed at high strain rate, which are similar to the rotations observed for the same orientations at low strain rate in Figure 5.14b, except for specimen 2-158 where the low strain rate rotation is toward the [111] direction.

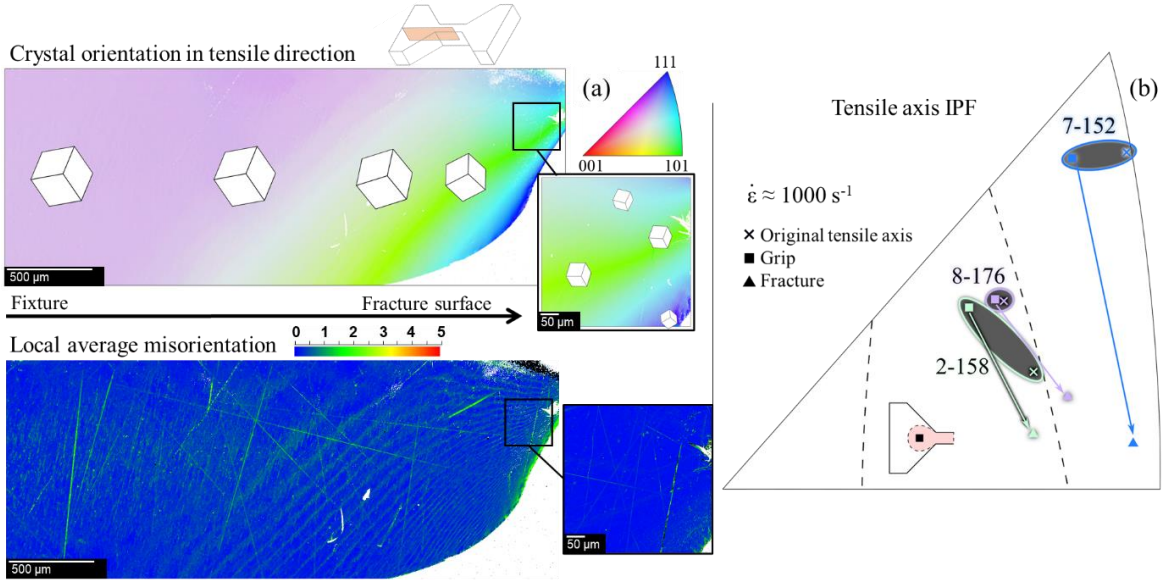

Figure 5.15: (a) EBSD orientation map in the tensile direction and misorientation of specimen 8-176 with an initial crystallographic orientation near the center of the tensile axis IPF deformed in tension at 10^3 s^{-1}. (b) Orientations in the grip (square), near the fracture surface (triangle) and theoretical (crosses) for three specimens deformed at high strain rates. A half-specimen schematically shows the location of the grip measurement and possibly deformed region within the grip in light red [176].

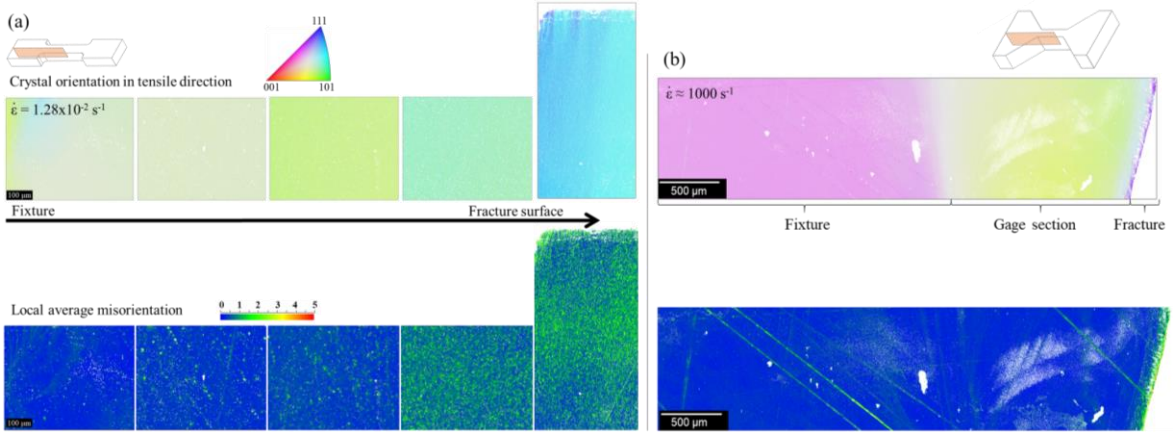

Figure 5.16: EBSD orientation map in the tensile direction and misorientation of specimen 2-158 with an initial crystallographic orientation near the center of the IPF deformed in tension at (a) $1.28x10^{-2}$ s^{-1} and (b) ~1 000 s^{-1}.

Specimen number 5-34, which has a tensile axis where there are equally low Schmid factors for the {110} and {112} slip systems, showed the highest hardening and lowest elongation for the tensile tests at $1.28x10^{-2}$ s^{-1}. The specimen also showed shear bands on its top and bottom surfaces after deformation, as illustrated in the image of the sample in the top of Figure 5.17. An EBSD analysis confirmed that the bands at the surface were shear bands with very different crystal orientations as shown by the contrasting colors in Figure 5.17. The heterogeneous slip behavior of the bands and the matrix resulted in a composite-like structure, which could account for the stress-strain curve with high hardening, associated with different slip directions in adjacent regions, and low ductility that results from

instabilities caused by formation of grain boundaries during deformation, and hence, adjacent orientations that are relatively harder or softer.

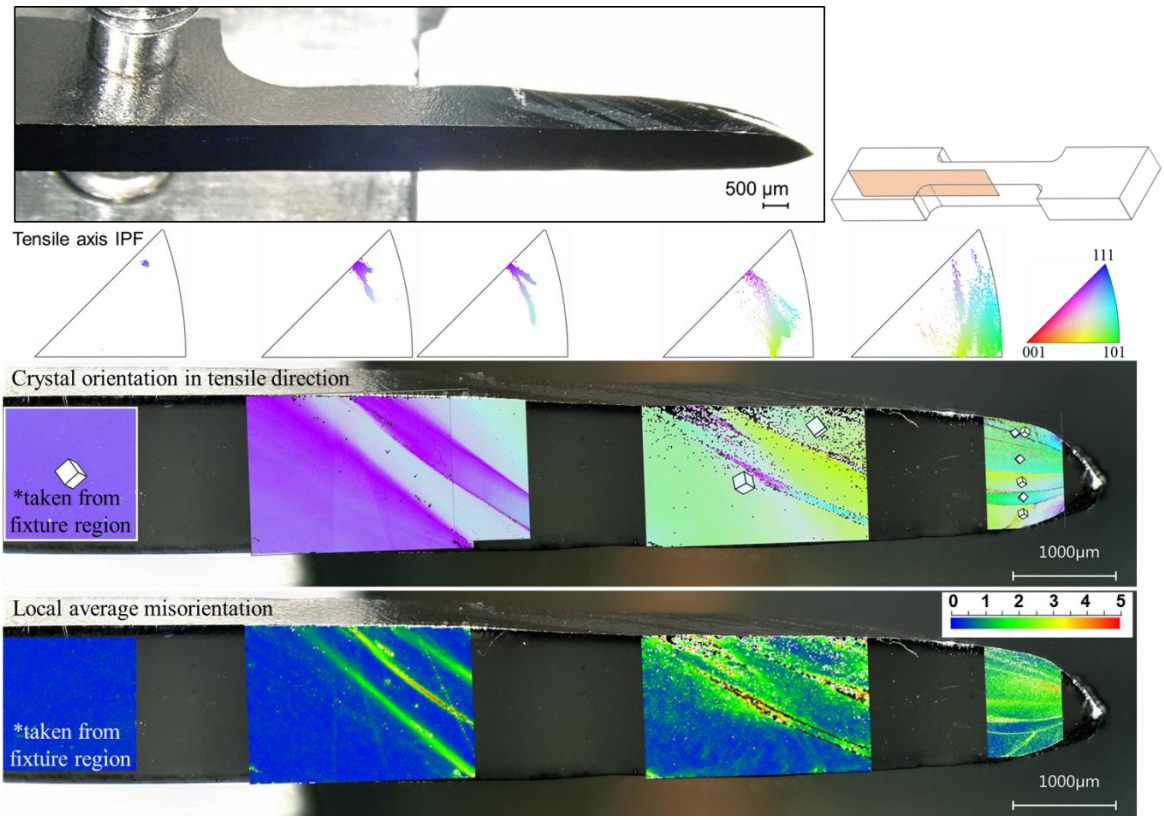

Figure 5.17: (Inset) optical image of specimen 5-34 showing large shear bands on the top surface of the specimen. EBSD orientation maps in the tensile direction with the corresponding orientation of 10 000 points of each map on tensile axis inverse pole figures, showing the crystal rotation from the fixture to the fracture surface, and LAM maps of the specimen deformed in tension at $1.28x10^{-2}$ s^{-1} [176].

Shear bands were also observed in specimen 4-99 (Figure 5.18), with an initial orientation close to specimen 5-34. The two slip systems with the highest Schmid factors in specimen 4-99 have similar resolved shear stresses on different slip planes sharing the same slip direction. This orientation also showed a low ductility and a high hardening rate. Softening shortly after yield was observed in the stress–strain curves of both specimens 4-99 and 5-34 and is likely caused by the formation of the shear bands [227], [228]. Baars et al. [148] also observed regions with distinct orientation splitting in specimens with the highest hardening and where slip is expected to occur in different <111> directions. Because some crystal orientations will deform in a manner that leads to orientation splitting, this can account for a wide range of ductility, such as observed in polycrystals with texture banding [229]. Clearly, it is important to be able to predict which crystal orientations are most likely to generate orientation splitting when considering formability of large grain material. However, this prediction is difficult to make since the initial orientation of specimens 4-99 and 5-34 are similar, with low Schmid factors, but the slip direction in the two slip systems

with the highest Schmid factors were the same for 4-99, and different for 5-34 (which showed orientation splitting).

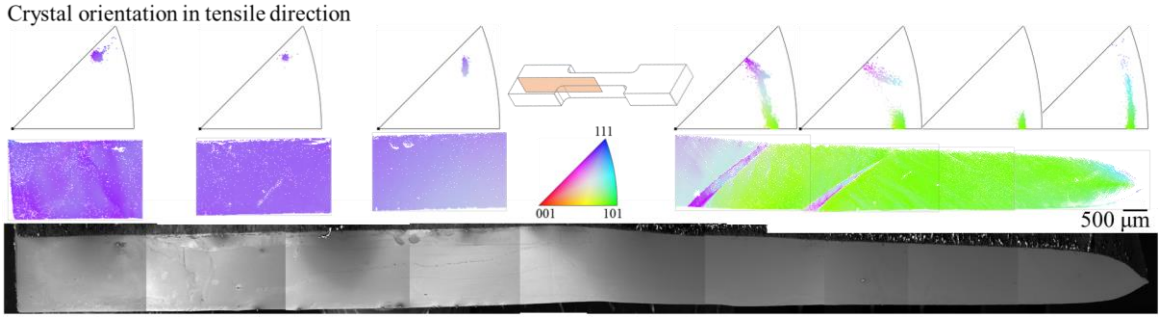

Figure 5.18: EBSD orientation map in the tensile direction of specimen 4-99 with an initial crystallographic orientation near the top of the IPF deformed in tension at $1.28x10^{-2}$ s^{-1}.

5.2.1.1. Slip Trace Analysis on Top and Side Surfaces of Specimen 5-34

Experimental slip trace analyses on deformed niobium single crystals were performed in two different studies. Duesbery and Foxall observed slip traces on both {110} and {112} planes [108], [109] and Maddin and Chen [110] observed slip traces only on {110} planes, both for temperatures above 175 K. The orientation dependence of operative slip system in tension and compression at 295 K showed differences compared with Schmid law-based theory [109], as previously shown in Figure 2.18 for tensile and compression tests.

Slip trace analysis of the top and side surfaces of specimen 5-34 deformed at a nominal strain rate of $1.28x10^{-2}$ s^{-1} was performed after fracture using an SEM. Detailed analyses, such as the identification of the activated slip planes was not performed for two main reasons. Firstly, the specimen was deformed up to failure, equivalent to a large engineering strain of ~0.55, which resulted in significant crystal rotation and the activation of multiple slip planes. The local orientation of the crystal should have been measured with EBSD post-mortem in the region of interest for any attempt at identifying the planes of the slip traces. Secondly, the possible annihilation of screw dislocations at the free surface of the specimen can lead to misinterpretation of slip trace analysis and TEM should be used for this purpose to characterize the bulk dislocation structure, which dictates the bulk plasticity of the specimen, instead of surface properties [114].

Before testing, the specimen was chemically polished which provided enough contrast to see slip steps (traces) at the surface of the specimen after deformation. Figure 5.19 shows the top and sides surfaces of the region studied. On the top surface (Figure 5.19b), wavy slip lines, which are common at room temperature in BCC metals [114], are observed and intersecting at an average angle of 23° (see the black and white lines). The wavy slip lines could be generated by the motion of the screw segment of long dislocation loops [230]. The wavy/intersecting slip traces are aligned along much longer and parallel features (green lines

in Figure 5.19b) that are at an average angle of 49° (counterclockwise angle with respect to a straight horizontal line parallel to the edge separating the top and side surfaces and the tensile axis).

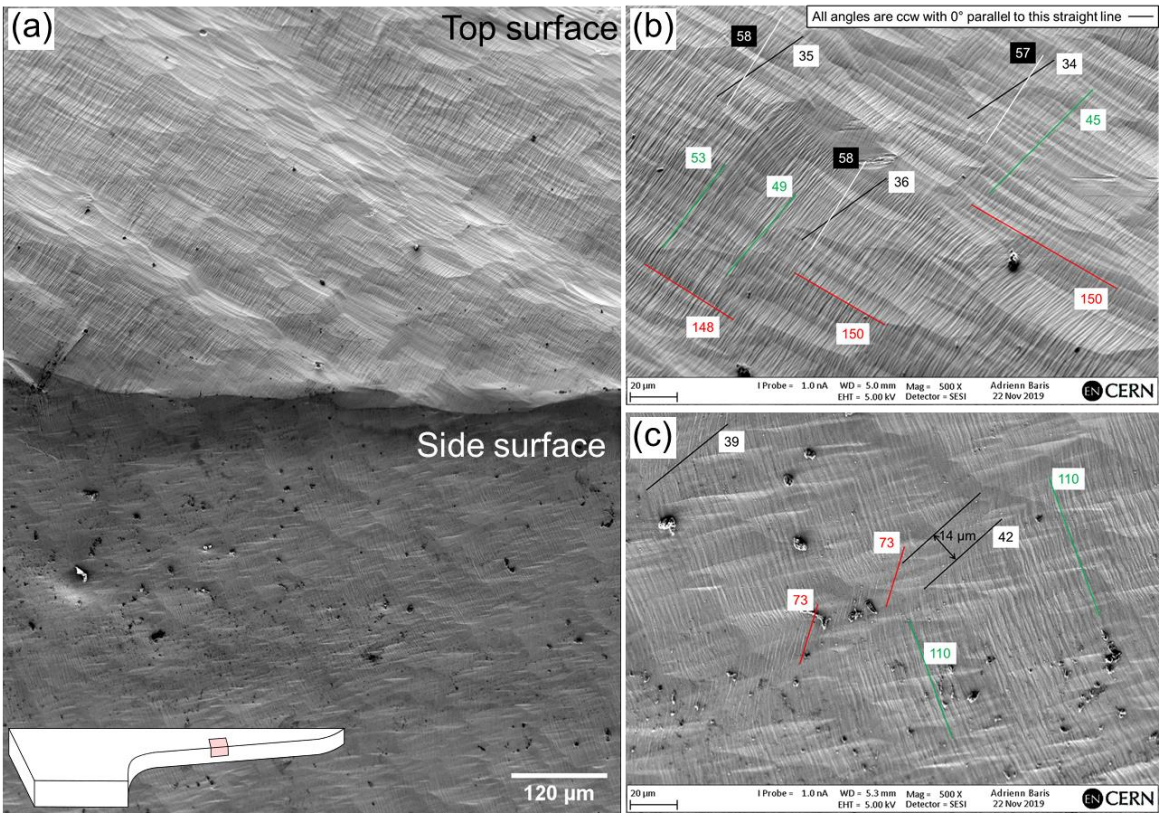

Figure 5.19: (a) Secondary electron images of the top and side surfaces of specimen 5-34 deformed at a nominal strain rate of 1.28×10^{-2} s^{-1}. Higher magnification images of the (b) top and (c) side surfaces with counterclockwise angular measurement, in degrees, of slip traces with respect to a horizontal line approximately parallel to the tensile axis of the specimen. (Inset) Schematic of the region of the tensile specimen captured with the SEM.

Note that slip in BCC metals is complex, as reviewed by Weinberger et al. [114], and slip could appear to take place on non-crystallographic slip planes [231], such as the maximum resolved shear stress (MRSS) plane, or a plane with low resolved shear stress, resulting in *anomalous slip*. However, anomalous slip observed in tungsten micropillars by Marichal et al. [232] was the consequence of a multidislocation process, cross kinks, which could result in the observation of multiple slip lines on the surface of the specimen since it was heavily deformed. Also, as previously discussed, the interaction of dislocations on the intersecting planes likely explains the EBSD results presented in Figure 5.17 and the highest hardening in Figure 4.2b.

Finally, nearly perpendicular larger scale features, described as hills and valleys and parallel to the red lines in Figure 5.19b, are visible. Those larger features are also visible with an optical microscope (inset of Figure 5.17) and likely correspond to the bands of different orientations previously presented in the IPF orientation maps of the specimen in Figure 5.17.

The side surface (Figure 5.19c) also shows intersecting slip traces suggesting that long dislocation loops on the {110} and {112} slip planes observed on the top surface extend to the side of the specimen. However, this surface also shows a ~14 µm wide band filled with short and parallel dislocation bands at an angle of 73°. The difference in slip traces between the perpendicular faces was previously observed in niobium single crystals [108] and caused by the observation of short edge segments and long screw segments of a dislocation loop on the different surfaces [230].

5.2.2. Microstructure of Compression Specimens

EBSD measurements were performed on cross-sections of specimens from grain 4, 7, and 9 deformed at quasi-static (4.4×10^{-3} s^{-1}) and dynamic strain rates (~4 000 s^{-1}). Figure 5.20 shows the IPF orientation and the local average misorientation maps measured for the different crystal orientations and strain rates. Dash lines indicate the approximate dimensions of the regions of the specimens that were not analyzed with EBSD.

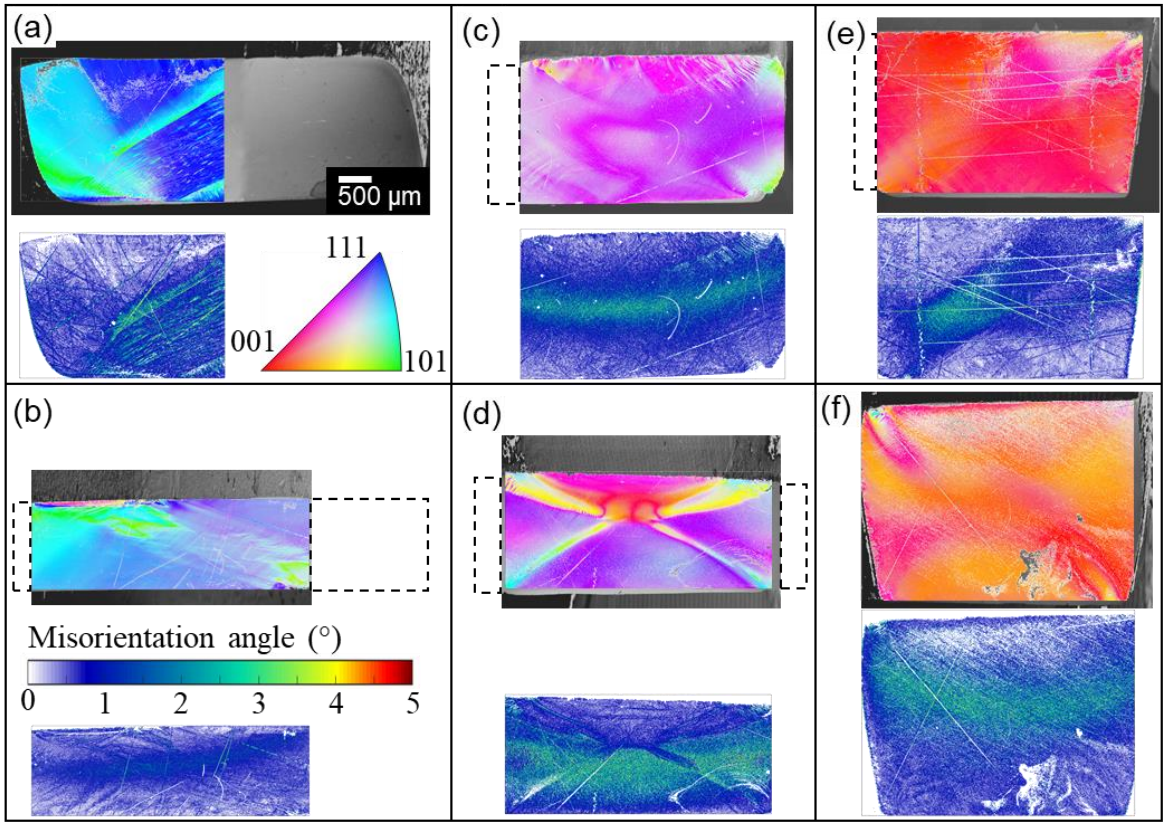

Figure 5.20: Orientation and LAM maps of specimens deformed at quasi-static (4.4×10^{-3} s^{-1} for a, c, and e) and dynamic (4 000 s^{-1} for b, d, and f) strain rates in compression for grains 4 (a and b), 7 (c and d), and 9 (e and f) showing different bands for the different orientations. All IPF orientation maps share the same scale bar. Dash lines show the approximate dimensions of the entire specimen's cross-section.

Specimens from grain 4 (Figure 5.20a and b), the orientation with the lowest flow stress and longest stage I hardening at all strain rates in Figure 4.15, show a diagonal band with different orientations across the whole specimens. The band connects the top left and bottom

right corners which correspond to the initial top and bottom surfaces of the specimens that glided on the anvils of the Instron machine or the faces of the split Hopkinson bars, as schematically shown in Figure 5.21. This relative motion between the faces of the specimen and the testing equipment was only observed for grain 4. Barreling, often not symmetrical about the center of the specimen due to dislocation glide on only few slip planes, was observed on specimens cut in the other grains. Since the same testing procedure, e.g. use of lubricant and strain rate, was used for all tests, the difference in specimen morphology is related to the activation of different slip systems. At low strain rate (Figure 5.20a) a band with a high misorientation angle was measured at the same location as the band with different orientations. Inversely, at high strain rate (Figure 5.20b), the region with a higher misorientation angle intersects the band with different orientations.

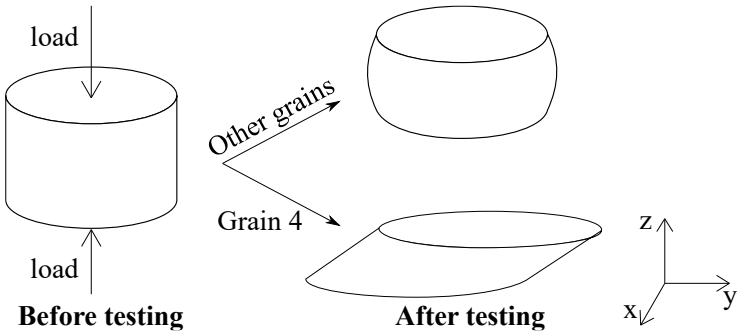

Figure 5.21: Schematic of the cylindrical compression specimen morphologies (left) before and (right) after testing.

In addition to barreling, specimens from grain 7 (Figure 5.20c and d) show a zone with little or no deformation, often called a dead metal zone [99], at the top of the specimens. The dead metal zone is observed due to important friction forces between the specimen and the testing equipment and intense shearing often in an "x" shape connecting the corners of the specimens, as shown in Figure 5.20d. The asymmetrical misorientation angle distribution in the specimen deformed at high strain rate could be caused by wave reflections [233]. Finally, IPF orientation maps for specimens from grain 9 (Figure 5.20e and f) show regions with different orientations close, but no clear trends. These specimens also have the lowest final strain, shown by the largest final thicknesses. For the low strain rate tests, the end-of-test-criterion was a maximum load of ~3.5 kN and, for the split Hopkinson tests, the same inlet pressure was used for all tests, equivalent to a constant striker velocity for all orientations. The higher final strain is then a consequence of the high resistance to deformation of specimens with a near-[001] crystal direction aligned with the compression axis, shown in Figure 4.15 with the highest flow stress at all strain rates (except at 4.4×10^{-4} s^{-1} since the tests for grain 5 were stopped at a higher load of ~4.0 kN).

Figure 5.22 shows the change in crystal orientation in a compression axis IPF along four lines (a, b, c, and d) intersecting bands with different orientations for a specimen from grain 7 deformed at ~4 000 s^{-1}. The change in crystal orientation is plotted on inverse pole figures with unit cells for lines (a) and (b). The orientations of lines (c) and (d) are similar than (a) and (b), respectively, and therefore not plotted. Figure 5.23 shows that the crystal orientation is nearly symmetric about the center of the compression specimen. Recall that single crystal specimens with an initial orientation in zone A or B of the IPF in Figure 4.16 deformed in compression rotate toward the terminal stable [001] and [111] orientations, respectively. The boundary between these zones is equal to the region of equal Schmid factors for the {110} and {112} slip planes closest to the [001] orientation and drawn with dash lines in the IPFs of Figure 5.22.

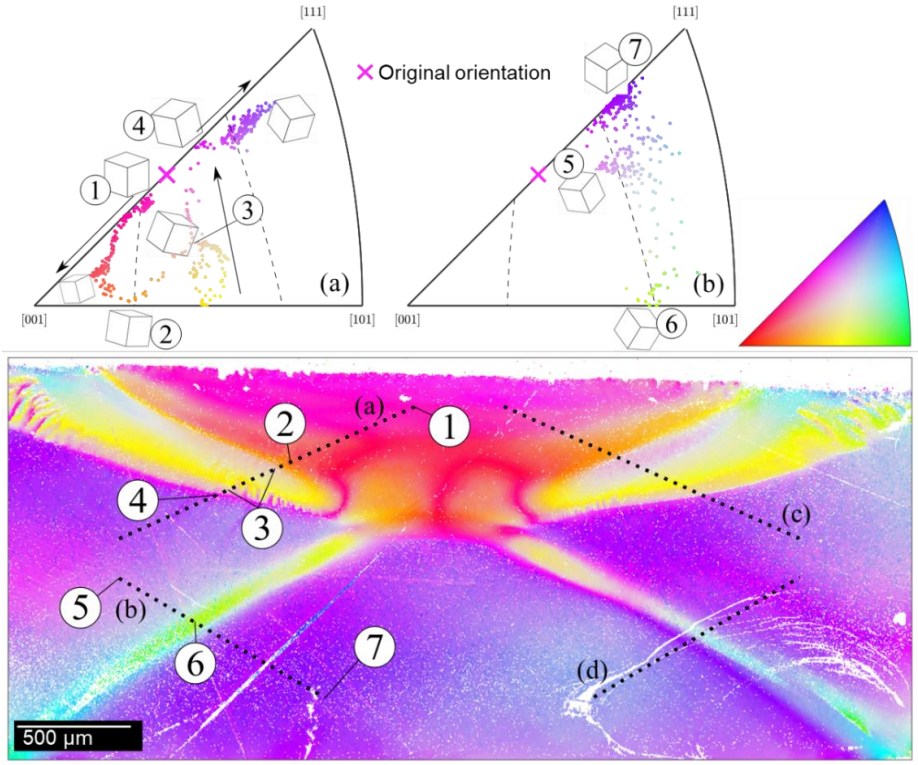

Figure 5.22: IPF orientation maps with line scans of four regions (a, b, c, d) of a specimen from grain 7 deformed at a strain rate of approximately 4 000 s^{-1}. Inverse pole figures (a) and (b) show the crystal rotation across the corresponding lines in the orientation maps. Unit cells are drawn for different orientations to help understanding how the crystal rotates. All IPFs are along the loading axes.

The initial crystal orientation is close to the boundary which lead to a rotation of the crystal toward the [001] direction between points 1 and 2. However, the shear band (region of high misorientation angle) around point 2 lead to a sudden change in orientation toward the center of the IPF (point 3). Note that the crystal rotation likely overshoots the [001]–[101] boundary of the IPF at point 2. This is not visible in the standard triangle of the IPF due to symmetries in the cubic structure. The crystal rotation from 3 to 4 due to slip on the primary slip system is in agreement with the literature and Figure 4.16. The activation of the conjugate plane at

the [101]–[111] boundary leads to a crystal rotation along this boundary of the IPF and toward the terminal stable [111] orientation.

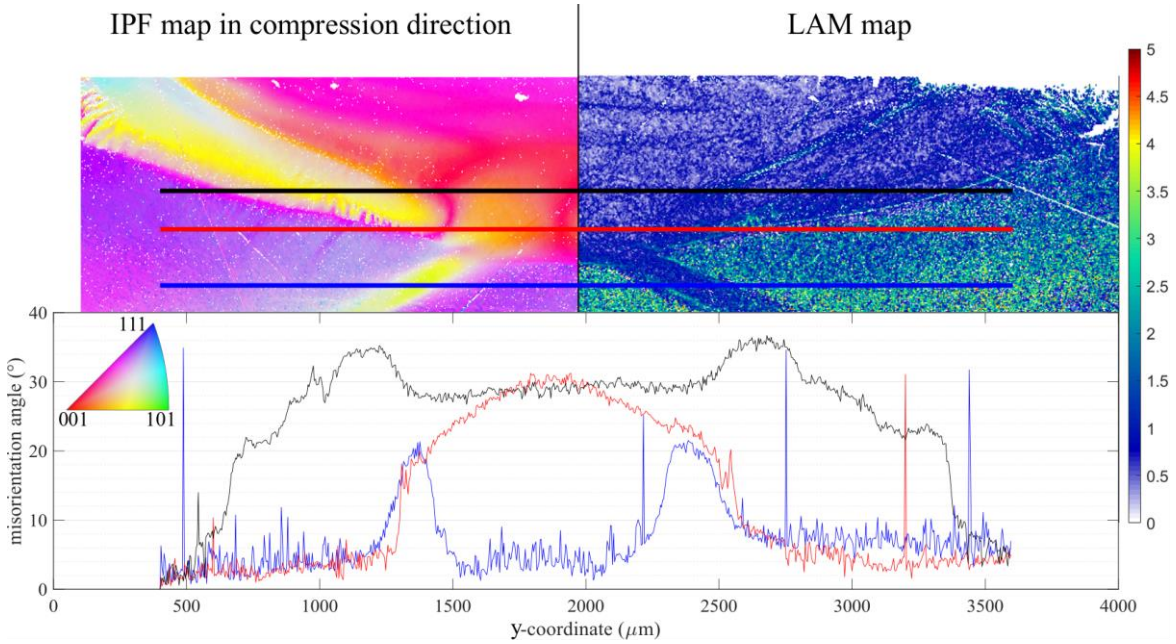

Figure 5.23: Horizontal line scans of three regions of specimen 7 deformed at ~4 000 s^{-1} intersecting the diagonal shear bands superposed on an IPF orientation map in the compression direction and a LAM map with corresponding plots of misorientation angle, with respect to the reference orientation (left extremity of the line scans).

Smaller changes in crystal orientation are measured along line (b). The green (orientation close to [101]) band at point 6 separates two regions of similar orientations (points 5 and 7) that are close to the [111] direction. The band at point 6 is also similar to the bands of intense shearing at the boundaries of the dead metal zone in the literature [99], spans over ~150 μm and have a misorientation of about 15 to 20° with respect to points 5 and 7. Finally, the "rebound" at point 5 could again be caused by an overshoot of the [001]–[101] boundary of the IPF.

5.3. Dislocation Substructures with STEM and TEM

Table 5.1 lists the niobium single crystal specimens analyzed with a transmission electron microscope at the German Federal Institute for Materials Research and Testing (BAM). An undeformed specimen from grain 4 was first analyzed to characterize the dislocation substructures of the as-received large grain niobium disk. The results obtained for this crystal orientation were then extrapolated to all other large grains and used as a comparison with deformed single crystal specimens to understand the change in dislocation substructure due to different testing conditions, i.e. different crystal orientations in the tensile direction and strain rates. The deformed specimens (5-34 and 2-158) were selected due to the different EBSD results (IPF orientation and LAM maps) measured and presented in the previous

section. Finally, the specimen deformed at a high strain rate has the same orientation than the quasi-static specimen 2-158 to evaluate the influence of strain rate on the dislocation substructure. All lamellae were prepared following the methodology described in section 3.1.1.6. and the majority of the bright field (BF) and dark field (DF) images presented in the following subsections were acquired in scanning transmission electron (STEM) mode due to sharper contrasts between dislocations and the matrix. Therefore, convergent-beam electron diffraction (CBED) patterns are more often shown than traditional selected-area diffraction (SAD) patterns of the reciprocal space obtained in traditional TEM mode with a parallel electron beam, instead of a converging beam in STEM mode. An advantage of CBED patterns is that Kikuchi lines are visible and can be associated with families of slip planes [234]. The abovementioned acronyms will be used throughout the following subsections.

Table 5.1: Characteristics of the niobium single crystal specimens analyzed with a TEM.

Specimen	Strain rate (s^{-1})	IPF map	LAM map
4-99	N/A	Undeformed	Undeformed
5-34	$1.28x10^{-2}$	Bands of different orientations	Shear bands with a high misorientation angle
2-158	$1.28x10^{-3}$	Rotated crystal	Gradient of increasing misorientation angle from grip to fracture regions
2-158	~1 000	Rotated crystal	High misorientation angle only close to the fracture surface

5.3.1. Reference Specimens from Grain 4

The first specimen analyzed was a reference undeformed quasi-static tensile specimen from grain 4 (4-99, close to the center of the large grain disk). This specimen was used to optimize the sample preparation technique for cross-section analyses using mechanical polishing and two electro-polishing (EP) steps. Analyses were conducted in the thin, electron transparent, regions of the specimens around the nearly oval hole with approximate principal dimensions of 99.8 μm and 185.2 μm formed during the last EP step and shown in the bottom right of Figure 5.24. Three areas of region A in Figure 5.24, namely areas A1, A2, and A3, where analyzed.

Figure 5.24 also shows the BF and DF STEM images obtained at a 20kx magnification for the three areas along zone axis z_5 (parallel to the <111> direction) and the CBED pattern acquired in area A2. The area closest to the hole (A1) shows a high dislocation density close to the hole and an abrupt reduction in dislocation density. Since this area is the thinnest, the

dislocation density is likely an artefact of the sample preparation. The high pressure of the EP jets could reasonably have deformed this thin area. Therefore, measurements that are too close to the hole are not considered representative of the bulk dislocation structure of a specimen. Likewise, the dislocations aligned with the {110} plane in area A2 and in the bottom left corner of area A3 are considered artefacts of the sample preparation, due the low thickness, shown in the DF images.The dislocation substructure of area A3, with a low dislocation density and short dislocation segments, is representative of an undeformed high-purity niobium single crystal specimen extracted from the large grain disk.

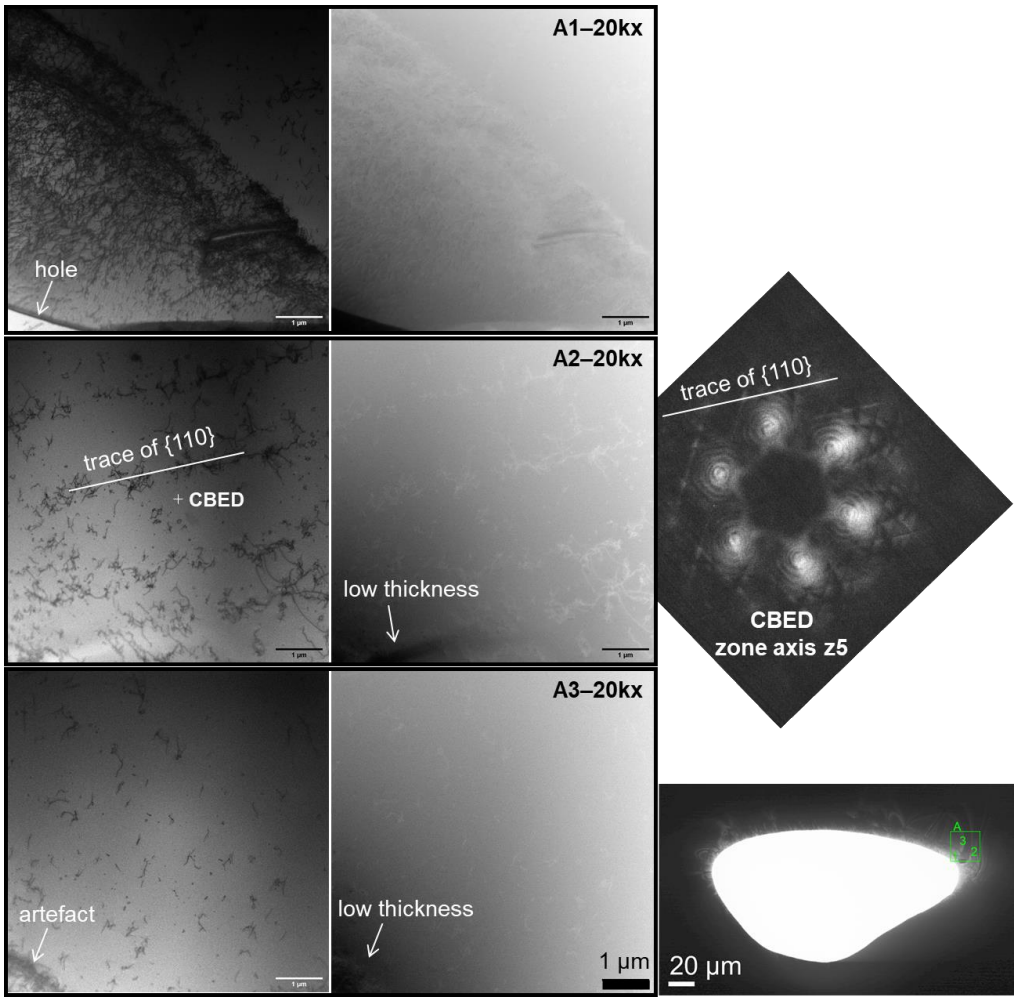

Figure 5.24: (left) BF and (right) DF STEM images of areas A1, A2, and A3 of the reference undeformed specimen from grain 4 along the zone axis z_5. CBED pattern of the z_5 axis, acquired in area A2, with the trace of a {110} plane. (Bottom right) BF STEM image of the hole formed during EP and the region (A) where high resolution images and diffraction patterns were obtained in the undeformed reference specimen from grain 4.

5.3.2. Specimen 5-34 QS – Low Strain Rate Test with Shear Bands

The objective of the TEM characterization of specimen 5-34 deformed at a nominal quasi-static strain rate of 1.28×10^{-2} s^{-1}, was to identify the dislocation substructure in the bands with different orientations and, more importantly, in the shear bands separating those regions

(see Figure 5.17 for EBSD results). A higher dislocation density is expected in the latter, based on the LAM maps presented in Figure 5.17. Before presenting the TEM results obtained at BAM, it is paramount to present STEM results obtained at CERN using a lamella prepared with a gallium focus ion beam (FIB) in a scanning electron microscope. This analysis was performed before the TEM study and the lack diffraction patterns acquisition and the lower resolution with the SEM in STEM mode justified the need for TEM.

The main steps of the lamella preparation with a FIB are shown in Figure 5.25 and detailed as follow: (a) selection of the area of interest (e.g. a shear band/low angle grain boundary perpendicular to the width of the lamella); (b) deposition of approximately 3 µm of platinum over the area of interest to prevent contamination of the top surface and deep cuts around this region; (c) undercut of the lamella; (d) introduction of the micromanipulator needle and soldering between the lamella and the needle using platinum deposition; (e) cutting the side of the lamella for extraction from the bulk to move and affix the lamella on a copper TEM grid using platinum; (f) removal of the micromanipulator needle by cutting the platinum and additional thinning and cleaning of the lamella with low FIB acceleration voltage and current to reach the thickness below 100 nm. The FIB parameters used for all the different steps are given in Appendix A.

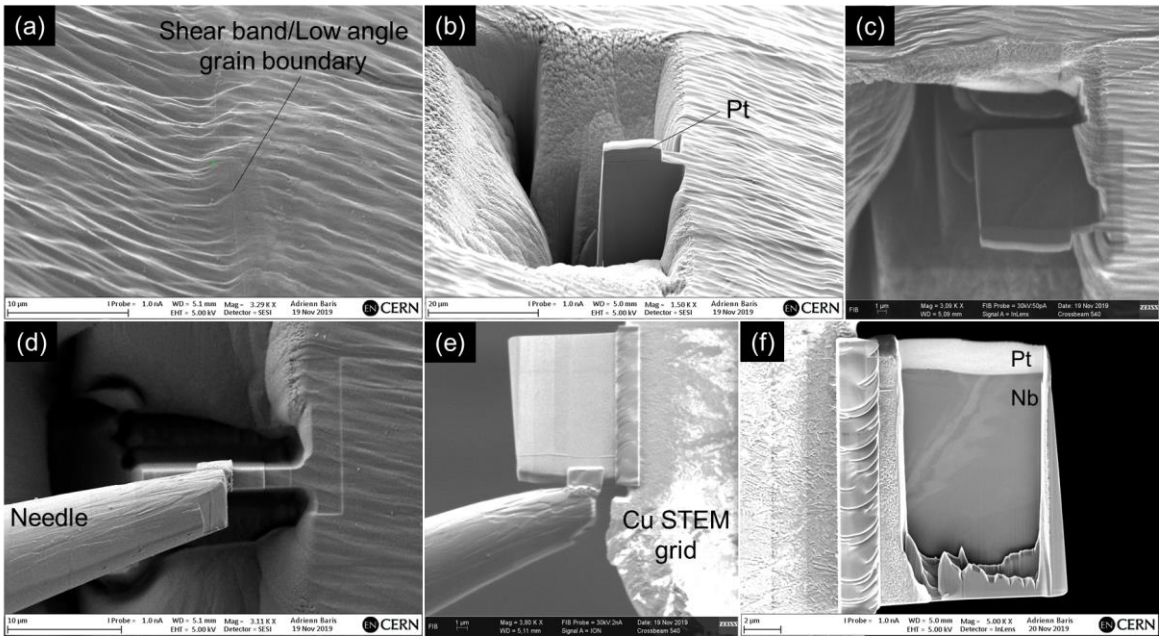

Figure 5.25: Steps for the extraction of a niobium single crystal lamella with a focus ion beam and imaging in STEM mode in an SEM.

Figure 5.26 shows the FIB lamella of specimen 5-34 analyzed at BAM with a TEM in STEM and conventional TEM (CTEM) modes. Large bend contours spanning across the entire specimen are visible and, in area G1, a line with a higher dislocation density appears to show a low angle grain boundary. While contrasts between dislocation rich and poor areas are

shown, individual dislocations are not visible, especially with CTEM. Gallium ion implantation is likely a source of distortion in the lattice and motivated the use of EP. However, it was possible with FIB to identify features on the surface of the specimen to prepare a lamella with a shear band. For example, in Figure 5.25a, a thin line is visible at the surface of the specimen and in valleys that are shown in the optical microscope image in Figure 5.17 and aligned with the shear band in the IPF orientation map of that same figure. Therefore, multiple disks punched out of the tensile specimen were electropolished in hope that a shear band intersects the electron-transparent region surrounding the hole.

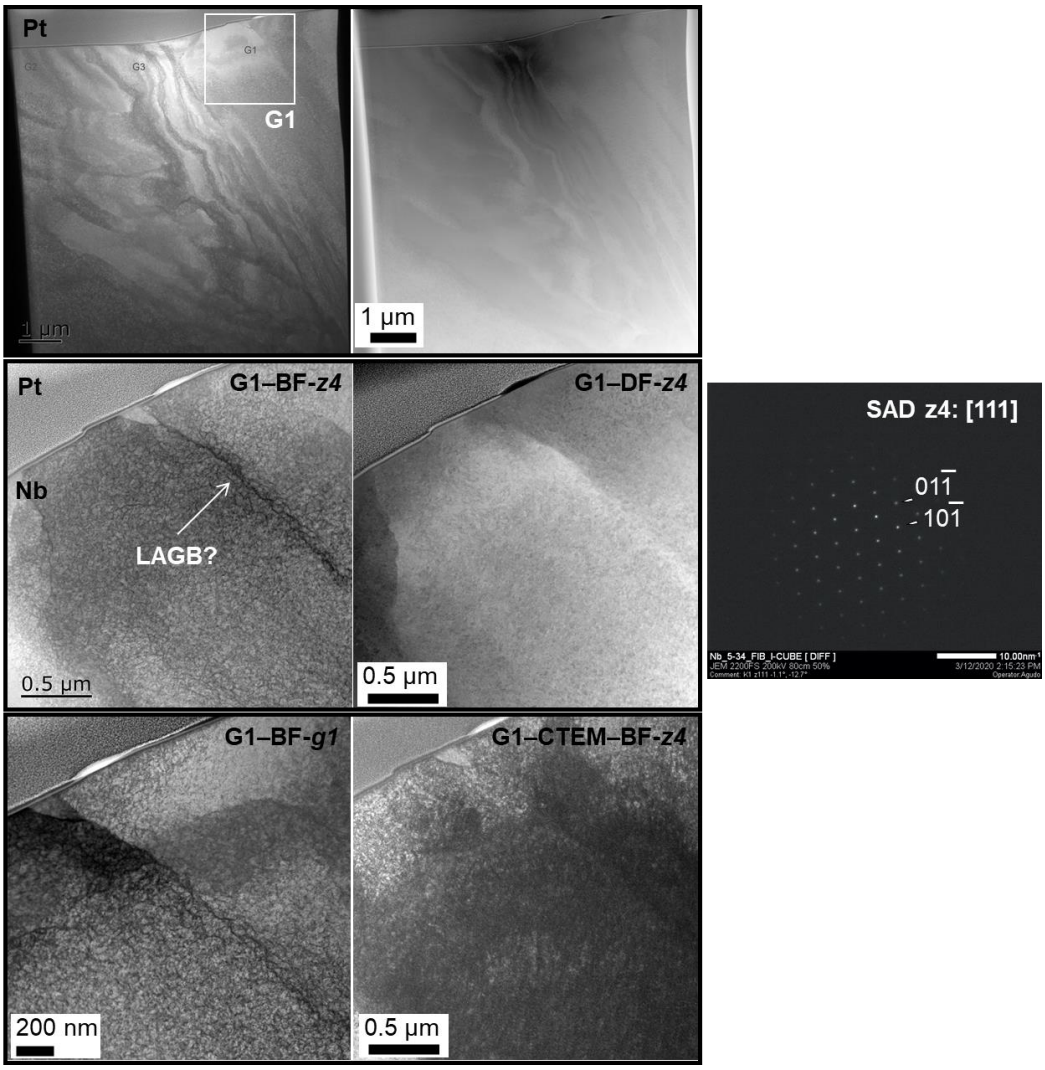

Figure 5.26: STEM and CTEM BF and DF images of the lamella prepared with FIB at CERN and analyzed at BAM. SAD pattern of the z_4 zone axis was acquired in area G1.

Figure 5.27 shows the hole formed during EP of a disk of specimen 5-34 and the five different regions that were analyzed with the TEM. As discussed for the reference specimen, sample preparation artefacts are more present in the thinnest regions of the specimen, that are closer to the hole. Regions A and E in Figure 5.27 showed such artefacts and are therefore not discussed.

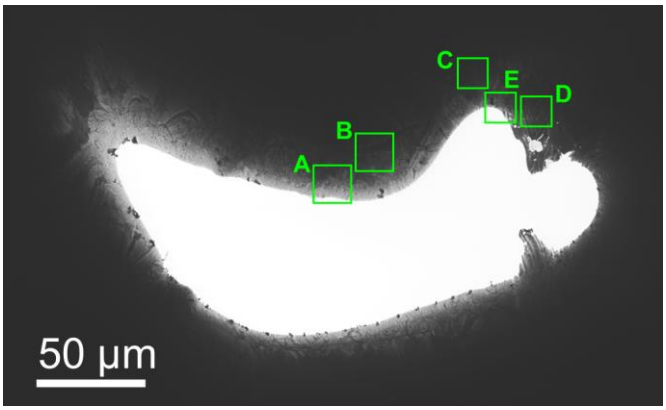

Figure 5.27: BF STEM image of the hole formed during EP and the five regions (A, B, C, D, E) where high resolution images and diffraction patterns were obtained in specimen 5-34 deformed at a nominal strain rate of 1.28×10^{-2} s^{-1}.

Figure 5.28 shows the BF and DF STEM images obtained in area B1 at magnifications of 20kx, 50kx, and 200kx with the corresponding CBED pattern. The four-fold symmetry of the CBED pattern indicates that the g vector is close to the [100] zone axis. The STEM images show a high density of entangled dislocations that are aligned in a preferred diagonal direction that appears to follow the trace of the {110} plane. Individual dislocations, instead of cell walls that are often found in heavily deformed materials, are observed. From those observations, region B is likely from the inside of a band with a normal direction close to [001] or [111], based on the orientation of bands measured with EBSD and the 90° rotation from the tensile axis IPF in Figure 5.17 and the direction normal to the cross-section of the specimen in this case. Figure 5.40 shows the corresponding IPF orientation map for specimen 5-34 deformed at low strain rate in the vicinity of the fracture surface.

Figure 5.29 shows DF and BF STEM images with different g vectors in region C of the same specimen. At all magnifications, regions with a sharp contrast separating topological features (different thicknesses) are visible. The nearly square white (black) features in the BF (DF) images are etch pits. Recall that the lighter (darker) shade of grey in the BF (DF) image indicates a lower thickness. Similar etch pits were also observed in specimen 2-158 deformed at a low strain rate, but not in bands. Individual dislocations are visible between the etch pits and follow the edges of the square pits, which is likely caused by a relaxation of the dislocations following the localized removal of material.

From the sudden change in dislocation substructure and surface morphology, area C1 of the specimen is presenting the effect of a shear band on the dislocation substructure. The higher dislocation density in a shear band likely explains the preferential etching, meaning that the bands containing the etch pits had a higher dislocation density than the region between the bands, where individual dislocations are visible. Also, a change in crystal orientation was measured across the dashed line drawn in Figure 5.29.

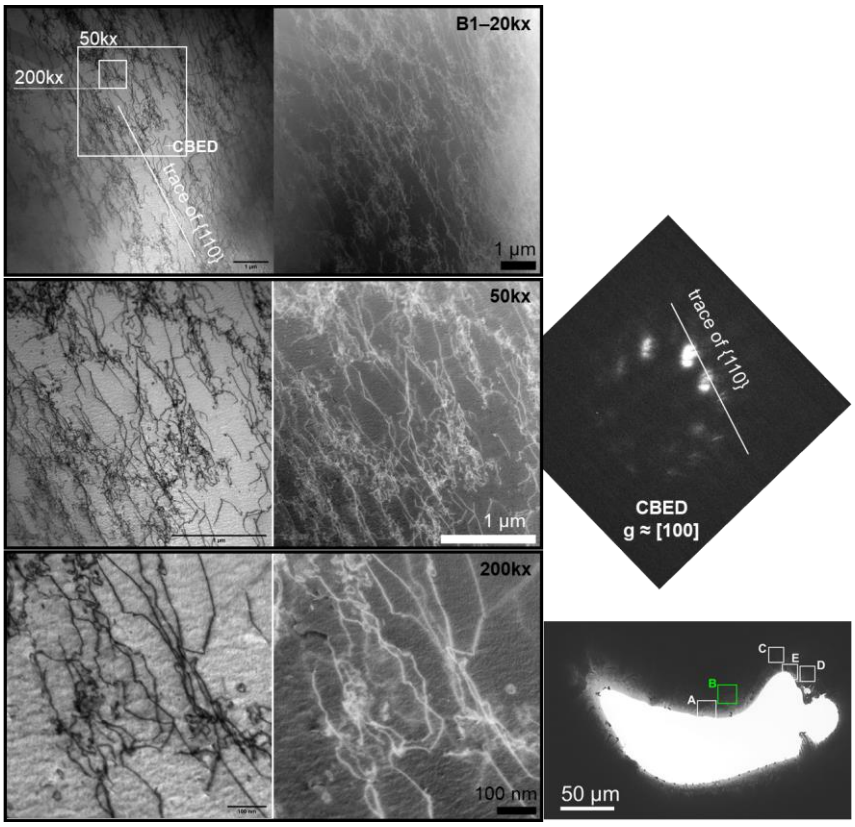

Figure 5.28: (left) BF and (right) DF STEM images of area B1 at 20kx, 50kx, and 200kx magnifications of specimen 5-34 along a g vector close to the [100] direction. CBED pattern of the g axis with the trace of a {110} plane.

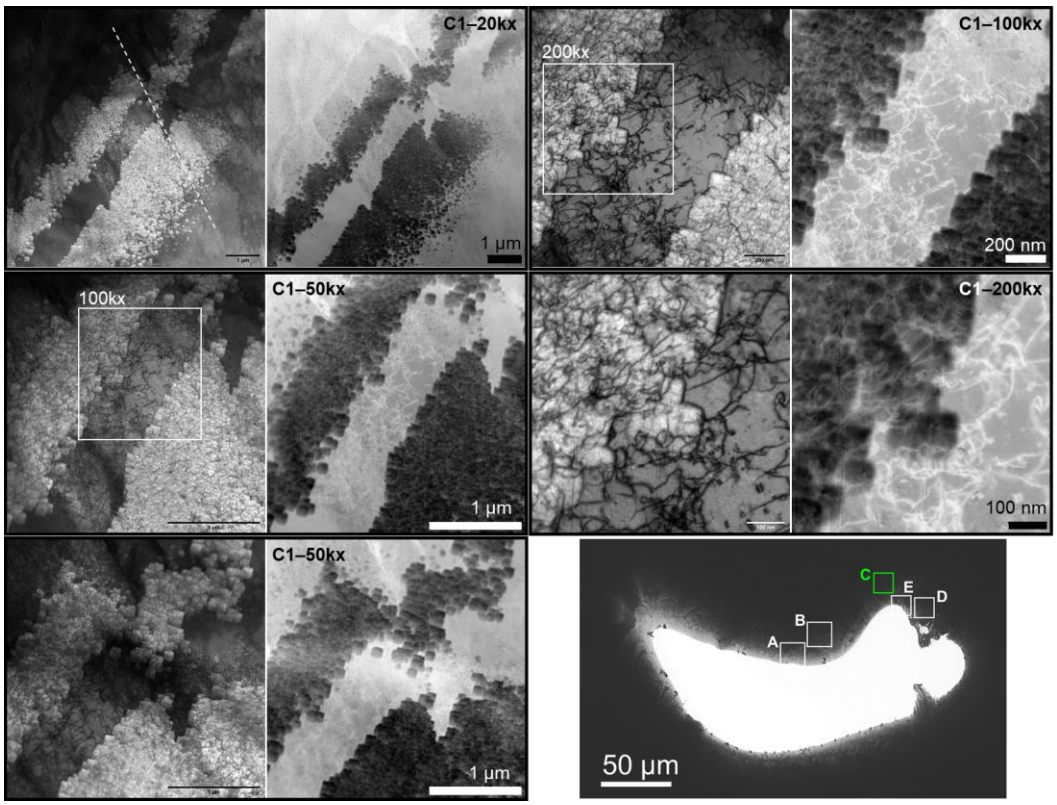

Figure 5.29: (left) BF and (right) DF STEM images of area C1 at 20kx, 50kx, 100kx, and 200kx magnifications of specimen 5-34 along different g vectors. The dashed line marks a region where a change in crystal orientation was measured.

Finally, region D of specimen 5-34 was analyzed and BF and DF STEM images are presented in Figure 5.30. This region of the specimen showed features that were not visible elsewhere. Bands with different thicknesses (contrasts) and widths of about 0.55 to 1.12 μm are intersecting at ~47°. Compared with the square etch pits Figure 5.29, preferential etching of bands did not leave marks on the surface of the specimen. The interior of the bands was difficult to image due to a high dislocation density. In sub-area D2-3 of Figure 5.30, different imaging conditions were used to reveal dislocations in the different quadrants of the intersecting bands. This indicates a strong change in crystal orientation in that sub-area.

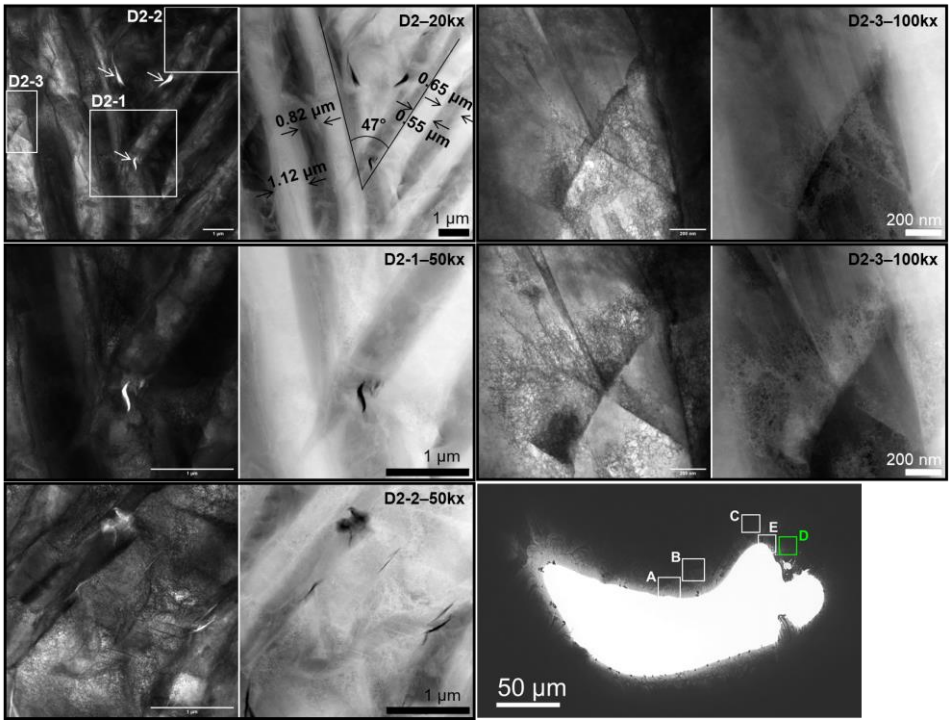

Figure 5.30: (left) BF and (right) DF STEM images of area D2 at 20kx, 50kx, and 100kx magnifications of specimen 5-34 along different *g* vectors. White arrows show the locations of small holes.

Since the substructure in this region is very different than regions B and C, the dislocation density is too high in the bands for adequate imaging, and no significant change in crystal orientation was measured between the bands, it is difficult to conclude what this corresponds. The high dislocation density and heterogeneous substructure suggests that this region is not inside a band of normal [001] or [111] direction, as suspected for region B (Figure 5.28). Also, the repeating pattern and similar crystal orientation between the bands of varying contrast does not suggest that region D is representative of a shear band, as suspected for region C (Figure 5.29). Finally, despite the three holes (identified with white arrows in Figure 5.30), this substructure is different than previously observed artefacts of sample preparation. Therefore, more regions of specimen 5-34 should be prepared for TEM characterization to see if this substructure is common.

5.3.3. Specimen 2-158 QS vs D – Low vs High Strain Rate Test

The effect of strain rate, from a quasi-static rate of $1.28x10^{-3}$ s^{-1} to a dynamic rate of ~1 000 s^{-1}, was studied by comparing the dislocation substructures in tensile specimens deformed up to rupture for specimen 2-158, with a tensile orientation in the center of the IPF. EBSD characterization were performed on quasi-static and dynamic specimens with the same crystal orientation and the IPF and LAM maps were presented in Figure 5.16.

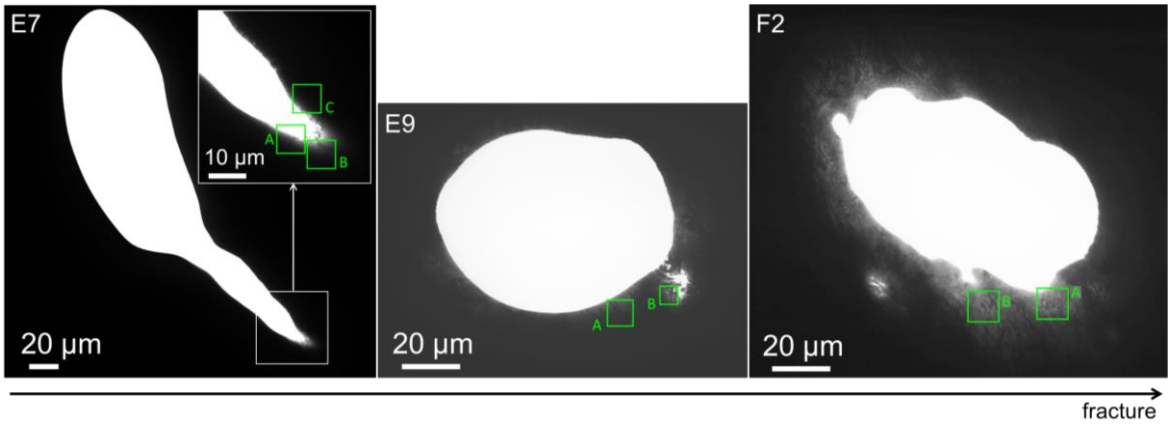

Figure 5.31: BF STEM images of the hole formed during EP of three punched disks, E7, E9, and F2, from specimen 2-158 deformed at a nominal strain rate of $1.28x10^{-3}$ s^{-1}. Disk F2 is closer to the fracture surface of the quasi-static tensile specimen.

Figure 5.32 shows BF and DF STEM images of areas B2 and C2 in disk E7 of specimen 2-158 deformed at a nominal strain rate of $1.28x10^{-3}$ s^{-1}. A lower dislocation density was observed in areas A (not shown in Figure 5.32) and B2 than in area C2. The short and dispersed dislocations are similar than in the reference (undeformed) specimen from grain 4 presented in Figure 5.24. Compared with the dislocation substructures observed in disks E9 (Figure 5.33) and F2 (Figure 5.34), the dislocation density is much lower in E7 and no cell walls are observed. This is likely due to a lower deformation the disk extracted the further away from the fracture surface.

Figure 5.33 shows BF and DF STEM images of area A1 in disk E9 of specimen 2-158 deformed at a nominal strain rate of $1.28x10^{-3}$ s^{-1}. A high dislocation density with no preferred orientation is observed. Screw dislocations normal to the surface of the specimen are visible in sub-area A1-1 at 50kx magnification and identified based on the black and white contrast, as shown in the schematic in Figure 5.33 [234]. The dislocation density in the bottom-right corner of sub-area A1-2 is so high that individual dislocations are impossible to distinguish. As seen in the DF image, this is due to an important increase in specimen thickness across the region scanned. The rapid increase in thickness is detrimental to observe the dislocation substructure of heavily deformed specimens. The circular hole formed during EP in disk E9 is related to this thickness distribution.

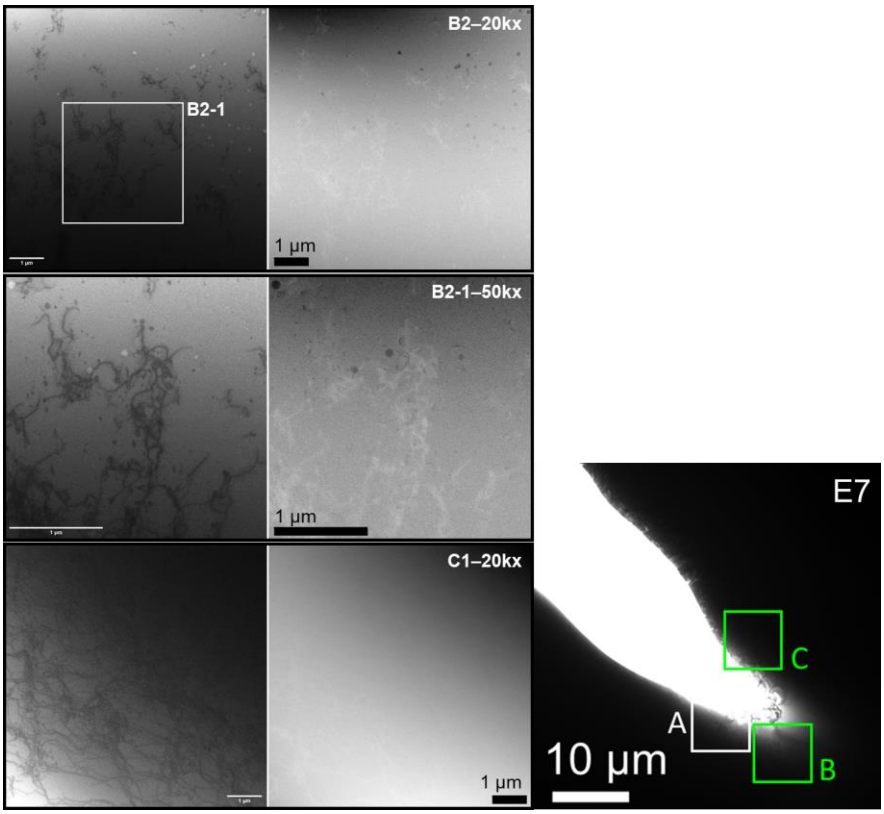

Figure 5.32: (left) BF and (right) DF STEM images of areas B2 and C2 in disk E7 at 20kx and 50kx magnifications along zone axis z_1 for specimen 2-158 deformed at 1.28x10^{-3} s^{-1}.

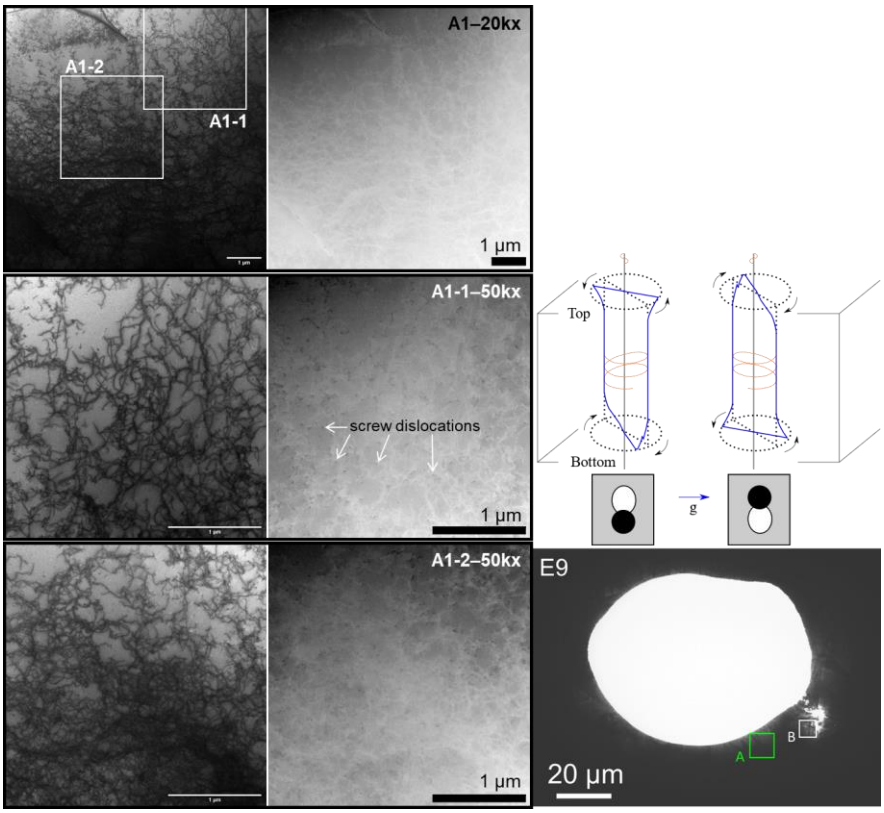

Figure 5.33: (left) BF and (right) DF STEM images of area A1 in disk E9 at 20kx and 50kx magnifications along g vector for specimen 2-158 deformed at 1.28x10^{-3} s^{-1}. Arrows in A1-1 point at screw dislocations normal to the surface of the specimen, based on the schematic on the right, redrawn from Williams and Carter [234].

A third disk, namely F2, from specimen 2-158 deformed at a quasi-static strain rate was electropolished and analyzed to compensate for the too high thickness in E9. Figure 5.34 shows BF and DF STEM images of area A2 of disk F2. Thick (~200 nm in width) cell walls with a high dislocation density were observed in this area and in region B. This dislocation substructure is different from disks E7 and E9, which were extracted from the same tensile specimen. As previously stated, this is probably caused by a higher deformation of the lattice in disk F2 that was punched closer to the fracture surface. This correlates with the higher misorientation angles measured close to the fracture surface with EBSD for single crystals with the same orientation but deformed at a nominal strain rate of 1.28×10^{-2} s^{-1} (Figure 5.16).

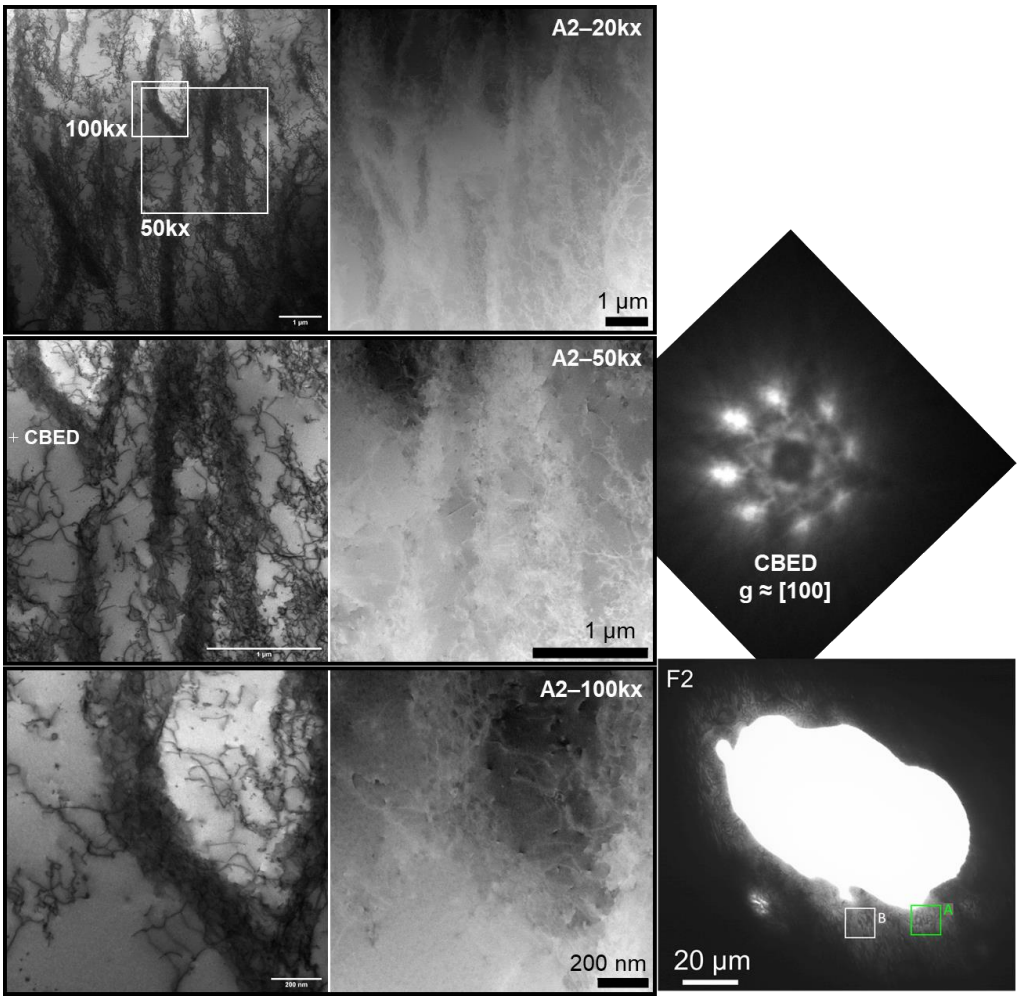

Figure 5.34: (left) BF and (right) DF STEM images of area A2 in disk F2 at 20kx, 50kx, and 100kx magnifications along zone axis z_1 for specimen 2-158 deformed at 1.28×10^{-3} s^{-1}. CBED pattern of the z_1 zone axis.

Figure 5.35 shows the hole formed with EP in the tensile specimen deformed at a strain rate of ~1 000 s^{-1}. Two regions, namely A and B, were characterized at high magnifications of up to 200kx. Region A is thicker and, therefore, has a dislocation substructure that is likely more representative of the bulk of the specimen.

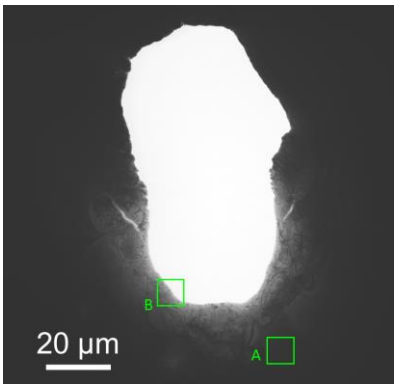

Figure 5.35: BF STEM image of the hole formed during EP and the two regions (A, B) where high resolution images and diffraction patterns were obtained in specimen 2-158 deformed at a strain rate of ~1 000 s^{-1}.

Figure 5.35 and Figure 5.36 show BF and DF STEM images of two areas (A1 and A2) in region A. The dislocation density is higher in A1, but, more importantly, both areas show short dislocation segments, no cell walls, and no preferred dislocation alignment directions. This differs from the low strain rate specimens with the same orientation (2-158) and with shear bands (5-34). Recall that a reduction of strength anisotropy at a strain rate of ~1 000 s^{-1} was measured (Figure 4.2) and explained by the activation of multiple slip systems at high strain rate to accommodate the imposed deformation. The short and homogeneously distributed dislocations in a specimen deformed at high strain rate support this hypothesis. The intersection of dislocations on different and intersecting slip planes leads to the formation dislocation dipoles (small loops), as shown in the high magnification images in Figure 5.36, and the activation of multiple slip systems explains the absence of preferred orientations.

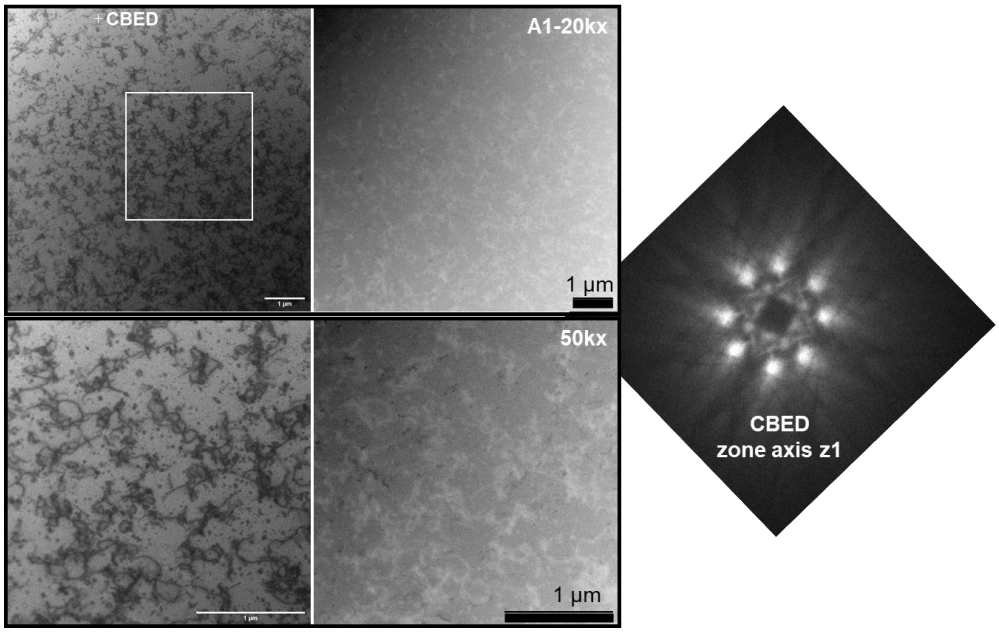

Figure 5.36: (left) BF and (right) DF STEM images of area A1 at 20kx and 50kx magnifications along zone axis z_1 for specimen 2-158 deformed at ~1 000 s^{-1}. CBED pattern of the z_1 zone axis.

Dislocations in the thinner B region of the high strain rate specimen, presented in Figure 5.38, also show a high density of dislocation dipoles. Slightly longer dislocation segments are visible and appear to be aligned in a preferred orientation. However, since this region is close to the hole, as shown with the darker region of the DF image at 20kx, artefacts from the sample preparation could affect the dislocation substructure. Therefore, the dislocation substructure obtained in the thicker A region is considered to be more representative of tensile specimens deformed at a high strain rate with an initial crystal orientation close to the center of the IPF.

Edington [155] observed similar differences in dislocation substructures in niobium single crystal specimens (with a lower purity) with an initial orientation close to the center of an IPF deformed in compression at strain rates of 1.2×10^{-4} s^{-1} and 1.5×10^{3} s^{-1}. Dislocations cells formed in specimens deformed at a low strain rate and a higher density of homogenously distributed dislocation dipoles was observed in the high strain rate specimens.

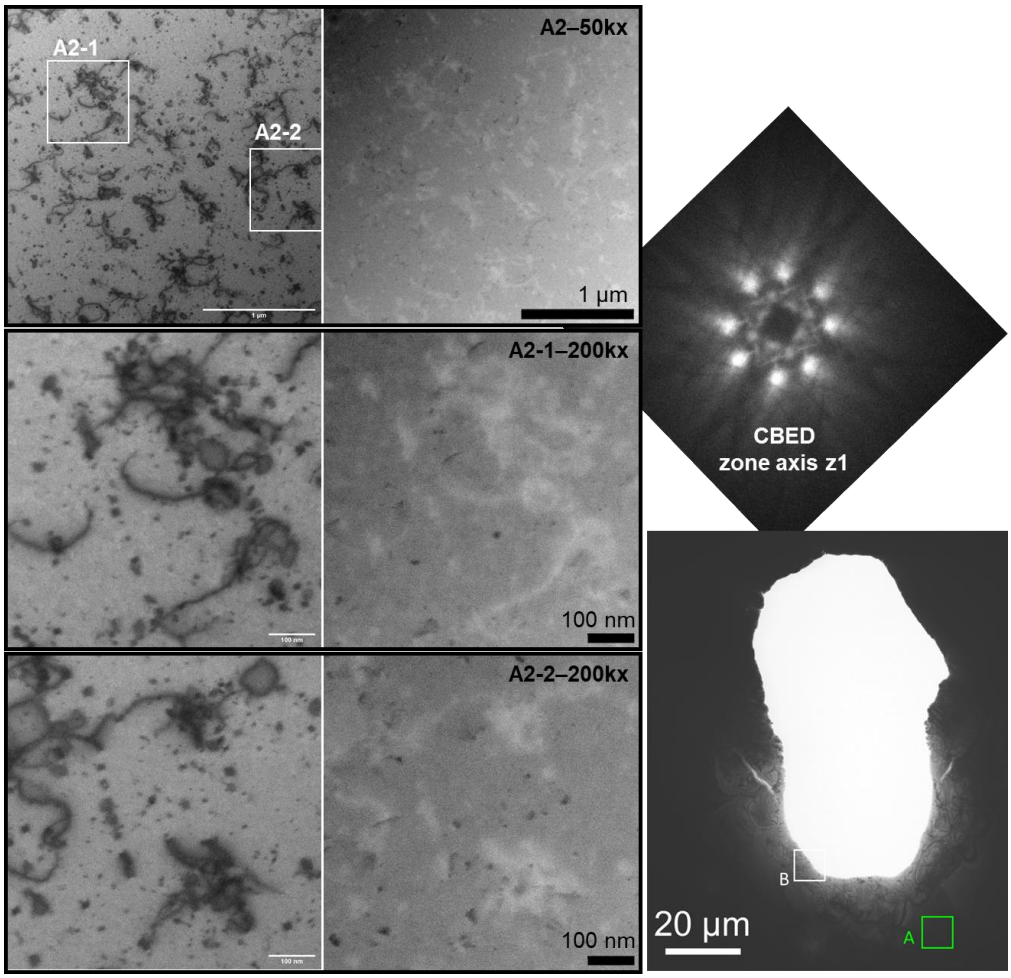

Figure 5.37: (left) BF and (right) DF STEM images of area A2 at 50kx and 200kx magnifications along zone axis z_1 for specimen 2-158 deformed at ~1 000 s^{-1}. CBED pattern of the z_1 zone axis.

5.3.4. Effect of the Different Dislocation Substructures on the Superconducting Properties

Since niobium SRF cavities are functional parts that operate in a superconducting state, it is essential to understand the effect of different defects on superconducting properties. Antoine [34] reviewed the influence of crystalline defects of different dimensions, i.e. from vacancies (0D) to inclusions (3D). The effect of dislocations was discussed for cell walls and low-angled grain boundary (LAGB) as flux penetration was observed by Sung et al. [183] using magneto-optical imaging on deformed tensile niobium single crystal specimens. Since a high dislocation density was measured in specimens deformed at low strain rates in the cell walls, close to the fracture surface of specimen 2-158, or in the shear bands, in the etch pits in specimen 5-34, similar flux penetration as observed by Sung et al. is expected. The homogeneously distributed short dislocation segments and loops in the specimen deformed at high strain rate have a lower dislocation density and are still considered as linear defects, compared with the previously cell walls and LAGB. This suggests that the dislocation substructure found at high strain rate has weaker pinning centers, which could reduce flux trapping and increase the performances of the SRF cavities. This hypothesis must however be experimentally confirmed with measurements, which were outside of the scope of this thesis.

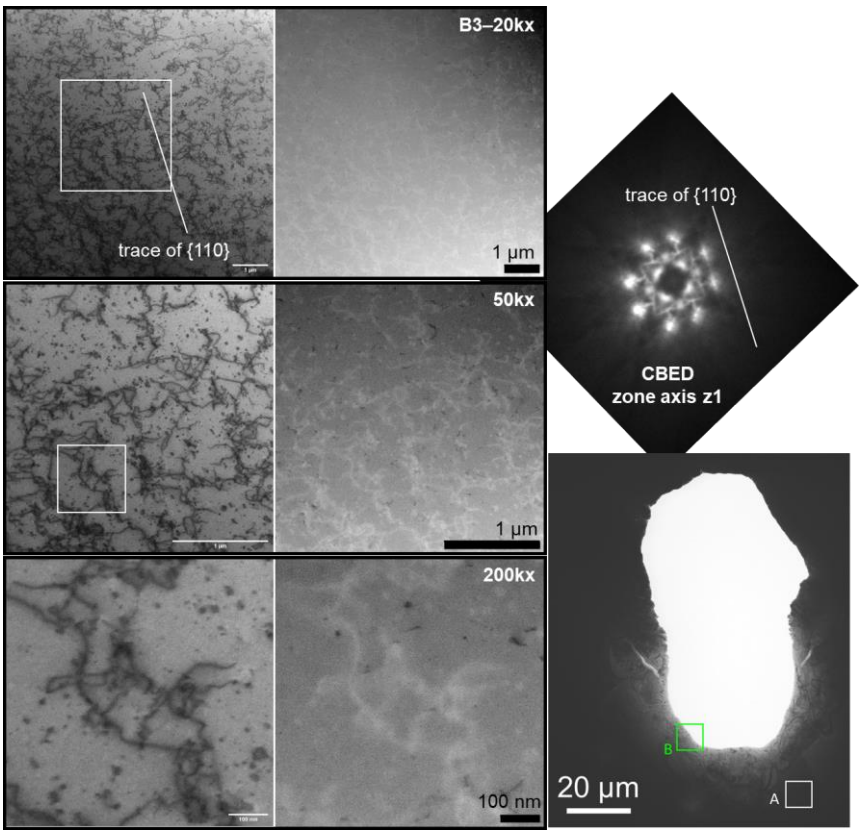

Figure 5.38: (left) BF and (right) DF STEM images of area B3 at 20kx, 50kx and 200kx magnifications along zone axis z_1 for specimen 2-158 deformed at ~1 000 s^{-1}. CBED pattern of the z_1 zone axis.

5.4. Nanoindentation of Deformed and Undeformed Single Crystals

Nanoindentation tests have been performed on undeformed and deformed niobium single crystals to quantify the indentation elastic modulus and hardness for different crystal orientations and misorientation angles measured with EBSD. First, undeformed compression specimens with different crystal orientations were analyzed and the effect of the crystal orientation on the elastic modulus and the hardness are presented. Second, results on the effect of the crystal orientation for a single crystal specimen deformed at low strain rate and with shear bands observed with EBSD are presented. Third, the effect of the strain rate on the hardness and elastic modulus is studied for tensile and compression specimens deformed at quasi-static (10^{-2} to 10^{-3} s^{-1}) and dynamic (10^{3} s^{-1}) strain rates. Fourth, the effect of crystal orientation from dynamic compression specimens with low and high hardening behavior is presented.

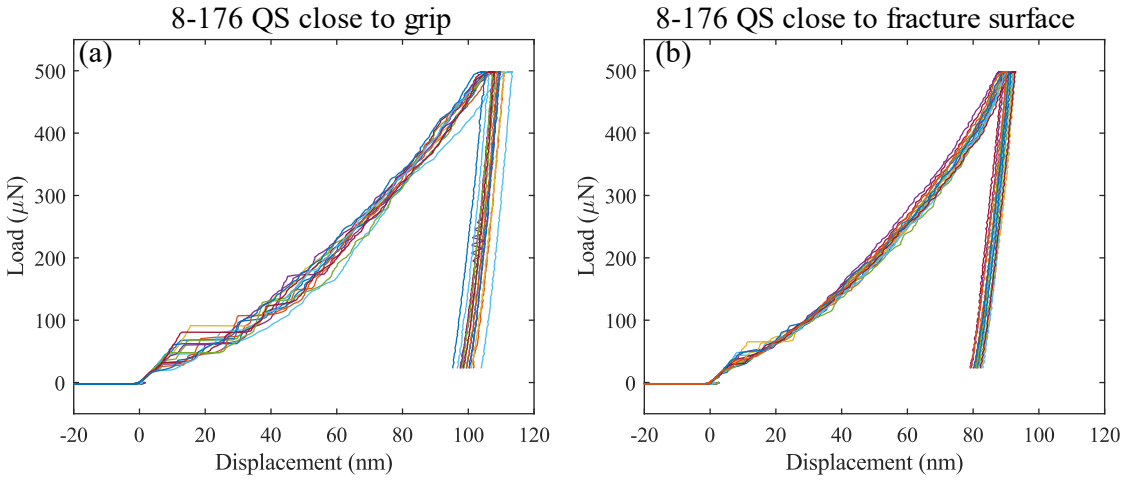

Figure 5.39: Load–displacement curves of specimen 8-176 deformed at a nominal strain rate of $1.28x10^{-2}$ s^{-1} (a) close to the region of the grip and (b) the fracture surface of the specimen.

The load–displacement curves were repeatable for all orientations. Large pop-ins were observed in most specimens, as shown in Figure 5.39, but not in all regions of the specimens. For example, in tensile specimen 8-176 deformed at a low strain rate, more pop-ins were observed in the less deformed region of the specimen (Figure 5.39a), i.e. the region farther away from the fracture surface. This could be a consequence of a lower pre-existing dislocation content in this region. The first pop-ins observed at penetration depths of about 10 nm are likely due to an oxide layer at the surface of the specimens. The tensile and compression specimens were polished for the EBSD study, which was performed 8 or 15 months before the nanoindentation study, and the specimens were not stored in vacuum. It has been reported by Grundner and Halbritter [235], Ma and Rosenberg [236], and Veit et al. [237] that a stable Nb_2O_5 oxide layer of about 5 nm forms at the surface of niobium surfaces. A Nb_2O_5 layer was then likely responsible for the first pop-ins observed in multiple

specimens. Finally, no general trend was measured for the pop-in length or depth or load of the occurrences.

5.4.1. Undeformed Specimens from Grains 4 and 7

First, the effect of crystal orientation on the elastic modulus and the hardness was measured with nanoindentations performed on undeformed compression specimens from grains 4 and 7. The specimens were vibratory polished at ENSTA Bretagne following a procedure similar to the one presented in section 3.1.1.5. and analyzed directly after polishing to minimize the growth of the stable Nb_2O_5 oxide layer. Grains 4 and 7 were chosen due to the large difference in hardening behavior measured in compression, as shown in Figure 4.15 (low flow stress and a long stage I for grain 4 and a high flow stress with parabolic hardening in the whole plastic domain for grain 7). While the stress state is more complex under the self-similar Berkovich tip than it is in uniaxial compression tests, similar differences in hardness were measured. Median hardness values of 1.53 ± 0.12 GPa and 2.07 ± 0.13 GPa were measured for grains 4 and 7, respectively. Different elastic moduli were also expected due to the difference in crystal orientation, as shown in Figure 5.40c. Median elastic moduli of 103.6 ± 8.39 GPa and 122.4 ± 9.97 GPa were measured for grains 4 and 7, respectively. Based on experimental values of the elastic modulus of niobium single crystals along different crystal orientations measured by Armstrong and Dickinson [222] and reproduced in Figure 5.40c, the elastic modulus for the [100] direction should be higher than the [111] direction and approximately equal to 148.29 and 81.04 GPa, respectively, at room temperature. The crystal orientations of grains 4 and 7 are not located at the corners of an inverse pole figure, but the closer proximity of grain 7 with the [100] direction likely explains the higher elastic modulus of that grain.

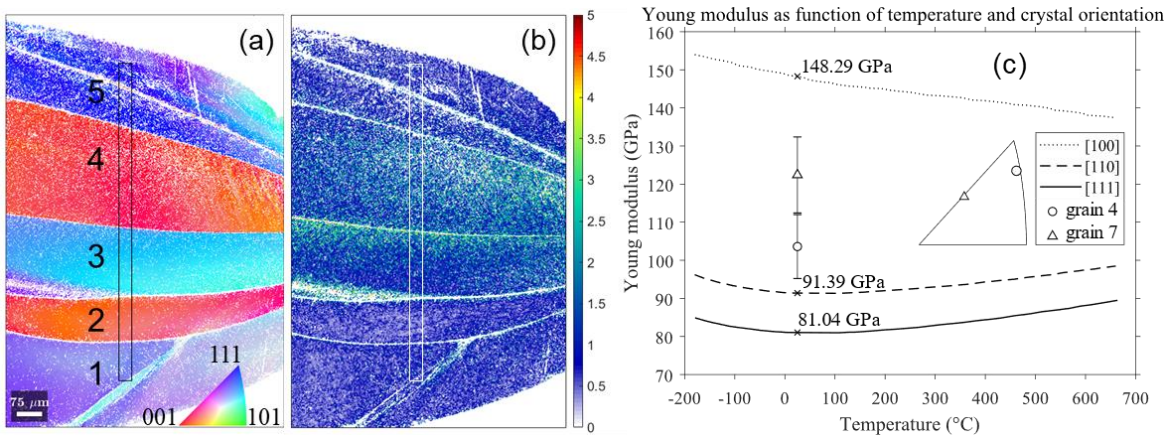

Figure 5.40: (a) IPF orientation map in the direction normal to the cross-section of the specimen with the approximate region indented (black rectangle) and the five bands analyzed and (b) corresponding LAM map. (c) Elastic modulus of niobium single crystals along different crystal directions and at different temperatures from Armstrong and Dickinson [222] with approximate values at 25°C.

5.4.2. Specimen 5-34 QS – Low Strain Rate Test with Shear Bands

Second, the tensile specimen 5-34 deformed at a nominal strain rate of 1.28×10^{-2} s^{-1} that showed bands of different crystal orientations with EBSD (Figure 5.17) was analyzed. Figure 5.40a shows the IPF orientation map of the specimen close to the fracture surface and normal to the cross-section of the specimen, i.e. along the indentation direction, the approximate region that was indented and the five bands with different crystal orientations. The crystal orientation of the different bands is close to [100] (bands 2 and 4) and [111] (bands 1, 3, and 5). Again, based on experimental values of the elastic modulus of niobium single crystals along different crystal orientations measured by Armstrong and Dickinson [222] (Figure 5.40c), the elastic modulus for the [100] bands should be higher than the [111] bands.

Figure 5.41 shows the elastic modulus and hardness distribution as function of the vertical position in the indented area. The median elastic modulus in the five bands, with approximate locations highlighted in red and blue in the plot, clearly show higher values in regions with a near-[100] orientation. This result confirms that the sensitivity of nano indentation is sufficient to measure differences in crystal orientations. However, the average elastic moduli measured in each band are different in absolute and relative values than the literature [222]. The relative difference measured by Armstrong and Dickinson [222] is given by the following relation:

$$E_{[001]} \approx 1.83\, E_{[111]}$$

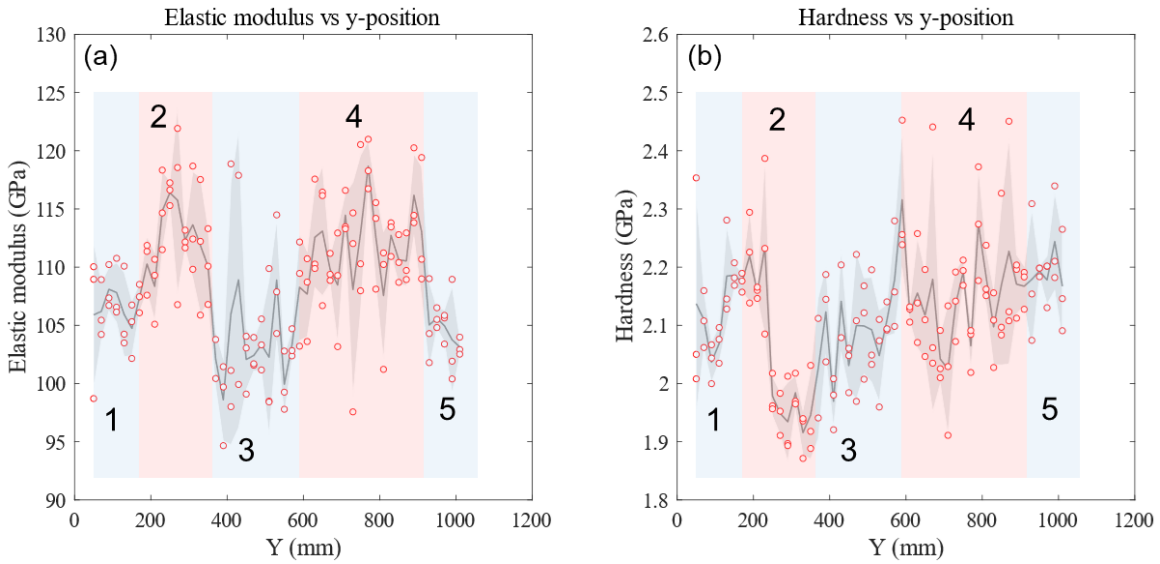

Figure 5.41: (a) Elastic modulus and (b) hardness as function of the vertical position in specimen 5-34 QS deformed at a nominal strain rate of 1.28×10^{-2} s^{-1}, with respect to the bottom of the indented area. The black line represents the median value at each height, the grey area is the standard deviation, and the red and blue areas are the approximate locations of the five bands.

Elastic moduli between 110–150 GPa and 100–110 GPa were measured for the [100] and [111] bands, respectively. The high misorientation angle due to the proximity of the indent with the fracture surface and the crystal orientations that are not exactly aligned with [100] and [111] are probably responsible for the differences with the literature. Also, the elastic moduli measured by Armstrong and Dickinson [222] was obtained from the resonance frequency of the different single crystals and might differ from the indentation modulus that is affected by material behaviors, such as dislocation pile-up [238].

A high hardness was expected at the boundary of two bands due to a higher misorientation angle and a similar hardness inside the bands, due to similar levels of strain. An increase in hardness was measured between bands 1 and 2 and bands 3 and 4. However, the former increase spans over few tens of hundreds of micrometers, which is larger than the width of the boundary between bands 1 and 2. The sharp increase between bands 3 and 4 appears to be more in agreement with the expected result and was then analyzed with a higher resolution, i.e. smaller step size between the indents.

Figure 5.42 shows the elastic modulus and hardness measured with the high-resolution scan done between bands 3 and 4. A sharp increase in hardness to ~2.5 GPa was measured between the bands and shown with an arrow in Figure 5.42b. This is explained by a local higher dislocation density due to the sudden change in crystal orientation between the two bands.

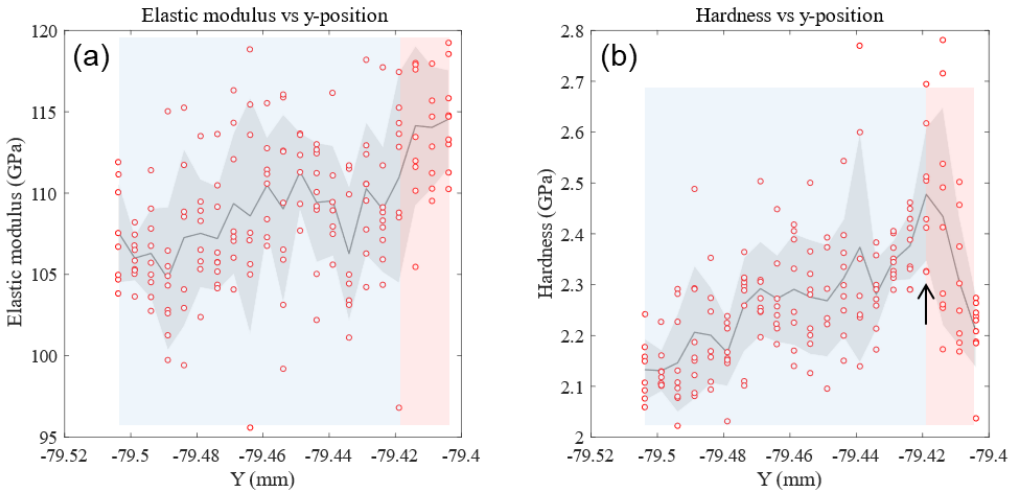

Figure 5.42: (a) Elastic modulus and (b) hardness as function of the vertical position between bands 3 (blue) and 4 (red) in specimen 5-34 QS. The black arrow indicates the region with a sharp increase in hardness and, therefore, the location of the shear band.

5.4.3. Specimen 8-176 QS vs D – Low vs High Strain Rate Test

Tensile specimens 8-176 deformed at strain rates of 1.28×10^{-2} s^{-1} and ~1 000 s^{-1} that showed rotated crystals between the grip and fracture surfaces in the EBSD measurements were analyzed with nano indentation. The objective of these analyses was to measure differences

in elastic modulus and hardness between the specimens deformed at quasi-static (QS) and dynamic (D) strain rates. In the QS specimen, the LAM map (Figure 5.14) shows a gradual increase in misorientation angle between the grip and the fracture surface while the dynamic specimen shows a low misorientation angle in the majority of the specimen and a sharp increase close to the fracture surface (Figure 5.15).

Figure 5.43 compares the elastic modulus and hardness of the specimens deformed at quasi-static and dynamic strain rates. The normalized position on the x-axis corresponds to the relative distance between the grip (0) and the fracture surface (1). The hardness of the specimen deformed at a high strain rate is consistently lower than the specimen deformed at a quasi-static strain rate. This is explained by the lower misorientation angle in the gage length and is probably also linked to the different dislocation substructures observed with TEM. The high dislocation density and thick cell walls observed in the low strain rate specimen (Figure 5.33 and Figure 5.34) are likely impeding the motion of dislocations more importantly than the short and homogeneously distributed dislocations observed in the high strain rate specimen (Figure 5.36 to Figure 5.38), as suggested by Edington [155] for specimens deformed in compression at strain rates of 1.2×10^{-4} s^{-1} and 1.5×10^{3} s^{-1}. The TEM and nanoindentation specimens were not cut from the same grain in the large grain sheet, specimens 2-158 and 8-176, but have an initial tensile orientation close to the center of the IPF and EBSD measurements showed homogeneous and rotated crystals. The strain rate of the quasi-static TEM specimens is of the order of 10^{-3} s^{-1}, compared with 10^{-2} s^{-1} for the nanoindentation specimens. However, similar dislocation substructures are expected in both specimens since both strain rates are in the quasi-static regime.

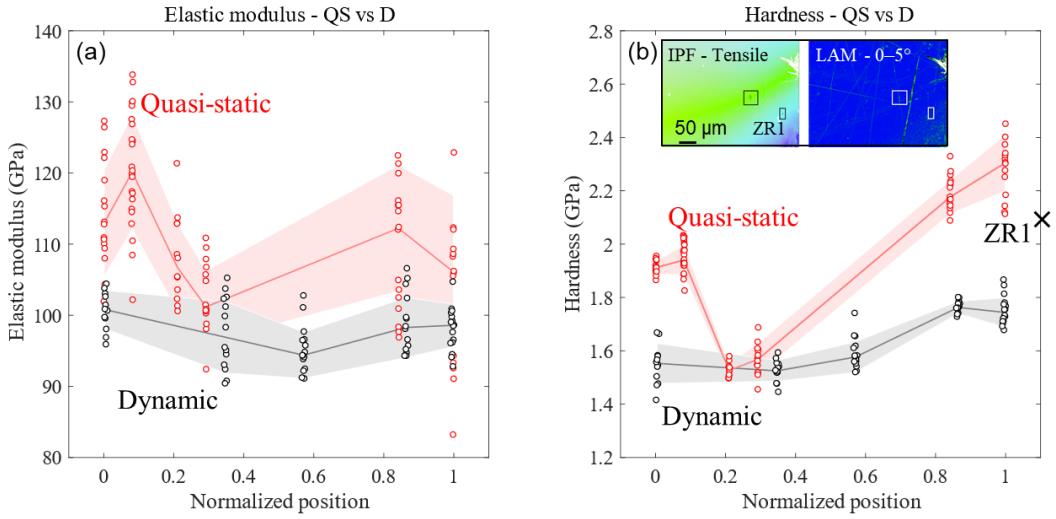

Figure 5.43: Plots of (a) elastic modulus and (b) hardness as function of the normalized position from the grip (0) to the fracture surface (1) of tensile specimens 8-176 deformed at (red) low (1.28×10^{-2} s^{-1}) and (black) high strain rates (~1 000 s^{-1}). (Inset) tensile axis IPF orientation map and LAM map of the region where the ZR1 indents were performed, closer to the fracture surface (see Figure 5.15 for the location of the IPF and LAM maps in the specimen).

A higher hardness was measured at ZR1, with indent locations closer to the fracture surface as shown in Figure 5.43, but for a fewer number of indents. The LAM map of the high-resolution EBSD scan (with a step size of 0.5 μm) does not show a high misorientation angle in the region analyzed. However, the misorientation angle is about 2° in the lower resolution image (with a step size of 2 μm) shown in Figure 5.15. This explains the higher hardness and the influence of the step size in EBSD measurements to observe features with different length scales. For this single crystal, the apparent reduction in misorientation angle at higher resolution is a consequence of the continuous crystal rotation with no heterogeneities.

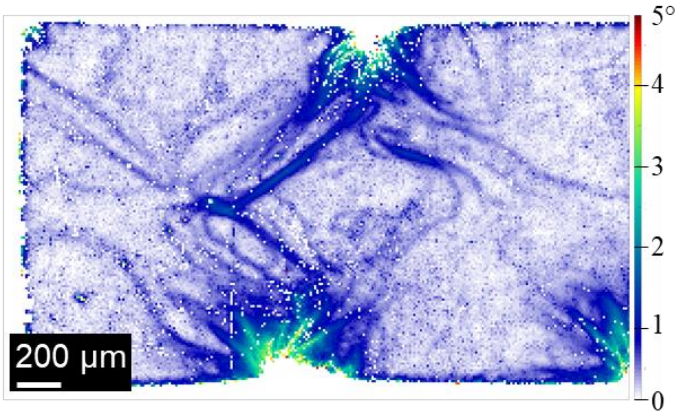

Figure 5.44: LAM maps of the cross-section of specimen 10-64 QS showing complex bands with a misorientation angle of 1–2° generated by the indents left by the fixture of the tensile machine.

The linear increase in hardness between normalized positions of 0.2 and 1 for the quasi-static specimen is related to the increase in GND density in the gage length of the broken specimen. The lowest hardness of ~1.52 GPa is similar to the values measured in the dynamic specimens and is defined as the hardness of the cross-section of an undeformed 8-176 specimen. The increase in hardness (up to ~1.94 GPa) between the shoulder of the tensile specimen, i.e. the beginning of the gage length (normalized position of 0.2), and the gripping end of the specimen (normalized position of 0) is caused by an interaction between the dislocations generated by the tip of the indenter and the complex dislocation networks left by the indents of the grip of the tensile machine. Figure 5.44 clearly shows that the GND density is high below the indents left by the grip of the tensile machine and a complex residual strain field with bands of 1–2° misorientation angles through the whole thickness of the specimen. The motion of the dislocations generated by the nano indenter is then likely impeded by the pre-existing dislocations and this explains the higher hardness measured in the grip region of specimen 8-176 QS. While the LAM map in Figure 5.44 is not for specimen 8-176 QS, but for specimen 10-64 QS, a similar result is expected for all tensile specimens deformed at low strain rate since the same equipment (thus the same fixtures) and methodology was used. Since the small specimens deformed at high strain rate were not

clamped in the split Hopkinson bars by a fixture applying a load on the top and bottom faces of the specimens, the grip region of those specimens is still likely undeformed, as confirmed with the low hardness measured in specimen 8-176 D.

5.4.4. Specimen 7 QS vs D – Low vs High Strain Rate Test

Compression specimens from grain 7 deformed at a quasi-static strain of $4.4x10^{-3}$ s^{-1} and at a high strain rate of ~4 000 s^{-1} were also analyzed with nano indentation measurements. The IPF orientation map along the indentation direction of the low strain rate specimen showed a similar crystal orientation for the majority of the cross-section of the specimen (Figure 5.45a). The EBSD measurements on the high strain rate specimen showed very different crystal orientations with two large diagonal bands spanning between opposite corners of the specimens and intersecting above the middle of the height of the specimen (Figure 5.45b). The LAM map of the quasi-static specimen shows a band of higher misorientation angle of up to ~3.5° across the width of the specimens. A wider band with a higher misorientation angle of up to ~4.25° located below the highest bands with distinct crystal orientations is visible in the LAM map of the high strain rate specimen.

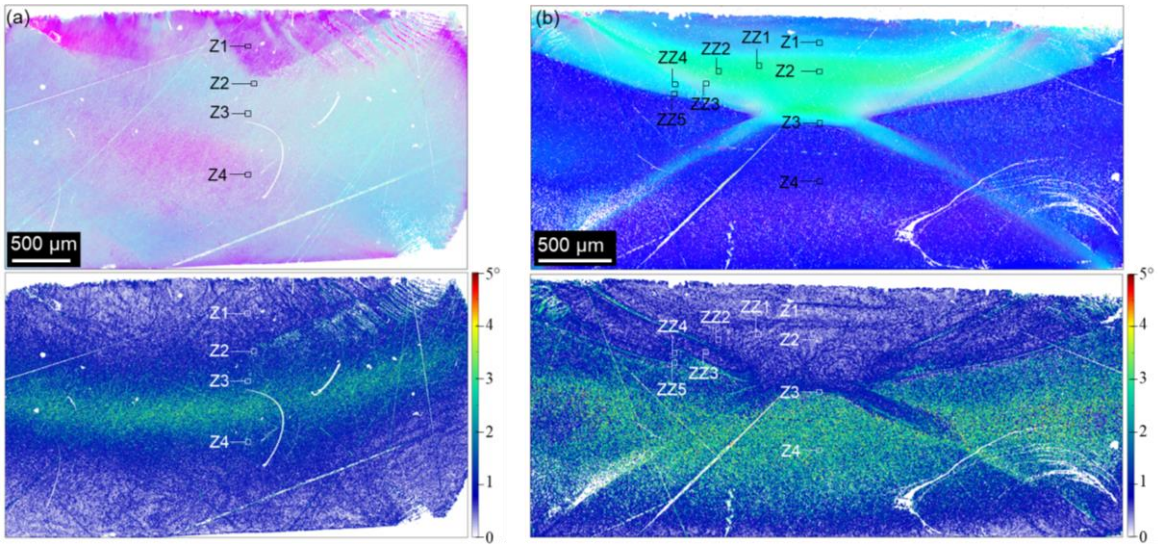

Figure 5.45: (top) IPF orientation maps along the indentation direction and (bottom) LAM map of compression specimens from grain 7 deformed at strain rates of (a) $4.4x10^{-3}$ s^{-1} and (b) ~4 000 s^{-1}.

The elastic modulus and indentation hardness of the specimens at different vertical positions, identified by the Z1 to Z5 markers in Figure 5.45, were measured and the results are compared in Figure 5.46. Similar elastic moduli were measured for both strain rates at most positions in the specimens. The distribution is much higher for the dynamic specimen and likely caused by the multiple different crystal orientations shown in the IPF orientation map.

The indentation hardness is the closest near the top surface of the specimen, i.e. at Y = 0 mm, which is linked to a zone with little to no deformation at the center of the specimen due

to high friction forces between the specimen and the anvil and split Hopkinson bars. This region is referred to as the dead metal zone [99]. However, like for tensile specimen 8-176, the hardness is consistently lower in the dynamic specimen. Since the GND density is higher in the dynamic specimen for zones Z3 and Z4, visible by comparison of the LAM maps in Figure 5.45 and caused by a higher final strain at the end of the high strain rate test, a higher hardness was expected for the dynamic specimen. As suggested for the tensile specimen, this difference in hardness is then most likely related to the different dislocation substructures formed during the compression test at different strain rates. Based on Edington's study [155] on the effect of strain rate on the dislocation substructure of niobium specimens deformed in compression, dislocation cell walls in the specimen deformed at a low strain rate are expected to act as more effective hardeners than the homogeneously distributed dislocation dipoles in the specimen deformed at a high strain rate.

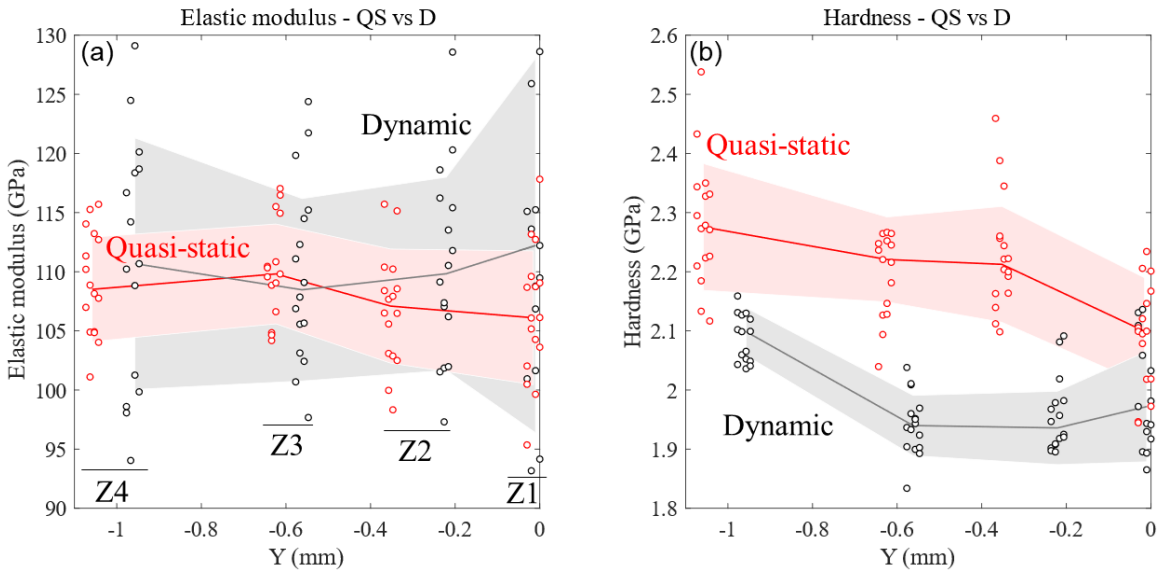

Figure 5.46: (a) Elastic modulus and (b) hardness as function of the vertical position in compression specimen 7 deformed at strain rates of (QS) 4.4×10^{-3} s^{-1} and (D) ~4 000 s^{-1}, with respect to region Z1. The black and red lines are the median in each region and the light shaded areas are the standard deviation.

The change in elastic modulus and hardness across the top left shear band of the dynamic specimen was also studied. Sixteen indents, 4x4 arrays of indents, were taken at each ZZ1 to ZZ5 regions in Figure 5.45b and the corresponding scatter plots are presented in Figure 5.47. The highest hardness was measured at ZZ5, which is in agreement with the high misorientation angle of that region in the LAM map of Figure 5.45b. No trends were measured for the elastic modulus as the median of each region is within the standard deviations of the other regions. A higher modulus was expected for regions ZZ1 to ZZ3 since the crystal orientation along the indentation direction is closer to the [101] direction while zones ZZ4 and ZZ5 are closer to the [111] direction.

5.4.5. Specimens 4 D vs 7 D – Different Crystal Orientations

To measure the effect of the crystal orientation and the effect of strain rate on hardness and elastic modulus, the compression specimen of grain 4 deformed at a strain rate of ~4 000 s^{-1} was analyzed with nano indentation and the results are compared with those of specimens from grain 7. The choice of specimen was based on the contrasting hardening behavior measured in the stress–strain curves of specimens from grains 4 and 7 (Figure 4.15). Recall that the specimens cut in grain 4 had the lowest hardening with the longest stage I hardening and the specimens from grain 7 had the highest hardening with no stage I, for orientations rotating toward the terminal stable [111] orientation.

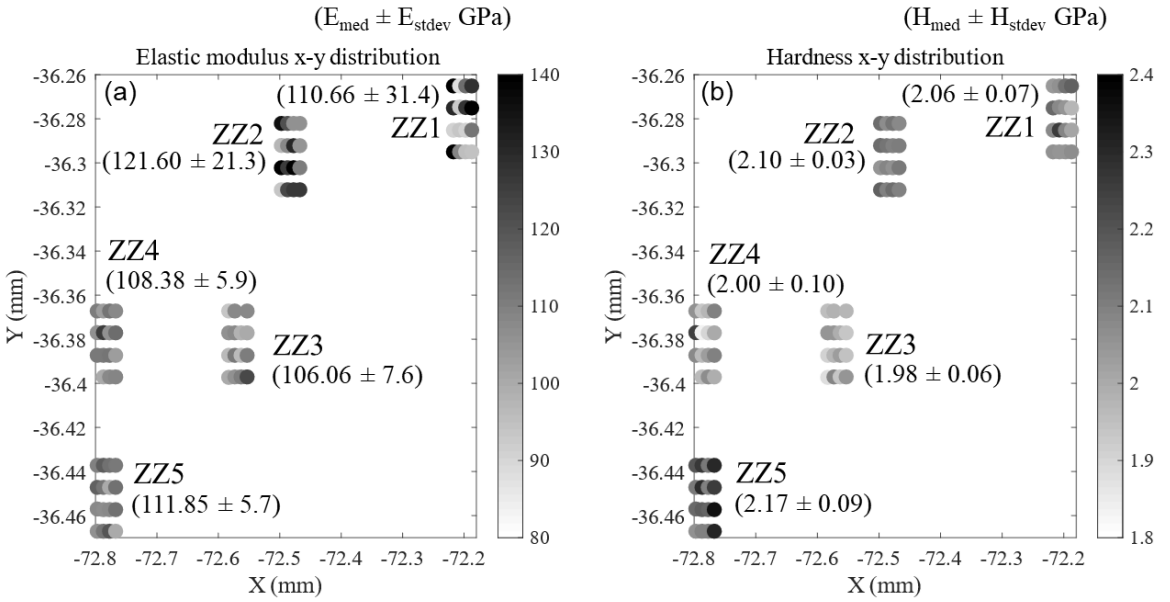

Figure 5.47: Scatter plots of the (a) elastic modulus and (b) hardness across a shear band of compression specimen 7 deformed at a strain rate of ~4 000 s^{-1}.

Measurements were taken at three vertical positions across the center of the cross-section of the compression specimen, as shown with the Z1 to Z3 markers in Figure 5.48. The values of the elastic modulus and hardness values measured in those zones are compared to grain 7 in Figure 5.49. The elastic modulus is similar for the two specimens with different orientations and hardening behaviors and a narrower distribution was measured in grain 4. According to Figure 5.40b, the elastic modulus of the grain 4 specimen should be higher than for grain 7 since the indent is performed close to the [110] and [111] crystal direction, respectively. Similar than for the bands of different orientations in specimen 5-34, this is probably a consequence measuring the elastic modulus of a heavily deformed lattice compared to an annealed crystal and to the indentation modulus being affected by microstructural effects [238].

The indentation hardness of the dynamic compression specimen from grain 4 is highest in the middle of the specimen, i.e. at Z2. This is directly related to the higher misorientation in that zone, as shown in the LAM map in Figure 5.48b. The indentation hardness of the grain 4 specimen is higher than the grain 7 specimen deformed at a similar strain rate in the order of 10^3 s^{-1}, for regions with a similar misorientation angle. Recall from Figure 4.15 that specimens from grains 4 and 7 had very different hardening behaviors, which likely resulted in different dislocation substructures. Note that the indentation hardness of specimens 4 D remains lower than for the grain 7 specimen deformed at a low strain rate in the order of 10^{-3} s^{-1}.

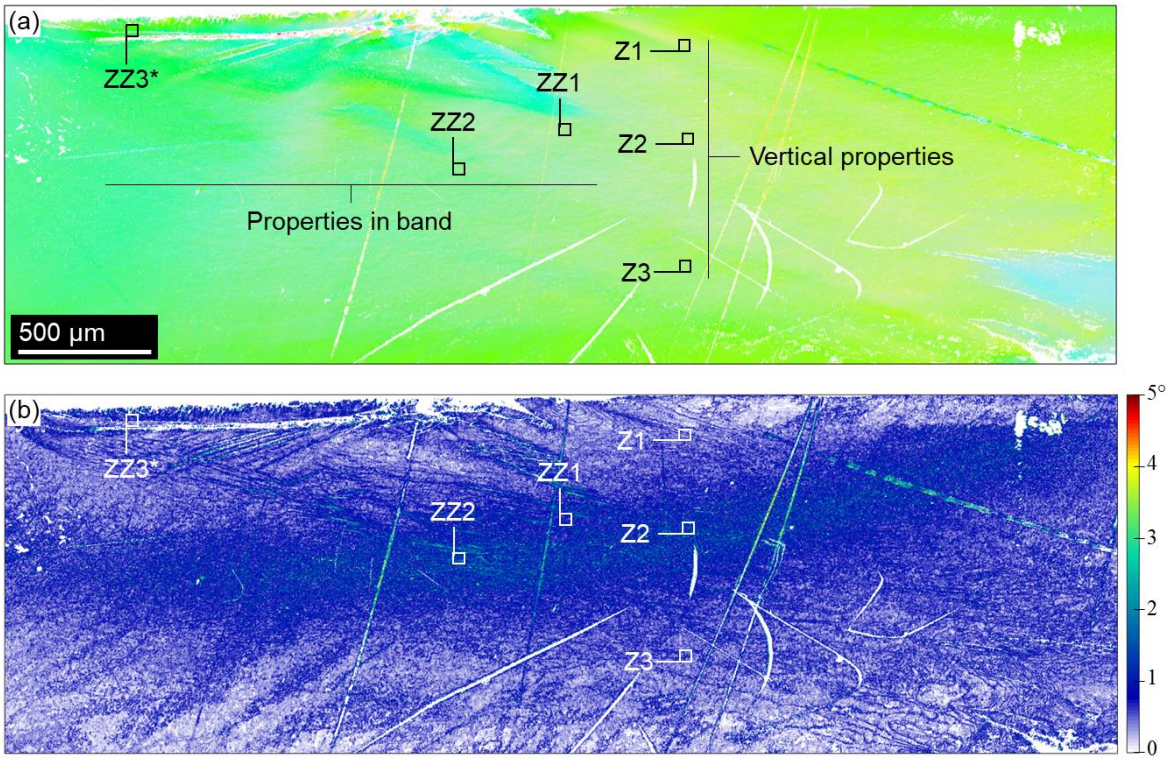

Figure 5.48: (a) IPF orientation map normal to the cross-section of the specimen (along the indentation direction) and (b) LAM map of a compression specimen from grain 4 deformed at ~4 000 s^{-1}. *The position of the ZZ3 zone is approximate.

The ZZ1 to ZZ3 regions analyzed in the split Hopkinson compression specimen from grain 4 had similar indentation elastic modulus and hardness. The average modulus and hardness measured are of 111.00 ± 3.67 GPa and 2.08 ± 0.06 GPa, respectively. Those values are also similar to the average elastic modulus and hardness of 109.59 ± 3.36 GPa and 2.10 ± 0.08 GPa of the Z1 to Z3 regions.

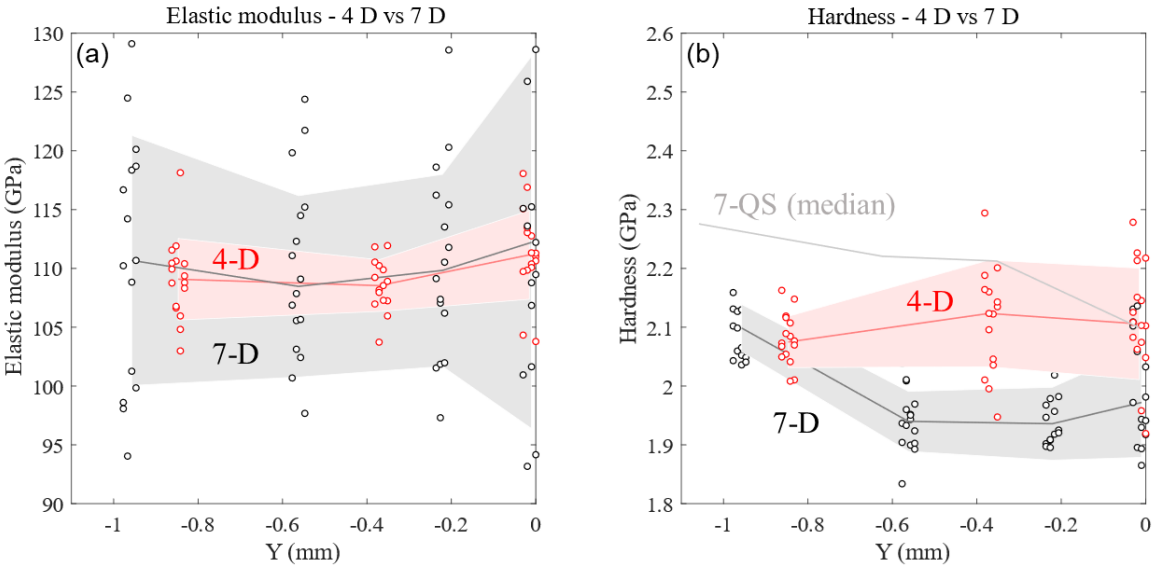

Figure 5.49: (a) Elastic modulus and (b) hardness as function of the vertical position in compression specimens 4 and 7 deformed at strain rates of (D) ~4 000 s^{-1} and (QS) $4.4x10^{-3}$, with respect to region Z1 (Y = 0). For specimens 4 D and 7 D, the black and red lines are the median in each region and the light shaded areas are the standard deviation. The grey line of specimen 7-QS in (b) is the median hardness.

5.5. Conclusions on the Microstructure of Niobium Single Crystals

In conclusion, similar fracture surfaces were observed in specimens deformed at quasi-static and dynamic strain rates, but no orientation-based trends were observed. EBSD orientation measurements of the cross-section of tensile specimens showed rotated crystals from the undeformed grip region to the fracture surface for most crystal orientations. Shear bands separating regions with different crystal orientations were observed in specimens deformed at a low strain rate and with an initial crystal orientation with similar Schmid factors for two slip systems of the {112} family. Despite the differences in IPF orientation maps and LAM maps, specimens deformed at low and high strain rates consistently rotated toward the [101] stable end orientation.

In compression, a more complex IPF orientation map was measured in specimens deformed at high strain rate. Different deformed specimen morphologies were observed for specimens with different orientations, which suggested that specimens from grain 4 with a long stage I hardening in their stress–strain curves mostly deformed by glide on the primary slip system.

TEM measurements on tensile specimens deformed at low and high strain rates revealed different dislocation substructures in the shear bands observed with EBSD and in rotated region of the crystals. More importantly, a homogeneously distributed high dislocation dipoles density was observed at high strain rate compared with long dislocation segments and dislocation cells at low strain rate.

Finally, a lower hardness was measured with nanoindentations in the cross-section of tensile and compression specimens deformed at high strain rates compared with specimens with the same initial crystal orientation deformed at low strain rates. This result was measured for different crystal orientations, which suggests that this result is caused by the different dislocation substructures observed with TEM. Nanoindentation measurements were also capable of detecting the location of the shear bands observed with EBSD and measure different elastic moduli for different crystal orientations.

PART II

POLYCRYSTALLINE NIOBIUM AND OFE COPPER

Chapter 6 Background

6.1. Forming Limit Diagram

A forming limit diagram (FLD) is a useful tool to represent the formability of metal sheets. The major and minor strains, ε_1 and ε_1, are measured at the onset of localized necking for different loading conditions, such as uniaxial tension, plane strain, and biaxial tension. Figure 6.1 schematically shows a forming limit diagram with the main modes of deformations and where they lay on the major strain as function of minor strain plot. During sheet–metal forming operations, multiple deformation modes are often present in the same part. The FLD is an engineering tool that is often used in finite element software packages to determine if a part will fail or if defects are expected during a forming operation. All points above the forming limit curve (FLC) are expected to lead to necking, the formability limit. Wrinkling of the sheet is expected for points below the uniaxial tension strain path.

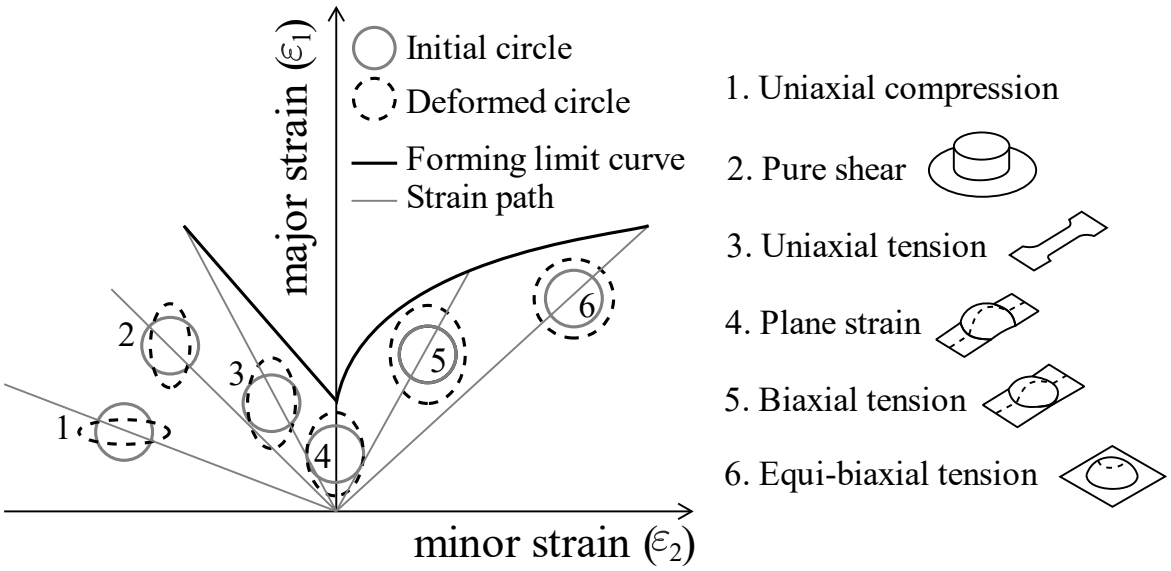

Figure 6.1: Schematic of a forming limit diagram with the main linear strain paths and states of strain with corresponding specimen geometries. Redrawn from [239].

Sheet formability was first extensively studied by Keeler [240]. The ISO 12004-2:2008 [241] and ASTM E2218-15 [242] standards are now available to experimentally obtain the FLD of a material. The Nakajima (out-of-plane) and Marciniak (in-plane) [243], [244] tests have been widely used to obtain the FLD of materials at different temperatures and strain rates. With both techniques, blanks with different geometries are used to obtain the different mode of deformation shown in Figure 6.1.

6.1.1. Experimental Determination of the FLD: Nakajima and Marciniak Tests

Figure 6.2a shows the schematic of the cross-section of a hemispherical punch used in a Nakajima test with recommended dimensions from the ISO 12004-2:2008 standard [241]. In-situ measurements of strain are not trivial in this test since the sheet is deformed out-of-plane. Stereo-correlation with two cameras is required for 3D digital image correlation analyses. Also, the ISO 12004-2:2008 standard states that the blank should fail at a maximum distance from the top of the hemispherical punch of 15% of the punch diameter. Failure may occur at greater distances from the top of the punch due to friction forces between the punch and the blank. The standard recommends two different combinations of oil/grease and polymer films to reduce friction in the cases of thin sheets and soft materials and thick sheets and stiff materials. Since annealed OFE copper and high-purity niobium, the two materials studied during this thesis, are ductile and the sheets are 1 mm thick, only the approach for ductile materials is summarized: oil or grease should be applied on the punch and on the blank. A thin film, in the order of 50 μm, of polyethylene (PE) or polytetrafluoroethylene (PTFE), commercially known as Teflon^{TM}, should then be placed between the punch and the blank. Finally, the effect of sheet curvature and punch radius was also found to influence FLC obtained with Nakajima tests [245]–[247].

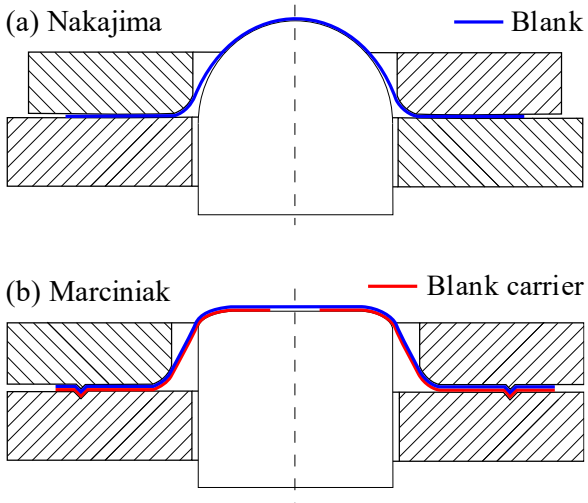

Figure 6.2: (a) Schematic of the cross-section of a hemispherical punch for a Nakajima test and (b) schematic of the cross-section of a flat-bottomed punch for a Marciniak test. Redrawn from [241].

Figure 6.2b shows the schematic of the cross-section of a flat-bottomed punch used in a Marciniak test with dimensions from the ISO 12004-2:2008 standard [241]. As shown in this figure, two sheets are required in the Marciniak test: a blank and a blank carrier. The role of the blank carrier is to ensure that a uniform deformation and ultimately necking occurs above the flat region of the punch and not at the radius of the punch. In-situ measurements are more easily done in Marciniak tests since the blank is deformed in-plane. Only one camera is required and 2D DIC is used. However, the blank carrier design is

complicated since the blank must fail before the blank carrier. If the blank carrier fails first, a stress concentration over the crack during crack opening leads to near plane strain deformation of the blank, resulting in a bi-linear strain path that underestimates the strain at necking [248]. A sheet–metal made of a more ductile material or the same material is then generally used and friction forces between the blank and the blank carrier is maximized to avoid relative motion between the sheets. More details about both techniques are available in the ISO standard [241].

6.1.2. Effect of Pre-Straining and Strain Path

With both experimental techniques, linear strain paths must be obtained from the beginning of the test to the onset of necking. However, non-linear strain paths are often found during sheet–metal forming of complex parts with multiple forming steps. Graf and Hosford [249] studied the effect of changes in strain path after pre-straining on the forming limit curve of Al 2008-T4 sheets (with mean strain hardening rate (n_m), strain rate sensitivity (m_m), and *r*-value (r_m) of n_m = 0.284, m_m < 0, r_m = 0.583). Different pre-straining levels for uniaxial, biaxial, and plane strain tension were induced parallel and perpendicular to the rolling direction of the sheets. They observed (1) an increase of the FLC for $\varepsilon_2 > 0$ for sheets that were pre-strain in uniaxial tension, (2) a decrease in formability for the entire FLC for biaxially pre-strained sheets (see Figure 6.3a and b), and (3) an increase of the overall FLC for sheets that were pre-strained in plane strain [249]. The location of the lowest point of the FLC, hereafter *FLC₀*, also changed for sheets that were pre-strained in uniaxial and biaxial tension. A translation of the FLC_0 and the entire FLC to negative values of minor strain was measured for uniaxial pre-strain and a translation to positive values of minor strain was observed for biaxial tension pre-strain.

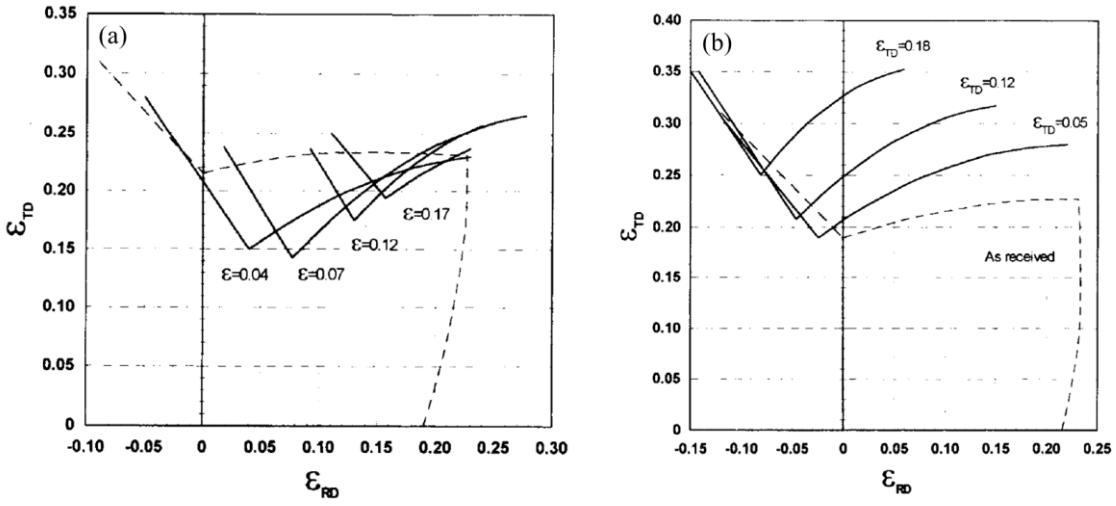

Figure 6.3: Forming limit diagrams of Al 2008-T4 for different levels of (a) equi-biaxial and (b) uniaxial pre-straining. The strain values in the figure indicate the pre-straining amount and the dotted-lines are the as-received FLDs. From Graf and Hosford [249].

6.1.3. Effect of Sheet Thickness

The forming limit diagram of a material is not an intrinsic property. Parameters such as the sheet thickness may influence formability. An increase in formability is generally expected for thicker sheets [250], but the opposite has also been measured for few aluminum and steel alloys [251]. Since forming limit diagrams have been developed for *thin sheets* with thicknesses between 0.2 and ~4 mm [251], the thickness of the sheet used to obtain a FLD must be specified and care must be taken when implementing it in FE models to predict the formability of a component.

6.1.4. Effect of Strain Rate Sensitivity and Strain Rate

An increase in formability has been observed for materials with a high positive strain rate sensitivity exponent m. A local increase of strain rate in the neck results in hardening. Tests and models of forming limit diagrams at quasi-static strain rates for materials with different strain rate sensitivity exponents m showed higher formability for increasing values of m [98], [204], [252], [253].

The effect of strain rate on the FLC can be important for materials with viscoplastic mechanical properties. An increase in ductility has been reported for stainless steel [254], interstitial-free iron [255], copper [49], [256], high strength steel [257], titanium alloys [258], aluminum alloys (AA) EN AW-7075 [233], AA 1050a-H24, AA EN AW-5083-H111 [259], and Al 6061-T4 and 5754 [260], magnesium alloys AZ80 [233], AZ31 [259], [261], and ZEK 100 [261]. However, a reduction in ductility in uniaxial tensile tests at room temperature for tantalum [262], a refractory metal, and an increase followed by a reduction of ductility for titanium alloys [261] were measured.

Three main factors are contributing to the increase in formability often measured at high strain rates. First, the die–sheet interaction in high-speed sheet forming processes, e.g. electro-hydraulic forming leads to enhanced formability due to through-thickness compressive stresses [263] or bending–unbending of the sheet upon impact [51] that both result in a decrease in damage development. Since the through-thickness stress component is non-zero during impact, a forming limit diagram obtained from tests with a die–sheet interaction is not valid [251]. Second, a stabilization of the neck due to inertial effects has also been reported [48], [50], [259]. Third, materials with a high strain rate hardening exponent experience local hardening in the neck due to a locally higher strain rate. This hardening behavior delays necking and increases formability. Finally, different mechanisms that delay sheet failure, such as void collapse [264], are sometimes observed at high strain rates.

6.1.5. Literature for High-Purity Copper and Niobium Polycrystalline Sheets

The forming limit diagram of annealed oxygen-free electronic copper sheets was not found in the literature. However, the FLD of other high-purity copper grade sheets, such as oxygen-free high conductivity (OFHC) copper, was experimentally measured by Melander [265] and Gerdooei and Dariani [256]. The study of Melander [265] focused on the development of the geometrical defect-based numerical model discussed in the previous sub-section that accurately predicted their experimentally measured FLD. Stachomicz [266] also measured the FLD of copper sheets (grade and purity not specified) with different annealing heat treatments using Marciniak (in-plane) tests and identified the initial and evolving geometric defect in a modified M–K model based on surface roughness measurements. The experimental results of Melander [265] and Gerdooei and Dariani [256] will be compared to the FLD of OFE copper measured in Chapter 8 to assess the validity of the Marciniak testing setup and the data analysis methods.

For high-purity niobium, only one forming limit diagram was found in literature. Daumas and Collard [1] performed modified Nakajima tests on 1 and 2 mm thick sheets. The setup holding the blank was filled with oil above the blank, instead of ambient air, and was lowered on the punch using a mechanical press. The forming limit curves only span for minimum and maximum minor strains of about −0.1 and 0.1, respectively. The low maximum minor strain of 0.1 was likely caused by important friction forces between the die and the sheet and this could be optimized to increase the sheet formability. The experimental results of Daumas and Collard [1] will be compared to the FLD obtained in this study in Chapter 8.

6.2. Electron Beam Welding

Electron beam welding is used in different applications because of its power efficiency and high welding speed [267]. This versatile welding technique is capable of welding metals with thicknesses ranging from 0.025 to 300 mm for the automotive, aerospace, electronics, energy, and many other industries [267]. The main advantages of this technique for SRF applications are: (1) the ability to weld refractory metals, like niobium, (2) a low impurity content due to operation in vacuum, (3) production of deep and narrow welds that minimize workpiece deformation, essential to respect the high tolerances, and (4) no filler is required.

The high welding speed produces narrow welds resulting in small workpiece deformation and a narrow heat affected zone compared with other welding techniques, see Figure 6.4 [267]. An electron beam welding machine is similar to a scanning electron microscope, but with a much more powerful beam. Electrons are emitted from a source and the beam is focused and stirred on the workpiece using magnetic lenses. For the manufacturing of SRF

cavities in a conventional manner, as shown in Figure 1.6, two half-cells are welded together by melting the copper or niobium of both half-cells with the energy of the electron beam.

Welding parameters for niobium sheets have been reviewed by Demyanov et al. [268] for sheet thicknesses of about 1.5 to 3.0 mm. A linear increase in weld energy per unit length was found, see Fig. 1 of [268]. However, other studies (unpublished) performed at CERN used a much lower energy, compared with the expected linear trend, and a full weld penetration was observed. A similar low energy was used during this study and the microstructure and mechanical properties of the welded OFE copper and niobium sheets are presented in Chapter 9.

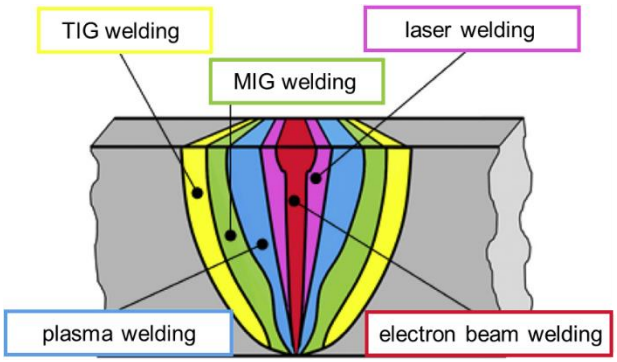

Figure 6.4: Geometry of a butt joint made from different welding techniques showing the narrower HAZ for electron beam welding [267].

6.2.1. Mechanical Properties of EB Welded Copper and Niobium Sheets

The mechanical properties of EB welded high-purity niobium specimens have been measured in tension at CERN (unpublished) and at Michigan State University by Jiang et al. [269] at quasi-static nominal strain rates of ~$3x10^{-4}$ s^{-1}, but never at intermediate or high strain rates. Jiang et al. [269] reported a yield stress similar to unwelded specimens and a lower strain hardening in the fusion region.

To the best of the author's knowledge, the mechanical properties of EB welded OFE copper and high-purity niobium at strain rates greater than the quasi-static regime, i.e. in the 10^{-4} to 10^{-3} s^{-1} range, are not documented in the literature. In this study, the yield and tensile strengths and ductility of both materials are investigated in tension at strain rates between 10^{-3} s^{-1} and approximately 10^{3} s^{-1}. The yield stress measured in tension is compared with compression specimens deformed at similar strain rates and with unwelded specimens tested at similar strain rates from this study for OFE copper and from Peroni and Scapin [182] for niobium. Peroni and Scapin [182] reported an important increase in yield stress for increasing strain rates and a transition from hardening to softening. The objectives of this study are to quantify and understand the effect of strain rate on the mechanical properties of

EB welded OFE copper and high-purity niobium for the fabrication of seamless SRF cavities from a bent and EB welded tube using a high-speed sheet forming technique.

6.3. Conclusions and Research Objectives

In conclusion, the formability of high-purity polycrystalline niobium and OFE copper sheets will be experimentally measured by performing Marciniak (in-plane) tests at a quasi-static strain rate. The strain paths will be measured to ensure linearity from the start of the test until localized necking is observed or to discuss the effect of non-linear strain paths on the FLD.

The FLDs measured in this study will provide a useful prediction tool for most traditional low strain rate forming techniques, such as deep-drawing and hydroforming, for SRF cavity manufacturing. The effect of strain rate on the forming limit diagrams will not be studied due to logistic constraints, e.g. setup development for high strain rate tests and material cost.

The production of high-purity niobium tubes, discussed in section 1.4. is not trivial and SRF cavities manufactured with electro-hydraulic forming showed promising performances, discussed in section 1.3. Therefore, the possibility of manufacturing tubes by bending and electron beam welding sheets and using EHF to form seamless SRF cavities is of interest. The study on the effect of strain rate of up to 10^3 s^{-1} on electron beam welded high-purity polycrystalline niobium and OFE copper sheets, presented in Chapter 9, will provide important data on the mechanical properties and the ductility of those materials to predict forming of EB welded components with EHF. A gap in the literature will be filled for EB welded high-purity niobium and OFE copper sheets deformed at strain rates greater than 10^{-3} s^{-1}. The potentially heterogeneous deformation in the fusion and heat affected zones of the weld will be analyzed with digital image correlation and links with the measured mechanical properties and ductility will be made.

Chapter 7 Materials and Methods

Experiments and microstructure analyses were performed at different institutes on polycrystalline niobium and oxygen-free electronic copper. In order to ensure repeatability between measurements and analyses performed in different laboratories, it is paramount to develop and respect detailed experimental procedures. This chapter describes the thermomechanical histories of the copper specimens. The experimental procedures that were used for the different mechanical tests (uniaxial tensile and compression tests at strain rates between 10^{-4} s^{-1} and 10^{3} s^{-1} and Marciniak tests for forming limit diagrams) and data analysis are presented.

7.1. Materials

7.1.1. Oxygen-Free Electronic Copper

The tensile and compression mechanical properties of OFE copper (ASTM C10100), a standardized copper with high purity and electrical conductivity, were studied. According to the ASTM standard B170-99 [270], OFE copper has a minimum copper content of 99.99% and chemical impurities should follow the content presented in the standard. This specific copper was selected since it is the substrate material used at CERN in niobium coated superconducting radiofrequency cavities.

Annealed specimens were heat treated at 600°C for 2 hours in vacuum before testing. Hard specimens were tested in the as-received condition (results are presented in Appendix E). More details about the different temper designations for copper are available in ASTM standard B152-06 [271]. The annealed and hard specimens supplied by CERN had average Vickers hardness of 52.6 and 89.0 HV0.2, respectively. The hard specimens supplied by Imperial College London for compression tests were slightly harder, with an average hardness of 100.0 HV. Specimens with different thermomechanical histories were selected to study the effect on the mechanical response at different strain rates.

The annealed and hard OFE copper supplied by CERN was in 1, 2, and 4 mm thick sheets. Specimens from the sheets were extracted using waterjet cutting for tensile, compression, and Marciniak tests. The hard cylindrical compression specimens that were supplied by the Imperial College London were machined from a rod using a lathe.

7.1.2. Polycrystalline Niobium Sheets

High-purity (RRR > 300) polycrystalline niobium sheets supplied by Ningxia were used for Marciniak and tensile tests to measure the forming limit of niobium and for EB welded

specimens deformed in tension and compression. As mentioned in section 1.2.2., the high-purity sheets were manufactured with multiple rolling and heat treatment steps after the production of a high purity ingot using electron beam melting [21]–[23]. The final sheet manufacturing steps are an annealing heat treatment and levelling of the sheet with rollers to ensure that a thickness tolerance of ± 0.1 mm was respected. The sheets used to measure the forming limit diagram had a thickness of 1 mm and the EB welded sheets had a thickness of 4 mm.

7.1.3. Electron Beam Welded OFE Copper and Niobium Specimens

OFE copper and high-purity polycrystalline niobium sheets were electron beam welded to study the effect of strain rate on the mechanical properties of welded specimens. Sheets with an initial thickness of 4 mm were electron beam welded at CERN with one pass on each side of the sheet. The following EB welding parameters were used for both materials: accelerating voltage of 100 kV, current of 22–23 mA, workpiece distance of 400 mm, and beam speed of 600 mm/min. Compared with other reported EB welding parameters for high-purity niobium [33], [59], [268], [269], [272], [273], the welding energy-to-sheet thickness ratio is lower. However, a full penetration was observed at CERN in previous internal studies with similar welding energies. The top and bottom surfaces of the welded sheets were milled to remove surface defects produced during welding and obtain flat and parallel surfaces. Tensile and compression specimens were cut using wire EDM. The weld was located at the center of the gage section and perpendicular to the tensile direction, as specified in the ISO 4136:2012 standard [274]. For compression specimens, the weld was located at the center of the specimens. OFE copper specimens were annealed at 600°C for 2 hours in vacuum after EB welding.

7.2. Specimen Geometries and Surface Preparation for Digital Image Correlation

7.2.1. Tensile and Compression Tests

Four different tensile sample geometries with rectangular cross-sections were used: (a) short dog bones with or without holes in the fixture for intermediate strain rate tests on OFE copper, (b) standardized large dog bones for quasi-static strain rate tests on OFE copper, EB welded specimens, and sheets used to obtain the forming limit diagram of polycrystalline niobium, and (c) small customized tensile specimens for EB welded specimens deformed at high strain rate with split Hopkinson bars. Figure 7.1 shows the three different specimens with labels for their main dimensions. The applied strain rates, materials and the length of the main dimensions for each geometry are listed in Table 7.1.

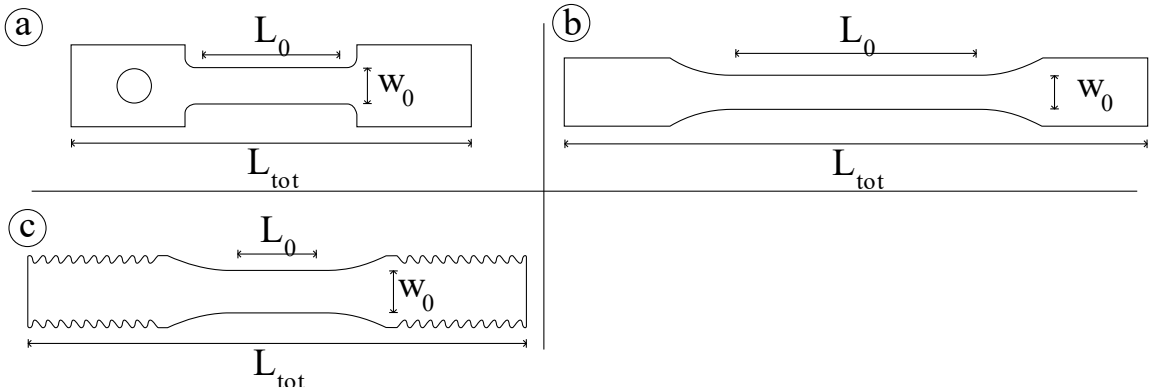

Figure 7.1: Tensile specimen geometry and main dimensions for all tests performed in Part II of this thesis. Specimen (a) was used in two different configurations, with or without the hole shown on the left side.

The geometry of the largest specimen (Figure 7.1b) was based on the recommendations in the ASTM E8 standard [196] and the geometry in Figure 7.1a is a reduced version of the subsize specimen in the same standard. Finally, the geometry in Figure 7.1c was developed at the JRC during this study. From finite element simulations of tensile tests with this geometry, it was found that the stress state is not uniaxial. An optimal initial gage length of 5 mm, equal to the length of the straight section L_0, was found by calculating the stress–strain curve using the output force and displacement of the specimen from the simulation for different gage lengths and compared with the expected response with a standardized geometry (Figure 7.1b). Digital image correlation was also used with this specimen geometry to measure the strain in the gage section, independently of the stiffness of the tensile machine. Compression tests were performed on cylindrical specimens and the copper (Appendix E) and EB welded specimens (Chapter 9) were 4 mm thick and had a diameter of 8 mm.

Table 7.1: Characteristics of the different tensile specimens used in Part II of this study.

	Strain rate (s^{-1})	**Material**	**L_0 (mm)**	**L_{tot} (mm)**	**w_0 (mm)**
a	1 to 100	Cu	13	35	3.2
b	10^{-4} to 10^{-2}	Cu	70	170	10
c	2.0×10^{-3} to 1 600	Nb, Cu (EB welded)	5	35	3

7.2.2. Forming Limit Diagram Blank and Blank Carrier

Rectangular blanks with a constant length of 200 mm and varying widths were used to obtain the forming limit curves (FLC) of annealed OFE copper and high-purity polycrystalline niobium, as specified in the ISO 12004-2:2008 standard [241]. Other studies, often using the Nakajima test instead of the Marciniak test, like in this study, use circular blanks with a central section with parallel edges and different widths. The rectangular geometry was used

due to previous experience with other materials at the Laboratoire d'étude des microstructures et de mécanique des matériaux (LEM3), where the tests were performed.

Seven different specimen geometries were used to obtain seven different points of the FLC of annealed OFE copper. Rectangular blanks with widths of 80, 100, 120, 140, 160, and 180 mm were used. The seventh point was obtained using a circular blank with a diameter of 200 mm. All sheets used were 1 mm thick and the material was annealed in vacuum at 600°C for 2 hours. Since Marciniak tests (described in section 6.1.) were performed, a blank carrier was used. A sheet of the same material and the same dimensions and thickness served as blank carrier and was placed between the blank and the punch for OFE copper. Two types of blank carriers were used to initiate localized necking on the flat surface of the punch. Figure 7.2 shows a schematic of the two different blank/blank carrier assemblies. The configuration with two half-sheets (Figure 7.2a) was used for rectangular specimens with a width of 80, 100, and 120 mm. The configuration with a hole is used for rectangular specimens with a width of 140, 150, 160, and 180 mm and for the circular blank with a diameter of 200 mm. Different hole diameters were used, from 5 to 30 mm, and the effect of the hole diameter on the strain paths and the FLC are presented in section 8.2. For consistency throughout the thesis, the blank carrier with two half-sheets (Figure 7.2a) is hereafter called the *split blank carrier* and the one with a hole (Figure 7.2b) is called the *pierced blank carrier*.

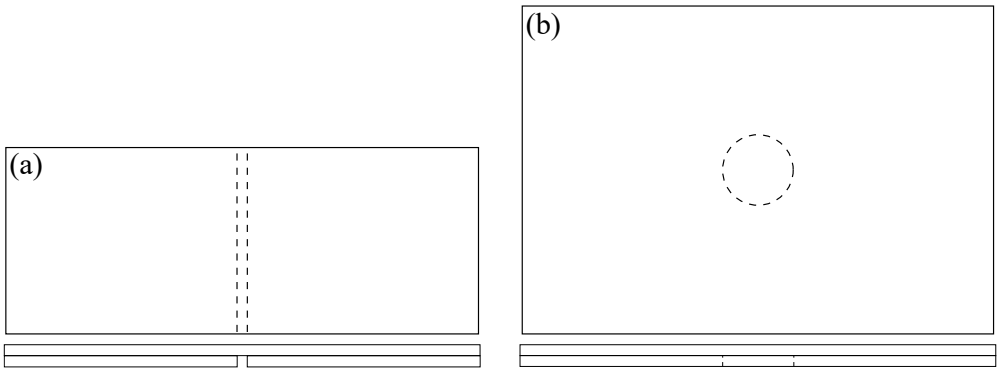

Figure 7.2: Schematic of the different blank/blank carrier assemblies with a blank carrier with (a) two half-sheets (*split blank carrier*) or (b) a central hole with a diameter of 5 to 30 mm (*pierced blank carrier*).

The FLC of small grain high-purity niobium sheets was obtained using six rectangular blank geometries with a constant length of 200 mm and widths of 80, 100, 120, 140, 150, and 180 mm. The blank carriers were made of annealed OFE copper due to similar ductility in uniaxial tension with polycrystalline high-purity niobium and because OFE copper is less expensive than niobium. Again, split blank carriers were used for rectangular sheets with a width of 80, 100, and 120 mm and pierced blank carriers with a hole diameter of 30 mm for the wider rectangular sheets. The blank carriers and blanks had a sheet thickness of 1 mm.

The left most point of the FLC of niobium was obtained with a tensile test performed on a specimen with the geometry presented in Figure 7.1b and analyzed with DIC for accurate measurements of the major and minor strains at the onset of localized necking. A tensile specimen with a large gage section, shown in Figure 7.3, was also used to obtain the strain at localized necking for a strain path near plane strain. The uniaxial and plane strain tensile specimens were all 1 mm thick and cut with water jet cutting at angles of 0°, 45°, and 90° between the tensile axis and the sheet rolling direction. Figure 7.4 shows the expected location of the point of the FLC for each specimen geometry for the tests performed with niobium sheets. This specimen geometry selection was based on test results obtained with annealed OFE copper sheets.

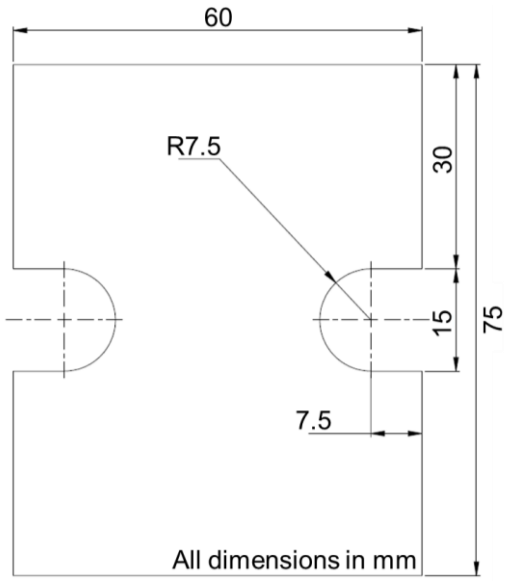

Figure 7.3: Main dimensions of the plane strain tensile specimen. Adapted from [275].

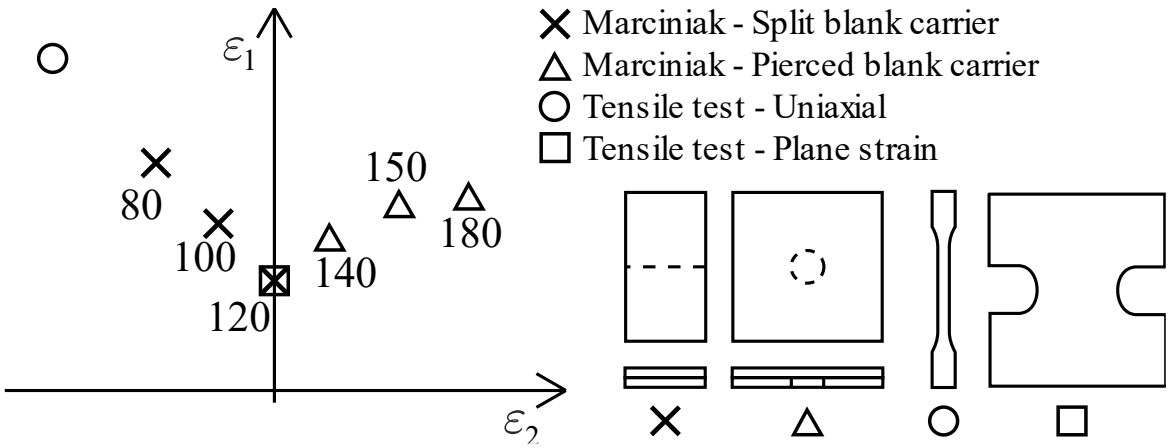

Figure 7.4: Schematic of (bottom-right) the different blank geometries (not to scale) used to obtain the FLC of high-purity niobium and (left) the expected strain state for the different geometries. The values in the FLD correspond to the width, in mm, of the 200 mm long rectangular sheets.

7.2.3. Surface Preparation for Digital Image Correlation

The strain during multiple tensile tests and for all Marciniak specimens was measured with digital image correlation (DIC). In DIC, a grid or stochastic pattern is applied on the surface of the specimen and pictures are acquired with a camera during the test. In this study, a stochastic paint pattern was used on all specimens with DIC measurements. The following steps were followed to generate the pattern. Any deviation from this methodology and the tests that used this technique are specified in section 7.3.

First, the surface of the specimen was cleaned with a solvent, such as ethanol or isopropyl alcohol, to remove oil or dust particle that would hinder the adhesion of the paint on the metallic surface. Second, a thin and uniform matte white paint layer was applied on the section of interest, i.e. the gage section of the tensile specimens and the entire sheet for the forming limit diagram tests. Finally, small and randomly distributed black speckles were sprayed on the white paint to provide tracking features between pictures for the DIC software.

7.3. Methods for Material Characterization

Tensile and compression tests were performed at strain rates of 10^{-4} to 10^{3} s^{-1} in different institutes. Screw-driven (mechanical) and hydraulic systems were used for tests at strain rates lower or equal to about 100 s^{-1}. Tests at higher strain rates were performed with split Hopkinson bar systems. Table 7.2 provides a summary of the different institutes where the tests were performed and the range of strain rate and materials studied. The following acronyms are used in the table for the name of the institutes: ENSTA Bretagne (ENSTA), Imperial College London (ICL), European Commission Joint Research Centre in Ispra (JRC), and Laboratoire d'Étude des Microstructures et de Mécanique des Matériaux in Metz (LEM3); and the following ones for the tested materials: oxygen-free electronics copper (Cu), polycrystalline niobium (Nb), and electron beam welded specimens (EBW). Detailed procedures for the different test rigs and the relevant equations for the data analysis are provided in the following subsections.

Table 7.2: Summary of the different tensile and compression tests performed during this study, grouped per testing system and institutes. (All acronyms are defined in the text.)

System	Institute	Strain rate (s^{-1})	Materials	Tension/Compression
Mechanical	ENSTA	10^{-4} to 1	Cu	T, C
	ICL	10^{-2} to 10^{-1}	Cu	T
	LEM3	10^{-3}	Nb	T

Hydraulic	JRC	10^{-3} to 10	Cu-EBW, Nb-EBW	T, C
Split Hopkinson	ENSTA	10^{3}	Cu	C
	JRC	10^{2} to 10^{3}	Cu-EBW, Nb-EBW	T, C

Finally, in addition to tensile and compression tests, Marciniak tests were performed to obtain the quasi-static forming limit diagrams of annealed OFE copper and high-purity polycrystalline niobium at the LEM3. The method and system used are detailed in this section.

7.3.1. Low Strain Rate Testing Methodologies (10^{-4} to 1 s^{-1})

7.3.1.1. ENSTA Bretagne – Annealed and Hard OFE Copper

Tensile tests at constant crosshead speeds of 1, 10, and 100 mm/min, equivalent to nominal strain rates of $2.38x10^{-4}$ s^{-1}, $2.38x10^{-3}$ s^{-1}, and $2.38x10^{-2}$ s^{-1}, were performed on annealed and hard OFE copper at the ENSTA Bretagne. The screw-driven tensile machines shown in Figure 7.5 (UTS) and in Figure 7.6 (Instron 5969) were used. Specimens cut parallel and perpendicular to the sheet rolling direction were tested to verify if the sheets had anisotropic properties. The strain in the specimens deformed with the former tensile machine was measured with a long travel extensometer. This type of extensometer was required to measure the total displacement of ductile specimens with an initial gage length of 70 mm. The elastic modulus of the annealed copper was not accurately measured during this study since the specimens were preloaded to remove any gap between the specimen and the holder and this unfortunately resulted in a small plastic deformation of the soft annealed specimens. Tests were not redone since this value was measured at CERN on the same material during a previous study. An optical extensometer tracking two white points was used to measure the strain in the gage section of hard OFE copper tensile specimens deformed with the table-top Instron 5969 machine.

Compression tests at constant crosshead speeds of 0.5 mm/min, 5 mm/min, 50 mm/min, and 250 mm/min, equivalent to nominal strain rates of $2.08x10^{-3}$ s^{-1}, $2.08x10^{-2}$ s^{-1}, $2.08x10^{-1}$ s^{-1}, and 1.04 s^{-1}, were also performed with the table-top machine (Figure 7.6). Instead of tracking the distance between two points on the compression samples, the displacement of two white dots located on the compression anvils was measured by the optical extensometer, as shown in Figure 7.6. The proximity of the dots with the specimen and the high rigidity of the anvils ensures that the displacement measurements are independent of the stiffness of the machine and the fixture.

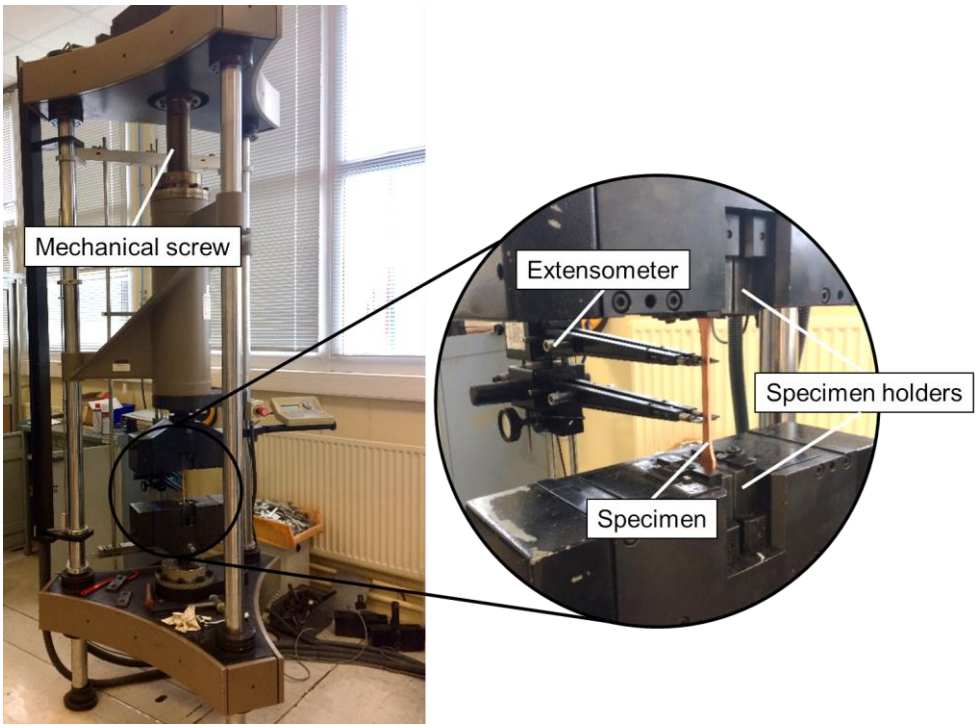

Figure 7.5: Screw-driven tensile testing UTS machine used at the ENSTA Bretagne with a close-up view of the specimen and the long travel extensometer.

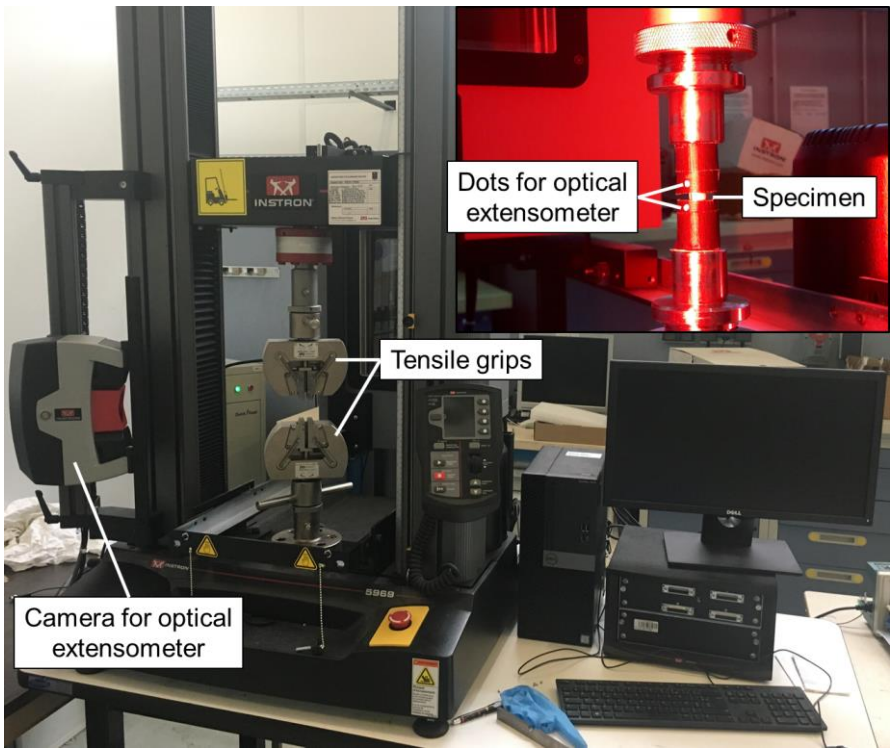

Figure 7.6: Table-top Instron machine used for tensile and compression tests at the ENSTA Bretagne. (Inset) compression fixture with dots for displacement measurement with an optical extensometer.

The engineering stress and strain for the compression and tensile machines were calculated using the load measured with the load cell and the displacement measured with the long

travel or the optical extensometers. The following standard equations were used to calculate the engineering stress and strain:

$$\sigma_{eng} = \frac{F}{A_0} \qquad (7.1) \qquad\qquad \varepsilon_{eng} = \frac{L - L_0}{L_0} \qquad (7.2)$$

where F is the applied load in N, A_0 is the initial specimen cross sectional area in mm^2, L and L_0 are the specimen current and initial lengths (or height in compression) in mm.

The true stress and strain are calculated using the following equations:

$$\sigma_T = \sigma_{eng}\left(1 + \varepsilon_{eng}\right) \qquad (7.3) \qquad\qquad \varepsilon_T = \ln\left(1 + \varepsilon_{eng}\right) \qquad (7.4)$$

Note that the same equations can be used for the tensile and compression tests, but the following details must be respected for compression tests. Since the specimen height reduces, the engineering strain is negative, $\varepsilon_{eng} < 0$. The stress is also negative, if a negative load is recorded. Consequently, the true strain is also negative. The following equation can also be used to calculate the true strain in compression:

$$\varepsilon_T = \ln\frac{L}{L_0} \qquad (7.5)$$

Note that in the following, the results of the compression tests are presented in terms of the absolute value of the stress $|\sigma_T|$ as a function of the absolute value of the strain $|\varepsilon_T|$.

7.3.1.2. LEM3 – Polycrystalline Niobium Sheets

Tensile tests were performed on polycrystalline niobium specimens cut at 0°, 45°, and 90° with respect to the rolling direction at the LEM3 with a screw-driven machine (ZwickRoell, with a 10 kN load cell) at a constant crosshead speed of 5 mm/min. A large displacement extensometer (ZwickRoell multiXtens) was used to accurately measure the displacement in the gage section. Pictures were acquired during the tests at 4 frames per second with a charged-coupled device (CCD) camera (Pike) and 50 mm focal lens. DIC was used to measure spatial strain distributions to obtain the minor and major strains at localized necking and to calculate the plastic strain anisotropy.

The plastic strain anisotropy coefficients, also called the *r*-values or the Lankford coefficients, were calculated using the uniaxial tensile tests with their tensile axis at 0°, 45°, and 90° with respect to the rolling directions. The manual method specified in the ASTM E517 standard [276] was used with digital image correlation. The change in axial length in the gage section from an initial length (L_0) of approximately 50 mm was measured at true

strains of 0.15 and 0.2. The transversal change in width for an initial width (w_0) of approximately 10 mm, averaged over three different regions of the specimen, was also measured at the same strains. The final lengths (L_f) and widths (w_f) were used in the following equation to calculate the *r*-value for each rolling direction and value of true strain:

$$r_\theta^\varepsilon = \frac{\ln\left(\frac{w_0}{w_f}\right)}{\ln\left(\frac{L_f w_f}{L_0 w_0}\right)} \tag{7.6}$$

where ε represents the true strain at which the value is calculated ($\varepsilon = 0.15$ or $\varepsilon = 0.2$) and θ represents the angle, in degree, between the rolling direction and the tensile axis of the specimen (θ = 0°, θ = 45° or θ = 90°).

The weighted average *r*-value, r_m^ε, of high-purity niobium was calculated at each level of strain using the following equation:

$$r_m^\varepsilon = \frac{r_0^\varepsilon + r_{90}^\varepsilon + 2r_{45}^\varepsilon}{4} \tag{7.7}$$

The degree of planar anisotropy, Δr^ε, was calculated with the following equation:

$$\Delta r^\varepsilon = \frac{r_0^\varepsilon + r_{90}^\varepsilon - 2r_{45}^\varepsilon}{2} \tag{7.8}$$

Tensile tests were also performed at a constant crosshead speed of 5 mm/min on specimens with the near-plane strain geometry shown in Figure 7.3. The load and displacement were not measured for those tests since the strain state at localized necking was the only value of interest. The method used to calculate this strain state is detailed in section 7.3.4.

7.3.2. Intermediate Strain Rate Testing Methodologies (1 to 100 s^{-1})

7.3.2.1. Joint Research Centre – Electron Beam Welded OFE Copper and Niobium

Tensile and compression tests were performed on electron beam welded OFE copper and niobium at quasi-static (10^{-3} s^{-1}) and intermediate strain rates (20 s^{-1}) with a servo-hydraulic machine (MTS 810) at the European Commission Joint Research Centre in Ispra. Specimen geometries in Figure 7.1b and c were used for tensile tests and cylindrical specimens with a diameter of 8 mm and a thickness of about 3.96 mm were used for compression tests. More precisely, the short specimens were deformed at nominal strain rates of $2.0\text{x}10^{-3}$ s^{-1}, $2.0\text{x}10^{-1}$ s^{-1}, and 20 s^{-1} and the long specimens at nominal strain rates of $1.0\text{x}10^{-3}$ s^{-1}, $1.0\text{x}10^{-2}$ s^{-1}, and $1.0\text{x}10^{-1}$ s^{-1}. Figure 7.7 shows the servo-hydraulic machine configured for tensile tests with the short specimen geometry and its main components. Compression specimens were deformed at nominal strain rates of 10^{-3} s^{-1}, 10^{-1} s^{-1}, and 10 s^{-1}.

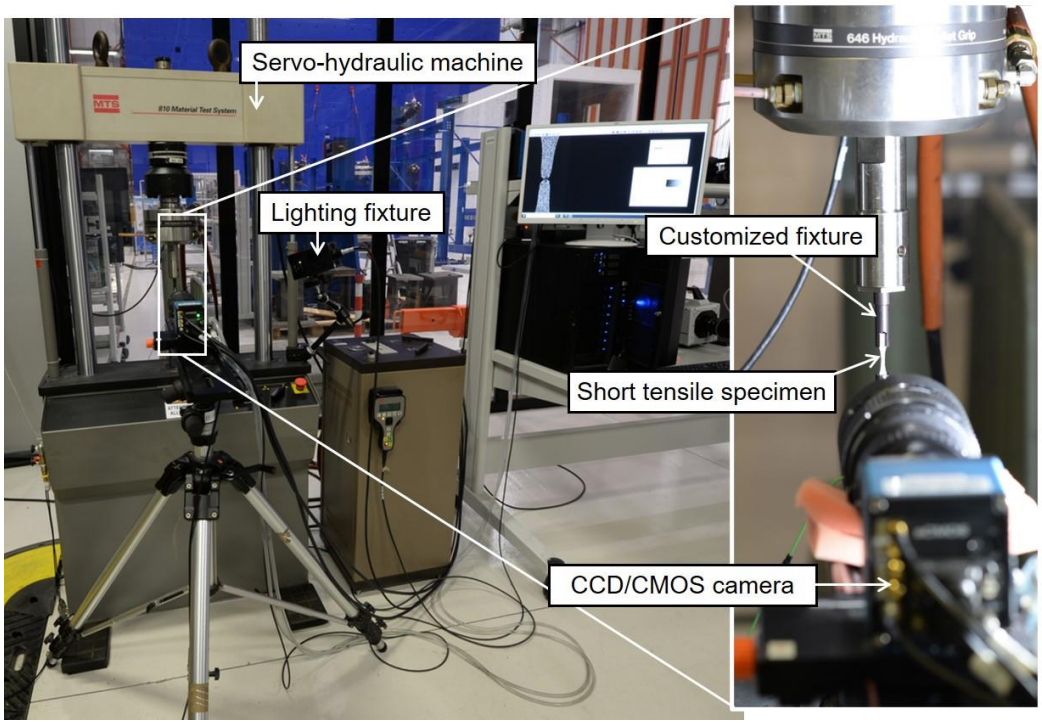

Figure 7.7: Servo-hydraulic machine configured for tensile tests with the short specimen with the main components. (Inset) Higher magnification picture of the tensile specimen and the customized fixture, as seen from the camera used for in-situ image acquisition and DIC analyses.

Pictures of the gage length of the tensile specimens were acquired at frame rates of 0.5 to 50 Hz with a hybrid CCD and complementary metal–oxide–semiconductor (CMOS) camera (pco.edge 5.5) for strain rates lower or equal to 2.0×10^{-1} s^{-1} and with a high-speed camera (IDT OS8-S3) for higher strain rates. Digital image correlation was used for the short specimens (Figure 7.1c) to measure the displacement between two points of the gage section with an initial distance of about 5 mm. The engineering strain was calculated using the increasing distance and the initial gage length L_0, as detailed in section 3.3.2. The deformation of the gage section of the long tensile specimens (Figure 7.1b) was measured using the displacement of the machine. The influence of the stiffness of the machine on the measured displacement was negligible since the measured elastic modulus was similar to the one calculated with DIC on short specimens. The reduction in height of the compression specimens was calculated with the crosshead displacement and the stiffness of the machine was found by performing a void test, i.e. a test with no specimen, and removed it from the displacement measurements.

7.3.3. High Strain Rate Testing Methodologies (> 1 000 s^{-1})

7.3.3.1. ENSTA Bretagne – Annealed and Hard OFE Copper

Compression tests at strain rates in the order of 10^3 s^{-1} were performed at ENSTA Bretagne using split Hopkinson bars. Cylindrical specimens with a diameter of 8 mm and a thickness of 4 mm were used. Figure 7.8 shows a picture and a schematic of the split Hopkinson bar

system used at the ENSTA Bretagne. The striker bar was projected on the incident bar upon discharge of the compressed air. Pressures of 2.5 to 5.0 bar, corresponding to strain rates of about 2 000 to 4 000 s^{-1}, were used for hard and annealed OFE copper. The strain waves were measured with one strain gage on the incident and the transmitted bars. All bars were made of maraging steel with a diameter of 20 mm, an elastic modulus of 184 GPa, a density of 7 819 kg/m^3, and a Poisson ratio of 0.3.

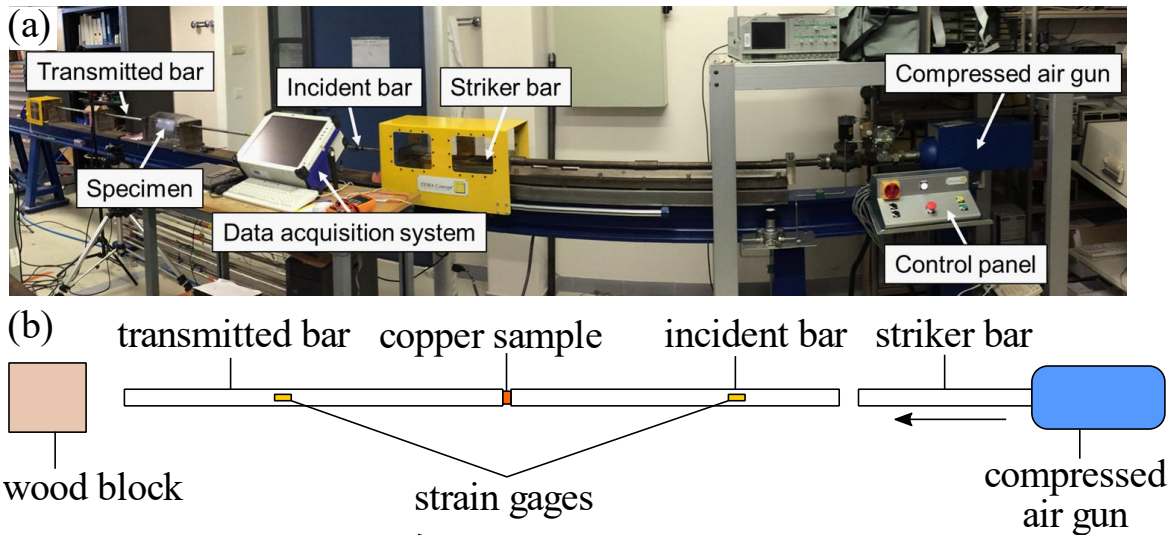

Figure 7.8: (a) Picture and (b) schematic of the split Hopkinson bar setup used at the ENSTA Bretagne for compression tests on OFE copper samples.

The acquired signals of the input and output bars were analyzed using the PostBarre software developed at ENSTA Bretagne. The stress–strain curves and strain rate calculated with PostBarre was also compared to a MATLAB code developed by the author and its accuracy was confirmed. Both software packages used the standard equations associated with the analysis of an elastic strain wave in split Hopkinson bars, as summarized in section 2.2.

7.3.3.2. Joint Research Centre – Electron Beam Welded OFE Copper and Niobium

High strain rate tensile and compression tests were performed on electron beam welded OFE copper and niobium specimens at the Joint Research Centre using split Hopkinson bars. Strain rates of up to approximately 1 600 s^{-1} and 4 000 s^{-1} were obtained in tension and compression, respectively. Pictures were acquired at up to 50 000 frames per second with a high-speed camera (Photron FASTCAM SA1.1).

A standard dynamically loaded system with a striker bar projected using compressed gas was used for the compression tests (Figure 7.9). The striker, input, and output bars had a diameter of 10 mm and were made of 17-4PH high-strength stainless steel.

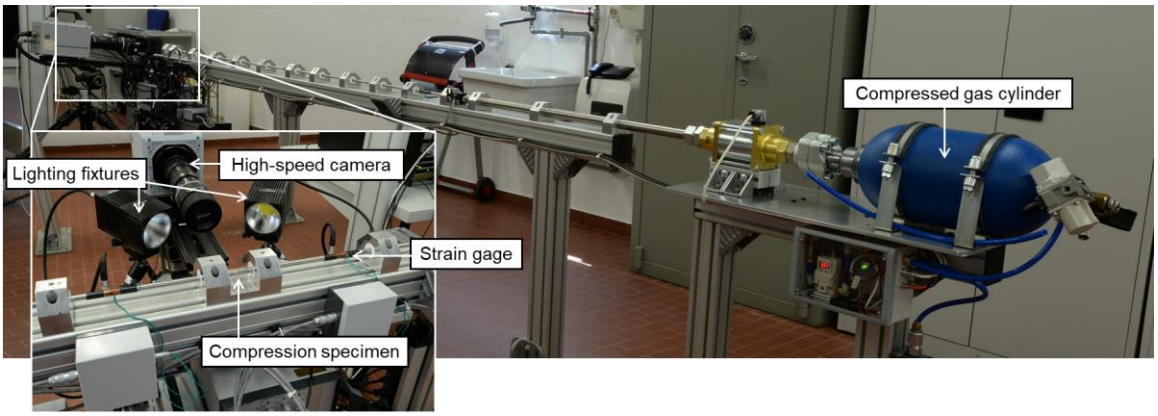

Figure 7.9: Split Hopkinson bar system used at JRC for the compression tests at high strain rate.

The split Hopkinson bar apparatus used for the tensile tests was designed at the Hopkinson bar laboratory (HopLab) of the JRC (Figure 7.10). Compared with traditional split Hopkinson bar systems, the tensile strain pulse is not generated by projecting a striker bar, but by pre-straining a section of the input bar [277], [278]. This is defined as a statically loaded system [96]. A hydraulic jack was used to pre-strain the input bar and a hydraulic clamp was used to hold and release the strain pulse, as shown in Figure 7.11. The input and output bars were made of 17-4H stainless steel (E_b = 197 GPa, ρ_b = 7780 kg/m^3, and $\emptyset_b$ = 10 mm) with lengths specified in the diagram shown in in Figure 7.11. The strain pulse was sufficiently long (~3.3 ms) to deform the specimens up to failure and was measured using three strain gages (Tokyo Measuring Instruments Laboratory FLA-2-350-11) affixed on both the input and output bars. However, the long strain pulse, with respect to the length of the bars, resulted in overlapping incident, reflected, and transmitted waves in the sections of the bars with the strain gages. Therefore, the algorithm proposed by Bussac et al. [279] to separate the waves traveling in different directions was used. This technique requires at least two independent strain measurements per bar and allows the reconstruction of the strain history at any location in the bars. More details about the implementation of this technique are found in the work of Peroni et al. [280].

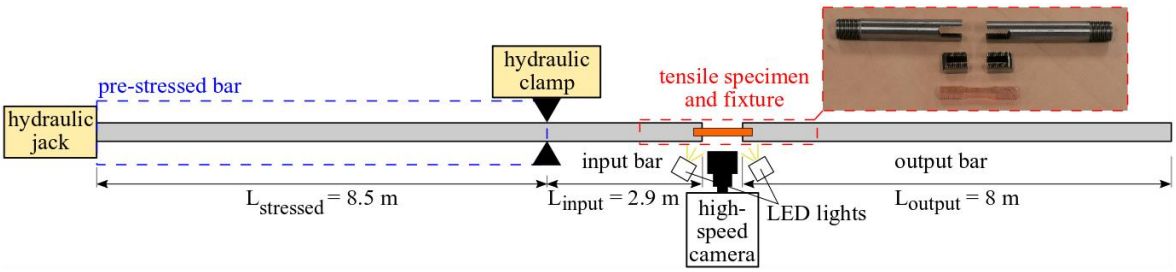

Figure 7.10: Schematic of the split Hopkinson bars system developed at the JRC HopLab for tensile tests at high strain rates [277]. (Inset) OFE copper tensile specimen, adaptors to align the specimen with the center of the bars, and holders with threaded to fix on the input and output bars.

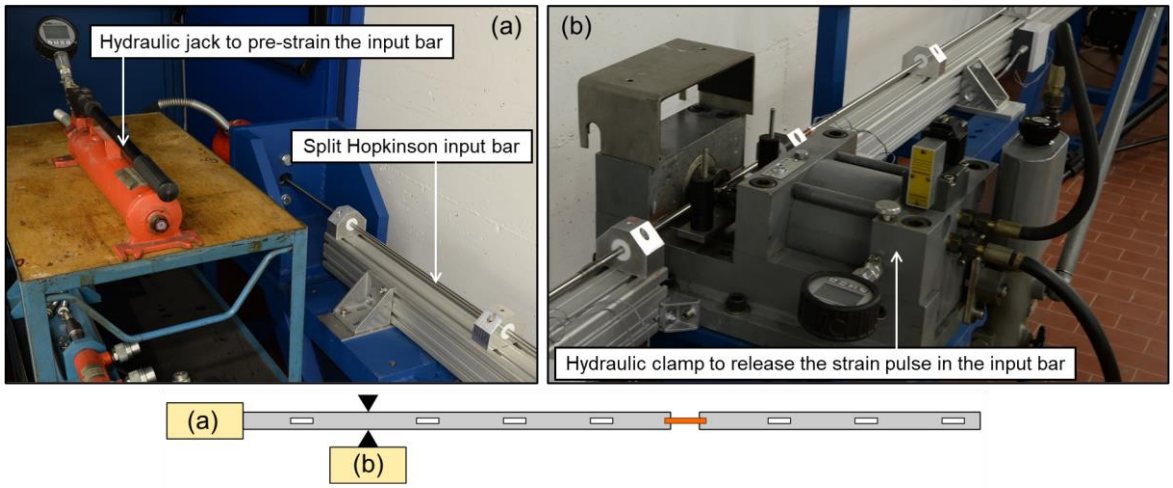

Figure 7.11: Hydraulic jacks to (a) pre-strain the input bar and (b) to clamp the input bar and release the strain pulse with their respective locations in the schematic from Figure 7.10.

7.3.4. Forming Limit Diagrams

Tests to obtain the quasi-static forming limit diagram (FLD) at localized necking were performed at the laboratoire d'étude des microstructures et de mécanique des matériaux (LEM3) of the University of Lorraine in Metz. Both the Marciniak and Nakajima tests, described in section 6.1. were used at the LEM3, but the results obtained with the latter technique are not considered in this study, as explained in Chapter 8. The experimental method used to obtain the FLD of OFE copper and niobium sheets detailed in the following sections are only applicable to the Marciniak test.

7.3.4.1. Marciniak Setup and Sheet Metal Preparation for DIC

As shown in Figure 6.2, the punch used in the Marciniak test has a flat bottom. A brass punch with an outer diameter of 75 mm, smaller than the 100 mm diameter recommended in the ISO 12004-2:2008 standard [241], was used in this study. Since the largest blank deformation for this punch geometry is at the radius, which results in non-linear strain paths and requires three-dimensional digital image correlation to measure strains, a blank carrier is used to force localized necking to occur on the top and flat surface of the punch.

Two blank carrier geometries were used, as shown in Figure 7.2. The cut sheets and pierced blank carriers were sticked to a blank with double-sided tape, as shown in Figure 7.12a. This step is important to maximize friction forces between the two sheets during the Marciniak test. The ISO standard also suggests to increase the surface roughness of the blank carrier using a silicon carbide paper sandpaper with a small grit to increase friction forces [241], if required.

The top surface of the blank, the one studied, was cleaned with a solvent to remove any oil and grease and painted for in-situ 2D strain measurements with DIC. A thin uniform and

matte white layer of paint was applied on the sheet to remove reflections and provide a high contrast with the black paint speckles that are tracked by the DIC software, as shown in Figure 7.12b and c. The blanks were painted shortly before the beginning of the tests to minimize the risk of dry paint flacking due to the large deformations. A stochastic paint pattern was used since spray painting is easier to use and has less health risks compared with chemical etching of circles or lines to form a uniform grid. Also, the stochastic patterns, if done with sufficiently small speckles, allows for local measurements of the whole blank. The blank carrier–blank assembly, hereafter the *blank-assembly*, was then inserted under the screw-driven mechanical press following the three steps schematically presented in Figure 7.13 and detailed below.

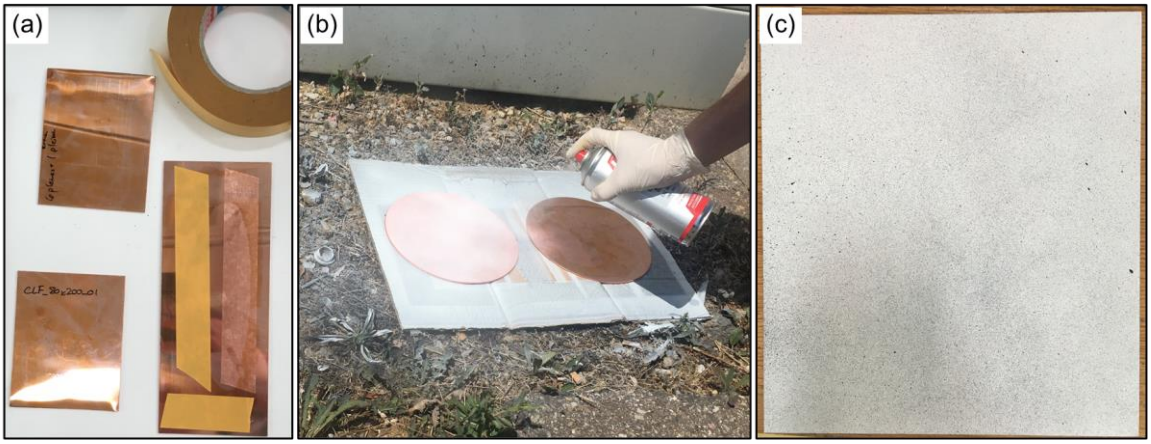

Figure 7.12: Sample preparation before Marciniak tests with (a) sticking a cut blank carrier with a 80 mm x 100 mm blank with double-sided tape, (b) painting of a circular blank with the mate white paint, and (c) the resulting stochastic pattern for DIC made with black paint speckles.

First, the press is lowered to clamp the blank-assembly in the blank holder with a loading force of about 170 kN. Six screws were used to lock the top and bottom parts of the blank holder into place and maintain the preloading force that prevents draw-in of the blank-assembly.

Second, the assembly is raised and the brass punch is inserted under the blank carrier. A 200 μm thick polyvinyl chloride (PVC) film was placed on the punch to reduce the friction with the blank carrier for the tests on OFE copper. A 50 μm thick polytetrafluoroethylene (PTFE) film was used instead of PVC for the FLD of niobium. The lower friction forces between the brass punch and the OFE copper blank carrier with the latter film was beneficial for the Marciniak tests. More details about the advantages of the PTFE film are presented with the obtained results in Chapter 8.

Finally, the press lowers the blank-assembly on the punch until failure is observed on the blank. Since the punch is stationary, the flat region of the blank, where localized necking occurs, is at a constant height and on a two-dimensional plane. A 45°-angled mirror was

affixed above the blank and images of the top surface of the assembly were acquired with a camera placed away from the press. The mirror never moved during the process since it was fixed on additional posts that are independent of the press and not shown in Figure 7.13 to avoid confusion.

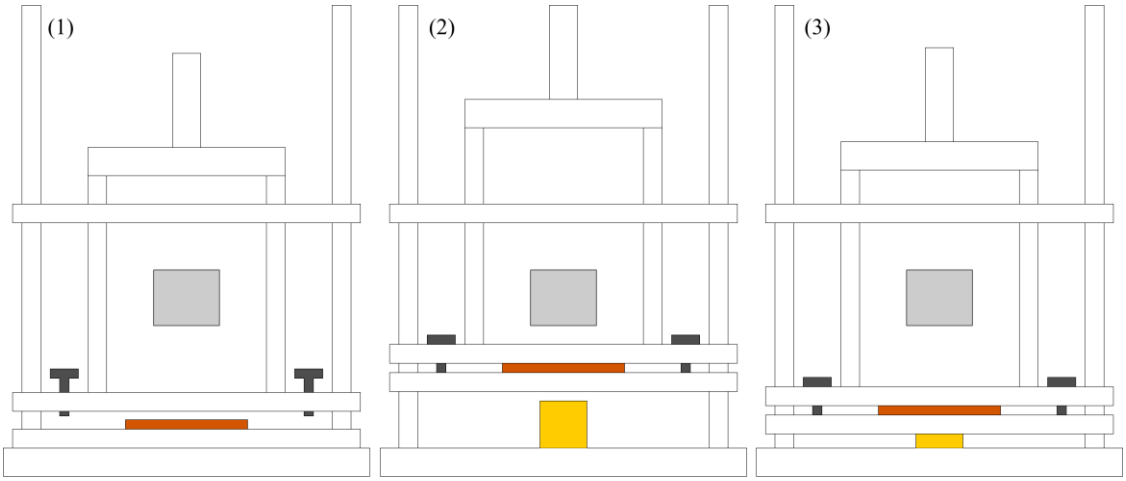

Figure 7.13: Schematic of the different steps to deform the blank with a flat-bottomed punch. Different colors are used for the following important components: mirror (grey), screws for the top and bottom parts of the blank holder (black), blank-assembly (orange), and brass punch (yellow).

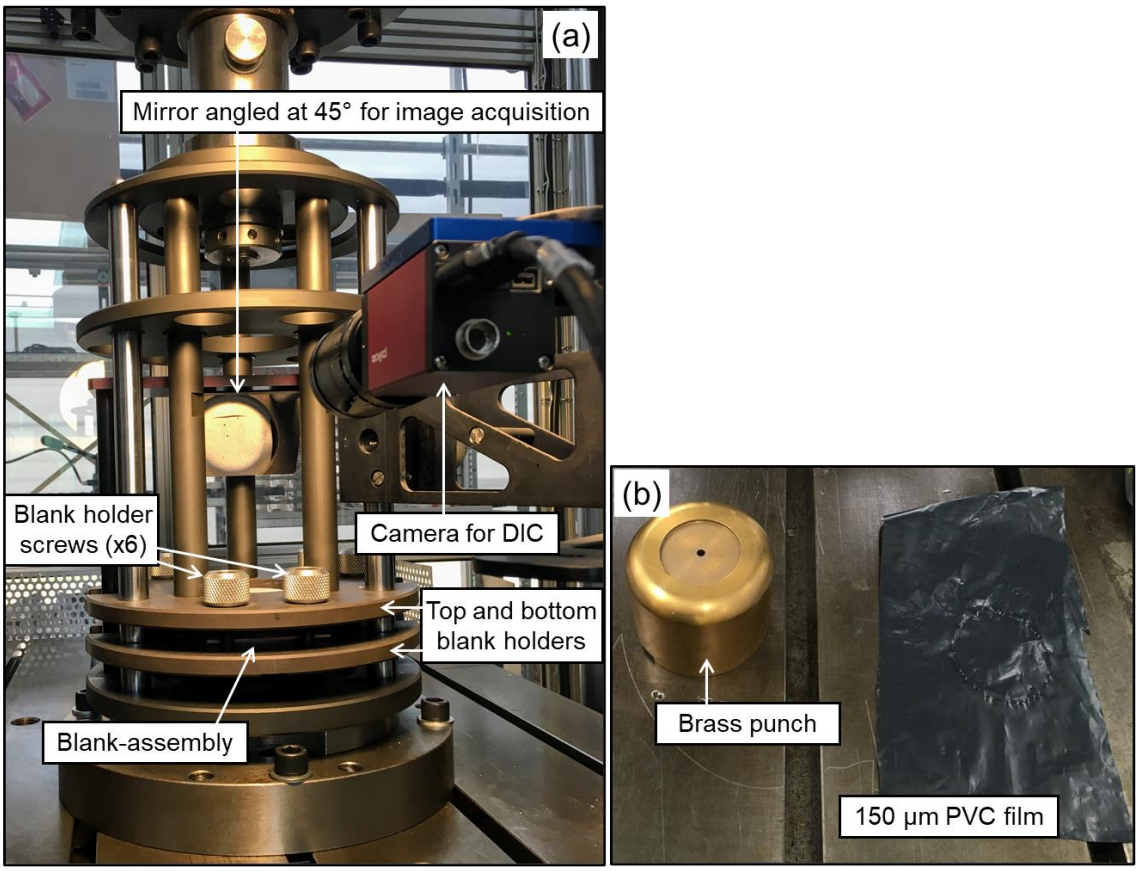

Figure 7.14: Pictures with (a) the main components of the setup for the Marciniak tests and (b) the punch and PVC films that are below the blank-assembly.

Figure 7.14 shows the main components of the Marciniak setup that were schematically presented in Figure 7.13. A CCD camera (Pike) with a 50 mm focal lens was used to acquire pictures every 500 ms, equivalent to 2 frames per second. Light emitting diodes (LED) were used to provide sufficient lighting and remove shadows caused by the assembly and the natural lighting of the room. The in-situ images were then imported in two DIC software packages, namely GOM Correlate and VIC 2D, to calculate the minor and major strains at each frame. VIC 2D was only used with the tests performed on OFE copper to confirm that the method used in GOM Correlate was adequate.

7.3.4.2. Methodology to Calculate the Strain at Localized Necking for the FLD and Strain Paths

To measure the major and minor strains at the onset of localized necking and define the FLD, a methodology based on the recommendations of the ISO standard was developed and implemented in MATLAB. The three steps of this methodology are presented below.

Step 1. Frame Identification from Visual Observation of Necking

First, the picture used for the analysis was selected based on visual observation and comparison of the different frames. Different other approaches have been proposed in the literature to determine the onset of necking, e.g. a sudden local increase in strain rate or from a load drop in the applied load as function of punch displacement curve [241], [251]. The latter method was initially used for the tests on OFE copper. However, the signals of the mechanical press and the camera were not synchronized, which resulted in an uncertainty of few frames in the manual synchronization process. Since the final selection of the appropriate frame to perform the analysis was done by comparison of few consecutive pictures, it was decided to always rely on a visual selection of the frame of interest. The main disadvantage of this method is that it leads to a higher variability in the obtained FLD between different users. However, Dr. Guillaume Robin of the LEM3 and the author independently analyzed the results for OFE copper and similar frames were used for the different tests, which resulted in a small and reasonable error in the FLD and justified the use of this method. Note that the load drop method remains useful to identify tests where the pierced blank carrier failed before the blank, further discussed in section 8.2., since two drops in load are measured.

The visual criterion used to select a frame was based on the appearance of light reflections in the neck due to a rupture of the paint, as shown in Figure 7.15. This subtle detail in the appearance of the neck was used for the frame selection of all specimens tested in this study. To easily locate the region where necking occurred and to select the frame of interest, all the

pictures acquired during the tests were imported in the DIC software GOM Correlate. A contour plot of the major strain was used to highlight the location of the neck.

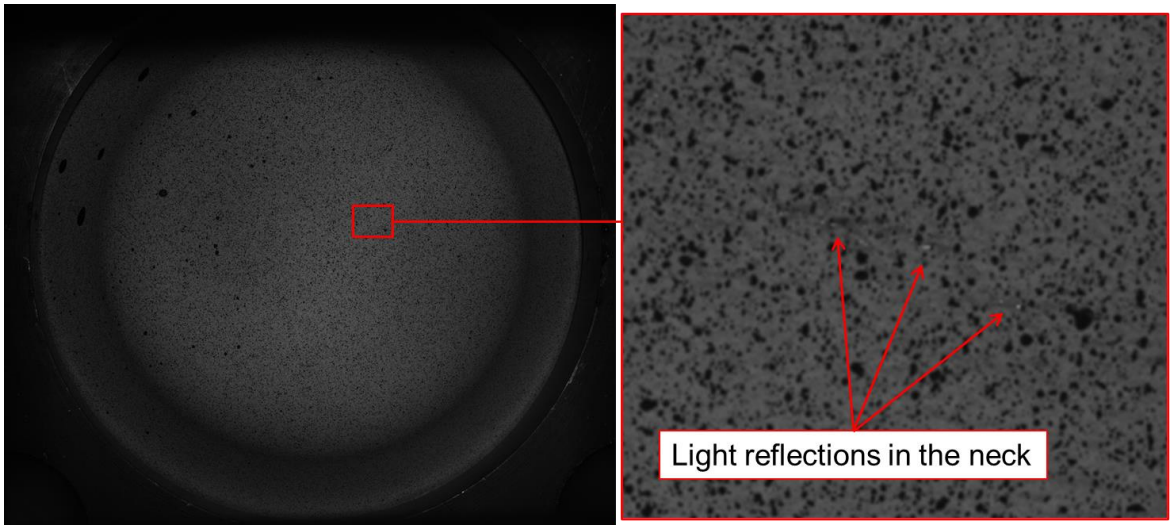

Figure 7.15: Visual inspection of a niobium sheet to identify the frame to be analyzed for the FLD based on light reflections due to flacking paint.

Step 2. Line Scans of the Major and Minor Strains

Second, major and minor true strains (ε_1 and ε_2) were measured at the selected frame with three line scans perpendicularly intersecting the neck. Figure 7.16 shows the sections of the line scans and the corresponding plots of major and minor strains as function of position on the blank, ε_1–x and ε_2–x, respectively, for each line. The data from those plots was exported in the comma separated value (CSV) format to be used as input data in the MATLAB code described in the next step.

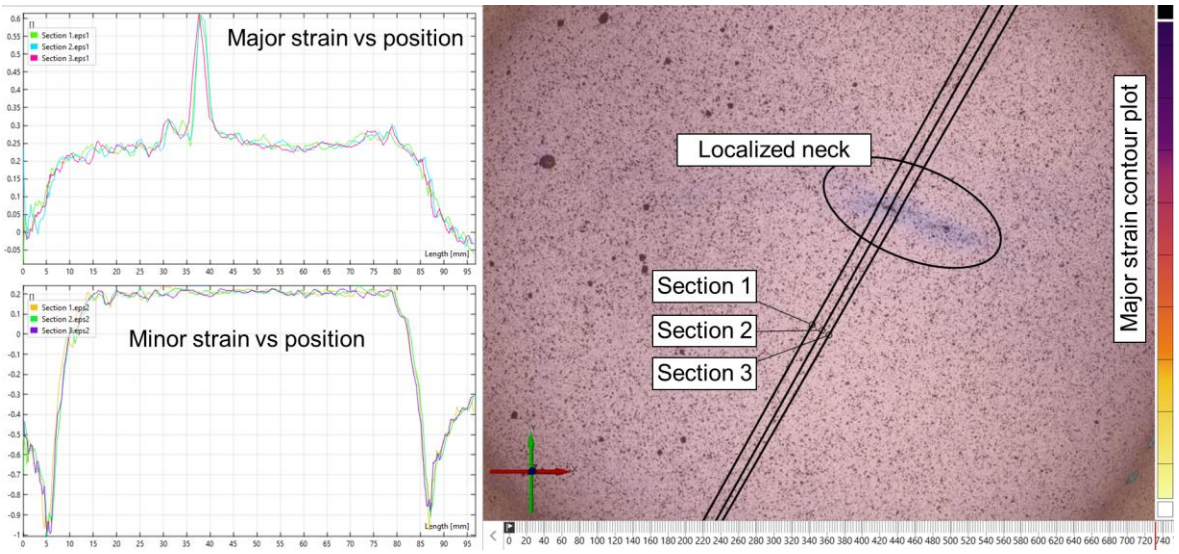

Figure 7.16: Extract from GOM Correlate of (right) the major strain contour plot with the three sections traced perpendicular to the neck to extract (left) the major and minor strains.

Step 3. Maximum Major Strain and Corresponding Minor Strain

Third, the ε_1–x and ε_2–x data sets of each line scan were imported in MATLAB to calculate the major and minor strains of the FLD. As specified in the ISO standard and as schematically shown in Figure 7.17, data in the center of the localized neck is not considered and only 4 mm on both sides of the 1 mm central gap is used in the numerical fit of the major strain distribution with the following equation:

$$\varepsilon_1(x) = \frac{1}{a_1 x^2 + a_2 x + a_3} \tag{7.9}$$

where parameters a_1, a_2 and a_3 are constants. Equation 7.9 is rearranged to solve a linear system of equations in MATLAB for n (ε_{1_i},x_i) points:

$$\underline{\underline{A}}\underline{a} = \underline{b} \rightarrow \begin{bmatrix} x_i^2 & x_i & 1 \\ x_{i+1}^2 & x_{i+1} & 1 \\ \vdots & \vdots & \vdots \\ x_n^2 & x_n & 1 \end{bmatrix} \begin{bmatrix} a_1 \\ a_2 \\ a_3 \end{bmatrix} = \begin{bmatrix} 1/\varepsilon_{1_i} \\ 1/\varepsilon_{1_{i+1}} \\ \vdots \\ 1/\varepsilon_{1_n} \end{bmatrix} \tag{7.10}$$

Since $\underline{\underline{A}}$ is not a square matrix and has more equations than unknowns, MATLAB finds the minimum-norm-residual solution of the overdetermined system using its built-in QR Solver [281], i.e. an orthogonal-triangular decomposition solver. The a_1, a_2 and a_3 constants found by the QR Solver are then used in equation 7.9 to plot the numerical approximation with the experimental data and confirm the adequacy of the fit with a visual inspection.

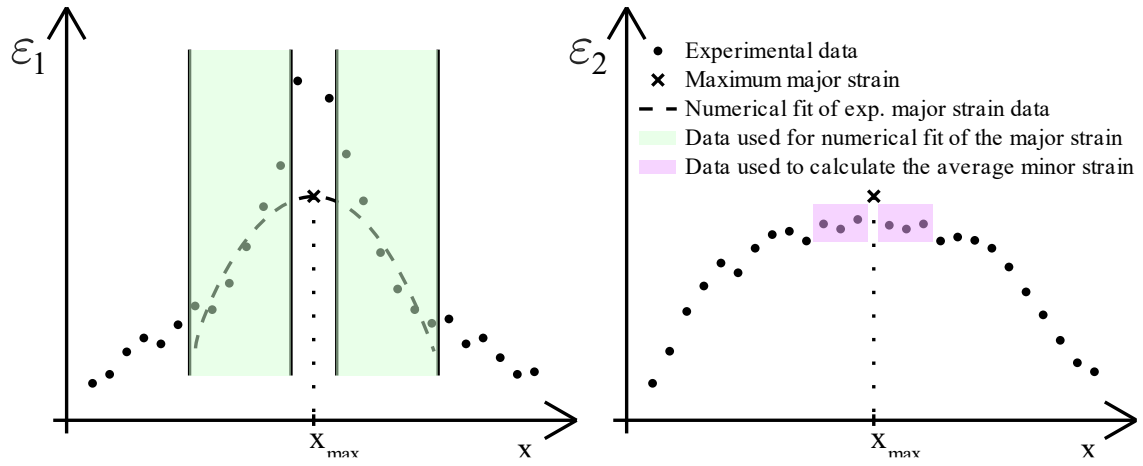

Figure 7.17: Schematic of the numerical fit of the major strain experimental data and the regions considered in the calculations of the points of the FLD.

The maximum of equation 7.9 is the ε_1 point of the FLD and the corresponding x position on the blank is found using the first derivative:

$$\frac{d\varepsilon_1(x)}{dx} = \frac{-(2a_1 x + a_2)}{a_1 x^2 + a_2 x + a_3} \tag{7.11}$$

Since equation 7.9 has only one maximum, the position on the blank satisfying the equation $\frac{d\varepsilon_1(x)}{dx} = 0$ is found in equation 7.12 and also used to calculate the minor strain point of the FLD:

$$x_{max} = -\frac{a_2}{2a_1} \tag{7.12}$$

The major strain at the onset of localized necking, corresponding to value of the point of the FLD is then calculated with the following equation:

$$\varepsilon_1 = \frac{1}{a_1 {x_{max}}^2 + a_2 x_{max} + a_3} \tag{7.13}$$

Finally, since deformation in the localized neck is close to pure plane strain, the minor strain is nearly constant in the neck and simply extracted at the position of the fitted maximum major strain. To avoid unrepresentative values of the minor strain due to local fluctuations of the 2D DIC results, the average minor strain of three points on each side of the location of maximum major strain x_{max}, as shown in Figure 7.17, is calculated as follow and used with the value found in equation 7.13 to define the location of a point of the FLD:

$$\varepsilon_2 = \frac{1}{6} \sum_{i=i_{max}-3}^{i_{max}+3} \varepsilon_{2_i} \tag{7.14}$$

where i_{max} correspond to the fictive i^{th} experimental point located at x_{max}. This point is defined as *fictive*, since there is no experimental point at the exact location of x_{max}. The notation $i_{max} \pm 3$ in equation 7.14 is then used to describe the selection the three closest points located before and after x_{max}.

7.3.4.3. Experimental Strain Paths

To ensure the validity of the FLD for each test, the strain paths around the neck was plotted. As specified in the ISO standard, the strain paths should be linear. More details about the effect of pre-straining on the FLD are presented in section 6.1.2. The major and minor strains at each frame are extracted at five points close to the neck, as shown in Figure 7.18. Finally, the extracted data was imported in MATLAB and ε_1 and ε_2 are plotted against each other.

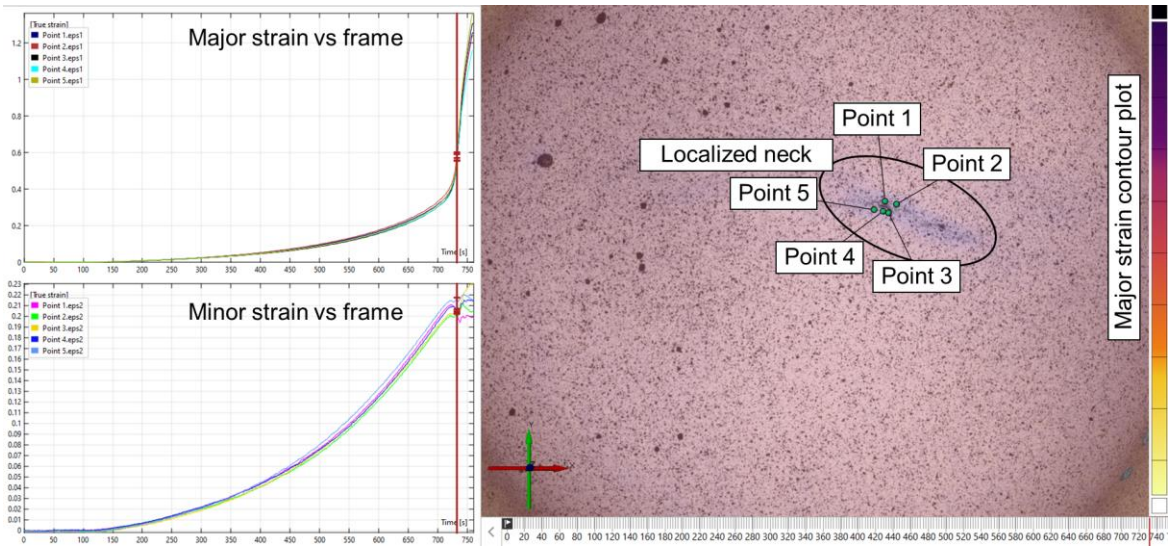

Figure 7.18: Extract from GOM Correlate of (right) the major strain contour plot with five points extracting the major and minor strains close to the neck at each frame and (left) the corresponding plots.

Chapter 8 Forming Limits of OFE Copper and Polycrystalline High-Purity Niobium

In this chapter, the quasi-static forming limit diagrams (FLD) of annealed oxygen-free electronic copper and high-purity polycrystalline niobium are presented. Experimental tests were performed at the Laboratoire d'étude des microstructures et de mécanique des matériaux (LEM3) in Metz, France. More details about forming limit diagrams are available in section 6.1. and the experimental procedures and the technique used to analyze the data are given in section 7.3.4.

8.1. Selection of the Marciniak Test

The Marciniak test (flat-bottomed punch) was selected over the Nakajima test (hemispherical punch) based on experiments with OFE copper using the setup available at the LEM3. Since high-purity copper is much cheaper than high-purity niobium, annealed OFE copper was used as a trial material to select and improve the experimental setup to obtain valid forming limit diagrams for both materials.

The Nakajima test was used on OFE copper sheets with a thickness of 1 mm and 2 mm and with different widths to obtain few points of a forming limit diagram. Since the punch is hemispherical, images were acquired using two cameras and stereographic digital image correlation (3D DIC) was used to extract the major and minor strains in the vicinity of the neck. Non-linear strain paths were measured and a very narrow range of minor strain was obtained. In addition, necking did not occur at the apex of the punch. This is caused by too important friction forces between the blank and the punch and is likely explaining the non-linear strain path and small minor strain distribution. In addition to those problems, the data analysis with 3D DIC is complicated to implement and motivated the use of the Marciniak test.

While the strain in Marciniak tests is easier to acquire and analyze because the region of interest is flat and 2D DIC can be used, the design of the blank carrier, the sheet placed between the punch and the blank that is studied, is non-trivial. A short study was then performed to select blank carriers with appropriate dimensions and the main findings are presented in the next section.

8.2. Blank Carrier Design for Marciniak Tests

For tests with negative minor strain, i.e. where the width of the blank reduces during deformation, the blank carrier was simply a sheet with the same dimensions as the blank, but

cut in two pieces at the center of the longest dimension. Figure 8.1a and c show the strain distribution in the blank and lines of higher strain corresponding to the end of the half-sheets of the blank carrier. No problems were observed with this design, as linear strain paths were measured and necking and failure occurred on the flat region of the punch. However, as shown in Figure 8.1b, localized necking did not occur above the space between the half-sheets of the blank carrier, but closer to the edge of the punch for the OFE copper blank. Similar to the Nakajima tests where necking did not occur at the apex of the punch but major strain localized above and below the apex, this is probably friction between the blank carrier and the punch. This problem was avoided for niobium, see Figure 8.1d, by reducing the friction between the brass punch and the OFE copper blank carrier by changing the polymer film between the two bare metal surfaces from 200 μm of polyvinyl chloride (PVC) to 50 μm of polytetrafluoroethylene (PTFE), commercially known as Teflon^{TM}. In addition to resulting in necking far from the radius of the punch, the forming limit curve covered a larger range of negative values of minor strain (presented in the following sections).

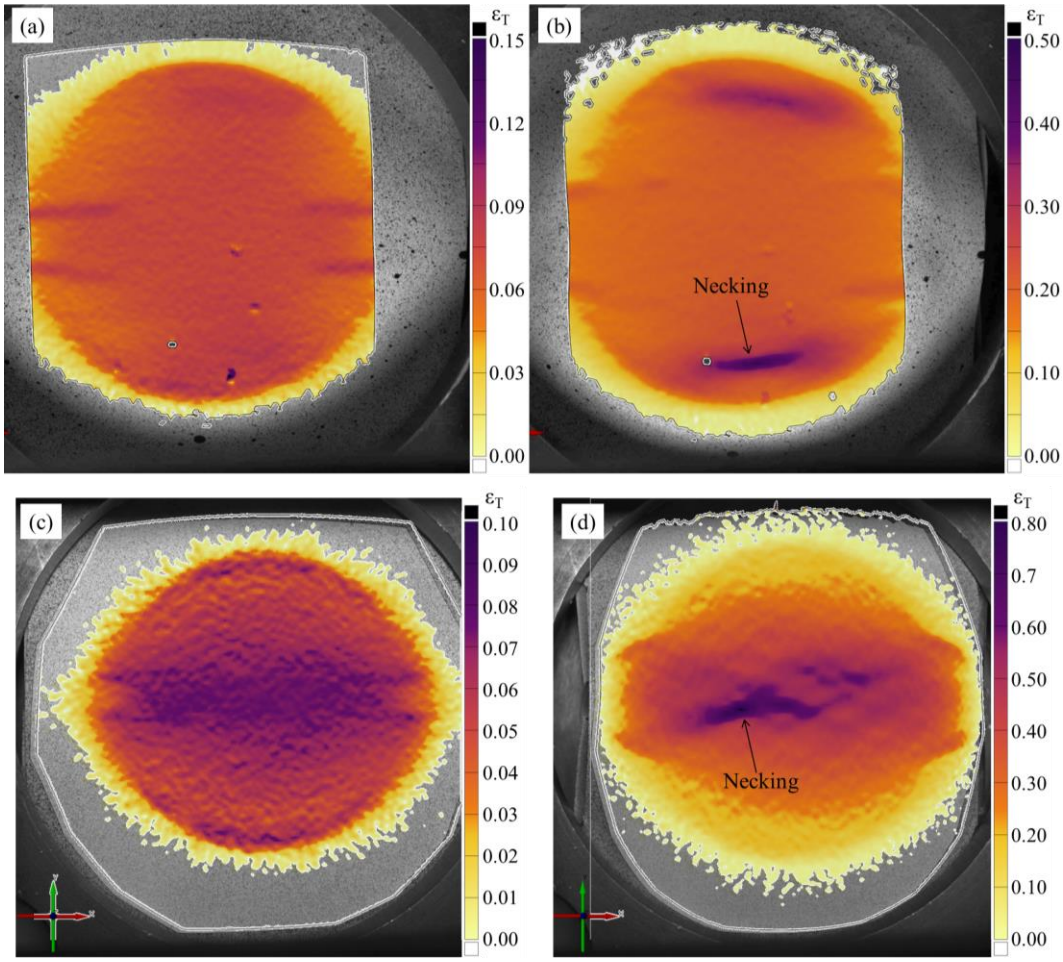

Figure 8.1: True major strain contour plots for specimens with a width of 100 mm showing (a and c) strain concentration from blank carrier and (b and d) at the onset of localized necking for OFE copper with a PVC film (a and b) and niobium with a PTFE film (c and d).

For tests with positive minor strain, i.e. with bi-axial extension, a blank carrier with the same dimensions as the blank but with a circular hole in center of the sheet was used. The selection of an appropriate hole diameter that ensures that the blank fails before the blank carrier proved to be non-trivial. The rupture of the blank carrier before the blank leads to a change of the strain path in the blank and an underestimation of the necking strains [248]. This phenomenon is visible in strain path plots that exhibit bi-linear strain paths. The first linear segment corresponds to the expansion of the hole and the second segment corresponds to crack propagation and opening after failure of the blank carrier. The opening of the cracks, as shown schematically in Figure 8.2, leads to strain localization in the blank above the crack and a nearly vertical strain path due a to a near plane strain deformation of the blank in this region. Figure 8.3a and c show digital image correlation contour plots of the major strain during bi-axial deformation, i.e. before failure of the blank carrier. Figure 8.3b shows four regions with localized strain on an OFE copper blank after failure of the blank carrier and Figure 8.3d shows the ideal case for niobium where necking occurred in the blank above the expanding hole of the blank carrier.

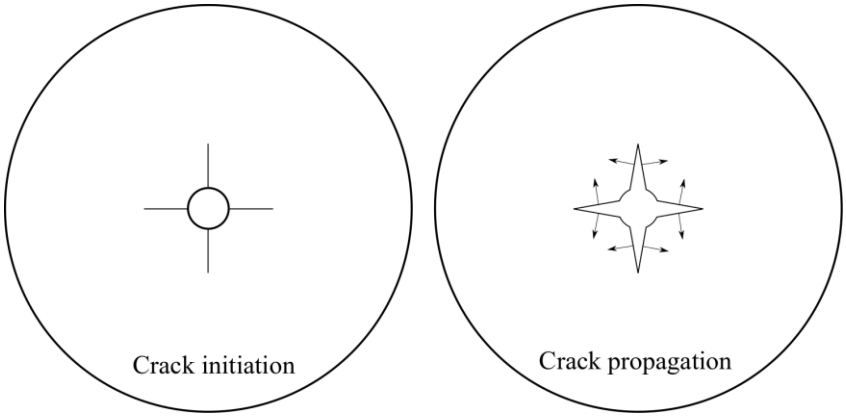

Figure 8.2: Crack initiation and propagation in the blank carrier explaining the plane strain-like deformation of the blank.

To delay the rupture of the blank carrier, the size of the hole was varied. The ISO 12004-2:2008 standard [241] recommends hole diameters of 32 to 34 mm for a punch diameter of 100 mm and a minimum blank carrier thickness of 0.8 times the thickness of the blank. Since the flat-bottomed punch used at LEM3 had a diameter of 75 mm, it is assumed that a smaller blank holder hole of 24 to 25.5 mm is acceptable. Tests with blank carrier hole diameters of 5, 10, 15, 20, 25, and 30 mm were performed for two sheet dimensions to quantify to effect of the hole on the strain path. Figure 8.4 shows the strain paths for 140 mm x 200 mm and 180 mm x 200 mm OFE copper blanks for the six blank carrier hole diameters previously mentioned. The effect of the hole diameter on the increase in minor strain at necking is more pronounced with the wider sheet, indicating that the rupture of the hole is more delayed for strain paths that are closer to an equi-biaxial deformation. A ~25% increase

in minor strain was measured for an increase in blank carrier hole diameters from 5 to 30 mm. Note that the last point of the strain path curves is higher than the forming limit curve for all hole diameters but 10 mm.

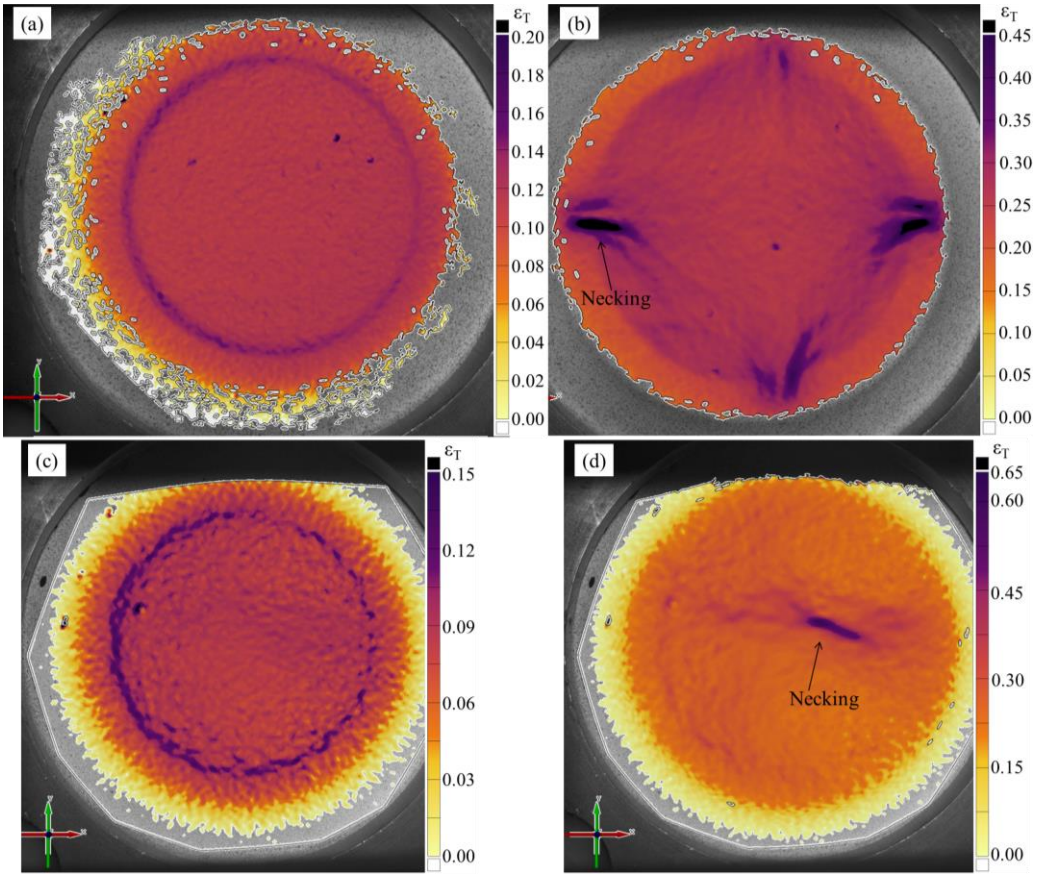

Figure 8.3: True major strain contour plots for specimens with positive minor strain ($\varepsilon_2 > 0$). (a) and (b) correspond to a OFE copper blank and a blank carrier hole diameter of 15 mm. In this case, necking of the blank is caused by the failure of the blank carrier. (c) and (d) correspond to a niobium blank and a blank carrier hole diameter of 30 mm. Necking takes place above the blank carrier hole.

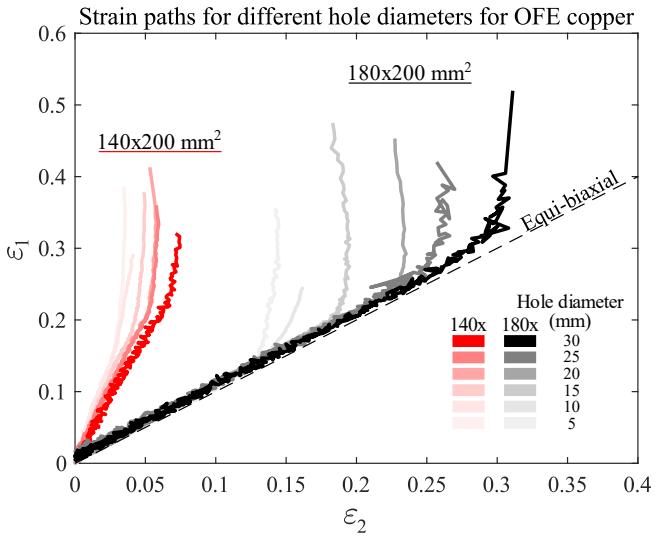

Figure 8.4: Strain paths for 140 mm x 200 mm and 180 mm x 200 mm OFE copper sheets with blank carrier hole diameters of 5 mm, 10 mm, 15 mm, 20 mm, 25 mm, and 30 mm. Only one representative strain path is plotted per blank carrier hole diameter for clarity.

The study on the effect of the blank holder hole diameter showed a reduction of the distance travelled by the punch between the rupture of the blank carrier and the blank. The rupture of the blank carrier is identified by a sudden load drop and a localization of the strain in the digital image correlation results. While the change in slope appears at larger values of minor strains, the extent of the second slope, in the near plane strain mode, is similar. An analysis of the distance travelled by the punch after rupture of the blank carrier was performed. The distance was measured using the raw load vs displacement curves, as shown in Figure 8.5a for two 180 mm x 200 mm sheets with blank carrier hole diameters of 5 mm and 30 mm. The black arrow indicates the rupture of the blank carrier and the grey arrows the rupture of the blank. The absence of a black arrow for the specimen with a hole diameter of 30 mm indicates that the blank failed before or at the same time as the blank carrier. A lower load was measured for sheets with hole diameters of 25 mm and 30 mm due to the lower friction coefficient of the PTFE film, compared with the PVC film. A reduction of the distance travelled by the punch between rupture of the blank carrier and the blank for increasing hole diameter is observed in Figure 8.5b. This distance is equal to the displacement of the punch between the locations of the black and grey arrows in Figure 8.5a. The reduction in distance travelled by the punch is more pronounced for the 180 mm x 200 mm blanks, despite the absence of data for holes of 25 mm and 30 mm for the 140 mm x 200 mm sheets, and this explains the larger difference in strain path observed in Figure 8.4.

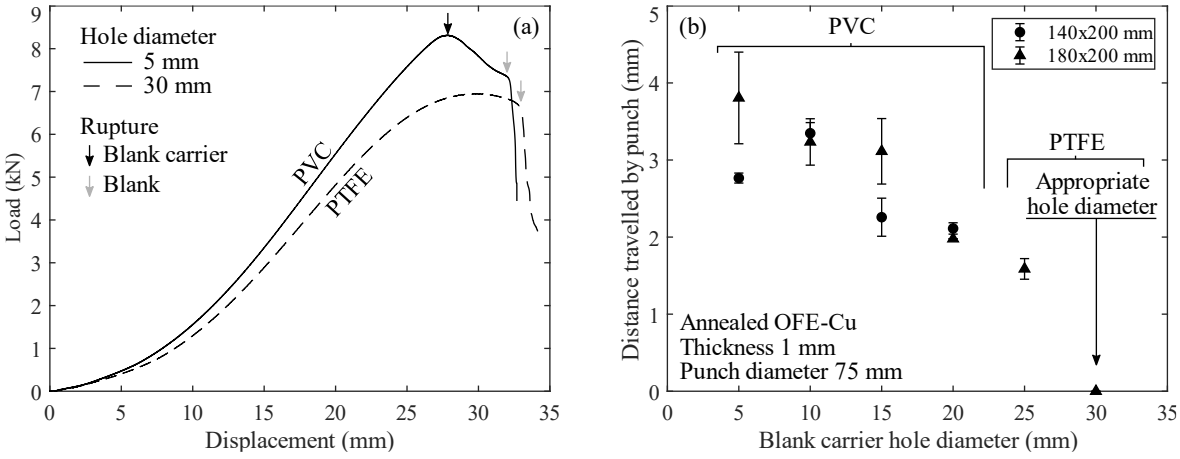

Figure 8.5: (a) Typical raw load vs displacement curves for tests performed on 180 mm x 200 mm copper sheets with arrows identifying the rupture of the blank carriers and blanks. (b) Distance travelled by the punch after rupture of the blank carrier and until the rupture of the blank for annealed OFE copper sheets with thicknesses of 1 mm and different polymer films. This distance is equal to the displacement between the black and grey arrows in (a).

8.3. Forming Limit Diagram of Annealed OFE Copper

The forming limit diagram OFE copper sheets annealed at 600°C for 2 hours in vacuum with a thickness of 1 mm was experimentally obtained with Marciniak tests. As detailed in the previous section, 1 mm thick blank carriers made of the same material were used. Tests were

performed on rectangular sheets with a length of 200 mm and varying widths of 80, 100, 120, 140, 160, and 180 mm and circular blanks with a diameter of 200 mm. Since the 180x200 mm^2 sheets were fully clamped in the setup, they yielded the same results as the circular disks. Pictures of the flat region of the blank being deformed were acquired during the test and used to calculate the strain with digital image correlation. More details about the experimental setups are available in section 7.3.4.

The strain paths on both sides of the localized neck were measured by extracting the minor and major strains, ε_2 and ε_1, at each frame and plotting ε_1 as a function of ε_2. Different software packages, namely GOM Correlate and VIC 2D, were used by the author and Dr. Robin of the University of Lorraine, respectively, and the results were compared. Similar results were obtained with the two software packages and users, which confirmed that the method used with GOM Correlate produces reproducible results for the strain path. The same exercise was repeated for the estimation of the points of the forming limit curve (FLC) and, again, the variation was small enough to confirm the validity of the data analysis method. It was found that the main source of error in results obtained between different users is the selection of the frame used to perform the measurements and calculations of the point of the FLC.

8.3.1. Tensile Mechanical Properties, Strain Paths and Forming Limit Curve

Tensile tests with DIC were not performed on specimens cut from the sheets used for the Marciniak tests. However, the 2 mm thick OFE copper sheets used to study the effect of strain rate on the tensile properties of this material, presented in Appendix E, came from the same supplier and were also annealed at 600°C for 2 hours in vacuum at CERN. The mechanical properties at a quasi-static nominal strain rate of 2.38x10^{-3} s^{-1} and the plastic strain anisotropy (*r*-value) at ~0.65 s^{-1} are used for this formability study and are summarized in Table 8.1. Parameters found at different strain rates are used with the quasi-static forming limit diagram since annealed OFE copper has a moderate strain rate sensitivity in tension, m = 0.011 (Appendix E). Recall from Appendix E that the *r*-value could only be calculated from subsize specimens pulled along the rolling direction with a servo-hydraulic machine since DIC was only used for these tests. The fully recrystallized microstructure obtained after the annealing heat treatment was previously characterized at CERN and isotropic properties were found, which is in agreement with the results obtained in this study.

Figure 8.6 shows the strain paths measured on either side of a neck in Marciniak tests for different blank carrier design, as discussed in section 8.2. For specimens with a positive minor strain and pierced blank carriers, the strain paths in blue and red are for blank carrier holes of 10 mm and 25 mm or 30 mm, respectively. The specimens with the 10 mm hole

diameter are not considered in the estimation of the forming limit curve as bi-linear strain paths (induced by the failure of the blank carrier) will result in an underestimation of the FLC.

Table 8.1: Tensile mechanical properties of annealed OFE copper at a nominal strain rate of 2.38×10^{-3} s^{-1} and at ~0.65 s^{-1} for the *r*-value.

Strain rate (s^{-1}):	2.38×10^{-3}			0.65
Rolling direction (°)	0.2% yield (MPa)	UTS (MPa)	ε_{fail} (-)	r (-)
0	47.0	220.0	0.484	0.95
90	47.4	217.2	0.509	N/A

The strain paths of specimens with a negative major strain are only covering a small fraction of the formability domain between the uniaxial and plane strain conditions. This is likely an artefact of friction forces that were too high between the blank carrier and the punch, leading to fracture closer to the punch radius and often not over the expending gap between the cut sheets of the blank carrier, as shown in Figure 8.1. As previously mentioned, this problem was solved for niobium by replacing the film material between the punch and the blank carrier from PVC to PTFE.

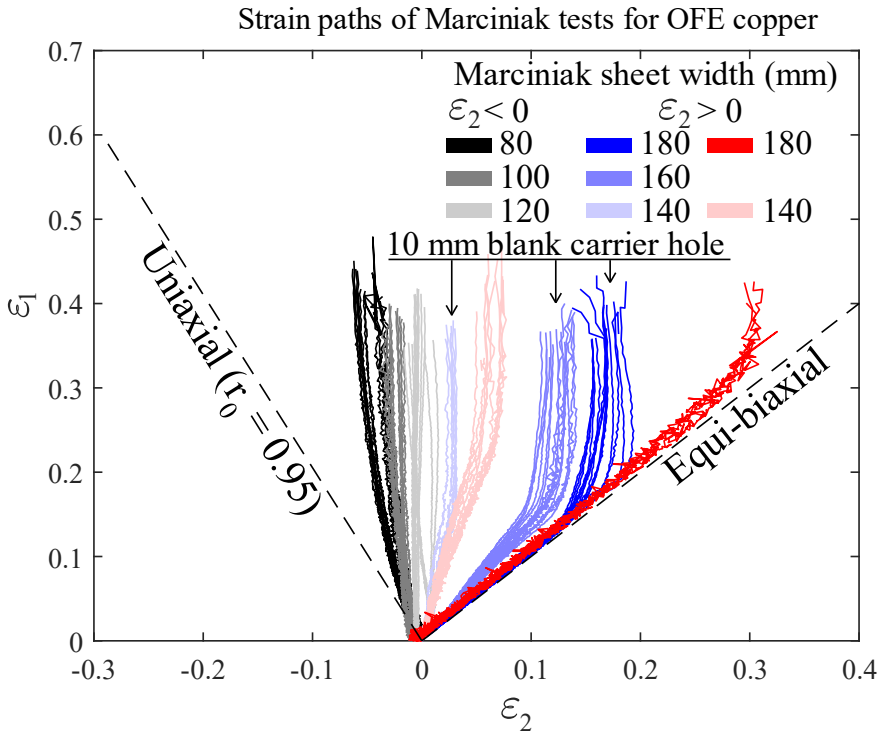

Figure 8.6: Strain paths of the Marciniak tensile tests for OFE copper with different colors for different blank holder geometries (black: cut sheets, blue: 10 mm hole, and red: 25 mm or 30 mm holes).

Figure 8.7 shows the experimental FLC of annealed OFE copper for tests that were considered valid, based on strain path analysis. Six experimental points describe the forming limit curve, four and two with a negative and positive minor strain, respectively. The location of the point corresponding to a uniaxial tensile test is determined based on the *r*-value along the rolling direction (r_0) of 0.95 and the logarithmic strain to failure of 0.484 presented in Table 8.1. Localized necking is often theoretically defined to occur at a true strain of $\varepsilon = 2n$ for a uniaxial tensile test, which would be equal to 0.97 for the hardening exponent of 0.485 of annealed OFE copper calculated from tensile tests at a quasi-static strain rate. However, this value is beyond the experimentally measured logarithmic strain of 0.484. The more conservative experimental value is then used in the FLC.

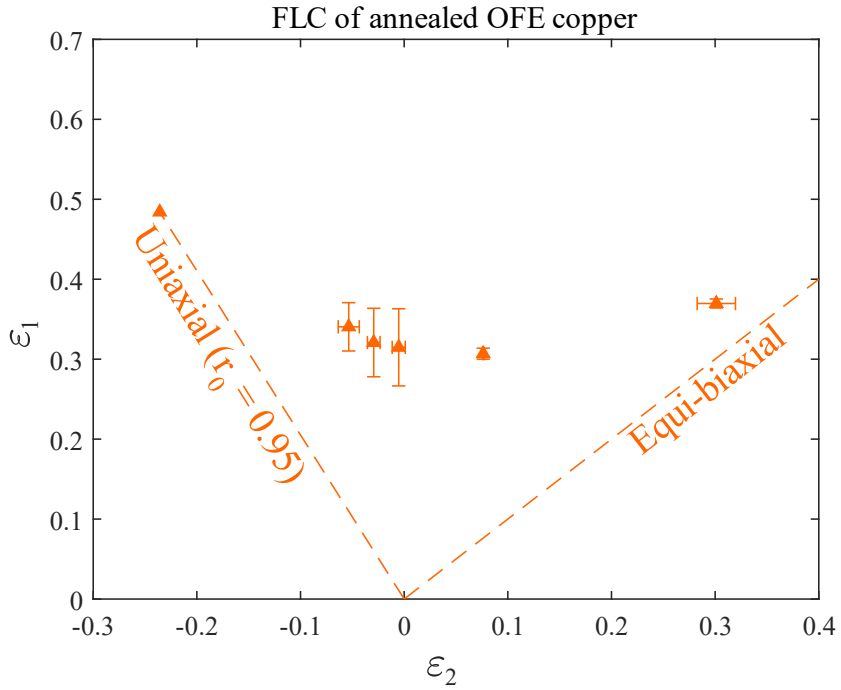

Figure 8.7: Experimental FLC of annealed OFE copper. Error bars represent the standard deviation for tests performed with the same sheet dimensions.

The lowest point of the FLC is around the plane strain condition, which is typical for materials with no pre-straining. Points with a negative minor strain appear to follow a linear trend with a steeper slope than the results with a positive minor strain. Also, larger variations in major strain for different tests with the same sheet dimensions, quantified with error bars of the standard deviation, are measured for Marciniak tests with $\varepsilon_2 < 0$.

8.3.2. Comparison with the Literature

Oxygen-free electronic copper is not the only commercially used grade of copper with a high purity. Thus, a comparison of the experimental forming limit diagram with other studies from the literature can be conducted. Figure 8.8 compares the FLC of annealed OFE copper presented in Figure 8.7 with experimental results for oxygen-free high conductivity (OFHC)

copper from Melander [265] and Gerdooei and Dariani [256]. The FLCs from the literature are slightly higher and lower than the one of OFE copper for the former and latter studies, respectively.

The similar FLCs obtained between the three studies are an indicator that the setup, data acquisition system, and data analysis methods used in this study provide reliable results. This is also an indicator that the formability of high-purity copper does not significantly varies between different grades of copper.

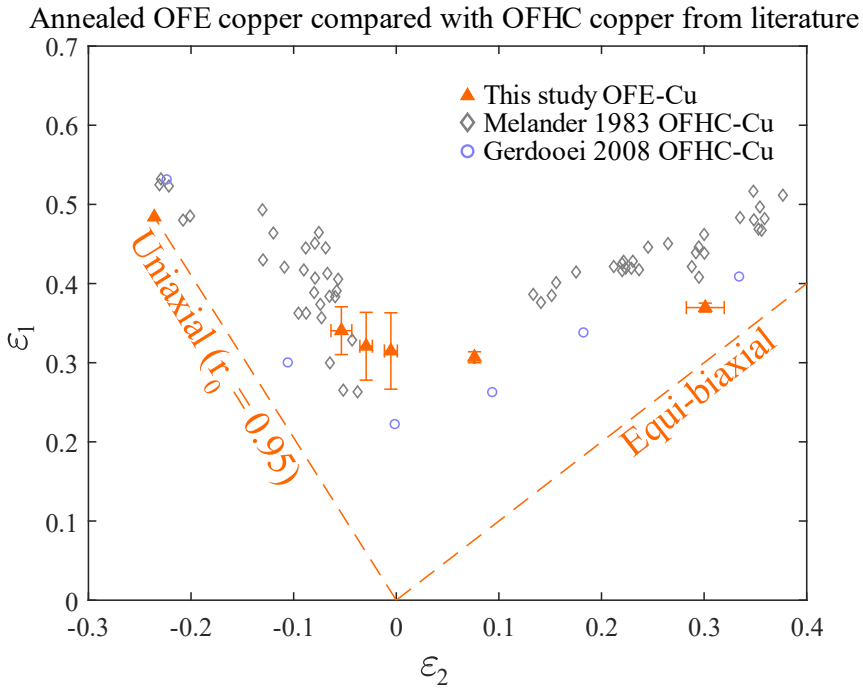

Figure 8.8: Comparison of the experimental FLC of annealed OFE copper with literature data for OFHC from Melander [265] and Gerdooei and Dariani [256]. Error bars represent the standard deviation for tests performed with the same sheet dimensions.

8.3.3. Forming Limit Diagram of High-Purity Niobium

Similarly, the forming limit diagram of high-purity niobium sheets with a thickness of 1 mm was obtained with Marciniak tests. Annealed OFE copper blank carriers with an equal sheet thickness were used. This choice was motivated by the lower cost of OFE copper and due to similar elongation at failure for both materials in standard tensile tests. Recall that the ISO 12004-2:2008 standard [241] specifies that the blank carrier can be made of a different material, as long as it fails after the sheet of interest. Tests were performed on rectangular sheets with a length of 200 mm and varying widths of 80, 100, 120, 140, 150, and 180 mm. In addition to the Marciniak tests, uniaxial tensile tests, based on ASTM E8 standard [196], and plane strain tensile tests, a non-standardized test with the geometry presented in section 7.3.4. were performed and DIC was used to measure the strain fields. Tensile specimens were cut at angles of 0°, 45°, and 90° with respect to the rolling direction in order to calculate

the plastic anisotropy (*r*-value). More details about the method and the material are available in section 7.3.4.

8.3.4. Validity of the Marciniak Tests

The validity of each test was assessed based on the location of the localized neck and the measured strain path. If failure occurred too close to the radius of the punch or with the circular shape of the hole of the blank carrier, the test was discarded and not considered in the following analyses. Three tests were repeated for each condition to ensure repeatability and that enough points are obtained to trace the FLC of high-purity niobium and fully understand the formability for different states of strain. Two tests for both the 140 mm x 200 mm and 150 mm x 200 mm sheet geometries were not considered due to failure at the vicinity of the radius of the punch and with a circular shape. All other tests are considered valid and used in the following sections.

8.3.5. Plastic Strain Anisotropy (*r*-value)

Table 8.2 shows the calculated plastic anisotropy values, following the methodology described in section 7.3.1.2., for the different tensile directions and the mean value r_m at true strains of 0.15 and 0.2. Since the difference is negligible between the two levels of strain, the average value is used in the following section. Those results show that high-purity niobium sheets have anisotropic plastic properties and a higher resistance to thinning in the 0 and 90° directions, i.e. r_0 and $r_{90} > 1$. A high r_m generally enhances the drawability of the sheet, but a non-zero degree of planar anisotropy Δr indicates that earing and other shape defects are expected during the forming process [42].

Table 8.2: Plastic anisotropy coefficients (*r*-value) of niobium in for different rolling directions and strain levels.

r_θ^ε	$\varepsilon = 0.15$	$\varepsilon = 0.2$	average
$\theta = 0°$	1.67	1.66	1.66
$\theta = 90°$	2.30	2.30	2.30
$\theta = 45°$	1.00	0.99	1.00
r_m	1.49	1.49	1.49
Δr	0.982	0.986	0.984

The *r*-value is the largest for the transversal (90°) direction at 2.30 and the smallest for the angled (45°) direction at 1.00. A lower value for the 45° direction is common in other materials, such as cold-rolled and annealed low carbon steel [276]. Since the sheets used in

the Marciniak tests were aligned with the rolling direction parallel to the major strain axis, the *r*-value in the longitudinal (0°) direction of 1.66 is the one used to determine the slope of the straight-line characteristic of a uniaxial tensile test in the forming limit diagram. Yamaguchi et al. [282] studied the recrystallization of cold rolled niobium sheets and measured a residual texture in annealed sheets due to a low dislocation energy that hinders recrystallization. This result could explain the plastic strain anisotropy measured in this study.

8.3.6. Tensile Mechanical Properties and Stress Anisotropy

The tensile mechanical properties of the high-purity niobium polycrystalline sheets used to obtain the forming limit curve of the material were measured. Tensile tests were performed at a nominal strain rate of about 1.0×10^{-3} s^{-1} for the 0°, 45°, and 90° sheet rolling orientations and the stress–strain curves are presented in Figure 8.9. These curves show that the niobium sheets have similar mechanical properties in the different loading directions. The low variation in yield stress and ultimate tensile strength presented in Table 8.3 support the observation made from the stress–strain curves. The mean yield stress and ultimate tensile stress are equal to 98.52 MPa and 180.20 MPa, respectively, using a formulation analogue to the one presented in equation 3.11 to calculate the mean plastic strain anisotropy.

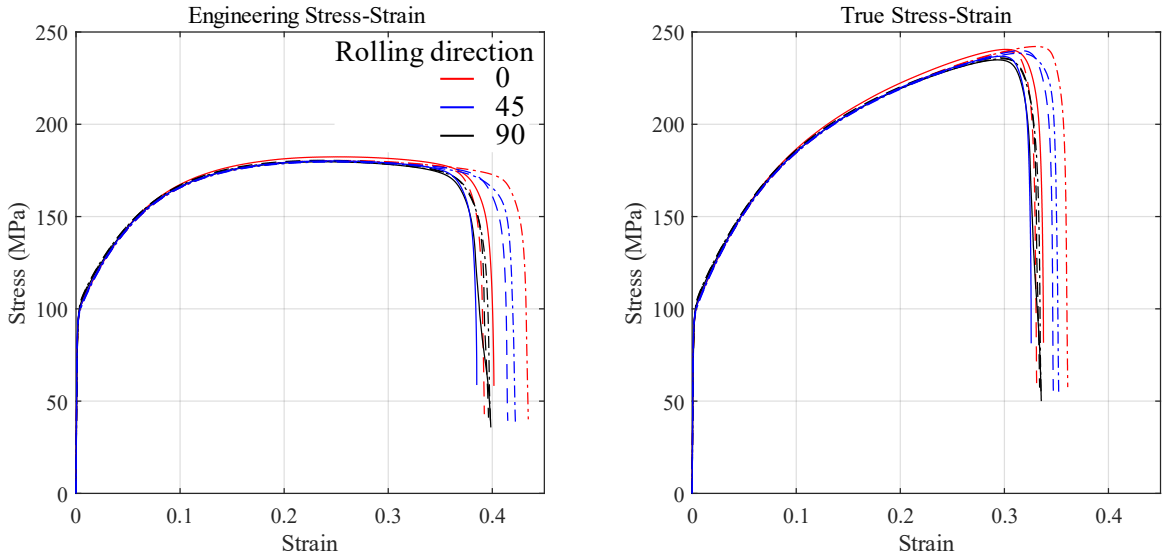

Figure 8.9: (a) Engineering and (b) true tensile mechanical properties of high-purity niobium polycrystalline sheets at a nominal strain rate of 10^{-3} s^{-1} for different rolling directions. Dashed and dash-dotted lines are repetitions of tests with the same rolling direction.

A parabolic hardening coefficient *n* of the Hollomon equation ($\sigma_T = K\varepsilon_T^n$) of 0.236 has been found for the stress–strain curves of Figure 8.9b. However, a simple parabolic hardening constitutive equation, like the Hollomon equation, is not appropriate for niobium since its

strain rate sensitivity is not considered (see Chapter 9). However, the value of *n* was still identified to allow comparisons with different studies.

Table 8.3 also presents the engineering strain at UTS and the post-uniform elongation (difference between the engineering strain at failure and at UTS). The post-uniform elongation is similar for all sheet rolling directions and rather large, with an average value of 0.159. Note that the post-uniform elongation is highest for materials with a large strain rate sensitivity such as niobium. Ghosh [98] reported a monotonically increasing dependence between post-uniform elongation and the strain rate sensitivity exponent m, explained by hardening of the necked region of the specimen due to a local increase in strain rate.

Table 8.3: Tensile mechanical properties at yield and at the maximum load for all rolling directions.

Rolling direction (°)	0.2% yield (MPa)	UTS (MPa)	Eng strain at UTS (-)	Post-Uniform elongation (-)
0	98.60	180.98	0.250	0.159
90	100.35	180.05	0.238	0.159
45	97.56	179.89	0.248	0.160

8.3.7. Marciniak Tests, Strain Paths and the Forming Limit Curve

By extracting the minor and major strain of the valid Marciniak tests, the strain paths and forming limit curve of niobium are found. Since the sheet material showed high anisotropic plastic strain properties, the strain paths and FLC presented in the following section are only valid for the 0° rolling direction.

Figure 8.10 shows the strain paths measured on either side of a neck in Marciniak and tensile test specimens. Since the measurements are taken close to the neck, the last points in this figure are higher than the forming limit curve. Dashed lines are also plotted to present the theoretical strain paths for (1) uniaxial tensile tests, based on the average *r*-value of 1.66 for the 0° orientation, and (2) equi-biaxial tension. As expected, the strain paths of the Marciniak tests are all between those boundaries. At least three specimen geometries yield results for negative and positive minor strains, which ensures that the FLC is representative of the material in all regions of the major–minor strain plot.

The strain paths for tests with negative minor strains are all fairly linear from the beginning of the test (0,0) up to necking, as required by the ISO 12004-2:2008 standard [241]. For the wider sheets with strain paths with positive minor strains, the bi-linear strain path due to a failure of the blank carrier before the blank, as discussed section 8.2. is visible in few

instances for sheets with widths of 150 mm and 180 mm. After inspection of the DIC results and the load vs. punch displacement curves, the blank fails only few frames after the failure of the blank carrier for the 150 mm x 200 mm sheet, which limits the impact of the bi-axial pre-straining on the forming limit curve. For the 180 mm x 200 mm sheets, the change in strain path appears to be more important. Those specimens, identified in Figure 8.10, are then not considered in the elaboration of the FLC as underestimation of the forming limit diagram are expected for tests with highly non-linear strain paths and biaxial pre-straining [248].

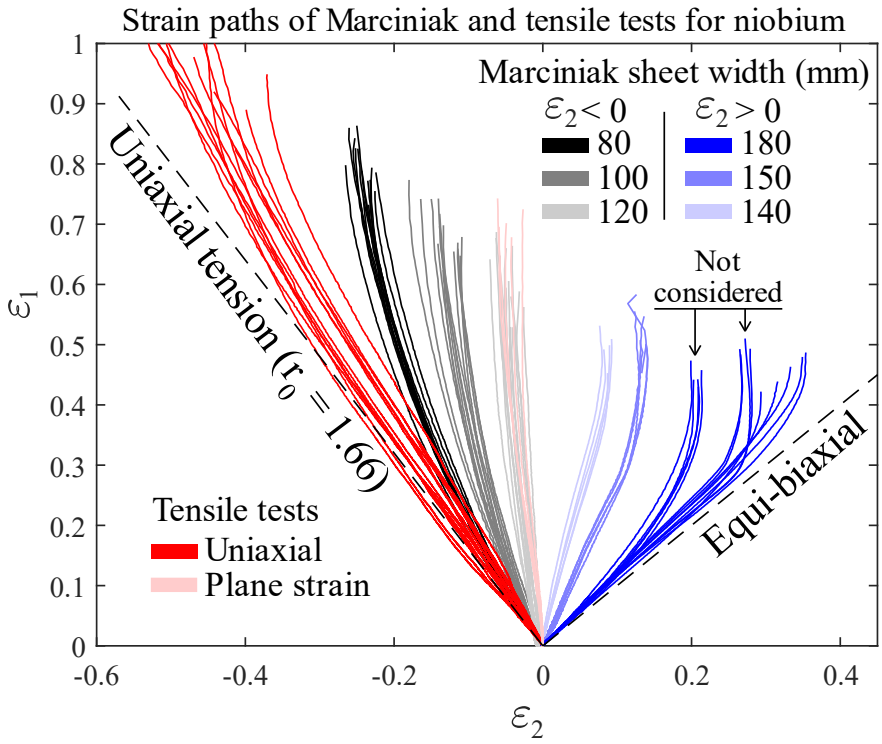

Figure 8.10: Strain paths of the Marciniak and tensile tests for niobium sheets with the major strain aligned with the 0° rolling direction.

Figure 8.11 shows the points of the forming limit curve for all sheets aligned with the rolling direction parallel to the major strain axis for the Marciniak tests and tensile tests in the longitudinal direction. The points of the FLC are determined by fitting the major strain data extracted across the neck, as detailed in section 7.3.4.

For the points with a negative minor strain, a linear trend with a negative slope is visible and characteristic of most forming limit curves. However, the red points corresponding to the uniaxial tensile tests are higher than the straight dashed line plotted based on the plastic strain anisotropy value obtained using the same specimens. The higher points determined using the same method as the one used for the Marciniak tests suggest that the *r*-value of the material is ~1.0. However, calculations of the *r*-value for the 0°, 45°, and 90° specimens in section 8.3.5. clearly show that the sheets have anisotropic plastic strain properties. The major strain

difference of approximately 18% is likely caused by the slightly non-linear strain path in Figure 8.10, which could be due to the failure of the tensile specimens at approximately 45 degrees. Human factors in the calculation of the *r*-values, especially due to the high sensitivity to changes in width [276], could also affect the mean *r*-value. This difference shows the necessity of using a safety margin of about 10% [283][283] when using a FLC in finite element models to predict the formability of a part.

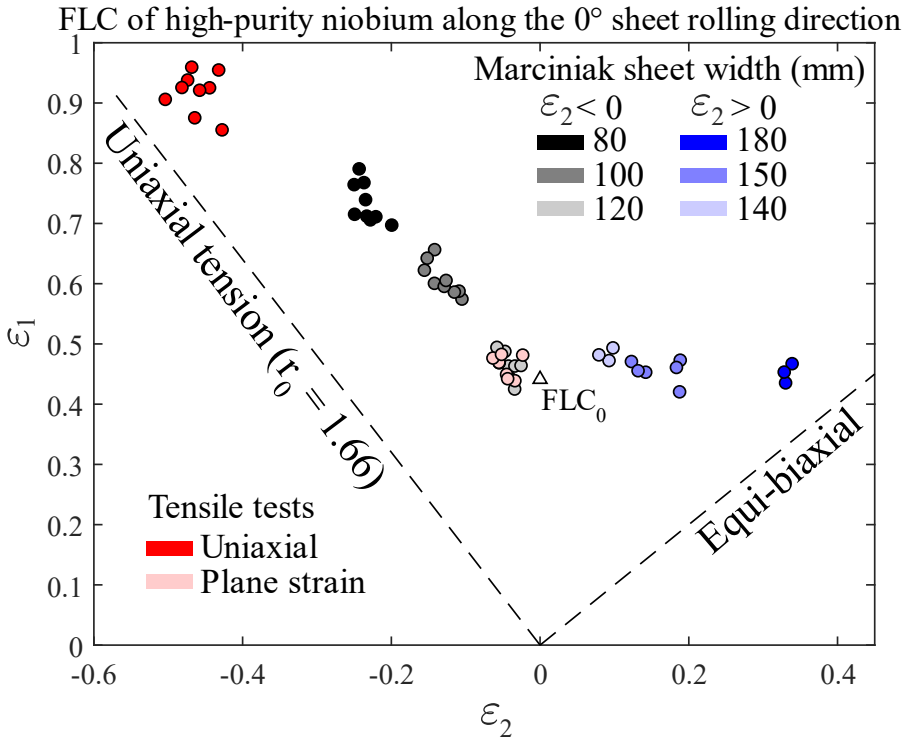

Figure 8.11: Forming limit curve of high-purity niobium for sheets aligned with the rolling direction parallel to the major strain axis and an approximated value of FLC_0 for pure plane strain deformation (n = 0.236 and m = 0.112).

Similar (ε_2,ε_1) points were extracted from the plane strain tensile tests in the longitudinal direction and the 120 mm x 200 mm sheets used in the Marciniak tests. This confirms that the non-standardized plane strain tensile test used in this study is adequate to characterize the formability of the sheet metal for a linear strain path close to the plane strain condition. This specimen geometry and test is much easier to perform than the traditional Nakajima and Marciniak tests as it only requires a standard tensile machine and one camera for 2D DIC. Problems associated with frictions are inexistant, the complex blank carrier design work is not required, and, therefore, it should easily be extrapolated to other materials. Xavier et al. [275] previously used this specimen geometry for interstitial-free and spheroidized SAE 1050 steels and compared the results of the near plane strain tensile tests with Nakajima tests. Experimental results using both techniques and from the literature

confirm the efficacy of the plane strain tensile test to determine the lowest point of the FLC, called FLC_0.

However, for the FLC of niobium, the points obtained from the plane strain tensile and Marciniak tests have $\varepsilon_2 < 0$, which is not a pure plane strain condition. For materials with no initial pre-straining, like the high-purity niobium sheets used in this study, the FLC_0 point is often for $\varepsilon_2 = 0$. A linear extrapolation of the experimental data with negative minor strains was then performed and the intersection of the major strain axis was found at a true strain of 0.441, which corresponds to an estimate of the formability limit for pure plane strain deformation. Recall from section 6.1. that translations of the lowest point of the FLC in the negative or positive minor strain quadrants are expected for uniaxial and equi-biaxial pre-straining, respectively [284]. The former also overestimates the formability limit for biaxial stretching, while the latter underestimates the whole forming limit curve. It is interesting to notice that all points with positive minor strains are approximately at the same major strain. This finding is consistent with the theoretical results reported by Marciniak et al. [252] for viscoplastic materials with a high strain rate sensitivity (see Figure 4 in [252]). The strain rate sensitivity exponent m of the high-purity niobium used in this study is equal to 0.112, based on results from Chapter 9. Also, as discussed in the previous section, a high strain rate sensitivity results in neck stabilization and a higher ductility. An increase in the forming limit diagram from the traditional Swift-Hill model, which predicts that isotropic and strain rate independent materials have their FLC_0 point at a true strain equal to n, is expected for those materials and was reported by Ghosh [98]. The strain hardening coefficient n and the FLC_0 were estimated at 0.236 and 0.441, respectively, suggesting that the high strain rate sensitivity of pure niobium explains its high formability.

8.3.8. Comparison with the Literature

To the best of the author's knowledge, only one previous study published a forming limit curve of high-purity niobium. Daumas and Collard [1] obtained this FLC in 1986 by performing Nakajima tests on 1 mm and 2 mm thick sheets. The sheet was deformed by hydroforming using oil on the top of the sheet and a fixed punch. Table 8.4 shows the mechanical properties that were obtained for the 1 mm thick high-purity niobium sheets used in the study of Daumas and Collard for the 0°, 45°, and 90° rolling directions. By comparison with Table 8.3, the niobium used in the present study has a lower yield and ultimate tensile stress, a higher strain to failure, and different plastic anisotropy coefficients. The lower mechanical properties and higher ductility are probably caused by a higher material purity and a different metallurgical state and pre-deformation history. The fabrication of high-purity niobium sheet requires several steps of lamination and full final recrystallization and

is therefore expensive [23]. It is reasonable to assume that progress was made in the 34 years separating the two studies. Also, the sheets used in this current study were supplied by Ningxia, a Chinese manufacturer that is relatively new in this industry, but delivering sheet with very high purity and residual resistivity ratio (RRR) values.

Table 8.4: Mechanical properties of 1 mm thick niobium sheets used by Daumas and Collard [1].

Rolling direction θ (°)	0.2% yield (MPa)	UTS (MPa)	A% (-)	A% total (-)	$r_\theta^{0.2}$ (-)
0	131	215	0.235	0.37	0.89
90	185	250	0.252	0.41	1.81
45	201	264	0.204	0.32	1.63

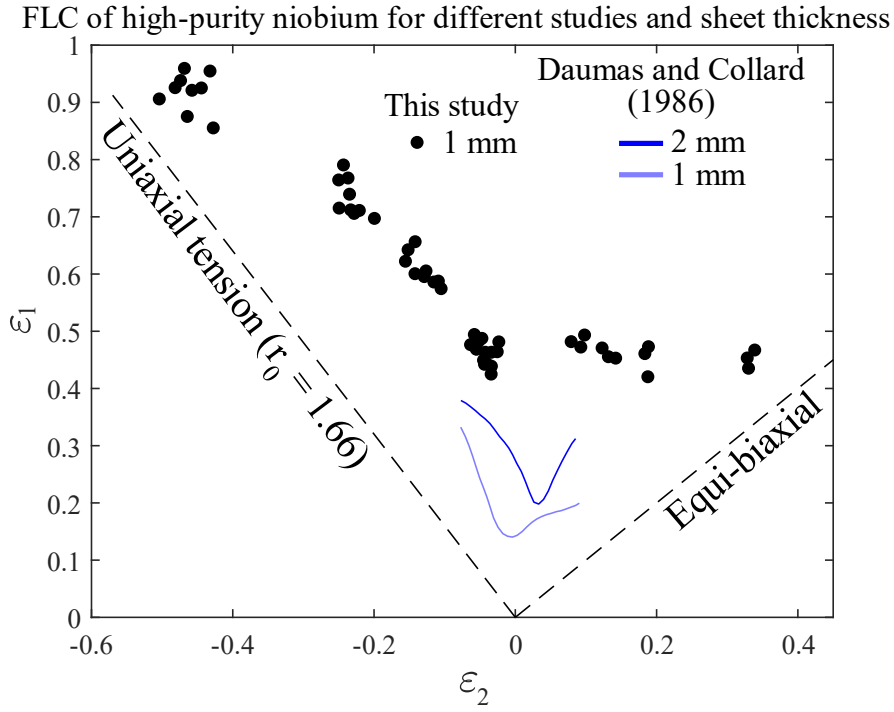

Figure 8.12: Comparison of FLCs of high-purity niobium from this study and Daumas and Collard [1] for sheet thicknesses of 1 mm and 2 mm, respectively.

Figure 8.12 compares the forming limit curves obtained by Daumas and Collard [1] and in the present study. The large difference in FLC and the lower formability of the material used in 1986 is probably related to the different sheet mechanical properties. The very narrow span of that FLC could be caused by friction forces resulting in a facture away from the apex of the punch and non-linear strain path. The translation of the minima of the FLC for the 1 mm thick sheet is likely caused by uniaxial pre-straining, as it was observed in the present study when a Nakajima setup was used.

8.4. Conclusion and Closing Remarks on Forming Limit Diagrams

In conclusion, the forming limit curves of annealed OFE copper and high-purity polycrystalline niobium sheets used to form SRF cavities have been experimentally obtained. Marciniak (in-plane) tests were performed at quasi-static strain rates and annealed OFE copper blank carriers were used for both materials. A blank carrier hole diameter of 30 mm was found to be adequate for both materials. A PTFE sheet was placed between the brass punch and the blank carrier for the study of niobium to reduce friction forces and for necking to occur in the opening of the split blank carrier. The formability limit of niobium is higher than OFE copper for all strain states, as shown in Figure 8.13.

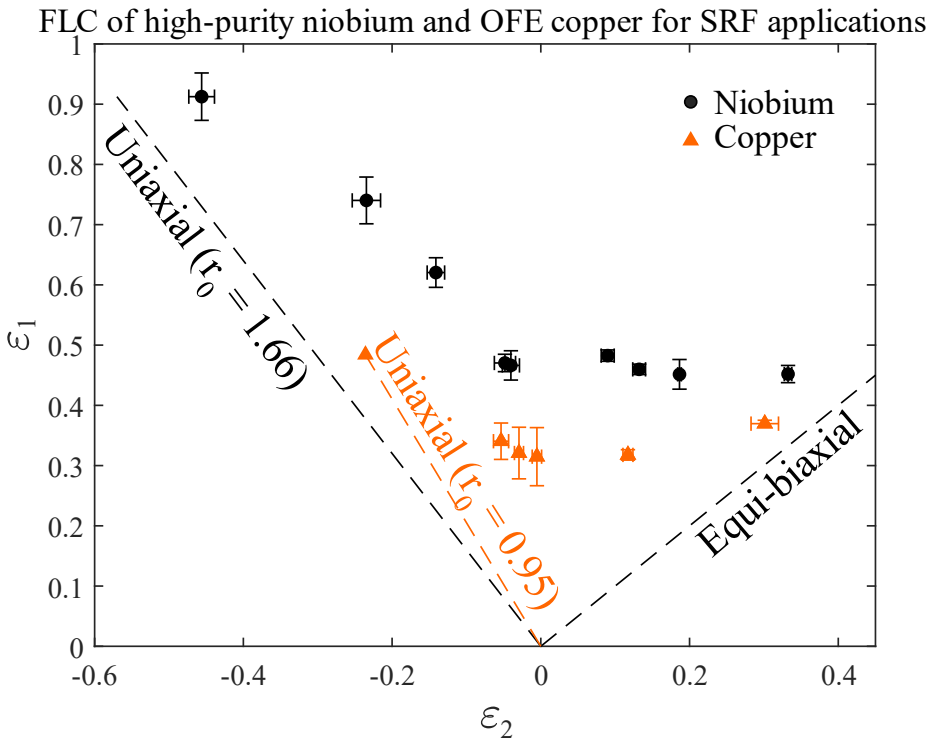

Figure 8.13: Comparison of the forming limit curves of OFE copper ($0.347 < n < 0.485$ and $m = 0.011$) and high-purity niobium ($n = 0.236$ and $m = 0.112$) sheets. Error bars represent the standard deviation for tests performed with the same sheet dimensions.

Since niobium is strain rate sensitive, its formability is expected to be rate dependent. Forming limit curves at strain rates of up to 10^3-10^4 s^{-1} should be experimentally obtained for application to electro-hydraulic forming. Uniaxial tensile tests on niobium single crystals and electron beam welded polycrystalline sheets performed during this study and presented in Chapters 4 and 9, respectively, indicate a reduction in strain to failure for strain rates greater than 10^{-1} s^{-1}. The effect of the strain rate on other modes of deformation for high-purity niobium remains unknown. High strain rate FLC are complicated to obtain due to issues such as friction [285], data acquisition and processing with a high-speed camera, the development of a setup that results in linear strain paths and more. Due to the limited

duration of a PhD and no access to such a setup, this study has not been pursued, but it is recommended as future work.

Note that some work on the formability of OFHC copper at different strain rate has already been done. Gerdooei and Dariani [256] reported an increase in sheet formability for increasing strain rate between 0.01 s^{-1} and 500 s^{-1} for this material. If a high strain rate setup is developed in the future for niobium, an initial study with OFE copper sheets should again be used to optimize the setup and data acquisition system. A BCC sheet metal with a strain rate sensitivity similar to niobium, such as iron or a ferritic steel (i.e. low strength steels), could also be used since the material will probably be cheaper and react to increasing strain rates in a similar manner as niobium.

Finally, the large difference between the FLC of high-purity niobium obtained in the 1986 study of Daumas and Collard [1] motivates the author to recommend the use of the FLC obtained in this study to individuals forming bulk niobium SRF cavities with traditional low strain rate techniques, such as deep drawing and spinning. The high-purity niobium sheets (RRR > 300) produced by Ningxia and used in this study are likely more representative of current state of the art sheets used to manufacture SRF cavities.

Chapter 9 Mechanical Properties of Electron Beam Welded OFE Copper and Niobium

In this chapter, the mechanical properties at low and high strain rates of electron beam (EB) welded oxygen-free electronic copper and high-purity polycrystalline niobium are presented. The objective of this first study of the mechanical properties of EB welded OFE copper and niobium specimens at high strain rate is to explore alternative forming strategies to manufacture seamless SRF cavities, such as the use of rolled and EB welded sheets to produce tubes and form them at high-speed with electro-hydraulic forming. Niobium tubes previously manufactured by sheet rolling and EB welding lacked the required ductility to manufacture cavities, but were only deformed at low strain rates.

Tensile and compression tests were performed at strain rate ranging from 10^{-3} to 10^{3} s^{-1} on the specimen geometries presented in Figure 9.1. The mechanical properties are compared with unwelded specimens (see Appendix E for OFE copper and Peroni and Scapin [182] for niobium) and used to understand the influence of strain rate on welded specimens. All tests were performed at the Joint Research Centre (JRC) in Ispra. The tensile and compression tests at strain rates of 10^{-3} to 20 s^{-1} and 10^{-3} to 10 s^{-1}, respectively, were performed with a servo-hydraulic universal testing machine, as described in section 7.3.2.1. Tests at higher strain rates were performed on tensile and compression split Hopkinson bars systems, described in section 7.3.3.2.

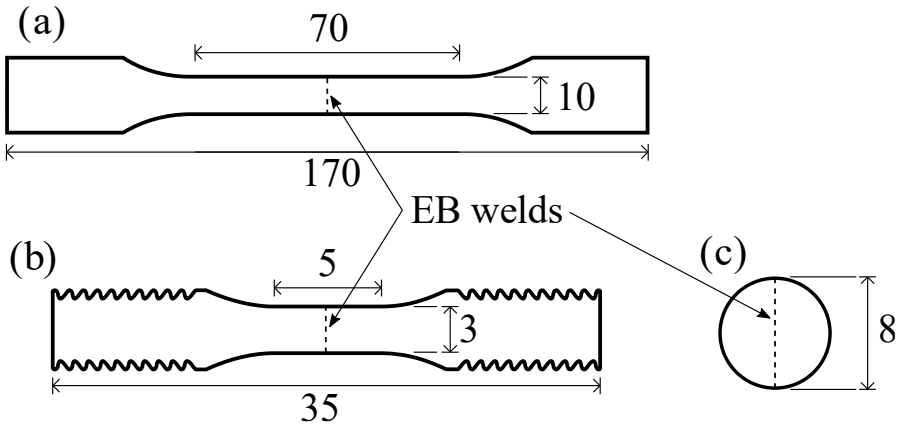

Figure 9.1: Location of the EB welds in (a) long and (b) short tensile and (c) compression specimens. The tensile specimen geometries are the same as in Figure 7.1b and c, with the addition of the location of the EB weld. (All dimensions are in mm).

This chapter is organized as follow. First, the hardness and the microstructure of the EB welded OFE copper and niobium specimens are presented. Second, the tensile mechanical properties of both materials are analyzed with stress–strain curves, and plots of the strength

and the ductility as function of strain rate. Third, strain heterogeneities in tensile specimens with in-situ DIC measurements are presented. Finally, the mechanical properties of compression specimens are presented.

The tensile results presented below have been published in an Open Access research article [286] in the *Journal of Dynamic Behavior of Materials*. Many of the analyses and figures in the following sections have been reproduced from this article.

9.1. Hardness and Microstructure

First, the hardness and microstructure of the EB welded specimens were studied. Hardness was measured across the weld of the cross-section of polished specimens using a Vickers indenter and a load of 200 gf (~1.96 N) applied for 10 s. Measurements were taken in the parent material, HAZ, and fusion zone. The cross-section of undeformed EB welded specimens were polished and etched for microstructure analysis with an optical microscope. Copper was etched with a solution of 5 g $FeCl_3$, 50 mL HCl and 100 mL H_2O and niobium was etched with a solution of 15 mL HF, 35 mL HNO_3, and 75 mL H_2O.

Figure 9.2 shows the Vickers microhardness profile of niobium and OFE copper as a function of the distance from the weld. The hardness of niobium is nearly constant in the fusion zone, the heat affected zone (HAZ), and the parent material (variations between 53 and 58 HV 0.2). Similar values were obtained by Jiang et al. [269]. However, a higher hardness in the HAZ (55 to 60 HV 0.3) compared with regions taken more than 80 mm away from the weld center (49 to 55 HV 0.3) was measured. The nearly constant hardness is consistent with the high-purity of the material and the low contamination during EB welding, due to the vacuum in the chamber. A larger variation in hardness was measured in the OFE copper specimens. The hardness is highest in the fusion zone, with a maximum of 58.2 HV 0.2, lowest in the HAZ with an average of 41.5 HV 0.2, and intermediate in the parent material of the specimen, with an average of 47.1 HV 0.2. The higher hardness in the fusion zone could be due to a combination of multiple factors such as a recrystallized microstructure with smaller grains [287] and residual stresses induced by the welding process [288], [289] and not completely removed by the post-welding annealing heat treatment. Despite the heterogeneous hardness properties in the fusion zone, the measured tensile mechanical properties, i.e. the stress–strain curves up to necking, are similar to unwelded specimens (section 9.2.) and fracture occurred in the region of the fusion zone (section 9.5.).

Figure 9.3 shows the etched microstructure in the cross-section of welded OFE copper and niobium specimens revealing grains and annealing twins. The grains in the HAZ of the OFE copper specimen are larger than in the parent material and the fusion zone. Annealing twins

are also visible in the HAZ and parent material, but not in the center of the weld, where the grains have smoother edges and often converge to a region where crystal nucleation likely started. The niobium specimen, shown in Figure 9.3b, has much larger grains close to center of the weld and in the HAZ (500–1 200 µm), compared to the parent material (20–200 µm). Similar grain dimensions were measured by Jiang et al. for EB butt welds of high-purity niobium [269]. The welded microstructures were not further analyzed as this study focuses on the macroscopic mechanical properties.

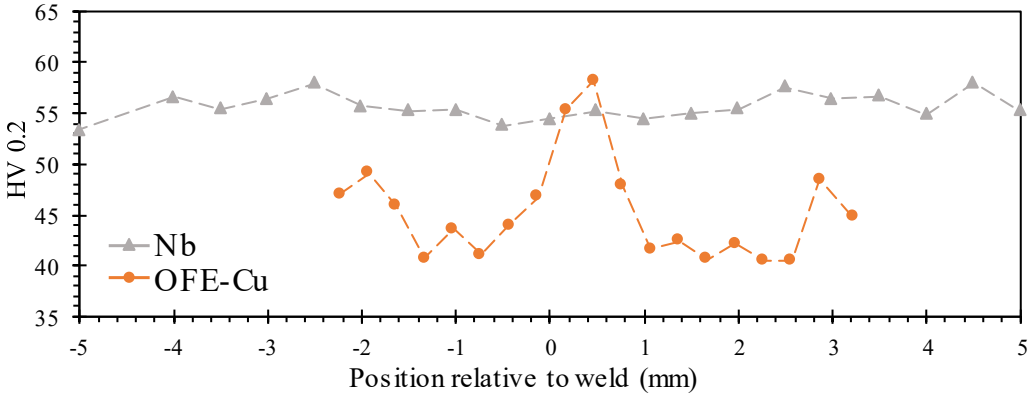

Figure 9.2: Vickers microhardness at different locations along niobium and OFE copper cross-sections.

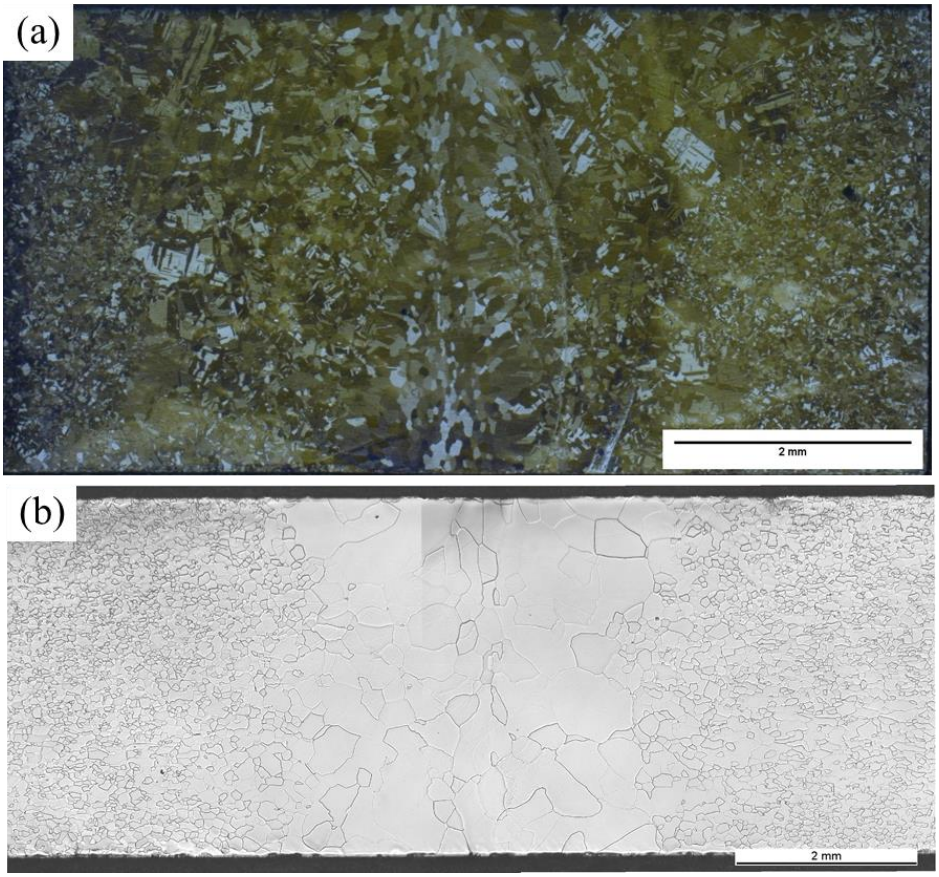

Figure 9.3: Microstructure of the cross-section of etched (a) OFE copper and (b) niobium specimens. The weld is approximately at the center of the pictures [286].

9.2. Tensile Mechanical Properties

Second, tensile tests were performed on EB welded OFE copper and niobium specimens with the standard long specimen geometry and the short specimen geometry, shown in Figure 9.1a and b, respectively. Tests were performed at nominal strain rates of 10^{-3} to 10^{-1} s^{-1} for the long specimens and 10^{-3} and ~1 600 s^{-1} for the short specimens, following the methodologies described in section 7.3.

The engineering stress–strain curves of the short and long specimens are compared in Figure 9.4 for quasi-static strain rates at the same order of magnitude (10^{-3} s^{-1} and 10^{-1} s^{-1}). Similar mechanical properties are measured pre-necking, i.e. before the nominal stress reaches its maximum value. The strain in the small specimens was calculated using DIC by measuring the displacement between two points that were initially separated by about 5 mm and using the displacement of the cross-head of the tensile machine for the long specimens. Note that the initial gage length of 5 mm was selected based on finite element modelling of the quasi-static tensile test of an unwelded OFE copper specimen using known material properties. The stress–strain curve was calculated using the output force and displacement of the specimen from the simulation for a given gage length and compared with the expected response. The similarities in mechanical properties for the long and short specimens confirm that the methodology using DIC and the short specimen geometry are appropriate to characterize the tensile mechanical properties (yield stress and ultimate tensile stress) of welded specimens.

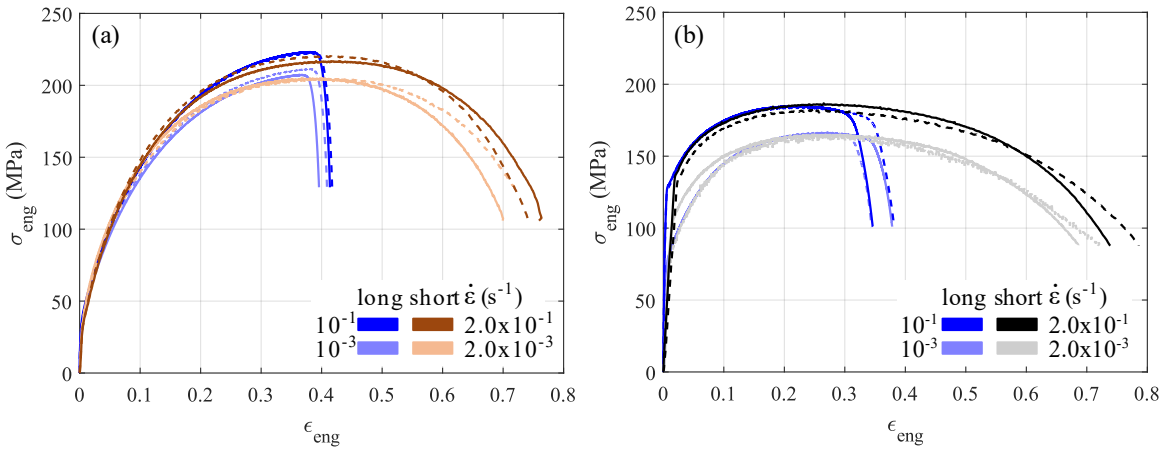

Figure 9.4: Comparison of the tensile mechanical properties of the short and long specimen geometries for EB welded (a) OFE copper and (b) niobium specimens. Dashed lines represent the repetition of a test performed at the same strain rate [286].

Figure 9.5 shows the engineering stress–strain curves of OFE copper and niobium for the short specimen geometry at strain rates of $2.0x10^{-3}$ to ~1 600 s^{-1}. DIC was used for all tests to ensure consistent strain measurements between tests performed with the servo-hydraulic

tensile machine ($\dot{\varepsilon} \leq 20$ s^{-1}) and the split Hopkinson bars and to measure the strain in the gage length only.

The strain rate sensitivity of EB welded copper and niobium are typical of FCC and BCC metals, respectively. The 0.2% yield stress of OFE copper specimens is nearly constant at all strain rates and the flow stress slightly increases for increasing strain rate due to increases in strain hardening, as shown in Figure 9.5a. Note that the 0.2% yield stress was calculated using the apparent elastic modulus in the linear section of the stress–strain curve. However, the end of the elastic domain is ill-defined for OFE copper since plastic deformation appears at low stress. The yield stress of high-purity niobium strongly increases for increasing strain rates (Figure 9.5b). The apparent hardening rate observed in the engineering stress–strain curve decreases and the ultimate tensile stress is reached at a lower strain for increasing strain rate. A similar increase in yield stress and reduction of the apparent hardening was obtained by Peroni and Scapin [182] for unwelded high-purity niobium specimens and by Croteau et al. [176] for niobium single crystals.

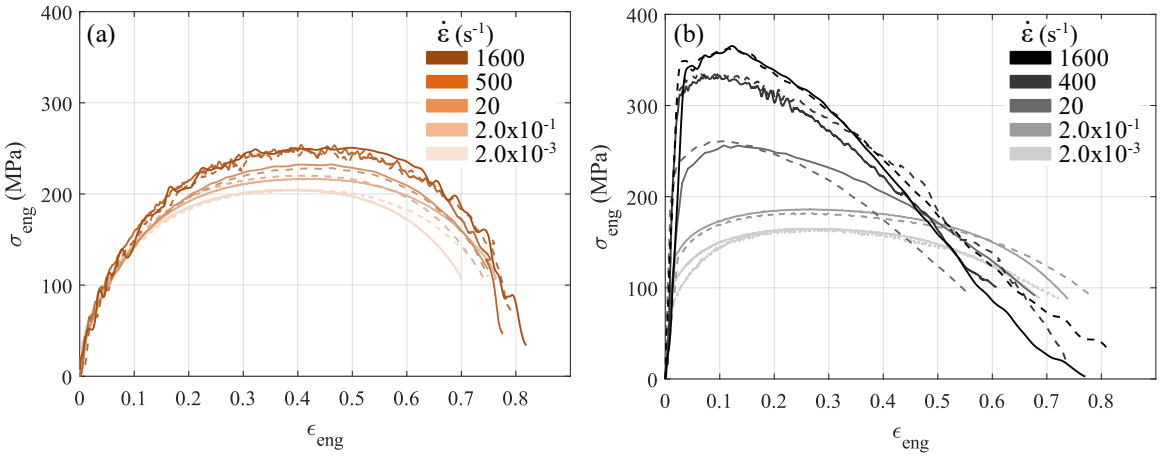

Figure 9.5: Engineering stress–strain curves of EB welded (a) OFE copper and (b) niobium for short specimens deformed at strain rates between 2.0x10^{-3} s^{-1} and ~1 600 s^{-1}. Dashed lines represent the repetition of a test performed at the same strain rate [286].

9.3. Tensile Strength Strain Rate Sensitivity

Figure 9.6 shows the yield stress (YS) and ultimate tensile stress (UTS) as function of strain rate (denoted by $\dot{\varepsilon}$ hereafter) for OFE copper and high-purity niobium for the short (for 2.0x10^{-3} s^{-1} $\leq \dot{\varepsilon} \leq$ ~1 600 s^{-1}) and long (for 10^{-3} s^{-1} $\leq \dot{\varepsilon} \leq$ 10^{-1} s^{-1}) EB welded specimens. The same marker is used for both geometries since similar values are measured at strain rates of the same order of magnitude. The stresses of the welded specimens are compared with those of unwelded specimens from Peroni and Scapin [182] for niobium and from unpublished results obtained by the authors and collaborators from the Imperial College London for OFE copper. The UTS is very similar for the welded and unwelded specimens

for both materials at strain rates between 10^{-3} s^{-1} and 20 s^{-1}. The yield stress is, however, lower by approximately 10 to 18 MPa for the welded OFE copper specimens and within the dispersion of the data for the niobium specimens, for the same strain rate range.

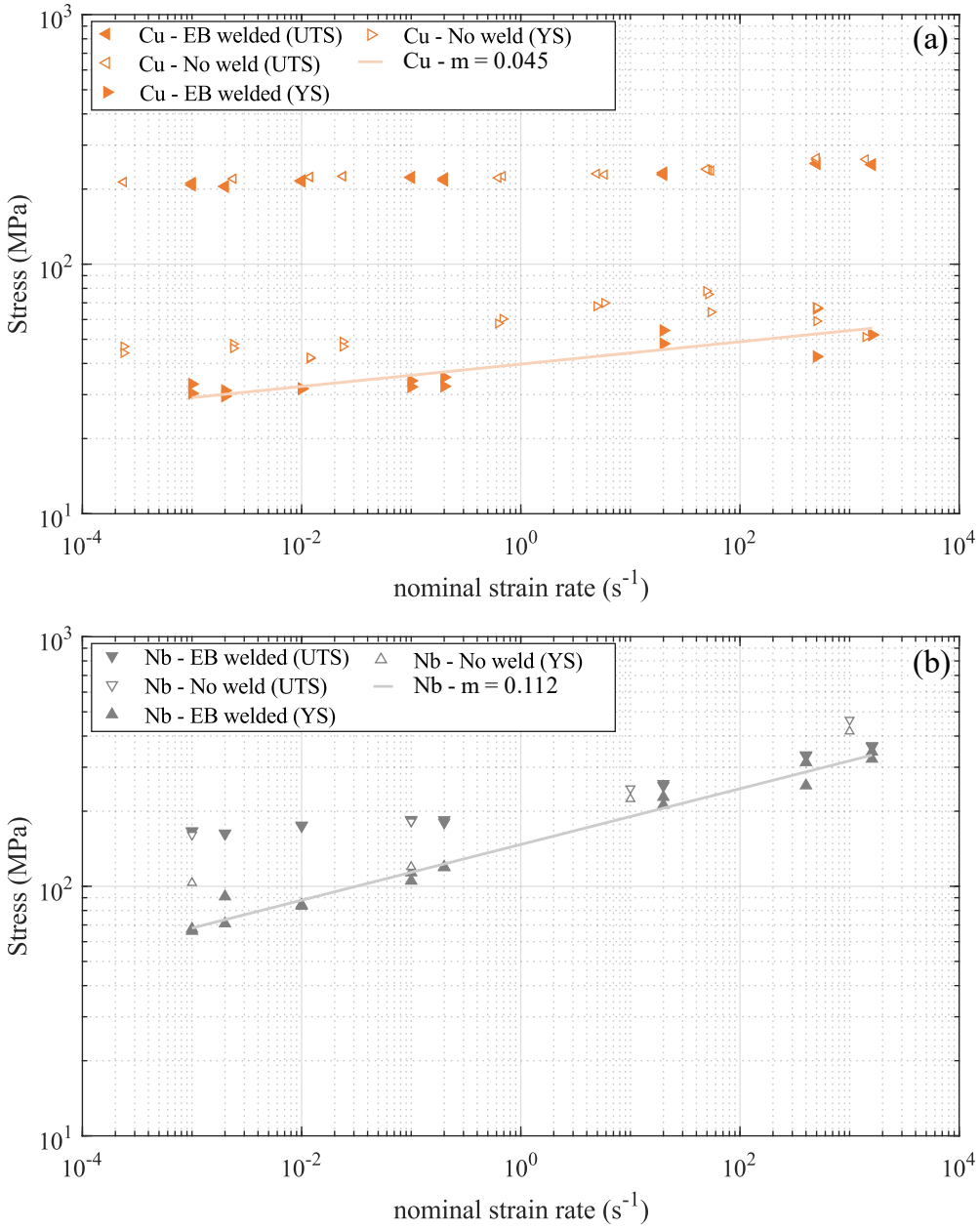

Figure 9.6: UTS and 0.2% yield stress as function of strain rate for (a) OFE copper and (b) niobium EB welded specimens compared with unwelded specimens [182]. Light shaded lines show the strain rate sensitivity (m) of the yield stress [286].

The tensile strength is likely preserved after EB welding due to the high-purity of the parent materials and the low contamination during the welding process. Recall that high-purity OFE copper and niobium have microstructures with a single phase and the welds are performed under vacuum. The welded microstructures are then still composed of a single phase, but with different grain sizes, as described in section 3.1. Thus, the conservation of mechanical

properties is different from what is found for other materials, e.g. high strength low alloy (HSLA) steel, that can have lower and higher tensile strengths for different compositions, welding techniques, and welding parameters [290], [291].

The strain rate sensitivity at yield ($m = \partial \ln \sigma_y / \partial \ln \dot{\varepsilon}$) is approximately constant for both materials and equal to 0.045 for OFE copper and to 0.112 for niobium. A constant strain rate sensitivity at all strain rates in the range studied, shown with two light shaded straight lines in Figure 9.6a and b, indicates that the same dominant deformation mechanism operates at all strain rates. Since the strain rate sensitivity m is derived from a power law relationship ($\sigma_y \propto \dot{\varepsilon}^m$), the use of a log–log plot is more appropriate in the stress as function of strain rate plot to show the differences in m between different materials. A linear scale is often used in literature for the stress axis, but could lead to the false impression that a sudden increase in flow stress is measured at the highest strain rate. The apparent "upturn" in flow stress at strain rates between ~10^3 s^{-1} and 10^4 s^{-1} has been contradicted for few materials and reviewed by Rosenberg et al. [292]. While this upturn phenomenon is not happening in this study, mainly because the highest strain rate is too low, the authors still want to stress the importance of using a logarithmic scale to clearly see changes in strain rate sensitivity, which are caused by a change in deformation mechanism, e.g. from thermal activation to dislocation drag.

A reduction in absolute difference in stress between the UTS and the YS ($\Delta\sigma = \sigma_{UTS} - \sigma_y$) is measured for niobium for increasing strain rates, from approximately 99.3 MPa at 10^{-3} s^{-1} to 28.8 MPa at ~1 600 s^{-1}. This is explained by the lower apparent strain hardening rate (in engineering stress–strain curves) for specimens tested at a higher strain rate. This behavior is typical for BCC metals, see for instance the analysis conducted by Zerilli and Armstrong [207] using dislocation mechanics arguments. For OFE copper, a small increase in $\Delta\sigma$ from ~177.6 MPa at 10^{-3} s^{-1} to ~198.6 MPa at about 1 600 s^{-1} is measured and due to an increasing strain hardening rate for increasing strain rates.

9.4. Ductility Strain Rate Sensitivity

As previously mentioned, and shown in Figure 9.4, the post-necking behavior of the long and short specimens is different for similar strain rates. Higher elongation at break, measured with the crosshead displacement of the tensile machine, was found for short specimens deformed at strain rates in the order of 10^{-3} s^{-1} and 10^{-1} s^{-1}. This is likely explained by the highest thickness-to-width ratio of the short specimens. While the different specimen geometries yield different absolute values of elongation at break, the change in strain to failure is similar for both geometries and materials between strain rates of 10^{-3} s^{-1} and

10^{-1} s^{-1}. Therefore, the effect of strain rate on the ductility of the short specimens, from $2.0x10^{-3}$ to ~1 600 s^{-1}, can reasonably be extrapolated to the standardized geometry.

Due to the high ductility of the materials it is difficult to accurately measure the cross-sectional area of the broken specimens, so the area reduction at failure (A%) is not used to quantify the ductility of the materials [293]. Also, measuring the elongation at break by aligning the broken specimens, as specified in ASTM's E8 standard [196], is difficult due to the non-standardized geometry and, again, the high ductility of both materials. The *nominal strain to failure* (ε_f), defined as the elongation measured using DIC for the last frame before specimen failure (Δy_{DIC}) divided by the initial gage length (L_0) of approximately 5 mm ($\varepsilon_f = \Delta y_{DIC}/L_0$), is used. The last frame was selected based on a visual criterion. The specimen was considered to be broken when a translation of the specimen in the neck perpendicular to the loading direction was observed, even if both ends of the specimen still looked attached. The absolute values of nominal strain to failure are not intrinsic to each material, but the variation across approximately 7 orders of magnitude of strain rate provides valuable information for high-speed sheet forming of SRF cavities.

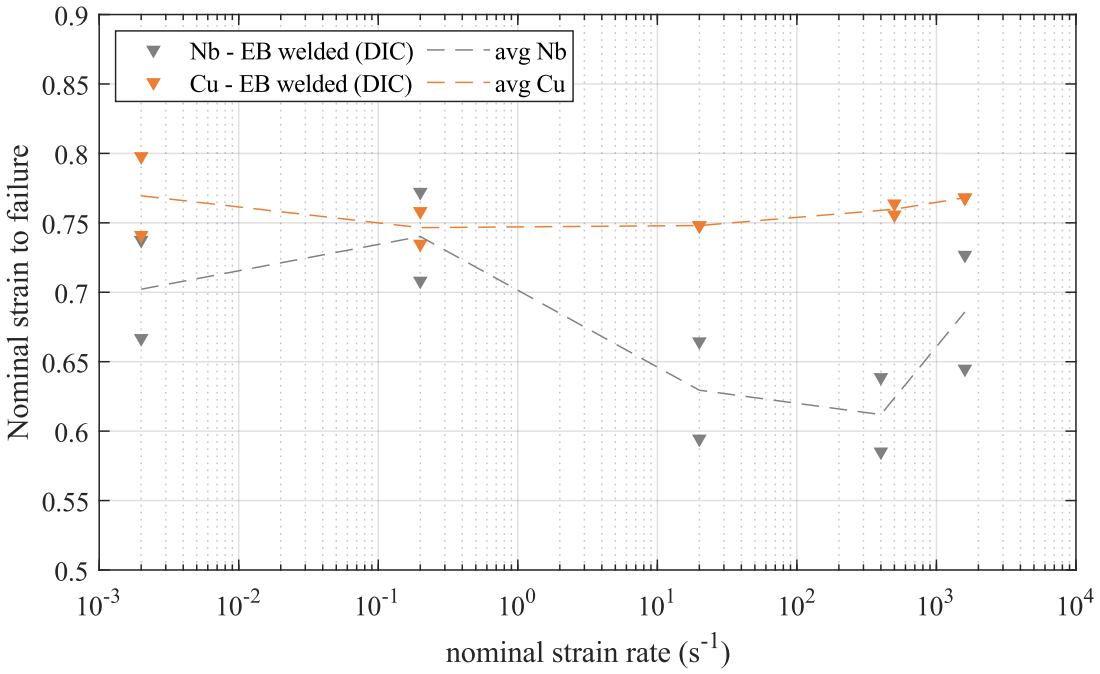

Figure 9.7: Nominal strain to failure measured with DIC for short EB welded OFE copper and niobium specimens for strain rates of $2.0x10^{-3}$ s^{-1} to approximately 1 600 s^{-1}. Dashed lines are used to show trends by connecting the average nominal strain to failure at each strain rate [286].

Figure 9.7 shows the nominal strain to failure as function of strain rate for short OFE copper and niobium welded specimens. Similar to the variation in yield and tensile strengths with strain rate (Figure 9.6a and b), the nominal strain to failure is almost constant between $2.0x10^{-3}$ s^{-1} and ~1 600 s^{-1} for EB welded OFE copper (the mean and standard deviation of

ε_f for all strain rates are equal to 0.75 and 0.01, respectively). The ductility of niobium is lower, less repeatable between tests performed at the same strain rate, and more strain rate sensitive than OFE copper. Average maximum and minimum nominal strains to failure of 0.74 ± 0.03 and 0.61 ± 0.03 were measured at strain rates of 2.0×10^{-2} s^{-1} and 400 s^{-1}, respectively.

Peroni and Scapin [182] reported a relative reduction in strain to failure of about 20% between strain rates of 10^{-1} s^{-1} and 10 s^{-1} for unwelded high-purity niobium (calculated using the engineering strain at an engineering stress of zero at the end of the published stress–strain curves). EB welded specimens deformed at the same order of magnitude of strain rate showed a similar relative reduction in nominal strain to failure of approximately 15%. The increase in strain rate between quasi-static and intermediate rates is then reducing the ductility of welded and unwelded high-purity niobium. A reduction in ductility varying from 16 to 50% was also reported by Croteau et al. [176] (Chapter 4) for niobium single crystals with different crystallographic orientations deformed at strain rates of 10^{-2} s^{-1} and ~10 s^{-1}.

The nominal strain to failure for the welded niobium specimens deformed at ~1 600 s^{-1} is higher than for specimens deformed at 20 s^{-1} and ~400 s^{-1}. The cause of the increase in ductility when the strain rate goes from ~400 s^{-1} to ~1 600 s^{-1} is unknown, but it could be due to inertia effects that yield a stabilizing effect and enhance the ductility at very high strain rate [50]. However, the ductility remains lower than at quasi-static strain rates, which could be detrimental for high-speed sheet forming. Nevertheless, strain rates achieved in high-speed forming operations are generally larger than the maximal strain-rate considered in the present experiments. This can contribute to enhance inertia effects and the resulting formability improvement [294], [295]. Moreover, in high-speed sheet forming, part of the deformation takes place during the impact of the sheet on the die. This phenomenon can also contribute to enhance formability [51], [52].

9.5. Strain Heterogeneities and Necking

Figure 9.8 shows the true (logarithmic) axial strain distribution in EB welded niobium specimens (short geometry) deformed at nominal strain rates of 2.0×10^{-3} s^{-1}, 2.0×10^{-1} s^{-1}, and ~1 600 s^{-1}. The axial true strain line scans in the gage section shown in Figure 9.8a1, b1, and c1 reveal a region of lower strain close to the center of the specimen and surrounded by two peaks. This behavior is probably due to microstructural heterogeneity in the vicinity of the weld. The large strain heterogeneities, compared with OFE copper in Figure 9.9, suggest that the anisotropic properties in the large niobium grains in the center of the specimen, as shown in Figure 9.3b, affect the localization process. Moreover, Figure 9.3b shows that the grain size is larger in the HAZ than in the fusion zone. These grain size heterogeneities may

be responsible for the two peaks observed in the strain distribution (Figure 9.8). In contrast, the more homogenous strain distribution in OFE copper specimens is probably due to the more homogeneous grain size distribution. Note that plastic flow localization takes place near the center of the specimens for both materials and at all strain rates. It is believed that this phenomenon is due to the presence of the weld (and not to the rather short specimen length) as it also occurs with the long specimens. Figure 9.10 shows a comparison of the true strain distribution in the gage length between long and short specimens deformed at strain rates in the order of 10^{-3} s^{-1}. The neck appears to be skewed to the right side of the gage length (corresponding to the upper-half of the specimen, which is closer to the moving end of the tensile machine) for the long specimens due to a reduced field of view to capture details in the fracture at a high resolution. However, fracture occurred at the center of the specimen at all strain rates for both materials. This suggests that the weld acts as an imperfection that promotes plastic flow localization in its vicinity.

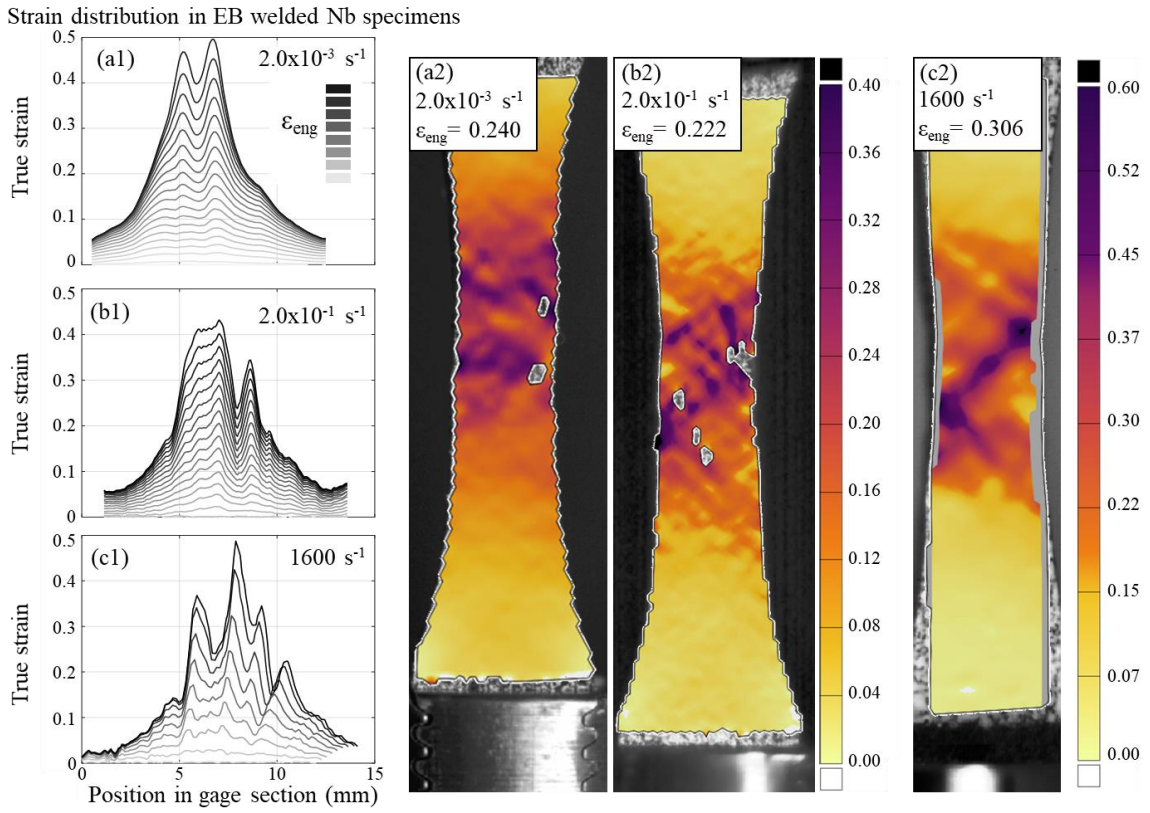

Figure 9.8: Axial strain distribution along the centerline of the gage section of the short EB welded niobium specimens for increasing engineering strain and spatial strain distribution from DIC at strain rates of (a1, a2) 10^{-3}, (b1, b2) $2.0x10^{-1}$, and (c1, c2) ~1 600 s^{-1} [286].

The true strain peaks and valley around the center of the short niobium specimen (Figure 9.8), which was attributed to grain size heterogeneities, is not as pronounced for the long niobium specimen (which has a larger width). The influence of the weld on the mechanical properties seems to be more important for the short niobium specimens. This is probably

because size effects from the large grains in the fusion region begin to be apparent (at the scale of the short specimen). Based on the grain size measured in the fusion zone in section 9.1, there are approximately 3 to 6 grains across the width of the short specimens compared with about 10 to 100 grains for the long specimens.

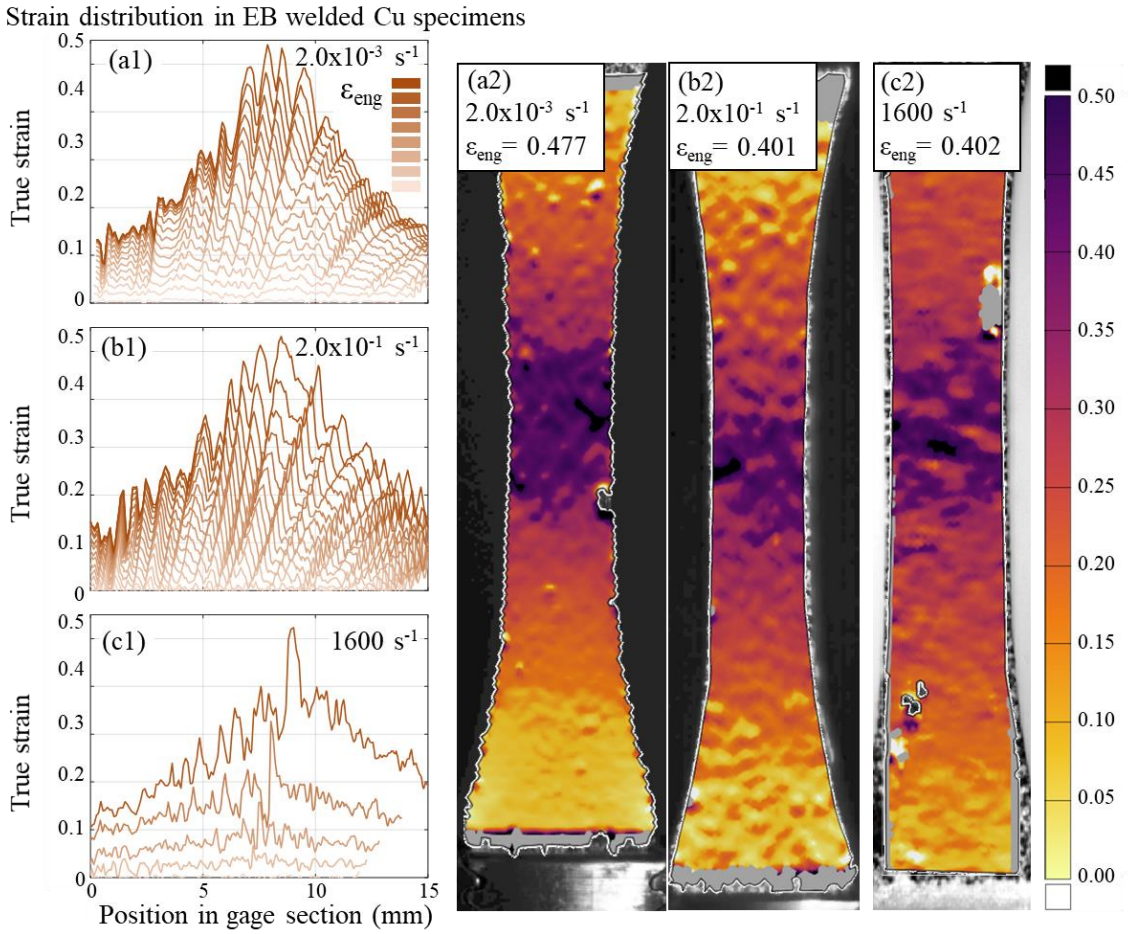

Figure 9.9: Axial strain distribution along the centerline of the gage section of the short EB welded copper specimens for increasing engineering strain and spatial strain distribution from DIC at strain rates of (a1, a2) $2.0x10^{-3}$ s^{-1}, (b1, b2) $2.0x10^{-1}$ s^{-1}, and (c1, c2) ~1 600 s^{-1} [286].

Figure 9.11 shows long and short OFE copper and niobium specimens deformed at strain rates in the order of 10^{-3} s^{-1} during necking and after failure. Those pictures were acquired in-situ and used in the digital image correlation analyses. The long niobium specimen shows a more acute neck (the section reduction is more marked) and a narrower fracture surface than the long copper specimen. This indicates larger plastic strain in the neck of niobium specimens after the onset of localization, which suggests that niobium is intrinsically more ductile than OFE copper (the local strain to failure, at the center of the neck, is larger for niobium than for OFE copper[2]). The difference in dimensions in the gage section of the short

[2] The local strain to failure (at the neck center) should not be confused with the nominal failure strain (Figure 9.7). The latter corresponds to an average strain between two points of the specimen. It does not characterize only the failure of the material, but also the plastic flow localization process.

and long specimens (e.g. higher thickness-to-width ratio for the short specimen) resulted in different neck morphologies for both materials. The short OFE copper specimen has a narrower fracture surface than the long one and a non-symmetric neck is observed in the short niobium specimen. The latter is probably caused by material heterogeneities and anisotropic properties at the center of the specimen from the low amount of grains across the width and thickness of the specimens. During the manufacturing of SRF cavities, size effects should be negligible due to the large sheet dimensions and a more uniform strain distribution (Figure 9.10b) is expected.

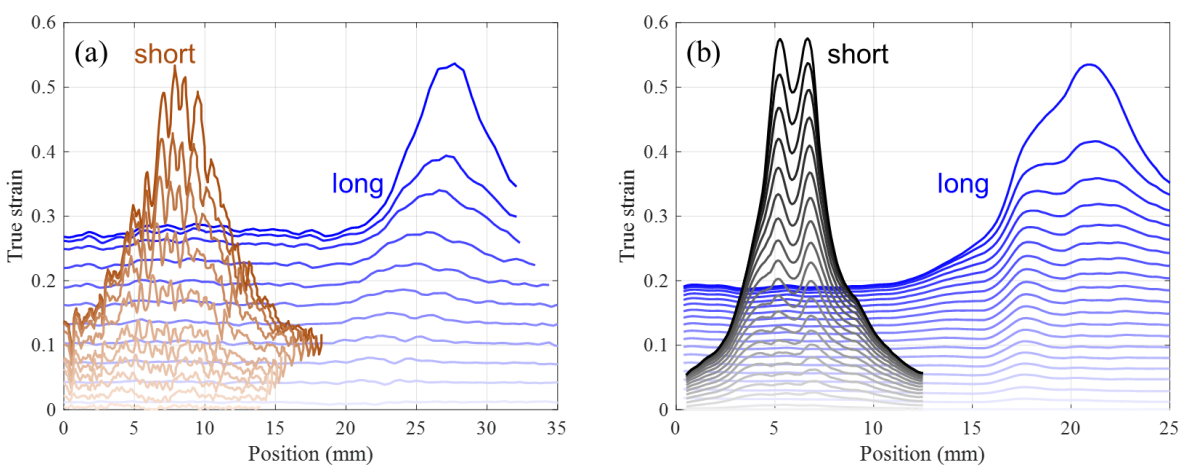

Figure 9.10: Axial strain distribution in the gage length of long and short (a) OFE copper and (b) niobium specimens deformed at strain rates in the order of 10^{-3} s^{-1} [286].

9.6. Compression Results

Cylindrical EB welded OFE copper and niobium specimens with the geometry shown in Figure 9.1c (diameter of 8 mm and initial thickness of 3.96 mm) have been deformed in compression at strain rates of 10^{-3} to ~1 500 s^{-1}. The servo-hydraulic universal testing machine, used at strain rates of up to 10 s^{-1}, and the split Hopkinson bars system used at higher strain rates are presented in section 7.3. The weld of the specimens was aligned with the center of the field of view of the camera to observe potential heterogeneities. This study is of interest for high-velocity sheet forming with techniques like electro-hydraulic forming (EHF), since through-thickness stresses can be generated upon impact of the blank on the die. The mechanical behavior of the EB welds at high strain rate is then of interest for manufacturing of seamless SRF cavities with rolled and welded tubes and EHF. Figure 9.12 shows the true stress–true strain curves for both materials. Similar to the tensile specimens, low average 0.2% yield stresses of 53.40 MPa and 123.25 MPa were measured for OFE copper at strain rates of 10^{-3} s^{-1} and ~1 500 s^{-1}, respectively. The calculation of the yield stress at an offset of 0.2% is not trivial for OFE copper since the elastic region is short and the transition from elastic to plastic deformation is gradual. A significant increase in yield

stress from 90.35 MPa to 521.64 MPa was measured for niobium at strain rates of 10^{-3} s^{-1} and ~1 000 s^{-1}. The noise in the stress–strain curve is not affecting the estimation of the 0.2% yield stress, since the interception of a line with a slope equal to the apparent elastic modulus and the stress–strain curves occurs before the first oscillation. A saturation of the flow stress was measured in the niobium specimens deformed at strain rates of 10 s^{-1} or higher.

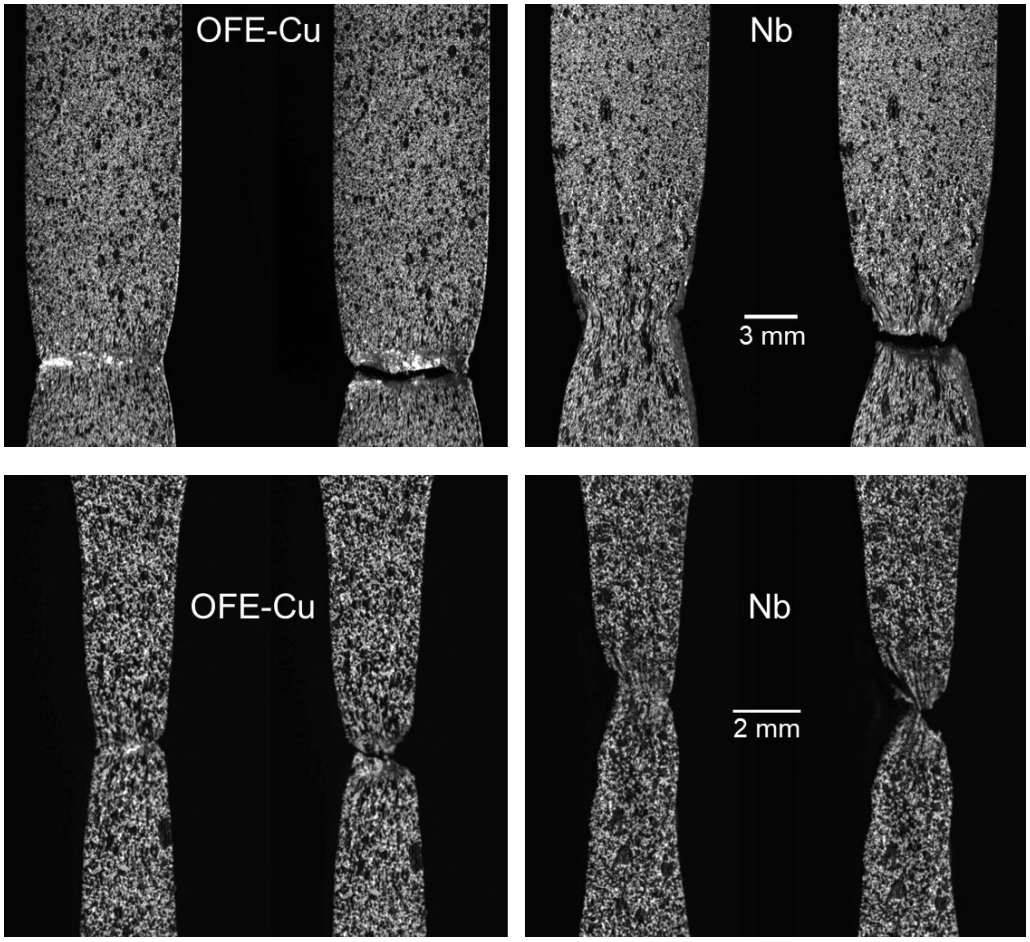

Figure 9.11: In-situ images of OFE copper and niobium during necking and at fracture for tests performed on (top) long and (bottom) short specimens deformed at nominal strain rates in the order of 10^{-3} s^{-1} [286].

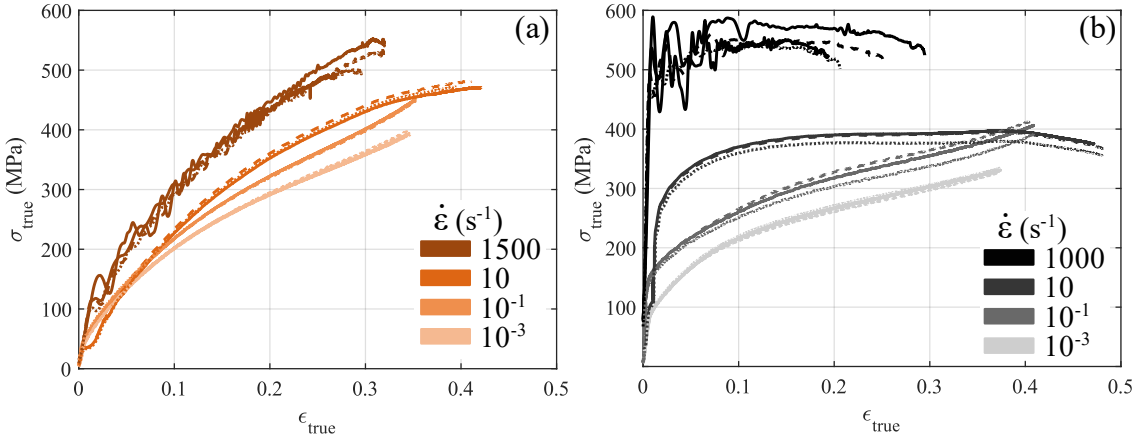

Figure 9.12: True stress–strain curves of EB welded (a) OFE copper and (b) niobium compression specimens deformed at strain rates between 10^{-3} s^{-1} and ~1 500 s^{-1}. Dashed lines represent the repetition of a test performed at the same strain rate.

Figure 9.13 shows the evolution of the yield stress as function of strain rate for both materials in compression and in tension. A higher yield stress was constantly measured in compression for both materials. More precisely, the yield stress was higher by about 19 MPa and 212 MPa at strain rates of 10^{-3} s^{-1} and 1 000 s^{-1}, respectively, for niobium and by about 17 MPa and 62 MPa at strain rates of 10^{-3} s^{-1} and 1 000 s^{-1}, respectively, for OFE copper. Higher strain rate sensitivity exponents m of 0.130 and 0.065 were measured in compression for niobium and OFE copper, respectively. A higher strain rate sensitivity at a true strain of 0.05 was also measured for unwelded annealed OFE copper specimens deformed in compression (m = 0.021), compared to tension (m = 0.010), see Appendix E. This tension/compression asymmetry is likely independent of the presence of a weld.

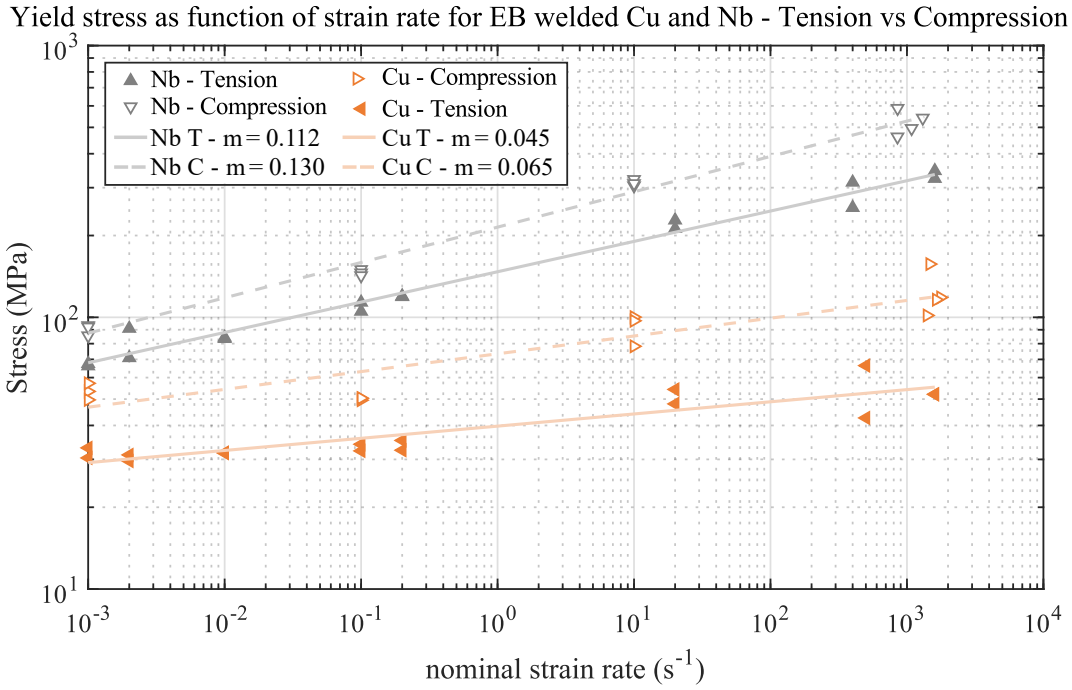

Figure 9.13: Yield stress as function of strain rate in tension and compression for EB welded OFE copper and niobium specimens.

Digital image correlation can also be used with tests on compression specimens. However, the out-of-plane deformation quickly brings the side of the specimen out of focus and the curved sides require the use of two cameras to perform 3D DIC. Only one camera was used in this study to observe possible heterogeneous deformations due to the presence of a weld. The EB weld was always placed toward the aperture of the camera. Figure 9.14 shows in-situ images acquired from the beginning (0 s) to the end (8 min) of a compression test at a strain rate of 10^{-3} s^{-1}. An asymmetrical barreling shape is visible from 4 min 54 s onward. This might be caused by slightly different friction coefficients between the top and bottom surfaces of the specimen and the compression testing setup. No heterogeneous deformations due to the presence of a weld were observed on specimens deformed at low and high strain

rates, which suggests that the influence of the weld on final geometry of the specimen is negligible in compression.

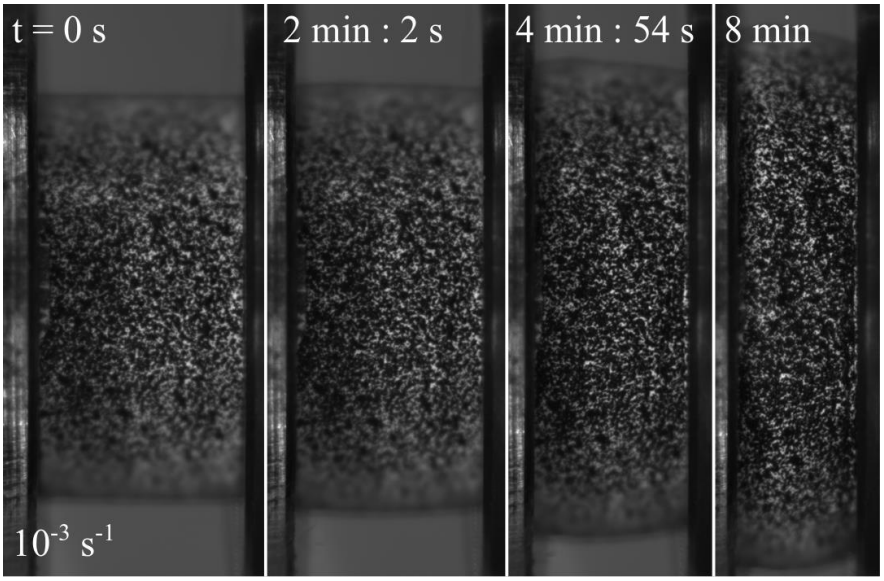

Figure 9.14: In-situ pictures of the profile of an EB welded niobium specimen deformed in compression at a quasi-static strain rate of 10^{-3} s^{-1}.

9.7. Conclusions on the Study of EB Welds

In conclusion, the microstructure and the mechanical properties of electron beam welded high-purity polycrystalline niobium and annealed OFE copper sheets were measured in tension and compression at strain rates of 10^{-3} to 10^{3} s^{-1}. Large grains were observed in the fusion and heat affected zone of niobium specimens and grains smaller than the HAZ were found in OFE copper specimens. The 0.2% yield and ultimate tensile stresses of welded specimens was similar to unwelded specimens for both materials and at all strain rates. The nominal strain to failure ε_f of niobium reached a maximum value of 0.74 ± 0.03 at 2.0×10^{-1} s^{-1} and a minimum value of 0.61 ± 0.03 at 400 s^{-1}. The ductility of OFE copper was higher than niobium, at an average ε_f of 0.75 ± 0.01 at strain rates of 2.0×10^{-3} to 1 600 s^{-1}. The low standard deviation showed that the effect of the strain rate is negligible, which is promising for high-speed sheet forming processes like electro-hydraulic forming. All niobium and OFE copper specimens failed approximately at the center of the gage length, i.e. in the fusion zone. Finally, the mechanical properties were measured in compression. A strain rate sensitivity higher than in tension was calculated and no heterogeneous deformations were observed around the weld.

Chapter 10 Conclusion and Perspectives

In this thesis, a thorough study of the mechanical and formability properties of OFE copper and high-purity niobium, the substrates of SRF cavities, was presented for quasi-static (10^{-4} s^{-1}) to high (10^{3} s^{-1}) strain rates. Notable contributions to the scientific knowledge are (1) the mechanical properties of niobium single crystals in tension and compression at strain rates greater than 10^{-1} s^{-1} and the associated microstructures, (2) the forming limit diagram of high-purity polycrystalline niobium, and (3) the mechanical properties of electron beam welded annealed OFE copper and high-purity polycrystalline niobium at strain rates greater than the quasi-static regime. Those results will help researchers and industrials to manufacture SRF cavities with conventional techniques, such as deep drawing and spinning, and with high-speed sheet forming techniques, such as electro-hydraulic forming.

Chapter 1 introduced SRF cavities, from their roles in particle accelerators to their manufacturing process. Chapters 2 and 6 summarized important concepts and the relevant literature to understand the results presented in Chapters 4, 5, 8, and 9.

In Chapters 3 and 7, details about the materials studied and the experimental methods are presented. The methodology used to select niobium single crystal orientations of interest for tensile tests is presented. This method and the associated plots could be used for other BCC metals and adapted for other lattice structures where a selection of crystal orientation is possible. The different instruments used to measure mechanical properties at quasi-static, intermediate, and high strain rates and forming limit diagrams, and to analyze the microstructure of deformed specimens, from features visible at the surface of specimens to dislocations, are presented. The associated data analysis techniques are also detailed. These chapters can be used as references for researchers and professionals that are conducting similar tests or analyses or for individuals who want to reproduce the results presented in this study.

10.1. Part I – Niobium Single Crystals

10.1.1. Conclusions

Chapter 4 presents the mechanical properties of high-purity niobium single crystals deformed in tension and compression at strain rates of about 10^{-4} to 10^{3} s^{-1}. The results at strain rates higher than 10^{-1} s^{-1} are fundamental to understand the behavior of niobium single crystals as function of strain rate for different crystal orientations and, ultimately, for sheet forming of a large-grain niobium disk into a half-cell at high-speed with electro-hydraulic forming. The tensile stress–strain curves at strain rates of 1.28×10^{-3} s^{-1} and 1.28×10^{2} s^{-1}

showed anisotropic mechanical properties in the plastic domain. A significant increase in yield stress, expected for a BCC metal, and, more importantly, a reduction of anisotropic properties were measured at ~10^3 s^{-1}. The latter is likely caused by the activation of more slip systems at high strain rate than at low strain rate and the dislocation substructure observed in a specimen deformed at a ~1 000 s^{-1} supports this explanation. A possible implication of this result on high-speed sheet forming of SRF cavities is a higher shape accuracy. However, a reduction of strain to failure was measured at strain rates greater than $1.28x10^{-2}$ s^{-1}.

The mechanical properties of compression specimens showed three-stage hardening for most crystal orientations and a linear correlation between the sum of the projection angles of the initial crystal orientation in the loading direction on the [001]–[111] and the [101]–[111] boundaries of an inverse pole figure with the true stress at a strain of 0.05. Asymmetrical tensile and compression mechanical properties were measured. The flow stress was higher in compression at low strain rates for specimens with an initial orientation close to [001] and higher in tension at low strain rates for specimens with an initial orientation close to [111]. The flow stress in tension was consistently higher than in compression at strain rates in the order of 10^3 s^{-1}. This result could not be physically explained by a change in dominant deformation mechanism, such as a transition from a thermally activated mechanism to viscous drag of dislocations, or to effects of the geometry of the tensile specimens. The log–log strain rate sensitivity of specimens deformed in tension and compression was found to be dependent on the initial crystal orientation. The lowest strain rate sensitivity was measured close to the [001] direction, while the highest strain rate sensitivity was measured close to the [111] direction and the [101]–[111] boundary of an inverse pole figure.

In Chapter 5, the microstructure of the deformed single crystals was extensively studied with electron backscattered diffraction. Tensile specimens deformed at low strain rates showed a gradual crystal rotation from the grip region of the specimen to the fracture surface and, in some instances, a microstructure with shear bands in the gage section. The latter heterogeneous microstructure is believed to be formed in specimens where the Schmid factor is similar on two {112}<111> slip systems with Burgers vectors in different orientations.

An investigation of differences of dislocation substructures for different crystal orientations and strain rates, observed with transmission electron microscopy, was presented. A high density of long dislocations, often preferentially aligned on a {110} plane, was observed on specimens deformed at low strain rates. A specimen deformed at a strain rate of ~10^3 s^{-1} and with an initial crystal orientation close to the center of an inverse pole figure showed short and homogeneously distributed dislocations with multiple loops. This suggests that

dislocations were gliding on multiple slip systems and intersected each other, which explains the homogeneous distribution and the short dislocation segments, respectively. The absence of cell walls and low angle grain boundaries, i.e. regions with a high dislocation density, in the specimen deformed at high strain rate might lead to a lower magnetic flux trapping and penetration at superconducting conditions. This could increase the performances of SRF cavities and be an important advantage of high-speed sheet forming.

10.1.2. Perspectives

The measurement of the mechanical properties of niobium single crystals at high strain rate in this study give important information for electro-hydraulic forming of SRF cavities with large-grain disks. Due to the anisotropic mechanical properties measured at low and intermediate strain rates and due to the apparent higher effect of non-Schmid behavior at high strain rate, a crystal plasticity model should be developed to accurately predict the deformation of the disk during EHF. The development of such model was beyond the scope of this thesis. Note that crystal plasticity modeling of niobium single crystals is the subject of current investigations in the group of Dr. Philip Eisenlohr at Michigan State University. The experimental stress–strain curves presented in this thesis can be used to validate a crystal plasticity model.

This hypothesis on the lower flux penetration due to shorter dislocations that are homogeneously distributed in specimens deformed at high strain rate shall be experimentally verified with techniques such magneto optical imaging. This measurement has previously been performed at the National High Magnetic Field Laboratory in the United States. If this hypothesis is confirmed, the advantages of high-speed sheet forming of SRF cavities with EHF would be beyond a higher shape accuracy and an inner surface with a lower roughness. The dislocation substructures of specimens deformed in compression at different strain rates will also be analyzed with transmission electron microscopy and compared with the tensile specimens and the results of Edington [155]. The effect of a heat treatment, which is always performed between cavity manufacturing and operation, on the dislocation substructure should be measured.

Finally, nanoindentation tests at high strain rates ($\sim 10^3$ s^{-1}) should be conducted to investigate size and strain rate effects. Hardness measurements as function of strain rate for different crystal orientation could be compared to the strain rate sensitivity measured in tension and compression in this study. The dislocation substructures below indents made at different strain rates on single crystals with different initial orientations could provide information and answers about orientation dependent strain rate sensitivity.

10.2. Part II – Polycrystalline Niobium and OFE Copper

10.2.1. Conclusions

In Chapter 8, the forming limit diagrams of annealed OFE copper and high-purity polycrystalline niobium were measured at a quasi-static strain rate in the order of 10^{-3} s^{-1} for sheets with a thickness of 1 mm. Marciniak (in-plane) tests were performed and a study of the selection of an appropriate hole diameter in the blank carrier for the material, sheet thickness, and setup used was presented. The FLD of annealed OFE copper was similar to results available in the literature for other high-purity copper sheets, which confirmed the validity of the setup and the analysis approach.

The forming limit diagram of high-purity niobium showed a higher formability (higher major strain) than copper, with an estimated FLC_0 of 0.441, and is likely explained by the higher strain rate sensitivity m of 0.112 for niobium, compared to 0.011 for copper (values calculated in Appendix E). The forming limit diagram of niobium was also compared with the only published FLDs found in the literature and a much higher formability was measured over a wider range of minor strains. The difference with the literature is likely explained by differences in purity of niobium sheets (lower mechanical properties were measured with the material used in this study, indicating potentially higher purity or more homogeneous recrystallization) or the testing methodology.

In Chapter 9, the mechanical properties of electron beam welded annealed OFE copper and polycrystalline niobium in tension and compression were measured at strain rates of 10^{-3} to 10^{3} s^{-1}. An observation of grains in the fusion zone, the heat affected zone, and the parent material showed large grains (500 to 1 200 μm) in the fusion and heat affected zones for niobium and a nearly constant Vickers hardness. Grains in the fusion zone of an OFE copper specimen were smaller than those in the HAZ and also had a different shape with no annealing twins. An increase in hardness was also measured across the weld. The yield and ultimate tensile stresses of both materials were similar for welded and unwelded specimens at all strain rates. The ductility of OFE copper was nearly constant at all strain rates, while niobium had a maximum nominal strain to failure at $2.0x10^{-1}$ s^{-1} and a minimum at about 400 s^{-1}. The mechanical properties in compression measured in this studied showed a higher strain rate sensitivity and flow stress at all strain rates compared with tensile tests. The results from this chapter in terms of ductility indicate that the manufacturing of seamless cavities from rolled and welded tube is more appropriate with OFE copper tubes. However, an increase in ductility can be achieved with high-speed sheet forming using intermediate dies, due to complex stress-states with through-thickness compressive components upon impact of the blank on the die.

10.2.2. Perspectives

This study of the formability and the effect of strain rate on electron beam welded polycrystalline high-purity niobium and OFE copper sheets provides important data to the SRF community and answers previously open questions, respectively. The forming limit diagram of OFE copper and niobium can be implemented in finite element models of low strain rate forming techniques, such as deep-drawing and hydroforming. This gives all manufacturers a numerical engineering tool that predicts necking and, therefore, allows them to reduce the risk of sheet failure during forming operations with a new setup. The cost of setup development should then be reduced, and parts formed closer to the forming limits of OFE copper and high-purity niobium can be produced.

The efforts to develop a setup to measure the forming limit diagram of both materials at high strain rate should be continued to obtain FLDs useful for electro-hydraulic forming [49], [52], [294]. This task is not trivial. Therefore, a significant amount of resources will likely be required. A two-step material characterization approach, i.e. a validation of the setup with a material cheaper than niobium, but with similar properties, is again recommended due to the high cost of high-purity niobium sheets. Due to the large difference in strain rate sensitivity between OFE copper and niobium, sheet-metals with a BCC lattice structure, e.g. α-iron, should be used to validate the setup.

Numerical modeling of the forming limit curves obtained at a quasi-static strain rate in this study should be conducted to allow researchers to adapt the FLCs to polycrystalline OFE copper and high-purity niobium sheets with different mechanical properties. Theoretical models adapted for high strain rate tests, e.g. the model of Jacques [295] that considers inertia effects, should be preferred. Predicting the FLCs obtained at low to high strain rates with the same model would make it more useful for electro-hydraulic forming.

The study of the effect of strain rate on EB welded high-purity niobium and OFE copper sheets opens opportunities for the manufacturing of bent and welded tubes for seamless cavity production. The use of small 6 GHz SRF cavities developed and used at the INFN LNL (shown in Figure 1.14) to design a setup to manufacture seamless cavities with such tube is recommended. This small setup and the smaller tubes require less initial investment than larger 1 300 MHz or 800 MHz cavities, allows for easier alterations to optimize the forming process with high-speed sheet forming operations, e.g. EHF, and OFE copper cavities can be coated with niobium, which allows for performance measurements. Due to the measured reduction in strain to failure with increasing strain rate for high-purity niobium, more success is expected with OFE copper tubes formed with electro-hydraulic forming. However, the production of seamless OFE copper tubes is already well understood and

controlled. Therefore, the potential cost reductions from a bent and EB welded tube are likely not significant enough to justify the use of this forming approach with OFE copper.

References

[1] M. T. Daumas and J. Collard, “Pure Niobium Sheet Formability Limits Hydroforming,” presented at the 14. International deep drawing research group biennal (IDDRG-14), Apr. 1986.

[2] International Organization for Standardization, “ISO 80000-1:2009 - Quantities and units — Part 1: General.” 2009. [Online]. Available: https://www.iso.org/standard/30669.html

[3] E. Cantergiani *et al.*, “Niobium superconducting rf cavity fabrication by electrohydraulic forming,” *Phys. Rev. Accel. Beams*, vol. 19, no. 11, Nov. 2016, doi: 10.1103/PhysRevAccelBeams.19.114703.

[4] S. Atieh *et al.*, “First Results of SRF Cavity Fabrication by Electro-Hydraulic Forming at CERN,” presented at the SRF2015, Whistler, Canada, 2015. [Online]. Available: https://s3.cern.ch/inspire-prod-files-0/0bd570decddba6068d33b8f8d07f04bd

[5] “Future Circular Collider Study. Volume 2: The Lepton Collider (FCC-ee) Conceptual Design Report, preprint edited by M. Benedikt et al. CERN accelerator reports, CERN-ACC-2018-0057,” Geneva, Dec. 2018.

[6] “Future Circular Collider Study. Volume 3: The Hadron Collider (FCC-hh) Conceptual Design Report, preprint edited by M. Benedikt et al. CERN accelerator reports, CERN-ACC-2018-0058,” Geneva, Dec. 2018.

[7] ATLAS Collaboration, “Observation of a new particle in the search for the Standard Model Higgs boson with the ATLAS detector at the LHC,” *Phys. Lett. B*, vol. 716, no. 1, pp. 1–29, Sep. 2012, doi: 10.1016/j.physletb.2012.08.020.

[8] R. W. Hamm and M. E. Hamm, Eds., *Industrial accelerators and their applications*. Hackensack, NJ: World Scientific Pub, 2012.

[9] TIARA project, “Accelerators for Society.” http://www.accelerators-for-society.org/ (accessed Apr. 15, 2020).

[10] D. De Bruyn, H. A. Abderrahim, P. Baeten, and P. Leysen, “The MYRRHA ADS Project in Belgium Enters the Front End Engineering Phase,” *Phys. Procedia*, vol. 66, pp. 75–84, 2015, doi: 10.1016/j.phpro.2015.05.012.

[11] H. Padamsee, J. Knobloch, and T. Hays, *RF superconductivity for accelerators*, 2nd ed. Weinheim: Wiley-VCH, 2008.

[12] H. Padamsee, *RF superconductivity: science, technology, and applications*. Weinheim: Wiley-VCH, 2009.

[13] A. Grassellino *et al.*, “Unprecedented quality factors at accelerating gradients up to 45 MVm^{-1} in niobium superconducting resonators via low temperature nitrogen infusion,” *Supercond. Sci. Technol.*, vol. 30, no. 9, p. 094004, Sep. 2017, doi: 10.1088/1361-6668/aa7afe.

[14] “Taking a closer look at LHC - RF cavities.” https://www.lhc-closer.es/taking_a_closer_look_at_lhc/0.rf_cavities (accessed Mar. 01, 2018).

[15] A.-M. Valente-Feliciano, “Superconducting RF materials other than bulk niobium: a review,” *Supercond. Sci. Technol.*, vol. 29, no. 11, p. 113002, Nov. 2016, doi: 10.1088/0953-2048/29/11/113002.

[16] B. Hillenbrand, “The Preparation of Superconducting Nb_3Sn Surfaces for RF Applications,” Karlsruhe, Germany, 1980, p. 12.

[17] S. Posen and D. L. Hall, “Nb_3Sn superconducting radiofrequency cavities: fabrication, results, properties, and prospects,” *Supercond. Sci. Technol.*, vol. 30, no. 3, p. 033004, Mar. 2017, doi: 10.1088/1361-6668/30/3/033004.

[18] E. A. Ilyina *et al.*, “Development of sputtered Nb_3Sn films on copper substrates for superconducting radiofrequency applications,” *Supercond. Sci. Technol.*, vol. 32, no. 3, p. 035002, Mar. 2019, doi: 10.1088/1361-6668/aaf61f.
[19] Fermilab, “About ILC-SRF at Fermilab.” https://ilc.fnal.gov/ilc-srf.html (accessed Apr. 16, 2020).
[20] P. Kneisel, G. R. Myneni, G. Ciovati, J. Sekutowicz, and T. Carneiro, “Preliminary Results from Single Crystal and Very Large Crystal Niobium Cavities,” in *Proceedings of the 2005 Particle Accelerator Conference*, Knoxville, TN, USA, 2005, pp. 3991–3993. doi: 10.1109/PAC.2005.1591693.
[21] K. Saito and F. Furuta, “Multi-wire Slicing of Large Grain Ingot Material,” presented at the SRF2009, Berlin, Germany, 2009. [Online]. Available: https://accelconf.web.cern.ch/SRF2009/papers/thoaau05.pdf
[22] C. Antoine, “Materials and surface aspects in the development of SRF Niobium cavities,” DSM IRFU CEA Centre d’Etudes de Saclay, EuCARD-BOO-2012-001, 2012. [Online]. Available: http://cdsweb.cern.ch/record/1472363
[23] W. Singer, “SRF Cavity Fabrication and Materials,” *CERN Yellow Rep. CERN-2014-005*, pp. 171–207, 2015, doi: 10.5170/CERN-2014-005.171.
[24] G. Rosaz, “Cu electrodeposition for the manufacturing of seamless SRF cavities,” FCC Week, Brussels, 2019.
[25] J. Brau, Y. Okada, and N. Walker, “ILC Reference Design Report Volume 1 - Executive Summary,” *ArXiv07121950 Hep-Ph Physicsphysics*, Dec. 2007, Accessed: Apr. 10, 2020. [Online]. Available: http://arxiv.org/abs/0712.1950
[26] P. Kneisel, “Progress on large grain and single grain niobium - ingots and sheet and review of progress on large grain and single grain niobium cavities,” presented at the SRF2007, Beijing, China, 2007.
[27] W. Singer *et al.*, “Development of large grain cavities,” *Phys. Rev. Spec. Top. - Accel. Beams*, vol. 16, no. 1, Jan. 2013, doi: 10.1103/PhysRevSTAB.16.012003.
[28] J. E. Chen and K. Zhao, “The growth of SRF in China,” presented at the SRF2007, Beijing, China.
[29] S. Quan *et al.*, “3.5-cell large grain niobium superconducting cavity for a dc superconducting rf photoinjector,” *Phys. Rev. Spec. Top. - Accel. Beams*, vol. 13, no. 4, Apr. 2010, doi: 10.1103/PhysRevSTAB.13.042001.
[30] Z. G. Zong *et al.*, “Electro-polished cavities using china ningxia large grain niobium material,” in *2007 IEEE Particle Accelerator Conference (PAC)*, Albuquerque, NM, 2007, pp. 2143–2145. doi: 10.1109/PAC.2007.4441177.
[31] J. Gao, J. P. Dai, Z. D. Guo, and I. Beijing, “First Test Result of the IHEP-01 Large Grain 9-Cell Cavity”.
[32] P. Kneisel *et al.*, “Review of ingot niobium as a material for superconducting radiofrequency accelerating cavities,” *Nucl. Instrum. Methods Phys. Res. Sect. Accel. Spectrometers Detect. Assoc. Equip.*, vol. 774, pp. 133–150, Feb. 2015, doi: 10.1016/j.nima.2014.11.083.
[33] A. Schmidt *et al.*, “1.3 GHz Niobium Single-Cell Fabrication Sequence,” TTC Report 2010-01, 2010.
[34] C. Z. Antoine, “Influence of crystalline structure on rf dissipation in superconducting niobium,” *Phys. Rev. Accel. Beams*, vol. 22, no. 3, p. 034801, Mar. 2019, doi: 10.1103/PhysRevAccelBeams.22.034801.
[35] V. Palmieri, “The Way of Thick Films toward a Flat Q-curve in Sputtered Cavities,” presented at the SRF2017, 2017. doi: 10.18429/JACOW-SRF2017-TUYBA03.

[36] C. Pira, “Nb thick films in 6 GHz superconducting resonant cavities,” PhD Thesis, University of Padova, Padova, Italy, 2018. [Online]. Available: http://paduaresearch.cab.unipd.it/10986/1/Pira_Cristian_tesi.pdf

[37] P. Garg, S. Balachandran, I. Adlakha, P. J. Lee, T. R. Bieler, and K. N. Solanki, “Revealing the role of nitrogen on hydride nucleation and stability in pure niobium using first-principles calculations,” *Supercond. Sci. Technol.*, vol. 31, no. 11, p. 115007, Nov. 2018, doi: 10.1088/1361-6668/aae147.

[38] V. Palmieri, “Seamless Cavities: the Most Creative Topic in RF Superconductivity,” in *1997 Workshop on RF Superconductivity*, Padova, Italy, 1997, pp. 553–589.

[39] “Copper Round Circle Stamping Blanks (1-5/8 to 3-5/8).” https://copperlab.com/copper-circle-stamping-blank.html (accessed Apr. 15, 2020).

[40] G. Ciovati *et al.*, “Final Surface Preparation for Superconducting Cavities,” TTC-Report 2008-05, 2008. [Online]. Available: https://flash.desy.de/sites/site_vuvfel/content/e403/e1644/e2271/e2272/infoboxContent2354/TTC-Report2008-05.pdf

[41] D. Franco and C. Pira, *Argon plasma during deposition of the 6 GHz Monocell Copper Cavity with a niobium superconductive thin film at INFN LNL, Italy*. 2018.

[42] S. Kalpakjian and S. R. Schmid, *Manufacturing engineering and technology*, Seventh edition. Upper Saddle River, NJ: Pearson, 2014.

[43] “A Complete Introduction to Sheet Metal Forming and Its Benefits,” *StampingSimulation*, Mar. 15, 2018. https://stampingsimulation.com/complete-introduction-sheet-metal-forming-benefits/ (accessed Apr. 20, 2020).

[44] S. S. Todkar, N. K. Chhapkhane, and S. R. Todkar, “Investigation of Forming Limit Curves of Various Sheet Materials Using Hydraulic Bulge Testing With Analytical, Experimental and FEA Techniques.,” *Int. J. Eng. Res. Appl.*, vol. 3, no. 1, pp. 858–863, 2013.

[45] “R&D Update: Processes for hydroforming sheet metal, Part I.” https://www.thefabricator.com/stampingjournal/article/stamping/r-d-update-processes-for-hydroforming-sheet-metal-part-i (accessed Apr. 17, 2020).

[46] “Bmax commercial website,” *Bmax*. https://www.bmax.com/ (accessed Apr. 22, 2018).

[47] S. F. Golovashchenko, “Electrohydraulic Forming of Near-Net Shape Automotive Panels,” DOE-FORD-GO18128, 1094831, Sep. 2013. doi: 10.2172/1094831.

[48] G. Regazzoni and F. Montheillet, “High Strain Rate Ductility in Uniaxial Tension: A Review,” *J. Phys. Colloq.*, vol. 46, no. C5, pp. C5-435-C5-444, Aug. 1985, doi: 10.1051/jphyscol:1985554.

[49] V. S. Balanethiram and G. S. Daehn, “Hyperplasticity: Increased forming limits at high workpiece velocity,” *Scr. Metall. Mater.*, vol. 30, no. 4, pp. 515–520, Feb. 1994, doi: 10.1016/0956-716X(94)90613-0.

[50] X. Hu and G. S. Daehn, “Effect of velocity on flow localization in tension,” *Acta Mater.*, vol. 44, no. 3, pp. 1021–1033, Mar. 1996, doi: 10.1016/1359-6454(95)00228-6.

[51] J. M. Imbert, S. L. Winkler, M. J. Worswick, D. A. Oliveira, and S. Golovashchenko, “The Effect of Tool–Sheet Interaction on Damage Evolution in Electromagnetic Forming of Aluminum Alloy Sheet,” *J. Eng. Mater. Technol.*, vol. 127, no. 1, pp. 145–153, Jan. 2005, doi: 10.1115/1.1839212.

[52] S. F. Golovashchenko, A. J. Gillard, and A. V. Mamutov, “Formability of dual phase steels in electrohydraulic forming,” *J. Mater. Process. Technol.*, vol. 213, no. 7, pp. 1191–1212, Jul. 2013, doi: 10.1016/j.jmatprotec.2013.01.026.

[53] V. Palmieri and R. Vaglio, “Thermal contact resistance at the Nb/Cu interface as a limiting factor for sputtered thin film RF superconducting cavities,” *Supercond. Sci. Technol.*, vol. 29, 2016, doi: https://doi.org/10.1088/0953-2048/29/1/015004.
[54] C. Z. Antoine, “How to Achieve the Best SRF Performance: (Practical) Limitations and Possible Solutions,” Gif-sur Yvette, France.
[55] R. Russo, “Quality measurement of niobium thin films for Nb/Cu superconducting RF cavities,” *Meas. Sci. Technol.*, vol. 18, no. 8, pp. 2299–2313, Jul. 2007, doi: 10.1088/0957-0233/18/8/003.
[56] S. Atieh, “Novel Technologies applied to SRF (cavity) fabrication,” presented at the TTC 2020, Geneva, Switzerland, Feb. 05, 2020. [Online]. Available: https://indico.cern.ch/event/817780/contributions/3716472/
[57] E. Chiaveri and H. Lengeler, “Welding of Nb cavities at CERN,” presented at the SRF84, Geneva, Switzerland, 1984. [Online]. Available: https://accelconf.web.cern.ch/srf84/papers/srf84-33.pdf
[58] G. Wu *et al.*, “Investigations of Surface Quality and SRF Cavity Performance,” in *FERMILAB-CONF-10-430-TD*, Batavia, USA, 2010, pp. 1–4. [Online]. Available: https://lss.fnal.gov/archive/2010/conf/fermilab-conf-10-430-td.pdf
[59] J. L. Kirchgessner, “Forming and Welding of Niobium for Superconducting Cavities,” in *The Third Workshop on RF Superconductivity*, Argonne National Laboratory, IL, USA, 1987, pp. 533–544.
[60] C. Hauviller, “Fully hydroformed RF cavities,” 1989, pp. 485–487. doi: 10.1109/PAC.1989.73087.
[61] S. Dujardin, J. Genest, C. Hauviller, R. Jaggi, and B. Jean-Prost, “Hydroforming Monolithic Cavities in the 300 MHz Range,” pp. 1100–1102.
[62] V. Palmieri, I. I. Kulik, R. Preciso, V. L. Ruzinov, and S. Y. Stark, “A New Method for Forming Seamless 1.5 GHz Multicell Cavities starting from Planar Disks,” pp. 2212–2214.
[63] T. Fujino *et al.*, “Status of the Seamless L-Band Cavity Fabrication at KEK,” in *1995 Workshop on RF Superconductivity*, Gif-sur-Yvette, France, 1995, pp. 741–745.
[64] C. Antoine, J. Gaiffier, and H. Chalaye, “Hydroforming at C.E.A. Saclay: First Results,” in *1997 Workshop on RF Superconductivity*, Padova, Italy, 1997, pp. 598–605.
[65] W. Singer, H. Kaiser, X. Singer, and G. Weichert, “Hydroforming of Superconducting TESLA Cavities,” in *10th Workshop on RF Superconductivity*, Tsukuba, Japan, 2001, pp. 170–176.
[66] C. Compton *et al.*, “Studies of alternative techniques for niobium cavity fabrication,” in *SRF 2007*, Beijing, China, 2007, pp. 429–433.
[67] M. Yamanaka, H. Inoue, H. Shimizu, and K. Umemori, “Hydroforming SRF Cavities from Seamless Niobium Tubes,” in *SRF 2015*, Whistler, Canada, 2015, pp. 1176–1180.
[68] W. Singer, X. Singer, I. Jelezov, and P. Kneisel, “Hydroforming of elliptical cavities,” *Phys. Rev. Spec. Top. - Accel. Beams*, vol. 18, no. 2, Feb. 2015, doi: 10.1103/PhysRevSTAB.18.022001.
[69] K. Fujii *et al.*, “Physics Case for the 250 GeV Stage of the International Linear Collider,” *ArXiv171007621 Hep-Ex Physicshep-Ph*, Aug. 2018, Accessed: Apr. 17, 2020. [Online]. Available: http://arxiv.org/abs/1710.07621
[70] E. Chyhyrynets *et al.*, “Vibro-Tumbling as an Alternative to Standard Mechanical Polishing Techniques for SRF Cavities,” presented at the SRF2019, Dresden, Germany, 2019.
[71] Y. Guolong, “Development of a new mechanical surface treatment for the internal finishing of 6 GHz superconducting cavities,” Master Thesis, University of Padova,

Padova, Italy, 2013. [Online]. Available: http://www.infn.it/thesis/thesis_dettaglio.php?tid=8850

[72] H. Kaiser, W. Singer, and X. Singer, “Hydroforming of Back Extruded Niobium Tubes,” Santa Fe, USA, 1999, pp. 528–531. [Online]. Available: https://accelconf.web.cern.ch/SRF99/papers/wep042.pdf

[73] K. T. Hartwig, D. C. Foley, and R. E. Barber, “Seamless Nb tubes for SRF cavities,” Shear Form, Inc., Final Scientific/Technical Report DE-SC0007601, Nov. 2019. doi: 10.2172/1574927.

[74] I. Gonin, I. Jelezov, H. Kaiser, and W. Singer, “Hydroforming Test of Back Extruded Niobium Tube,” in *1997 Workshop on RF Superconductivity*, Padova, Italy, 1997, pp. 590–597.

[75] R. Crooks, “Fabrication and Testing of ILC Cavities Produced from Seamless Nb Tubes,” presented at the Fifth International Workshop on Thin Films and New Ideas for Pushing the Limits of RF Superconductivity, Newport News, VA, Jul. 2012.

[76] P. D. Roy Crooks, “Production of Seamless Superconducting Radio Frequency Cavities from Ultra-fine Grained Niobium, Phase II Final Report,” *Digital Library*, Oct. 31, 2009. https://digital.library.unt.edu/ark:/67531/metadc931842/m1/1/ (accessed May 17, 2018).

[77] R. Crooks, “Production of Seamless Superconducting Radio Frequency Cavities from Ultra-fine Grained Niobium,” Black Laboratories, L.L.C., SBIR DE-FG02-04ER83909, Nov. 2009.

[78] S. Balachandran, R. C. Elwell, D. Kang, R. E. Barber, T. R. Bieler, and K. T. Hartwig, “Nb Tubes for Seamless SRF Cavities,” *IEEE Trans. Appl. Supercond.*, vol. 23, no. 3, pp. 7100904–7100904, Jun. 2013, doi: 10.1109/TASC.2013.2243492.

[79] S. Balachandran, “Microstructure Development in Bulk Niobium Following Severe Plastic Deformation and Annealing,” PhD Thesis, Texas A&M University, College Station, TX, 2015.

[80] F. Carra *et al.*, “Crab Cavity and Cryomodule Development for HL-LHC,” in *SRF2015*, 2015, pp. 1460–1467.

[81] F. C. Salvado, F. Teixeira-Dias, S. M. Walley, L. J. Lea, and J. B. Cardoso, “A review on the strain rate dependency of the dynamic viscoplastic response of FCC metals,” *Prog. Mater. Sci.*, vol. 88, pp. 186–231, Jul. 2017, doi: 10.1016/j.pmatsci.2017.04.004.

[82] G. R. Johnson and W. H. Cook, “A constitutive model and data for metals subjected to large strains, high strain rates and high temperatures.” 1983.

[83] F. J. Zerilli and R. W. Armstrong, “Dislocation-mechanics-based constitutive relations for material dynamics calculations,” *J. Appl. Phys.*, vol. 61, no. 5, pp. 1816–1825, Mar. 1987, doi: 10.1063/1.338024.

[84] D. J. Steinberg and C. M. Lund, “A constitutive model for strain rates from 10^{-4} to 10^{6} s^{-1},” *J. Appl. Phys.*, vol. 65, no. 4, pp. 1528–1533, Feb. 1989, doi: 10.1063/1.342968.

[85] D. J. Steinberg, S. G. Cochran, and M. W. Guinan, “A constitutive model for metals applicable at high-strain rate,” *J. Appl. Phys.*, vol. 51, pp. 1498–1504, 1980.

[86] H. Mecking and U. F. Kocks, “Kinetics of flow and strain-hardening,” *Acta Metall.*, vol. 29, no. 11, pp. 1865–1875, 1981, doi: https://doi.org/10.1016/0001-6160(81)90112-7.

[87] P. S. Follansbee and U. F. Kocks, “A constitutive description of the deformation of copper based on the use of the mechanical threshold stress as an internal state variable,” *Acta Metall.*, vol. 36, no. 1, pp. 81–93, Jan. 1988, doi: 10.1016/0001-6160(88)90030-2.

[88] D. L. Preston, D. L. Tonks, and D. C. Wallace, “Model of plastic deformation for extreme loading conditions,” *J. Appl. Phys.*, vol. 93, pp. 211–220, 2003.

[89] A. Rusinek and J. R. Klepaczko, “Shear testing of a sheet steel at wide range of strain rates and a constitutive relation with strain-rate and temperature dependence of the ¯ow stress,” *Int. J. Plast.*, p. 29, 2001.
[90] A. Rusinek, J. A. Rodríguez-Martínez, and A. Arias, “A thermo-viscoplastic constitutive model for FCC metals with application to OFHC copper,” *Int. J. Mech. Sci.*, p. 16, 2010.
[91] ASM International, Ed., *Atlas of stress-strain curves*, 2nd ed. Materials Park, OH: ASM International, 2002.
[92] S. Yoo, D. Schueler, M. Brodbeck, N. Toso, G. Catalanotti, and H. Voggenreiter, “An Improved Load Introduction Technique for Dynamic Material Characterisation at Intermediate Strain Rate,” *Proceedings*, vol. 2, no. 8, p. 381, May 2018, doi: 10.3390/ICEM18-05203.
[93] M. A. Meyers, *Dynamic behavior of materials*. New York, NY: Wiley, 1994.
[94] G. T. (Rusty) Gray, “High-Strain-Rate Testing of Materials: The Split-Hopkinson Pressure Bar,” in *Characterization of Materials*, E. N. Kaufmann, Ed. Hoboken, NJ, USA: John Wiley & Sons, Inc., 2012. doi: 10.1002/0471266965.com023.pub2.
[95] B. A. Gama, S. L. Lopatnikov, and J. W. Gillespie, “Hopkinson bar experimental technique: A critical review,” *Appl. Mech. Rev.*, vol. 57, no. 4, pp. 223–250, Jul. 2004, doi: 10.1115/1.1704626.
[96] W. W. Chen and B. Song, *Split Hopkinson (Kolsky) bar: design, testing and applications*. New York, NY: Springer, 2011.
[97] G. T. (Rusty) Gray, “High-Strain-Rate Deformation: Mechanical Behavior and Deformation Substructures Induced,” *Annu. Rev. Mater. Res.*, vol. 42, no. 1, pp. 285–303, 2012, doi: 10.1146/annurev-matsci-070511-155034.
[98] A. K. Ghosh, “The Influence of Strain Hardening and Strain-Rate Sensitivity on Sheet Metal Forming,” *J. Eng. Mater. Technol.*, vol. 99, no. 3, pp. 264–274, Jul. 1977, doi: 10.1115/1.3443530.
[99] F. C. Campbell, *Elements of Metallurgy and Engineering Alloys*. ASM International, 2008. [Online]. Available: https://www.asminternational.org/search/-/journal_content/56/10192/05224G/PUBLICATION
[100] H. Conrad, “Thermally activated deformation of metals,” *JOM*, vol. 16, no. 7, pp. 582–588, Jul. 1964, doi: 10.1007/BF03378292.
[101] M. Tang, L. P. Kubin, and G. R. Canova, “Dislocation mobility and the mechanical response of b.c.c. single crystals: A mesoscopic approach,” *Acta Mater.*, vol. 46, no. 9, pp. 3221–3235, May 1998, doi: 10.1016/S1359-6454(98)00006-8.
[102] Q. Wei, S. Cheng, K. T. Ramesh, and E. Ma, “Effect of nanocrystalline and ultrafine grain sizes on the strain rate sensitivity and activation volume: fcc versus bcc metals,” *Mater. Sci. Eng. A*, vol. 381, no. 1–2, pp. 71–79, Sep. 2004, doi: 10.1016/j.msea.2004.03.064.
[103] Y. Wang, A. Hamza, and E. Ma, “Temperature-dependent strain rate sensitivity and activation volume of nanocrystalline Ni,” *Acta Mater.*, vol. 54, no. 10, pp. 2715–2726, Jun. 2006, doi: 10.1016/j.actamat.2006.02.013.
[104] M. Dao, L. Lu, R. Asaro, J. Dehosson, and E. Ma, “Toward a quantitative understanding of mechanical behavior of nanocrystalline metals,” *Acta Mater.*, vol. 55, no. 12, pp. 4041–4065, Jul. 2007, doi: 10.1016/j.actamat.2007.01.038.
[105] D. Hull and D. J. Bacon, *Introduction to dislocations*, 5. ed. Amsterdam: Elsevier/Butterworth-Heinemann, 2011.
[106] J. W. Christian, “Some surprising features of the plastic deformation of body-centered cubic metals and alloys,” *Metall. Trans. A*, vol. 14, no. 7, pp. 1237–1256, Jul. 1983, doi: 10.1007/BF02664806.

[107] W. D. Callister, *Materials science and engineering: an introduction*, 7th ed. New York: John Wiley & Sons, 2007.
[108] M. S. Duesbery, R. A. Foxall, and P. B. Hirsch, "The plasticity of pure niobium single crystals," *J. Phys. Colloq.*, vol. 27, no. C3, pp. C3-193-C3-204, Jul. 1966, doi: 10.1051/jphyscol:1966325.
[109] R. A. Foxall, M. S. Duesbery, and P. B. Hirsch, "The deformation of niobium single crystals," *Can. J. Phys.*, vol. 45, no. 2, pp. 607–629, Feb. 1967, doi: 10.1139/p67-052.
[110] R. Maddin and N. K. Chen, "Plasticity of Columbium Single Crystals," *JOM*, vol. 5, no. 9, pp. 1131–1136, Sep. 1953, doi: 10.1007/BF03397601.
[111] D. Ali, N. Mushtaq, and M. Z. Butt, "Investigation of active slip-systems in some body-centered cubic metals," *J. Mater. Sci.*, vol. 46, no. 11, pp. 3812–3821, Jun. 2011, doi: 10.1007/s10853-011-5295-0.
[112] A. Seeger and U. Holzwarth, "Slip planes and kink properties of screw dislocations in high-purity niobium‡," *Philos. Mag.*, vol. 86, no. 25–26, pp. 3861–3892, Sep. 2006, doi: 10.1080/14786430500531769.
[113] W. F. Hosford, *The mechanics of crystals and textured polycrystals*. New York: Oxford University Press, 1993.
[114] C. R. Weinberger, B. L. Boyce, and C. C. Battaile, "Slip planes in bcc transition metals," *Int. Mater. Rev.*, vol. 58, no. 5, pp. 296–314, Jun. 2013, doi: 10.1179/1743280412Y.0000000015.
[115] D. Shilo and E. Zolotoyabko, "Chapter 80 X-Ray Imaging of Phonon Interaction with Dislocations," in *Dislocations in Solids*, vol. 13, Elsevier, 2007, pp. 603–639. doi: 10.1016/S1572-4859(07)80012-X.
[116] M. Z. Butt, "Kinetics of flow stress in crystals with high intrinsic lattice friction," *Philos. Mag.*, vol. 87, no. 24, pp. 3595–3614, Aug. 2007, doi: 10.1080/14786430701370850.
[117] M. S. Duesbery and V. Vitek, "Plastic Anisotropy in B.C.C. Transition Metals," *Acta Metall.*, vol. 46, no. 5, pp. 1481–1492, 1998.
[118] M. R. Fellinger, H. Park, and J. W. Wilkins, "Force-matched embedded-atom method potential for niobium," *Phys. Rev. B*, vol. 81, no. 14, p. 144119, Apr. 2010, doi: 10.1103/PhysRevB.81.144119.
[119] S. Takeuchi, "Core structure of a screw dislocation in the b.c.c. lattice and its relation to slip behaviour of α-iron," *Philos. Mag. A*, vol. 39, no. 5, pp. 661–671, May 1979, doi: 10.1080/01418617908239296.
[120] A. Sato and K.-I. Masuda, "Screw-dislocation motion in b.c.c. transition metals model calculation using a tight-binding-type electronic theory," *Philos. Mag. B*, vol. 43, no. 1, pp. 1–17, Jan. 1981, doi: 10.1080/01418638108225797.
[121] G. Regazzoni, U. F. Kocks, and P. S. Follansbee, "Dislocation kinetics at high strain rates," *Acta Metall.*, vol. 35, no. 12, pp. 2865–2875, Dec. 1987, doi: 10.1016/0001-6160(87)90285-9.
[122] G. K. Williamson and R. E. Smallman, "X-Ray Extinction and the Effect of Cold Work on Integrated Intensities," *Proc. Phys. Soc. B*, vol. 68, p. 577, 1955.
[123] H. Lim, J. D. Carroll, C. C. Battaile, S. R. Chen, A. P. Moore, and J. M. D. Lane, "Anisotropy and Strain Localization in Dynamic Impact Experiments of Tantalum Single Crystals," *Sci. Rep.*, vol. 8, no. 1, p. 5540, Dec. 2018, doi: 10.1038/s41598-018-23879-1.
[124] H. Lim, J. D. Carroll, J. R. Michael, C. C. Battaile, S. R. Chen, and M. D. Lane, "Investigating active slip planes in tantalum," *Acta Mater.*, 2019.

[125] R. E. Rudd *et al.*, "Multiscale strength (MS) models: their foundation, their successes, and their challenges," *J. Phys. Conf. Ser.*, vol. 500, no. 11, p. 112055, May 2014, doi: 10.1088/1742-6596/500/11/112055.
[126] K. G. Hoge and A. K. Mukherjee, "The temperature and strain rate dependence of the flow stress of tantalum," *J. Mater. Sci.*, vol. 12, no. 8, pp. 1666–1672, Aug. 1977, doi: 10.1007/BF00542818.
[127] M. R. Nadler and C. P. Kempter, "Niobium Crystallographic Data," *Anal. Chem.*, vol. 31, no. 11, pp. 1922–1923, Nov. 1959, doi: 10.1021/ac60155a002.
[128] S. Nemat-Nasser and W. Guo, "Flow stress of commercially pure niobium over a broad range of temperatures and strain rates," *Mater. Sci. Eng. A*, vol. 284, no. 1–2, pp. 202–210, May 2000, doi: 10.1016/S0921-5093(00)00740-1.
[129] L. Dezerald, L. Proville, L. Ventelon, F. Willaime, and D. Rodney, "First-principles prediction of kink-pair activation enthalpy on screw dislocations in bcc transition metals: V, Nb, Ta, Mo, W, and Fe," *Phys. Rev. B*, vol. 91, no. 9, p. 094105, Mar. 2015, doi: 10.1103/PhysRevB.91.094105.
[130] G. Taylor, "Thermally-activated deformation of BCC metals and alloys," *Prog. Mater. Sci.*, vol. 36, pp. 29–61, Jan. 1992, doi: 10.1016/0079-6425(92)90004-Q.
[131] C. Y. Ho, R. W. Powell, and P. E. Liley, "Thermal Conductivity of the Elements: A Comprehensive Review," *J. Phys. Chem. Ref. Data*, vol. 3, pp. 1–796, 1974.
[132] J. E. Dorn and S. Rajnak, "Nucleation of kink pairs and the Peierls' mechanism of plastic deformation," *Trans. Metall. Soc. AIME*, vol. 230, pp. 1052–1064, 1964.
[133] P. Guyot and J. E. Dorn, "A Critical Review of the Peierls Mechanism," *Can. J. Phys.*, vol. 45, no. 2, pp. 983–1016, Feb. 1967, doi: 10.1139/p67-073.
[134] S. Takeuchi, T. Hashimoto, and K. Maeda, "Plastic Deformation of bcc Metal Single Crystals at Very Low Temperatures," *Trans. Jpn. Inst. Met.*, vol. 23, no. 2, pp. 60–69, 1982.
[135] V. A. Al'shitz and V. L. Indenbom, "Dynamic dragging of dislocations," vol. 18, no. 1, p. 21.
[136] D. Klahn, A. K. Mukherjee, and J. E. Dorn, in *Proceedings of the second International Conference Strength of Metals and Alloys*, Pacific Grove, CA, USA, 1970, vol. 3, p. 951.
[137] D. Blaschke, "Properties of Dislocation Drag from Phonon Wind at Ambient Conditions," *Materials*, vol. 12, no. 6, p. 948, Mar. 2019, doi: 10.3390/ma12060948.
[138] G. Taylor, "The deformation of crystals of β-brass," *Proc. R. Soc. Lond. Ser. Contain. Pap. Math. Phys. Character*, vol. 118, no. 779, pp. 1–24, Mar. 1928, doi: 10.1098/rspa.1928.0032.
[139] G. Po *et al.*, "A phenomenological dislocation mobility law for bcc metals," *Acta Mater.*, vol. 119, pp. 123–135, Oct. 2016, doi: 10.1016/j.actamat.2016.08.016.
[140] D. Baars, "Investigation of active slip systems in high purity single crystal niobium," Ph. D. Thesis, Michigan State University, East Lansing, MI, 2013.
[141] A. Mapar, "Crystal Plasticity Modeling of the Deformation of BCC Iron and Niobium Single Crystals," Michigan State University, East Lansing, MI, 2017.
[142] A. Mapar, D. Kang, T. R. Bieler, F. Pourboghrat, and C. C. Compton, "Crystal Plasticity Modeling of Single Crystal Nb," in *SRF2015*, Whistler, Canada, 2015, pp. 228–232.
[143] W. A. Spitzig and A. S. Keh, "Orientation and temperature dependence of slip in iron single crystals," *Metall. Trans.*, vol. 1, no. 10, pp. 2751–2757, 1970, doi: 10.1007/BF03037811.
[144] A. D. Rollet and U. F. Kocks, "A review of the stages of work hardening," Apr. 1993.

[145] T. E. Mitchell, R. A. Foxall, and P. B. Hirsch, “Work-hardening in niobium single crystals,” *Philos. Mag.*, vol. 8, no. 95, pp. 1895–1920, Nov. 1963, doi: 10.1080/14786436308209081.
[146] M. S. Duesbery and R. A. Foxall, “A detailed study of the deformation of high purity niobium single crystals,” *Philos. Mag.*, vol. 20, no. 166, pp. 719–751, Oct. 1969, doi: 10.1080/14786436908228040.
[147] A. Ermakov *et al.*, “Physical properties and structure of large grain/single crystal niobium for superconducting RF cavities,” *J. Phys. Conf. Ser.*, vol. 97, p. 012014, Feb. 2008, doi: 10.1088/1742-6596/97/1/012014.
[148] D. C. Baars, T. R. Bieler, and C. Compton, “Microstructure Studies of Niobium,” presented at the SRF2009, Berlin, Germany, 2009.
[149] D. Kang, D. C. Baars, and T. R. Bieler, “Study of Slip and Deformation in High Purity Single Crystal Nb for Accelerator Cavities,” presented at the SRF2015, 2015.
[150] G. R. Myneni, “Physical and Mechanical Properties of Niobium for SRF Science and Technology,” in *AIP Conference Proceedings*, Araxa, Brazil, 2007, vol. 927, pp. 41–47. doi: 10.1063/1.2770677.
[151] T. Gnäupel-Herold, G. R. Myneni, and R. E. Ricker, “Investigations of Residual Stresses and Mechanical Properties of Single Crystal Niobium for SRF Cavities,” in *AIP Conference Proceedings*, Araxa (Brazil), 2007, vol. 927, pp. 48–59. doi: 10.1063/1.2770678.
[152] R. E. Ricker, D. J. Pitchure, and G. R. Myneni, “Mechanical properties as an indicator of interstitials in niobium for superconducting accelerator cavities,” presented at the Science and Technology of Ingot Niobium for Superconducting Radio Frequency Applications, Virginia, USA, 2015. doi: 10.1063/1.4935319.
[153] J. Nagakawa and M. Meshii, “The deformation of niobium single crystals at temperatures between 77 and 4.2 K,” *Philos. Mag. A*, vol. 44, no. 5, pp. 1165–1191, Nov. 1981, doi: 10.1080/01418618108235801.
[154] T. S. Byun, S.-H. Kim, and J. Mammosser, “Low-temperature mechanical properties of superconducting radio frequency cavity materials,” *J. Nucl. Mater.*, vol. 392, no. 3, pp. 420–426, Aug. 2009, doi: 10.1016/j.jnucmat.2009.03.058.
[155] J. W. Edington, “Effect of Strain Rate on the Dislocation Substructure in Deformed Niobium Single Crystals,” in *Mechanical Behavior of Materials under Dynamic Loads*, U. S. Lindholm, Ed. Berlin, Heidelberg: Springer Berlin Heidelberg, 1968, pp. 191–240. doi: 10.1007/978-3-642-87445-1_10.
[156] T. R. Bieler *et al.*, “Physical and mechanical metallurgy of high purity Nb for accelerator cavities,” *Phys. Rev. Spec. Top. - Accel. Beams*, vol. 13, no. 3, Mar. 2010, doi: 10.1103/PhysRevSTAB.13.031002.
[157] D. K. Bowen, J. W. Christian, and G. Taylor, “Deformation properties of niobium single crystals,” *Can. J. Phys.*, vol. 45, no. 2, pp. 903–938, Feb. 1967, doi: 10.1139/p67-069.
[158] P. J. Sherwood, F. Guiu, H. C. Kim, and P. L. Pratt, “Plastic Anisotropy of Tantalum, Niobium, and Molybdenum,” *Can. J. Phys.*, vol. 45, no. 2, pp. 1075–1089, Feb. 1967, doi: 10.1139/p67-079.
[159] R. Maddin and N. K. Chen, “Geometrical aspects of the plastic deformation of metal single crystals,” *Prog. Met. Phys.*, vol. 5, pp. 53–95, Jan. 1954, doi: 10.1016/0502-8205(54)90004-0.
[160] B. A. Loomis and S. B. Gerber, “The Yield Stress of Niobium and Niobium-Oxygen Solutions,” *Scr. Metall.*, vol. 4, pp. 921–924, 1970.

[161] K. V. Ravi and R. Gibala, “Low temperature strengthening in niobium-hydrogen single crystals,” *Metall. Trans.*, vol. 2, no. 4, pp. 1219–1225, Apr. 1971, doi: 10.1007/BF02664255.
[162] S. Ikeno and E. Furubayashi, “Behavior of dislocations in niobium under stress,” *Phys. Status Solidi A*, vol. 12, no. 2, pp. 611–622, Aug. 1972, doi: 10.1002/pssa.2210120234.
[163] M. G. Ulitchny and R. Gibala, “The effects of interstitial solute additions on the mechanical properties of niobium and tantalum single crystals,” *J. Common Met.*, vol. 33, no. 1, pp. 105–116, Oct. 1973, doi: 10.1016/0022-5088(73)90061-1.
[164] A. J. Garratt-Reed and G. Taylor, “Stress-strain curves for niobium crystals deformed at temperatures below ambient,” *Philos. Mag.*, vol. 33, no. 4, pp. 577–590, Apr. 1976, doi: 10.1080/14786437608221120.
[165] S. Ikeno, “Direct observation of cell formation in niobium by a high-voltage electron microscope,” *Phys. Status Solidi A*, vol. 36, no. 1, pp. 317–328, Jul. 1976, doi: 10.1002/pssa.2210360134.
[166] L. N. Chang, G. Taylor, and J. W. Christian, “Stress asymmetries in the deformation behaviour of niobium single crystals,” *Acta Metall.*, vol. 31, no. 1, pp. 37–42, Jan. 1983, doi: 10.1016/0001-6160(83)90061-5.
[167] W. Wasserbäch and V. Novák, “Optical investigation of anomalous slip-line patterns in high purity niobium and tantalum single crystals after tensile deformation at 77 K,” *Mater. Sci. Eng.*, vol. 73, pp. 197–202, Aug. 1985, doi: 10.1016/0025-5416(85)90308-8.
[168] M. I. Wood and G. Taylor, “Niobium—an athermal plateau in the low-temperature yield stress,” *Philos. Mag. A*, vol. 56, no. 3, pp. 329–342, Sep. 1987, doi: 10.1080/01418618708214389.
[169] W. Wasserbäch, “Anomalous Slip in High-Purity Niobium and Tantalum Single Crystals,” *Phys. Status Solidi A*, vol. 147, no. 2, pp. 417–446, Feb. 1995, doi: 10.1002/pssa.2211470213.
[170] G. R. Myneni *et al.*, “Mechanical Properties of High Purity Niobium Novel Measurements,” presented at the SRF2003, 2003.
[171] G. R. Myneni, “Physical and Mechanical Properties of Single and Large Crystal High-RRR niobium,” presented at the SRF2005, Ithaca, NY, USA, 2005.
[172] D. Baars, T. R. Bieler, A. Zamiri, F. Pourboghrat, C. Compton, and M. S. University, “Crystal Orientation Effects During Fabrication of Single or Multi-Crystal NB SRF Cavities,” Beijing, China, 2007, p. 5.
[173] T. R. Bieler, M. S. University, and E. Lansing, “Advances in Material Studies for SRF,” Berlin, Germany, 2009, p. 7.
[174] D. Kang, D. C. Baars, T. R. Bieler, and C. C. Compton, “Characterization of Large Grain Nb Ingot Microstructure Using EBSP Mapping and Laue Camera Methods,” Virginia, (USA), 2011, pp. 90–99. doi: 10.1063/1.3579228.
[175] T. R. Bieler *et al.*, “Deformation mechanisms, defects, heat treatment, and thermal conductivity in large grain niobium,” Virginia, USA, 2015, p. 020002. doi: 10.1063/1.4935316.
[176] J.-F. Croteau *et al.*, “Effect of strain rate on tensile mechanical properties of high-purity niobium single crystals for SRF applications,” *Mater. Sci. Eng. A*, p. 140258, Sep. 2020, doi: 10.1016/j.msea.2020.140258.
[177] J. P. Hirth, “Effects of hydrogen on the properties of iron and steel,” *Metall. Trans. A*, vol. 11, no. 6, pp. 861–890, Jun. 1980, doi: 10.1007/BF02654700.
[178] I. M. Robertson, “The effect of hydrogen on dislocation dynamics.,” *Eng. Fract. Mech.*, vol. 68, pp. 671–692, 2001.

[179] I. M. Robertson *et al.*, “Hydrogen Embrittlement Understood,” *Metall. Mater. Trans. B*, vol. 46, no. 3, pp. 1085–1103, Jun. 2015, doi: 10.1007/s11663-015-0325-y.
[180] M. Nagumo, *Fundamentals of Hydrogen Embrittlement*. Singapore: Springer Singapore, 2016. doi: 10.1007/978-981-10-0161-1.
[181] K. V. Ravi and R. Gibala, “The strength of niobium-oxygen solid solutions,” *Acta Metall.*, vol. 18, no. 6, pp. 623–634, Jun. 1970, doi: 10.1016/0001-6160(70)90091-X.
[182] L. Peroni and M. Scapin, “Experimental analysis and modelling of the strain-rate sensitivity of sheet niobium,” *EPJ Web Conf.*, vol. 183, 2018, doi: 10.1051/epjconf/201818301014.
[183] Z.-H. Sung *et al.*, “Development of low angle grain boundaries in lightly deformed superconducting niobium and their influence on hydride distribution and flux perturbation,” *J. Appl. Phys.*, vol. 121, no. 19, p. 193903, May 2017, doi: 10.1063/1.4983512.
[184] M. Wang, D. Kang, and T. R. Bieler, “Direct observation of dislocation structure evolution in SRF cavity niobium using electron channeling contrast imaging,” *J. Appl. Phys.*, vol. 124, no. 15, p. 155105, Oct. 2018, doi: 10.1063/1.5050032.
[185] R. Srinivasan, G. B. Viswanathan, V. I. Levit, and H. L. Fraser, “Orientation effect on recovery and recrystallization of cold rolled niobium single crystals,” *Mater. Sci. Eng. A*, vol. 507, no. 1–2, pp. 179–189, May 2009, doi: 10.1016/j.msea.2008.12.013.
[186] A. V. Dobromyslov, N. I. Taluts, G. V. Dolgikh, and E. A. Kozlov, “Deformation behavior of a niobium single crystal upon loading by spherically converging shock waves,” *Phys. Met. Metallogr.*, vol. 111, no. 4, pp. 375–384, Apr. 2011, doi: 10.1134/S0031918X11030033.
[187] S. Xu, “Dislocation Multiplication from a Frank-Read Source in Six Body-centered Cubic Refractory Metals,” presented at the TMS 2020, San Diego, CA, USA, 2020.
[188] M. G. Wang and A. H. W. Ngan, “Indentation strain burst phenomenon induced by grain boundaries in niobium,” *J. Mater. Res.*, vol. 19, no. 8, pp. 2478–2486, Aug. 2004, doi: 10.1557/JMR.2004.0316.
[189] M. A. Mamun *et al.*, “Nanomechanical properties of NbN films prepared by pulsed laser deposition using nanoindendation,” *Appl. Surf. Sci.*, vol. 258, no. 10, pp. 4308–4313, Mar. 2012, doi: 10.1016/j.apsusc.2011.12.089.
[190] M. A. A. Mamun, A. H. Farha, Y. Ufuktepe, H. E. Elsayed-Ali, and A. A. Elmustafa, “Investigation of the crystal structure on the nanomechanical properties of pulsed laser deposited niobium nitride thin films,” *J. Mater. Res.*, vol. 27, no. 13, pp. 1725–1731, Jul. 2012, doi: 10.1557/jmr.2012.167.
[191] Y. Ufuktepe *et al.*, “Superconducting niobium nitride thin films by reactive pulsed laser deposition,” *Thin Solid Films*, vol. 545, pp. 601–607, Oct. 2013, doi: 10.1016/j.tsf.2013.08.051.
[192] M. A. A. Mamun, A. H. Farha, Y. Ufuktepe, H. E. Elsayed-Ali, and A. A. Elmustafa, “Nanoindentation study of niobium nitride thin films on niobium fabricated by reactive pulsed laser deposition,” *Appl. Surf. Sci.*, vol. 330, pp. 48–55, Mar. 2015, doi: 10.1016/j.apsusc.2014.12.144.
[193] S. A. Turnage, “Anomalous Dynamic Behavior of Stable Nanograined Materials,” PhD Thesis, Arizona State University, Tempe, AZ, 2017. [Online]. Available: https://repository.asu.edu/items/46327
[194] S. A. Turnage *et al.*, “Influence of variable processing conditions on the quasi-static and dynamic behaviors of resistance spot welded aluminum 6061-T6 sheets,” *Mater. Sci. Eng. A*, vol. 724, pp. 509–517, May 2018, doi: 10.1016/j.msea.2018.03.120.

[195] W. R. Whittington *et al.*, “Capturing the effect of temperature, strain rate, and stress state on the plasticity and fracture of rolled homogeneous armor (RHA) steel,” *Mater. Sci. Eng. A*, vol. 594, pp. 82–88, Jan. 2014, doi: 10.1016/j.msea.2013.11.018.
[196] ASTM International, “ASTM E8 / E8M-16ae1, Standard Test Methods for Tension Testing of Metallic Materials.” 2016. [Online]. Available: astm.org
[197] C. Kale *et al.*, “On the roles of stress-triaxiality and strain-rate on the deformation behavior of AZ31 magnesium alloys,” *Mater. Res. Lett.*, vol. 6, no. 2, pp. 152–158, Feb. 2018, doi: 10.1080/21663831.2017.1417923.
[198] C. Kale, S. Turnage, D. Z. Avery, H. El Kadiri, J. B. Jordon, and K. N. Solanki, “Towards dynamic tension-compression asymmetry and relative deformation mechanisms in magnesium,” *Materialia*, vol. 9, p. 100543, Mar. 2020, doi: 10.1016/j.mtla.2019.100543.
[199] S. A. Turnage *et al.*, “Anomalous mechanical behavior of nanocrystalline binary alloys under extreme conditions,” *Nat. Commun.*, vol. 9, no. 1, p. 2699, Jul. 2018, doi: 10.1038/s41467-018-05027-5.
[200] D. J. Barton, C. Kale, B. C. Hornbuckle, K. A. Darling, K. N. Solanki, and G. B. Thompson, “Microstructure and dynamic strain aging behavior in oxide dispersion strengthened 91Fe-8Ni-1Zr (at%) alloy,” *Mater. Sci. Eng. A*, vol. 725, pp. 503–509, May 2018, doi: 10.1016/j.msea.2018.04.016.
[201] G. Nolze and R. Hielscher, “Orientations – perfectly colored,” *J. Appl. Crystallogr.*, vol. 49, no. 5, pp. 1786–1802, Oct. 2016, doi: 10.1107/S1600576716012942.
[202] “The microscope that digs deep for answers,” *CERN*. https://home.cern/news/news/engineering/microscope-digs-deep-answers (accessed Dec. 14, 2020).
[203] T. E. Mitchell and W. A. Spitzig, “Three-stage hardening in tantalum single crystals,” *Acta Metall.*, vol. 13, no. 11, pp. 1169–1179, Nov. 1965, doi: 10.1016/0001-6160(65)90054-4.
[204] J. W. Hutchinson and K. W. Neale, “Influence of strain-rate sensitivity on necking under uniaxial tension,” *Acta Metall.*, vol. 25, no. 8, pp. 839–846, Aug. 1977, doi: 10.1016/0001-6160(77)90168-7.
[205] Y. Rotbaum and D. Rittel, “Is There An Optimal Gauge Length for Dynamic Tensile Specimens?,” *Exp. Mech.*, vol. 54, no. 7, pp. 1205–1214, Sep. 2014, doi: 10.1007/s11340-014-9889-8.
[206] P. Verleysen, J. Degrieck, T. Verstraete, and J. Van Slycken, “Influence of Specimen Geometry on Split Hopkinson Tensile Bar Tests on Sheet Materials,” *Exp. Mech.*, vol. 48, no. 5, pp. 587–598, Oct. 2008, doi: 10.1007/s11340-008-9149-x.
[207] F. J. Zerilli and R. W. Armstrong, “Description of tantalum deformation behavior by dislocation mechanics based constitutive relations,” *J. Appl. Phys.*, vol. 68, no. 4, pp. 1580–1591, Aug. 1990, doi: 10.1063/1.346636.
[208] G. Z. Voyiadjis and F. H. Abed, “Effect of dislocation density evolution on the thermomechanical response of metals with different crystal structures at low and high strain rates and temperatures,” p. 45, 2005.
[209] M. A. Bhatia, S. Groh, and K. N. Solanki, “Atomic-scale investigation of point defects and hydrogen-solute atmospheres on the edge dislocation mobility in alpha iron,” *J. Appl. Phys.*, vol. 116, no. 6, p. 064302, Aug. 2014, doi: 10.1063/1.4892630.
[210] T. E. Mitchell, “Dislocations and plasticity in single crystals of face-centered cubic metals and alloys,” *Prog. Appl. Mater. Res.*, vol. 6, pp. 119–237, 1964.
[211] T. Suzuki, S. Takeuchi, and H. Yoshinaga, *Dislocation Dynamics and Plasticity*. Berlin, Heidelberg: Springer Berlin Heidelberg, 1991. Accessed: Oct. 08, 2019. [Online]. Available: http://public.eblib.com/choice/publicfullrecord.aspx?p=3092676

[212] T. Suzuki, H. Koizumi, and H. O. K. Kirchner, “Plastic flow stress of b.c.c. transition metals and the Peierls potential,” *Acta Metall. Mater.*, vol. 43, no. 6, pp. 2177–2187, Jun. 1995, doi: 10.1016/0956-7151(94)00451-X.

[213] A. Rusinek, R. Zaera, J. Klepaczko, and R. Cheriguene, “Analysis of inertia and scale effects on dynamic neck formation during tension of sheet steel,” *Acta Mater.*, p. S1359645405004775, Oct. 2005, doi: 10.1016/j.actamat.2005.08.019.

[214] K. J. Bowman and R. Gibala, “Stress asymmetry in cyclic deformation of b.c.c. metals,” *Acta Metall. Mater.*, vol. 40, no. 1, pp. 193–200, Jan. 1992, doi: 10.1016/0956-7151(92)90213-X.

[215] L. N. Chang, G. Taylor, and J. W. Christian, “A stress asymmetry in niobium single crystals deformed at 77 K,” *Scr. Metall.*, vol. 16, no. 1, pp. 95–98, Jan. 1982, doi: 10.1016/0036-9748(82)90410-0.

[216] A. Rohatgi, “WebPlotDigitizer,” Apr. 2019. https://automeris.io/WebPlotDigitizer

[217] G. K. Williamson and R. E. Smallman, “III. Dislocation densities in some annealed and cold-worked metals from measurements on the X-ray debye-scherrer spectrum,” *Philos. Mag.*, vol. 1, no. 1, pp. 34–46, Jan. 1956, doi: 10.1080/14786435608238074.

[218] K. J. Carroll, “Elastic constants and thermal expansion of niobium as a function of temperature,” p. 36.

[219] W. C. Hubbell and F. R. Brotzen, “Elastic constants of niobium-molybdenum alloys in the temperature range −190 to +100°C,” *J. Appl. Phys.*, vol. 43, no. 8, pp. 3306–3312, Aug. 1972, doi: 10.1063/1.1661712.

[220] D. I. Bolef, “Elastic Constants of Single Crystals of the bcc Transition Elements V, Nb, and Ta,” *J. Appl. Phys.*, vol. 32, no. 1, pp. 100–105, Jan. 1961, doi: 10.1063/1.1735933.

[221] R. J. Wasilewski, “Wasilewski_1965_Elastic constants of Nb by resonance at sonic frequencies.pdf,” *J. Phys. Chem. Solids*, vol. 26, p. 1643, 1965.

[222] P. E. Armstrong and J. M. Dickinson, “Temperature Dependence of the Elastic Stiffness Coefficients of Niobium(Columbium),” *Trans. Metall. Soc. AIME*, vol. 236, pp. 1404–1408, Oct. 1966.

[223] R. J. Farraro and R. B. McLellan, “High temperature elastic properties of polycrystalline niobium, tantalum, and vanadium,” *Metall. Trans. A*, vol. 10, no. 11, pp. 1699–1702, Nov. 1979, doi: 10.1007/BF02811703.

[224] S. Simoto, W. F. Hosford, and W. A. Backofen, “Ductile fracture in copper single crystals,” *Philos. Mag.*, vol. 12, no. 116, pp. 319–333, Aug. 1965, doi: 10.1080/14786436508218874.

[225] “Fracture Types: 2 Main Types of Fracture in Metals | Metallurgy,” *Engineering Notes India*, Apr. 21, 2018. http://www.engineeringenotes.com/metallurgy/metal-fracture/fracture-types-2-main-types-of-fracture-in-metals-metallurgy/42598 (accessed Jan. 29, 2020).

[226] A. F. Liu, *Mechanics and mechanisms of fracture: an introduction*. Materials Park, Ohio: ASM International, 2005.

[227] N. Jia, P. Eisenlohr, F. Roters, D. Raabe, and X. Zhao, “Orientation dependence of shear banding in face-centered-cubic single crystals,” *Acta Mater.*, vol. 60, no. 8, pp. 3415–3434, May 2012, doi: 10.1016/j.actamat.2012.03.005.

[228] D. Dorner, Y. Adachi, and K. Tsuzaki, “Periodic crystal lattice rotation in microband groups in a bcc metal,” *Scr. Mater.*, vol. 57, no. 8, pp. 775–778, Oct. 2007, doi: 10.1016/j.scriptamat.2007.06.048.

[229] Z. Zhao, T. R. Bieler, and D. Kang, “An Investigation of Correlations Between Mechanical and Microstructural Properties of High Purity Polycrystalline Niobium,” Whistler, Canada, Sep. 2015, vol. C08, pp. 219–222.

[230] R. Gröger, Z. Chlup, I. Kuběna, and T. Kruml, “Slip activity in molybdenum single crystals compressed at 77 K,” *Philos. Mag.*, vol. 98, no. 30, pp. 2749–2768, Oct. 2018, doi: 10.1080/14786435.2018.1505056.
[231] C. Marichal, H. Van Swygenhoven, S. Van Petegem, and C. Borca, “{110} Slip with {112} slip traces in bcc Tungsten,” *Sci. Rep.*, vol. 3, no. 1, p. 2547, Dec. 2013, doi: 10.1038/srep02547.
[232] C. Marichal *et al.*, “Origin of Anomalous Slip in Tungsten,” *Phys. Rev. Lett.*, vol. 113, no. 2, p. 025501, Jul. 2014, doi: 10.1103/PhysRevLett.113.025501.
[233] El-Magd, E. and Abouridouane, M., “High speed forming of the light-weight wrought alloys,” in *Proceedings of the 1st International Conference on High Speed Forming*, Dortmund, Germany, 2004, pp. 3–12. [Online]. Available: http://dx.doi.org/10.17877/DE290R-12924
[234] D. B. Williams and C. B. Carter, *Transmission electron microscopy: a textbook for materials science*, 2nd ed. New York: Springer, 2008.
[235] M. Grundner and J. Halbritter, “XPS and AES studies on oxide growth and oxide coatings on niobium,” *J. Appl. Phys.*, vol. 51, no. 1, pp. 397–405, Jan. 1980, doi: 10.1063/1.327386.
[236] Q. Ma and R. A. Rosenberg, “Surface study of niobium samples used in superconducting rf cavity production,” in *PACS2001. Proceedings of the 2001 Particle Accelerator Conference (Cat. No.01CH37268)*, Chicago, IL, USA, 2001, vol. 2, pp. 1050–1052. doi: 10.1109/PAC.2001.986573.
[237] R. D. Veit, N. A. Kautz, R. G. Farber, and S. J. Sibener, “Oxygen dissolution and surface oxide reconstructions on Nb(100),” *Surf. Sci.*, vol. 688, pp. 63–68, Oct. 2019, doi: 10.1016/j.susc.2019.06.004.
[238] A. C. Fischer-Cripps, *Nanoindentation*, 2nd ed. Springer-Verlag New York, 2004. Accessed: Nov. 05, 2020. [Online]. Available: https://doi.org/10.1007/978-1-4757-5943-3
[239] S. K. Paul, G. Manikandan, and R. K. Verma, “Prediction of entire forming limit diagram from simple tensile material properties,” *J. Strain Anal. Eng. Des.*, vol. 48, no. 6, pp. 386–394, Aug. 2013, doi: 10.1177/0309324713488886.
[240] S. P. Keeler, “Plastic instability and fracture in sheets stretched over rigid punches,” PhD Thesis, Massachusetts Institute of Technology, Cambridge, MA, 1961. [Online]. Available: https://dspace.mit.edu/handle/1721.1/120282
[241] International Organization for Standardization, “ISO 12004-2:2008 - Metallic materials - Sheet and strip - Determination of forming-limit curves - Part 2: Determination of forming-limit curves in the laboratory.” 2008. [Online]. Available: https://www.iso.org/standard/43621.html
[242] ASTM International, “ASTM E2218-15, Standard Test Method for Determining Forming Limit Curves.” 2015. [Online]. Available: astm.org
[243] Z. Marciniak and K. Kuczyński, “Limit strains in the processes of stretch-forming sheet metal,” *Int. J. Mech. Sci.*, vol. 9, no. 9, pp. 609–620, Sep. 1967, doi: 10.1016/0020-7403(67)90066-5.
[244] K. S. Raghavan, “A simple technique to generate in-plane forming limit curves and selected applications,” *Metall. Mater. Trans. A*, vol. 26, no. 8, pp. 2075–2084, Aug. 1995, doi: 10.1007/BF02670679.
[245] J. Min, T. B. Stoughton, J. E. Carsley, and J. Lin, “Compensation for process-dependent effects in the determination of localized necking limits,” *Int. J. Mech. Sci.*, vol. 117, pp. 115–134, Oct. 2016, doi: 10.1016/j.ijmecsci.2016.08.008.

[246] J. Min, T. B. Stoughton, J. E. Carsley, and J. Lin, “A Method of Detecting the Onset of Localized Necking Based on Surface Geometry Measurements,” *Exp. Mech.*, vol. 57, no. 4, pp. 521–535, Apr. 2017, doi: 10.1007/s11340-016-0232-4.

[247] J. Min, T. B. Stoughton, J. E. Carsley, and J. Lin, “An improved curvature method of detecting the onset of localized necking in Marciniak tests and its extension to Nakazima tests,” *Int. J. Mech. Sci.*, vol. 123, pp. 238–252, Apr. 2017, doi: 10.1016/j.ijmecsci.2017.02.011.

[248] J.-L. Geoffroy, J. Goncalves, and X. Lemoine, “Adequately used FLC’s for Simulations,” presented at the International Deep-drawing Research Group (IDDRG 2007), Győr-Hungary, May 2007.

[249] A. Graf and W. Hosford, “Effect of changing strain paths on,” *Metall. Trans. A*, vol. 24A, no. 11, pp. 2503–2515, Nov. 1993, doi: 10.1007/BF02646529.

[250] S. Keeler and W. Brazier, “Relationship between laboratory material characterization and press-shop formability,” in *Conference on Microalloying*, 1975, vol. 75, pp. 517–528.

[251] A. Col, *Emboutissage des tôles - Importance des modes de déformation*. 2011.

[252] Z. Marciniak, K. Kuczyński, and T. Pokora, “Influence of the plastic properties of a material on the forming limit diagram for sheet metal in tension,” *Int. J. Mech. Sci.*, vol. 15, no. 10, pp. 789–800, Oct. 1973, doi: 10.1016/0020-7403(73)90068-4.

[253] D. Dudzinski and A. Molinari, “Perturbation analysis of thermoviscoplastic instabilities in biaxial loading,” *Int. J. Solids Struct.*, vol. 27, no. 5, pp. 601–628, 1991, doi: 10.1016/0020-7683(91)90216-3.

[254] W. W. Wood, “Experimental Mechanics at Velocity Extremes – Very High Strain Rates,” *Exp. Mech.*, vol. 7, pp. 441–446, 1967, doi: https://doi.org/10.1007/BF02326303.

[255] V. S. Balanethiram and G. S. Daehn, “Enhanced formability of interstitial free iron at high strain rates,” *Scr. Metall. Mater.*, vol. 27, no. 12, pp. 1783–1788, Dec. 1992, doi: 10.1016/0956-716X(92)90019-B.

[256] M. Gerdooei and B. M. Dariani, “Strain-rate-dependent forming limit diagrams for sheet metals,” *Proc. Inst. Mech. Eng. Part B J. Eng. Manuf.*, vol. 222, no. 12, pp. 1651–1659, Dec. 2008, doi: 10.1243/09544054JEM1193.

[257] Meyer, L.W., Kunze, H.D., and Seifert, S., “Dynamic behaviour of high strength steels,” in *Shock Waves High Strain Rate Phenomena in Metals*, 1981, pp. 51–63.

[258] Takeda, N. and Kobayshi, A., “High-velocity tensile properties of Ti–15V–3Cr–3Al–3Sn alloys,” in *Shock Waves and High Strain Rate Phenomena in Metals*, 1990, pp. 97–106.

[259] K. Demir, S. Goyal, M. Hahn, and E. Tekkaya, “Novel Approach and Interpretation for the Determination of Electromagnetic Forming Limits,” *Materials*, vol. 13, no. 18, p. 4175, Sep. 2020, doi: 10.3390/ma13184175.

[260] S. F. Golovashchenko, “Material Formability and Coil Design in Electromagnetic Forming,” *J. Mater. Eng. Perform.*, vol. 16, no. 3, pp. 314–320, 2007.

[261] V. Psyk, D. Risch, B. L. Kinsey, A. E. Tekkaya, and M. Kleiner, “Electromagnetic forming—A review,” *J. Mater. Process. Technol.*, vol. 211, no. 5, pp. 787–829, May 2011, doi: 10.1016/j.jmatprotec.2010.12.012.

[262] J. C. Giannotta, G. Regazzoni, and F. Montheillet, “Ductility and Flow Rule of Tantalum at 20°C and 500°C,” *J. Phys.*, vol. 46, no. C5, pp. C5-49-C5-54, Aug. 1985, doi: 10.1051/jphyscol:1985507.

[263] A. Jenab, D. E. Green, and A. T. Alpas, “Microscopic investigation of failure mechanisms in AA5182-O sheets subjected to electro-hydraulic forming,” *Mater. Sci. Eng. A*, vol. 691, pp. 31–41, Apr. 2017, doi: 10.1016/j.msea.2017.03.007.

[264] Subramani, Manoj, “Dynamic Response of Porous Ductile Materials Containing Cylindrical Voids,” PhD Thesis, Université de Lorraine, Metz, France, 2019. [Online]. Available: https://hal.univ-lorraine.fr/tel-02860800/file/DDOC_T_2019_0310_SUBRAMANI.pdf
[265] A. Melander, “A new model of the forming limit diagram applied to experiments on four copper-base alloys,” *Mater. Sci. Eng.*, vol. 58, no. 1, pp. 63–88, Mar. 1983, doi: 10.1016/0025-5416(83)90138-6.
[266] F. Stachowicz, “Inhomogeneity and forming limits of copper sheets,” *Int. J. Eng. Model.*, vol. 17, no. 1, pp. 7–12, 2004.
[267] M. St. Węglowski, S. Błacha, and A. Phillips, “Electron beam welding – Techniques and trends – Review,” *Vacuum*, vol. 130, pp. 72–92, Aug. 2016, doi: 10.1016/j.vacuum.2016.05.004.
[268] S. E. Demyanov *et al.*, “Superconducting properties of ultra-pure niobium welded joints,” *Low Temp. Phys.*, vol. 41, no. 7, pp. 522–527, Jul. 2015, doi: 10.1063/1.4927078.
[269] H. Jiang, T. R. Bieler, C. Compton, and T. L. Grimm, “Mechanical properties, microstructure, and texture of electron beam butt welds in high purity niobium,” in *Proceedings of the 2003 Bipolar/BiCMOS Circuits and Technology Meeting (IEEE Cat. No.03CH37440)*, Portland, OR, USA, 2003, vol. 2, pp. 1359–1361. doi: 10.1109/PAC.2003.1289705.
[270] ASTM International, “ASTM B170-99(2015), Standard Specification for Oxygen-Free Electrolytic Copper—Refinery Shapes,” West Conshohocken, PA, 2015. doi: 10.1520/B0170-99R15.
[271] ASTM International, “ASTM B152 / B152M-06, Standard Specification for Copper Sheet, Strip, Plate, and Rolled Bar.” 2006. [Online]. Available: asm.org
[272] R. L. Geng, J. Knobloch, and H. Padamsee, “Micro-Structures of RF Surfaces in the Electron-Beam-Weld Regions of Niobium,” in *1999 Workshop on RF Superconductivity*, Padova, Italy, 1999, pp. 238–245.
[273] J. Brawley, J. Mammosser, and L. Phillips, “Electron Beam Weld Parameter Set Development and Cavity Cost,” in *1997 Workshop on RF Superconductivity*, Padova, Italy, 1997, pp. 518–522.
[274] International Organization for Standardization, “ISO 4136:2012 - Destructive tests on welds in metallic materials - Transverse tensile test.” 2012. [Online]. Available: https://www.iso.org/standard/62317.html
[275] M. D. Xavier, R. L. Plaut, and C. G. Schön, “Uniaxial near plane strain tensile tests applied to the determination of the FLC0 formabillity parameter,” *Mater. Res.*, vol. 17, no. 4, pp. 982–986, Jun. 2014, doi: 10.1590/S1516-14392014005000083.
[276] ASTM International, “ASTM E517-19, Standard Test Method for Plastic Strain Ratio r for Sheet Metal.” 2019. [Online]. Available: astm.org
[277] M. Peroni, A. Caverzan, and G. Solomos, “A New Apparatus for Large Scale Dynamic Tests on Materials,” *Exp. Mech.*, vol. 56, no. 5, pp. 785–796, Jun. 2016, doi: 10.1007/s11340-015-0123-0.
[278] M. Peroni and G. Solomos, “Advanced Experimental Data Processing for the Identification of Thermal and Strain-Rate Sensitivity of a Nuclear Steel,” *J. Dyn. Behav. Mater.*, vol. 5, no. 3, pp. 251–265, Sep. 2019, doi: 10.1007/s40870-019-00207-w.
[279] M.-N. Bussac, P. Collet, G. Gary, and R. Othman, “An optimisation method for separating and rebuilding one-dimensional dispersive waves from multi-point measurements. Application to elastic or viscoelastic bars,” *J. Mech. Phys. Solids*, vol. 50, no. 2, pp. 321–349, Feb. 2002, doi: 10.1016/S0022-5096(01)00057-6.

[280] M. Peroni, G. Solomos, and N. Babcsan, “Development of a Hopkinson Bar Apparatus for Testing Soft Materials: Application to a Closed-Cell Aluminum Foam,” *Materials*, vol. 9, no. 1, p. 27, Jan. 2016, doi: 10.3390/ma9010027.
[281] MATLAB, “QR Solver.” https://www.mathworks.com/help/dsp/ref/qrsolver.html (accessed Nov. 04, 2020).
[282] Y. Yamaguchi, H. Doryo, M. Yuasa, H. Miyamoto, and M. Yamanaka, “Deformation and recrystallization behavior of super high-purity niobium for SRF cavity,” *IOP Conf. Ser. Mater. Sci. Eng.*, vol. 194, p. 012029, May 2017, doi: 10.1088/1757-899X/194/1/012029.
[283] S. K. Paul, “Theoretical analysis of strain- and stress-based forming limit diagrams,” *J. Strain Anal. Eng. Des.*, vol. 48, no. 3, pp. 177–188, Apr. 2013, doi: 10.1177/0309324712468524.
[284] A. Barata Da Rocha, F. Barlat, and J. M. Jalinier, “Prediction of the Forming Limit Diagrams of Anisotropic Sheets in Linear and Non-linear Loading,” *Mater. Sci. Eng.*, vol. 68, pp. 151–164, 1984.
[285] L. Corallo and P. Verleysen, “High-speed sheet metal forming: Numerical study of high speed Nakajima testing,” in *DYMAT Winter School 2020*, Les Houches, France, 2020, pp. 29–34.
[286] J.-F. Croteau, M. Peroni, S. Atieh, N. Jacques, and E. Cantergiani, “Effect of Strain Rate on the Tensile Mechanical Properties of Electron Beam Welded OFE Copper and High-Purity Niobium for SRF Applications,” *J. Dyn. Behav. Mater.*, 2021, doi: 10-1007/s40870-021-00293-9.
[287] R. Satish, V. Seshagiri Rao, D. Ananthapadmanaban, and B. Ravi, “Tensile Strength and Hardness Correlations with Microscopy in Friction welded Aluminium to Copper,” *J. Inst. Eng. India Ser. C*, vol. 97, no. 1, pp. 121–126, Jan. 2016, doi: 10.1007/s40032-015-0187-8.
[288] P. Kapadia *et al.*, “Quantification of residual stresses in electron beam welded fracture mechanics specimens,” *Int. J. Solids Struct.*, vol. 106–107, pp. 106–118, Feb. 2017, doi: 10.1016/j.ijsolstr.2016.11.028.
[289] N. Huber and J. Heerens, “On the effect of a general residual stress state on indentation and hardness testing,” *Acta Mater.*, vol. 56, no. 20, pp. 6205–6213, Dec. 2008, doi: 10.1016/j.actamat.2008.08.029.
[290] S. Ragu Nathan, V. Balasubramanian, S. Malarvizhi, and A. G. Rao, “Effect of welding processes on mechanical and microstructural characteristics of high strength low alloy naval grade steel joints,” *Def. Technol.*, vol. 11, no. 3, pp. 308–317, Sep. 2015, doi: 10.1016/j.dt.2015.06.001.
[291] P. Cavaliere, G. Campanile, F. Panella, and A. Squillace, “Effect of welding parameters on mechanical and microstructural properties of AA6056 joints produced by Friction Stir Welding,” *J. Mater. Process. Technol.*, vol. 180, no. 1–3, pp. 263–270, Dec. 2006, doi: 10.1016/j.jmatprotec.2006.06.015.
[292] Z. Rosenberg, R. Kositski, Y. Ashuach, V. Leus, and A. Malka-Markovitz, “On the upturn phenomenon in the strength vs. strain-rate relations of metals,” *Int. J. Solids Struct.*, vol. 176–177, pp. 185–190, Nov. 2019, doi: 10.1016/j.ijsolstr.2019.06.015.
[293] J. R. Davis, Ed., *Tensile testing*, 2nd ed. Materials Park, Ohio: ASM International, 2004.
[294] A. Rohatgi, A. Soulami, E. V. Stephens, R. W. Davies, and M. T. Smith, “An investigation of enhanced formability in AA5182-O Al during high-rate free-forming at room-temperature: Quantification of deformation history,” *J. Mater. Process. Technol.*, vol. 214, no. 3, pp. 722–732, Mar. 2014, doi: 10.1016/j.jmatprotec.2013.07.015.

[295] N. Jacques, “An analytical model for necking strains in stretched plates under dynamic biaxial loading,” *Int. J. Solids Struct.*, vol. 200–201, pp. 198–212, Sep. 2020, doi: 10.1016/j.ijsolstr.2020.05.028.

BOOK OF APPENDICES

Table of Contents

List of Figures

List of Tables

Appendix A – FIB Parameters of Niobium Lamella Preparation

Below are the FIB parameters used to prepare a ~100 nm thick lamella at CERN for STEM analysis. The lamella was prepared by Dr. Adrienn Baris and further analyzed at BAM with a conventional TEM.

Machine: Zeiss XB540 Focused Ion Beam – Scanning Electron Microscope

Ions: Gallium (Ga+)

Coating and soldering material: Platinum (Pt), 3 μm layer deposited on the specimen before milling.

Preparation steps:

Cut in bulk specimen:

1. Coarse milling: 30 kV, 65 nA (far from the specimen);
2. Fine milling #1: 30 kV, 30 nA;
3. Fine milling #2: 30 kV, 3 nA;
4. Undercut: 30 kV, 1.5 nA;

Extraction of the lamella with the micromanipulator (lower current, lower amount of ions):

5. Thinning #1: 30kV, 700 pA (first side)
6. Thinning #2: 30kV, 300 pA (first side);
7. Thinning #3: 30kV, 100 pA(first side);
8. Thinning #4: 30kV, 50 pA (first and second side);

Cleaning of the lamella (lower voltage, lower energy/ion):

9. Cleaning #1: 5 kV, 200 pA;
10. Cleaning #2: 5 kV, 10 pA (low magnification imaging with sample extra tilt of 3° on both sides for 2 minutes);
11. Cleaning #3: 2 kV, 10 pA (low magnification imaging with sample extra tilt of 3° on both sides for 2 minutes).

Appendix B – Niobium Single Crystal Tensile Orientation Selection

This first section of this appendix presents flowcharts of MATLAB codes written to (1) plot an inverse pole figure from Bunge Euler angles or an orientation vector, (2) plot the possible tensile crystal orientations for each grain in an IPF for a rotation of 180° about the normal to the niobium disk, and (3) to calculate the Schmid factors of all 24 slip systems that could activate and print important details about the two slip systems with the highest Schmid factors. A breakdown of the orientations selected in each grain, based is presented in the second section of this appendix.

B.1. Flowchart of Important MATLAB Codes Used to Analyze the Large-Grain Niobium Disk

The flowchart of the MATLAB code to convert Bunge Euler angles or an orientation vector into coordinates in a standard triangle inverse pole figure is presented in Figure B.1, with subfunctions in Figure B.2. This code was often used during this study to plot results from different sources, such as EBSD measurements and the selection of tensile orientations. For IPF coordinates calculated from Bunge Euler angles, the return variable (`coord_IPF`) contains the coordinates for the IPF in the *x*, *y*, and *z* directions. Based on the coordinate system defined in Figure 3.2, the direction normal to the disk, the orientations measured, is along *z* (third column) and the tensile orientation is along *y* (second column).

Next, the flowchart of the MATLAB code developed to plot the IPFs with all possible tensile orientations, i.e. for a rotation from 0 to 180 degrees around the *z* axis, is presented in Figure B.3. This code was used to produce the IPFs for each grain in Figure B.7 to Figure B.16.

After selecting the tensile orientations of interest, the Schmid factor was calculated for all 24 slip systems (Table 2.1) to identify the two systems with the highest Schmid factors and their respective values. Figure B.4 and Figure B.5 show the flowcharts of the MATLAB codes developed to perform those tasks and print relevant information about the two slip systems of interest. Figure B.6 shows an example of the text printed from this analysis for tensile samples cut in grain 2. Also, the code in Figure B.4 was used to produce Table 4.1 and the one in Figure B.5 was combined with the giveIPFCoord code of Figure B.1 to produce the inverse pole figures with different values of Schmid factors and slip systems in Figure 2.11 and 2.12.

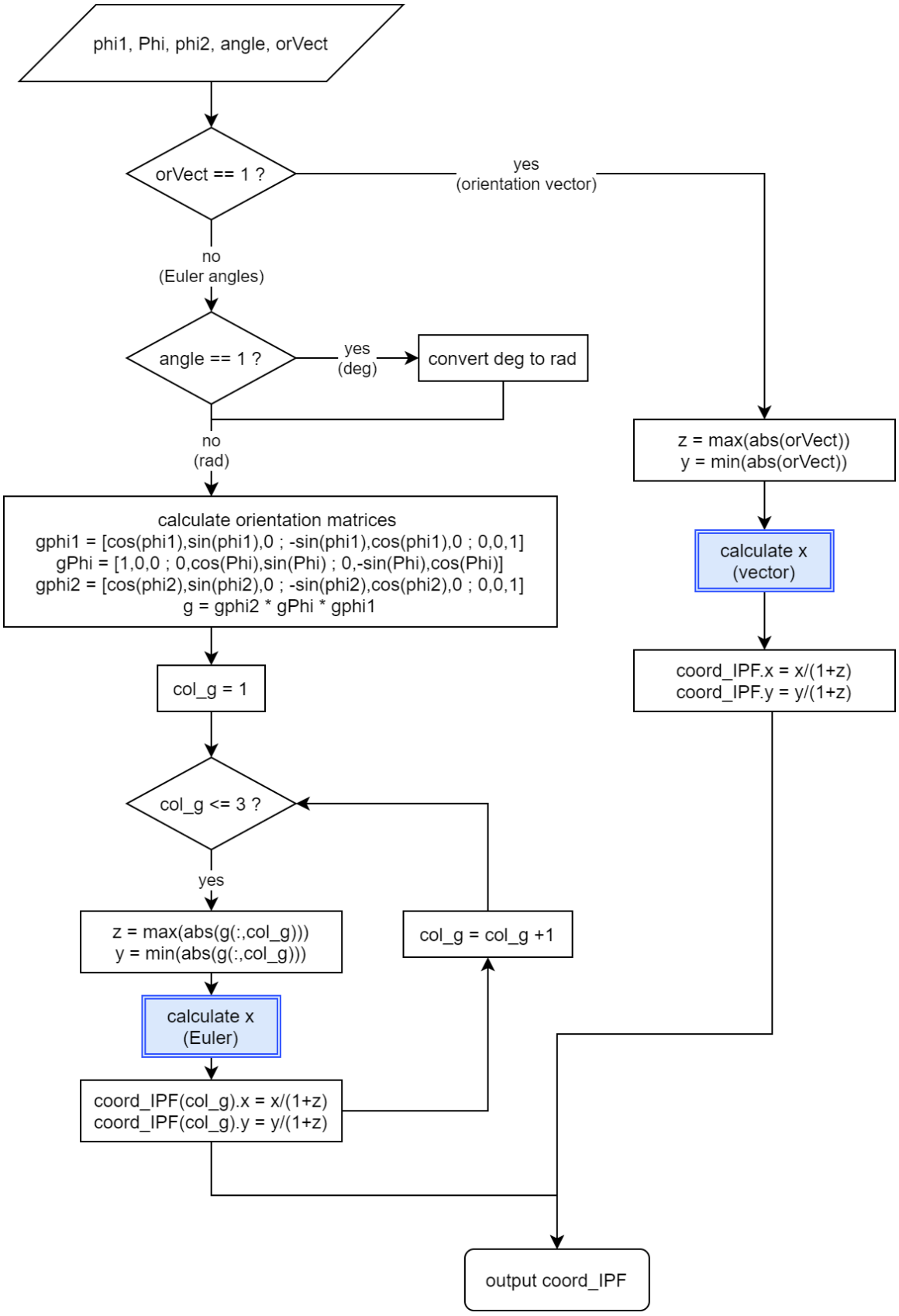

Figure B.1: Part 1/2 of the flowchart for the giveIPFCoord MATLAB code.

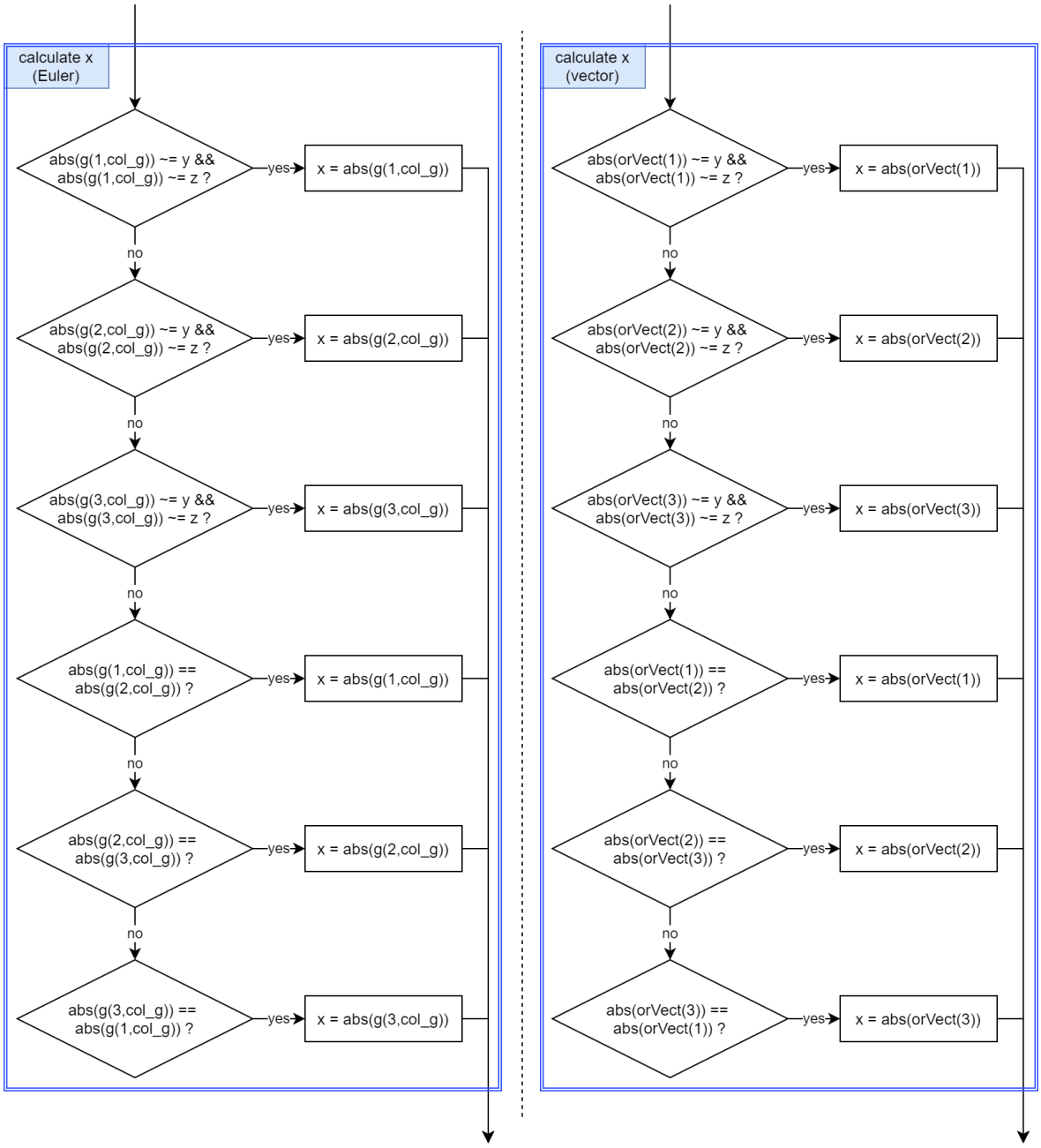

Figure B.2: Part 2/2 of the flowchart for the giveIPFCoord MATLAB code, which deals with the calculation of x for (left) Bunge Euler angles and (right) an orientation vector.

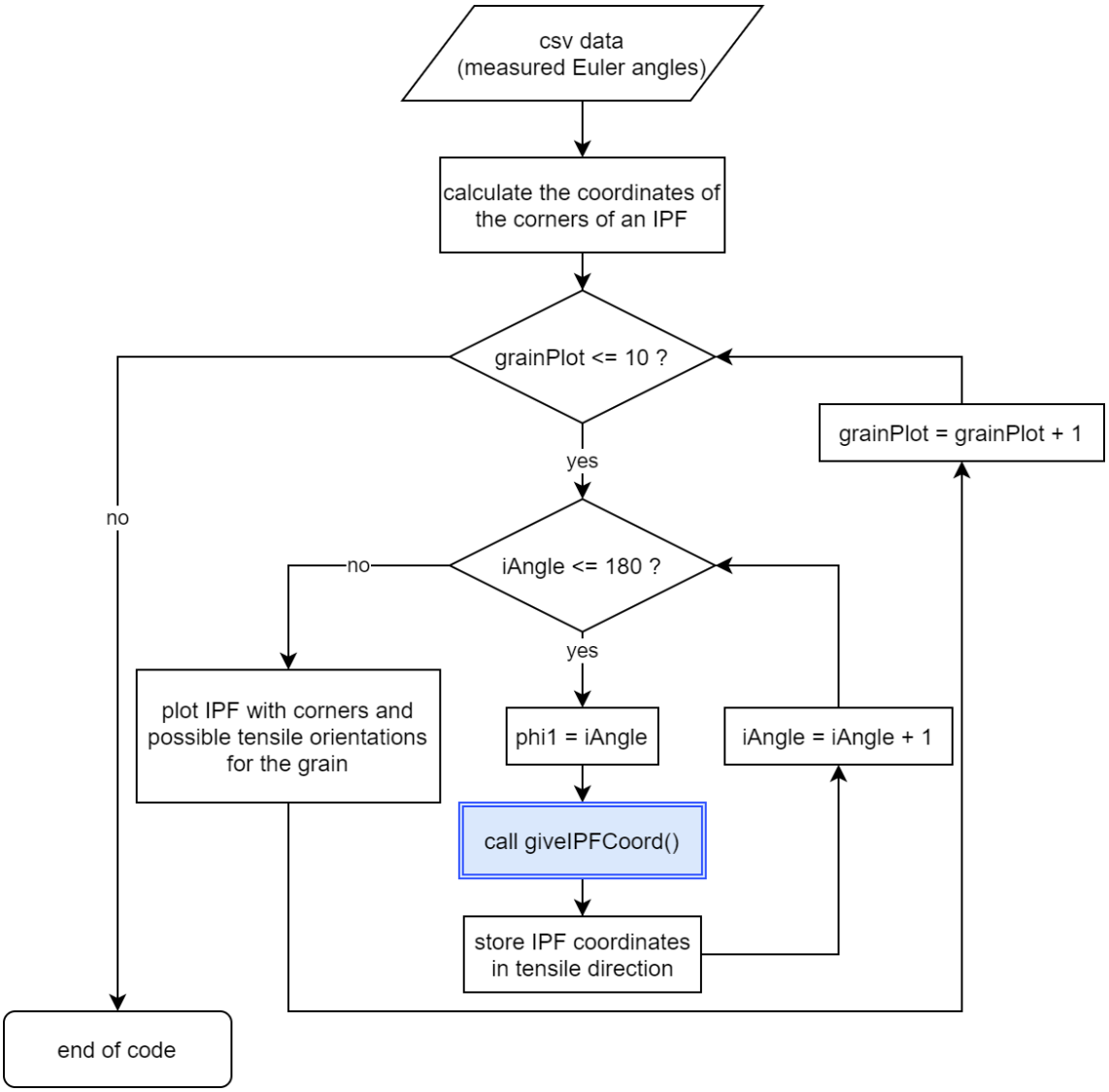

Figure B.3: Flowchart of the MATLAB code to plot the possible tensile orientations by a rotation of 0 to 180 degrees around *z* for a given single crystal.

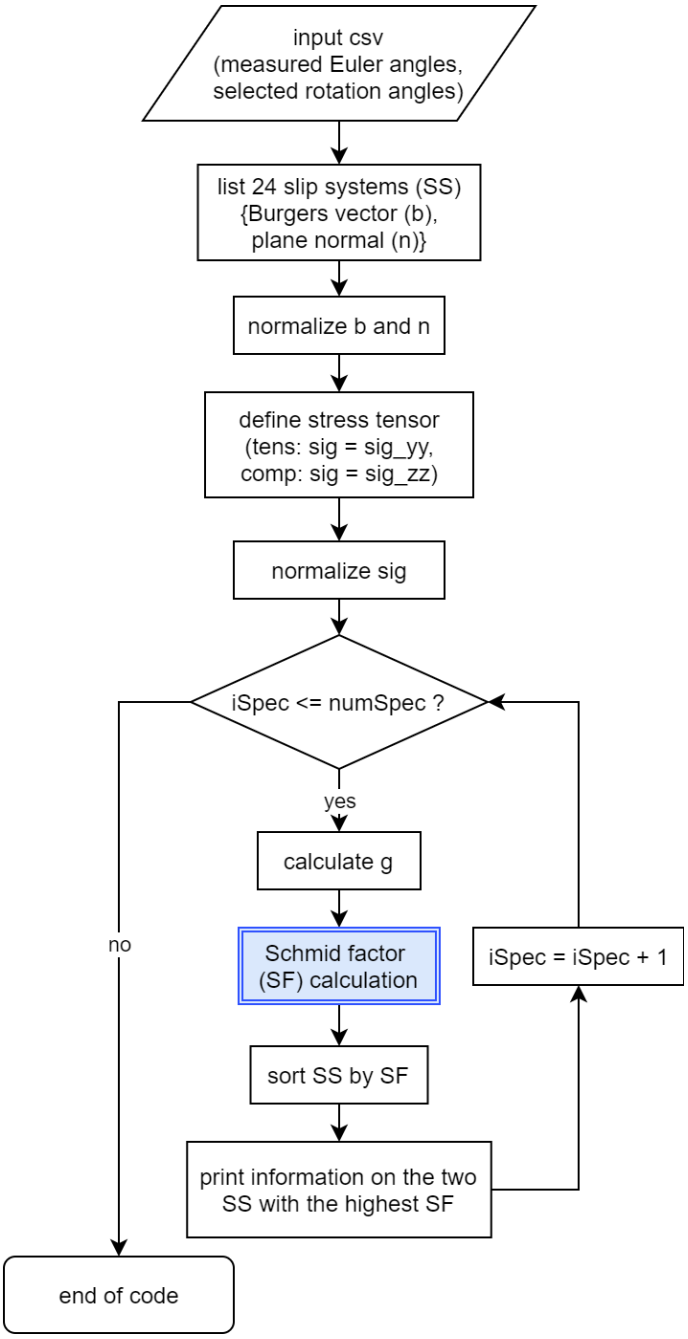

Figure B.4: Flowchart of the MATLAB code to print the Schmid factor, slip direction, and slip plane normal of the two slip systems with the highest Schmid factors for each tensile or compression specimen.

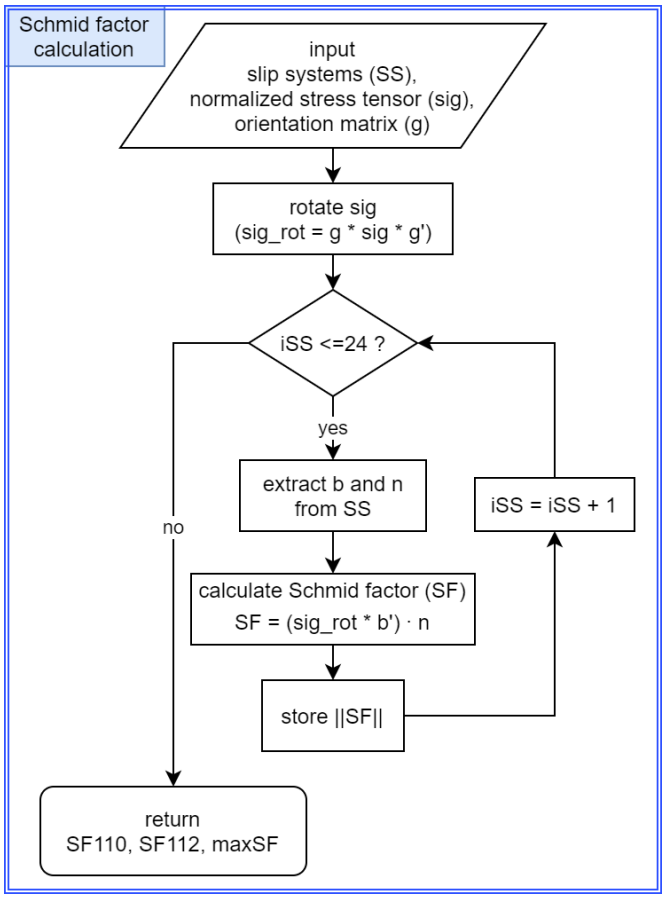

Figure B.5: Flowchart of the MATLAB code to calculate the Schmid factor of all slip systems for a given stress tensor and crystal orientation.

```
Grain2 Angle 14 SF1 0.412 SS1 [1-11](-2-11) SF2 0.393 SS2 [1-11](110)
Grain2 Angle 43 SF1 0.437 SS1 [111](-101) SF2 0.428 SS2 [111](-1-12)
Grain2 Angle 59 SF1 0.471 SS1 [-1-11](2-11) SF2 0.459 SS2 [111](-101)
Grain2 Angle 87 SF1 0.496 SS1 [1-11](-2-11) SF2 0.483 SS2 [-111](211)
Grain2 Angle 123 SF1 0.459 SS1 [-111](1-12) SF2 0.418 SS2 [-111](101)
Grain2 Angle 158 SF1 0.484 SS1 [-1-11](1-10) SF2 0.479 SS2 [-1-11](2-11)
```

Figure B.6: Example of text printed from the MATLAB code depicted in Figure B.4 for the tensile specimens cut in grain 2.

B.2. Breakdown of Each Grain

Figure B.7 to Figure B.16 show the tensile crystal orientations selected for the ten largest grains of the high-purity niobium disk. Each figure presents (a) the location of the specimens in the disk before cutting colored based on the IPF orientation in the loading direction, (b) the possible crystal tensile orientations in an inverse pole figure for the specific grain, and the orientations that were selected and cut, and (c) the same information as in the IPF in (b), but superposed on the color code defined for ratios of Schmid factors (Figure 2.12).

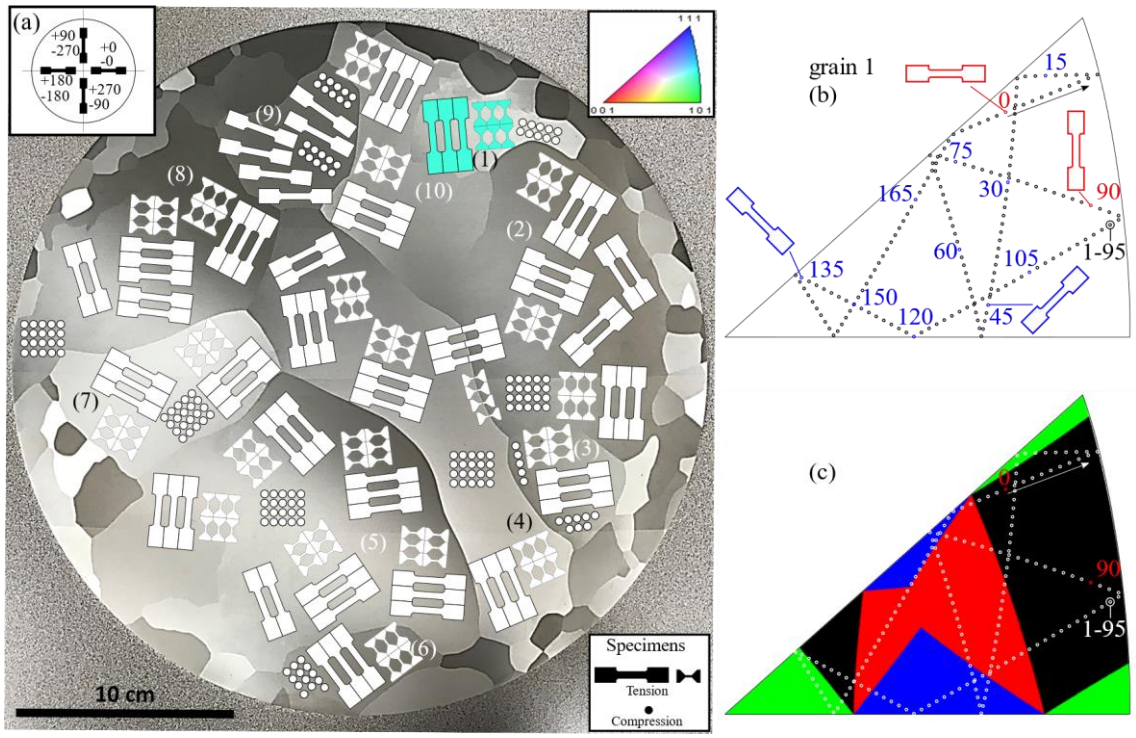

Figure B.7: (a) Large grain disk with colored specimens for grain 1, (b) an inverse pole figure with all potential crystal orientations (small black circles) and the ones selected (larger circles) for grain 1, and (c) an IPF of the ratio of two slip systems with the highest Schmid factor with the chosen orientations.

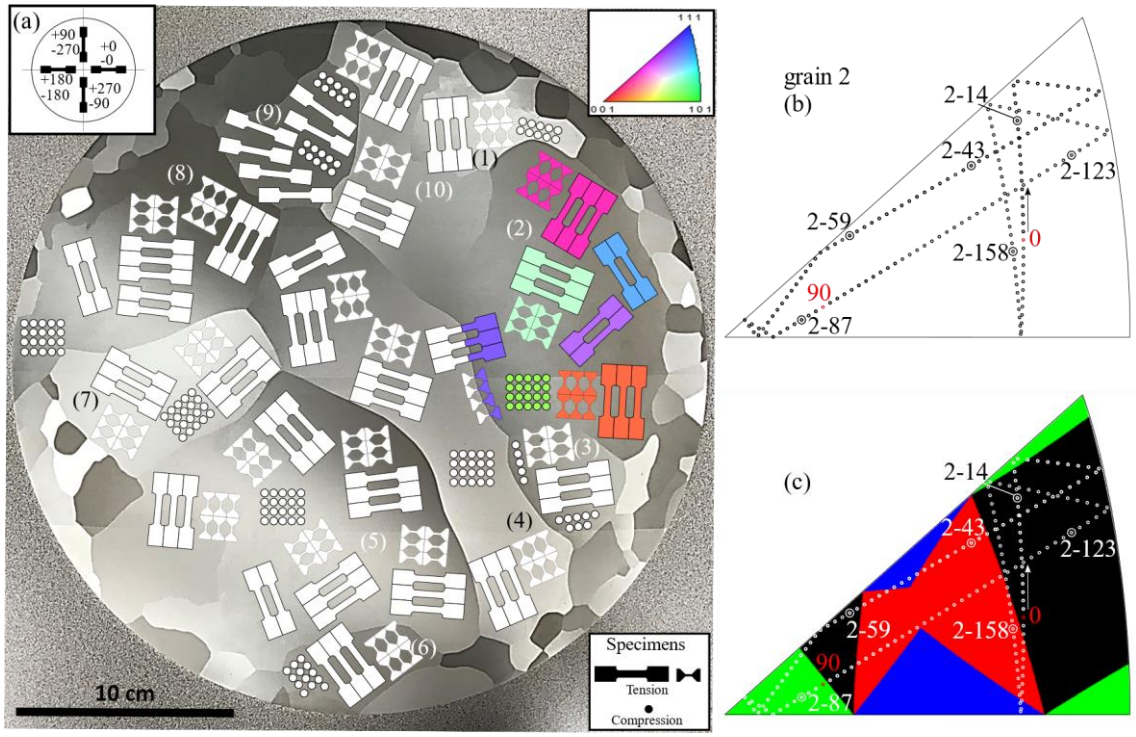

Figure B.8: (a) Large grain disk with colored specimens for grain 2, (b) an inverse pole figure with all potential crystal orientations (small black circles) and the ones selected (larger circles) for grain 2, and (c) an IPF of the ratio of two slip systems with the highest Schmid factor with the chosen orientations.

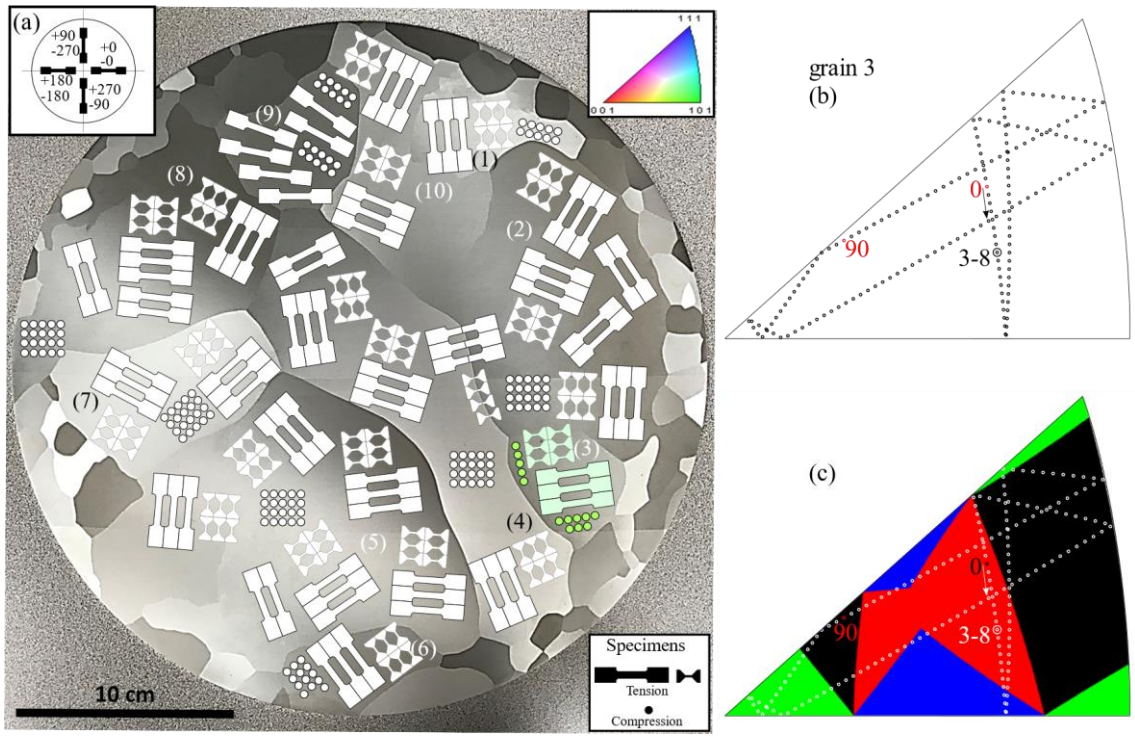

Figure B.9: (a) Large grain disk with colored specimens for grain 3, (b) an inverse pole figure with all potential crystal orientations (small black circles) and the ones selected (larger circles) for grain 3, and (c) an IPF of the ratio of two slip systems with the highest Schmid factor with the chosen orientations.

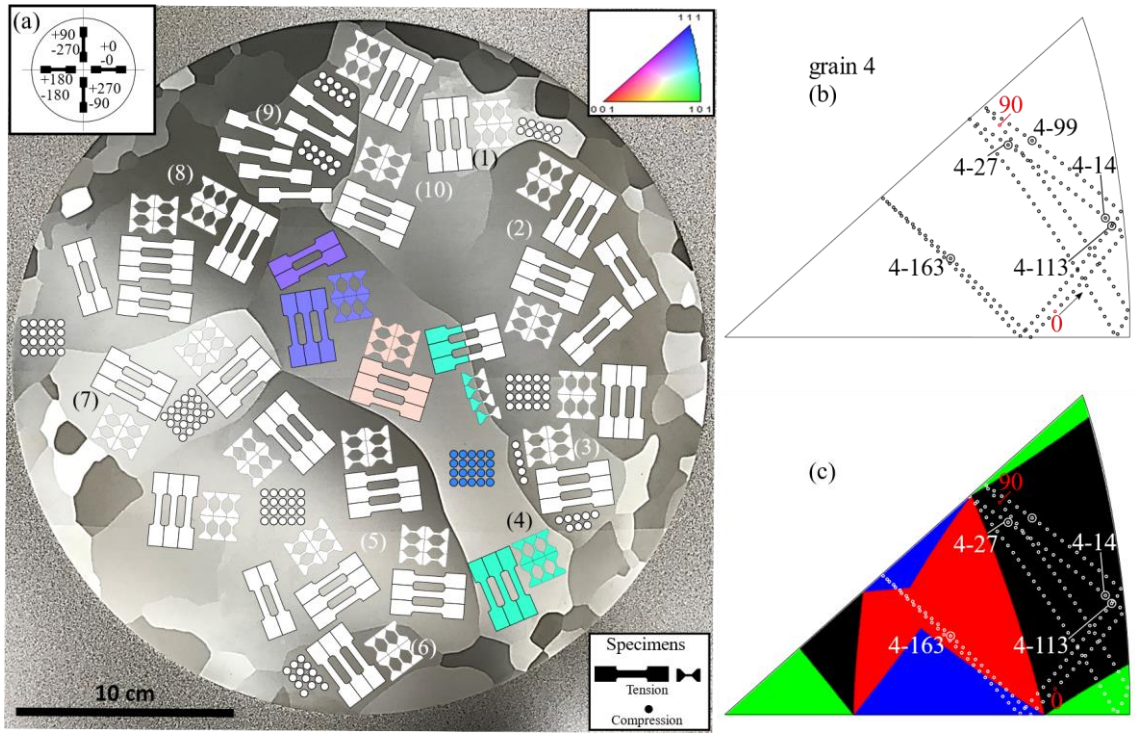

Figure B.10: (a) Large grain disk with colored specimens for grain 4, (b) an inverse pole figure with all potential crystal orientations (small black circles) and the ones selected (larger circles) for grain 4, and (c) an IPF of the ratio of two slip systems with the highest Schmid factor with the chosen orientations.

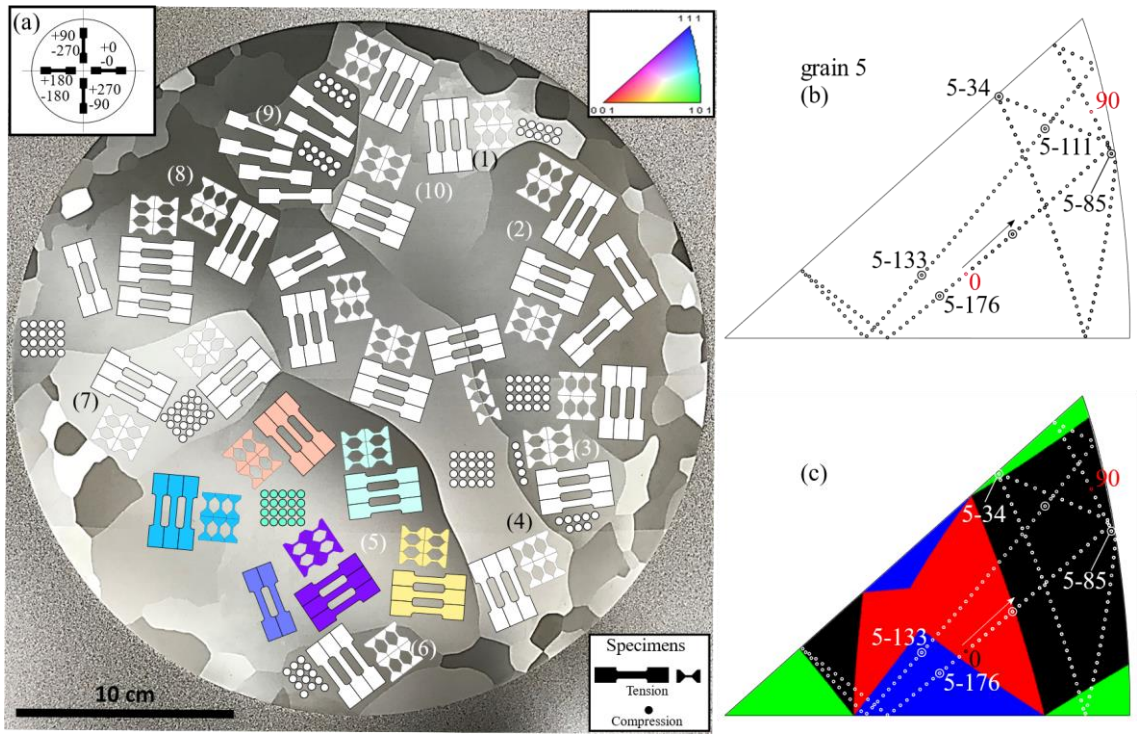

Figure B.11: (a) Large grain disk with colored specimens for grain 5, (b) an inverse pole figure with all potential crystal orientations (small black circles) and the ones selected (larger circles) for grain 5, and (c) an IPF of the ratio of two slip systems with the highest Schmid factor with the chosen orientations.

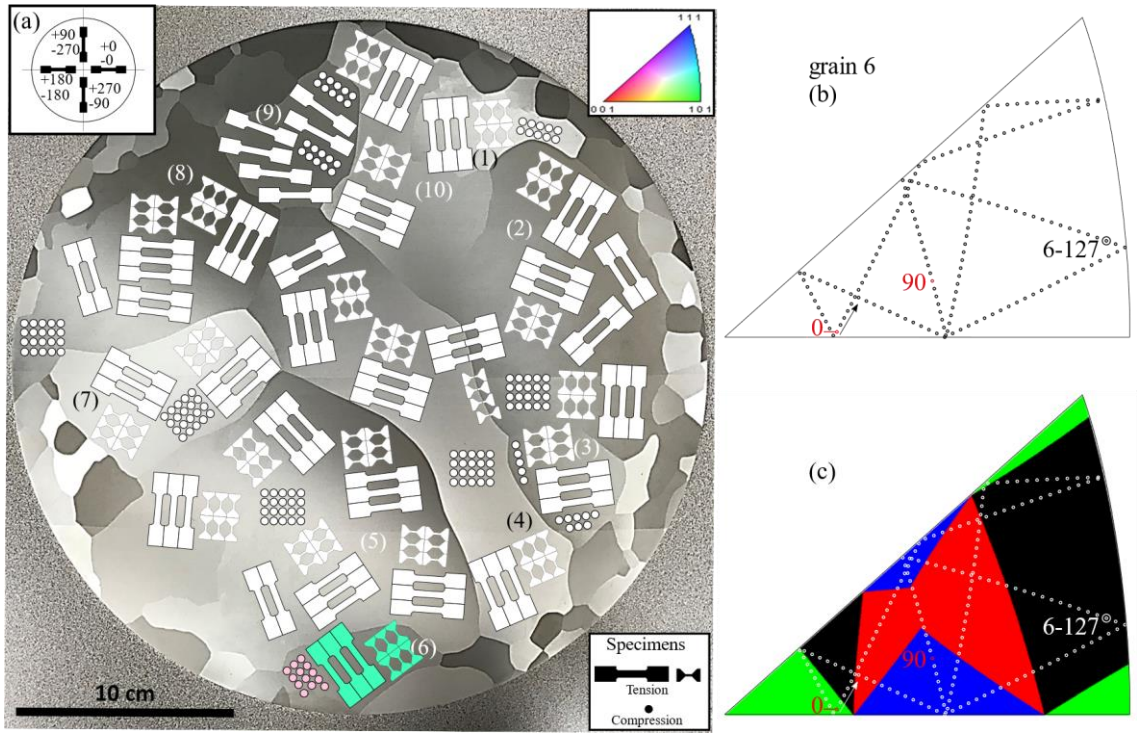

Figure B.12: (a) Large grain disk with colored specimens for grain 6, (b) an inverse pole figure with all potential crystal orientations (small black circles) and the ones selected (larger circles) for grain 6, and (c) an IPF of the ratio of two slip systems with the highest Schmid factor with the chosen orientations.

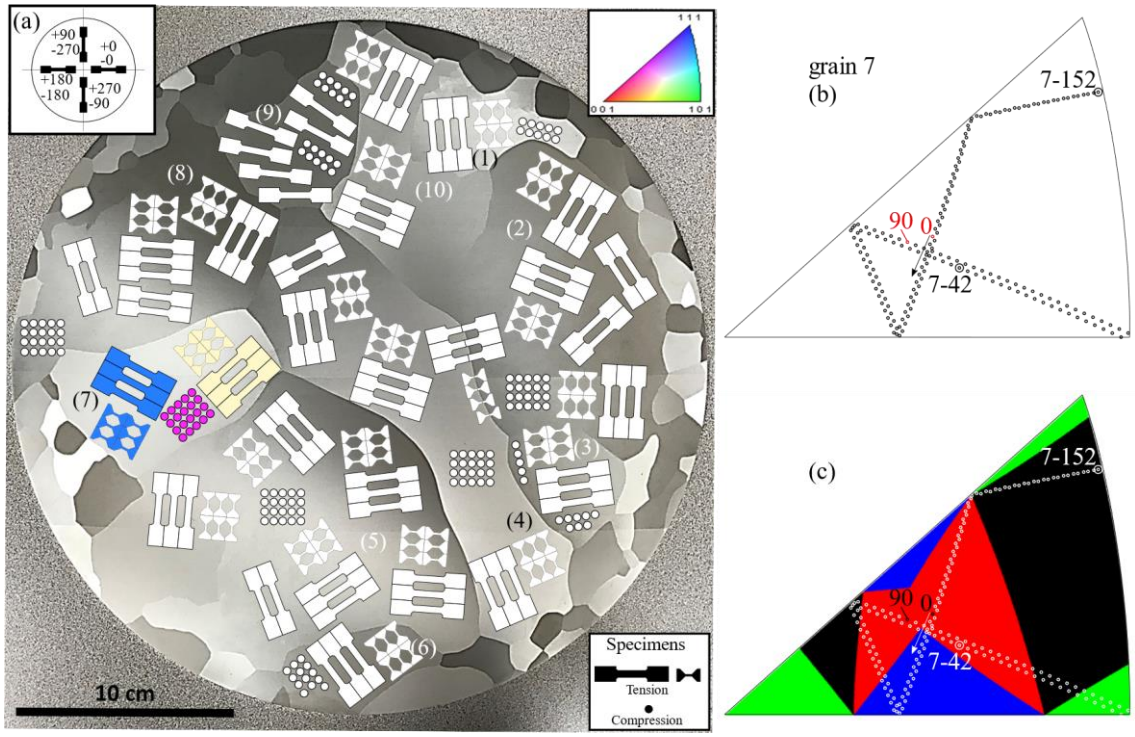

Figure B.13: (a) Large grain disk with colored specimens for grain 7, (b) an inverse pole figure with all potential crystal orientations (small black circles) and the ones selected (larger circles) for grain 7, and (c) an IPF of the ratio of two slip systems with the highest Schmid factor with the chosen orientations.

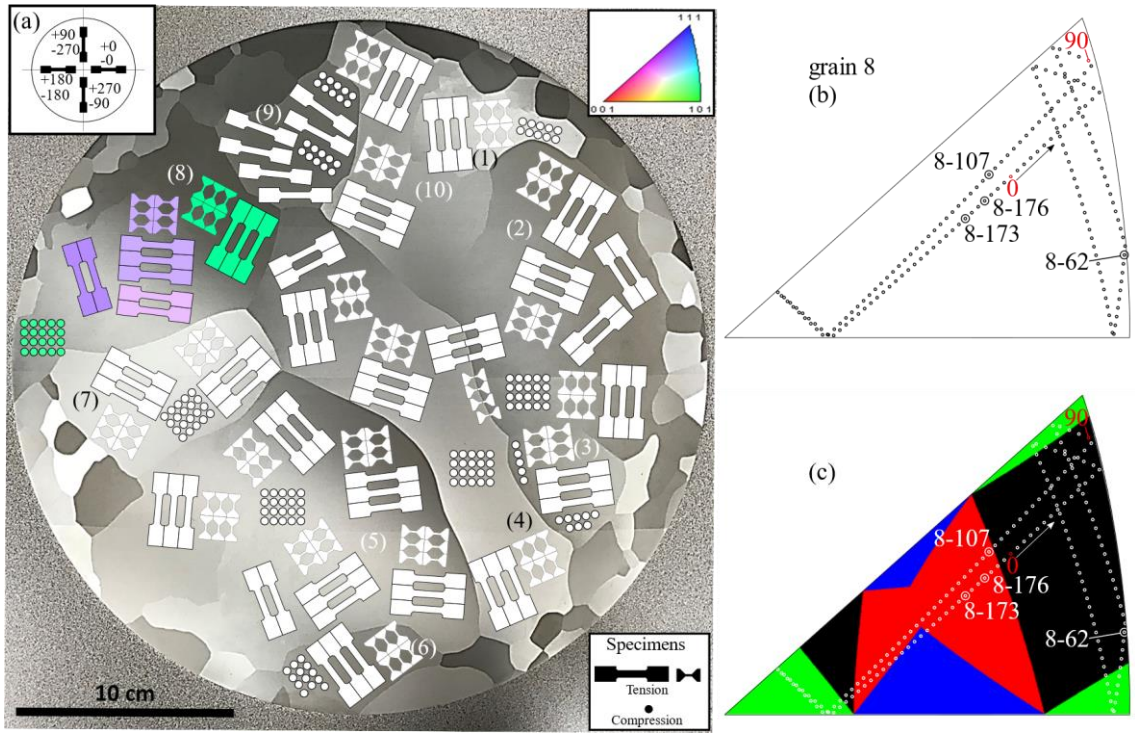

Figure B.14: (a) Large grain disk with colored specimens for grain 8, (b) an inverse pole figure with all potential crystal orientations (small black circles) and the ones selected (larger circles) for grain 8, and (c) an IPF of the ratio of two slip systems with the highest Schmid factor with the chosen orientations.

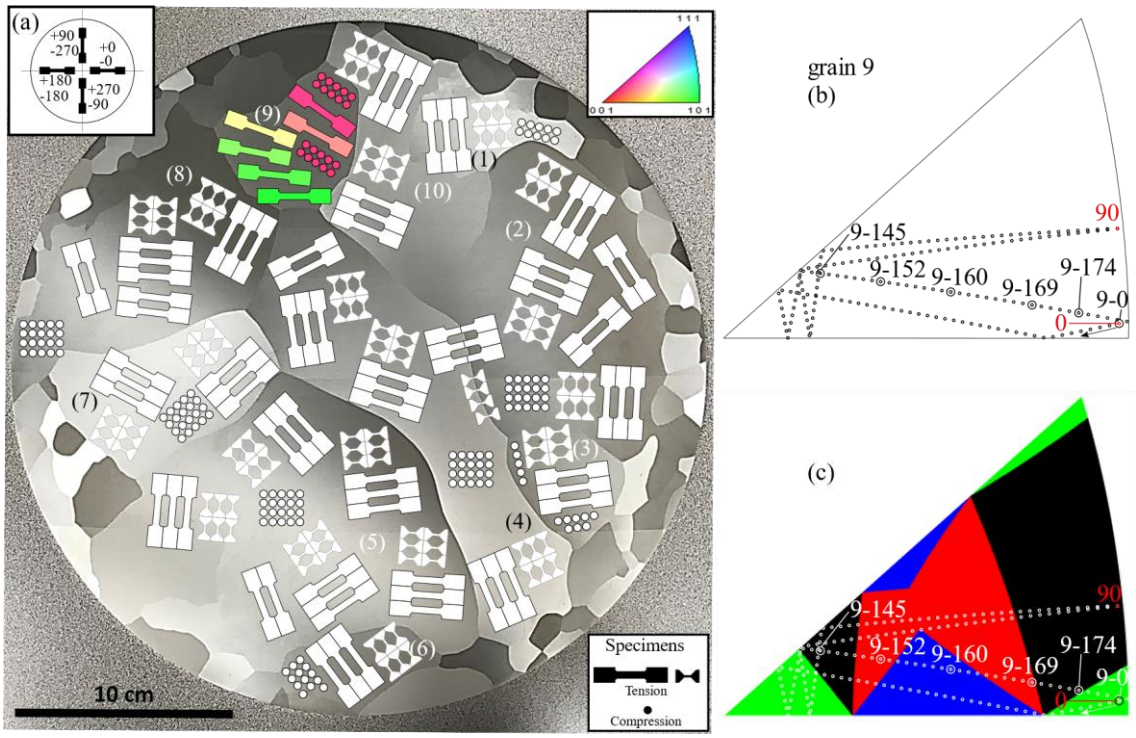

Figure B.15: (a) Large grain disk with colored specimens for grain 9, (b) an inverse pole figure with all potential crystal orientations (small black circles) and the ones selected (larger circles) for grain 9, and (c) an IPF of the ratio of two slip systems with the highest Schmid factor with the chosen orientations.

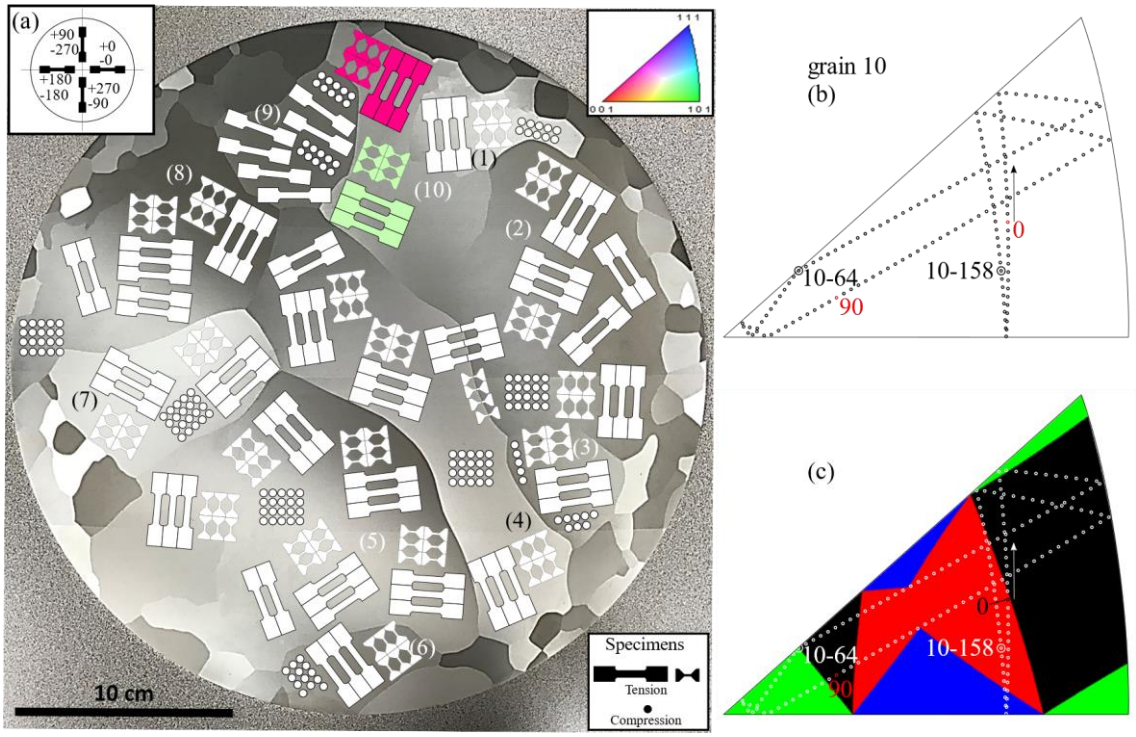

Figure B.16: (a) Large grain disk with colored specimens for grain 10, (b) an inverse pole figure with all potential crystal orientations (small black circles) and the ones selected (larger circles) for grain 10, and (c) an IPF of the ratio of two slip systems with the highest Schmid factor with the chosen orientations.

Appendix C – Code to Calculate the FLD from Experimental Marciniak Tests

An overview of the MATLAB code used to calculate the forming limit diagram of OFE copper and niobium in Chapter 8 was provided in section 7.3.4.2. More details about the code are given in the flowcharts in Figure C.1. and Figure C.2. The former figure provides details about the function written to numerically fit the experimental data to calculate ε_1 and to calculate ε_2 and the latter presents an overview of the entire MATLAB code. Recall from section 7.3.4. that three line-scans of the major strain as function of position, perpendicularly intersecting the neck, were extracted from the 2D DIC software package GOM Correlate for each Marciniak specimen. Those csv files were the input data of the code presented in Figure C.2. Finally, the plots for each FLD were saved in the MATLAB figure format and the Scalable Vector Graphics (SVG) format. The free and open-source software Inkscape was used with the SVG files for simple editions of the appearance of the figures.

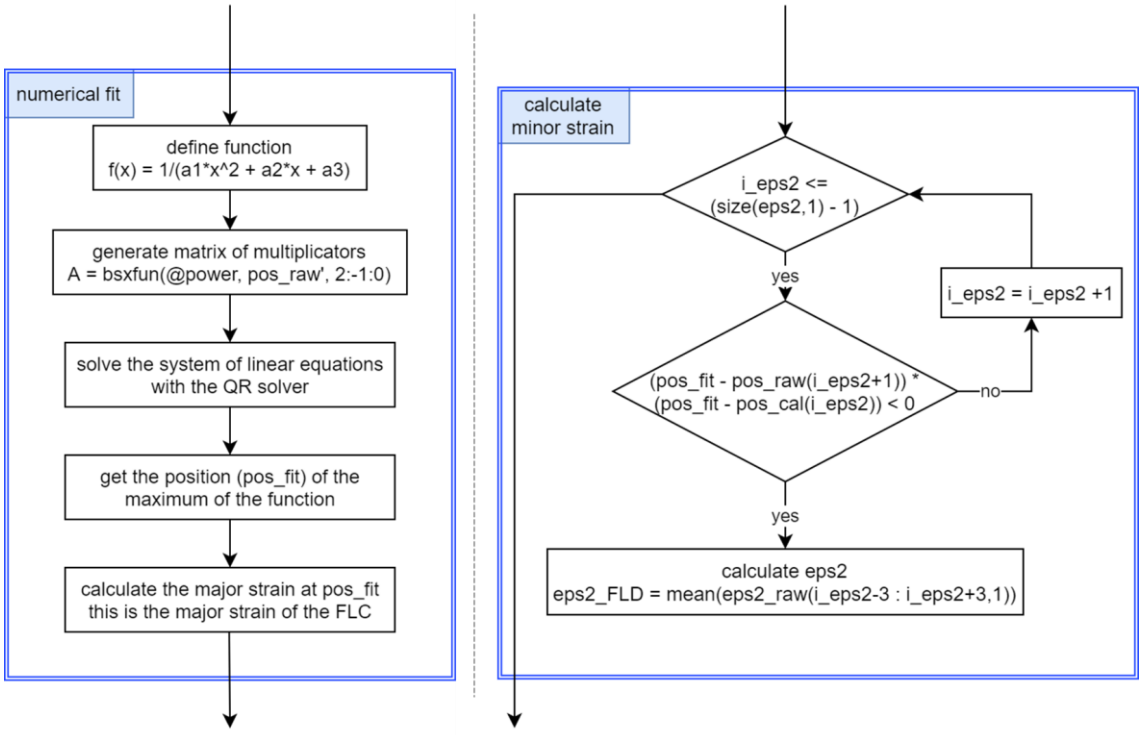

Figure C.1: Part 1/2 of the flowchart of the MATLAB code used to calculate the FLD of OFE copper and niobium, showing the functions used for the numerical fit of experimental data to calculate the major strain (ε_1) and to calculate the average minor strain (ε_2) around the position of the maximum numerically fitted ε_1.

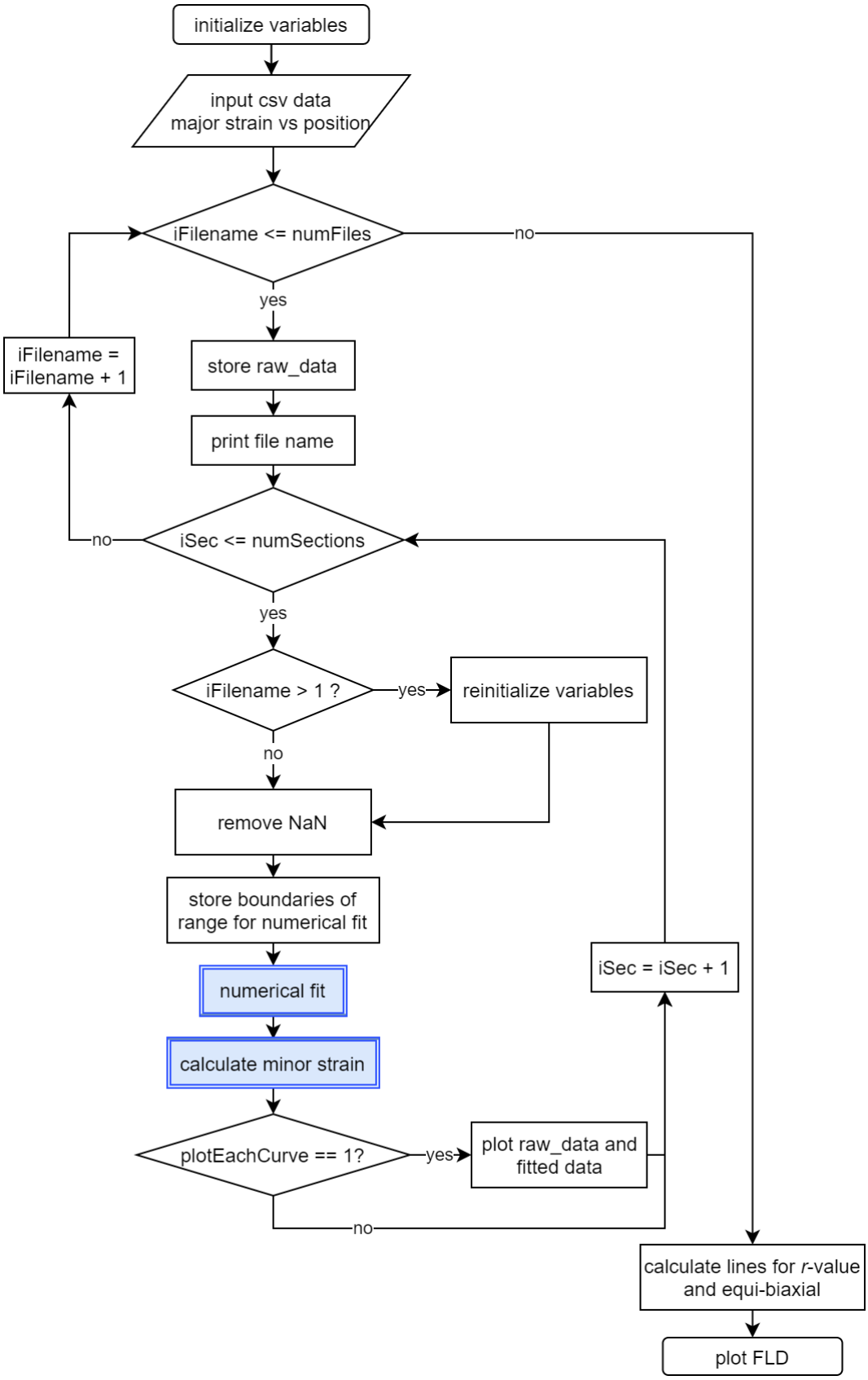

Figure C.2: Part 2/2 of the flowchart of the MATLAB code used to calculate the FLD of OFE copper and niobium showing an overview of the entire code.

Appendix D – Pictures of Marciniak Sheets after Testing

Deformed and broken blanks following Marciniak tests provide valuable information to help improve a setup and methodology and explain measured results. This appendix shows some of the deformed OFE copper and niobium blank-assembly (the blank carrier–blank assembly).

Figure D.1a shows three 80 mm x 200 mm annealed OFE copper blank-assemblies. Necking is visible on the painted blanks, but not in the bottom view of the blank carriers. This indicates that the sheets necked away from the gap between the halves of the blank carriers. As discussed in section 8.2. and shown in the Figure 8.1, this is likely caused by high friction forces between the brass punch and the blank carrier due to the use of PVC films instead of PTFE films.

Figure D.1b shows three 140 mm x 200 mm annealed OFE copper blank-assemblies with a blank carrier with an initial hole with a diameter of 10 mm. The blank of the first one (labelled 01) failed at the radius of the punch, which invalidated the test. This is a consequence of using a too small hole, recall that a hole diameter of 30 mm was found to be adequate for the blank to fail before the blank carrier. Note that the other specimens were not used to estimate the FLD of OFE copper since the blank carriers failed before the blank. This type of information cannot be found from the post-mortem pictures of the specimens, but from in-situ DIC and the load–displacement curve of the mechanical press (Figure 8.5).

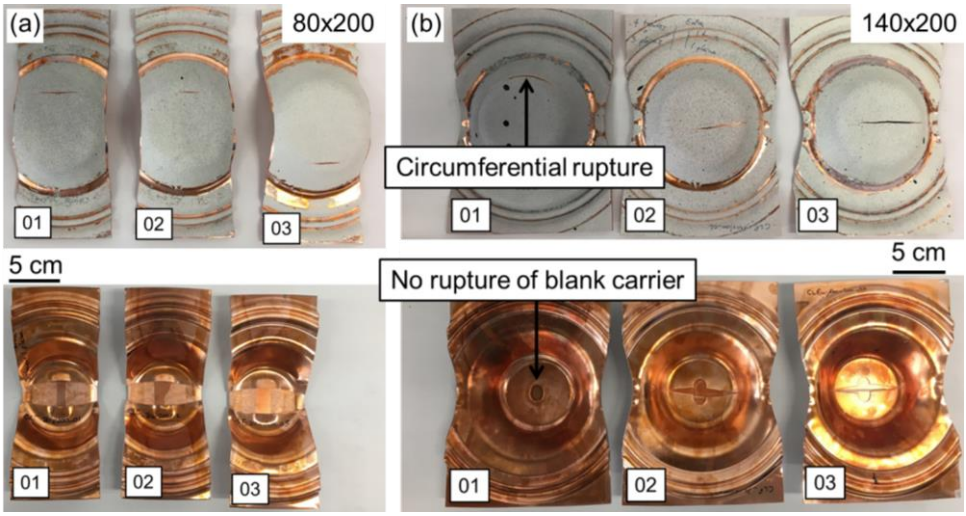

Figure D.1: (a) Top and bottom views of deformed 80 mm x 200 mm annealed OFE copper blank-assemblies with a neck not located above the gap between the halves of the blank carrier. (b) Top and bottom views of deformed 140 mm x 200 mm annealed OFE copper blank-assemblies with a hole of 10 mm showing a circumferential rupture at the radius of the punch for specimen 01.

Figure D.2a shows deformed Marciniak specimens with 2 mm thick niobium blanks and 1 mm thick annealed OFE copper blank carriers. These tests were performed at the beginning of the study, since niobium sheets with this thickness, compared to 1 mm thick like in Chapter 8, were already available and more commonly produced by the manufacturer. However, three issues occurred during tests with specimens with different widths, as shown in Figure D.2a. The narrower specimen (80 mm x 200 mm) did not neck and the mechanical press was at its maximum displacement. As discussed in section 6.1.3., thicker sheets often have a higher formability, which motivated the reduction in sheet thickness to 1 mm to use the same setup and blank carrier. Wider specimens showed folded sheets on both sides of the middle of the blank-assembly, see Figure D.2b for more views of the 140 mm x 200 mm specimen. This was again due to the high sheet thickness and ductility of niobium. Finally, the 160 mm x 200 mm specimen had a circumferential rupture at the radius of the punch, as previously discussed for a copper blank. Those issues motivated the use of 1 mm thick niobium sheets to measure the FLD of the material using the same setup as for OFE copper.

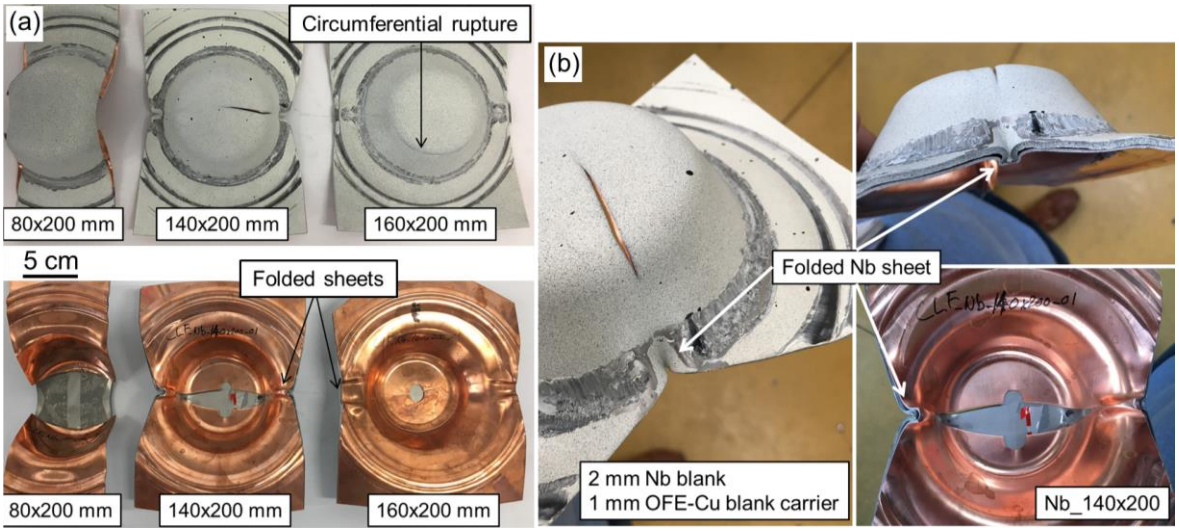

Figure D.2: (a) Top and bottom views of deformed 80 mm x, 140 mm x, and 160 mm x 200 mm 2 mm thick niobium blanks and 1 mm thick annealed OFE copper blank carriers, and (b) additional views of the folded sheet for the 140 mm x 200 mm specimen.

Appendix E – Mechanical Characterization of OFE Copper

This short appendix presents the mechanical properties of OFE copper specimens deformed in tension and compression, at different strain rates and with different thermomechanical histories. The results presented in this appendix are also used in Chapter 8 to estimate the strain at necking for uniaxial tensile tests and in Chapter 9 to compare the mechanical properties of electron beam welded specimens with unwelded specimens.

E.1. Mechanical Properties

Tensile specimens were cut parallel to the rolling direction and deformed at quasi-static strain rates of 2.38×10^{-4} to 2.38×10^{-2} s^{-1} at ENSTA Bretagne with two mechanical universal testing machines, as described in section 7.3.1.1, and at intermediate strain rates of 0.65 to ~61 s^{-1} at Imperial College London with a servo-hydraulic tensile machine, as described in section 3.3.2.1. The geometry of the specimens deformed at ENSTA Bretagne follows the ASTM E8 standard [1] and is shown in Figure 7.1b. A subsize specimen, shown Figure 7.1a, was used at Imperial College to reach higher strain rates. Compression tests were all performed at ENSTA Bretagne on cylindrical specimens with a diameter of 8 mm and a thickness of 4 mm. A mechanical universal testing machine was used at strain rates of 2.08×10^{-3} to 1.1 s^{-1}, described in section 7.3.1.1, and split Hopkinson bars were used for strain rates of about 4 000 s^{-1}, as described in 7.3.3.1.

Figure E.1 shows the stress–strain curves of OFE copper specimens deformed at different strain rates in tension and in compression for the annealed (600°C for 2 hours in vacuum) and hard (as-received) conditions. Similar stress–strain curves with an initial yield stress of about 50 MPa were obtained at different strain rates for annealed specimens deformed in tension (Figure E.1a). A small increase in flow stress was measured for increasing strain rates and is explained by an increase in strain hardening exponent n, a common result for FCC metals [2]. Annealed specimens cut perpendicular to the rolling direction were also tested at similar strain rates. The results are not presented in Figure E.1a since the stress–strain curves were similar to those of specimens cut along the rolling direction, which confirms that the specimens were fully recrystallized during the heat treatment. Annealed compression specimens also showed similar mechanical properties at strain rates of 2.08×10^{-3} to 1.1 s^{-1} (Figure E.1c), but a significant increase in flow stress was measured at ~4 000 s^{-1}.

Hard tensile and compression specimens showed a much higher initial yield stress than annealed specimens deformed at the same strain rate. A higher ultimate tensile stress was also measured for hard specimens deformed at all strain rates and tensile specimens deformed at quasi-static strain rates showed very low hardening (Figure E.1b). A lower yield stress and a higher strain hardening exponent were measured for tensile specimens deformed at intermediate strain rates. This result was unexpected, but repeatable for multiple specimens. Finally, similar to annealed specimens, compression specimens showed a significant increase in flow stress between strain rates of 1.1 s^{-1} and ~4 000 s^{-1} (Figure E.1d).

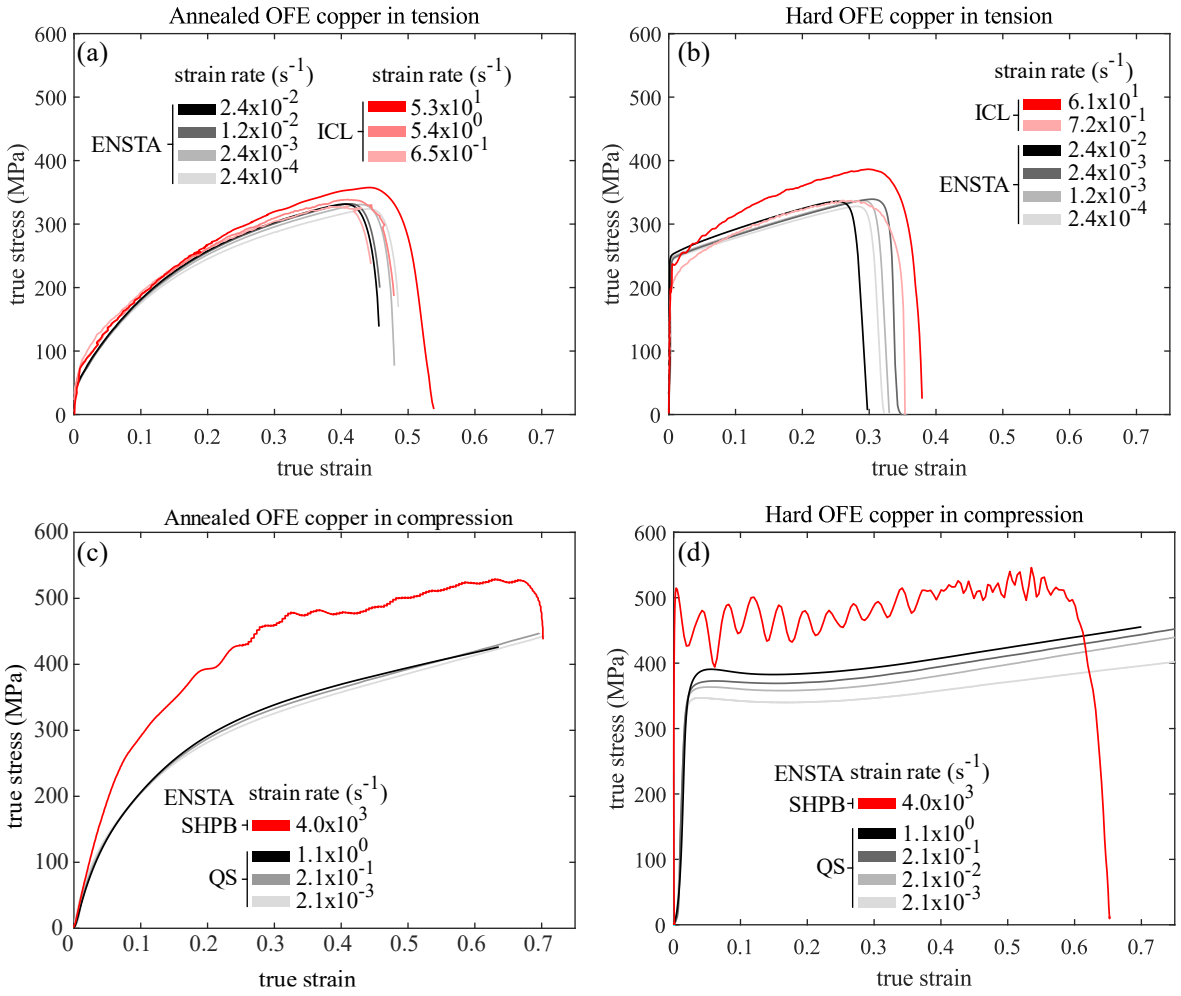

Figure E.1: Stress–strain curves of OFE copper specimens deformed at different strain rates in tension and compression with different thermomechanical histories: (a) annealed and (b) hard in tension, and (c) annealed and (d) hard in compression.

E.2. Strain Rate Sensitivity

Figure E.2 shows the true stress at a true strain of 0.15 as function of the nominal strain rate for annealed and hard OFE copper specimens deformed in tension (Figure E.2a) and compression (Figure E.2b). Data from Follansbee and Kocks [3] on annealed high-purity copper deformed in compression at strain rates of 10^{-4} to 10^{4} s^{-1}, a study that is often cited in the analysis of the mechanical properties of copper at high strain rates (see for example the

PhD thesis of Dr. Lewis Lea [4]), are plotted in Figure E.2a and b for comparison with this study. The flow stress of the data from the literature is slightly lower than the annealed specimens deformed in compression in this study. Follansbee and Kocks [3] also noted a change in slope on a semi–log plot at strain rates exceeding ~10^3 s^{-1}, which has not been observed in this study.

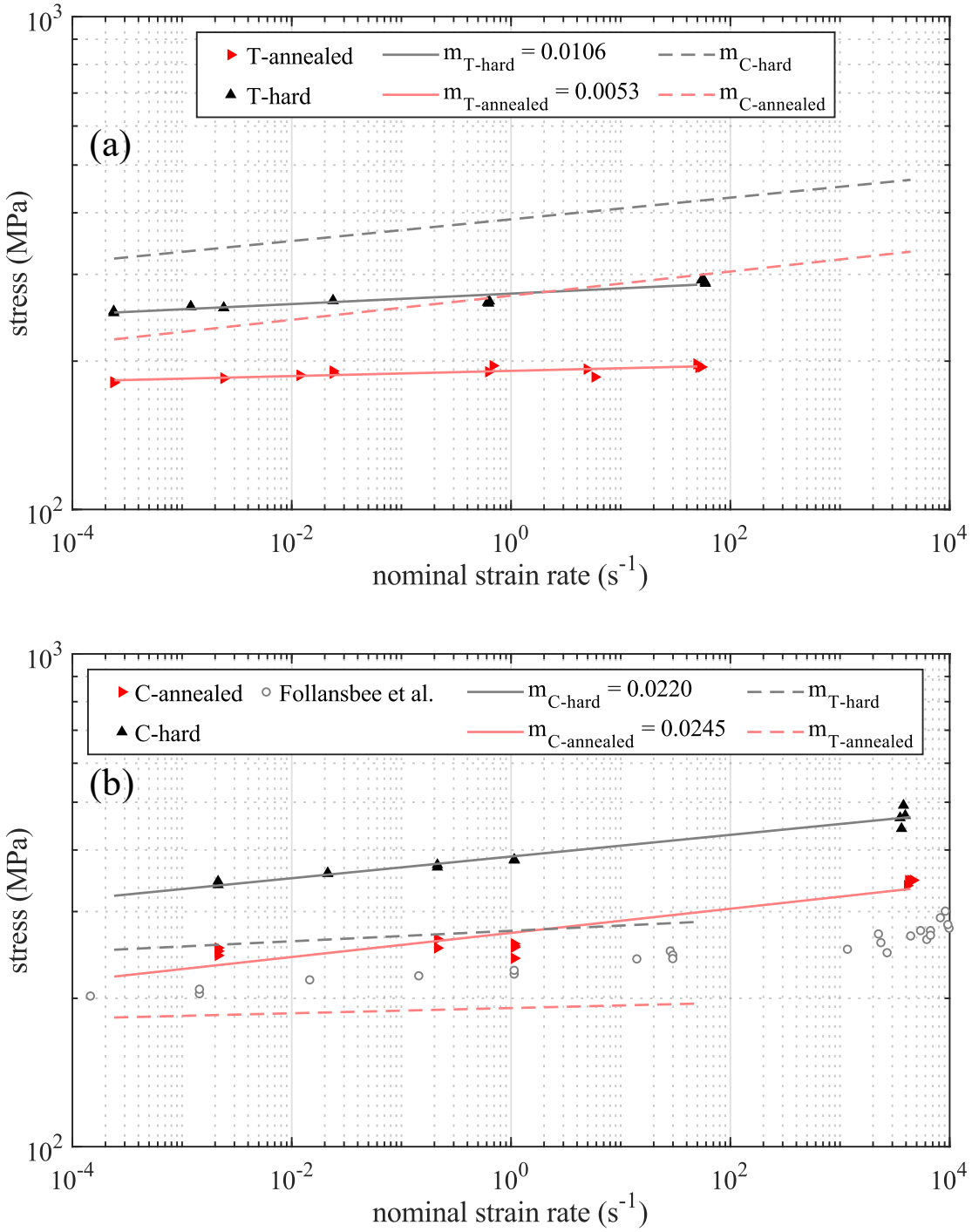

Figure E.2: True stress at a strain of 0.015 as function of strain rate in (a) tension and (b) compression for hard and annealed OFE copper, compared with annealed high-purity copper from Follansbee and Kocks [3]. Dashed lines in the tension (compression) plot represent the solid lines of constant strain rate sensitivity in the compression (tension) plots and are presented for comparison between the two loading cases.

Strain rate sensitivity exponents m were calculated in tension and compression for the hard and annealed specimens at strains of 0.05 and 0.15 and are presented in Table E.1. The levels of strain were selected to, first, have a low work hardening to minimize the effect of changes in dislocation substructures with the initial state of the specimens and be beyond the yield stress due to uncertainties in the measurements of the elastic domain, and, second, for comparisons with the study of Follansbee and Kocks [3]. An increase in strain rate sensitivity exponent was measured for an increasing strain for all conditions, except the annealed specimens deformed in tension.

Solid lines of constant m at a strain of 0.15 are plotted in Figure E.2 and the majority of the measured points follow the linear trend in the log–log plot. Dashed lines of constant m are also plotted for the opposite loading cases, e.g. $m_{compression}$ in Figure E.2a, for comparison of effect of strain rate on the flow stress in tension and compression. The calculated strain rate sensitivity exponents at a strain of 0.15 were 2 and 4.9 times greater in compression for the hard and annealed specimens, respectively. The true stress at ε_T = 0.15 is also greater in compression at all strain rates.

Table E.1: Strain rate sensitivity m at true strains of 0.05 and 0.15 in tension and compression at strain rates of 2.4×10^{-4} to ~60 s^{-1} and 2.1×10^{-3} to ~4 000 s^{-1}, respectively, for hard and annealed OFE copper deformed.

	Tension		Compression	
True strain (ε_T)	0.05	0.15	0.05	0.15
m_{hard}	0.002	0.011	0.013	0.022
$m_{annealed}$	0.010	0.005	0.021	0.024

E.3. Plastic Strain Anisotropy

Finally, the plastic strain anisotropy (*r*-value) of annealed OFE copper was calculated using the tensile tests performed on subsize specimens (Figure 7.1a) at an intermediate strain rate of 0.65 s^{-1}. Only these tests could be used since in-situ DIC measurements were performed and the spatial resolution was sufficient to measure changes in width and length, as discussed in the experimental procedure in section 7.3.1.2. However, no specimens were cut at angles of 45° and 90° between the loading and rolling directions. Therefore, the mean plastic strain anisotropy r_m and the planar anisotropy Δr could not be calculated. Nevertheless, the *r*-value at 0° (r_0) was used in the study of the forming limit diagram of annealed OFE copper (Chapter 8), to estimate the point of the forming limit curve corresponding to a uniaxial tensile test. This specimen orientation is of particular interest since the Marciniak (in-plane) tests were performed with the direction of the major strain aligned with the sheet rolling direction. An average *r*-value in the rolling direction of 0.95 was calculated for three specimens deformed at the same nominal strain rate.

References

[1] ASTM International, “ASTM E8 / E8M-16ae1, Standard Test Methods for Tension Testing of Metallic Materials.” 2016, [Online]. Available: astm.org.

[2] G. T. (Rusty) Gray, “High-Strain-Rate Deformation: Mechanical Behavior and Deformation Substructures Induced,” *Annu. Rev. Mater. Res.*, vol. 42, no. 1, pp. 285–303, 2012, doi: 10.1146/annurev-matsci-070511-155034.

[3] P. S. Follansbee and U. F. Kocks, “A constitutive description of the deformation of copper based on the use of the mechanical threshold stress as an internal state variable,” *Acta Metall.*, vol. 36, no. 1, pp. 81–93, Jan. 1988, doi: 10.1016/0001-6160(88)90030-2.

[4] Lewis J. Lea, “Structural Evolution in the Dynamic Plasticity of FCC Metals,” PhD Thesis, University of Cambridge, Cambridge, UK, 2018.

DOCTORAT BRETAGNE SCIENCES LOIRE POUR L'INGENIEUR

ENSTA Bretagne

Titre : Niobium monocristallin et polycristallin et cuivre OFE pour les cavités SRF : caractérisation mécanique de basse à haute vitesse de déformation et investigation de la microstructure

Mots clés : niobium, cuivre OFE, propriétés mécaniques, courbe limite de formage, microstructure, cavité SRF

Résumé : La fabrication de cavités SRF à hautes performances est essentielle pour augmenter l'énergie de collision dans de nouveaux accélérateurs de particules. L'utilisation de procédés de fabrication à haute vitesse, comme l'électro-hydro formage, peut être bénéfique, mais requiert une compréhension détaillée des propriétés mécaniques des matériaux déformés à haute vitesse et de l'impact sur leurs microstructures. Les objectifs de cette thèse sont d'étudier les propriétés mécaniques de monocristaux de niobium et de tôles polycristallines de niobium à haute pureté et de cuivre OFE déformés à des taux de déformation d'environ 10^{-4} s^{-1} à 10^{3} s^{-1}. Les résultats de cette étude sont séparés en deux parties selon le matériau étudié.

En partie I, la caractérisation de monocristaux de niobium se concentre sur les propriétés mécaniques en traction et en compression à des taux de déformation d'environ 10^{-4} s^{-1} à 10^{3} s^{-1} et sur la microstructure (MEB, EBSD, MET et nanoindentation) d'éprouvettes déformées. Les effets de l'orientation des cristaux, la vitesse de déformation et de la direction de chargement sur les propriétés mécaniques, la rotation des cristaux et la structure de dislocations sont présentés.

En partie II, la formabilité de tôles polycristallines de niobium et de cuivre OFE sont présentées à l'aide de courbes limites de formage (CLF) obtenues à un taux de déformation quasi-statique. Les CLFs de ces matériaux offrent des données importantes pour les techniques de formage conventionnel, tels que l'emboutissage et le repoussage. Cette seconde partie présente aussi les propriétés mécaniques d'éprouvettes de cuivre OFE recuites et de tôles de niobium polycristallines soudées par faisceau d'électron et déformées en traction et en compression à des taux de déformation de 10^{-3} à 10^{3} s^{-1}.

Title : Single Crystal and Polycrystalline Niobium and OFE Copper for SRF Cavities Applications: Mechanical Characterization at Low to High Strain Rates and Microstructural Investigations

Keywords : niobium, OFE copper, mechanical properties, forming limit diagram, microstructure, SRF cavity

Abstract : Manufacturing of superconducting radiofrequency (SRF) cavities with high performances is paramount to increase the collision energy in new particle accelerators. The use of high-speed sheet forming techniques, such as electro-hydraulic forming, can be beneficial, but requires a detailed understanding of the mechanical properties of the materials being deformed and the consequence on their microstructure. This thesis focuses on the characterization of high-purity niobium single crystals, polycrystalline niobium sheets, and polycrystalline OFE copper sheets. The results from this study are separated in two parts.

In Part I, the characterization of niobium single crystals focused on the mechanical properties in tension and compression at strain rates of 10^{-4} to 10^{3} s^{-1} and on the microstructure (analyzed using SEM, EBSD, TEM, and nanoindentation) of the deformed specimens. The effect of crystal orientation, strain rate, and loading direction on the mechanical properties, the crystal rotation, and the dislocation substructures are presented.

In Part II, the forming limit diagram (FLD) of polycrystalline niobium sheets and OFE copper sheets were measured at a quasi-static strain rate. The FLDs of those materials should provide important data for manufacturers using conventional techniques, such as deep-drawing and spinning. The second part also presents the mechanical properties of electron beam (EB) welded polycrystalline niobium sheets and OFE copper sheets deformed in tension and compression at strain rates of 10^{-3} to 10^{3} s^{-1}.